Structural Analysis of Radar Meteoroid Orbital Data

A THESIS
SUBMITTED IN PARTIAL FULFILMENT
OF THE REQUIREMENTS FOR THE DEGREE
OF
DOCTOR OF PHILOSOPHY IN PHYSICS
IN THE
UNIVERSITY OF CANTERBURY

by
David P. Galligan

2000

To Janine

Abstract

The structure of a radar-derived meteoroid orbit data set is examined in the current study. Biases in the parameter distributions and measurement uncertainties for the orbits are determined. Meteoroid stream related substructure is searched for in order to determine the level to which the dust population probed retains memory of the assumed progenitors of the current meteoroid population: the short-period comets. The detectable consequence of streams within the data set are meteor showers: several methods of shower detection are discussed and tested. The data set provided by the AMOR meteoroid orbit radar system is used for these tests, though the techniques developed and the comparative survey of earlier techniques are of value to searches of similar radar meteor data sets and indeed in many cases to such data derived by other methods (e.g. photographically). AMOR is situated near Christchurch, New Zealand (172°39′ E,43°34′ S) and has been operating with increasing time-coverage since 1990. It is one of the most sensitive orbit-determining meteor detection systems ever deployed, routinely measuring to a limiting radio magnitude of +14 which corresponds to a dust particle size of ~ 40 μm (similar to those which form the zodiacal light). From the time of the vernal equinox in 1995 to mid-1999 the characteristics of $\sim 5.3 \times 10^5$ meteors, of sufficient quality for orbit calculation, were measured using a static equipment setup. The large homogeneous meteoroid orbit catalogue resulting is the main data source used currently.

Searching for fluctuations, associated with shower presence, in the meteor rate curve is found to be inapplicable due to the relative weakness of even the major showers against the background (the strongest shower comprises approximately 5% of the total meteors observed per day at their activity peak). A new direct search approach for associations of data set orbits with mean stream orbits from other surveys is defined and tested. Only the major showers (η Aquarids (ETA), Southern δ Aquarids (SDA), α Capricornids (CAP) and Daytime Sextantids (DSX)), in addition to a few other minor showers, have associations at the 95%/99% significance levels under this Poisson statistic based test. A new method using wavelet enhancement to search for showers in radiant-speed-time space is introduced. This method is found to be effective and relatively straightforward in implementation; it detects the four major showers in addition to a number of other peaks—the significance of most of the latter is attributed to low background meteor activity at the time. Finally, the single-linkage cluster analysis technique, as used in many photographic meteor surveys, is applied. This again discovers the four major showers but it is found that the cutoff level in the hierarchy at which these showers are complete is rather unstable and subjective. Randomisation tests, in an attempt to determine a statistically significant cutoff level, indicate that all structure including the major showers is essentially randomly formed from the background. This extreme result contradicts other methods. The conclusion reached is that the randomisation tests and the single-linkage method itself are inappropriate for their current use.

The AMOR data set is found to be dominated by sporadic (non-shower) meteors and most traces of past cometary passages have been erased. This is particularly

true of the $\approx 50\%$ of the data set which are in retrograde orbits: their importance, after correction for a large detection bias is found to be negligible. The antihelion, helion and apex sporadic sources appear strongly in the AMOR data set. These virtual sources, formed by the combination of the true spatial dust distribution with the observation biasing conditions, are explored further to reveal any orbital structure appearing within. The only definite meteor showers found using several different methods are the major showers. These comprise less than 1% of the total meteors observed per year over the five year data set: approximately 1×10^3, 2×10^3, 3×10^2 and 4×10^2 meteors are detected in total from the ETA, SDA, CAP and DSX respectively. Two other showers appearing under the wavelet enhancement method, labelled Peaks A and C (approximately 3×10^2 and 9×10^2 meteors respectively), are found to be significant. These showers, which also appear significantly under the direct search method, are studied and Peak C is identified with the omicron Cetids. Due to their long-lived activity it is found to be difficult to determine whether Peaks A and C are true showers, or instead, simply favourable alignments of the sporadic biased regions in which they lie.

It is found to be unlikely that showers, of lesser activity than those above, are detectable against the strong sporadic meteor background. One reason for this scarcity is that owing to the size range probed by AMOR the coherence of a stream may be lost over a relatively short time-interval: typical shower mass distributions favour larger particle sizes and hence many of the smaller particles detected by AMOR are non-shower "noise". The biases on the data set demonstrated in this study are so strong that these will also act to remove the detectability of minor showers. The presence of large measurement uncertainties on radar-derived orbits, as compared with those detected photographically, also has a major effect on detectability. Two methods for the calculation of individual orbit uncertainty are tested and found to provide generally equivalent results. The uncertainty in the AMOR orbital parameters varies greatly, with a general increase as the geocentric speed of the meteoroid increases. Representative uncertainties in the orbit-defining heliocentric velocity components are found to range between 6% and 55% (uncertainties close to the latter correspond to retrograde orbits). The prograde meteoroid orbit region close to the ecliptic, in which most meteoroid streams are detected, is found to have the lowest orbital element uncertainties—representative values for which are: $\Delta q = 0.03$ AU, $\Delta e = 0.03$, $\Delta \omega = 5°$, $\Delta i = 2°$ and $\Delta \Omega = 0°$.

The orbital statistics and character of the four major showers, in addition to the two shower candidates Peaks A and C, are further analysed. Daily motion in the radiant position, generally occurring in a plane parallel to the ecliptic, is seen for all showers. Daily motion in the orbital elements is also measured: the SDA provide a particularly good example in q and ω. It is found that the spread in the orbital parameters of each shower is similar to, or smaller in magnitude than, that expected from the individual meteor measurement uncertainties: measurement of the physical spread in such parameters is generally not possible. Good agreement is reached between the mean orbits of the showers and a variety of published sources, indicating the correct calibration of the AMOR system; the large number of shower orbits in each case ensure a high level of reliability in their respective means.

Contents

Figures

Tables

Chapter 1

Introduction

1.1 Meteoroids, Meteors and Meteorites

Objects smaller than 10 m found in space are termed meteoroids. Due to their small size and large speed, our information about them comes exclusively from effects produced when they collide with various types of detector.

The primary detector used is the atmosphere of the Earth. When a meteoroid comes close to the Earth it may enter the atmosphere. At atmospheric heights of $\sim 100 \pm 20$ km there are sufficient air molecules to ablate the incoming body by friction. Owing to the high temperature of this interaction the meteoroid will ionise forming a train of free electrons and positive ions (Fe^{2+}, Na^{2+} etc.) along the trajectory taken: particularly large meteoroids may cause visible light to be emitted due to the energy released. The appearance of the electron train is termed a meteor: typically, meteor trains are 1–10 km in length and last for a few seconds before dissipating via ambipolar diffusion into the background. A particularly large and bright meteor may be termed a fireball. Should a meteoroid have a shallow enough entry angle and a particular composition, some of the original body may arrive intact at the Earth's surface: these remains are termed a meteorite.

Often during the year we are treated to a display of meteors all seemingly emerging from a single "radiant" point in the sky. Such displays are called meteor showers and result when the Earth's orbit intersects a particularly dense and spatially coherent set of meteoroid orbits, collectively termed a meteoroid stream. Meteoroids in a specific stream have the same parent, they are in similar orbits to each other and to their parent—this similarity may be only evident in historical behaviour which may be studied by analysis of the perturbations which have shaped the current state of the orbits. When the stream node (crossing of the ecliptic plane) occurs near the Earth's orbit a meteor shower may occur for a short period each year. Such an occurrence is the opportunity for an Earth-based observer to measure a small part of the total stream. (One should note that in the current study the distinction

between "meteoroid streams" and "meteor showers" often becomes a little blurred. These words are sometimes used interchangeably as the only way to detect a stream is by the detection of the corresponding shower in the data set.)

There are several major showers each year which have in some cases been studied for centuries. These are characterised by a high influx rate which remains constant for showers caused by older streams but may fluctuate from year to year for those cause by newer streams. Most of these streams have well known parent bodies which, through their past dust emissions, formed the showers now being seen. There are still questions as to the parent bodies of some streams such as those making up the Taurid complex.

In addition to the major showers there are a multitude of minor showers. These typically exhibit low influx rates and/or diffuse radiants. Such characteristics make the shower more difficult to distinguish against the background pseudo-random sporadic orbit population—many of their constituents may be mistakenly classified as sporadic meteors.

McKinley (1961) defines a sporadic meteor: "A sporadic meteor is one that is not a member of a recognised shower". In the past these meteors were dismissed as oddities from which little of scientific value could be gleaned, however now it is realised that much of the sporadic orbit population originally existed in distinct streams which over time have experienced perturbative forces which destroyed their distinct characters. If one were to integrate backward in time over the motion of such particles it is possible that their original stream identities could be restored.

One of the goals of meteor study is to understand the origin of incoming meteoroids. We may work towards this goal by two broad approaches. The first being the study of the mineralogical aspects of meteorites, meteoroids, comets and asteroids. The second involving the study of their orbital characteristics. The current study attempts to survey the AMOR radar meteoroid orbit data set in order to search for coherent streams based on orbital character. Well-known major streams are verified by a variety of methods. The number of members of these streams detected by AMOR allows excellent statistical mean orbits to be determined. Searches for minor showers are based in large part on their annual repetitiveness, distinctiveness and compactness with respect to the background. The implications of orbital uncertainty which is often large in the case of radar derived orbits are discussed and where possible accounted for.

1.1.1 Meteoroid Streams and Their Parent Bodies

Meteoroids are presently believed to be on the whole cometary in origin (Hughes 1993) with some indications that asteroids are also involved in a more minor role[1] (Štohl and Porubčan 1993). It is important in a study of meteoroids and their orbits to begin with a discussion of these progenitor bodies.

The study of cometary motions in the heavens dates back to ancient times. Many events of historical significance have been influenced or marked by a passing comet, an example which springs to mind is the image of Halley's comet emblazoned on the Bayeux tapestry. Until relatively recently comets were little understood and consequently viewed with superstition.

It is believed that comets were formed in the equatorial plane of the dusty pre-planetary disc somewhere beyond the present location of Saturn (Hughes 1993). The primitive silicate dust in this region mixed and bonded with volatile "snows" in order to form dirty snowflakes which further agglomerated by collision to form an icy conglomerate nucleus. This first modern view of the comet nucleus construction, often called "the dirty snowball model", was proposed by Whipple (1950). Here he visualises the nucleus as being composed of a conglomerate of ices (H_2O, NH_3 etc.) and other materials (volatile at room temperature) together with "meteoric materials"[2].

The characteristic tail which is seen when the comet is near perihelion is formed by solar radiation evaporation of the nucleus gases, the meteoric material which had been locked into the icy conglomerate with this outer layer of volatiles is then only constrained to the nucleus body by gravity. Larger material for which gravitational attraction is significant can only be removed by gas shocks or it must remain as an insulating layer (Whipple 1950). However, for material below a limiting size, this gravitational attraction will be not sufficient to hold it and a dust trail will be left in the comet's wake[3]. This trail is a signature marker of the comet's path through the heavens and it will, over time, form a meteoroid stream.

It is obvious that comets must have a finite supply of the icy volatiles. This suggests that comets cannot have existed near to the Sun for long: they must have

[1] One may note that in the specific mass interval 10^{-8} kg$< m < 10^{2}$ kg the cosmic flux to Earth of cometary dust is $\sim$ 900 times higher than the corresponding flux of asteroidal material (Hughes 1993). This ratio closes to $\sim$ 20 in the fireball size region.

[2] Whipple (1950) defines "ices" as substances with melting points below 300°C and "meteoric material" as those with greater melting points.

[3] Hughes (1993) estimates that the rate of dust emission from a large active comet is 10^{7} to 10^{8} g s^{-1}. As an example Comet P/Halley loses on average about 3×10^{14} g per apparition.

come from a colder area of the Solar System. It also implies that eventually a comet must lose all of its volatiles and become dormant—it is believed that some asteroids are in fact exactly this type of defunct comet. An example is 3200 Phaethon which in its present form is classified as an asteroid—this body has recently been shown to have in the past been the progenitor of the Geminid meteor shower (Whipple 1983).

An accepted composition of a meteoroid released from such an icy matrix is that of a collection of elemental rocky carbonaceous particles with a low density (~ 3 g cm^{-3}) and low mass ($\sim 10^{-12}$ g) which are strong, solid and of random shape. Hughes (1978) notes that 80% of the dust emitted by a comet near perihelion is made up of particles with masses between 10^{-4} and 10^{2} g. It is these particles which produce radar, telescopic and visual detectable meteors. A visual class meteoroid of $\sim 10^{-1}$ g is ejected from the nucleus with a typical relative speed of between 0.03 and 0.3 km s^{-1}. A typical radar detectable meteoroid of between 10^{-4} and 10^{-3} g would attain a speed approximately three times that of the corresponding visual meteoroid. Solar System comets near 1 AU have orbital speeds up to 42 km s^{-1}, hence the relative dust emission speed is a second order quantity resulting in a very similar meteoroid orbit to that of the cometary nucleus. Due to the higher relative emission speeds, determined from cometary emission models, for radar detectable meteoroids relative to those in the visual size range, the spread in a particular stream's meteoroid orbits will still be relatively larger for the former than for the latter (Hawkes 1993).

Hughes (1993) notes that of the 135 short-period comets known at the time all had associated meteor streams. This subset of the total known $\sim 10^{4}$ cometary population is characterised by small perihelion distances, large nuclei and short periods[4]. All of these are fairly obvious requirements for an icy conglomerate model of cometary composition and meteoroid emission. It is possible that longer period comets could also have associated streams, these however would need to be very strongly defined as they would need to wait longer for the replenishment (compared to short-period comet streams) needed to combat the perturbational and collisional instances which act to diffuse the stream into the background distribution.

1.2 Formation and Evolution of Meteoroid Streams

Hughes (1993) notes that the meteoroid cloud formed by a typical comet will be

[4]A short-period comet is one with a period of less than 200 years while a long-period comet has a greater period than this.

doughnut shaped with a central hole which extends from the Sun out to about 0.5 AU and then a sharp density drop-off at 6 AU. On an Earth based observing platform meteoroids are only observed when they cross the Earth's orbit at a distance close to 1 AU from the Sun.

Babadzhanov and Obrubov (1992a) list five stages of short-period meteoroid stream formation. In the first stage a compact mass of meteoroids is left only in the vicinity of the cometary nucleus. When the Earth passes through this dense dust cloud a meteor shower results. Soon after this first stage a low density stream of dust has been left around the comets orbit while a high density component is still present about the nucleus of the comet. Weak meteor showers are observed when the Earth passes through the low density regime with meteor storms when it passes through the high density component[5]. By the third stage irregularities have been smoothed out with an even spread in stream volume, there are now no meteor storms but a stable year to year meteor shower. Southworth and Hawkins (1963) state that it typically takes $\sim$ 400 years for a specific emission of meteoroids to spread around the cometary orbit.

In the fourth stage the meteoroids are beginning to diffuse from the distinguishable stream centre. Dispersion in both argument of perihelion and longitude of the ascending node have broadened the stream volume in an even, but less dense manner. By the fifth stage intra- and extra-stream impacts, in addition to extreme broadening of the stream volume by dispersion, have combined to make the stream indistinguishable from the sporadic (or random) background.

Dispersion of meteor streams in the first and second stages stems from the difference between orbital periods due to ejection conditions from the parent comet and the radiative action of the Sun. In the later stages planetary perturbations and the Poynting-Robertson effect are of greater influence. At the final stage all of these effects, in combination with collisional interactions, will disperse the stream into the sporadic background. Interestingly enough the sporadic background was often in the past viewed as a nuisance having nothing to do with stream studies. However, as has been pointed out this background simply consists of stream particles which have been dispersed too far from their siblings in order for the recognition of these as a stream to be performed. By delving ever deeper into this background then we might attempt to unravel some of the mysteries of streams long thought to have perished. In addition study of the meteoroid orbit population by different methods

[5]An example of this regime is the Leonid meteor shower with its 33 year storm period.

(e.g. optical and radar) owing to the different meteoroid size ranges and hence also dispersion mechanisms that will have acted upon them, may reveal in one case a reasonably coherent stream while in the other a tangled mess of "random" orbits.

1.2.1 Orbital Perturbation Mechanisms

As we have seen in the later stages of stream development various perturbation mechanisms work to disperse a stream, in some cases totally destroying it. It is interesting to look at these processes and to ascertain the impact they can have on meteoroids of the size detected by radar—these being of particular interest in the current study.

Immediately upon release from the comet both Poynting-Robertson drag and direct radiation pressure act on the meteoroid. The former is a relativistic effect which occurs due to the difference between the Sun and meteoroid reference frames: the meteoroid receives solar radiation and re-radiates it, as seen from the meteoroid, isotropically; but from the platform of the Sun, it is seen that more momentum is being moved toward the Sun than away from it, hence a spiralling motion into the Sun results. This effect would tend to sweep the Solar System clear of a whole size range of meteoroids if there weren't constant replenishment. Meteoroids of the size range detected by radars are perturbed by Poynting-Robertson drag; direct radiation pressure meanwhile acts appreciably only on smaller non-radar visible meteoroids (diameter $\lesssim 5$ μm) (Gustafson and Adolfsson 1996), this mechanism tends to enlarge the semi-major axis of the orbits of these meteoroids.

Poynting-Robertson drag is generally a secondary effect to gravitational perturbation particularly when the meteoroids have orbital nodes near the orbits of the major planets. Short-period streams with aphelia in the vicinity of Jupiter are most difficult to define as the parent's orbit is changing so quickly. In such cases, a large perturbational effect is, of course, also applied to the streams themselves. Hughes (1993) notes that meteoroids with aphelia well removed from Jupiter's grasp hardly change at all due to gravitational perturbation. In the case of gravitational perturbation the most stable element is the inclination with respect to the ecliptic; close-encounters with the planets tend to change the size, shape and orientation of the meteoroid orbit on its orbital plane without changing the ecliptic inclination of that plane. The inclination angle is therefore particularly important in any stream search effort.

In general the smaller the particle mass the greater the effect of the perturbative

forces. Ceplecha et al. (1998) notes that meteor showers are stronger amongst meteors of medium size and brightness while being much less significant, relative to the background, for smaller particles. Very bright meteors, particularly those termed fireballs, also suffer from a dearth of shower particles. Radar meteoroid data sets therefore, due to the small meteoroids they detect, are expected to contain only a small percentage of shower particles, indeed various studies conclude that only a few percent of radar meteoroids have known showers while the percentage of known shower meteors in photographic data sets is an order of magnitude higher.

1.3 Meteor Detection Methods

For centuries meteors have been looked up at in their brief existence as man has appreciated, feared or simply tried to understand. Until relatively recently very little could be studied in an objective fashion as regards these wonderful apparitions in the sky.

During the past century various types of observational methods have been used in order to obtain essential characters of incoming meteors. The first studies consisted simply of naked-eye observations—here people, mostly amateurs, lay out at night and watched for meteors. Upon observing a visual meteor, the position in the sky from which it emerged (often determined using remarkably accurate techniques) in addition to an estimated magnitude, duration, and colour were noted; for meteor shower observations, data could also be obtained on the rate and dispersion of the radiant position. Unfortunately this information is insufficient for the calculation of a space orbit for the particle, however naked-eye observation is such a simple and inexpensive method of obtaining data that it persists to this day with a strong amateur network of observers who regularly publish work of interest to professional astronomers[6]. One must note that while this method has its many adherents there is a great deal of subjectivity to observations made in this fashion and the strength of the method comes not from its low quality individual results but rather from the very large number of these results.

In order to obtain velocity information and to preserve a more permanent record of the meteor event photographic methods were devised. The first known photograph of a meteor was taken by L. Weinek in 1885 in Prague (Ceplecha et al. 1998). Nowadays "standard" 35 mm cameras are normally used for this task: these cam-

[6]See for example Lovell (1954) for an early review of visual meteor astronomy work or Rendtel et al. (1995) for a more recent summary.

eras can measure down to 2nd stellar magnitude while the Super-Schmidt cameras used in the Harvard programs measured down to 4th magnitude. For a long exposure photograph, while the stars will leave short arcs on the film, a meteor train will be shown as simply a narrow straight line. The position of the train in azimuth and elevation, and therefore right ascension and declination, can be determined from a good quality photograph. McKinley (1961) commends photographs for their use in adding further data on a meteor event to radio data. But he notes a limitation in that one can only pick up zeroth to first magnitude meteors on a camera whereas the naked-eye can see to fifth or sixth magnitude while eighth or ninth magnitude can be seen through binoculars. The major advantage to photographs is of course their accuracy: positional measurements can be given accurate to minutes of arc as compared to the 1° to 2° usually quoted for radar methods or the typical $\sim 10°$ for visual plots.

Measurement of the meteoroid speed on photographs is generally by use of a rotating shutter device. Here a shutter is rotated at a (constant) high frequency in front of the camera lens in order to create a raster-like pattern of the meteor train. The spacing of the blank intervals on this train gives the angular velocity, if two or more separated cameras are used a linear velocity can be obtained from which a pre-impact orbit may be calculated.

Another method which is successful in accurately determining the orbits of meteors is the TV camera method where image intensifiers in combination with television cameras are used to detect meteor occurrences. Such systems have advantages of automation and a high degree of accuracy. Hawkes (1993) summarises some of the limitations and advantages of this method as it has been applied over time. He notes the improvement in the limiting sensitivity (see Table 1.1) and meteor rates gained over using photographic techniques and the lack of bias towards meteor train profile which this presents over radar systems. The radiant positions of the showers as determined by the TV method unfortunately suffer in accuracy due to the poor signal to noise ratio in the system and instability in the spatial characteristics of the detectors. The accuracy of the method is nevertheless very good, Hawkes quotes uncertainties of 0.2° in angular position, 3% in velocity and 0.2 km in height. Apart from the velocity uncertainty, this method yields uncertainties several times lower than radar methods.

Detection Method	Mass Range (g)	Magnitude Limit
photographic (small camera)	$10^{-1}..5 \times 10^{2}$	+2
photographic (Super-Schmidt)	$5 \times 10^{-4}..10^{0}$	+4
TV	$2 \times 10^{-5}..10^{-3}$	+10
radar	$10^{-7}..10^{-3}$	+8..+14

Table 1.1: Sensitivity of detection method to meteoroid mass. Baggaley (1995) and Ceplecha et al. (1998) are used as references for these estimates. The radar limiting magnitude is given in the equivalent radio magnitude scale which is related to the electron density in the meteor train.

1.3.1 Radar Meteor Measurement Theory

During the early years (1930s) of the study of ionisation in the E-region it had been noticed that there were strong enhancements in the local ionisation over short periods at night-time. Daytime anomalous enhancements had been previously explained by solar radiation however no mechanism existed to explain this new phenomena. Eventually both day and night enhancements were attributed to meteor events. During World War II the early radar systems operated at wavelengths of 7–15 m. At such wavelengths meteors were often detected which to the inexperienced might look to be enemy aircraft—at this time these meteor echoes were simply a nuisance. After the war some of these radar systems were adapted to conduct the early systematic meteor-observing programs (e.g. Hey and Stewart (1947), Eastwood and Mercer (1948)).

The basic assumption of classical radio theory, as applied to meteor detection, is the presence of an under-dense train (e.g. McKinley (1961)). This is defined as a stationary column of electrons, assumed to have infinite length, which has a small diameter in comparison to the radio wavelength being scattered by it. These electrons are expected to be sparsely distributed allowing for free oscillation with very few collisions and no secondary radiative or absorptive effects. Trains of greater electron concentration are termed over-dense, such trains can last longer before diffusing, but present greater problems for analysis.

A radar system such as AMOR emits radio pulses at regular time intervals into the ionosphere and awaits the return of a signal. Should a signal above the noise level be returned, for a number of consecutive pulses at a similar range, then a meteor has been detected.

The reflection from the under-dense column occurs when the incident radio wave penetrates and is scattered by the free electrons found therein—these electrons oscillate independently but coherently in sympathy with the applied electromagnetic field. Figure 1.1 shows the geometry for reflection from a meteor train: when the

specular reflection condition (at $t = t_0$, $s = 0$) is met, i.e. the radio wave is oriented perpendicular to the train, the signal is reflected back to the receiver stations.

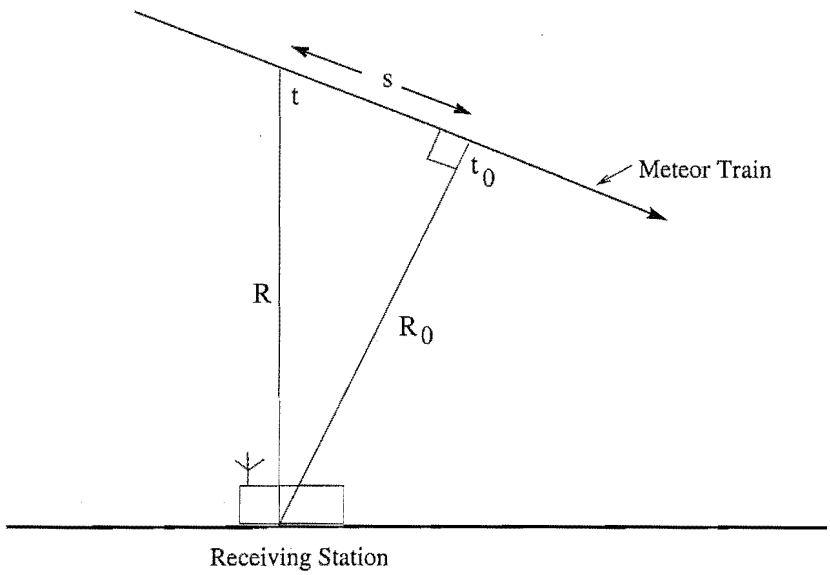

Figure 1.1: The specular reflection of radio waves off a meteor train.

The total power received at the receiver by all of the wavelets scattered by a single electron is

$$\Delta P_R = \frac{P_T G^2 \lambda^2 \sigma_e}{64\pi^3 R^4}, \tag{1.1}$$

where P_T is the transmitted power, G the antenna gain, λ the wavelength of the radio wave, σ_e the scattering cross-section of a free electron and R the distance to the train.

As R changes over time a phase modulation of the returned signal will be introduced. This modulation combined with the peak amplitude of the field vector due to a single scattering electron gives rise to an amplitude

$$dA_R = (2r\Delta P_R)^{0.5}\, q \exp j \left(2\pi f t - \frac{4\pi R}{\lambda}\right) ds, \tag{1.2}$$

where r is the receiver input impedance, f is the radio frequency, q the charge on an electron and t the time parameter.

The amplitude of the field generated by all electrons in the train between s_1 and s as seen at the receiver is thus given by

$$A_R = (2r\Delta P_R)^{0.5}\, q \int_{s_1}^{s} \exp j \left(2\pi f t - \frac{4\pi R}{\lambda}\right) ds. \tag{1.3}$$

As the radius changes very little near t_0, R can be approximated by $R \approx R_0 + s^2/(2R_0)$. Using the transformations $\chi = 2\pi ft - 4\pi R_0/\lambda$ and $2s = x(R_0\lambda)^{0.5}$, equation 1.3 becomes

$$A_R = \frac{\sqrt{2r\Delta P_R R_0 \lambda}}{2} q(C\cos\chi + S\sin\chi + j(C\sin\chi - S\cos\chi)), \qquad (1.4)$$

where C and S are the Fresnel integrals of optical theory defined by

$$C = \int_{-\infty}^{x} \cos\frac{\pi x^2}{2}\,dx \text{ and } S = \int_{-\infty}^{x} \sin\frac{\pi x^2}{2}\,dx. \qquad (1.5)$$

The maximum amplitude of this oscillating field is then given by

$$(A_R)_0 = |A_R^2| \qquad (1.6)$$

$$\propto \sqrt{C^2 + S^2}. \qquad (1.7)$$

The amplitude received changes with position (x) on the train. As the train forms the amplitude steadily rises: the specular reflection point (t_0) located on this part of the profile is used as a marker-point for meteor speed measurement. After the initial amplitude rise the profile begins to oscillate as the meteor moves through successive Fresnel half-period zones; at the same time the train expands by way of ambipolar diffusion, this decreases the received signal amplitude due to destructive interference between independent scatterers in the train.

These effects are shown, theoretically, in Figure 1.2 with the upper curve showing only Fresnel amplitude oscillation (no diffusion acting) and the lower curves showing diffusion increasing in strength by a factor of 2 as one proceeds lower in the diagram. Examples of experimental echo profiles obtained by AMOR are shown in Section 2.2.2. By measuring Fresnel oscillations the speed of the incoming meteoroid can be derived. The use of a minimum of 3 receiver stations in addition to this method of speed calculation allows an unambiguous meteoroid orbit to be obtained. Early radar systems applied this method. It works well when the train is well defined but McKinley (1961) was the first to note many meteor echo profiles suffer from smoothing of the Fresnel profile to the point where measurement is not possible.

The current AMOR system complements the Fresnel method with a time-lag method whereby a measurement of the time between detection of the meteoroid at each of three receiver sites, elevation angle (as determined by a dual-interferometer),

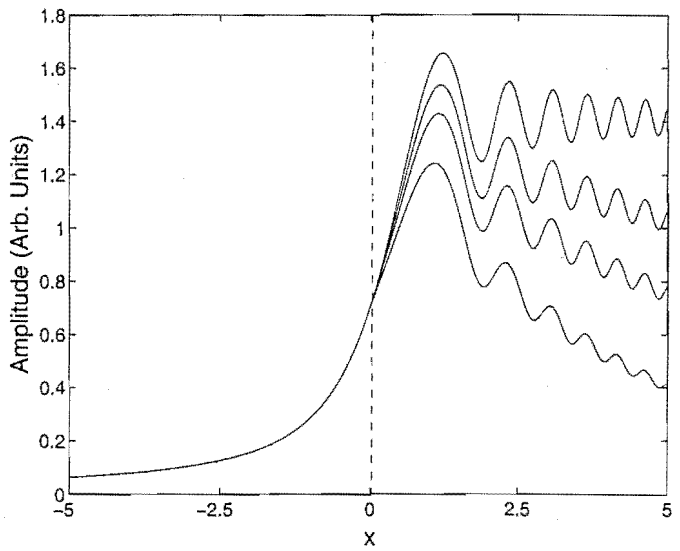

Figure 1.2: Four meteor diffraction patterns are shown with the level of ambipolar diffusion after the specular reflection point ($x = 0$) increasing towards the bottom of the figure. The uppermost curve is that obtained based on the assumption of no diffusion.

and range to the meteor train combine to provide a velocity for the incoming meteoroid which may then be reduced to a heliocentric orbit using the time of detection. For the time-lag measurements the point of maximum slope on each of the echo profiles, which is the specular reflection point, is used as a reference.

1.3.2 An Historical Overview of Meteor Radar Use

Table 1.2 summarises the contributions of all of the major orbit producing meteor radars over the past 50 years. Some of these radar systems are now briefly discussed so as to give an overview of the field.

As mentioned above, the first meteor radars in use were those in the immediate post-World War II time. Hey and Stewart (1947) used three separate receiver stations operating at 73 MHz in order to determine the radiant position within 10°. Other systems using slightly different methods were developed at Jodrell Bank (England) in the late 1940's, by the mid-1950's three station systems using Fresnel diffraction pattern correlation were in operation. The Harvard project of the 1960's was a watershed in modern radio meteor study. This project followed from principles laid down at Jodrell Bank, and resulted from the application of a large amount of money and technology to build the optimal equipment configuration. The radar system consisted of 8 spaced stations, rather than the necessary minimum of 3, in order to obtain additional coverage of meteor events. Additionally a powerful 2 MW peak power output transmitter, high-gain antennas and sensitive receivers

Location	Years of Operation	Number of Orbits	M_R	References
Ottawa,Canada	1948	1	-	McKinley and Millman (1949)
Jodrell Bank,U.K.	1949–50	4 mean stream orbits	+6	Almond (1951) Lovell (1954)
Jodrell Bank, U.K.	1954–55	2,509	+7	Davies and Gill (1960)
Adelaide, Australia*	1960–61	2,092	+6	Nilsson (1964)
Kharkov, Ukraine	1960–65	12,500	+7	Lebedinets (1968)
Illinois, U.S.A.*	1961–65	19,327	+12	Cook et al. (1972) Sekanina (1973)
Obninsk, Russia*	1967–68	9,358	+7.5	Lebedinets (1981,1982)
Kazan, Russia	1968	3,200	+8	Andrianov (1968,1970)
Adelaide, Australia*	1968–69	1,667	+8	Gartrell and Elford (1975)
Illinois, U.S.A.*	1968–69	19,818	+12	Cook et al. (1972) Sekanina (1976)
Mogadisho, Somalia*	1968–70	5,328	+8	Fedynski (1975,1977)
Kharkov, Ukraine*	1975	5,317	+12	Kashcheev and Tkachuk (1980)
Kharkov, Ukraine	1975–77	$\sim 1.5 \times 10^5$	+12	Kashcheev and Voloshchuk (1992)
AMOR, Christchurch, New Zealand	1990–1994	$\sim 3 \times 10^5$	+13	Baggaley et al. (1994)
AMOR, Christchurch, New Zealand	1995–1999	$\sim 6 \times 10^5$	+14	The Current Study

Table 1.2: Meteoroid orbit radars 1948-1994. This table after Baggaley (1995). *Orbits available from the IAU Meteor Data Center, Lund Observatory, Sweden. M_R is the limiting radio magnitude at which meteors are detectable.

were used in order to probe down to very faint meteors at a limiting radio magnitude +12. Normally if one is studying shower structure in a data set, one wishes to look at meteoroids which are larger, and therefore appear not so faintly because of the expected mass distributions for the contributing streams. By scanning for very small meteors a much larger data set is obtained, as the spatial density of meteoroids increases as the size/mass range decreases. Cook et al. (1972) notes that the increase in data set size thus obtained allows more reliable space distributions of meteoroids to be secured. Over the synoptic year from October 1968 to December 1969 a sample of 19,327 meteoroid orbits was obtained from this survey.

Various studies have been conducted at Adelaide, Australia including those of Weiss (1960), Nilsson (1964) and Gartrell and Elford (1975). The system at Adelaide used the 3 spaced receiver station method (employing the continuous wave (CW) technique) and detected orbit reduction quality meteors with magnitudes varying between +6 (Nilsson 1963) and +8 (Gartrell and Elford 1975). In each of these studies $\sim 2 \times 10^3$ orbits were recovered.

Studies at Kharkov in the Ukraine have also been performed over the past decades with the largest orbital data set having been collected between 1975–1977. The limiting magnitude of this system (+12) was similar to that of the

Harvard project but the number of orbits catalogued was an order of magnitude greater ($\sim 1.5 \times 10^5$), due to the observation continuity obtained (Kashcheev and Voloshchuk 1992). The results from this survey have never been published.

Other radar systems presently available tend to concentrate on the easier task of obtaining simple flux measurements of major meteor showers. They do so either based on the assumption that the shower under observation contributes all of the flux or with some knowledge of the radiant position of the meteors under study. Such systems may either work in forward-scatter mode, as used by many amateurs who study FM radio signal scattering by meteor trains, or they may work in a back-scatter mode. These systems illuminate the sky and scatter results off the general population of meteors at a given time. Porubčan et al. (1996) use an example of such a (back-scatter) system to study the Lyrid meteor shower. This three stations system was only able to measure the flux of particles. By looking at the appropriate two-station baseline for a given shower the presumed activity profile for that shower alone was obtained. Many other such systems have been deployed in recent years, particularly in the Leonid campaigns. The SKYiMET system (e.g. Arlt et al. 1999), which has been deployed in many places around the world in similar configurations, is an excellent example of an advanced implementation of the Forward Scatter technique. Here the radiant position is obtained in addition to activity profiles—hence one can be assured that one is measuring the shower under study and not simply fluctuations in the background.

The Arecibo radio telescope is used occasionally for the purpose of measuring meteoroid orbits (e.g. Janches et al. 2000). However there are challenges based on the necessity of head echo geometry and on the available observing time which limit the role of this method. Otherwise, at present the AMOR system is the only one in the world actively and routinely involved in measuring meteoroid orbits. It does so down to a lower limiting magnitude (+14 currently) than either the Harvard or Kharkov studies and therefore observes meteors derived from the smallest dust grains ever seen by such an orbit-calculating radar system. This limit is approaching the size range of the zodiacal dust and therefore the orbital structure obtained in the data set is expected to be essentially that due to the various strong biasing effects imposed on an Earth-intersecting dust population—there are expected to be very few discernible streams present. The number of meteor observations per year ($\sim 10^5$ orbits) using AMOR allows studies of distributions of dust in space and also provides an excellent resource in which to test for the presence of streams.

1.4 Thesis Overview

The aim of this thesis is to study the data set provided by the AMOR meteoroid orbit system in order to determine the structure contained therein. The layout of this presentation attempts to accomplish this by studying the biases, uncertainties, large- and small-scale structures present in a logical order. The purpose here is to determine general methods for studying meteor orbit data sets with a particular application to that provided by the AMOR system. Perhaps the most important part of the current study is the search for small-scale structure (showers) given in Chapter 7—several new and old methods are introduced and their relevance compared there. Applications of the chosen methods show clearly similar results and serve to confirm the generally randomised nature of the data set at the small-scale structure level: for the most part the AMOR data set is found to provide a poor record of past cometary activity, undoubtedly the information is present but measurement biases, uncertainties and perturbation mechanisms have acted to dull the distinctiveness of meteoroid streams once present.

This thesis is split into 11 chapters and 8 appendices. Appendix A is of special note, as it contains a glossary of acronyms and mathematical symbols. This appendix should be referred to should the reader require clarification while reading the main body of the text.

The current chapter has introduced the history of meteor measurement, with a particular emphasis on radar methods. It has discussed the meteoroid population and the methods by which streams are formed and removed from the population. Chapter 2 focuses on a particular meteor detection system: the AMOR meteoroid orbit radar whose data set is used in the current study. The reader is led through the process by which field meteor observations are translated to pre-impact heliocentric orbits. Chapter 3 gives an overview of the orbital distributions as detected by AMOR. A discussion of the various processes which bias these distributions is given leading to the presentation of bias-corrected distributions. Chapter 4 discusses a particular aspect of the biased distribution of meteors, that of radiant position. The seasonal motion of these sources is demonstrated. The reader is introduced to the so-called sporadic sources which appear as virtual sources of meteors. The orbital distributions within these sources are probed both in the case of all orbits and then on a seasonal basis. Chapter 5 introduces the topic of uncertainty analysis of meteoroid orbits. It then proceeds to discuss the application of two techniques which have been developed in the current study to measure individual orbital pa-

rameter uncertainties in the AMOR orbits. A comparison between these techniques is made later in this chapter. Representative uncertainties are determined for several subclasses of the orbit population. Chapter 6 presents a number of dissimilarity functions, called D-criteria, used for determining the closeness of orbit pairs to each other. These functions are discussed in terms of practical considerations involved in their implementation. Simulations are given of the effect the expected orbital spread due to measurement uncertainty (the dominant process in radar meteoroid stream spread) will have on D-criteria values. As mentioned above, Chapter 7 begins with an introduction to stream search methods which have been used in the past. It then proceeds to list the expected stream structure within the AMOR data set. The methods which have been applied in the current study and their results are discussed. These methods are, in the order in which they appear: gross-rate detection, direct search against published mean stream orbits, wavelet enhancement of the radiant-speed-time space and finally single-linkage cluster analysis. The direct search method is an adaptation of a previously used method while the wavelet enhancement method is a completely new technique. The latter is used further to define the showers detected: a section is dedicated to showers found in each of the source direction regions. Chapter 8 studies the showers revealed in the previous searches in-depth. Each shower, as defined by the wavelet transform definitions of Chapter 7, is systematically tested for daily motion in the orbital and directly observed parameters of the shower. The statistics of the orbit population of each shower are then determined and compared with the published literature. Finally the activity profile of each shower is presented for each year of coverage. Significant changes in activity are searched for. Chapter 9 presents overall conclusions and a summary of work accomplished; smaller, more basic, summaries are also included with several of the above chapters. Chapter 10 presents opportunities for future work on the AMOR data set and system.

Appendix B lists the contents of each AMOR meteor record. Appendix C presents program listings for many of the C and MATLAB programs developed in the current study. Appendix D discusses the characteristics of the orbit data files which are used throughout this study. Appendix E lists the results of the direct search applied in Section 7.6. Appendix F discusses methods of source characterisation using wavelet analysis, based on the assumption of idealised Gaussian shaped sources. Appendix G presents the output wavelet enhancement graphs obtained from the analyses described in Section 7.7. Appendix H contains a poster paper presented

at the Asteroids, Comets and Meteors '99 conference and referred to in Section 7.8.

Chapter 2

Meteoroid Orbits and the AMOR System

This chapter introduces the AMOR system and illustrates the process by which unprocessed meteor observations are reduced to obtain the pre-impact heliocentric orbits of the meteoroid particles. The information contained herein will constantly be referred to in later analysis, when discussing the origin of particular features of the data set.

2.1 The AMOR System

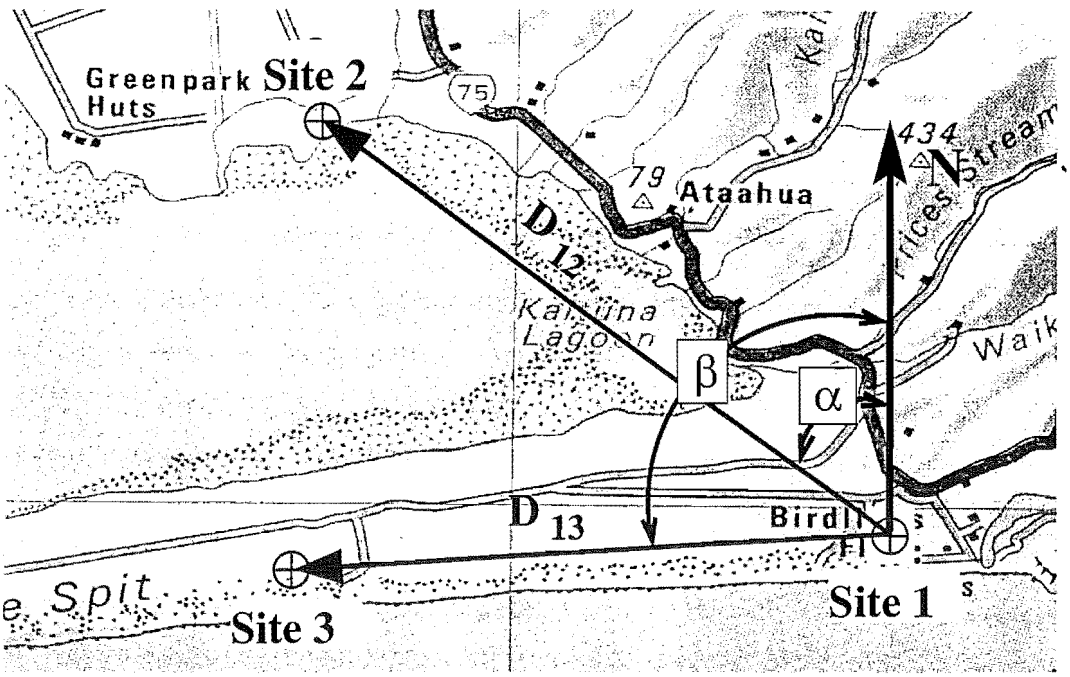

Figure 2.1: AMOR three station orientation. Here α, the angle between north and the Site 2, is 45°; β, the angle between north and the Site 3, is 93°.

The AMOR system consists of three sites near Christchurch in New Zealand. The central site consists of a transmitter, receivers and their respective antenna arrays. A dual interferometer is formed by three parallel antennas in order to unambiguously determine the elevation of the echo point. This site also houses the

computer data acquisition and storage setup and has FM radio links to two remote receiver stations which are situated at distances of $\approx$ 8 km and $\approx$ 11 km in different directions from it, as shown in Figure 2.1. The two remote sites are identical, they both consist of a receiver with its receiving array and an FM transmitter which relays echo reception information in real-time to the central site.

The transmitted antenna beam pattern is broad in elevation, as discussed later in Section 3.5.1, while being very narrow in azimuthal extent ($\approx 2^\circ$ wide). The latter feature implicitly determines the location of the echo-point on a meteor train to within 1°, thus constraining one of the dimensions of the problem.

Site monitoring and antenna maintenance have been carried out at least once a week. This dedication and a constant upgrade and repair programme have resulted in a near continuous observation mode over the past few years.

2.2 Orbit Determination

A meteoroid orbit is defined in terms of heliocentric orbital elements which in turn may be based on heliocentric velocity components of the meteoroid at the time of impact. In order to measure these components a number of steps must be taken by the AMOR system. The following sections detail these steps.

2.2.1 Determination of Fundamental Parameters

In order to determine the pre-atmospheric orbit of a meteoroid AMOR requires knowledge of the position and velocity of the meteor at the time of observation. The azimuth and zenith angles and the scalar velocity together provide this velocity vector. In order to determine the position of the meteor train its range and elevation are needed.

The range (R) is the distance between the receiving antenna and the meteor's ionisation trail. This is determined by timing the delay between an outgoing pulse and its reflected echo. In order to provide an unambiguous elevation angle (ψ), two radio interferometers are used. These are formed by two receiving antennas spaced at distances of 3 and 10.5 wavelengths respectively from a central receiving antenna. The original AMOR configuration (Taylor 1991) used only one interferometer with a 5 wavelength spacing: however this was changed in 1994 to the dual interferometer mode to provide less ambiguity and a greater consistency in the elevation measurement.

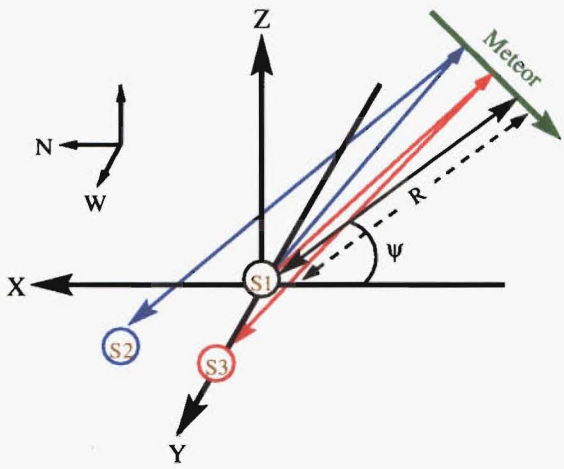

Figure 2.2: Specular reflection off a meteor train with AMOR. Reflection is received from the meteor train when the radio beam hits the train at an angle of 90°. Sites 2 and 3 are the remote sites and Site 1 is the central site.

Figure 2.2 illustrates the geometry of meteor measurement. Echoes from the north have elevations varying between 90° and 180° while those from the south have elevations from 0° to 90°. Meteor ionisation trains are detected at approximately right angles to the direction of motion, thus meteoroids moving from north to south are detected by the radar from towards the south. By determining which remote site the profile appears on first the north-south direction can be determined—e.g. if the profile appears on Site 2 before Site 3 then the train is to the south.

The principal method used in the past to determine velocities was the Fresnel method. As the meteor train passes the specular reflection point Fresnel oscillations may be observed. From McKinley (1961) the scalar velocity of the meteor in the atmosphere is given by

$$V = \sqrt{R_o \lambda} \frac{\sqrt{n} - \sqrt{m}}{\triangle \tau}, \tag{2.1}$$

where $\triangle \tau$ is the time between the mth and nth cycles; R_o is the direct-line distance between the observing station and the specular reflection point on the trail; and λ is the wavelength corresponding to the frequency of the transmitter. This formula is approximate only and valid for small n and m.

The Fresnel method when used on a *good quality* echo profile yields good results. However in about 70% of cases the Fresnel pattern is too badly distorted due to atmospheric turbulence, cascade fragmentation, gross fragmentation or rapid diffusion of the meteor body during the observation. Relying on this method to measure velocities thus reduces the usable data set size.

AMOR implements the traditional Fresnel speed measurements on any echoes

of sufficient quality. The principal method used on lower quality profiles involves measuring the time-lag between the echo profile being observed at each of the three receiver sites[1]. In practice the appearance of the point corresponding to the maximum gradient in the amplitude profile is used as a reference to allow the calculation of relative time-lags. Comparison of speeds measured simultaneously by Fresnel and time-lag techniques on suitable meteor detections verify the calibration of the time-lag method (e.g. Taylor et al. 1994).

An accepted meteor observation consists of an echo profile from each of the three receiver sites together with an elevation angle (ψ), range value (R), and time-lag between detections at each site. Section 2.2.2 gives examples of some typical detection records of this form.

2.2.2 Representative Meteor Detections

A recording day has been selected at random to display some of the typical detection scenarios one comes across. In each case the amplitude decay profiles from each of the three receiver sites have been displayed together with the range and elevation of each echo point and the time-lags between the appearance of the steepest increasing point of each profile at the respective receiving sites. This information, together with the time of meteor detection, constitutes a complete record for orbit determination. Additionally the derived pre-atmospheric geocentric and heliocentric speeds are displayed—the details of their calculation are given later in Section 2.4.

Most observations consist of an echo profile similar to Figure 2.5. Here there is a swift rise to the maximum and then an exponential decay as ambipolar diffusion of the ionised train occurs. As with the majority of the profiles recorded by AMOR there is evidence of Fresnel oscillations on the decay slope but in this case it is insufficient for determination of a Fresnel based speed. It is likely that other effects such as wind turbulence, sampling frequency and meteoroid fragmentation during observation have caused the Fresnel oscillations to be washed out in such a profile.

Fresnel oscillations are visible in $\sim 10\%$ of meteor observations (Baggaley et al. 1994), Figure 2.4 presents two such observations. Comparison of the Fresnel based speed (equation 2.1) with that obtained from time-lag measurements (equation 2.5) for such detections was used by Taylor (1991) to validate the time-lags velocity measurement method.

[1]The calculation of a time-lag velocity obviously requires that all three receiver sites record usable echo profiles.

Many other types of meteor observation are seen. An interesting example from which an orbit is still fully calculable is that shown in Figure 2.6—while the previous observations shown are for slower prograde orbit meteoroids, this observation is of a fast (55.6 $\mathrm{km\,s^{-1}}$ geocentric velocity) grain of dust. One can see clearly on all three profiles that at approximately 120 radar pulses a fragmentation/wind distortion event occurs, the early rise slope at $\approx$ 50 radar pulses however is distinct and as this is the important region for orbit calculation an orbit was still able to be determined from this record.

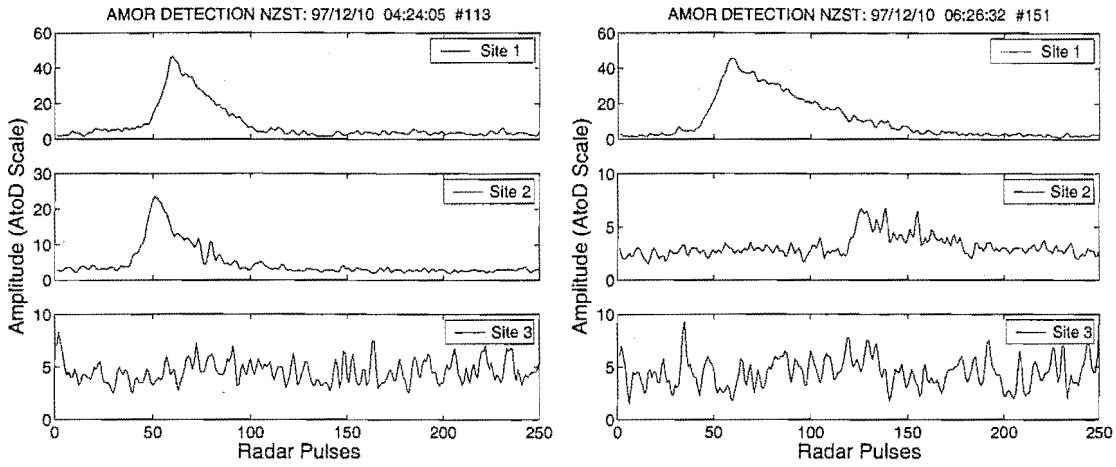

Figure 2.3: Meteor observation with insufficient data for orbit determination. Lag times are given in units of radar pulses (r.p.).

Many meteor detections are logged by AMOR which are found on subsequent quality control to be unsuitable for orbit determination, Figure 2.3 gives examples of two such observations[2]. The meteor detection shown on the left has a reasonable decay profile for Sites 1 and 2 with Site 3 displaying noise, that on the right has noise on both Sites 2 and 3. Notice the very low amplitude on the noisy sites corresponding to a lack of signal.

There are many reasons for the lack of a usable profile on all three sites. Recording of an observation triggers off the central site, hence there are more likely to be good central site profiles recorded than there are for the remote sites. The remote sites send data via VHF link at present hence transmission noise/problems with the VHF link equipment may cause lack of a usable profile. (As of April 2000 the remote links have been upgraded to UHF devices which are more robust both phys-

[2]Even though a meteor event may not be detected adequately at all three receiver sites, if it is detected on the central site then it is still useful for atmospheric measurements of such parameters as ambipolar diffusion (Thomas 1998), wind shear (Edsall 1996) and meridional wind speed (Marsh et al. 2000).

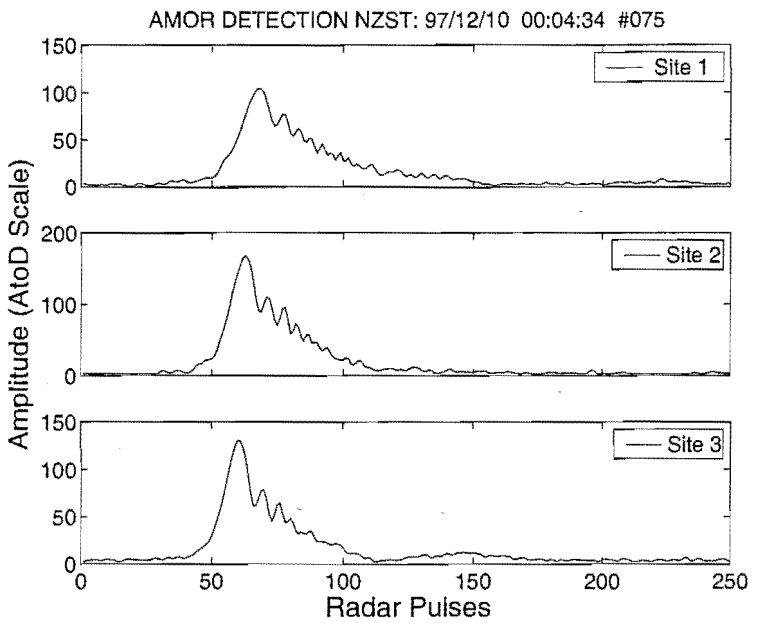

Range	216 km
Elev.	26.2°
Lag_{12}	-2.0 r.p.
Lag_{13}	-20.0 r.p.
V_x	18.6 km s^{-1}
V_y	25.6 km s^{-1}
V_z	21.9 km s^{-1}
V_H	38.5 km s^{-1}
V_G	35.5 km s^{-1}

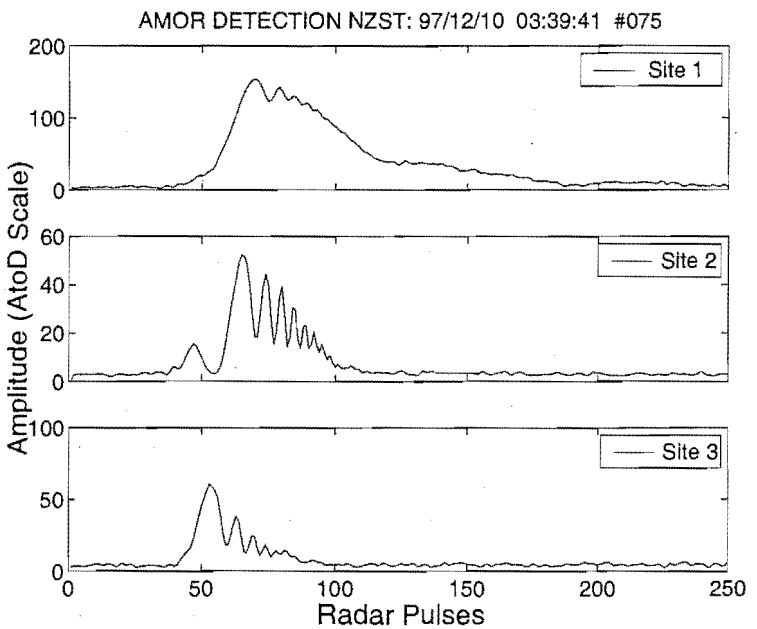

Range	209 km
Elev.	25.4°
Lag_{12}	24.0 r.p.
Lag_{13}	12.1 r.p.
V_x	14.0 km s^{-1}
V_y	31.5 km s^{-1}
V_z	28.9 km s^{-1}
V_H	45.0 km s^{-1}
V_G	45.6 km s^{-1}

Figure 2.4: Meteor observations with visible Fresnel oscillations. Lag times are given in units of radar pulses (r.p.). The derived heliocentric velocity components which define a space orbit are shown as V_x, V_y and V_z; the heliocentric speed resulting from these is given by V_H. The geocentric speed (V_G) is additionally given as this is close to the ground speed of the meteoroid as seen by the radar and may differ substantially from V_H particularly for meteoroids on retrograde orbits.

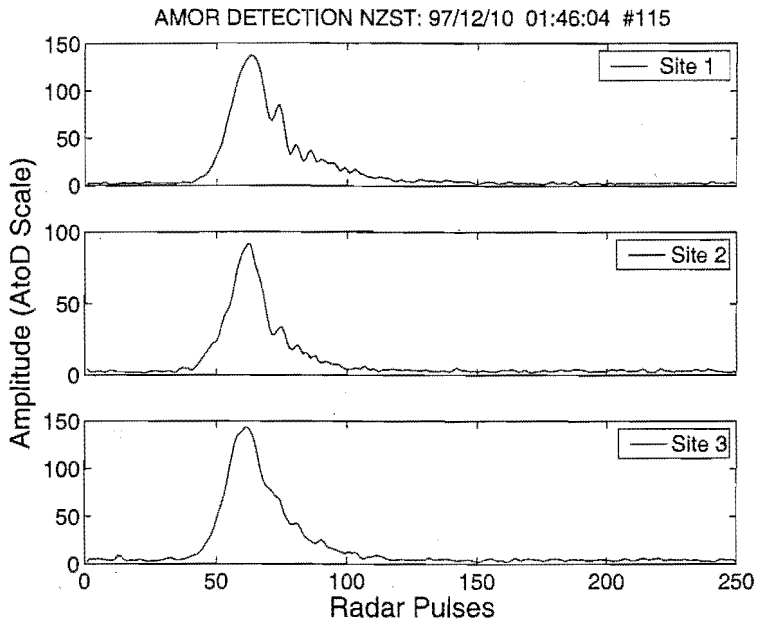

Range	300 km
Elev.	161.0°
Lag_{12}	-24.2 r.p.
Lag_{13}	-14.1 r.p.
V_x	13.9 km s^{-1}
V_y	-3.2 km s^{-1}
V_z	35.3 km s^{-1}
V_H	38.1 km s^{-1}
V_G	39.1 km s^{-1}

Figure 2.5: Meteor observation with no usable Fresnel pattern. See Figure 2.4 for more information on the layout.

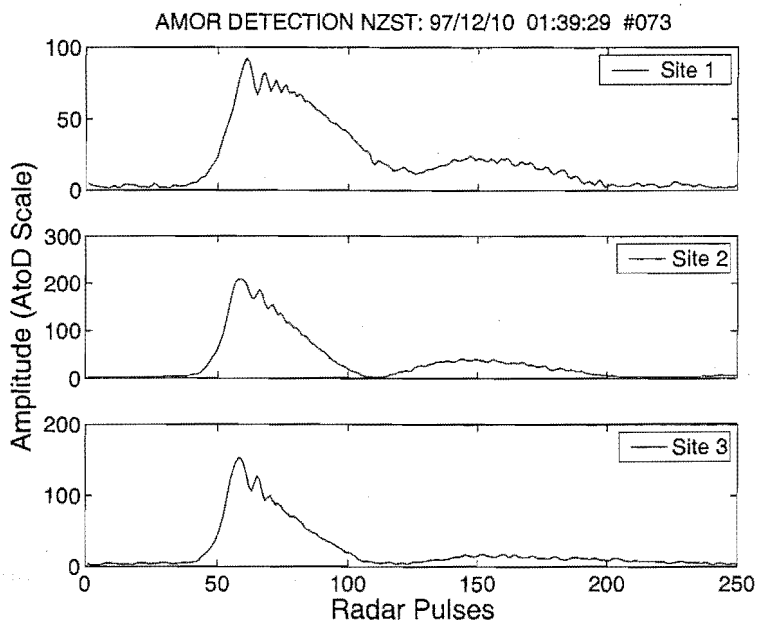

Range	286 km
Elev.	19.4°
Lag_{12}	-17.1 r.p.
Lag_{13}	-23.9 r.p.
V_x	-21.7 km s^{-1}
V_y	4.3 km s^{-1}
V_z	19.5 km s^{-1}
V_H	29.4 km s^{-1}
V_G	55.6 km s^{-1}

Figure 2.6: Observation of a fast meteoroid fragmenting or wind-induced train distortion. See Figure 2.4 for more information on the layout.

ically and with regards to corona discharge interference. The ambient noise level experienced currently is much lower than that found in the profiles used to provide the orbits studied in this thesis.) The slender azimuthal $\approx 1.5°$ width of the transmitted radio beam means that, depending on the geometry of the meteor ionisation train, very different amounts of radio power may be reflected to each of the receiver sites—this difference may cause one site to receive a very strong amplitude profile while at another, close by, the amplitude may fall below the noise level.

2.3 Observed Velocity in the Local Frame

In order to calculate the pre-atmospheric heliocentric velocity of the meteoroid a number of steps must be followed. These involve determining the velocity locally and then through a series of transformations removing all local and geocentric features of this velocity.

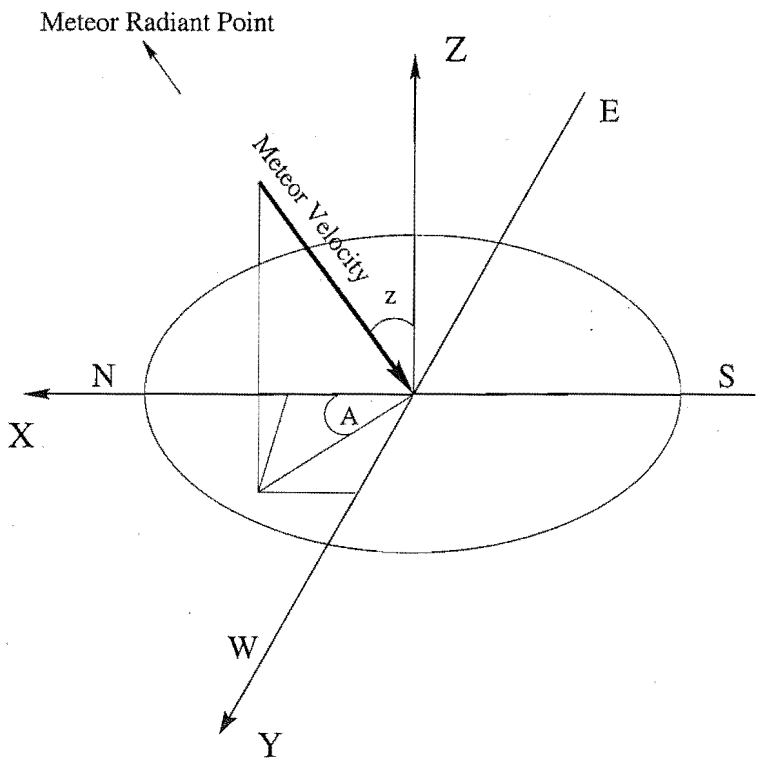

Figure 2.7: Parameters of interest in the local reference frame for meteor detection.

The time-lags, $t_{1k} = t_1 - t_k$, between the central site and each of the remote sites are given by

$$t_{12} = \frac{1}{2V_1} D_{12} \sin z \left[\cos\alpha \cos A + \sin\alpha \sin A\right] \qquad (2.2)$$

and

$$t_{13} = \frac{1}{2V_1} D_{13} \sin z \left[\cos\beta \cos A + \sin\beta \sin A\right], \tag{2.3}$$

where α, β, D_{12} and D_{13} as defined in Figure 2.1 refer to the relative positions of the received stations; A and z are the azimuth and zenith angles of the radiant respectively; and V_1 is the observed meteor speed in the local frame. A can be obtained by solving these equations simultaneously. For meteor trains appearing in the south $A \in [-90°, 90°)$ while for those in the north $A \in [90°, 270°)$. The azimuth and elevation angles, together with an assumption of zero azimuthal spread in the transmitted radio beam (see Section 2.1), allow the calculation of z using

$$\tan z = \frac{\tan\psi}{\cos A}. \tag{2.4}$$

With both A and z now known the magnitude of the speed (V_1), as observed in the local coordinate frame, may be calculated by rearranging equation 2.2 or 2.3. By further utilising these angles the components of the corresponding velocity (V_1) follow from

$$\mathrm{V}_1 = -V_1 \begin{pmatrix} \sin z \cos A \\ \sin z \sin A \\ \cos z \end{pmatrix}. \tag{2.5}$$

2.4 Reductions to Heliocentric Velocity

In the previous section we saw how parameters in the local reference frame may be determined. In this form these are of little use astronomically: the next step is to determine the pre-atmospheric velocity and orbit of the meteoroid itself. Corrections are applied to V_1 for atmospheric deceleration, the rotational velocity of the Earth, the gravitational acceleration of the Earth and zenith attraction. The velocity is then transformed from the local coordinate system to equatorial coordinates and finally to the heliocentric ecliptic coordinate system. Figure 2.8 shows this sequence of reductions graphically. The final velocity (V_H) is thus the corrected velocity of the meteoroid in its heliocentric orbit about the Sun prior to its gravitational attraction and collision with the Earth's atmosphere.

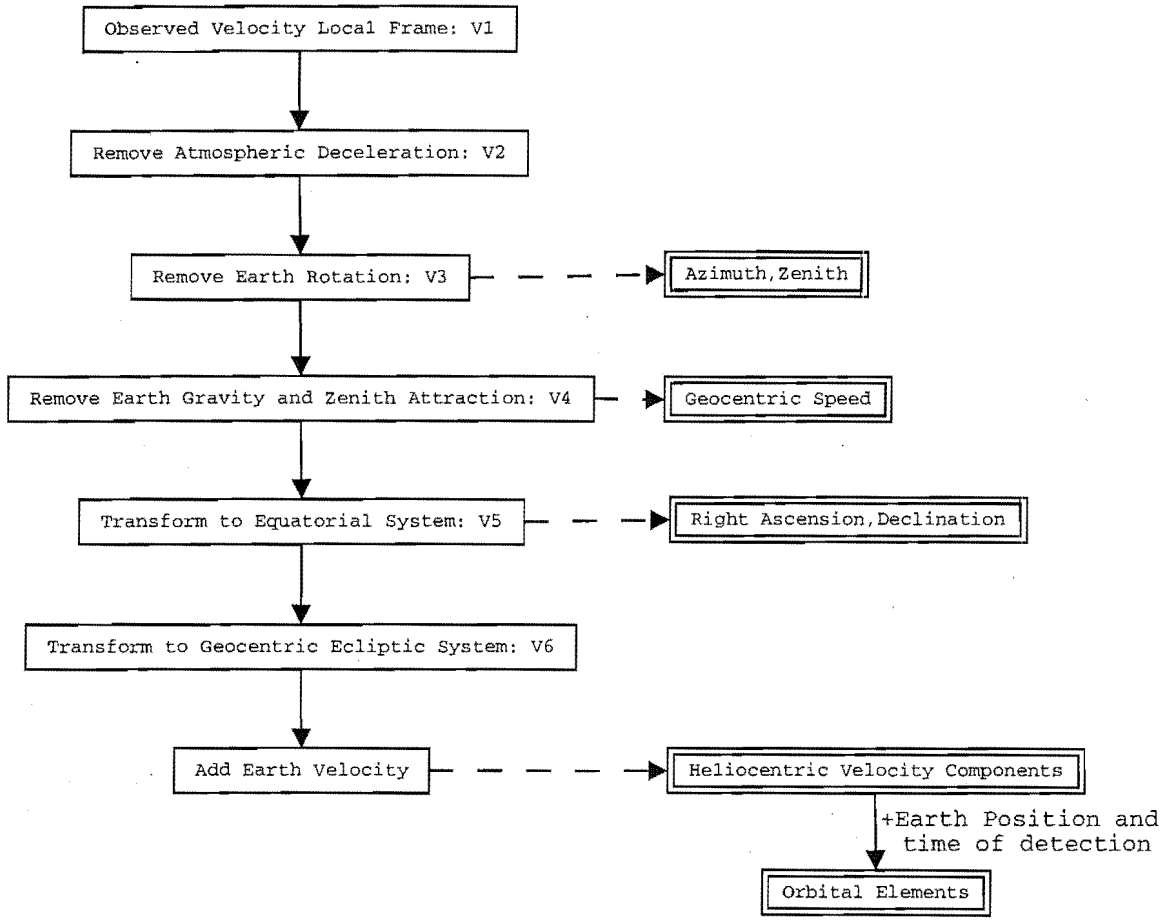

Figure 2.8: Velocity reduction steps used by AMOR. Each level shows the successive steps carried out by the reduction program. The outcomes from different levels appear at the right.

2.5 Orbital Element Calculations

The meteoroid's heliocentric velocity components (V_x, V_y, V_z) (see Figure 2.11) together with the epoch of detection make it possible to calculate conventional orbital elements for the orbit of the meteoroid.

2.5.1 Orbital Size and Shape

The shape of the orbit is defined by its semi-major axis length (a) and eccentricity (e), this is demonstrated in Figure 2.9 for parabolic/hyperbolic orbits and in Figure 2.10 for elliptic orbits. In order to determine these parameters one must first find the orbital parameter (p) and the true anomaly (ν) of the meteoroid at its point of detection. These parameters are in turn based on the position vector of the meteoroid and the radial $(V_r = -V_y)$ and angular $(V_\nu^2 = V_x^2 + V_z^2)$ components

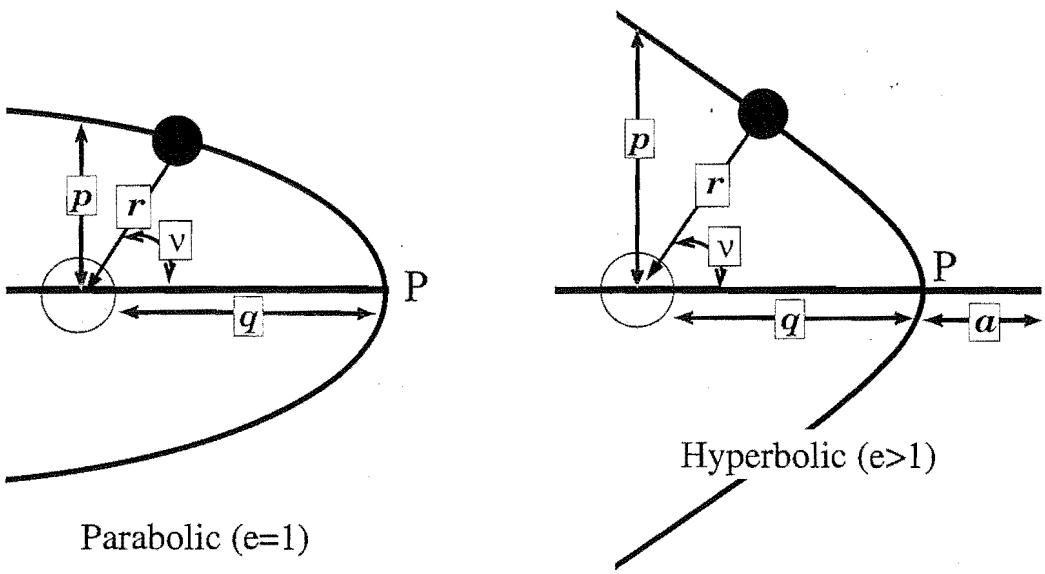

Figure 2.9: Solar system escape orbits. Orbits with $e \geq 1$ escape from the Solar System and do not return. 'P' marks the perihelion position. The light and dark circles represent the Sun and the meteoroid (shown at angular position ν) respectively.

of the heliocentric velocity via

$$p = \frac{r_m^2 V_\nu^2}{GM_\odot} \tag{2.6}$$

and

$$\tan\nu = \frac{V_r\sqrt{p/GM_\odot}}{p\,r_m^{-1} - 1}. \tag{2.7}$$

The equation for a conic section gives the distance (r) from the Sun, for a body at position ν, in an orbit defined by p and e as

$$r = \frac{p}{1 + e\cos\nu}. \tag{2.8}$$

The impact of the meteoroid with the Earth occurs at $r = r_\oplus$, where $r_\oplus$ is the distance from the Earth to the Sun. By substitution into equation 2.8, the eccentricity follows from

$$e = \frac{p\,r_\oplus^{-1} - 1}{\cos\nu}. \tag{2.9}$$

The semi-major axis length (a) is easily defined in terms of p and e via

$$a = \frac{p}{1 - e^2}. \tag{2.10}$$

The sign of a changes according to the type of conic section one is dealing with; the orbital parameter (p) is always positive. Equation 2.10 shows that a is positive for $e < 1$ (elliptical), negative for $e > 1$ (hyperbolic) and undefined for $e = 1$ (parabolic).

The meteoroid is closest to the Sun at perihelion ($q = a[1 - e]$) and furthest away at aphelion ($Q = a[1 + e]$). Often in meteoroid orbit studies the pair (q, e) is preferred to that of (a, e) because of the constrained range of possible q for Earth impact and also because a is undefined for parabolic orbits.

2.5.2 Orbital Orientation

V_z, the heliocentric velocity component perpendicular to the ecliptic plane, defines whether the meteoroid detection has occurred at the ascending ($V_z > 0$) or descending ($V_z < 0$) node of the orbit. Figure 2.12 illustrates the geometry involved for these two types of nodal impact.

The argument of perihelion (ω) orients the orbit on the orbital plane (Figure 2.11). This element is directly related to the true anomaly (Equation 2.7) via

$$\omega = \begin{cases} 360^\circ - \nu, & V_z > 0 \text{ (asc. node)} \\ 180^\circ - \nu, & V_z < 0 \text{ (des. node).} \end{cases} \tag{2.11}$$

As shown in Figure 2.11, the longitude of the ascending node (Ω) and inclination (i) fix the plane in which the orbit sits. Ω is defined in terms of the mean longitude of the Sun ($\lambda_\odot$) and the node at which the detection occurred:

$$\Omega = \begin{cases} \lambda_\odot - 180^\circ, & V_z > 0 \text{ (asc. node)} \\ \lambda_\odot, & V_z < 0 \text{ (des. node).} \end{cases} \tag{2.12}$$

$\lambda_\odot$ may be calculated from the epoch of observation (see for example *The Astronomical Almanac 1997,* page C24). AMOR catalogues Ω referred to the standard epoch of B1950.0. Finally the inclination (i) is given by

$$\tan i = \frac{V_z}{V_x}, \tag{2.13}$$

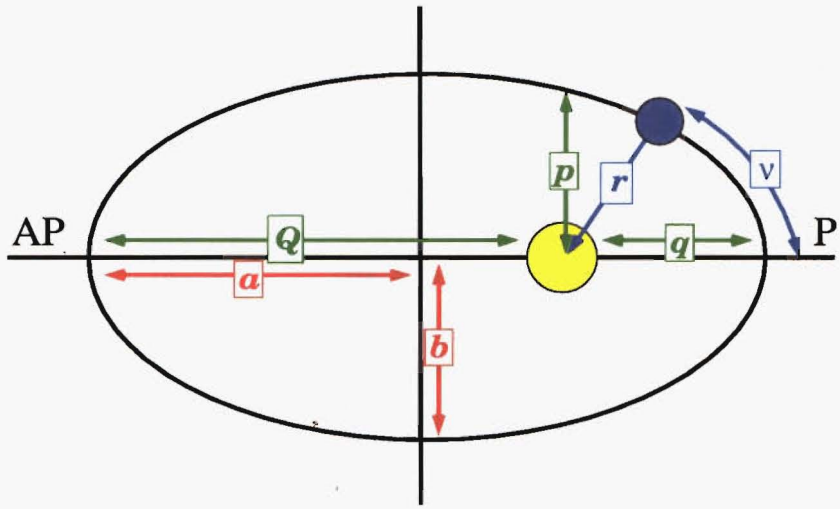

Figure 2.10: Orbital shape parameters. The elliptical orbit of a meteoroid is shown, with the meteoroid represented by a blue circle (not to scale) at its intersection point with the Earth's orbit and the Sun represented by a yellow circle. The perihelion position is marked by 'P' and the aphelion position by 'AP'. The semi-major axis length (a) determines the size of the orbit while the eccentricity (e) defines its curvature. The curvature varies from circular ($e = 0$) to elliptic ($0 < e < 1$) then to parabolic ($e = 1$) and finally to hyperbolic ($e > 1$). Alternative measures of orbital shape/size are perihelion distance ($q = a(1 - e)$), aphelion distance ($Q = a(1 + e)$), semi-minor axis length (b) and orbital parameter ($p = a(1 - e^2)$).

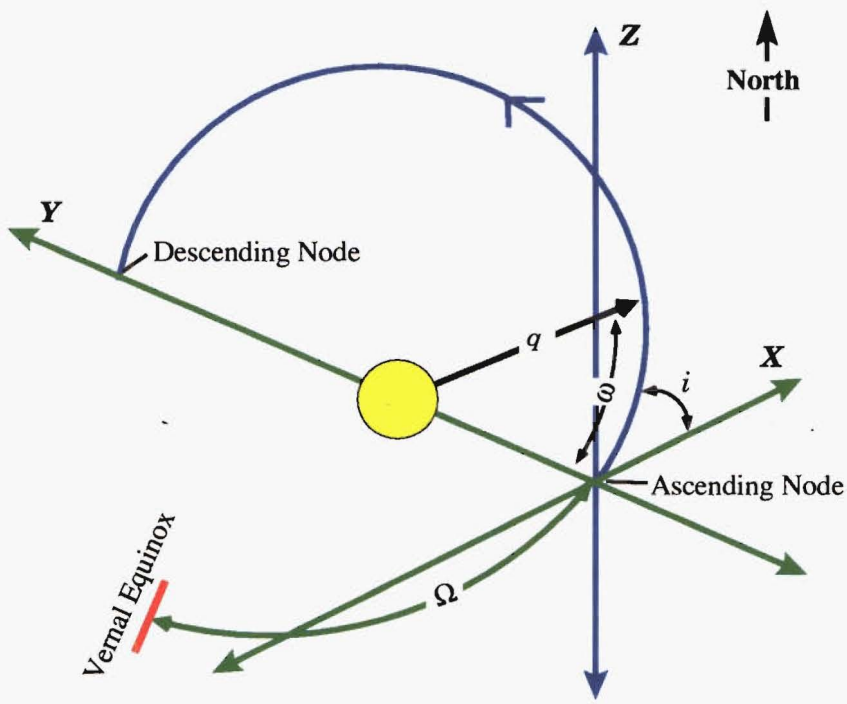

Figure 2.11: The orientation of the orbit within its orbital plane is fixed by the argument of perihelion (ω). This plane is itself inclined by an angle (i) with respect to the ecliptic. The points of intersection with the ecliptic are called the "nodes". The ascending and descending nodes correspond to meteoroids which impact while travelling in southerly or northerly directions respectively. The longitude of the ascending node (Ω) is the angle between the vernal equinox and the ascending node (measured in the ecliptic plane).

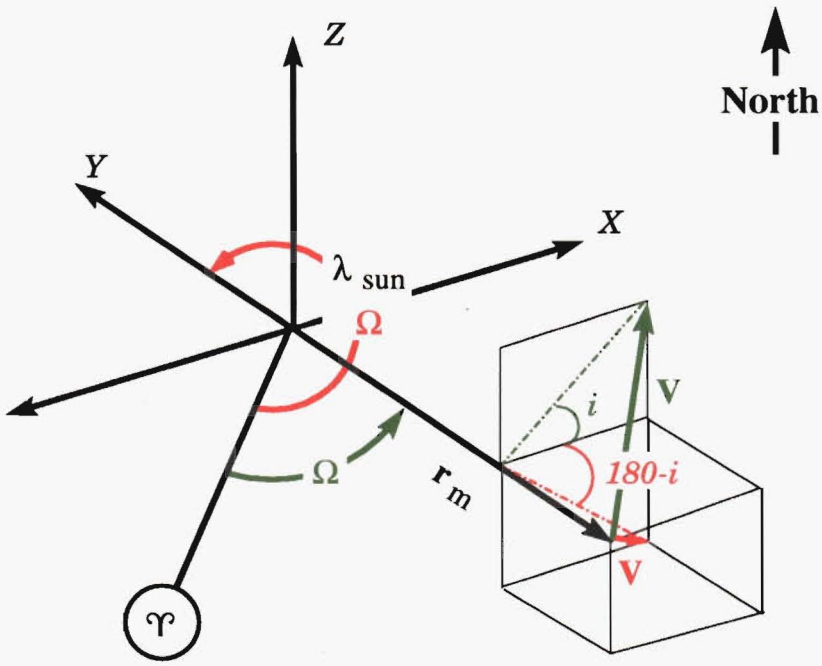

Figure 2.12: Geometry of meteoroid detection at ascending/descending node. The heliocentric velocity vector ($\mathbf{V}_H$) is shown in green in the case of ascending node detection ($V_z > 0$) and red in the alternative case of descending node detection ($V_z < 0$). This colour coding is extended to the selection of longitude of ascending node (Ω) and inclination (i) parameters. The vernal equinox is shown at Υ.

where for prograde orbits $i \in [0°, 90°)$ and for retrograde orbits $i \in (90°, 180°]$.

2.6 The Meteor Radiant

For each meteor detection the geocentric radiant position is determined. The radiant is the point from which the meteor appears to emerge on the celestial sphere—it defines the direction of the incoming meteor's velocity. This angular position is defined, in the equatorial system, by the coordinate set of right ascension (α) and declination (δ). Combination of these with the geocentric speed of the meteoroid and the time of detection allow the calculation of an unambiguous heliocentric orbit. The geocentric radiant used in the current study, unlike that in some studies, is corrected for the Earths' rotation, gravitational and zenith attraction—this process is summarised in Figure 2.8. Owing to this processing the current radiant position is referred to as "corrected" while radiant positions aimed towards visual observers generally quote an "apparent" radiant, the latter being the point on the sky from which the meteor directly appear to emerge. The apparent and corrected radiant positions are generally similar but for slow meteors there will be substantial differences.

In geocentric equatorial coordinates the radiant position is determined from

$$\alpha = \arctan\left(\frac{V_{5y}}{V_{5x}}\right)$$

and (2.14)

$$\delta = \arctan\left(-\frac{V_{5z}}{\sqrt{V_{5x}^2 + V_{5y}^2}}\right),$$

where $\mathbf{V_5}$ is the geocentric equatorial velocity (see Figure 2.8).

It is often useful to be able to translate these to the geocentric ecliptic system, which is defined by the coordinate set of ecliptic longitude (λ) and ecliptic latitude (β) where

$$\cos\beta\cos\lambda = \cos\delta\cos\alpha, \tag{2.15}$$

$$\cos\beta\sin\lambda = \sin\delta\sin\epsilon + \cos\delta\cos\epsilon\sin\alpha, \tag{2.16}$$

and

$$\sin\beta = \sin\delta\cos\epsilon - \cos\delta\sin\epsilon\sin\alpha, \tag{2.17}$$

where ϵ, the obliquity of the ecliptic, is equal to $\epsilon = 23.4393°$ for the epoch J2000.0.

2.6.1 Apparent Radiant Motion Due to the Earth's Orbital Motion

The Earth moves on the ecliptic with its longitude changing by approximately 1° of mean solar longitude per day. A static radiant with respect to the celestial sphere will appear to rotate about the Sun when observed from the moving reference frame provided by the Earth; this is illustrated in Figure 2.13. The use of the ecliptic coordinate system for geocentric radiant measurements becomes useful when we wish to attempt to remove the effect of the Earth's motion in order to provide radiant positions in a non-rotating frame. The equatorial system is cumbersome as the correction needs to be applied to two variables (α and δ) rather than just to one in the ecliptic case (λ). It is apparent from Figure 2.13 that the solar longitude changes by the same amount and in the same direction as does the ecliptic longitude of the radiant under observation. The ecliptic latitude is not affected, as the Earth's motion takes place purely in the ecliptic plane, i.e. at $\beta = 0°$. An inertial frame of reference is therefore simply defined by

$$(\lambda_R, \beta) = (\lambda - \lambda_\odot, \beta). \tag{2.18}$$

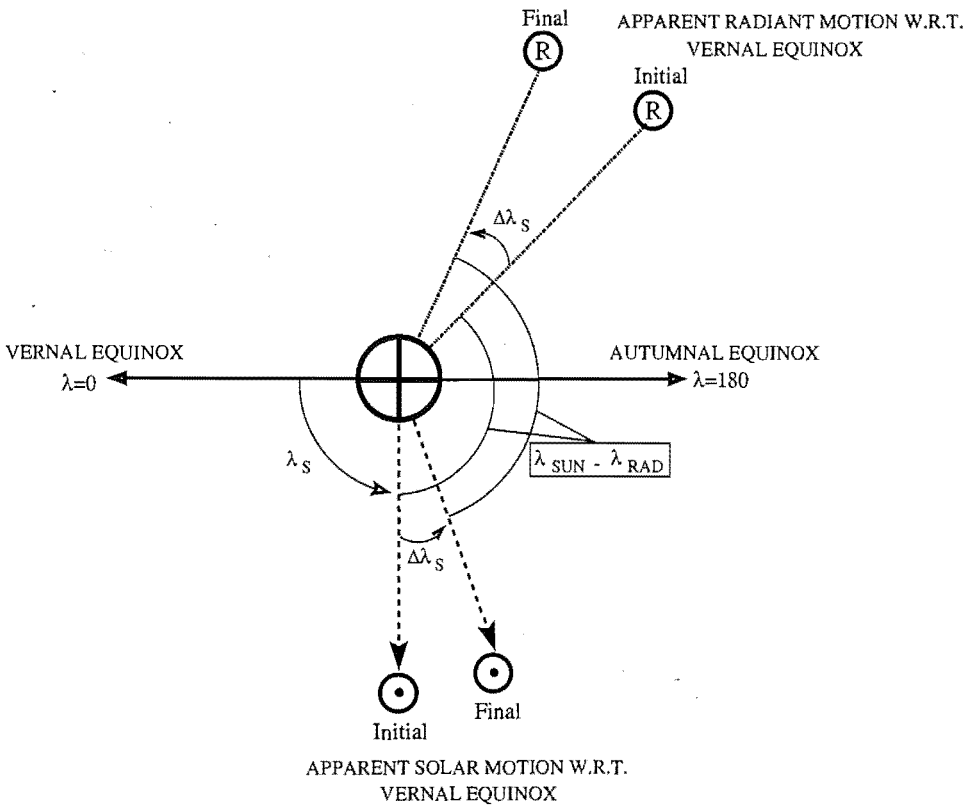

Figure 2.13: Apparent radiant motion caused by the motion of the Earth's reference frame. The Earth is shown at the centre with the Sun (⊙) and a meteor radiant appearing to rotate about it.

Unfortunately in the case of meteoroid streams the situation of a static radiant moving only due to the Earth's motion is not realised: instead the motion of the radiant is generally a fraction of that of the Sun in longitude. In addition to the motion of the Earth the physical orientation of the near-Earth meteoroid entry paths must be taken into account. For a stream approaching the Earth, with meteoroids appearing to travel on nearly parallel paths as seen over several days, an apparent motion in the longitude equivalent to that of the Sun is expected—in this case the ideal of a static radiant is valid. For any other orientations the fractional motion is observed. It is impossible to determine beforehand the likely daily motion of a shower, apart from the fact it is most likely to take place almost exclusively in longitude, hence pre-correction for stream observations over several days is not possible. The daily motion of a shower radiant must be measured and then subtracted from the observed radiant positions over time to provide an average centre radiant position for the shower. In the current study the determined daily motion is stated with respect to change in $\lambda_{\odot}$ as opposed to calendar day. The difference between these time-measurement regimes is minor, hence the magnitudes of the daily motion are negligibly affected. The motion is still termed "daily"

motion even given the $\lambda_\odot$ system used because of the ease of naming this provides. In later chapters the reader should be aware that daily motion detected in angular parameters is of course unit-less under the current regime.

2.7 Precessional Reduction

The contemporary standard is for orbital parameters to be given with respect to the epoch J2000.0. As mentioned previously, AMOR catalogues orbits with respect to epoch B1950.0, an older standard. For easy comparison with other data sets the affected orbital parameters are now given, in the current study, with respect to J2000.0.

Ecliptic longitude related parameters—the mean solar longitude ($\lambda_\odot$) and the longitude of the ascending node (Ω) are stored referred to B1950.0 in the catalogue so the following reduction is applied to correct for precession between B1950.0 and J2000.0:

$$\text{Julian Century}, J = \frac{\text{B1950.0} - \text{J2000.0}}{36525.0}, \tag{2.19}$$

$$\text{Precession} = 1.396971J + 0.0003086J^2, \tag{2.20}$$

$$\Omega_{2000} = \Omega_{1950} - \text{Precession} \tag{2.21}$$

and

$$\lambda_{2000} = \lambda_{1950} - \text{Precession}. \tag{2.22}$$

The right ascension and declination radiant angles are stored at the mean epoch of detection date in the catalogue. These should have been reduced to B1950.0 originally but were not. The correction while quite minor is now included.

The current scheme reduces directly from the mean epoch of date to that of J2000.0:

$$\text{Julian Century, } J_1 = \frac{\text{J2000.0} - \text{J}_{\text{DETECT}}}{36525.0}, \tag{2.23}$$

$$M = 1.2812323J_1 + 0.0003879J_1^2 + 0.0000101J_1^3, \tag{2.24}$$

$$N = 0.5567530J_1 - 0.0001185J_1^2 - 0.0000116J_1^3, \tag{2.25}$$

$$\overline{\alpha} = \alpha_P - 0.5(M + N \sin \alpha_P \tan \delta_P), \tag{2.26}$$

$$\overline{\delta} = \delta_P - 0.5N \cos \overline{\alpha}, \tag{2.27}$$

$$\alpha_{2000} = \alpha_P - M - N \sin \overline{\alpha} \tan \overline{\delta}, \tag{2.28}$$

and

$$\delta_{2000} = \delta_P - N \cos \overline{\alpha}, \tag{2.29}$$

where J_1 is the number of Julian centuries between the date of detection and J2000.0. The C function `ReducePresentTo2000` is used by the orbit output program `amr2asc.c` to implement all of the above equations in order to produce orbits fully reduced to J2000.0.

2.8 Summary of Available Reduced Quantities

This section summarises the available catalogued parameters available for meteoroid research, particularly those useful to orbital analysis. Further information on the catalogue contents for each AMOR orbit record may be found in Appendix B.

The fundamental parameters: inter-site time-lags (Lag_{12} and Lag_{13}), meteor detection time, meteor echo-point elevation (ψ), and range (R) combine to produce a local reference frame uncorrected meteoroid speed (V_1). These parameters are available together with the derived azimuth (A) and zenith (z) angles.

Following the reductions detailed previously, corrected pre-atmospheric quantities in both a geocentric and heliocentric sense are recorded. The corrected radiant position is given by the right ascension (α) and the declination (δ). These quantities are analogous to terrestrial longitude and latitude—the difference being that they are given with respect to an imaginary celestial sphere. The geocentric speed (V_G) tells us how fast the meteoroids are coming towards the Earth—for retrograde meteoroids this will be much faster than the corresponding heliocentric speed as V_H is combined in an additive sense with the Earth's velocity. An example of a meteoroid stream containing high geocentric velocity particles is the Halleyid stream,

the parent of the η Aquarids and Orionids meteor showers, which has an ecliptic inclination of $\approx 165°$ and a mean geocentric speed at detection of $\approx 65\ \mathrm{km\,s^{-1}}$.

The heliocentric speed (V_H) for each meteoroid is available together with the ecliptic longitude and latitude of perihelion. The latter angles are mainly used for the calculation of orbital dissimilarities.

Parameters derived from the heliocentric velocity together with the detection time (and the position of the Earth) are the orbital elements, as introduced in Section 2.5. The perihelion distance (q), eccentricity (e), inclination (i), argument of perihelion (ω), longitude of the ascending node (Ω) and semi-major axis length (a) are the reduced orbital parameters. Any two of q, e and a together with i, ω and Ω define the orbital path uniquely. The addition of the detection time allows one to trace the motion of the meteoroid in this orbital path over time.

The C program `amr2asc.c` implements a series of routines to output orbits in a form which may be read by the various MATLAB and C programs developed for this thesis. Details of this program are given in Appendix C.

Chapter 3

An Overview of the AMOR Data Set

The AMOR system has been in operation since 1990. It is experiencing an increasing degree of reliability and uptime due to a series of upgrades and constant technical supervision. This chapter presents aspects of the long-term statistical qualities of the data set obtained thus far. A particular emphasis is placed on an understanding of the inherent biases in data obtained by AMOR.

3.1 Meteor Detection Time/Date

Throughout this study the normal measure of time and date is not used. Instead, as is common in meteor astronomy, the time of year is measured by the mean longitude of the Sun ($\lambda_\odot$)[1]. This longitude cycles through 360° between vernal equinoxes (Υ). An equinoctial year containing one cycle of $\lambda_\odot$ and starting at Υ is used. This year is designated TYYYY where YYYY corresponds to the calendar year containing the initial Υ.

Why is $\lambda_\odot$ used? This variable is directly related to the longitude of the ascending/descending node at meteor detection (equation 2.12). Cyclic changes in the rate of meteor detections and in the distributions of various parameters appear naturally using this system. Inter-year comparisons are also more conveniently performed as particular $\lambda_\odot$ values correspond to the same position of the Earth relative to the Sun in successive equinoctial years.

3.2 Meteor Detection Rate Distribution

The rate of meteor detections is dependent upon the power output of the radar, the narrowness of the transmitted beam and on various diurnal and annual astronom-

[1]In the current study, for brevity, the mean solar longitude is often referred to, simply, as the "solar longitude".

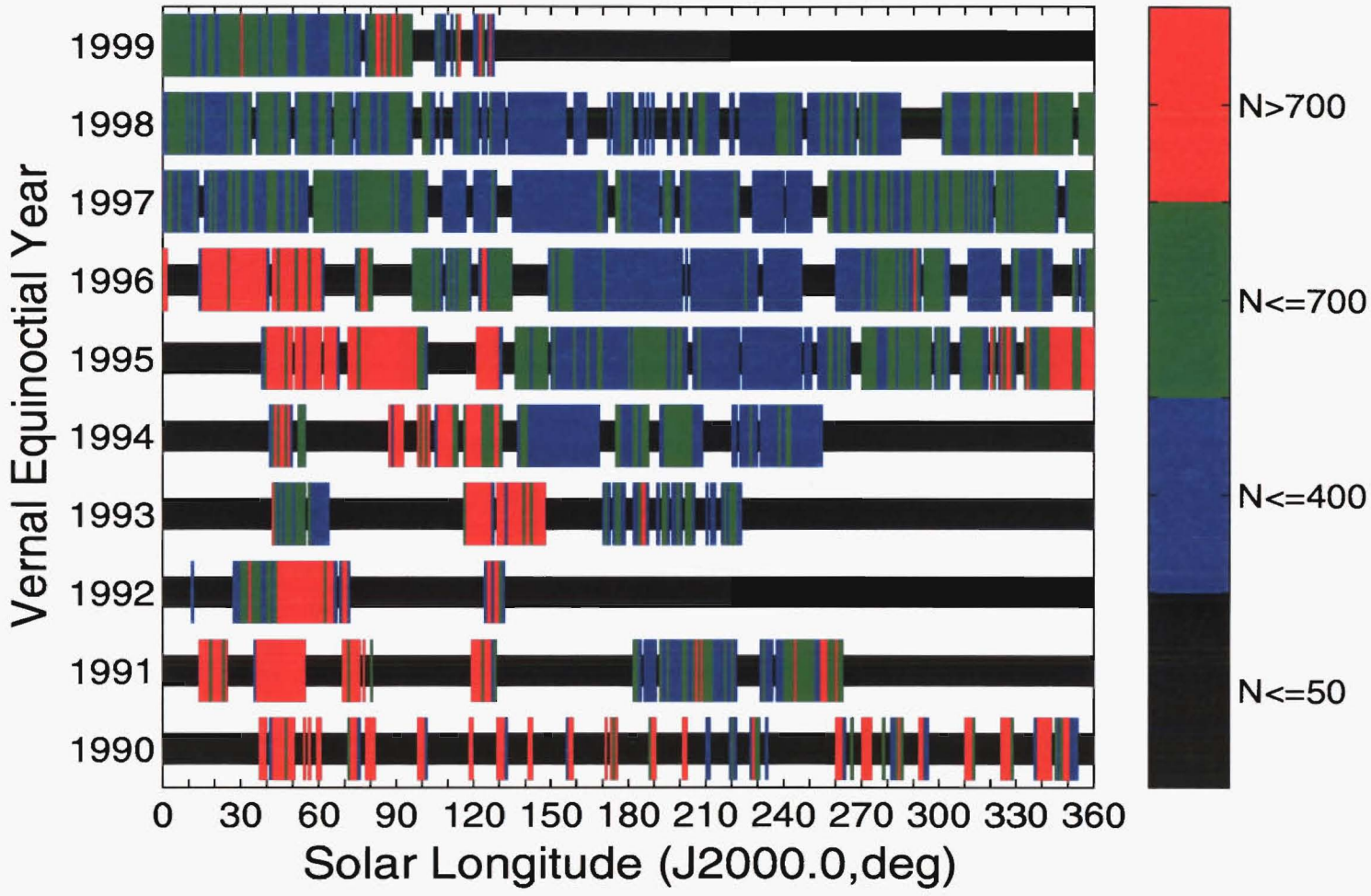

Figure 3.1: The rate of usable meteor detections. For each equinoctial year a line shows the number of orbits recorded per degree of solar longitude. Colours are assigned to each degree based on the number of orbits catalogued over that time.

ical influences. Atmospheric conditions (sporadic-E[2] and corona[3]) and equipment problems may also change the observed rate. The number of orbits reduced per day is less than the observed meteor rate as not all observations are of sufficient quality to enable the computation of a precise orbit[4].

To date $\sim 9 \times 10^5$ orbits have been reduced and catalogued, over the T1990–T1999 period. Typically several hundred orbits are reduced per day or degree of mean solar longitude. Figure 3.1 presents the number of orbits recorded over the past nine equinoctial years—the increasing system continuity is readily evident.

In T1990, the first year of operation, AMOR had good overall coverage but with many days missed due to equipment and processing limitations. T1991–93 exhibit continuity over longer periods with large gaps in between due to upgrades and system faults. In T1994 the radar entered the first year of its modern phase—here while the entire year is not fully covered, a sizeable portion between $\lambda_\odot = 90°$ and 270° shows almost continuous operation. It is extremely important to have such reliable operation in order to observe showers year after year and to systematically search for new structure in the data set.

In T1995–96, after a small gap at the beginning of T1995, reasonably complete coverage over $\lambda_\odot \in [0°, 360°)$ was achieved. One may note that where there are gaps in one of T1995/T1996 the other year does not generally exhibit a gap allowing the possibility of combining the data from both these years to create a continuous set. The homogeneity of these two years is evident in a gross sense by the similarity of their meteor detection rates.

In T1996 a Doppler winds module (Marsh 1996) was added to the AMOR system. This module was mostly separate from the core AMOR hardware and software, however due to its influence or perhaps some other unknown mechanism the rate of meteor detection decreased at this time. It is found that the meteoroid detection rates in prominent showers have decreased by the same amount as those of the sporadic component—this indicates that there has been no real decrease in the meteoroid impact rates at particular times of year, rather a change in equipment

[2]Sporadic-E interference is caused by the formation of ionised layers in the lower E-region (100–110 km height) during the daytime which provide strong reflections to the radar at times. This interference triggers false meteor detections.

[3]Coronal interference is due to atmospheric electrical discharges from high voltage supply connections at the central site.

[4]For each reduced orbit there are approximately three other meteor detection events which do not trigger on all three receiver sites or whose decay profiles are of insufficient quality. While these observations are often useful for atmospheric measurements they are neglected for orbital calculation purposes.

or in the average (long term) upper atmosphere conditions must be responsible.

Both T1997 and T1998 exhibit very good coverage with similar rate characteristics. As with T1995–96 these years may be combined so that one can obtain near continuous coverage. It is also possible to combine all of the data from T1995 to the end of the coverage of T1999. This does produce a relatively inhomogeneous data set when comparing rates: however if one is looking for shower structure which recurs year after year the inclusion of so many years of data should boast the signal (shower) to noise (background) ratio accordingly.

In the following chapters 5.3×10^5 orbits, corresponding to meteors detected between the time of the vernal equinox in 1995 to mid-1999, are studied. The equipment over this time has not changed markedly, therefore the data are expected to form a reasonably homogeneous set—the only concern here being the decrease in meteor rate in T1997 and T1998. Section D.2 lists the various data subsets used in the current study.

3.3 Diurnal and Annual Rate Variations

The Earth's orbital velocity at any time is directed towards a point called the apex of the Earth's way, this is located on the ecliptic and lags the solar longitude by approximately 90°. Meteoroids are detected most strongly when they collide with the Earth from a direction near the apex. The meteoroids detected in this region are, almost entirely, on retrograde orbits—this is because the orbital speed of the Earth has been added almost in its entirety to that of the meteoroid, thus increasing its apparent speed and therefore the ionisation density of the resulting meteor train (see Section 3.4.2). Some observers refer therefore to an apex source of meteors although it is purely an observational effect.

Due to the 24 hour rotation of the Earth about its polar axis there is a diurnal variation in the rate of meteoroids detected. This coincides with the change in the altitude of the apex—the apex transits the meridian at approximately 0600 hrs[5] and sets below the horizon at approximately 1200 hrs. Therefore the highest rate is generally obtained in the early morning as radiants may be seen both above and below the ecliptic while a dearth of meteors is experienced in late afternoon and early evening when the apex is low, on or below the horizon. Figure 3.2 presents a representative image of the diurnal variation using all orbits from T1997,

[5]Times are quoted in the local standard time at Birdlings Flat: NZST = UT + 12^h.

this picture smoothes over the variation in the diurnal variation itself between one vernal equinox and the next—sharper peaks are found about the times of the solstices with broader peaks at the times of the equinoxes. The reason for these broader equinoctial peaks is the presence of two weaker sporadic sources called the helion and antihelion sources. These are approximately 70° out of phase with the apex source and therefore transit the meridian at approximately midday and midnight respectively. The maxima of these sources occur at the equinoxes while the maximum of the apex source occurs at the summer solstice.

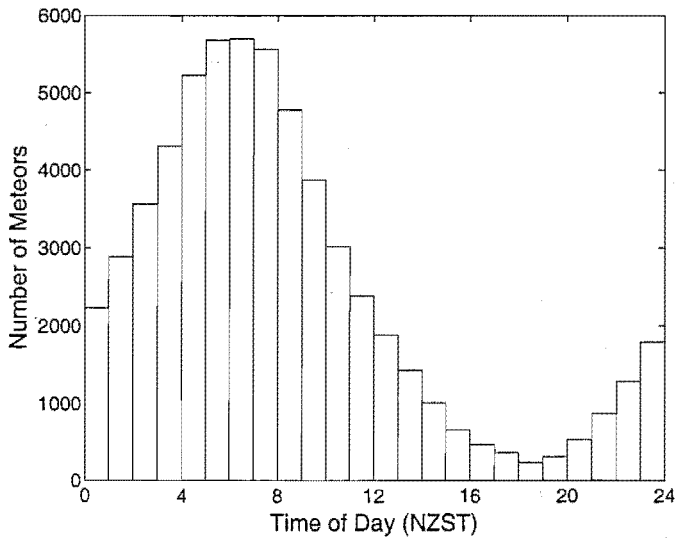

Figure 3.2: Diurnal variation in usable meteor detections (T1997).

Different types of orbits are detected at different times of day due to the variation in the altitude of the apex. When the apex is at its maximum altitude (transit) there are a greater number of retrograde than prograde orbits detected. These meteoroids are always detected with velocities greater than the terrestrial orbital velocity—the minimum geocentric speed recorded for any retrograde meteoroid detected by AMOR is 29.7 $\mathrm{km\,s^{-1}}$. Retrograde meteoroids collide head-on with the Earth, in the apex region, while prograde orbits are swept-up as the Earth overtakes their position or they may catch-up with the Earth and then collide, should their orbital speeds be high enough. Figure 3.3 schematically illustrates these regimes. As the apex of the Earth's way is the direction in which the terrestrial velocity is directed, the higher the altitude of the apex the more retrograde meteoroids will become visible due to their collision at this point. In contrast when the apex is at lower altitudes or below the horizon mostly prograde orbits will be detected as those meteoroids colliding with the Earth from the helion and antihelion source directions will then become

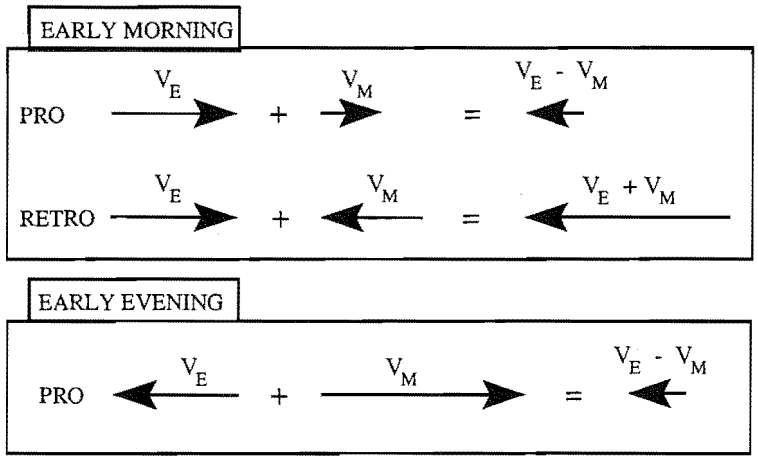

Figure 3.3: A simplistic explanation of diurnal variation. In the early evening retrograde meteoroids are undetectable as they are accelerating away from the observer while prograde meteoroids must have a large heliocentric velocity to be detected with a moderate geocentric velocity. (On the right hand side in each case the observed velocity vector is shown.)

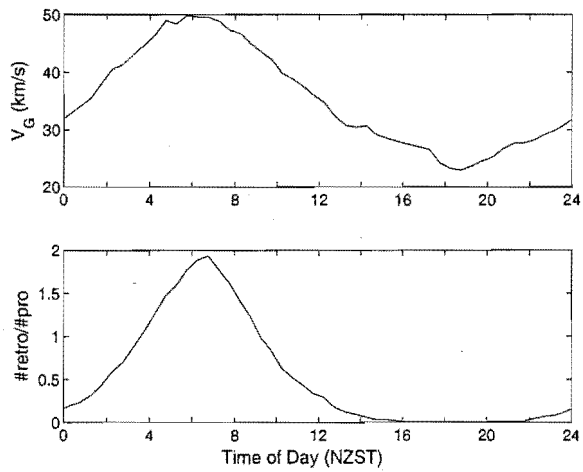

Figure 3.4: Diurnal variation in the orbital orientation and average geocentric speed of meteoroid detections. (Data from all orbits in the T1997 year).

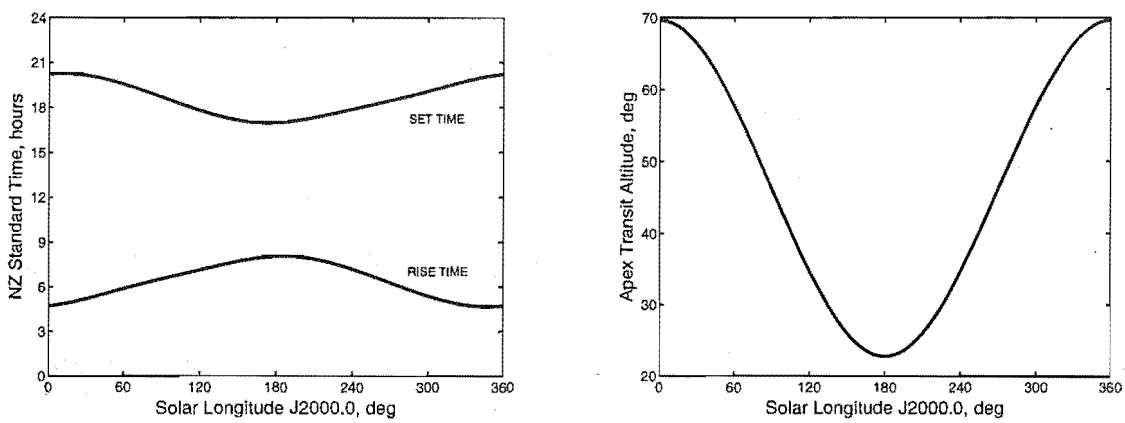

Figure 3.5: Variation in the transit altitude and rise/set times of the apex of the Earth's way as seen at the Birdlings Flat field site (latitude=43°49′30″ S, longitude=172°41′12″ E).

visible. Figure 3.4 shows the change in orbital speed and orientation regimes present in the data set, over an average day.

At the time of the vernal equinox the apex rises to the highest altitude at transit and remains above the horizon for the longest time as shown in Figure 3.5; by the autumnal equinox the opposite is true. The majority of meteor detections occur near the time of apex transit, the higher the altitude of this transit the larger the range of radiant positions which may be seen both above and below the ecliptic. Hence at the vernal equinox the maximum meteoroid detection rate is expected while at the autumnal equinox the minimum is expected. This pattern is indeed found in the AMOR data as shown in Figure 3.6. T1995 presents a very strong variation[6] as does T1996 up to the region about the autumnal equinox where the change in rate character discussed earlier appears. Thereafter the rate variation is not so strongly defined but maxima and minima at the equinoxes are still visible. Further work needs to be done to enquire into the cause of this large-scale rate change over the more recent years.

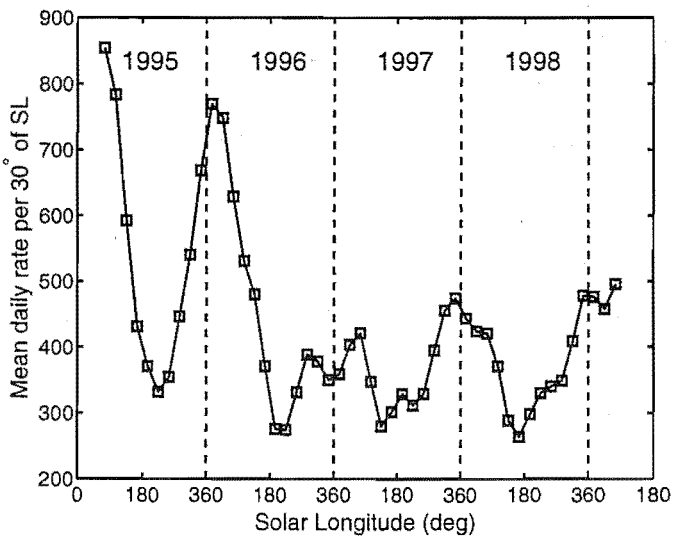

Figure 3.6: Annual meteor rate variation. The change in the rate of high quality meteor detections suitable for orbital analysis is shown. An annual cycle is visible with a maximum at the vernal equinox and a minimum at the autumnal equinox.

As with the diurnal variation there is also an annual variation in the types of meteoroid orbits which may be detected. Radiant points of meteor detections are

[6]Some of the strong variation in T1995 may be attributed to an unexplained block of time during which the radar appears to have picked up no meteoroids. This block occurred over the period $\lambda_\odot \in [120°, 180°]$ from 0400 to 0600 NZST. It is likely that for this block of time there was some strong radio interference present at that time of the year. As these times are some of the most productive, the decrease in the rate curve towards the autumnal equinox was steeper than it should have been. No other years data show the peculiar lack of meteors at these times.

generally higher in declination at the time of the autumnal equinox than at the vernal equinox—this variation corresponds to maxima and minima of the declination of apex of the Earth's way respectively. Most meteoroids are detected at their ascending nodes at the autumnal equinox while equal numbers are detected at their ascending/descending nodes as shown in Figure 3.7. This is due to changes in the maximum altitude of the apex of the Earth's way—as the maximum altitude decreases mainly meteor radiants below the ecliptic are illuminated by the radar beam while for higher altitudes radiants both above and below the ecliptic are visible.

One should remember that while the apex source is the strongest the weaker sources mentioned above have maxima at different times of the year hence while all of the changes here are ascribed to the apex source there are in fact contributions from the other sources which muddy the waters.

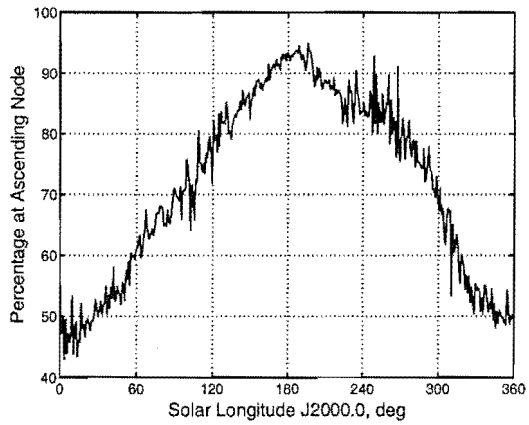

Figure 3.7: Variation in the percentage of total meteoroids detected at their ascending node (data from T1995–T1998).

3.4 Biases in the AMOR Data Set

An Earth-based radar meteoroid orbit data set is biased by two major factors. The geographic position and antenna pattern of the radar very strongly influence the speed and direction ranges in which detections may occur. The orbit of the Earth causes strong biases in the orbital distribution perceived over the year.

3.4.1 Impact With the Earth

For a meteoroid to impact the Earth its unperturbed orbit must come within $\sim 10^3$ km (velocity dependent) in order for gravitational attraction to cause an impact. The Earth's orbital plane is by definition the ecliptic, hence for an impact

to occur a meteoroid must be at its ascending or descending node at the time of detection ($\lambda_\odot$). Ω is equal to $\lambda_\odot$ for detection at the meteoroid's descending node and to $(\lambda_\odot - 180°)$ for detection at its ascending node. During one equinoctial year the complete range of possible ascending and descending orbital nodes is scanned, assuming AMOR is active continuously. With a data set spanning over several years it is possible to revisit the streams at the same nodal crossings several times.

For Earth impact the perihelion distance (q) and aphelion distance (Q) are also constrained. The perihelion distance is the closest the meteoroid comes to the Sun—hence we require $q \leq r_\oplus$, where $r_\oplus$ is the radius of the Earth's orbit[7]. Q is the furthest distance the meteoroid gets from the Sun—we require $Q \geq r_\oplus$ as otherwise the meteoroid orbit is completely enclosed within that of the Earth and may never impact the Earth[8]. In summary: based on the assumption of a circular Earth orbit with orbital radius of 1 AU, q and Q are constrained by

$$q \leq 1 \leq Q. \tag{3.1}$$

One should note that this equation only holds for elliptical orbits. Parabolic and hyperbolic orbits do obey $q \leq 1$ AU but their aphelion distances are undefined.

Figure 3.8 presents the distributions of q and Q as they relate to e. Data from T1997 are shown with firstly all orbits and then prograde and retrograde orbits separately being selected. On all of the graphs the limiting conditions imposed by equation 3.1 are clearly visible—in fact there appears to be a strong bias towards the region of these limits with increased populations appearing about $q = r_\oplus$ and $Q = r_\oplus$. Orbits with $Q \approx 1$ AU are completely constrained within the Earth's orbit, they spend longer in close proximity to this orbital path and therefore have a greater probability of detection. Likewise orbits with $q \approx 1$ AU make an almost tangential pass by the Earth's orbit and hence spend longer in the detection region. As the retrograde orbit population is almost completely a purely observational bias effect it is not surprising, when looking at Figure 3.8, that almost all of these orbits fall on the identified bias limit lines with very few falling elsewhere. The prograde population shown is quite different as more orbits well off the bias lines are seen—comparison with the retrograde population yields the essential difference between a

[7]Due to the slight eccentricity of the Earth's orbit the Earth-Sun distance ($r_\oplus$) varies over approximately 1.000 ± 0.016 AU during the course of a year.

[8]An orbit interior to the Earth's could impact Earth only if perturbed into an Earth crossing orbit. However as it would be so close to the Sun it is more likely to spiral into the Sun than out to the orbit of the Earth.

purely bias driven population and one which is sampling real orbital distributions in space.

The impact condition with the Earth also carries other important considerations. Argument of perihelion (ω), q and e are also linked together due to their common association with the meteoroid's true anomaly (ν) (Section 2.5). The conic equation states that for any orbit

$$r = \frac{a(1-e^2)}{1+e\cos\nu}. \tag{3.2}$$

According to equation 2.11, ω is equal to $(360° - \nu)$ or $(180° - \nu)$ depending on whether the meteor corresponds to an ascending or descending node impact respectively. Combining this and $r_\oplus \approx 1$ AU with equation 3.2 yields a relationship between q, e and ω which is necessary for orbital impact, and therefore detection, to occur. This is given by

$$q = \frac{1 \pm e\cos\omega}{1+e}, \tag{3.3}$$

where the $\pm$ sign relates to detection at the ascending node $(+)$ or descending node $(-)$.

The factors mentioned above imply a strong link between q, e and ω in orbital distributions seen on the Earth, as illustrated in Figure 3.9. This link is entirely caused by the observing platform and bears no resemblance to astronomical reality. As orbits can only be detected at their nodes and only then with nodes close to the Earth's orbit we are only sampling a very small proportion of the true meteoroid distribution.

3.4.2 Orbit Detection Probability

The probability of collision (per revolution) of a particle in an orbit described by particular values of semi-major axis length (a), eccentricity (e) and inclination (i) with a planet of radius R is derived by Öpik (1951) as

$$P_1 = \frac{R^2 V_\infty^2}{\pi V_G \sin i}\left[2 - \frac{1}{a} - a(1-e^2)\right]^{-\frac{1}{2}}. \tag{3.4}$$

Here the term π/R^2 may be neglected when dealing with a single planet, such as the Earth, as only a relative probability of detection is needed. All speeds in the above expression are expressed in terms of the Earth's average orbital velocity (≈ 29.76 km s^{-1})—V_G is the geocentric speed of the meteoroid and V_∞ is the speed in the atmosphere relative to the station (corrected for deceleration). For hyperbolic

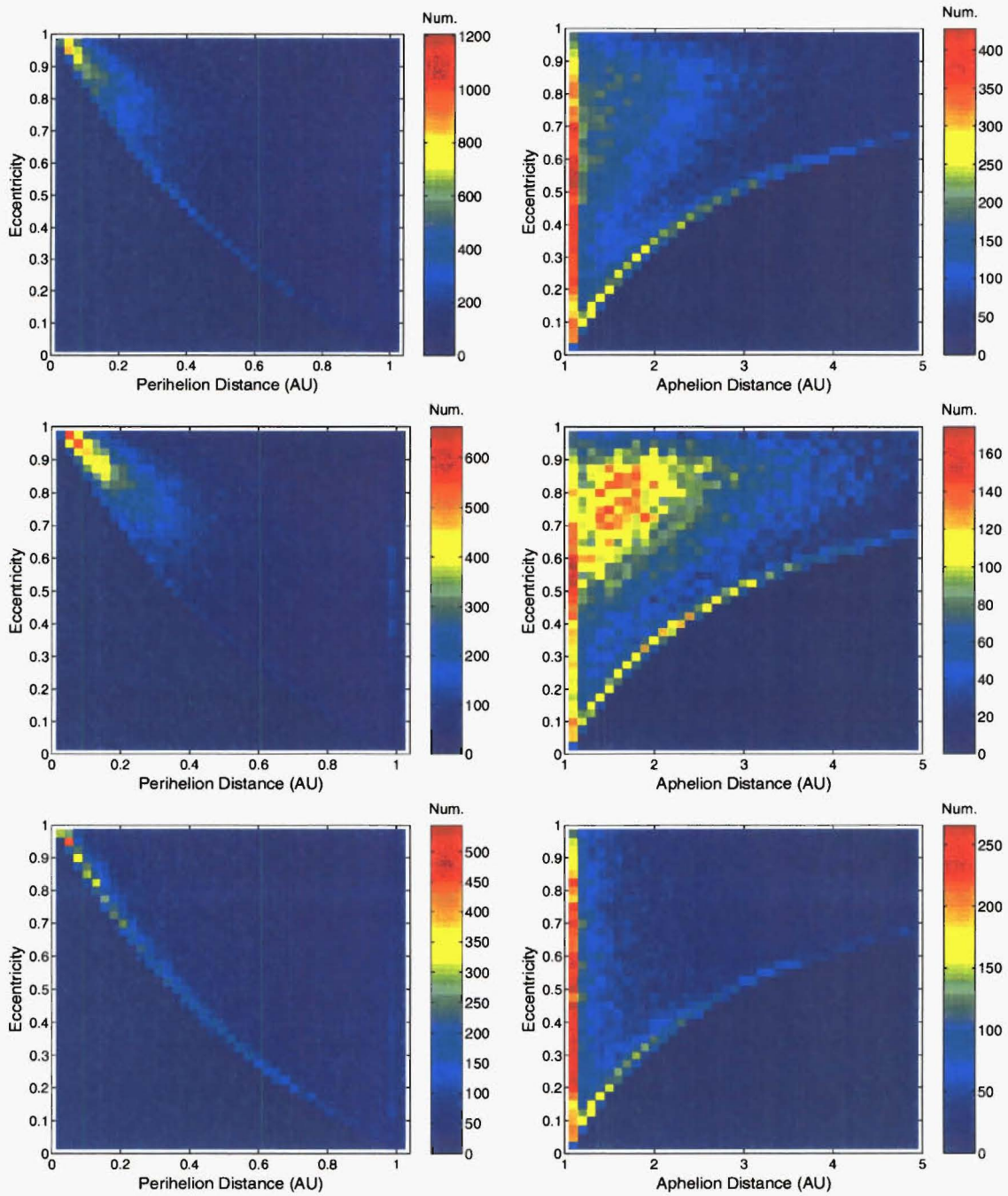

Figure 3.8: Distributions of orbit size and shape biased by impact conditions. Data from the T1997 year is used to illustrate the biased distributions in the associated perihelion distance, aphelion distance and eccentricity parameters. The first row contains the distributions for all orbits, the second and third contain prograde and retrograde selected subsets respectively.

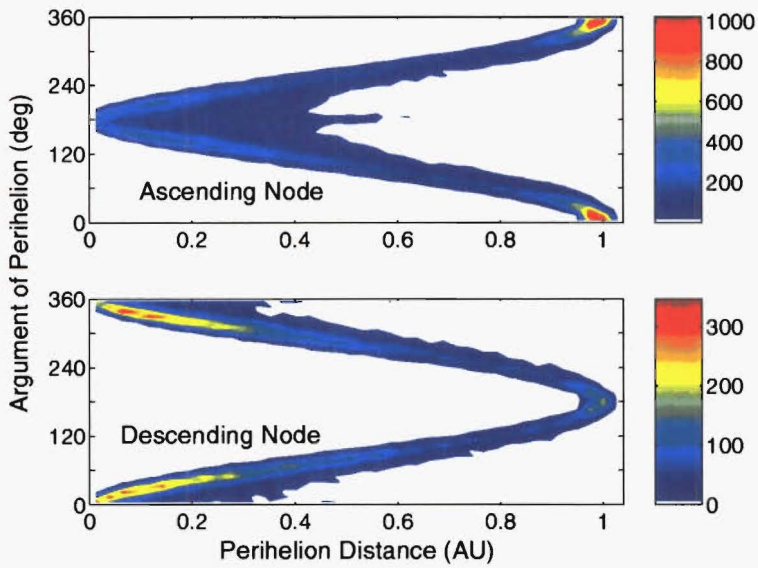

Figure 3.9: Association of perihelion distance and the argument of perihelion. Data from the 1997 equinoctial year is shown. Note that the colour scales, corresponding to number density, differ for the two graphs.

orbits the semi-latus rectum, $p = a(1 - e^2)$, is set to $p = 2q$ and $1/a$ replaced by 0.

Ḱresak (1967) makes use of a slightly modified cosmic weight in order to correct (a, e) diagrams for meteoroid orbits. Whipple (1954) uses P_1 in order to weight a distribution of photographic meteors, he defines a weighting function $(P_1 V_\infty^2)^{-1}$ and names it the "cosmic weight". The V_∞^2 term used by Whipple is included to correct for the change in the luminous efficiency of meteors as a function of their incoming speeds—faster meteoroids are brighter. In the context of equation 3.4, Whipple's V_∞^2 could be viewed as a probability of detection due to meteor train quality (P_2). For radar meteors the form of P_2 must change, here the concept of luminous efficiency is replaced by an equivalent concept: the ionisation coefficient (β). This parameter is equal to the average number of free electrons per vapourising atom. The magnitude of the scattered radio power from a meteor train is proportional to β, the power returned to the receiver increases as β increases. β is normally expressed by a power law

$$\beta = \beta_o V^k, \tag{3.5}$$

where V is the meteoroid's speed and k an exponent to be chosen by laboratory experiment. Bronshten (1983) surveys several papers on the subject and assuming an ordinary chondrite composition for meteoroids arrives at an average β given by

$$\overline{\beta} = 4.36 \times 10^{-24} V^{3.42}. \tag{3.6}$$

The detection of a meteor train depends on power received in the return signal hence a "probability" for the detection of a meteor may be written

$$P_2 \propto V^{3.42}. \tag{3.7}$$

Therefore, setting V equal to V_∞, we can arrive at a quantity P which is proportional to the probability of detection of a meteor on orbital impact and train quality grounds:

$$\begin{aligned} P &= P_1 P_2 \\ &= \frac{V_\infty^{5.42}}{V_G \sin i} \left[2 - \frac{1}{a} - a(1-e^2) \right]^{-\frac{1}{2}}. \end{aligned} \tag{3.8}$$

3.4.3 The Radar Response Function

The shape of the transmitted radar beam imprints a bias on the distribution. Meteors illuminated by high gain regions of the beam are more likely to be detected than similar meteors in lower gain regions. The antenna gain[9] (G), taken in the azimuthal centre of the beam[10], is given by

$$G(\psi, R) = R^{-1.5} \sin^2 \left(\frac{2\pi h \sin \psi}{\lambda} \right), \tag{3.9}$$

where ψ is the elevation of the meteor echo point, h the height of the antennas above the ground (for AMOR $h \approx 0.6\lambda$), λ the wavelength of the radar and R the range to the meteor train[11]. All of these parameters are known and therefore $G(\psi, R)$ can be calculated. Figure 3.10 presents a theoretical beam pattern for AMOR as defined by equation 3.9. Limits of the meteor detection region are marked on this figure corresponding to atmospheric heights 70 and 120 km respectively[12]. This figure also presents data from the T1997 year in order to show the detected distribution. This detected distribution is not a true measure of the beam pattern given the nonuniform distribution of meteors, the rotation of the Earth and the orbital motion of the Earth.

[9] Antenna gain is given in terms of elevation response for horizontal polarisation.

[10] As noted in Section 2.1 the antenna beam has a width of $\approx 2°$ in azimuth.

[11] The range is stored for all three of the receiver stations with the value for the central station being taken as representative.

[12] The meteor detection height range is dictated by the atmospheric density: above $\sim$ 120 km this density is too low to ablate incoming meteoroids while below $\sim$ 70 km most meteoroids have already ablated. It is assumed in the AMOR reduction scheme that meteor heights determined outside these ranges are a result of measurement ambiguities, as such these meteors are discarded.

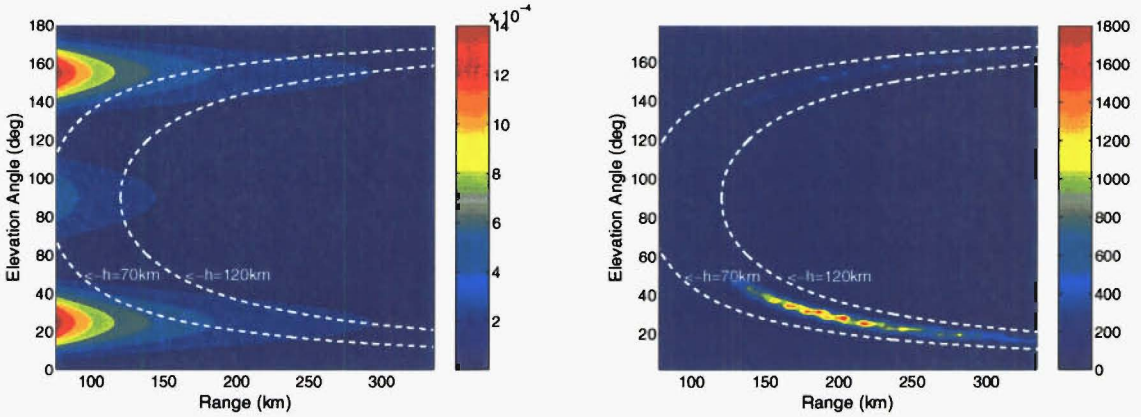

Figure 3.10: The shape of the AMOR transmitted radio beam. The theoretical shape is shown on the left and the meteor detection distribution on the right.

Another biasing factor is that due to the zenith angle (χ) of the radiant. For small χ a very large cross-section of ionised atoms is seen by the radar beam while for shallow angles a very thin cross-section interacts. A zenith correction may be simply formulated to correct this phenomenon in the form $\cos\chi$.

The antenna gain in combination with the zenith bias provides probability of detection as the gain is linearly proportional to the strength of the reflection received. Therefore one can define a probability of detection due to atmospheric and radar influences as given by

$$P_3 = \cos\chi\, G(\psi, R). \tag{3.10}$$

This function may be combined with P_1 and P_2 of Section 3.4 to give a probability of detection function combining orbital detection, atmospheric ionisation and radar response function considerations:

$$P = \frac{\cos\chi \sin^2(1.2\pi \sin\psi)\, V_\infty^{5.42}}{R^{1.5}\, V_G \sin i} \left[2 - \frac{1}{a} - a(1-e^2)\right]^{-\frac{1}{2}}. \tag{3.11}$$

3.5 Apparent and Corrected Distributions

Several factors have been presented in Section 3.4 which influence the distribution of various parameters in the data set. This section presents apparent distributions and then attempts to correct them in order to remove the principal biases. Equation 3.11 is used, for this process, but with the radar elevation pattern function removed—meteor detection at the height region in question is not much affected by the elevation function (Figure 3.10), the main effects are due to impact probability

with the Earth, ionisation efficiency and zenith angle.

3.5.1 Basic Parameters Determined at the Field Station

Several parameters are determined from the basic meteor echo profile which are then used to derive meteoroid orbits. These are the time-lags between the appearance of the profiles at each of the three receiving sites (see Figure 2.2 for station orientation): Lag_{12}, Lag_{13} and Lag_{23}. The distributions of these time-lags for T1995–T1998 years are shown in Figures 3.11(a), 3.11(b) and 3.11(c) respectively. The time-lag distributions for Lag_{12} and Lag_{13} are centred about zero. In the case of individual orbits it is often seen that one time-lag value will be large and the other near zero (Figure 3.12). Due to uncertainty considerations meteors with time-lags very close to zero are not included in the data set. There are plans to increase the pulse repetition frequency of AMOR next year, when this is done more orbits will be accepted and the quality of those just above the present acceptance criterion will be enhanced.

The elevation angle distribution shown in Figure 3.11(d) is interesting in its bi-modal distribution. There are two radar beam nodes of approximately equal strength one directed south ($0° \leq \psi \leq 90°$) and the other directed towards the north ($90° < \psi \leq 180°$). We cannot see echoes between elevations 70° to 120° due to the beams being too weak in these areas, likewise large echo ranges and elevation pattern falloff are found for elevations from the ground less than 15°. More meteors are detected towards the south due to the ecliptic being situated towards the north in combination with the specular reflection condition for detection[13].

3.5.2 Speed Parameters

The orbit is defined in terms of the heliocentric velocity which is itself defined in terms of the geocentric velocity in turn deriving from the speed in the topocentric reference frame at AMOR. The geocentric and heliocentric speed distributions are shown in Figure 3.13. Here little correction needs to be applied to the heliocentric distribution while the geocentric distribution's upper peak is removed and merged into the lower. The upper peak in geocentric speed is caused by retrograde orbit impacts in which the speed of the Earth is added, substantially, to that of the meteoroid. Due to the much increased level of train ionisation associated with

[13]There is a concentration of meteoroid orbits with inclinations close to the ecliptic, in contrast there are relatively few orbits as one approaches $i \approx 90°$ (as shown later in Figure 3.14).

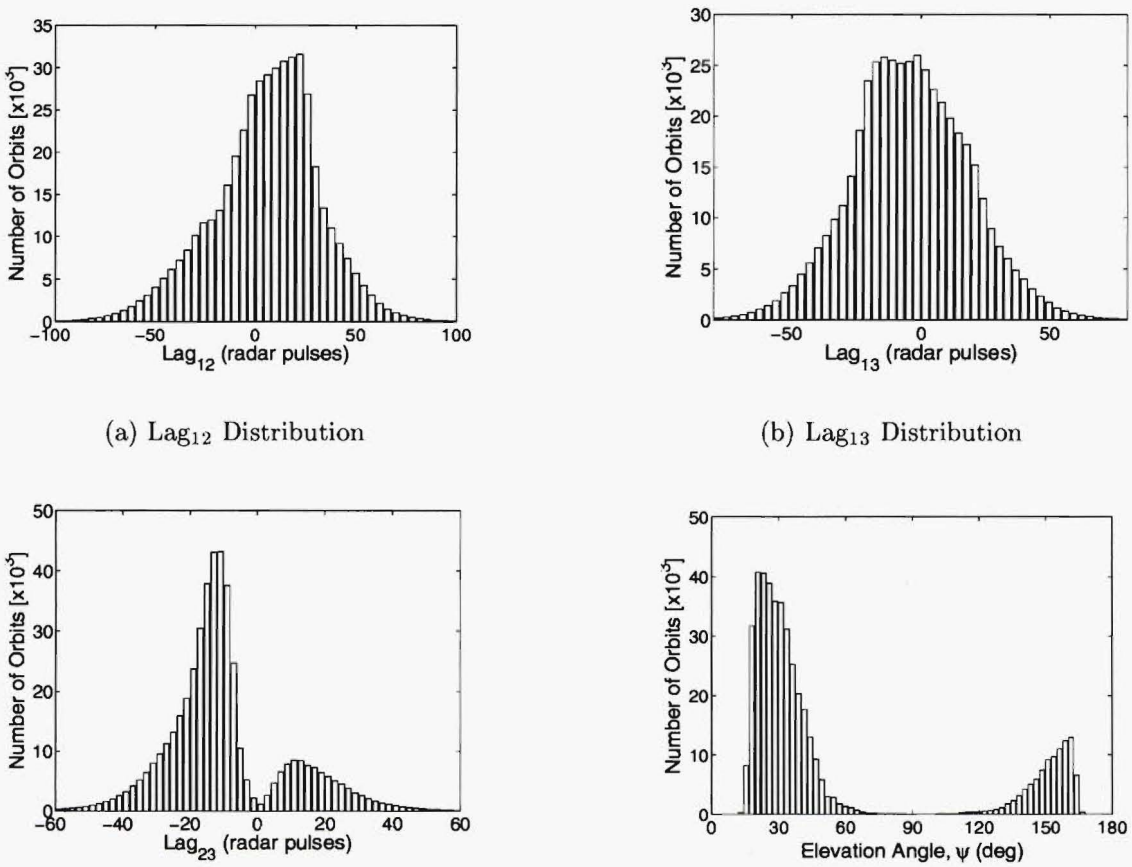

(a) Lag_{12} Distribution

(b) Lag_{13} Distribution

(c) Lag_{23} Distribution

(d) Elevation Angle Distribution

Figure 3.11: Distribution of time-lag and elevation values for T1995–T1998 orbits.

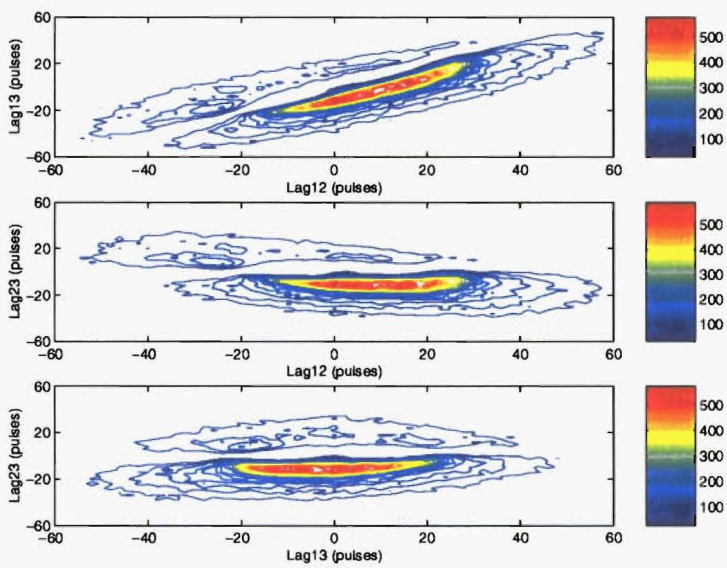

Figure 3.12: 2-D distribution of time-lag values for T1996 Orbits.

greater apparent speeds (equation 3.7) this peak develops artificially and is thus correctly removed.

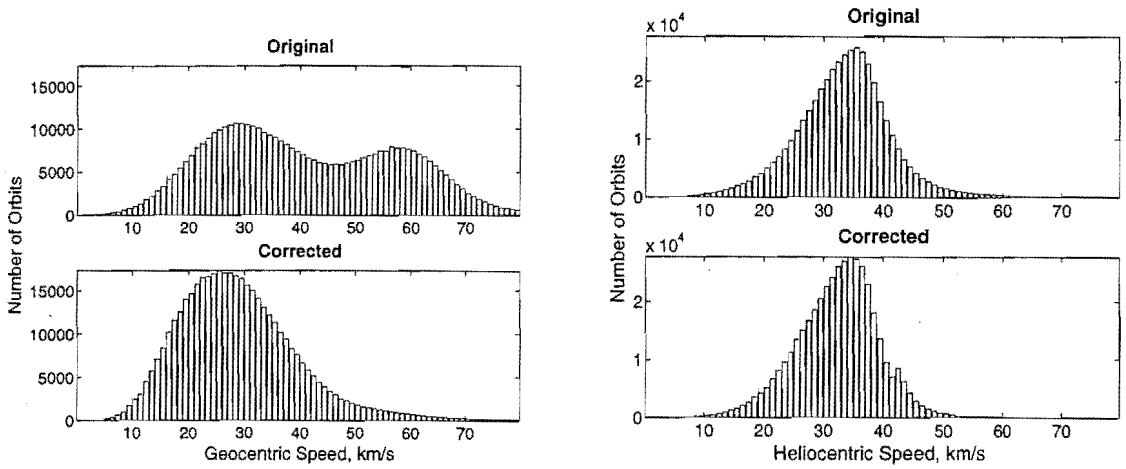

Figure 3.13: Speed parameter distributions recorded by AMOR in T1995–T1998. Both the directly observed and bias corrected distributions are shown for each parameter.

3.5.3 Orbital Orientation

The orientation of the orbit is defined by three angles: the inclination (i), the argument of perihelion (ω) and the longitude of the ascending node (Ω). The inclination angle distribution, as shown in Figure 3.14, is dominated by orbits close to the ecliptic. This bias is due to the increased probability of meteoroid detection close to the orbital plane of the Earth. The correction process recognises this and therefore the very near ecliptic population is diminished while the remainder of the prograde population, up to $i = 90°$, is raised in significance—in the corrected distribution there is an almost linear falloff in the meteoroid density as the inclination increases.

Retrograde orbits are vastly over-represented in the radar meteoroid data sets—a secondary peak appears at $i \approx 150°$ in Figure 3.14 due to this. The correction strongly diminishes the density of retrograde meteoroids in the data set to the point where they are almost insignificant. It is interesting to note that many of the meteoroid streams found in radar surveys, such as that of Gartrell and Elford (1975), are made up of retrograde orbits and the strong bias shown here may call into doubt the true size/significance of many such streams.

The argument of perihelion distribution, as shown in Figure 3.15, is very different for prograde and retrograde orbits. In the case of retrograde orbits there is a reasonably uniform distribution peaking at $\omega = 0°$ and 180°, i.e. there is an increased of detection of meteor detection when it is near perihelion or aphelion. This makes

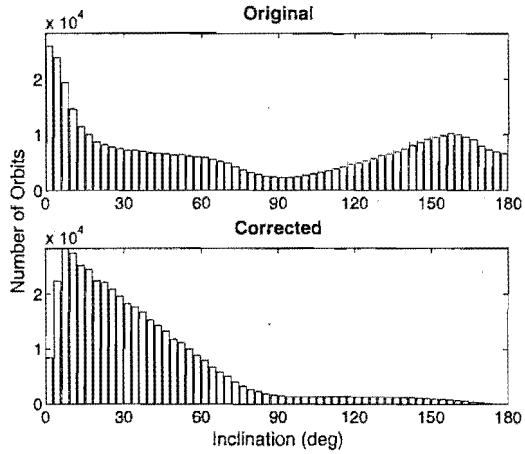

Figure 3.14: Orbital inclination distribution recorded by AMOR in T1995–T1998. Both the directly observed and bias corrected distributions are shown.

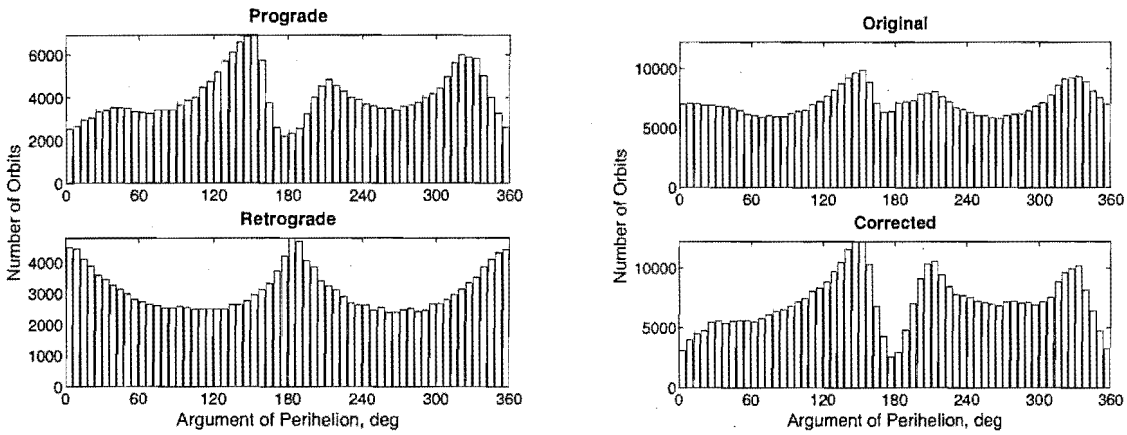

Figure 3.15: Argument of perihelion distributions recorded by AMOR in T1995–T1998. On the left the prograde and retrograde separated distributions are shown. On the right the complete directly observed and bias corrected distributions are shown.

sense as, at these points, the meteoroid will be facing exactly towards the apex of the Earth's way—for maximum apparent speed into the atmosphere. The prograde case is more difficult to interpret with the main features being reductions in the number of meteors detected at their perihelion points. At such points the Earth must often pursue the meteoroid and the apparent speed resulting will be much lower implying a lower probability of detection—the only prograde meteoroid orbits generally detected at $q \approx 1$ AU are the minority in the apex region. The corrected ω distribution for all orbits is, of course, biased strongly towards the prograde orbit population. The deficit at the perihelion/aphelion points is deepened compared with the original prograde distribution.

3.5.4 Orbit Size and Shape

The size of the orbit is given by the semi-major axis length (a), or alternatively by the perihelion (q) or aphelion (Q) distances, in combination with eccentricity (e). Eccentricity defines the orbital shape. Figure 3.16 shows the distributions in q, e and Q. As can be seen there is a very definite division between prograde and retrograde subsets. Retrograde orbits show a uniform distribution in q with a strong peak at ≈ 1 AU; similarly in Q there is a strong bias towards ≈ 1 AU. This fits in with the argument of perihelion distribution (Figure 3.15), where a bias towards perihelion/aphelion detections in the meteoroid orbit are identified. The eccentricity distribution, for the retrograde orbits, is shown to have a generally uniform structure with a decline as one approaches the circular or hyperbolic regions. There are known to be very few meteors on extra-Solar System orbits, hence the small number of orbits with $e > 1$ is explained; the diminished number as $e \rightarrow 0$ is explained by the clearing by perturbation or collision of meteoroids on such paths in addition to the limitation on the values of q and ω (equation 3.3) as one approaches this point.

The prograde distribution in q is more biased towards low-medium values with a broad peak between 0.1 AU and 0.4 AU—the secondary peak at $q \approx 1$ AU is less pronounced than that for the retrograde case and relies completely on higher inclination prograde orbits. As noted in the previous section, low inclination prograde orbits are unlikely to be detected at perihelion on Earth due to the unfavourable geometry; however higher inclination orbits may overcome this disadvantage as they approach the Earth from a quite different orientation—in fact due to their inclination $q \approx 1$ AU is very likely as their closest approach to the Sun is generally when they intersect the ecliptic: their inclination moves them quickly away. The lack of prograde orbits, meanwhile, near $q \approx 0$ AU is attributed to their being removed by solar perturbation/collision. The Q distribution is not so biased as that of the retrograde population: there is a smooth decrease as this distance increases as might be expected. The e distribution is more compact than its retrograde counterpart, this corresponds to the generally uniform (apart from perihelion/aphelion points) distribution in ω, in combination with the strong bias towards low-medium q values. Equation 3.3 cannot allow near-circular eccentricities for such q: there must therefore be a bias towards medium-high eccentricities, with a diminishing density after the parabolic limit due to the scarcity of extra-Solar System orbits.

The corrected distributions in q, Q and e are, again, biased towards prograde orbits. The maxima at low-medium q, identified for the prograde orbits, remains

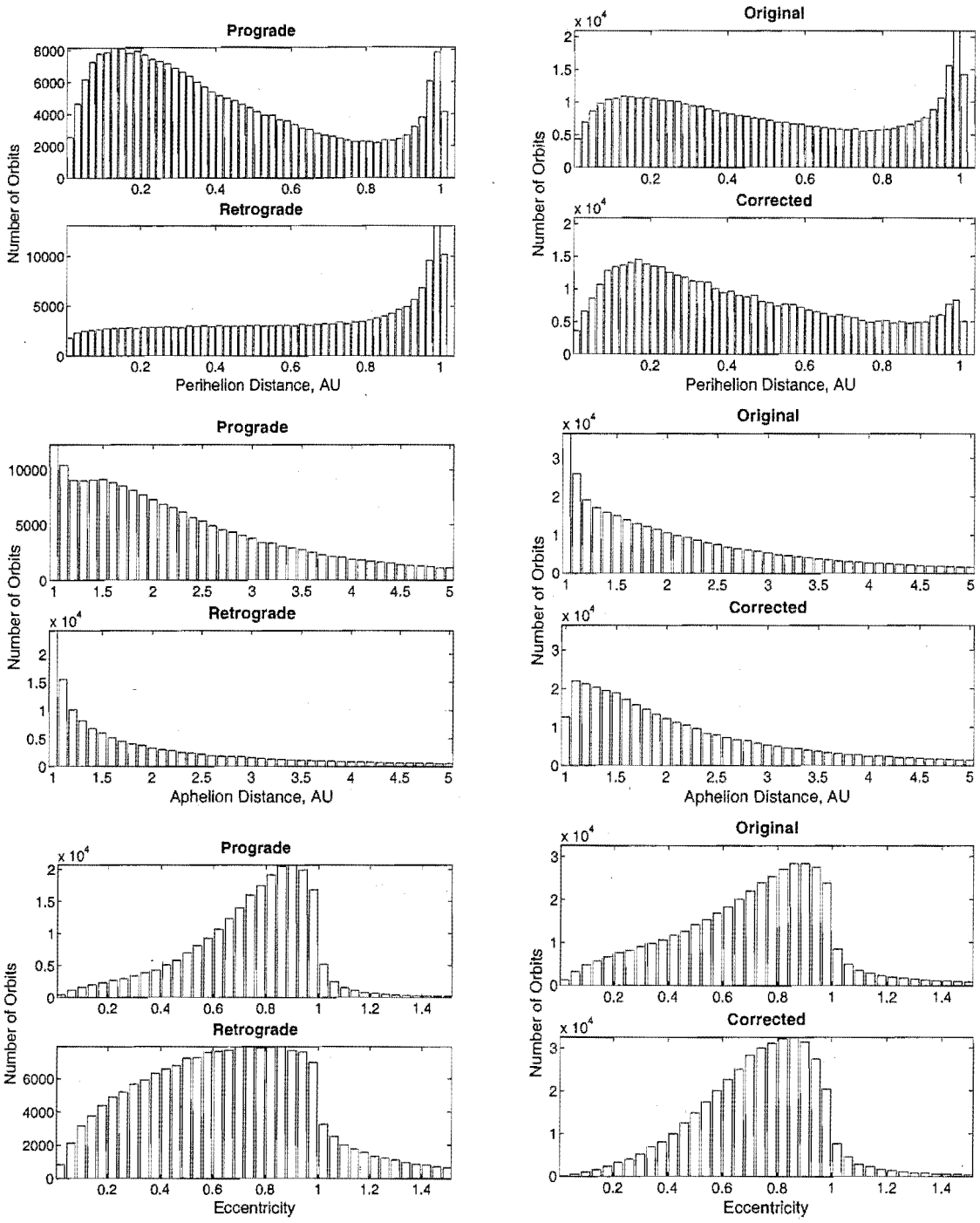

Figure 3.16: Size and shape distributions recorded by AMOR in T1995–T1998. On the left the original distributions are shown, partitioned on the basis of prograde/retrograde orbital direction. On the right the directly observed complete distribution, together with that corrected for bias effects, are shown for each parameter.

albeit in a more subdued form. The $q \approx 1$ AU and $Q \approx 1$ AU biases, particularly associated with retrograde and high prograde inclination orbits are likewise removed due to their being purely artifacts. The e distribution is similar to that for the prograde orbits with few near-circular or hyperbolic orbits being present for the same reasons as given above. The removal of most of the low eccentricity orbits removes the major link with asteroid and planetary population which both share low eccentricities. It provides a distribution in e which is more similar to the presumed progenitor bodies of most of the meteoroids: comets.

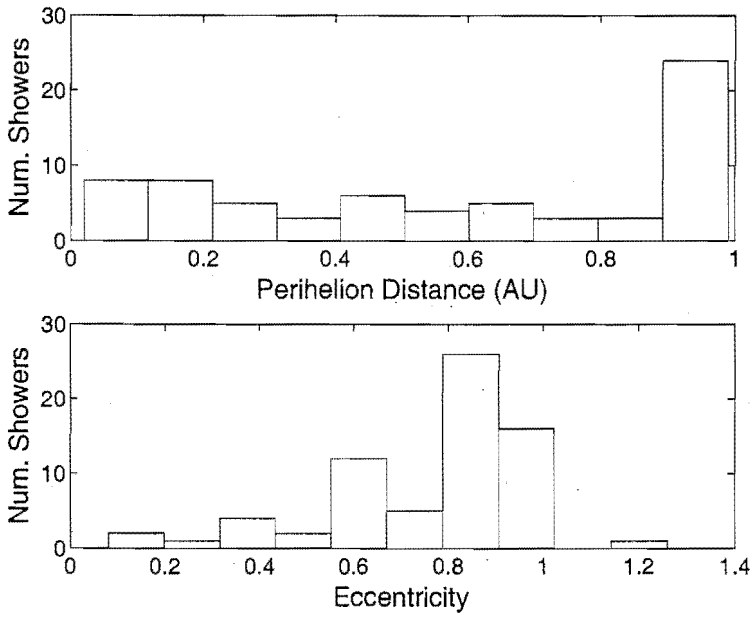

Figure 3.17: Perihelion distance and eccentricity distributions of the radar meteoroid stream orbits published in Gartrell and Elford (1975).

It is informative in the light of the biases shown in the q and e to look, once more as an example, at the results of the radar meteoroid stream survey of (Gartrell and Elford 1975). The distributions of the streams found in this data set in q and e are shown in Figure 3.17. As most of these streams are retrograde it is not surprising that there is a strong bias towards $q \approx 1$ AU. Such a bias is removed by correction in Figure 3.16, hence there is a definite risk that such results contain showers which are much larger than they truly are to the point where these may not have been considered actual showers without the magnifying effect of the bias.

3.6 Summary

A radar meteor detection system such as AMOR is strongly biased in sampling the true dust distribution in space due to a number of effects including the antenna beam function, the relationship between train ionisation and speed, the astronomical probability of collision with the Earth. This chapter has summarised the various effects and attempted to correct the apparent parameter distributions for these. It has been shown that the retrograde meteoroid population, which appears to be a large part of the data set, is in fact a very small part of the true dust distribution (Figure 3.14), as expected based on the orbital directions of most of the larger bodies in the Solar System. In the case of prograde meteors the apparent distributions have been found to be a lot closer to astronomical reality.

Chapter 4

The Meteor Radiant Distribution

When viewed in a geocentric equatorial coordinate system AMOR exhibits a strong bias towards radiants with declinations between $-30°$ and $10°$. A secondary much smaller maximum is found centred on $\delta = -60°$ which corresponds to meteor radiants from well below the ecliptic. The declination distribution is relatively constant throughout the year with variations in the more extreme measurements of declination. Figure 4.1 shows the radiant distributions taken over three years. There is a relatively sparse area between $-30°$ and $-60°$ which is caused by radiants appearing near the zenith and therefore being undetectable due to the beam pattern.

Each day all right ascension angles transit the meridian. Due to the diurnal variation in the meteor rate there is also a "gap" in right ascension detections per day over the hours of lowest rate, this feature is clearly shown in Figure 4.1. There is a strong central line shown in this diagram with two weaker lines at the edges. These lines correspond to the meteor radiant in the apex (AX), helion (HN) and antihelion (AH) sporadic sources respectively.

4.1 Bias in the Radiant Distribution

The orbital motion of the Earth, orientation of the radar system and the spatial distribution of meteoroid orbits themselves combine to produce a radiant distribution which changes on both a daily and an annual cycle. When viewed in an appropriate reference frame the radiant distribution appears to be dominated by several strong (apparent) sources of meteors. It is interesting to study the characteristics of these sources as they are clearly the most dominant feature of the AMOR data set and any shower will normally be a second-order effect when compared with them.

Early investigators (e.g. Hawkins (1956)) assume three adjacent sources designated helion, antihelion and apex. These sources are defined in a geocentric ecliptic coordinate system in which the Sun does not appear to move with respect to the Earth. Such a system has been defined in Section 2.6.1, where the ecliptic longi-

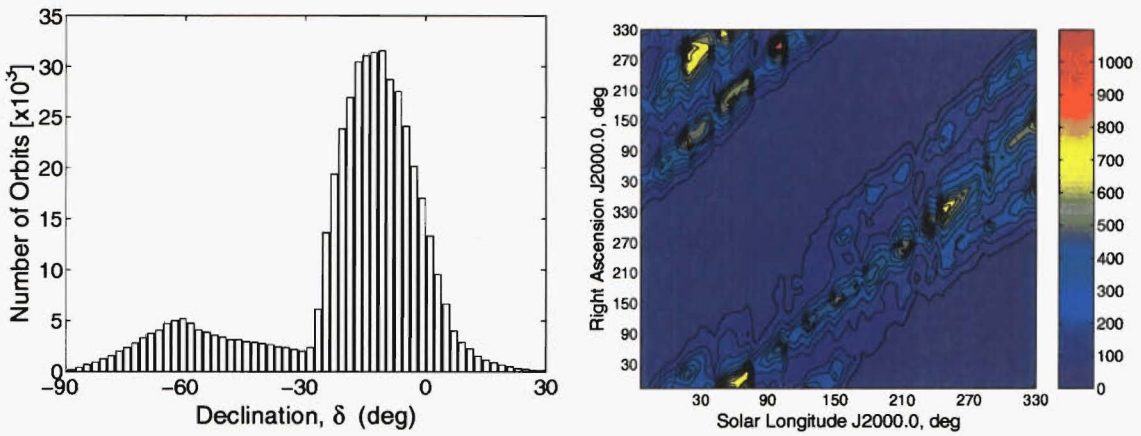

Figure 4.1: Radiant distributions recorded by AMOR in T1995–T1998.

tude (λ) of the radiant under observation is referred to the mean solar longitude at detection using equation 2.18, to give a new longitude value: λ_R.

Jones and Brown (1993) summarise the presence of the sporadic sources in a number of previous radio and photographic meteor campaigns. They extend the three-source model to include a toroidal source at a northern ecliptic latitude ($\beta \sim 60°$) and they split the AX source into three components with a northern/southern source being detected in surveys by systems in the northern/southern hemispheres respectively and a main AX source being found in all surveys near $\beta = 0°$. The HN and AH sources would be expected to occur at $\lambda_R = 0°$ and 180° if one were to take their names literally. Instead they are found to be centred on the ecliptic plane with $\lambda_R \approx 340°$ and $\lambda_R \approx 200°$ respectively.

All meteor detections from the AMOR data set in T1997 have been reduced to the geocentric ecliptic reference frame discussed above. The results of radiant density analysis in the space defined by (λ_R, β) on these data are shown in Figure 4.2. The HN, AH and AX sources are clearly evident in this diagram. The AX source is the widest in both latitude and longitude, its centre at $\lambda_R = 270°$ is very dense particularly for $\beta \in [-30°, -10°]$. There is a definite split in this source centred on the ecliptic with the part above the ecliptic being defined for $\beta > 10°$ and that to the south at $\beta < -10°$. The character of the sources within the AMOR data agrees well with other surveys. For example the source map (Figure 4.3) obtained by Jones and Brown (1993), for a survey performed using the meteor radar at Adelaide, Australia (35° S 138° E) shows good agreement with the AMOR result.

There is an obvious gap in the source distribution for almost 90° to each side of the anti-apex ($\lambda_\odot = 90°$)—this causes the well known decline in the meteor rate in

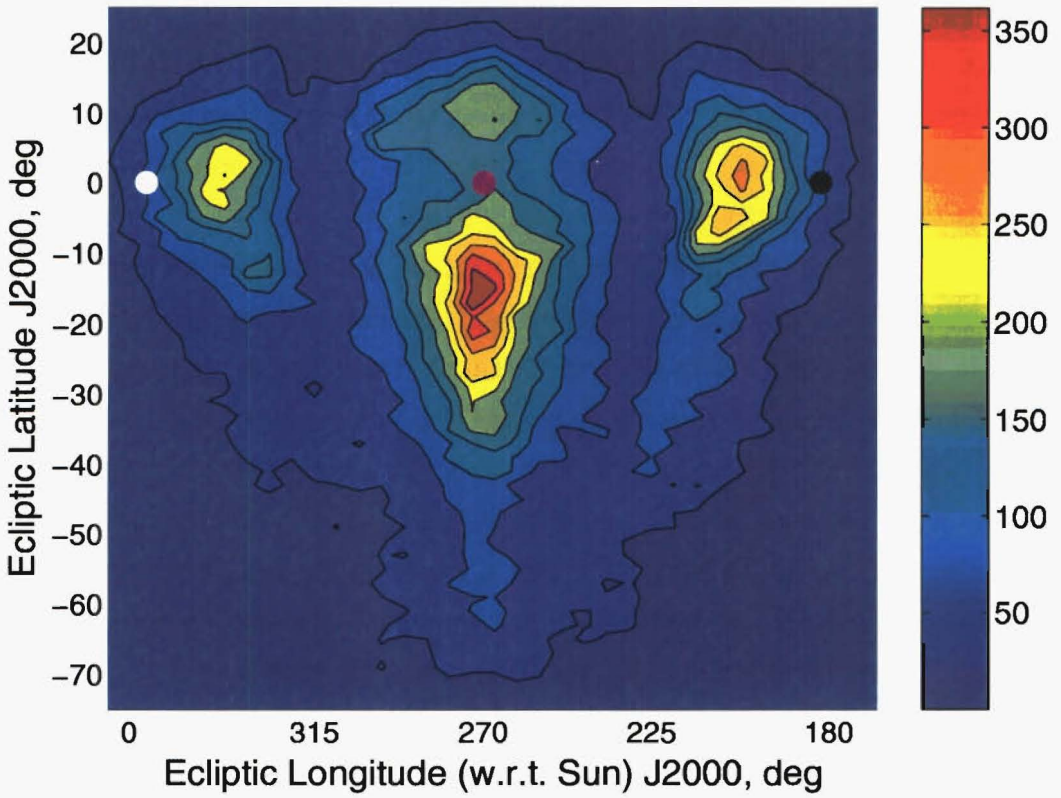

Figure 4.2: Sporadic sources of all meteors in T1997 shown in geocentric ecliptic Sun-referenced coordinates.

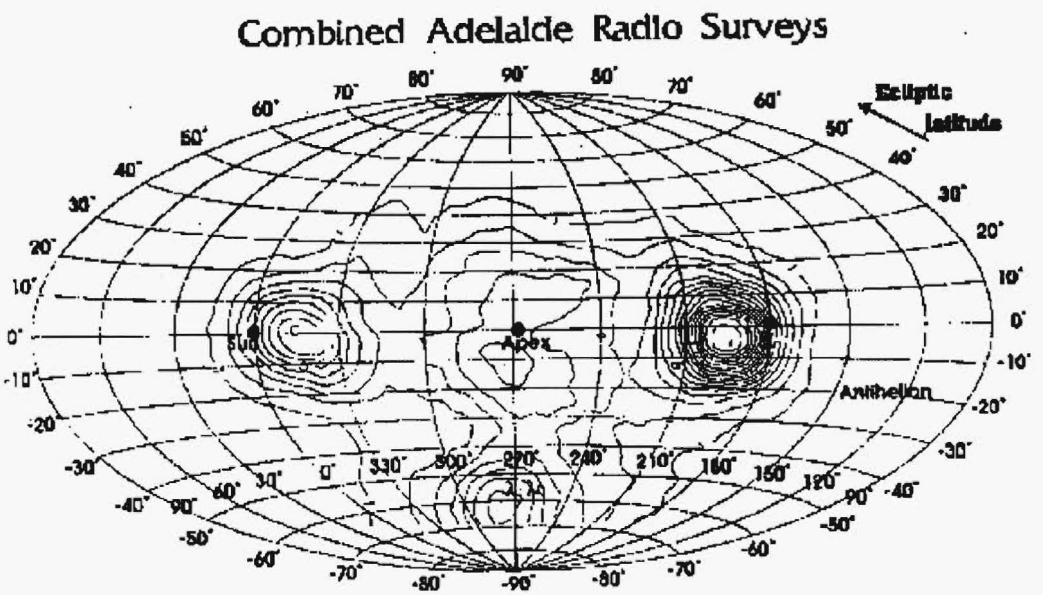

Figure 4.3: Sporadic source distributions from Adelaide radar survey data. Reprinted from Jones and Brown (1993).

the late afternoon between about 1600–1800 local time. This gap is caused by the low detection probability of meteor appearing to radiate from the direction opposite to that in which the Earth is moving—one cannot pick up retrograde meteors in this direction as the solid Earth blocks these while prograde meteors must achieve speeds larger than that of the Earth in order to achieve impact, such speeds are towards the higher range of that normally expected.

The sporadic sources defined in Figure 4.2 are averages over an equinoctial year. These sources actually change in shape and position, particularly in their average latitude, as the Earth orbits the Sun. Assuming a uniform distribution of orbits in solar longitude (azimuthal symmetry), the sporadic sources should not change in intensity or latitude throughout the year, if one assumes there to be an homogeneous population of meteoroids, with the highest density closest to the ecliptic, perfectly probed by the Earth. When one studies the motion of the sources throughout the year the results clearly support either an inhomogeneity in the meteoroid population or severe biases caused by Earth's orbital position over time.

In order to investigate the changes in the characteristics of the sporadic sources over the course of a year all available data from T1995–T1999 have been used. This data set comprises in excess of half a million orbits. Twelve virtual months have been formed which consist of 30° of solar longitude each, with all radiant detections being used to form an average structure for each month. The data set is divided into pixels of size 3° in longitude and 2° in latitude. For each virtual month the data from each equinoctial year is first analysed separately in order to normalise the strengths of the various pixels against those surrounding in that year. These normalised pixel strengths are then added together to form a picture for the month supported at all times by at least three years data with up to five years at times depending on equipment down-time. The final results are presented using a logarithm of the arbitrary pixel strength achieved, with all months using the same intensity scale to enable comparisons.

The use of several years of data to form virtual average months is justified by examination of the radiant distributions for each year. It is found that these distributions exhibit a high degree of similarity for the same period over the different years—the only difference being the variation over the years, due to equipment/atmospheric fluctuations, of the number of meteors detected in the month. These fluctuations are dealt with by the normalisation. Poole (1997) conducts a similar study into HN and AH sources in his Grahamstown, South Africa (33.3° S,26.5° E) all-sky meteor

radar data. He combines 8 years of data and finds that the inter-annual activity differences for a given month have upper limits lying between 10% to 30%—this lends support to the exclusion of an in-depth study of the annual variation in the AMOR data.

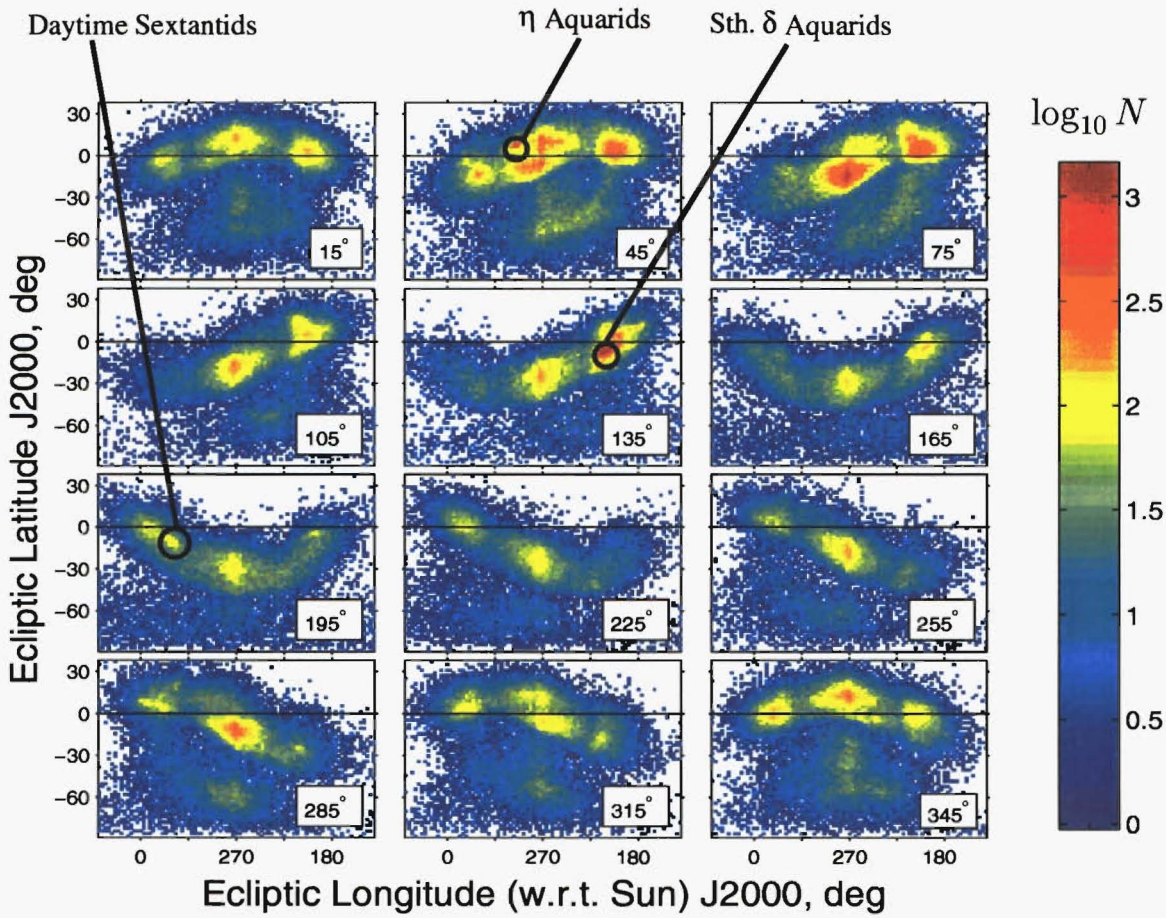

Figure 4.4: The radiant distributions (ecliptic coordinates) for the twelve virtual ($\Delta\lambda_\odot = 30°$ wide) months in the AMOR data set. Data from T1995–T1999 years are used with the normalised rates per region being used to form this composite picture. Each pixel is 3° by 2° and the ecliptic longitudes are given with respect to that of the Sun, viz equation 2.18. Note that the scale is logarithmic and in arbitrary units.

The source distributions for all meteors in the data set are presented in Figure 4.4. Cursory inspection reveals large-scale changes in the positions of the sources over the course of the year. The HN, AH and main AX sources are well defined in all of the months with the southern AX source being defined only in the months near to the vernal equinox. The main AX source is the strongest; this is to be expected as the AX source consists of meteors whose apparent speed is much greater than their orbital speed due to their detection having occurred from the direction in which the Earth's speed is most strongly added. For this reason most of the orbits de-

tected in the AX source are retrograde—the Earth must "catch-up" with prograde meteors from the AX while it "collides head-on" with retrograde meteors. In fact the AX source is the only one from which retrograde meteors are detected—this is easily shown by partitioning the meteors on the basis of inclination: the source distributions for retrograde and prograde meteors are displayed in Figures 4.5 and 4.6 respectively.

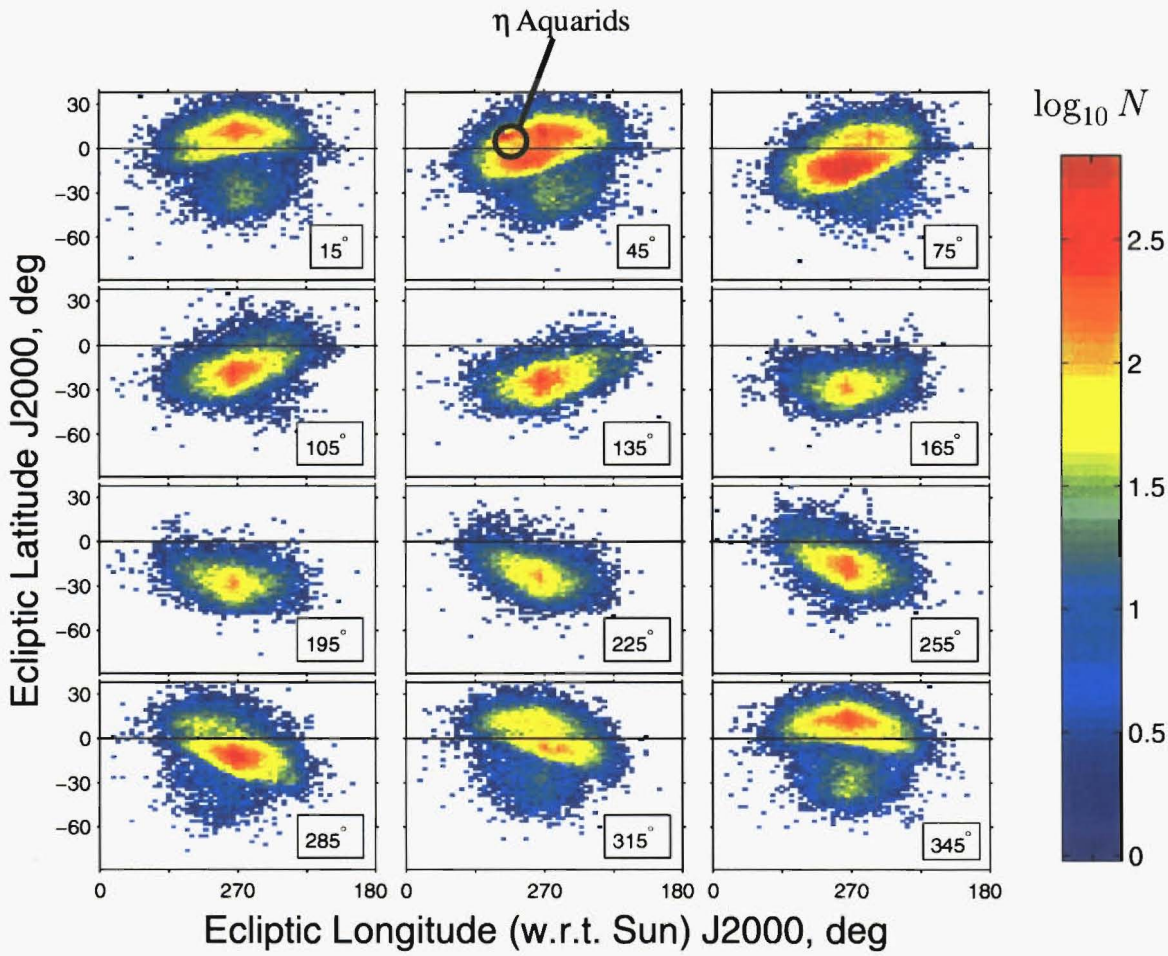

Figure 4.5: The average monthly radiant distributions (ecliptic coordinates) for all retrograde orbiting meteors in the AMOR data set. See Figure 4.4 for further details.

The source picture becomes much clearer once the retrograde and prograde orbits are split-up. Looking first at the prograde case (Figure 4.6) the HN and AH sources are well defined and oscillate in latitude completing a cycle over the course of a year. One may wonder why these sources should exist—what is so special about positions approximately 30° and 210° from the Sun? Sources are found in these positions owing to their closeness to the ecliptic, the plane at the centre of the densest distribution of meteoroid orbits. It should be noted that as the sources

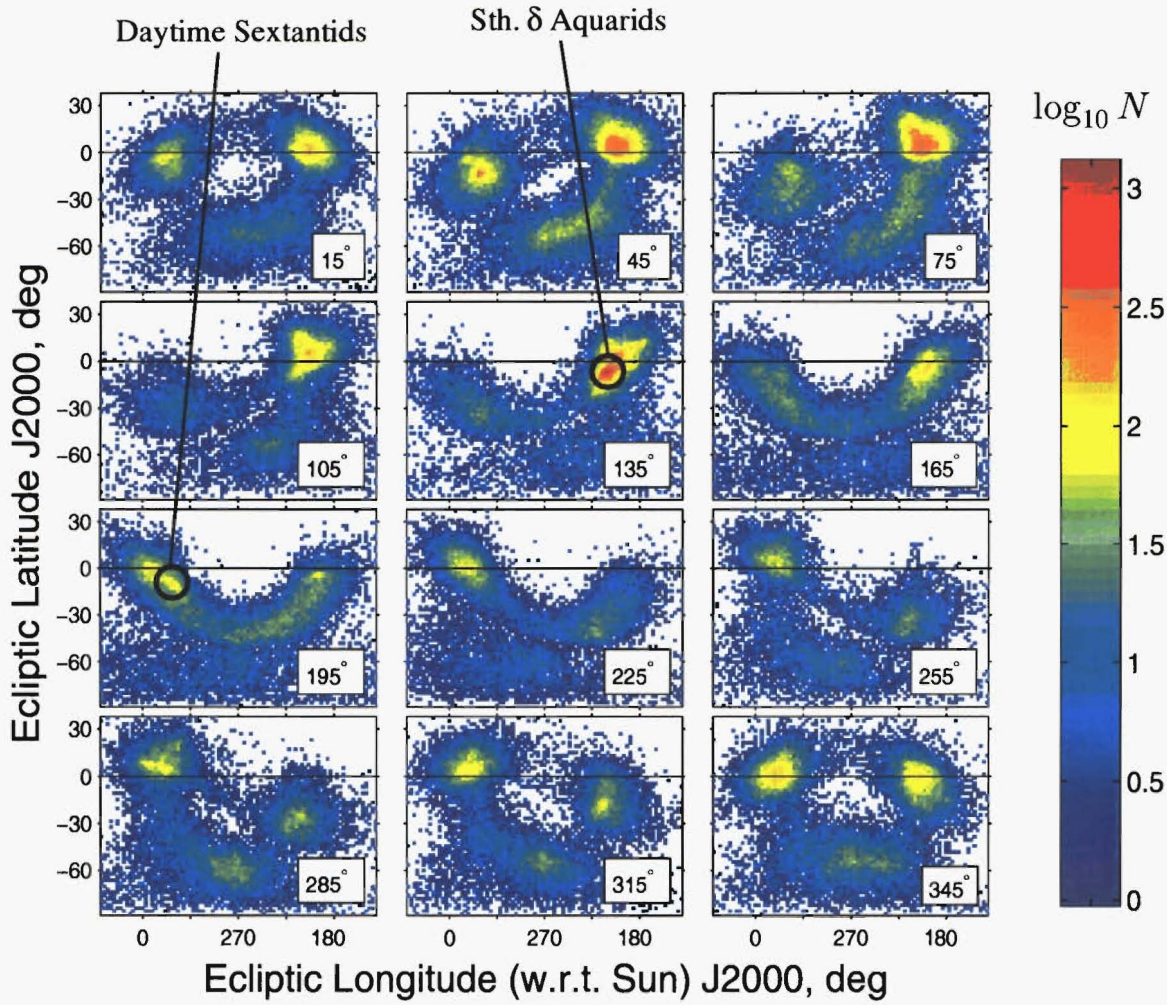

Figure 4.6: The average monthly radiant distributions (ecliptic coordinates) for all prograde orbiting meteors in the AMOR data set. See Figure 4.4 for further details.

move above or below the ecliptic their strength diminishes. The oscillation of the sources, as mentioned earlier, is not readily understandable until one understands that the symmetry of the radar system is with respect to the equator of the Earth and not to the ecliptic. The AMOR antenna is aligned along the East-West parallel and it radiates in a narrow azimuthal beam towards the north and south. The angle made by the equator to the celestial equator then determines the latitude of the sources. This is clear when one examines Figure 4.6 and finds at the time of the equinoxes, when this angle is zero, that the sources centre about the ecliptic latitude with extrema in the centre latitudes being reached in between equinoxes about the time of the solstices.

The latitude of the Earth's equator with respect to the ecliptic changes between vernal equinoxes as shown in Figure 4.7; the motion of the sources in latitude can

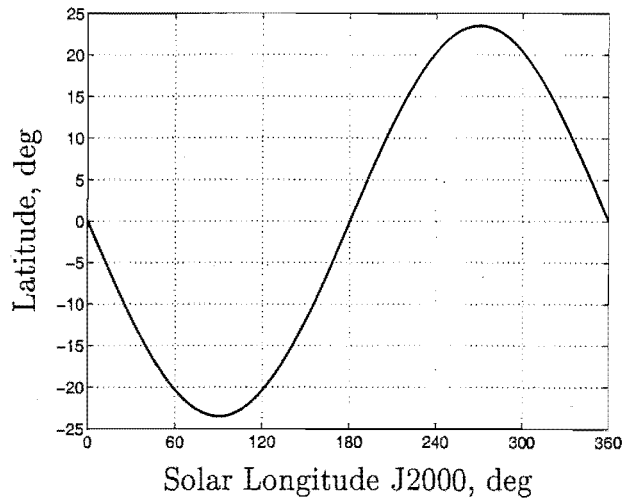

Figure 4.7: Variation in the altitude of the Earth's equator w.r.t. the ecliptic as the Earth moves in its orbit.

be related to this. As Figure 4.4 shows, the HN source falls below the ecliptic from the time of the vernal equinox up to that of the autumnal equinox; it then rises above the ecliptic for the second half of the year. This cycle follows that of the equator inclination cycle verifying that one is dealing with an Earth-related biasing effect as opposed to a real change in spatial density of meteoroids. The AH source also performs exactly as expected with a cycle 180° out of phase from that shown in Figure 4.7. The AX source shown most clearly for retrograde meteors in Figure 4.5 also follows this trend with its latitudinal centre on the ecliptic occurring at $\lambda_\odot = 90°$, i.e. 90° after the HN source. While the geocentric ecliptic sun-referenced system is used to help remove reference system induced apparent motion of the radiant, a similar equatorial system may be used to clearly display the symmetry of the radiant distribution with respect to the equator. Figure 4.8 shows the equatorial system where the right ascension (α) is referenced to the right ascension of Sun ($\alpha_\odot$) by

$$\alpha_R = \alpha - \alpha_\odot. \tag{4.1}$$

Over the course of the virtual months this distribution does not change markedly in declination. The only value which changes then is the right ascension of meteor detections. This picture is consistent with Figure 4.1 and should be compared with the large-scale shifts in source radiant latitudes experienced in the complementary Figure 4.4.

The reasons for the change in average latitude of the sources are now well established. As a source moves further from the ecliptic, its intensity weakens, showers within such a source region may only reasonably be detected when the source is

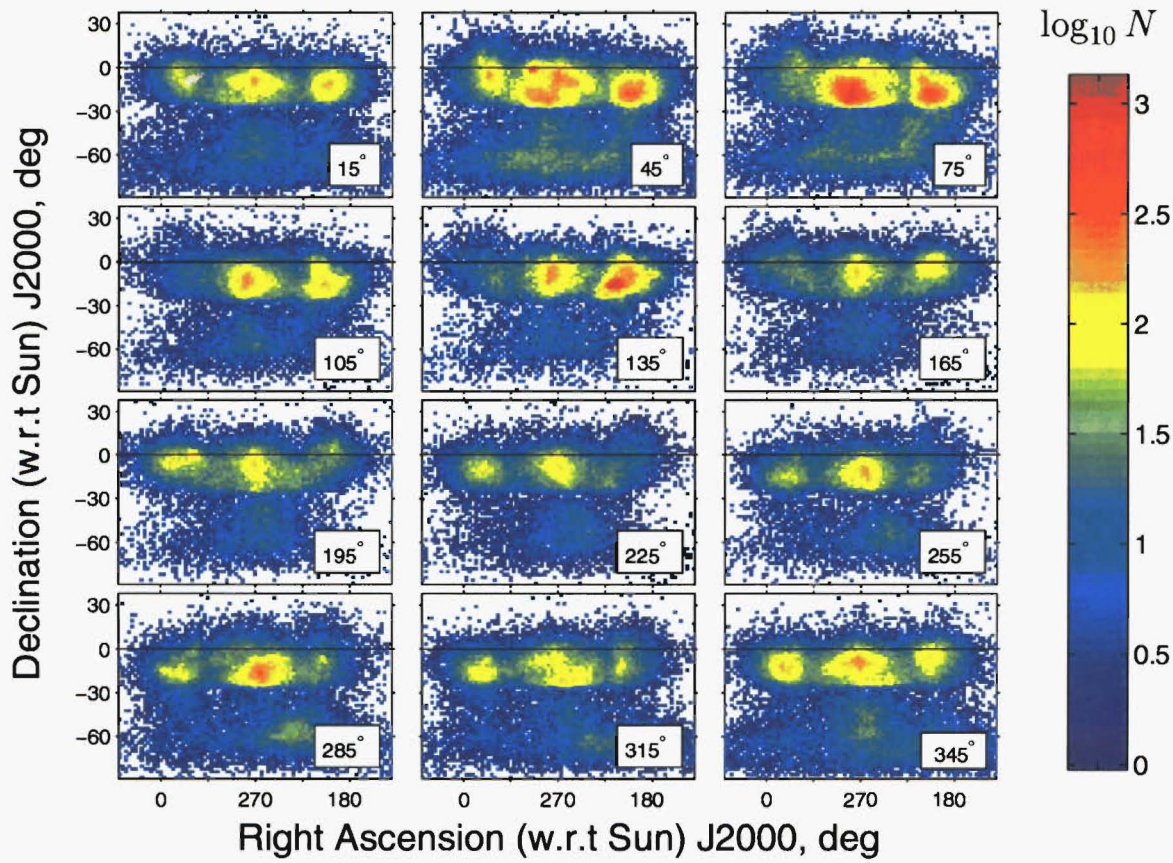

Figure 4.8: The average monthly radiant distributions (equatorial coordinates) in the AMOR data set. The declination of the celestial equator is marked at $\delta = 0°$. See Figure 4.4 for further details.

near to the ecliptic. It becomes less and less likely for detection to continue as the source moves its centre away from the ecliptic and in so doing sometimes almost completely disappears, an example of which occurs for the HN source in the fourth virtual month of Figure 4.4. This places a fundamental time limit of two to three months on a shower detection, although most detections last for much shorter spaces of time.

Even given the monthly averaging of the current part of this study, several major showers are in fact readily visible. These are identified in Figures 4.4, 4.5 and 4.6. The only obvious shower to be found in the AX region is the η Aquarids. The Daytime Sextantids is found in the HN region and the Southern δ Aquarids is found in the AH region. No other showers are immediately visible: however that may simply mean that such showers only last for a few days and/or have been split across the month boundaries, rendering it difficult to see them. A systematic search is carried out in later chapters to search for known and unknown showers within the radiant distributions in the AMOR data set. These searches use not only the

radiant positions and time of detection of the meteors but also the geocentric speed of the incoming particle. There is no doubt that such speed discrimination makes the detectability of a shower stronger against the background.

4.2 An Exact Definition of the Sporadic Source Regions

It is important in the current study to have an exact definition of the location of the sporadic source regions in order to form boundaries for analysis of these regions. Figure 4.9 presents the average radiant position and geocentric speed distributions from all meteors observed in T1995–T1999. These distributions are further partitioned based on whether the originating meteoroid was on a prograde or a retrograde orbit. The Sun-referenced geocentric ecliptic longitude shows a tri-modal structure for prograde meteoroids and a uni-modal structure for retrograde meteoroids. The AH and HN peaks are fitted by Gaussian curves, bounds to them are set by taking limits at the 2σ points on the inward apex side and at 3σ from the mean on the other side (as shown in the figure). The prograde AX source is assumed to lie between the 2σ boundaries imposed by these vastly stronger sources. The retrograde AX source meanwhile is very well defined as shown to the right of the figure.

It is interesting to note, in passing, the relative amplitudes of the AH and HN peaks, in the longitude distribution, of Figure 4.9. This figure shows five years of data and while it is true that due to gaps in the time-coverage there will be strong biases on these peaks, there is nevertheless such a strong difference between these peaks that it is unlikely that the unequal time-coverage is the only cause. Jones and Brown (1993) notes similar differences in the relative number of meteors detected in each of these sporadic source regions in the various surveys summarised therein. There is no reason that AH and HN sources should differ as they are sampling the same dust distribution from different sides of the Earth. The only possibility, also discussed by Jones and Brown, is that atmospheric conditions during the daytime make detecting meteors more difficult. For example the sporadic-E interference condition only occurs during daylight hours, resulting as it does from the interaction of the wind conditions induced by solar radiation and meteoric ions deposited aloft by incoming meteors themselves. Indeed the diurnal variation in meteors, as shown in Figure 3.2, shows little influence from meteors occurring about the time the helion source is expected to peak ($\approx$ 1200 hrs); the overwhelming population comes from the peak times of the apex and antihelion sources ($\approx$ 0600 hrs and $\approx$ 1800 hrs

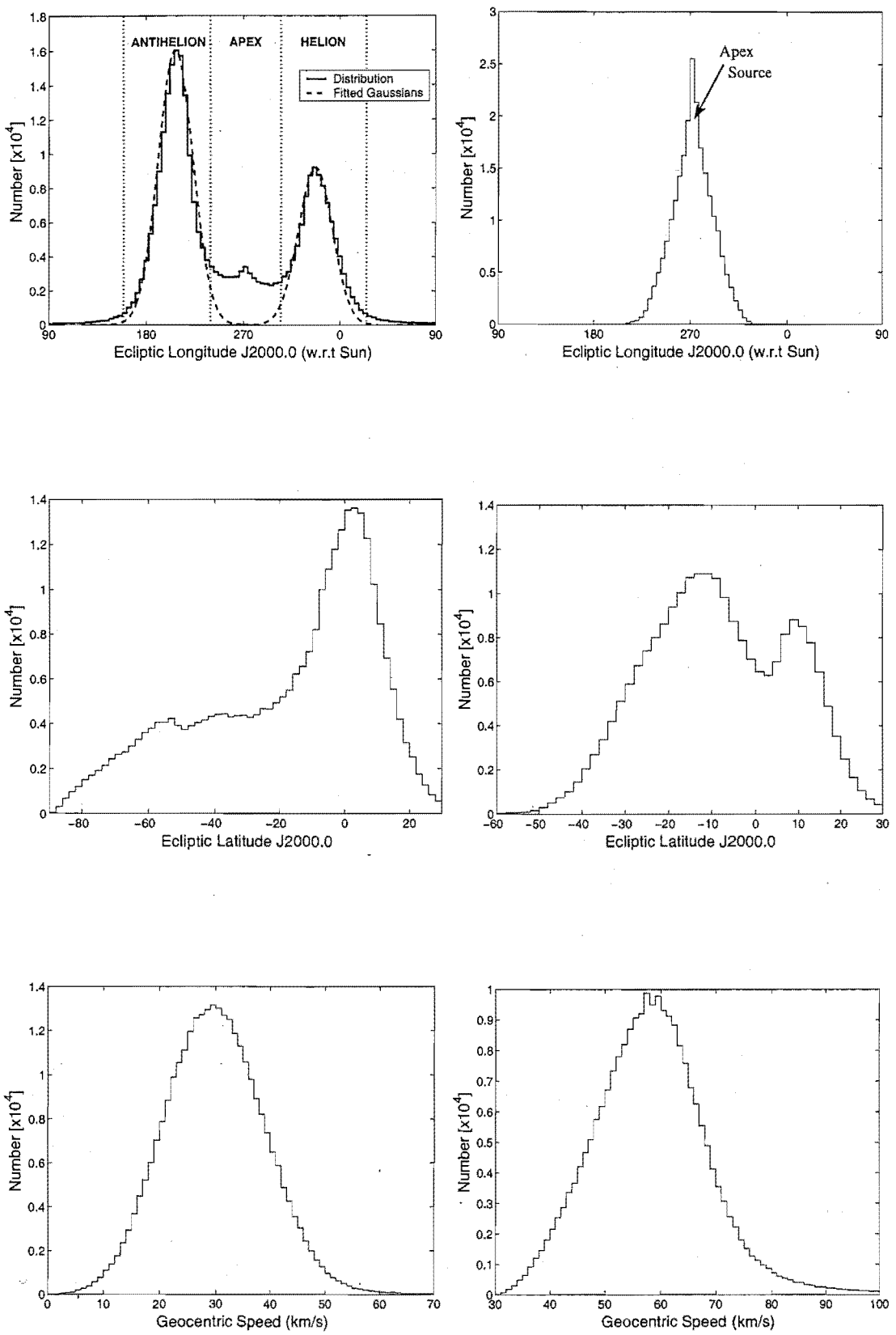

Figure 4.9: Gross distributions of the geocentric Sun-referenced ecliptic coordinates for meteors from T1995–T1999. The data set is partitioned according to the orbit rotational direction of the meteoroids: Prograde meteors are shown on the left and retrograde on the right. The sporadic source regions are identified on the longitude distribution plots; the AH region is defined by $\lambda_R \in [150°, 240°]$, the HN region by $\lambda_R \in [300°, 30°]$ and the AX region by $\lambda_R \in (270°, 330°)$.

respectively).

The latitude distributions reflect earlier discussions on the changing locations of the sporadic sources throughout each year. In the prograde case there is a strong bias towards near-ecliptic latitudes with a smooth curve extending to near-polar latitudes where the numbers gradually taper off. In the retrograde case the distribution is more Gaussian-like and centred about $\beta \sim -15°$, this is due to the fact that most retrograde meteors are simply a result of the observation bias—the average position of the apex of the Earth's way corresponds to the peak of the declination profile seen by AMOR which is at $\delta \sim -15°$. The geocentric speed distributions are very close to Gaussian about means of 30 $\mathrm{km\,s^{-1}}$ and 60 $\mathrm{km\,s^{-1}}$ respectively.

4.3 The Relationship of Meteoroid Geocentric Speed to Radiant Position

Up to this point the meteor radiant distribution has been considered apart from the speed at which the meteoroids are entering from these radiant points. There is a strong link however between speed and radiant position—the latter defines the direction in which the meteoroid speed is directed. The geocentric speed of the meteoroid includes a component of the velocity of the Earth: the radiant region in which the meteor is detected determines the size of this addition. In the case of those in the AX source region almost the full orbital speed of the Earth is added to the incoming meteoroid while for those few appearing from the anti-apex direction almost the full speed of the Earth is subtracted from their heliocentric speeds.

Figure 4.10 shows the distribution of geocentric speeds detected by AMOR, with partitioning based on radiant source direction. As shown in Figure 4.10(a) for all meteors, the speed distribution with Sun-referenced ecliptic longitude shows a clear pattern of increase in average speed, as one approaches the apex position, from each of the exact helion and antihelion positions. This pattern is shown in more depth for the AH and HN regions in subsequent sub-plots, it is clear that in general the speed regimes of these two regions can be treated in a similar fashion. The AX direction, shown in Figures 4.10(e) and 4.10(f), has much less variation in speed with longitudinal position, partly due to the reality that the population detected in this region is very much over emphasised due to its large geocentric speeds: meteors are essentially randomly distributed in this region with random speeds at Earth-

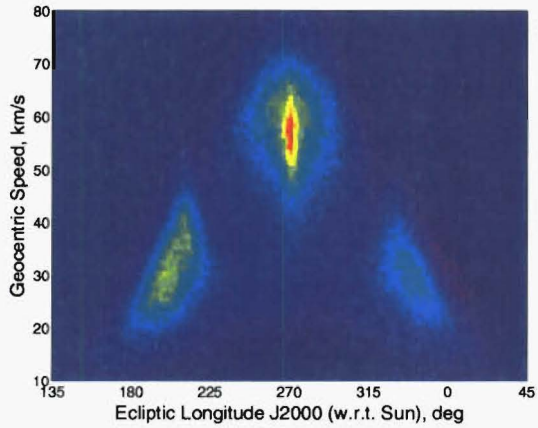

(a) All Meteors.

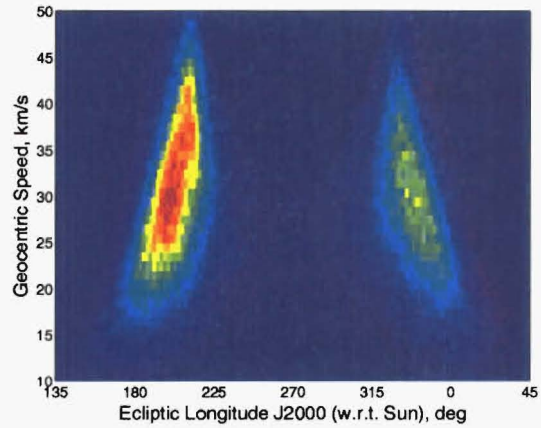

(b) Mid-latitude Prograde Meteors ($\beta > -30°$).

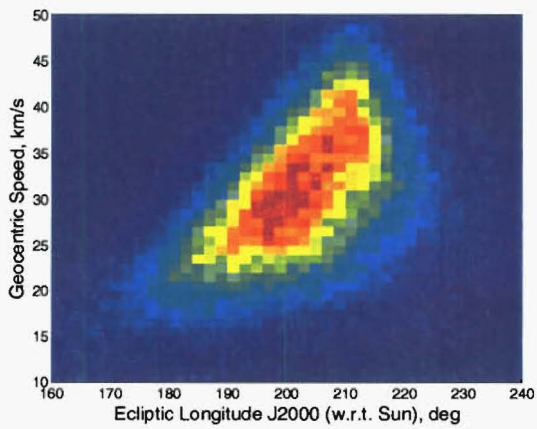

(c) Mid-latitude AH Source Prograde Meteors ($\beta > -30°$).

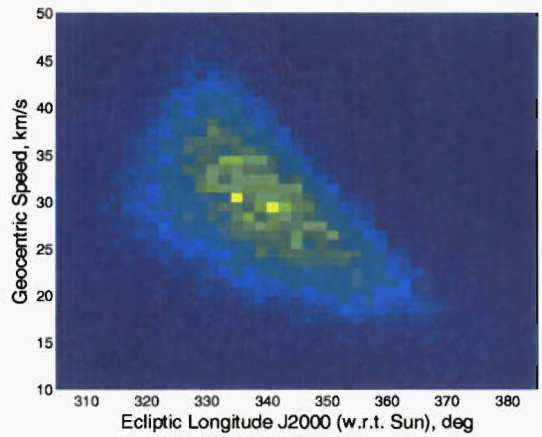

(d) Mid-latitude HN Source Prograde Meteors ($\beta > -30°$).

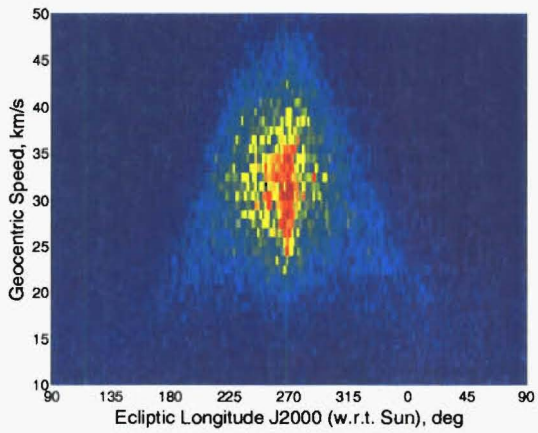

(e) Far-south Prograde (mainly AX source) Meteors ($\beta < -50°$).

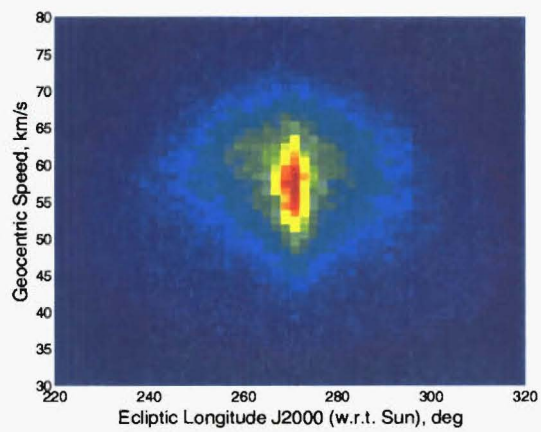

(f) All Retrograde Meteors (AX source).

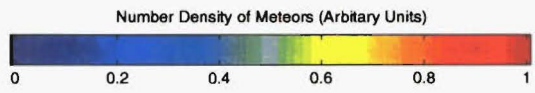

Figure 4.10: The relationship of geocentric speed to radiant position. All meteors from T1995–T1999 are used to provide this picture.

encounter—one is not sampling a close to astronomically true population such as that in the antihelion region, one is sampling a population defined almost purely by the biasing effect of the large geocentric speeds realised near the apex. The former has underlying structure while the latter boasts little such structure.

It is clear from Figure 4.10 that radiant position places a very strong bias on the geocentric speed of the meteor. In fact non-speed determining radar systems may still place limits on the likely speed range of particles given the radiant position from which the meteor is seen to appear.

The biases shown lead the author to the opinion that, where detection of meteor showers is concerned, the geocentric speed is in fact a more useful measure than the heliocentric speed owing to the severe constraints imposed by detection selection effects. As an example of this bias, prograde meteors appearing at $\lambda_R \approx 180°$ only have a speed range of ~ 10 km s^{-1} which contrasts with the much larger heliocentric speed range for all Solar System meteoroids of 0 km s^{-1} to ~ 42 km s^{-1}.

4.4 Orbital Distributions Within the Sporadic Source Regions

In previous sections we have looked at the distribution of meteor events in radiant position and speed. It has been clearly shown that there are well-defined regions of enhanced structure within this system which are often termed "sporadic sources". An unambiguous heliocentric orbit can be derived from the set comprising radiant position, geocentric speed and time of detection of a meteor. It is important to enquire into the orbital distributions found within these source regions to study the effect this link has on the types of orbits detected. It will be particularly interesting to note, as we proceed, that the orbital distributions change, often quite dramatically, as the year progresses and therefore the static distributions discussed in Chapter 3, as are commonly used in discussion of meteoroid orbit data sets (e.g. Steel 1996), are only valid from the perspective of an annually averaged view.

The HN region generally does not contain many published showers due to its invisibility to visual observers and to difficulties with sporadic-E and other interference mechanisms experienced by radars during the daytime. The showers found in this region are normally prefixed with "Daytime"—examples include the Daytime Arietids and Daytime Sextantids. Most such showers are found at close to ecliptic inclinations as befits the sporadic distribution of the region.

The AX region is dominated by retrograde sporadics however some clear showers such as the ETA and the Leonids are to be found there in addition to some minor showers, such as those of Gartrell and Elford (1975). There are also a few prograde showers, in this region, at high inclinations such as the Quadrantids ($i \approx 72°$) and the July Phoenicids ($i \approx 85°$).

The majority of the annual showers are to be found in the AH region simply because of the ease of detection and the low inclination regime which agrees better with the true prograde dominated inclination distribution of the spatial meteoroid population than the AX retrograde inclination biased distribution.

Using the sporadic region definitions of Figure 4.9 and by selecting firstly only prograde orbits ($i < 90°$) and then only retrograde orbits ($i \geq 90°$) from T1995–T1999, the orbital distributions within these regions are surveyed.

4.4.1 Prograde Orbital Distributions

The orbital parameter distributions in the AH and HN regions are found to be generally similar to each other and together they form the bulk of the prograde meteoroid population sampled by AMOR. The character of the small number of prograde orbits detected in the AX region is generally very different to those in the AH and HN. There are also marked variations through the time between vernal equinoxes in the distributions of the parameters in each region.

The average orbital distributions over all years in the radiant regions are shown in Figure 4.11. The AH and HN are typified by orbits with low inclinations (54% and 52% of orbits in the AH and HN regions respectively have orbital inclinations less than 20°), a bias towards low to medium perihelion distances (very few with q near 1 AU) and a bias towards medium to high eccentricities (the majority have e between 0.7 and 1.0 (the parabolic limit)). A bi-modal distribution is seen in the argument of perihelion distributions of these two radiant regions which is explained by the relationship between q, e and ω (equation 3.3): one mode consists of orbits detected at the ascending node and the other of those at the descending node. There is a clear deficit in $\omega \in [140°, 180°]$ and $\omega \in [180°, 220°]$ for HN and AH regions respectively. This is in line with the general lack of perihelion distances near 1 AU in these regions; ω close to 180° implies $q \approx 1$ AU regardless of eccentricity due to the $\cos\omega$ term in equation 3.3, the side of $\omega = 180°$ on which the gap takes place changes between AH and HN as the ascending/descending node distributions are reversed in these cases thus reversing the $\pm$ sign in equation 3.3.

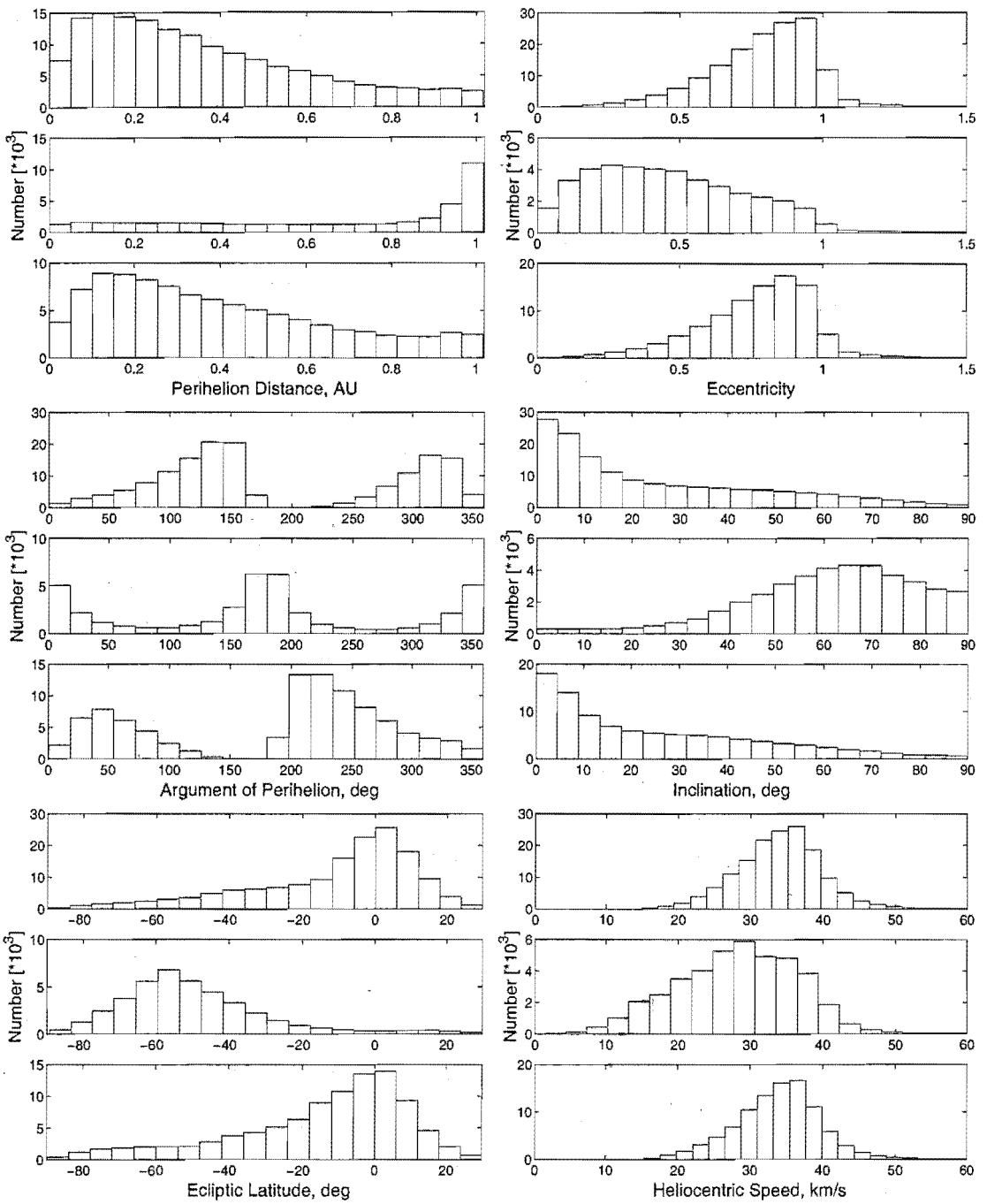

Figure 4.11: The orbital element distribution of all prograde meteoroids, from T1995–T1999, grouped by the sporadic source region in which the radiant of the meteor was detected. In each graph shown from top to bottom are the AH, AX and HN regions.

The AX source region is dominated by very different typical orbits. Here almost all orbits have perihelion distances close to 1 AU, with a broad spectrum of eccentricities biased slightly towards lower more circular eccentricities and with very few near-parabolic eccentricities. The argument of perihelion distribution for these orbits is again bi-modal however here the gaps between the modes cover most of the possible parameter range leaving a distribution which only takes $\omega \approx 0°$ or 180°—i.e. meteoroids are detected at points very close to or at their perihelion. This is not difficult to understand in the context of orbits which have $q \approx 1$ AU, the only possible detection time for these is near perihelion as the Earth's orbital diameter is ≈ 1 AU.

The differences between the AX and AH and HN regions are very much due to the differences in ecliptic latitudes at which the meteors are detected. As shown in Figure 4.11, the AX region is dominated by radiants at deep southerly ecliptic latitudes ($\overline{\beta} \sim -50°$) while the other regions are dominated by near-ecliptic latitudes ($\overline{\beta} \sim -12°$). The inclination distribution sampled follows from this, where AH and HN regions have generally low inclination orbits while the AX region has $i > 40°$. The q, e and ω differences between these regimes follow from this inclination distribution: orbits on higher inclination orbits generally come closest to the Sun when crossing the ecliptic as their inclination quickly increases the distance to the Sun as they move away from the ecliptic; additionally retrograde meteoroids are optimally placed to hit the Earth "head-on" when perihelion/aphelion occurs at the Earth intersection point as they are turned towards the apex direction. Detection by the Earth of meteoroids must occur at a solar distance of ≈ 1 AU and as perihelion normally occurs on or near the ecliptic then the bias in q, e and ω is explained. Conversely the low inclination regime of the AH and HN regions implies a much less constrained distribution in q, e and ω. These distributions are close to those expected in the corrected distributions of Chapter 3, in particular the inclination distributions of Figure 4.11 for AH and HN regions agree well with the corrected distribution of Figure 3.14, while the correction removes almost all of the inclination values occupied by the AX region.

It is also interesting to study the differences between the heliocentric speed (V_H) distributions for the different regimes. As shown in Figure 4.11, the AX region enjoys a wide range of orbital speeds at impact while that of the other regions is much more constrained—this is simply due to the AX region gaining the greatest benefit from the orbital speed of the Earth (V_E)—meteoroids with speeds close to 0 $\mathrm{km\,s^{-1}}$

and appearing at ecliptic latitudes near 0° obtain a geocentric speed equal to V_E by the Earth colliding with them while they wait pseudo-stationary. Conversely very fast meteoroids with speeds exceeding the escape speed from the Solar System (i.e. hyperbolic orbits with $V_H > 42$ km s^{-1}) are also found in the AX region at latitudes near the ecliptic South Pole; such meteoroids gain little in apparent speed at impact from $\mathbf{V}_E$ as the vector addition of their $\mathbf{V}_H$ with the latter at $\beta \sim 90°$ yields a geocentric speed close to $V_G \approx V_H$. The AH and HN regions meanwhile have much tighter distributions in V_H with higher mean speeds as these meteors generally appear approximately perpendicular to the apex of the Earth's way and therefore little of V_E adds to these meteors. In fact to obtain sufficient speed to be detected often these meteoroids must travel faster than V_E as some of their $\mathbf{V}_H$ is removed by the addition to a "speeding away" Earth. The tendency towards higher eccentricities in the AH and HN regions is related to this general increase in heliocentric speeds over the AX region—the faster the meteoroid, the nearer to hyperbolic it is.

Seasonal Changes in Prograde Orbital Distributions

The variations in the orbital elements and in heliocentric speed occurring between the three sporadic source regions have been discussed up to now. It is therefore timely to comment on the variation, with time of year, of each of these regional distributions. For this purpose the year has been partitioned into four virtual "seasons", each 90° of mean solar longitude apart, for which the orbital distributions are shown (in a similar fashion to Figure 4.11) in Figures 4.12, 4.13, 4.14 and 4.15.

As shown in these seasonal figures, the ecliptic latitude in the three regions is very changeable. The AH and HN while, on average, dominated by near-ecliptic latitudes experience motion in their distribution centres over the course of the year. This fact has already been established and explained for Figure 4.4—the one dimensional distributions shown here serve to underline the point.

In the AH region the first season is dominated by meteors at latitudes north of the ecliptic. Over the next two seasons the latitudes gradually become more southerly. The third season has the most southerly meteors with the situation returning to a similar intermediate phase as the second season in the fourth season. The HN region shows a similar change in latitude however this occurs approximately 180° out of phase as should be expected. The AX region shows a more definite variation between seasons with a narrow distribution centred on $\sim 50°$ in both the first and

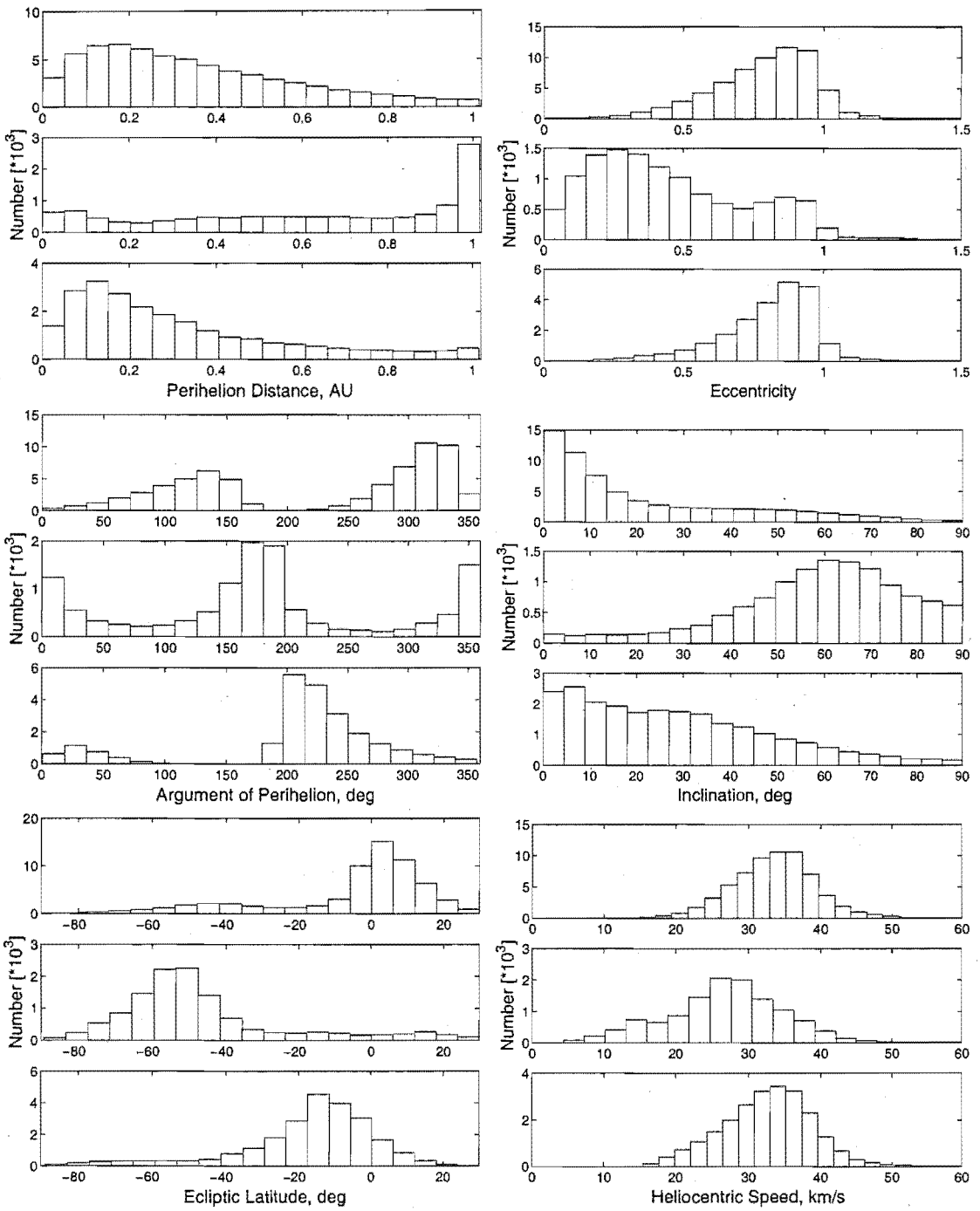

Figure 4.12: The orbital element distribution of prograde meteoroids, from T1995–T1999, in the first virtual season ($\lambda_\odot \in [0°, 90°]$). These are grouped by the sporadic source region in which the radiant of the meteor was detected. In each graph shown from top to bottom are the AH, AX and HN regions.

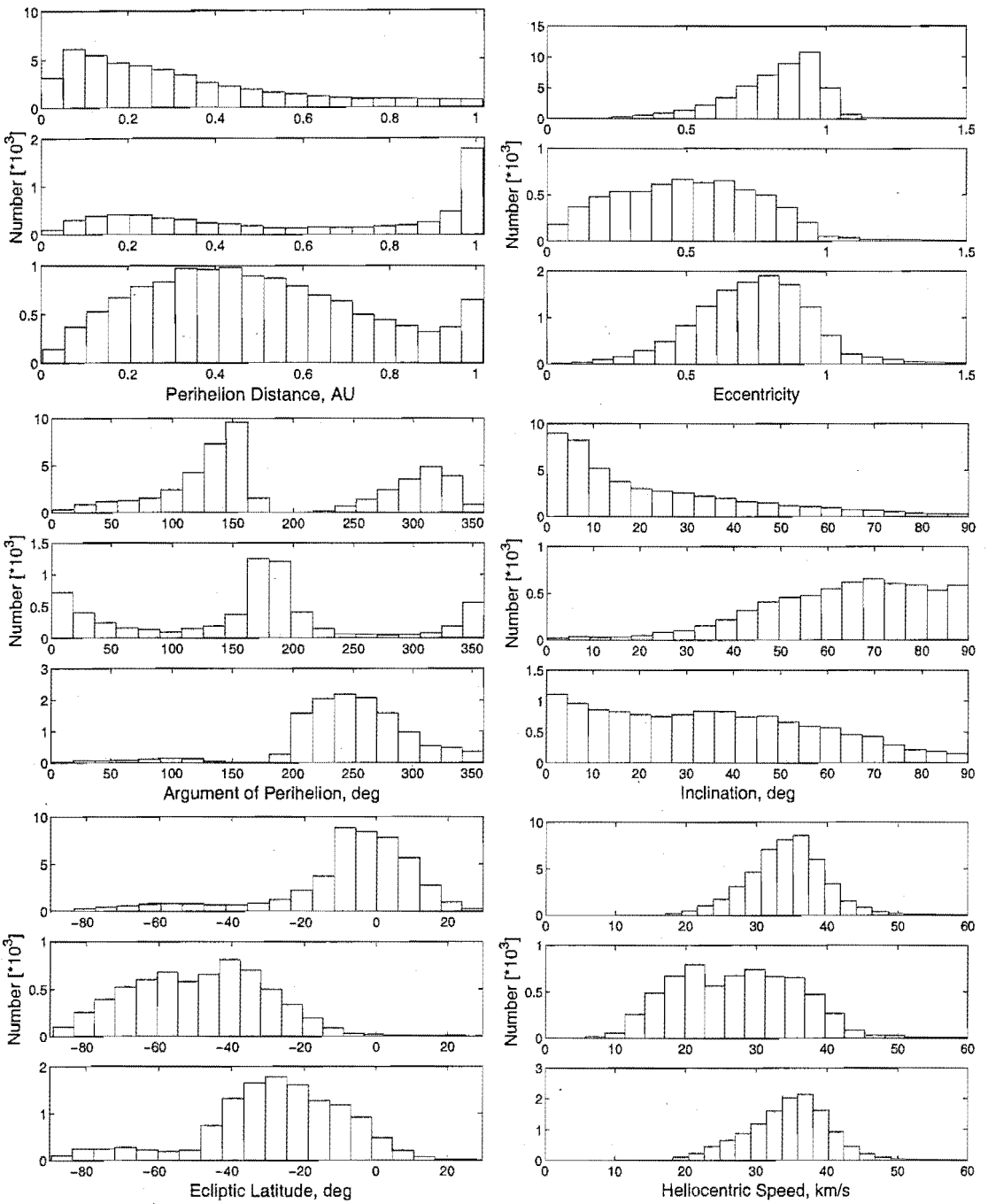

Figure 4.13: The orbital element distribution of prograde meteoroids, from T1995–T1999, in the second virtual season ($\lambda_\odot \in (90°, 180°]$). These are grouped by the sporadic source region in which the radiant of the meteor was detected. In each graph shown from top to bottom are the AH, AX and HN regions.

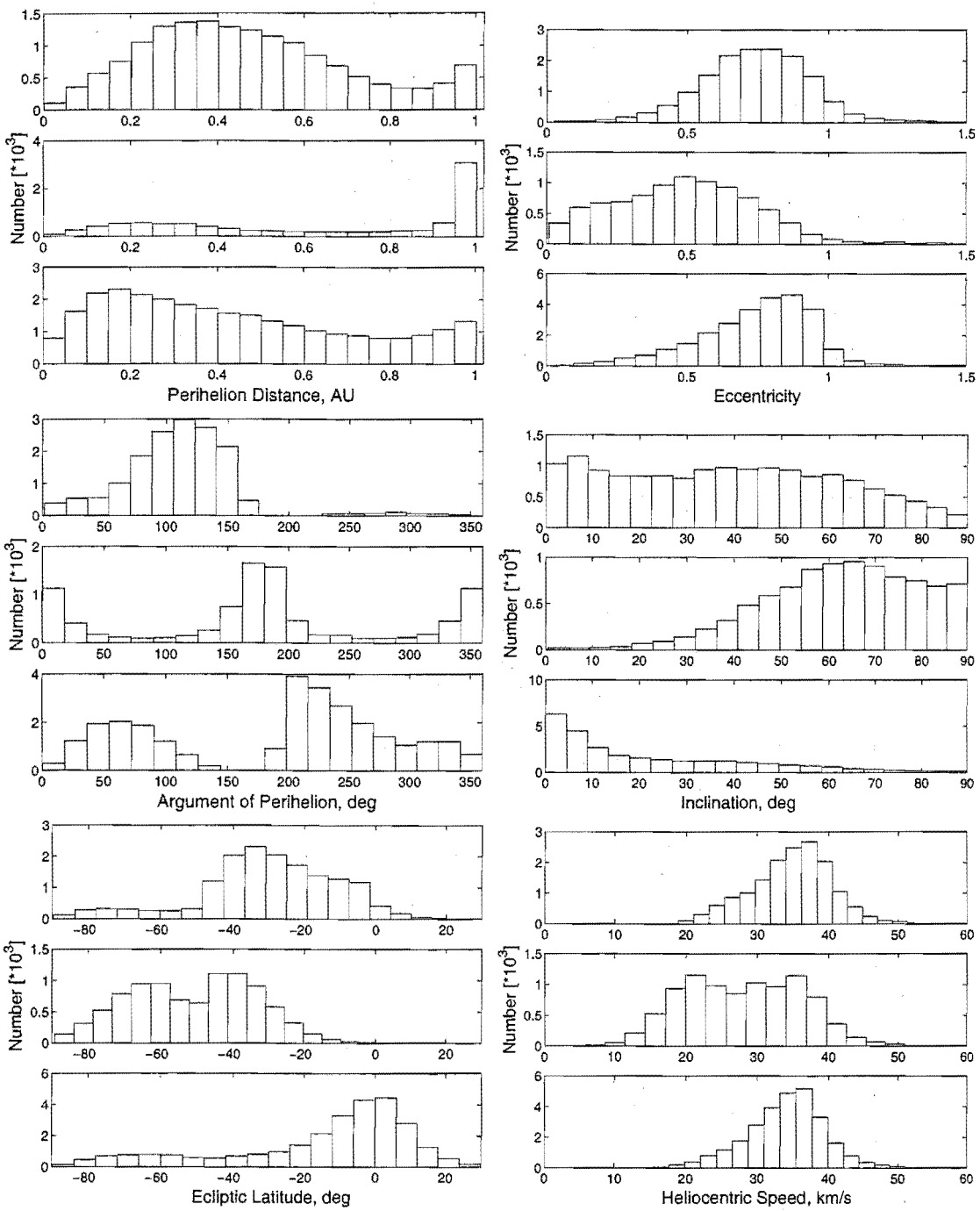

Figure 4.14: The orbital element distribution of prograde meteoroids, from T1995–T1999, in the third virtual season ($\lambda_\odot \in (180°, 270°]$). These are grouped by the sporadic source region in which the radiant of the meteor was detected. In each graph shown from top to bottom are the AH, AX and HN regions.

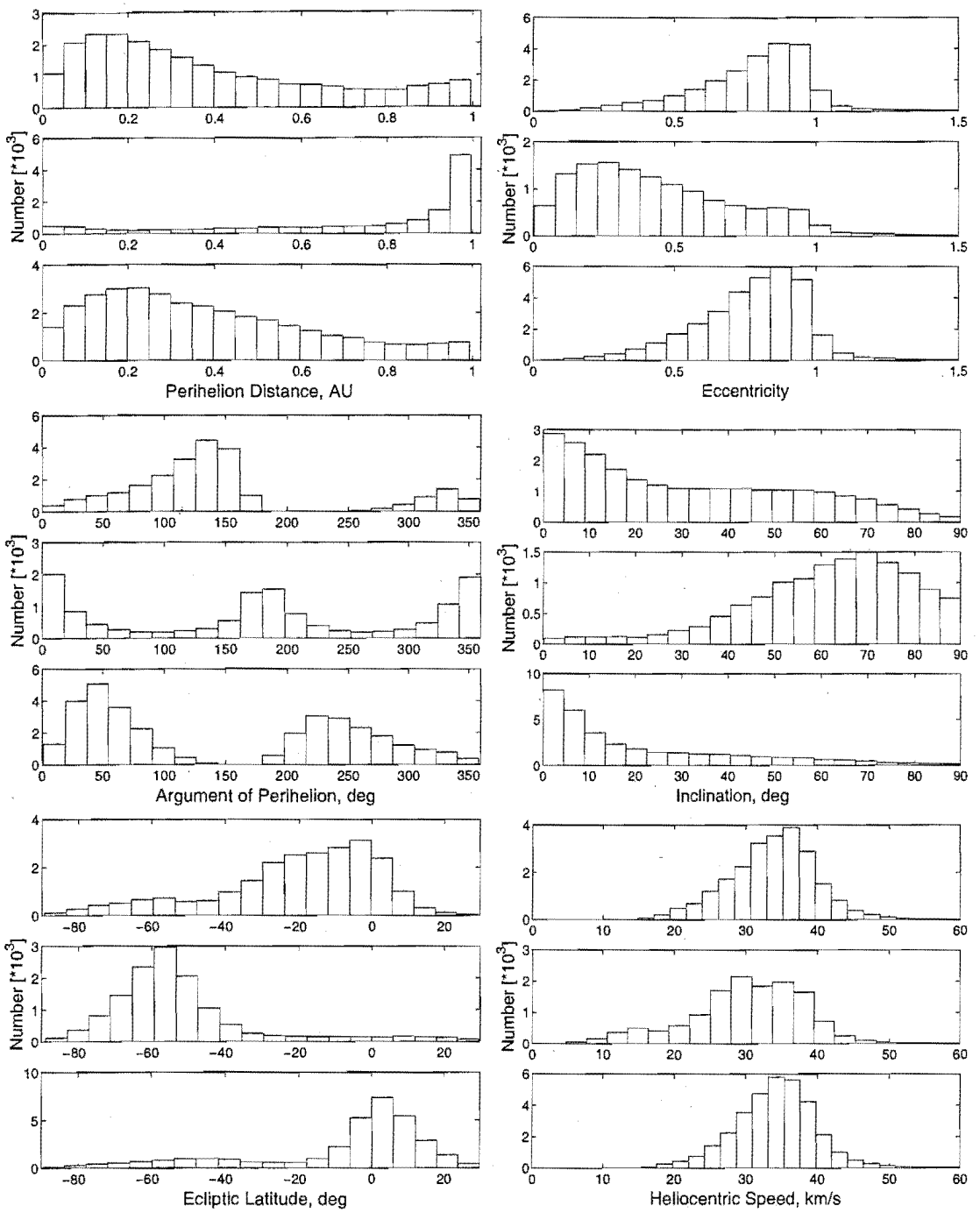

Figure 4.15: The orbital element distribution of prograde meteoroids, from T1995–T1999, in the fourth virtual season ($\lambda_\odot \in (270°, 360°)$). These are grouped by the sporadic source region in which the radiant of the meteor was detected. In each graph shown from top to bottom are the AH, AX and HN regions.

fourth seasons and a much wider distribution across much of the range south of the ecliptic in the intermediate seasons.

The inclination angle distribution of the orbits found in the AH and HN regions changes dramatically over time. As was noted for the full year distributions this angle is normally biased towards near-ecliptic values in these regions: however, it is found from the seasonal change figures, that the AH region only experiences this regime in the first season with an increase towards the higher inclinations in subsequent seasons. Conversely the HN region appears to experience increased high inclinations in the first season and a bias towards the expected lower inclinations in subsequent seasons. This is caused by the change in the ecliptic latitude regime throughout the year. As shown in Figure 4.4, the AH region meteoroid distribution achieves its most Southerly latitude in the first three virtual months while the AH region is mostly seen above the ecliptic position during this time. In later months the AH meteors are seen at lower latitudes in general particularly during the third season where the southerly component is strongest, corresponding to the inclination distribution being found to have the highest number of high values.

The change in inclination distribution is mirrored by changes in the other elements. Increased numbers of $q \approx 1$ AU are found in seasons where the inclination distribution above $\sim 45°$ is increased. The same reasons for this increase apply to the full year AX region propensity of $q \approx 1$ AU values shown earlier in Figure 4.11. It is found that removal of radiants at latitudes south of 30° completely removes both the higher inclination components to these regions and also the perihelion distance changes compared to the yearly distributions of Figure 4.11—hence verifying the relation between southerly latitudes and the yearly variations.

The eccentricity distribution changes little for the AH and HN regions from that discussed for the yearly case. The argument of perihelion also changes little in its bi-modal nature. However the lower mode of the distribution dominates in the HN in the second season while that in AH dominates to a large extent in the third and completely in the fourth season. This is due to the changes in the number of meteors detected at ascending/descending nodes in these periods—most of the meteoroids detected in the HN and AH regions collide at their descending nodes over these periods.

The AX region meanwhile only shows slight variations in its parameters throughout the year. The perihelion distribution shows its very strong bias towards near 1 AU values throughout all seasons. There is a uniform increase relative to this

peak in the first season corresponding to an increase in the relative numbers of near-ecliptic latitude meteor radiants. The eccentricity distribution in this season shows an increase in near parabolic orbits to offset this change in q: there are no other significant changes in the e in the other seasons from the average. The argument of perihelion also shows no significant changes apart from slight variations in the relative strengths of the 0° and 180° narrow-centred modes as the ascending/descending node ratio fluctuates by season. Likewise there are no significant changes in the inclination distributions by season.

The heliocentric speed distributions in the AH and HN regions show no significant changes between seasons however the AX region shows very definite changes. There is a decrease in low speed ($V_H < 20$ km s^{-1}) meteoroids in the first and second seasons with a subsequent increase in this region to a symmetrical level with those at higher speeds in the third season and reducing again in importance in the fourth season. This trend follows that towards meteors with near-ecliptic latitudes in the second and more strongly in the third season; as discussed previously such latitudes allow the detection of very slow heliocentric meteors. There are no such near-ecliptic distributions in latitude in the first or fourth seasons.

4.4.2 Retrograde Orbital Distributions

The retrograde orbit population is only sampled by AMOR in the AX radiant region. The latitudinal variation of this region is clearer than that seen for the prograde populations. The variation follows that shown in Figure 4.4, as the AX region is dominated by retrograde orbits. Much of the retrograde population is simply an observational bias induced effect—as discussed in Section 3.4 the high geocentric speeds associated with this population due to "head-on" collision with the Earth serve to exaggerate the importance of this population.

Once again orbital distributions of all meteors detected in T1995–T1999 (in the retrograde sense) are shown in Figure 4.16 while four 90° separated virtual seasons are shown in Figure 4.17, for the first half, and Figure 4.18, for the second half of the year.

The heliocentric speed distribution does not vary seasonally. This is because the meteoroids collide "head-on" with the Earth and therefore the ecliptic latitude is not a determining factor in whether they will be detected or not: they will always be detected when in the AX region as their geocentric speed will always be greater than or equal to the Earth's orbital speed. The perihelion distance distribution is

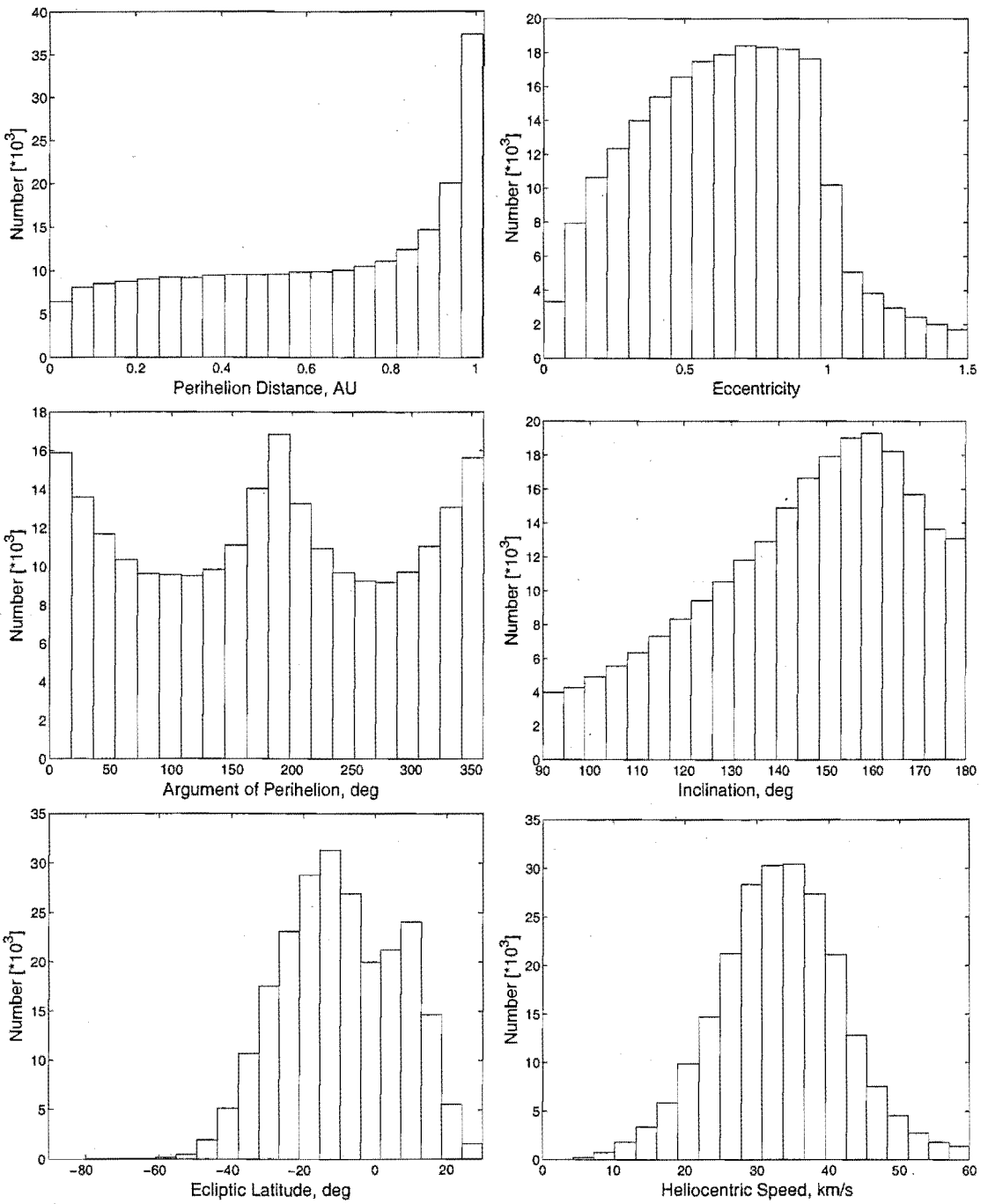

Figure 4.16: The orbital element distribution of all retrograde meteoroids, from T1995–T1999, grouped by the sporadic source region in which the radiant of the meteor was detected.

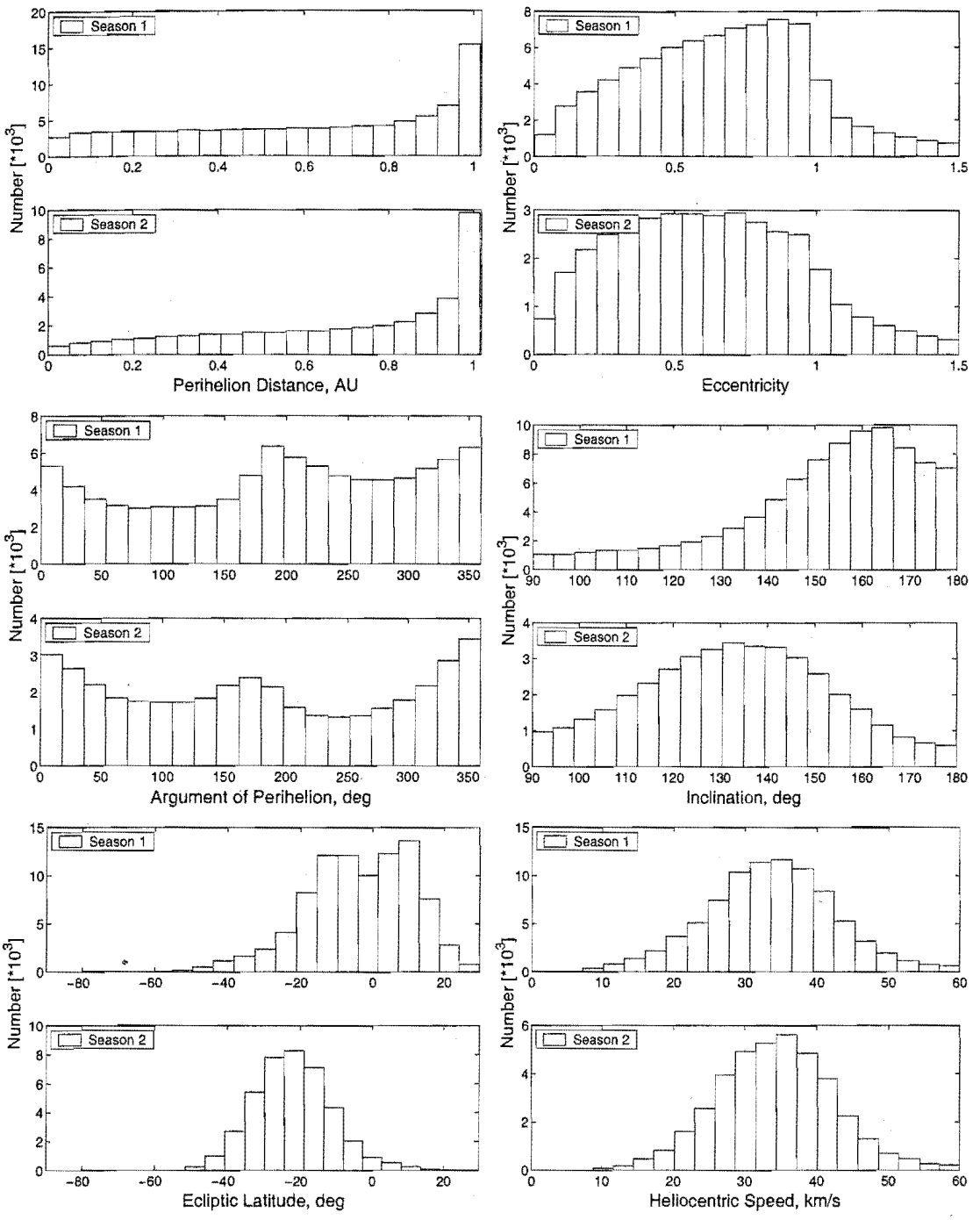

Figure 4.17: The orbital element distribution of retrograde meteoroids, from T1995–T1999, in the first and second virtual seasons ($\lambda_\odot \in [0°, 90°]$ and $\lambda_\odot \in (90°, 180°]$). These are grouped by the sporadic source region in which the radiant of the meteor was detected.

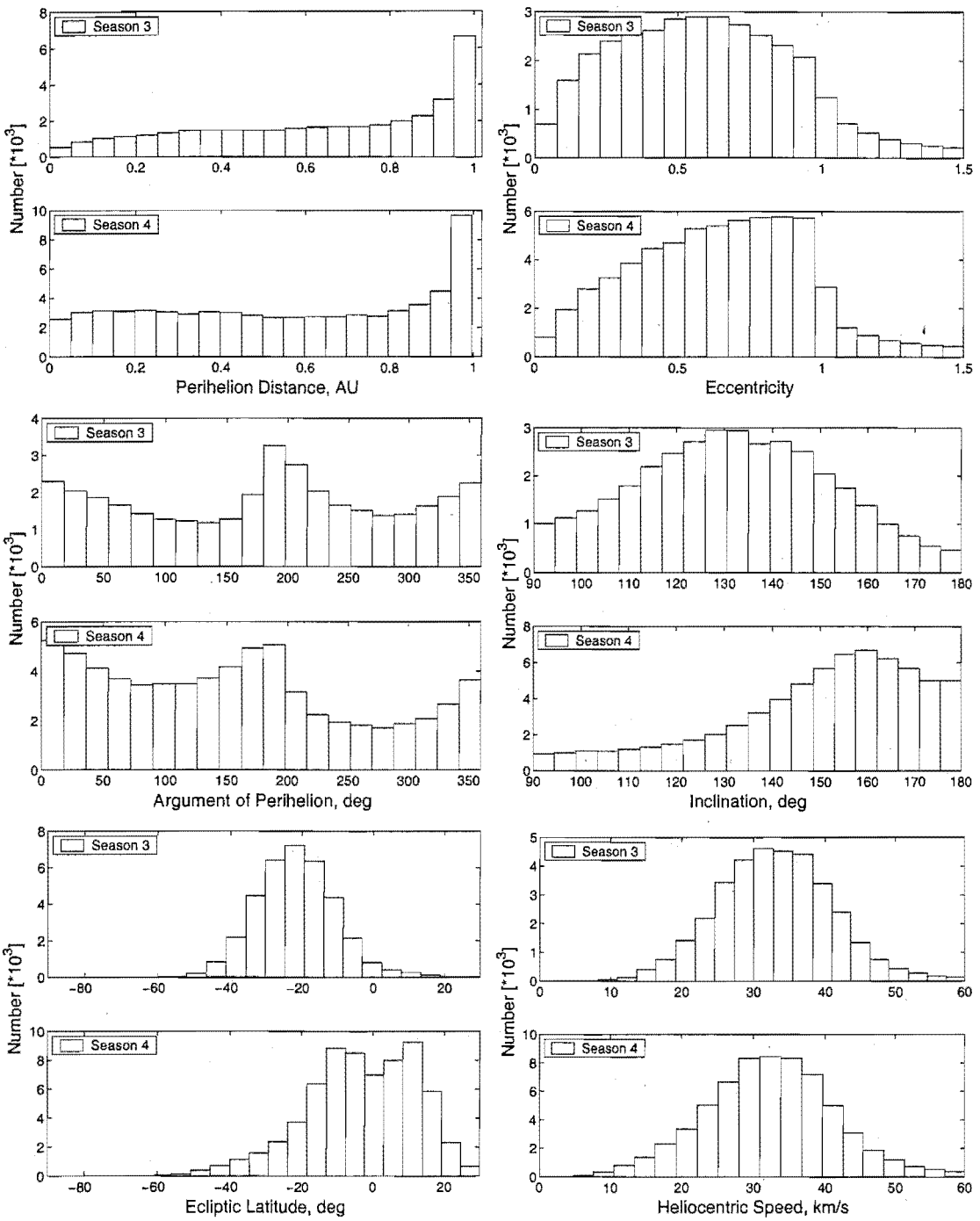

Figure 4.18: The orbital element distribution of retrograde meteoroids, from T1995–T1999, in the third and fourth virtual seasons ($\lambda_\odot \in (180°, 270°]$ and $\lambda_\odot \in (270°, 360°]$). These are grouped by the sporadic source region in which the radiant of the meteor was detected.

reasonably stable between seasons with a strong bias towards the $q \approx 1$ AU region. However, by contrast with the AH and HN regions of the prograde population, there is still a large fairly uniform number of meteoroids across all perihelion distances. In the second and third seasons there is a lowering of the number of lower perihelion distances, which corresponds to a decrease in the number of near-ecliptic latitude meteors compared to the first and fourth seasons. As noted above low latitude, and in this case correspondingly low inclination meteors, have a wider range of possible perihelion distances while those further away from the ecliptic tend to be biased towards the $q \approx 1$ AU region. The inclination and eccentricity distributions in the second and third seasons clearly show a different character differ from the first and fourth seasons having less orbits with $i \approx 180°$ and more with low eccentricities.

In the first and fourth seasons, the inclination distribution is biased towards medium to high (retrograde) inclination orbits. Few are found at $i < 130°$ corresponding to the bias towards near-ecliptic latitudes. This situation changes, as discussed above, for the other seasons where a symmetric distribution is found centred about $i \approx 130°$ with a decay to both sides corresponding to a further from south of ecliptic latitude distribution.

The argument of perihelion shows almost a flat distribution with small structure at $\omega = 0°$ and 180°—this corresponds to the slight bias towards detection at perihelion, it is not stronger as although there is an obvious $q \approx 1$ AU peak the remainder of the range of q is cumulatively stronger than this relegating it to a second-order perturbation by contrast to the situation in the case of the prograde AX source orbits. The $\omega = 0°$ and 180° peaks are more obvious in the first and third seasons respectively where the relative strength of the $q \approx 1$ AU peak is increased.

The argument of perihelion distribution is bi-modal but less obviously so with the modes being centred at 0° and 180°. The variation in the strength of these modes corresponds to the variation in the strength of the ascending node and descending node detected components.

4.5 Summary

It has been shown in this chapter that the radiant distributions are strongly guided by the effects of observational bias. The form of the transmitted radio beam, in combination with the true spatial distribution of the dust in space, is found to have a particularly strong effect on the resultant radiant distribution (Figure 4.8). The "sporadic sources" have been shown to be nothing more than an effect of the bias

and attempts to ascribe to them properties apart from this are misled. However, these virtual sources are still very useful to group together orbits which have been sampled in similar ways in the AMOR data set—for example the apex region is almost completely dominated by retrograde orbits.

It is particularly interesting to see the changes in meteor population orbital parameters with season. The changes in the retrograde inclination distribution of Figures 4.17 and 4.18, argue particularly for careful understanding of the orbital element distributions. It is clear from this that orbital distributions, such as those of Steel (1996), will be severely biased should the observation system not be run over regular time intervals throughout a year. For example, if several years of data are added together with part of some of the combined years having large time-gaps or should only a specific month of each year be studied with regard to the orbital parameter distributions, two studies from similar observation systems are likely to emerge with quite different distributions.

Chapter 5

Uncertainties in AMOR Orbital Parameters

5.1 Introduction

Many previous radar surveys list average or representative uncertainties on the directly observed meteor parameters and on the orbital elements which follow from these. This achieves a large-scale picture of the quality of the surveyed orbits; however, it does not allow detailed analysis of the quality of a small sample of orbits. It is important when performing stream analyses to decide whether a grouping is formed of reasonably accurate orbits. Many of the orbits collected by radar methods have large uncertainties and it might be that a grouping is formed of these in such a way as to look significant where even a slight change in the velocities, on which the orbits are based, would render them highly insignificant.

As discussed in Chapter 2, meteoroid orbits as calculated by AMOR are derived from the observed quantities: meteoroid speed, azimuth and zenith angles and the time of observation. These quantities are in turn calculated from the fundamental parameters: inter-station time-lags, elevation angle and time. By performing a study of the effect changes in these basic parameters can have on the each of the derived orbital elements Baggaley et al. (1994) have estimated the uncertainties.

Baggaley et al. assign the angular elements i and ω representative uncertainties of 2°; Ω is assumed to have no uncertainty due to its direct relation to the time of observation, which is measured highly accurately; eccentricity (e) and perihelion distance (q) are each assigned a 5% uncertainty.

The uncertainty in the heliocentric speed corresponds to the uncertainty in the raw observed time-lag speed (equation 2.5). Assuming an average one pulse detection uncertainty for AMOR[1] yields a 3% uncertainty for an average 40 $\mathrm{km\,s^{-1}}$ meteoroid—this leads to a corresponding $\triangle V_H$ of 3%. We would expect up to a 5% uncertainty in speed for meteors which are near the limiting sensitivities of AMOR.

[1]The pulse repetition frequency of AMOR is 379 $\mathrm{s^{-1}}$.

We can write the energy equation relating V_H and a as

$$V_H^2 = GM_\odot(2r^{-1} - a^{-1}). \tag{5.1}$$

By choosing units such that $V_E = 1$, $GM_\odot = 1$ and $R_E = 1$: at $r = 1$ AU (assuming the Earth to have a constant orbital radius of 1 AU about the Sun) we can write

$$V_H^2 = 2 - a^{-1}. \tag{5.2}$$

Differentiating this with respect to a yields

$$2V_H\, dV_H = \frac{da}{a^2}, \tag{5.3}$$

which upon rearrangement leads to

$$\left(\frac{\triangle a}{a}\right) = \frac{V_H^2}{1 - V_H^2/2}\left(\frac{\triangle V_H}{V_H}\right). \tag{5.4}$$

From the 3% uncertainty in V_H the uncertainty in a follows as

$$\left(\frac{\triangle a}{a}\right) = \frac{0.03V_H^2}{1 - V_H^2/2}. \tag{5.5}$$

This equation shows that the uncertainty in a will be small in lower velocity orbits and will become prohibitively high for those with higher velocities. As an example for a 30 km s^{-1} meteoroid the uncertainty is about 6%. However for a 40 km s^{-1} meteoroid the uncertainty will be 48%.

It is obvious from the above calculations that in the case of some meteoroid orbits we will have very significant uncertainties. When searching for streams within a large set of orbits often no regard is taken of these uncertainties. In some cases this disregard for uncertainties will not make much difference, however there is the possibility that in some instances we may get what are in fact very different meteoroid orbits being clustered together simply because of their measurement uncertainties. Hence it is advantageous to determine the uncertainties on each orbit under study. Baggaley et al. (1994) attempted to do this only in the grossest sense by simply considering a representative uncertainty in each parameter for the vast data set, hence their values are only useful as indicators in this study. The study presented in this chapter has the added advantage that detailed statistics have been obtained from it which permit a detailed study of the causes of high uncertainty in various

elements.

5.2 Uncertainties in the Fundamental Parameters

The orbital element calculation process may be viewed as a three stage process. From the raw meteor observation information the elevation angle of the echo point (Ψ), time-lags (Lag_{12} and Lag_{13}) between receiver stations and the time of detection of the meteor are gleaned from the reduction program `Calorb.pas`. These are then reduced in order to yield the heliocentric velocity of the meteoroid in its orbit at the time of detection. Finally the components of this heliocentric velocity are used to calculate the orbital elements of the meteoroid orbit.

Knowledge of the uncertainties inherent in the parameters used in the first stage of this reduction process may therefore, in principle, lead to determination of the uncertainties in those at the later two stages. Table 5.1 lists the absolute uncertainties on the necessary parameters. For the present day AMOR system,

Input Parameter	Uncertainty
Lag_{12}	1.4 pulses
Lag_{13}	1.4 pulses
Elevation	0.5°
Azimuth Angle	1°

Table 5.1: Representative uncertainties on fundamental AMOR parameters.

the uncertainties in each of the time-lags between stations were determined by Taylor (1991) as being equal to one radar pulse (corresponding to 2.64 ms). A representative uncertainty in the elevation angle is given as 0.5°. The elevation angle is measured using a dual interferometer—this provides two elevation angles, one from each interferometer, which should be the identical for each meteor. The difference between these angles for a large sample of meteor detections gives the uncertainty quoted above. The elevation uncertainty given at the time of Taylor (1991) was higher owing to the use of only a single interferometer. The angular width of the radar beam in azimuth is known to be approximately 2° to the 3 dB points, hence the uncertainty in the azimuthal position of the meteor is taken to be 1°.

5.3 Uncertainty Analysis Implementation

Two different methods are chosen in order to perform uncertainty analyses of the AMOR data set. These methods yield essentially the same results, as will be seen in Section 5.5.

5.3.1 A Monte Carlo Simulation Approach

A method, used briefly by Taylor (1991), involves creating a Gaussian distribution in each of the fundamental parameters with the measured value of the parameter becoming the distribution mean and the standard deviation being set equal to the uncertainty on the parameter. For a large number of sample runs a value for each of these parameters is randomly selected from the generated Gaussian distributions. Each of these sets of random parameter values is then used as input to the standard orbit calculation `Pascal` subroutine `GetOrbit` in order to obtain a full set of orbital parameters. The standard deviation over this large set of sample runs in each output parameter is taken as its uncertainty. This method effectively constitutes a Monte Carlo approach where the orbit calculation procedure is treated as a "black box" and the spread in an output parameter, corresponding to a spectrum of physically valid input parameter values, defines the uncertainty.

In the case of Taylor (1991), this method was used simply to check the uncertainty in a set of ETA orbits[2]. It is applied in an adapted form in the current study to provide routine uncertainty measurements for any given orbit.

In order to prevent unphysical extreme values of the fundamental parameters appearing from the distributions: ψ, Lag_{12}, and Lag_{13} are randomised according to Gaussian distributions with limits at three standard deviations while the azimuthal angle is randomised by a two standard deviation normal distribution[3]. Each orbit is subjected to 5×10^4 of these uncertainty smearing simulations[4].

[2]In that case Taylor found that the standard deviation in the various parameters approximately equalled the respective uncertainties; this means that little can be said about the true astronomical spread in the orbits of the approximately 300 ETA orbits per year. However the general region of orbital element space of this shower can be determined as can statistics such as mean velocity. The sheer number of orbits in this case so far exceeds those available by photographic and other methods that this statistical picture may be just as valuable as that obtained from a small number of more precise orbits.

[3]A Gaussian distribution is not an exact fit for the shape of the beam in azimuth but it is close enough to be used as representative of the essential form of the beam.

[4]It would be favourable to have used a greater number of sample runs per orbit uncertainty calculation, however 5×10^4 is the maximum practical limit when surveying the very large AMOR data set.

In order to demonstrate the different outcomes one may expect from this type of uncertainty analysis, two sets of histograms are presented. Figure 5.1 shows the distribution of orbital elements obtained from a randomised simulation based on the first meteor of 1996 (Meteor 96/01/01 00:01:14 (#29)). This orbit is subjected to 3×10^4 random variations in input parameters, producing a corresponding distribution in orbital elements. Notice the well defined and narrow peaks—e.g. the inclination range is only 3° while that for the perihelion distance is only 0.06 AU. This can be thus regarded as a highly accurate orbit and used with the utmost confidence when determining stream affiliations.

In contrast the 28th Meteor of 1996 (Meteor 96/01/01 02:22:02 (#22)), as displayed in Figure 5.2, is highly unstable with respect to variation of the input parameters. The distributions produced are much less clearly defined as compared with those of Figure 5.1, for example the inclination range is $\sim 40°$ while the perihelion distance is spread right across its whole range from 0 to 1 AU. Little weight should be placed on streams containing a reasonable proportion of such orbits. Minor streams, which by definition consist of few meteoroids, made up of such orbits should equally be accorded little weight.

An interesting problem raised by some orbits, such as that shown in Figure 5.2, is the ease with which minor variations in the fundamental parameters may change the node of detection of the meteoroid. Many meteoroids are detected in orbits close to the ecliptic hence this is not an unusual problem—the question is how to determine an uncertainty from such distributions as on a nodal change the longitude of the ascending node and the argument of perihelion will both change by 180°. In practice the computer program rejects the node at which the least randomised samples occur in favour of concentrating on the larger one. It is found that for 40% of meteoroid orbits which swap nodes in such a way, 1% of the randomised samples were at one node and 99% at the other. In the remaining 60% of node swapping orbits there is usually a dominant node.

Other difficulties presented by the randomisation method are its computational intensiveness, due to the large number of sample runs needed per orbit, and also the care which has to be taken in the determination of statistical parameters for the circular angular elements whose distributions may cross the 0°/360° equivalence point.

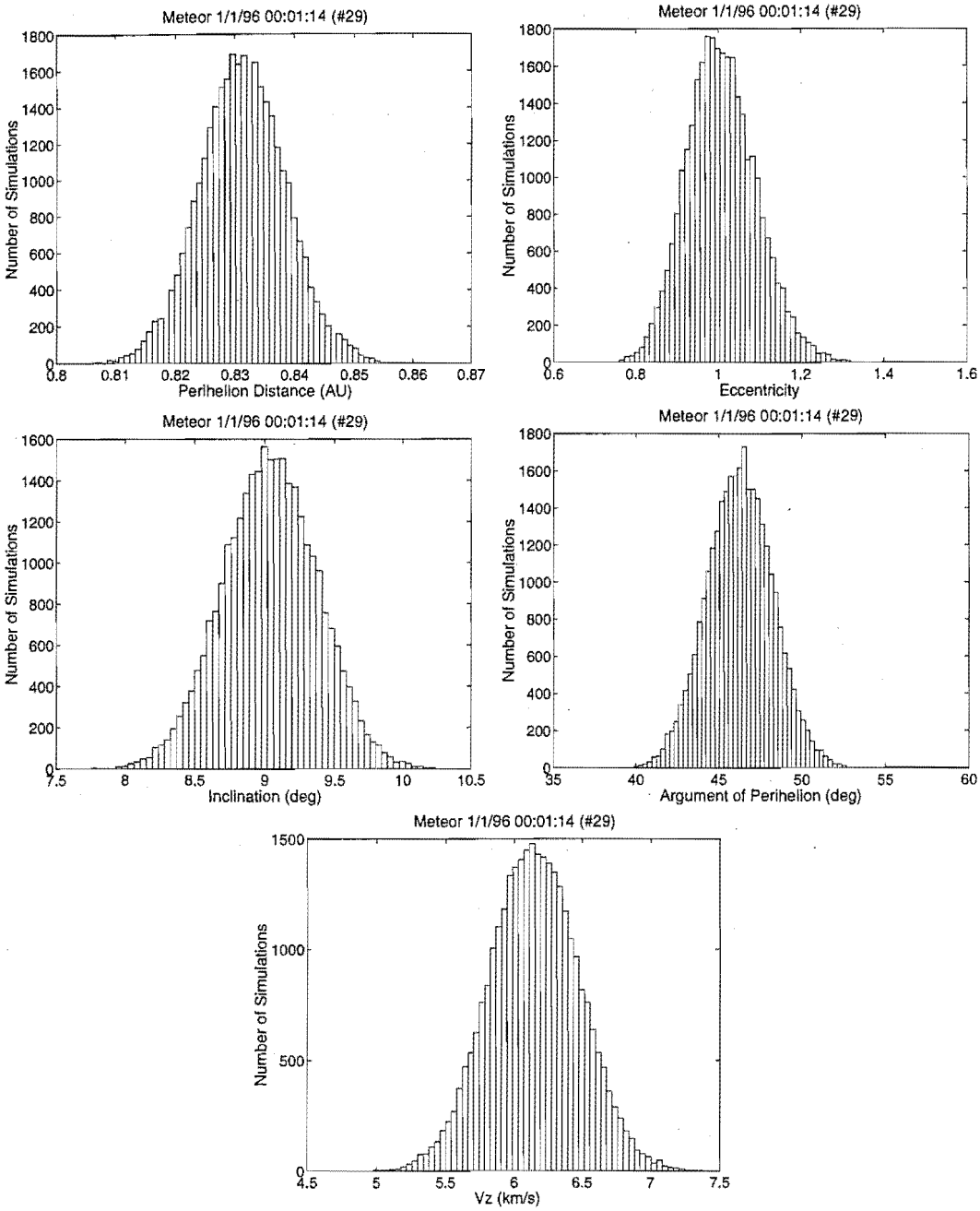

Figure 5.1: Stability testing, using 3×10^4 randomised simulations, of a well defined orbit. Distributions in the major orbital parameters are shown. The distribution in the heliocentric velocity z-component is given to show that this orbit does not change nodes easily.

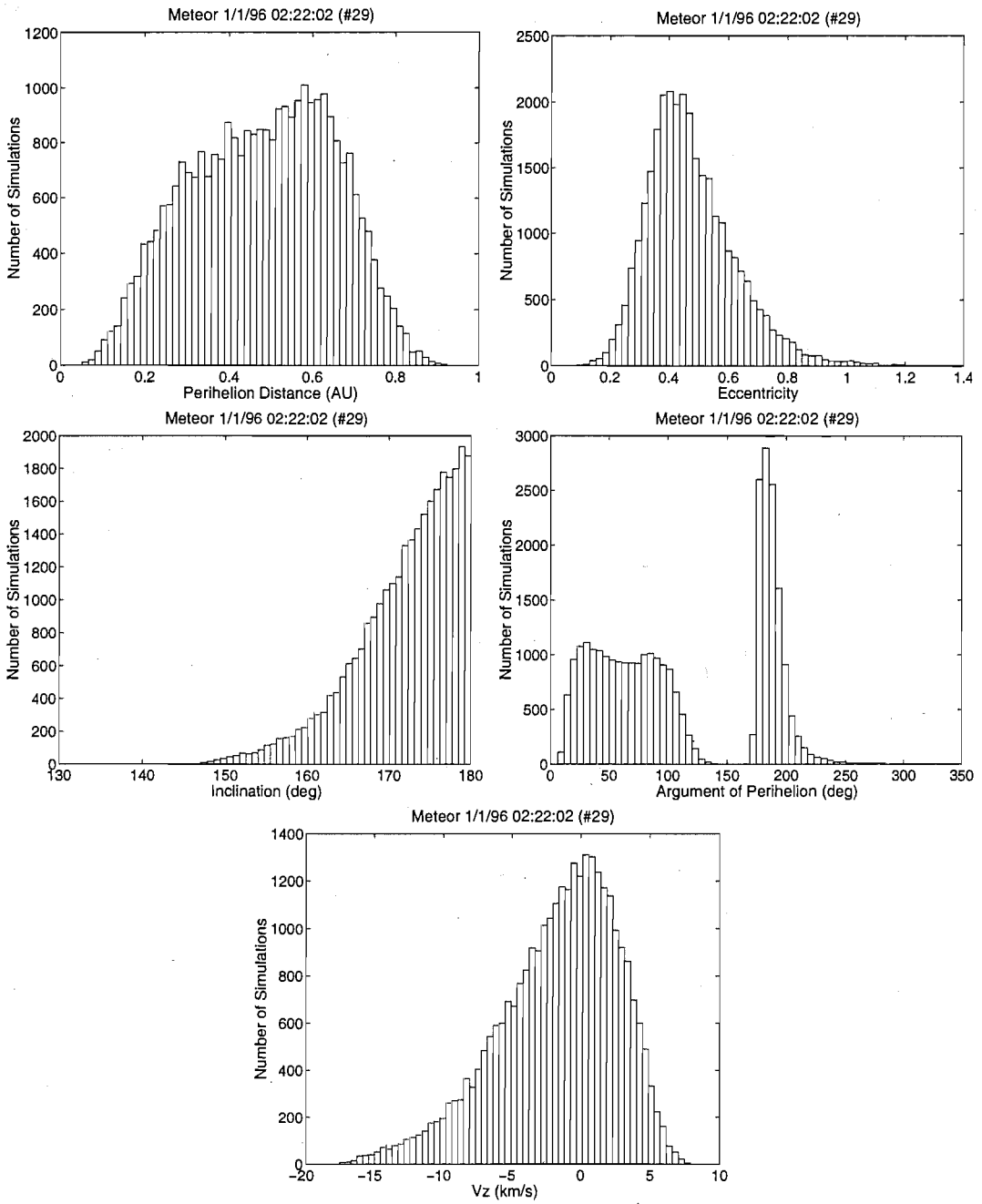

Figure 5.2: Stability testing, using 3×10^4 randomised simulations, of a very poorly defined orbit. Distributions in the major orbital parameters are shown. The distribution in the heliocentric velocity **z**-component is given to show that this orbit does change nodes very easily (the zero point in this component is also the node crossover point).

5.3.2 An Analytical Approach

A method which carries through uncertainties from the fundamental parameters to the orbital elements, using classical analytical uncertainty propagation techniques, is found to be too cumbersome. Instead a hybrid method using analytic uncertainty methods together with the subroutine at the core of the orbit calculation computer program is formed. This method has advantages of much greater speed and less problems with angular ambiguity problems than the randomisation method of the previous section.

Classically the uncertainty δf in a function $f(V_1, V_2, ...V_n)$ is given by

$$(\delta f)^2 = \sum_{k=1}^{n} \left(\frac{\partial f}{\partial V_k} \right)^2 (\delta V_k)^2, \tag{5.6}$$

where the partial derivatives follow from

$$\frac{\partial f}{\partial V_k} = \lim_{h \to 0} \frac{f(V_k + h) - f(V_k - h)}{2h}. \tag{5.7}$$

For the current analysis $V \in \{Lag_{12}, Lag_{13}, \psi, A\}$ are the variables on which the calculation of any orbital parameter depends. Analytic method uncertainties in the orbital elements are calculated by the computer program `Analytic_orbit_err.p`. `GetAzimuthOrbit`, a subroutine of this program, acts as the function f_j for each of the orbital parameters $j \in$ {perihelion distance, eccentricity, etc.}, calculating all of these in parallel. `GetAzimuthOrbit` is thus called eight times in total for each orbit in order to calculate $f_j(Lag_{12} + h)$, $f_j(Lag_{12} - h)$, $f_j(Lag_{13} + h)$ etc. Here $h = 10^{-3}$ is used as this is sufficiently small to give reasonable answers, but large enough to avoid stability problems which occur at lower values[5]. Subsequently, for each of the j parameters requiring uncertainty calculation the subroutine `calc_errors` which implements equation 5.6, with wraparound protection for circular elements, is called.

5.4 Statistics on Circular Angular Parameters

Angular elements which have ranges from 0° to 360° suffer from a well known problem when statistics are required on a distribution of values which extend across

[5]Values of $h = 10^n$, where $\{-8 \leq n \leq 0,\ n \in I\}$, have been tested and $h = 10^{-3}$ found to be optimal.

the 0°/360° equivalence point.

Two methods are applied in the current study to alleviate, where possible, these problems. The first aims to shift the distribution to a section of the angular element range where there are no wraparound problems; then to perform the appropriate statistical tests and shift the results back to the original range. Software has been developed to recognise three types of distribution: Type I distributions have a clear peak with no wraparound. Type II peaks have a clear peak which requires wraparound correction. Type III peaks have no clear peak and hence are not corrected before taking statistics. These peak types are shown in Figure 5.3. An example of the automated correction of a Type II peak is given in Figure 5.4: here an argument of perihelion distribution wraps around 360°, the program solves this by defining a pivot about the midway point between the tail of each part of the peak. The part to the left of the pivot then has 360° added to shift it to the far right of the graph. Statistics of the new (magenta) peak may now be freely taken.

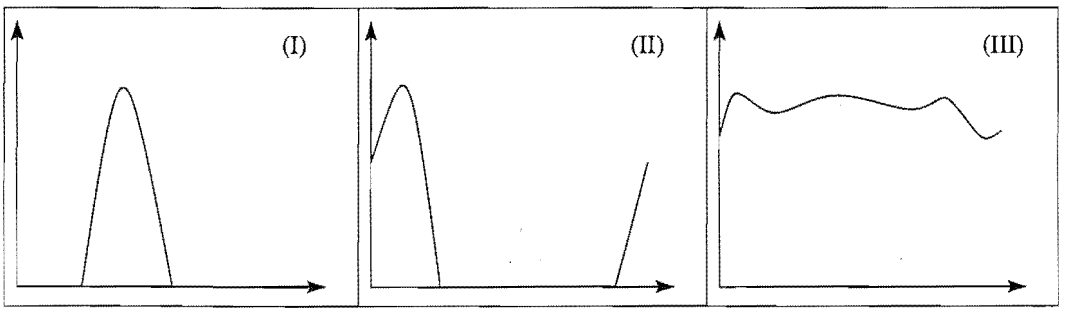

Figure 5.3: The three assumed generic types of angular distributions. A Type I peak has a clear peak well within the range $[0°, 360)$ and hence has no ambiguity. By contrast a Type II peak straddles the two extremes of the range and corrections can be applied to remove ambiguity. For a Type III peak the distribution is spread over the whole range and no corrections can be applied.

The angle correction scheme listed above is used in the implementation of randomisation method. A more convenient method for most cases was found after this implementation. This requirement of no automated peak detection or distribution corrections stands in its favour, as often a subjective decision must be made as to where the "main" part of the distribution lies in such processes. The method, often used in biology for similar problems, determines the mean and standard deviation of a sample of circular data using the trigonometric moment of that data. With reference to Fisher (1993), for a set of k angular data points (θ_k), the following preliminary calculations are made. The parameter values are split into sine and

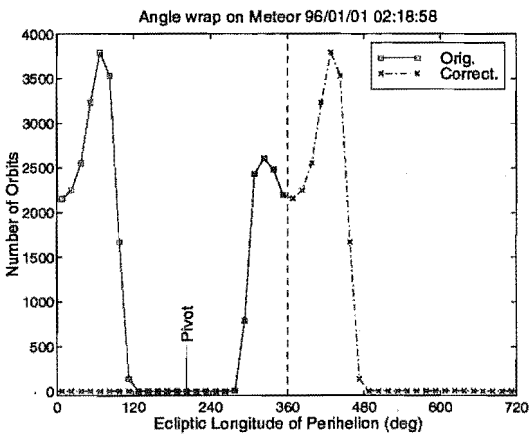

Figure 5.4: An example of computer based angular wraparound correction. The original peak (blue) is originally split in two due to this wraparound. Correction yields the magenta peak to which statistical tests may be applied normally.

cosine components defined respectively by

$$\begin{aligned} S &= \sum_{j=1}^{k} \cos\theta_j \\ \text{and} \qquad & \qquad (5.8) \\ C &= \sum_{j=1}^{k} \sin\theta_j. \end{aligned}$$

The mean direction $(\overline{\theta})$ follows from

$$\overline{\theta} = \tan^{-1}(S, C), \tag{5.9}$$

where the arctangent should be corrected to the appropriate quadrant. The mean resultant length $(\overline{R})$ associated with $\overline{\theta}$ is given by

$$\overline{R} = \frac{\sqrt{S^2 + C^2}}{k}. \tag{5.10}$$

The sample variance and sample standard deviation of the circular distribution follow respectively from

$$\operatorname{var}\theta = 1 - \overline{R}, \tag{5.11}$$

and

$$\operatorname{std}\theta = \sqrt{-2\log_e(1 - \operatorname{var}\theta)}. \tag{5.12}$$

Note that both $\overline{R}$, and therefore var θ, have ranges between zero and one.

This method is obviously much easier to implement and supervise than that the previous method; in terms of reliability it achieves very similar results to those obtained for standard deviations of wraparound corrected distributions, particularly for large samples such as those investigated presently. Therefore for future error analyses the above method is preferred as a replacement.

5.5 Uncertainty Analysis Results

While the purpose of the uncertainty analysis in the present study has been to determine uncertainties on individual orbits (for use later in this thesis), it is also instructive to look at the statistics of these for a large set of orbits. The preceding sections have described the methods leading to the derivation of individual orbital element uncertainties. This section concentrates on giving some indicative results obtained using the analytic method described in Section 5.3.2.

During the years T1995–T1997 361,380 meteor detections suitable for reduction to orbits and with eccentricities less than 1.5 were made. Each of these orbits is processed through `Analytic_orbit_err.p` to derive a set of uncertainties. The statistical results of these output sets are analysed to determine representative uncertainties on the various orbital parameters of interest.

In order to present some typical features of the uncertainty distributions in the parameters under study, two parameters have been selected in order to partition the data set into 4, more homogeneous, subsets. The parameters selected are the speed of the meteoroid in the local frame of reference of AMOR and the inclination of the orbit with respect to the ecliptic plane. The definitions of the subsets formed under the two regimes are given in Table 5.2. For increasing values of both of these parameters there is, in general, a corresponding increase in the uncertainties of the other parameters of the orbit. For parameters given relative to the Earth the local frame speed is preferred as it relates more directly while for heliocentric parameters the inclination is used for the same reason. Incidentally there is a direct link between the speed of the meteoroid measured locally at AMOR and the orbital inclination as shown in Figure 5.5. This occurs as, in general, apparently faster meteors are detected on retrograde orbits and slower ones on prograde orbits.

The method of presentation adopted uses one of the data set partition definitions of Table 5.2. For each parameter of interest a graph is shown with the cumulative number of orbits having less than a particular uncertainty being plotted. This is

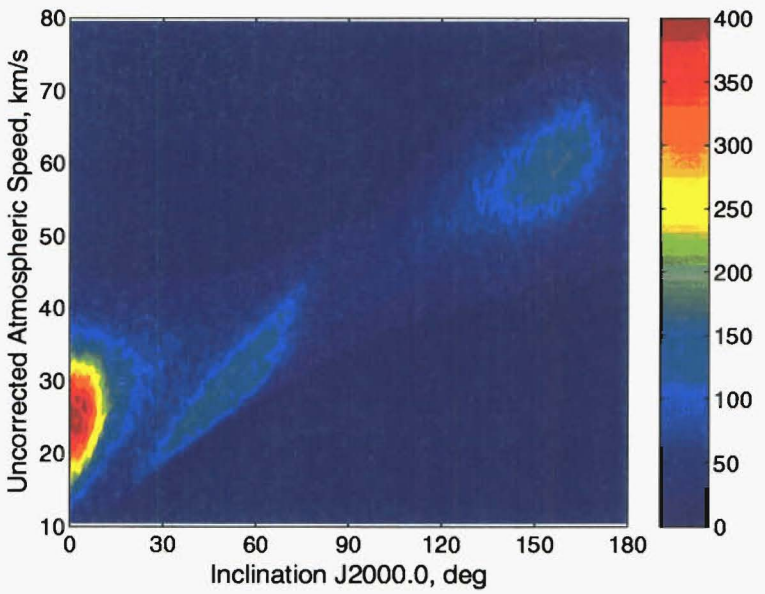

Figure 5.5: The link between atmospheric speed and orbital inclination.

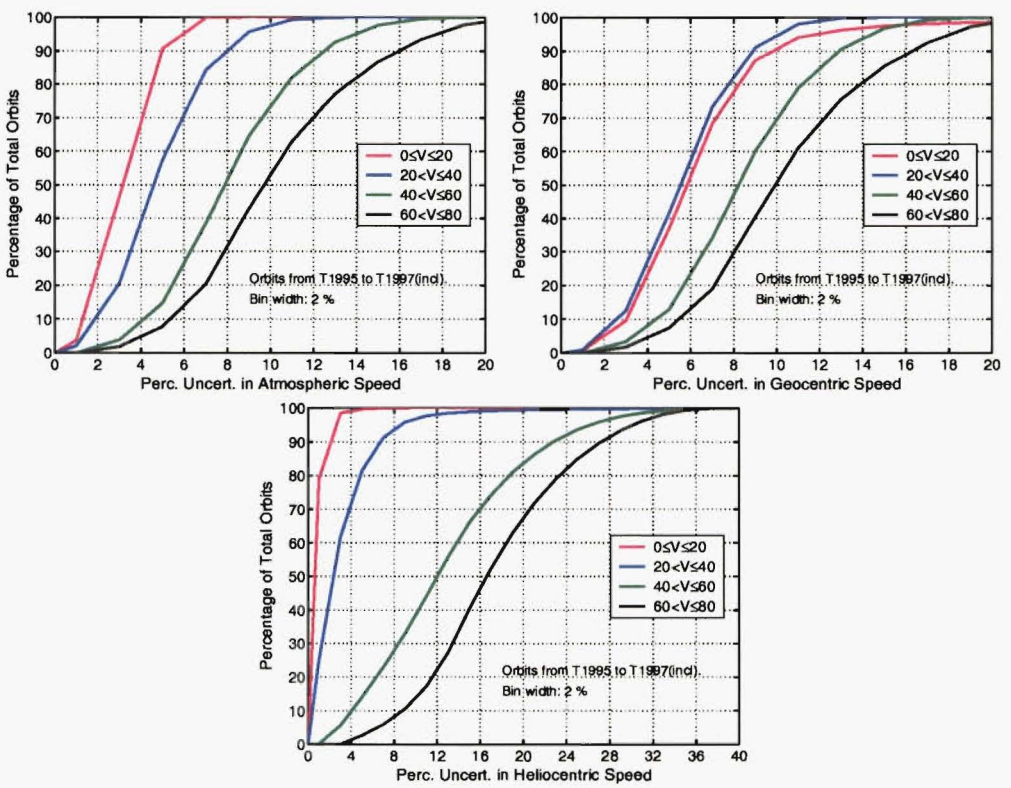

Figure 5.6: Relative uncertainties in T1995–T1997 speeds.

Subset	Atmospheric Speed Split ($\mathrm{km\,s^{-1}}$)	Inclination Split
I	$0 \leq V \leq 20$	$0° \leq i \leq 45°$
II	$20 < V \leq 40$	$45° \leq i \leq 90°$
III	$40 < V \leq 60$	$90° \leq i \leq 135°$
IV	$60 < V \leq 80$	$135° \leq i \leq 180°$

Table 5.2: Orbital subsets defined by atmospheric speed/inclination partitioning.

found to be an efficient way to see differences between the distributions in the various subsets. Graphs constructed in such a fashion also facilitate easy determination of representative uncertainties in the parameter.

The atmospheric local frame speed is used to calculate the geocentric speed, from which follows the heliocentric speed of the meteor. The heliocentric velocity components are then used to calculate the elements of the orbit. Uncertainties in each of these successive speed calculation stages will carry through to the orbit itself. Figure 5.6 demonstrates the increase in relative speed uncertainty with increasing local frame speed. This increase is caused by the lower time-lag values associated with faster meteoroids—as the absolute uncertainty in these time-lags is presumed to be constant lower values of the time-lags lead to greater relative uncertainties.

Figure 5.7 presents a summary of the uncertainties in the heliocentric velocity components. Each of the graphs shows the data set partitioned on the basis of inclination. The uncertainties increase as the inclination increases—this corresponding, in general, to a local frame speed increase in Figure 5.6. The distributions in V_x and V_z are different from what might be expected according to a simple increase in speed. In the case of V_x, one finds that the orbits in the two nearer ecliptic subsets I and IV have, in general, lower uncertainties than those in subsets II and III. This is due to the large values of V_x associated with subsets I and IV reducing the relative uncertainty in these cases. The unusual V_z uncertainty distribution follows from the high values of V_z for meteors appearing in subset II and III, these values act to reduce the relative uncertainties in these cases.

The five central orbital elements used in much orbit analysis work are the perihelion distance, eccentricity, argument of perihelion, inclination and the longitude of the ascending node. The longitude of the ascending node, as previously noted, has negligible uncertainty as it is based on the time of meteor detection. The uncertainties on the other four elements are presented in Figure 5.8, with the data set being partitioned on the basis of orbital inclination. One finds that prograde orbits have the lowest uncertainties in general. For both perihelion distance, eccentricity

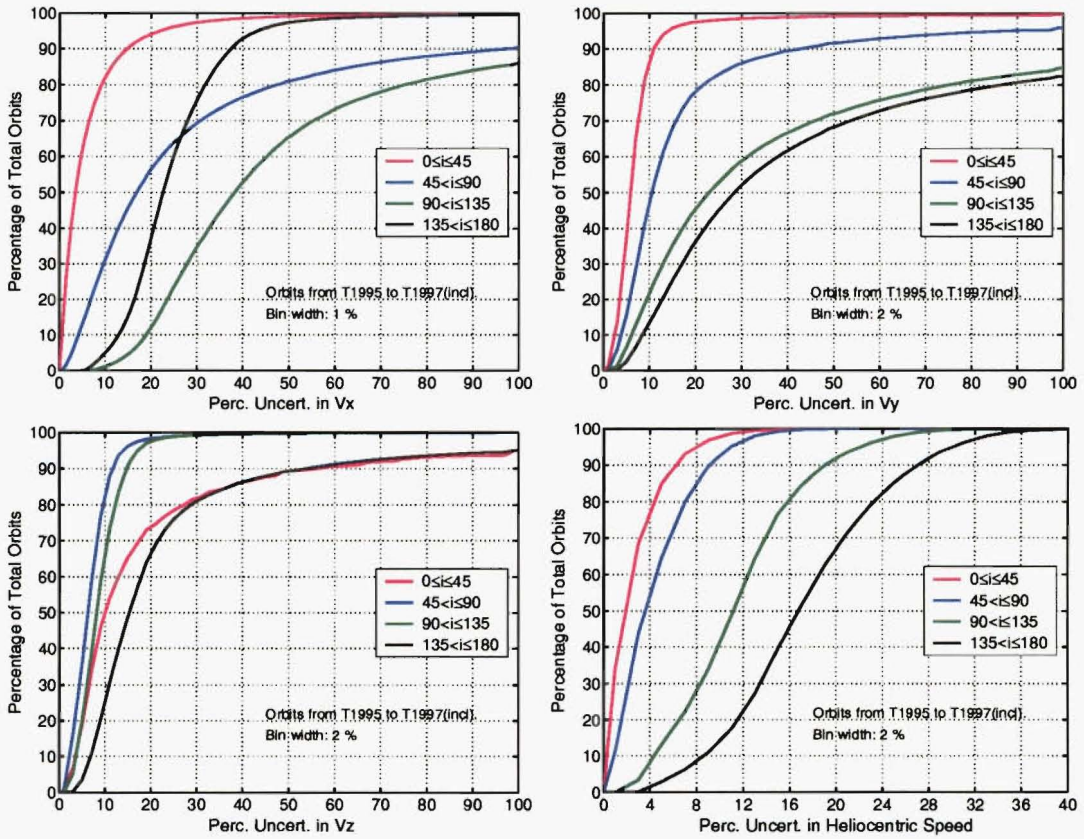

Figure 5.7: Relative uncertainties in T1995–T1997 heliocentric velocity components.

and argument of perihelion this is very true with large increases in the retrograde regime. Prograde orbits have generally slower local frame speeds (Figure 5.5) than their retrograde counterparts thus explaining this phenomenon.

The inclination angle has a different uncertainty regime than that shown for the other three orbital elements. In this case subset IV has lower uncertainties than subsets II and III. This can be explained by deriving the equation for the inclination uncertainty from Equation 2.13. Setting $\zeta = \tan i = V_z/V_x$, we have

$$\begin{aligned} \Delta i &= \frac{\Delta\zeta}{1+\zeta^2} \\ &= \frac{\zeta\sqrt{\left(\frac{\Delta V_x}{V_x}\right)^2 + \left(\frac{\Delta V_z}{V_z}\right)^2}}{1+\zeta^2} \\ &= \frac{|\sin 2i|}{2}\sqrt{\left(\frac{\Delta V_x}{V_x}\right)^2 + \left(\frac{\Delta V_z}{V_z}\right)^2}. \end{aligned} \tag{5.13}$$

According to equation 5.13 the uncertainty distributions in all four subsets will be ruled equally according to $|\sin 2i|/2$ with any differentiation being due to the

relative uncertainties in V_x and V_z. In the current case (Figure 5.7) the relative uncertainties in V_x dominate as these are generally larger than those in V_z. It has been shown that for the subsets I and IV the relative uncertainties in V_x are lower, in general, than those for subsets II and III—thus explaining the unusual order of the regions in the inclination uncertainty distribution graph.

The uncertainties in perihelion distance and eccentricity are often better stated as relative rather than absolute uncertainties. Figure 5.9 illustrates these distributions. These are especially useful in order for comparison with the representative uncertainties given in Section 5.1. Note the expected increase in uncertainty with inclination value as in most previous graphs.

The radiant position is another important source of information about a meteor shower. The radiant is defined by the right ascension and declination angles. These parameters are strongly related to the local speed—they are based on the components of the geocentric speed which differs from that in the local frame by a number of (normally small) corrections (Section 2.4). Due to this linkage the data set partitioning has been determined on the basis of local frame speed. As shown in Figure 5.10, the right ascension angle uncertainty increases almost linearly with local frame speed. The declination angle has the same very low uncertainty for all speed regimes—this is due to a strong link between the declination angle and the elevation angle of the meteor reflection point. The elevation angle has been assigned an uncertainty of 0.5° (Table 5.1). This carries through fairly directly to declination giving an uncertainty of approximately 0.5° for the majority of the orbits. Some orbits display a higher uncertainty than that expected, due simply to $\Delta\psi$, this is caused by the stronger role that the meteoroid velocity plays in these cases.

The radiant position may also be represented in ecliptic coordinates with the longitude being referenced to that of the Sun. The coordinates (λ_R, β) are defined as in Section 2.6.1. As one can see in Figure 5.10, the difference in uncertainty regimes between the longitudinal and latitudinal components corresponds to that between the right ascension and declination. The uncertainty in longitude for prograde orbits ranges from two to three times that in latitude while for retrograde orbits this figure increases to an extreme eight times. This large difference is considered later when searching for radiant shower sources in Chapter 7.

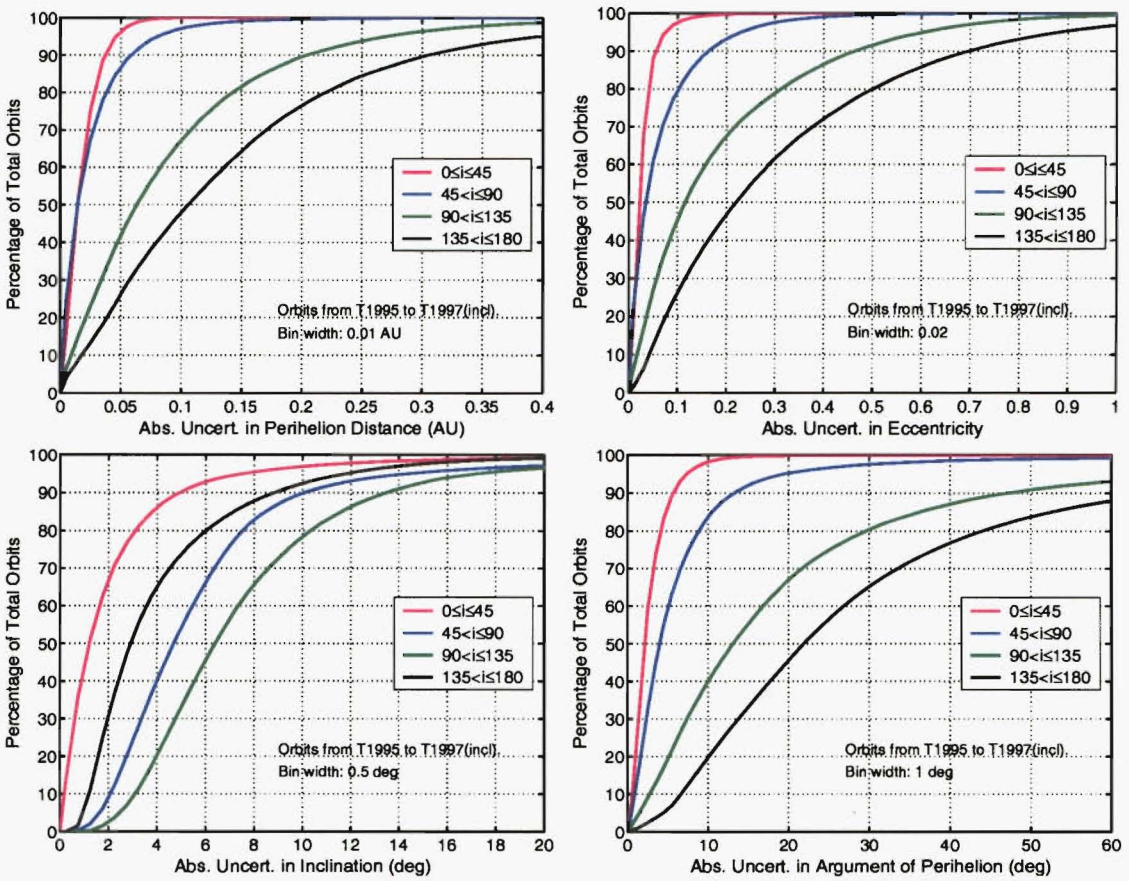

Figure 5.8: Uncertainties in T1995–T1997 main orbital elements.

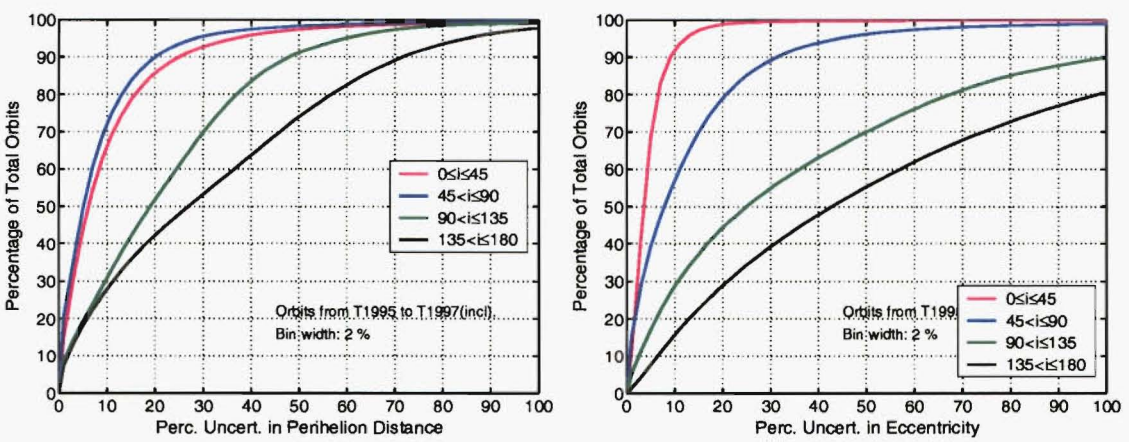

Figure 5.9: Relative uncertainties in T1995–T1997 perihelion distance and eccentricity.

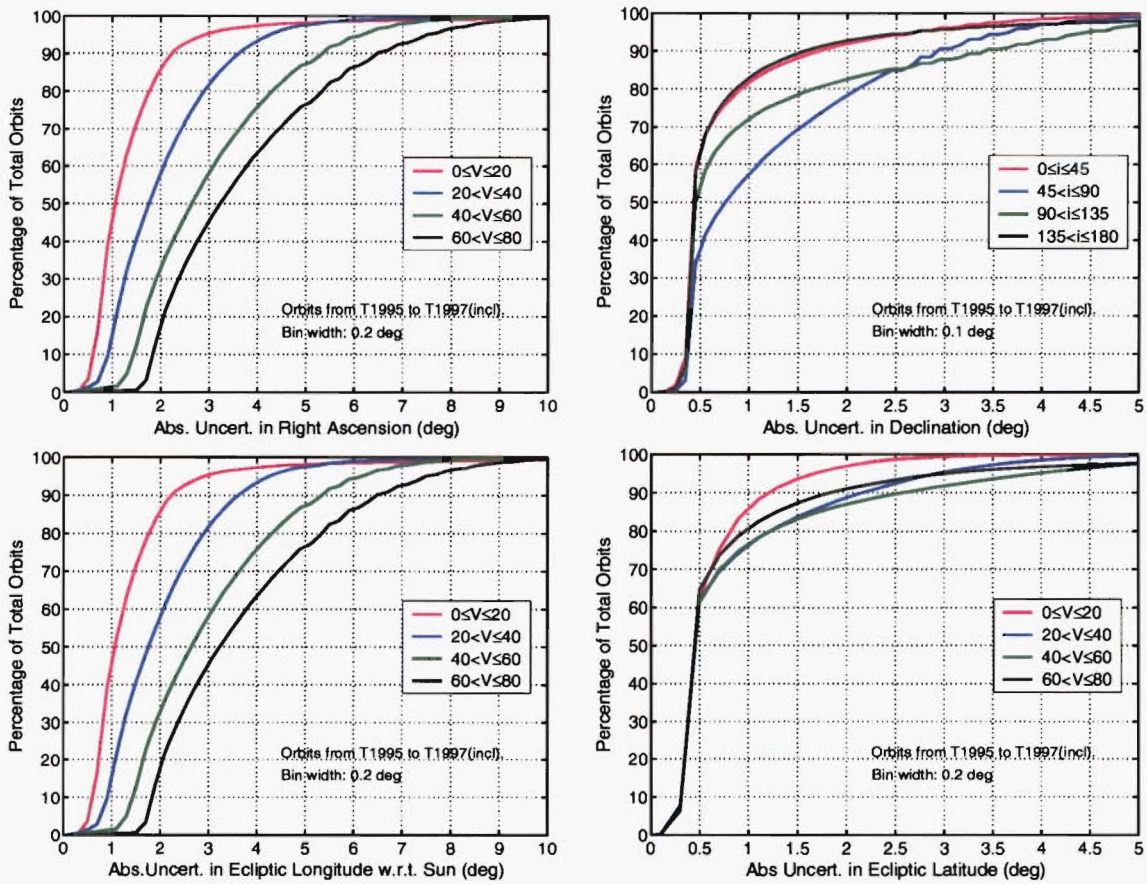

Figure 5.10: Uncertainties in T1995–T1997 radiant position are shown for both the equatorial and ecliptic systems. Note the similarity between the profiles for the pair of ecliptic longitude and right ascension and that of ecliptic latitude and declination.

5.5.1 Representative Uncertainties

From the figures of the preceding section, one can work out representative uncertainties easily by stipulating a certain percentage of orbits which must be below this representative uncertainty. Seventy percent is used as this representative cutoff in the current study. Table 5.3 presents representative uncertainties on the orbital parameters. It is easy to see from this table that as one increases the inclination of the orbits under study the uncertainties in the various orbital parameters increase, often rather sharply. This has important implications for the search for meteor shower presence in the data set. Meteoroid streams are normally found at low prograde inclinations. It is less likely to find streams at higher inclinations or in retrograde orbits, due to the predominant orbital direction of Solar System bodies and the very high density of meteoroid orbits with inclinations close to the ecliptic plane. This is just as well as the shower uncertainties at higher inclinations have been shown to become prohibitively large in this area. Only large streams, streams

with low velocities[6] at these inclinations or very strong streams whose showers occur at a time of year at which other showers in similar regions of orbital element space do not occur, are likely to be detected. One such shower is the ETA which is one of the most distinctive and of the highest activity detected by AMOR. The meteoroids from this shower are travelling in retrograde orbits at $i \approx 165°$ and are detected with geocentric speeds $V_G \approx 65$ km s^{-1}.

Parameter	Partitioning	I	II	III	IV	Unit
Perihelion Distance	INC	0.03	0.04	0.14	0.22	AU
Perihelion Distance	INC	12	9	30	47	%
Eccentricity	INC	0.03	0.07	0.23	0.39	
Eccentricity	INC	5	15	52	77	%
Argument of Perihelion	INC	5.3	11.2	37.2	57.9	deg
Inclination	INC	2.2	6.6	8.9	4.7	deg
Atmospheric Speed	SPD	0.6	1.8	5.2	8.3	km s^{-1}
Geocentric Speed	SPD	0.8	2.0	5.3	8.5	km s^{-1}
Heliocentric Speed	INC	0.3	1.2	4.8	8.3	km s^{-1}
Heliocentric Speed	INC	3	6	14	21	%
V_x	INC	6	31	57	28	%
V_y	INC	7	16	47	55	%
V_z	INC	18	8	11	22	%
Right Ascension	SPD	1.5	2.5	3.7	4.6	deg
Declination	SPD	0.6	1.5	0.9	0.6	deg
Rad. Ecliptic Longitude	SPD	1.5	2.4	3.7	4.5	deg
Rad. Ecliptic Latitude	SPD	0.6	0.8	0.8	0.6	deg

Table 5.3: Representative absolute uncertainties in the orbital parameters parameters. The uncertainties are given for each of the four subsets at the level at which 70% of all orbits are contained. In some cases the subset partition is based on local frame speed (SPD) and in others on inclination (INC). In some cases both absolute and relative uncertainties are given; the difference is clear based on the presence of a unit or percentage sign.

How do the representative uncertainties given in Table 5.3 compare with those of Baggaley et al. (1994)? The latter's representative relative uncertainty in eccentricity coincides with that for subset I and underestimates that for the other subsets. The relative uncertainty in perihelion distance is more than twice as large in this study in subset I. Again the gap increases further for the other subsets. The inclination angle uncertainty coincides for the first subset and is underestimated for the rest. The argument of perihelion uncertainty is underestimated by at least a factor of two and the uncertainty in this element increases for later subsets markedly. The relative uncertainty in the heliocentric speed is similar for the first two subsets

[6]Detection uncertainty may decrease with meteoroid speed: however, the detectability of lower speed orbits also decreases due to their weaker ionisation trains.

but increases for the rest. One must assume then, that Baggaley et al. (1994) base their estimates on lower inclination/speed orbits. This is to some extent a sensible approach, to determining a *representative* uncertainty, as although it is not globally valid it is applicable in the near-ecliptic region in which most streams are found.

When Taylor (1991) was investigating the ETA shower, he found similar uncertainties to those quoted for subset IV in which this shower falls. As shall be presented in later chapters, the standard deviations in the various elements of this relatively high uncertainty shower do validate the types of uncertainties being quoted here so there is little doubt that they are at least representative of the truth.

5.5.2 Analytic and Monte Carlo Simulation Method Comparison

It is important to compare the analytic and randomisation methods used for uncertainty analysis in order to confirm that they provide similar results. For this comparison the data set is not split into subsets, instead the differences between the uncertainties for each of the two methods are simply plotted in the style of the previous sections in order to show that they are small. This comparison is only performed for the T1997 year but is representative of the whole.

Parameter	Difference	Unit
Perihelion Distance	0.01	AU
Eccentricity	0.01	
Argument of Perihelion	3	deg
Inclination	0.1	deg
Atmospheric Speed	0.07	$\mathrm{km\,s^{-1}}$
Geocentric Speed	0.07	$\mathrm{km\,s^{-1}}$
Heliocentric Speed	0.06	$\mathrm{km\,s^{-1}}$
Right Ascension	0.08	deg
Declination	0.03	deg

Table 5.4: Representative differences between the analytic and randomisation uncertainty determination methods.

Figure 5.11 shows the comparison for the four central orbital elements and the two radiant position angles. Figure 5.12 presents a similar comparison for the various meteoroid speeds which may be measured. If we read off representative differences from these graphs, in the same way as we read representative uncertainties off the graphs in the previous section, i.e. at the 70% level, we obtain Table 5.4. When reading this table one must be careful to realise that there are no subset separations as there were in the Table 5.3, instead there is a single representative

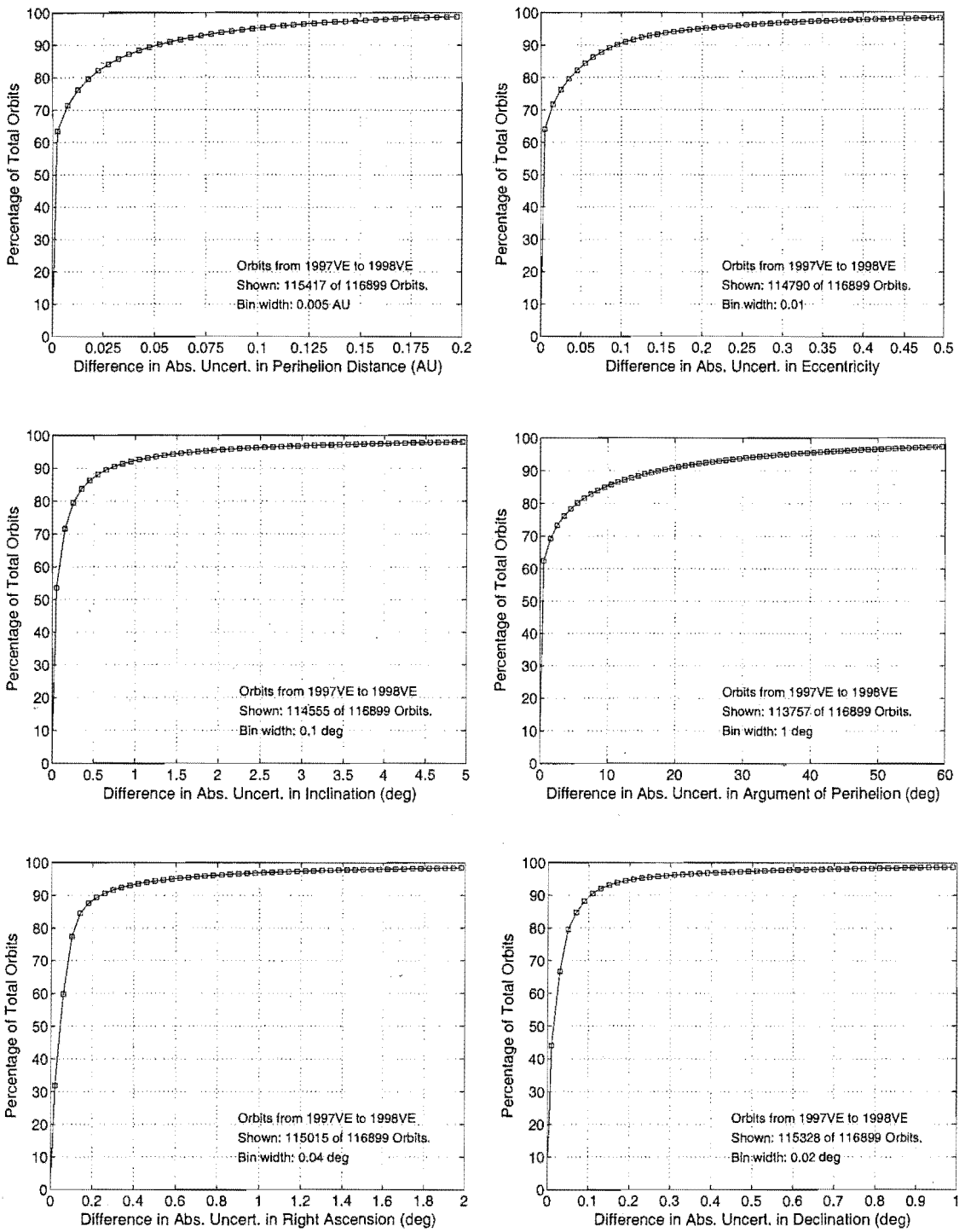

Figure 5.11: Differences between the analytic and randomisation uncertainty analysis methods for the T1997 meteoroid orbits.

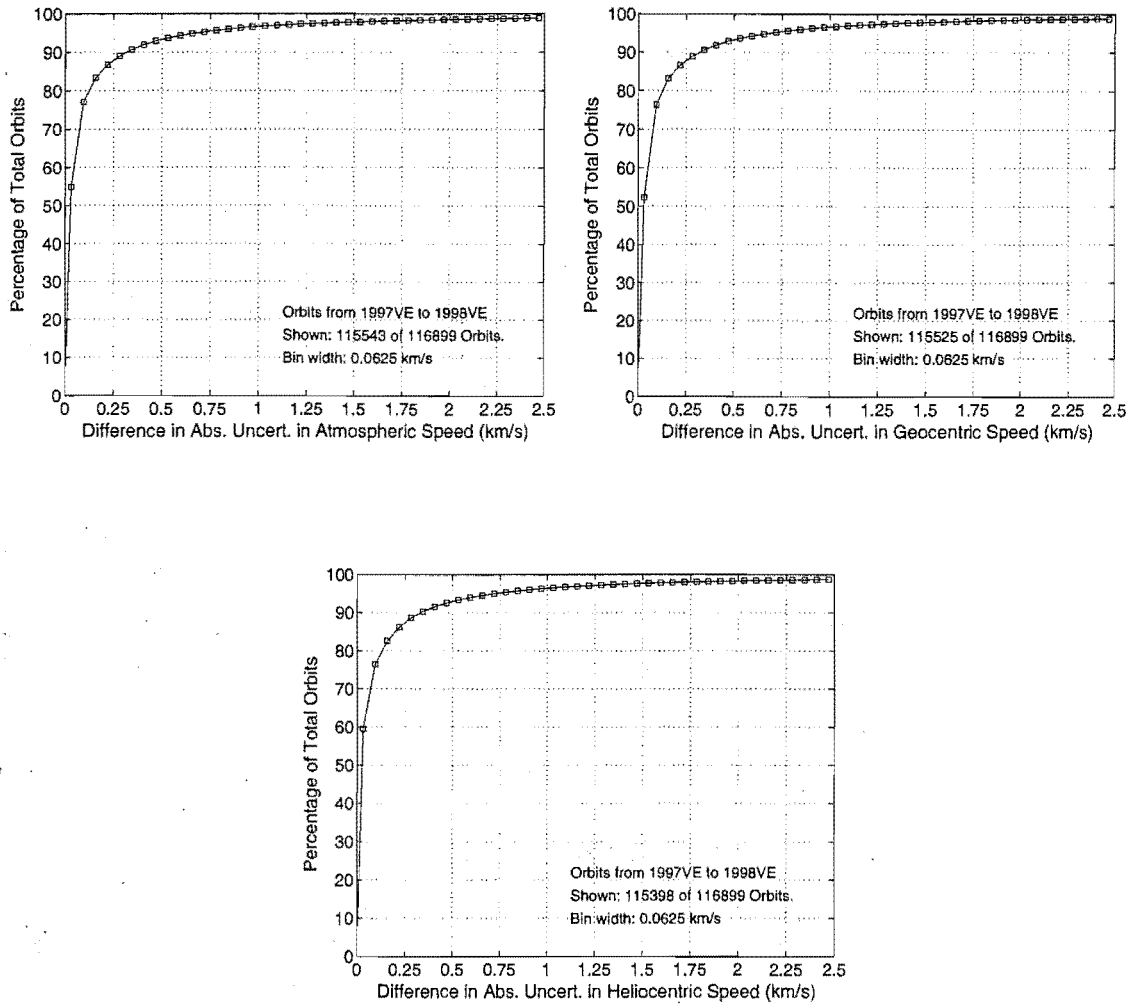

Figure 5.12: Differences between the analytic and randomisation uncertainty analysis in the study of meteoroid speed from the T1997 meteor observations.

difference encompassing all orbits. When this is taken into account all of the differences between the results of the two methods become trivial. For example the differences in right ascension angle are less than 0.1° which is much smaller than that found in the lowest uncertainty subset (I) of Table 5.3. The argument of perihelion has the largest difference. However this also has the largest angular range in the subsets—up to 58° uncertainty in subset IV in fact.

We can thus conclude that the two methods produce results which are equivalent in the main. This justifies the abandonment of the randomisation method and its replacement with the more efficient analytic method.

5.5.3 Improving on Existing Uncertainties

In the future it is anticipated that the pulse repetition frequency (PRF) of the AMOR radio transmitter will be doubled. The hardware is in place for this to

occur and it is a matter of implementing software upgrades—a nontrivial task due to timing difficulties. Such an upgrade promises to halve the uncertainties of the time-lag measurements. This is especially important for faster meteors, some of whose time-lags will be small. In the case of accurate hyperbolic meteoroid orbit determination, a topic not covered in this thesis, such PRF doubling promises to be especially beneficial due to the very high speeds involved.

Another area introducing potential errors which may need to be studied in the future are in the phase measurements from the interferometers. Determination of the elevation angle from these relies on the accurate calibration of the ground elevation to phase measurement. New equipment now being installed allows the detection of independent phases on all three antennas, as opposed to the present arrangement using relative phase. Under this new system there will then be three interferometers rather than two. Detections with a lack of agreement on all three interferometers may then be discarded.

5.6 Summary

Uncertainty analysis of the AMOR data set has been accomplished using two quite different methods and the results found to be in excellent agreement generally. The analytic uncertainty calculation method has been preferred due to its relative ease of implementation and the much greater computer efficiency achievable. A thorough uncertainty analysis of the AMOR data set has not been accomplished before and hence this work is an important step in the continuing program of radar work at the University of Canterbury.

Results have been presented from which representative uncertainties may be gleaned; the use of representative uncertainties has been shown to be inadequate to some extent due to the range of uncertainty regimes present in the data set. The increasing uncertainty with increased orbital inclination has been shown and explained through the link with geocentric speed. The uncertainty results obtained are used in later chapters in discussions of the observed spread in meteor showers observed by AMOR.

Chapter 6

Dissimilarity functions

In order to perform any analysis of orbital association a function representing the dissimilarity between any two orbits is required. Such a function must be able to differentiate orbits which appear to come from a similar progenitor from those which do not. This task is by no means easy due to the astronomical problem of orbital perturbations, in addition to the present subject of measurement uncertainty in the orbits. The latter is particularly high in radar derived orbits. Over the past 50 years several functions have been suggested.

6.1 A Survey of Dissimilarity Functions

Southworth and Hawkins (1963) introduce a dissimilarity function: the D-criterion (D_{SH}). This function uses the five orbital elements q, e, i, ω and Ω to represent the geometry of the orbit of each meteoroid; the true anomaly (ν) is ignored here due to lack of interest in the meteoroid's location within its orbit. The criterion is defined by

$$[D_{SH}]^2 = (e_2 - e_1)^2 + (q_2 - q_1)^2 + \left(2\sin\frac{I_{21}}{2}\right)^2 + \left(\frac{e_2 + e_1}{2}\right)^2 \left(2\sin\frac{\Pi_{21}}{2}\right)^2, \quad (6.1)$$

where I_{21} is the angle between the planes on which each of the two orbits lie and Π_{21} is the angle between their respective perihelion points. These angles are given by

$$I_{21} = \arccos\left[\cos i_1 \cos i_2 + \sin i_1 \sin i_2 \cos(\Omega_2 - \Omega_1)\right] \quad (6.2)$$

and

$$\Pi_{21} = \omega_2 - \omega_1 + 2\Gamma \arcsin\left(\cos\frac{i_2 + i_1}{2} \sin\frac{\Omega_2 - \Omega_1}{2} \sec\frac{I_{21}}{2}\right), \quad (6.3)$$

with Γ being defined by

$$\Gamma = \begin{cases} +1, & |\Omega_2 - \Omega_1| \leq \pi \\ -1, & |\Omega_2 - \Omega_1| > \pi \end{cases}. \quad (6.4)$$

It is interesting to note that for hyperbolic meteoroid orbits the fourth term of equation 6.1 will become very large even if the eccentricities and Π_{21} angles are very similar. This has implications for slightly hyperbolic meteoroids, such as some of those in the ETA shower, where measurement uncertainties may conspire to change near-hyperbolic elliptical orbits into hyperbolic orbits.

Since its introduction D_{SH} has been used in many stream searches and has become a de facto standard for the calculation of inter-orbital dissimilarities. Drummond (1979) introduces an alternative D-criterion (D_D) defined by

$$[D_D]^2 = \left(\frac{e_2 - e_1}{e_2 + e_1}\right)^2 + \left(\frac{q_2 - q_1}{q_2 + q_1}\right)^2 + \left(\frac{I_{21}}{\pi}\right)^2 + \left(\frac{e_2 + e_1}{2}\right)^2 \left(\frac{\theta_{21}}{\pi}\right)^2, \qquad (6.5)$$

where I_{21} is the angle between the orbital planes as defined in equation 6.2; θ_{21} is the angle between the perihelion points on each orbit (equation 6.6) and λ and β are the ecliptic longitude and latitude of perihelion. These parameters are respectively defined by

$$\theta_{21} = \arccos(\sin\beta_1 \sin\beta_2 + \cos\beta_1 \cos\beta_2 \cos(\lambda_2 - \lambda_1)), \qquad (6.6)$$

$$\lambda = \Omega + \arctan(\cos i \tan\omega) \quad [+\pi \text{ if } \cos\omega < 0], \qquad (6.7)$$

and

$$\beta = \arcsin(\sin i \sin\omega). \qquad (6.8)$$

The main difference between D_{SH} and D_D lies in the use of chords as opposed to actual angles to represent I_{21} and Π_{21} in D_{SH}. In order to balance out the effect of large perihelion distances and/or eccentricities the first two terms of D_{SH} are also divided by the sum of the respective orbital elements in D_D. Each term in D_D is weighted where necessary to provide a value which is unit-less and lies in the range 0 to 1.

Jopek (1993a) studies both the D_{SH} and D_D and concludes that they are unsatisfactory. He takes several orbits and perturbs them by an impulse, whose direction is chosen randomly, for two cases. In each case he perturbs the orbits by 10% of either their circular or orbital velocities respectively. He looks at the variation in the values of D_D and D_{SH} with changes in eccentricity of the reference orbit for a series of values of perihelion distance. He ignores elements Ω, ω and i as these have no statistical meaning given his random perturbing model.

In the case of D_{SH} a dependence on the q of the reference orbit is found. This

is not so for D_D, where the dependence is removed by the sum in the denominator of the second term. D_D shows itself to be strongly dependent on e. This problem is not present for D_{SH} until $e > 0.9$, however beyond this D_{SH} shows a much faster increase in dissimilarity than D_D, as e increases due to the third term in equation 6.1—near the parabolic limit $D_{SH} \sim 10 D_D$.

Jopek (1993a) also notes that the dependence on e for D_{SH} varies with q—this is another justification for the $1/(q_2+q_1)$ factor in D_D. He takes features from both D_{SH} and D_D to create a further D-criterion (D_H) defined by

$$[D_H]^2 = (e_2 - e_1)^2 + \left(\frac{q_2 - q_1}{q_2 + q_1}\right)^2 + \left(2\sin\frac{I_{21}}{2}\right)^2 + \left(\frac{e_2 + e_1}{2}\right)^2 \left(2\sin\frac{\Pi_{21}}{2}\right)^2 . \quad (6.9)$$

This corresponds to D_{SH} with the perihelion distance difference term changed to the form of that in D_D. Figure 6.1 shows the difference the change in this term makes.

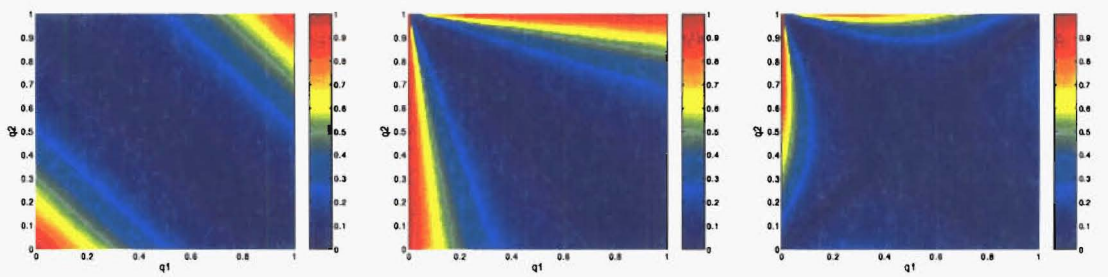

Figure 6.1: Differences between the perihelion distance difference terms of D_{SH} and D_H. On the left the $(q_2 - q_1)^2$ term values are shown for all q_1 and q_2 values between 0 and 1. The same is shown for the $((q_2 - q_1)/(q_1 + q_2))^2$ of D_H in the middle figure. The figure on the right shows the absolute difference between the values shown on the preceding figures.

The most recent attempt at the definition of a D-criterion is that of Valsecchi et al. (1999), designated D_N. The three criteria D_{SH}, D_D and D_H are all very similar with each introducing minor changes based on weightings of the various parameters but essentially preserving the measure of distance based on the conventional orbital elements q, e, i, ω and Ω. D_N introduces a departure from these earlier criteria. It is defined in terms of the geocentric velocity components of the orbit immediately prior to the gravitational influence of the Earth apply (U_x, U_y, U_z), as shown in Figure 6.2. The mass of the Sun and the gravitational constant G are set to 1. The heliocentric velocity of the Earth is set to a constant $V_\oplus = 1$, disregarding the Earth's mass. The geocentric speed (U) is then defined by

$$U = \sqrt{3 - T}, \quad (6.10)$$

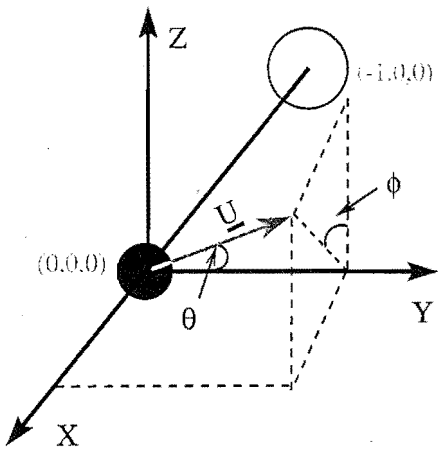

Figure 6.2: Geocentric velocity geometry. The velocity, **U** may be broken down into components U_x, U_y and U_z. U_x is measured in a negative direction from the Sun, U_y is in the direction of the Earth's motion and U_z is perpendicular to the ecliptic plane. Alternatively **U** may be represented by the speed U ($\|\mathbf{U}\|$) and two angles θ and ϕ. θ is the angle between the y-axis and **U**. ϕ is the angle between the yz-plane and **U**y-plane. The Sun is shown as a light ball located at (-1,0,0) and the Earth is shown in a darker colour at (0,0,0).

where T is the Tisserand parameter given by

$$T = \frac{1}{a} + 2\sqrt{a(1-e^2)}\cos i. \tag{6.11}$$

The components of U can be expressed in terms of orbital elements a, e and i:

$$U_x = \pm\sqrt{2 - \frac{1}{a} - a(1-e^2)}, \tag{6.12}$$

$$U_y = \sqrt{a(1-e^2)}\cos i - 1, \tag{6.13}$$

and

$$U_z = \pm\sqrt{a(1-e^2)}\sin i. \tag{6.14}$$

U_x and U_z must be multiplied by -1 for pre-perihelion impacts and descending node impacts respectively. The ascending/descending node of an orbit is readily gleaned from the sign of the heliocentric velocity component in the **z** direction (V_z). The intersection is at ascending node for $V_z > 0$ and descending mode for $V_z < 0$. The position with respect to perihelion is determined from the value of V_x. The radial velocity $V_r = -V_x$. Radial velocities which are positive are post-perihelion and those which are negative are pre-perihelion.

Alternatively the velocity components may be determined directly from the geocentric velocity and radiant position as measured by V_G and (α,δ) respectively

for the terrestrial longitude at detection ($\lambda^{\oplus}$):

$$\begin{pmatrix} U_x \\ U_y \\ U_z \end{pmatrix} = \mathbf{r}(\lambda^{\oplus})\ \mathbf{p}(\epsilon)\frac{V_G}{29.7}\begin{pmatrix} -\cos\delta\cos\alpha \\ -\cos\delta\sin\alpha \\ -\sin\delta \end{pmatrix}, \tag{6.15}$$

where $\mathbf{r}$ and $\mathbf{p}$ are the rotation matrices about the x- and z-axes respectively, and ϵ is the obliquity of the ecliptic.

The geocentric speed together with angles defining its direction (θ and ϕ) are used to calculate the similarity of orbits. These angles are illustrated in Figure 6.2 and defined by

$$\theta = \arccos\frac{U_y}{U} \tag{6.16}$$

and

$$\phi = \arctan\frac{U_x}{U_z}. \tag{6.17}$$

Here the calculated ϕ must be adjusted to the correct quadrant according to the signs of U_x and U_z as shown in Table 6.1

Rel. Perihelion	Node Type	U_x	U_z	ϕ
Post-perihelion	Ascending	>0	>0	$0 < \phi < \frac{\pi}{2}$
Post-perihelion	Desending	>0	<0	$\frac{\pi}{2} < \phi < \pi$
Pre-perihelion	Ascending	<0	>0	$\frac{3\pi}{2} < \phi < 2\pi$
Pre-perihelion	Descending	<0	<0	$\pi < \phi < \frac{3\pi}{2}$

Table 6.1: Adjustment of ϕ to correct quadrant.

Valsecchi et al. (1999) resolve to use $\cos\theta$ instead of θ in their dissimilarity function as this is linearly dependent on 1/a, the orbital energy of the meteoroid. This relationship to 1/a is given by

$$\cos\theta = \frac{1 - U^2 - 1/a}{2U}. \tag{6.18}$$

D_N is defined as

$$D_N^2 = [U_2 - U_1]^2 + w_1[\cos\theta_2 - \cos\theta_1]^2 + \Delta\xi^2, \tag{6.19}$$

where:

$$\Delta\xi^2 = \min[w_2\Delta\phi_A^2 + w_3\Delta\lambda_A^2, w_2\Delta\phi_B^2 + w_3\Delta\lambda_B^2], \quad (6.20)$$

$$\Delta\phi_A = 2\sin\frac{\phi_2 - \phi_1}{2}, \quad (6.21)$$

$$\Delta\phi_B = 2\sin\frac{\pi + \phi_2 - \phi_1}{2}, \quad (6.22)$$

$$\Delta\lambda_A = 2\sin\frac{\lambda_2^{\oplus} - \lambda_1^{\oplus}}{2}, \quad (6.23)$$

and

$$\Delta\lambda_B = 2\sin\frac{\pi + \lambda_2^{\oplus} - \lambda_1^{\oplus}}{2}. \quad (6.24)$$

The weighting factors w_i are all set to 1 in the current study as they are by Valsecchi et al. (1999). It is possible to use other weighting schemes however the possibilities presented by manipulating the three weightings are such that this could be the topic of a large study in itself.

The first two terms of D_N are obvious while the third requires further explanation. $\Delta\xi$ encapsulates the differences in the ϕ and $\lambda^{\oplus}$ angles between the two orbits. $\lambda^{\oplus}$ is the longitude of the Earth at the time of meteoroid detection: differences between $\lambda^{\oplus}$ correspond to differences in time of year and in Ω.

As shown in equation 6.20, $\Delta\xi$ is measured as the minimum of two choices. The first choice allows for both small differences in ϕ and λ between the orbits being compared. The second allows differences which are both near π radians, in this instance one is comparing two meteoroids sharing the same orbit but sampled at opposite nodes. In both cases the length of the chord between the angles is used.

6.2 Practical Implementation of the D-criteria

While the previous section has focussed on the definitions and implications of using the various dissimilarity functions D_{SH}, D_D, D_H and D_N, this section looks at issues involved in the computer implementation of these. While at first the definitions may seem simple there are a number of hidden pitfalls. Mostly these relate to division by zero problems.

One would not normally expect to obtain a floating point number exactly equal to 0.0 or the sum of two numbers being exactly equal to 180.0 (for angles stored in degrees). The probability of such occurrences is normally very low, however due to the storage precision of the AMOR data set (typically 1–3 decimal places in the

various parameters), combined with all of the possible inter-combinations of the several hundred thousand orbits available, the likelihood of obtaining such exact numbers is increased enormously.

6.2.1 Issue I

The first two problems impact both D_{SH} and D_H. When $I_{21} = \pi$, $\sec(I_{21}/2)$, used in equation 6.3 is undefined. In order to study the parameter combinations leading to this, we set $I_{21} = \pi$ in equation 6.2 to give

$$\Pi = \arccos(\cos i_1 \cos i_2 + \sin i_1 \sin i_2 \cos(\Omega_2 - \Omega_1)). \tag{6.25}$$

This has the solution $\Sigma i = \pi$ when $\Delta\Omega = \pm\pi$ and $i_1 = 0, i_2 = \pi$ or $i_1 = \pi, i_2 = 0$ for $0 \leq \Delta\Omega \leq \pi$. Hence we must have $\Sigma i = \pi$ accompanying $I_{21} = \pi$. Substituting this into equation 6.3 yields

$$\Pi_{21} = \Delta\omega + 2\Gamma \arcsin\left(\cos\frac{\pi}{2}\sin\frac{\Delta\Omega}{2}\sec\frac{\pi}{2}\right). \tag{6.26}$$

This simplifies to give an alternative equation for the Π_{21} calculation to be used instead of equation 6.3 whenever $I_{21} = \pi$:

$$\Pi_{21} = \Delta\omega + 2\Gamma \arcsin\left(\sin\frac{\Delta\Omega}{2}\right). \tag{6.27}$$

The other problem encountered by both D_{SH} and D_H is caused solely by computer storage precision. When $\cos \Sigma i/2 = \cos I_{21}/2$ the product $\cos(\Sigma i/2)\sec(I_{21}/2)$ in equation 6.3 equals 1. However due to storage precision one may obtain a product which is very slightly different from 1, e.g. 1.00000000002. This answer is a mathematical impossibility as the product of two cosine terms must by less than or equal to 1.0. The occurrence of this condition causes problems with the arcsine term in equation 6.3 when coincident $\Delta\Omega = \pi$. The nature of the returned error differs between different compiler implementations[1]. Functions `asin_protect` and `acos_protect` have been created to protect against this problem. Arguments greater than 1.0 are set to 1.0 while those less than -1.0 are set to -1.0 before the arcsine or arcosine are taken respectively.

[1]In fact in this case the DEC Alpha returns 0.0 as the arcsine while the Intel Linux Computer returns NaN.

6.2.2 Issue II

A problem faced by both D_H and D_D is division by zero in the first two terms of equation 6.5 for D_D and the second term of equation 6.9 for D_H. These terms are all structured in the form

$$\frac{\Delta x}{\Sigma x}, \tag{6.28}$$

where x is either q or e. As $x \geq 0$ the only possibility for division by zero to occur is for $\Delta x = \Sigma x = 0$, i.e. the $0/0$ case. The solution in such cases is to set the term equal to zero.

6.2.3 Issue III

Another aspect to consider with D_{SH} and D_D is the use of the $\pm$ sign in equation 6.3. The original paper introducing D_{SH} (Southworth and Hawkins 1963) as with most papers since does not mention the need for this sign on the arcsine. Drummond (1981) appears to be the only paper notifying this requirement. On examination it is found to be an important addition. If we take the case of $\cos \Sigma i/2 = \cos I_{21}/2$ then one is left with

$$\Pi_{21} = \Delta\omega \pm 2 \arcsin\left(\sin\frac{\Delta\Omega}{2}\right). \tag{6.29}$$

In this case by definition

$$\Pi_{21} = (\Omega_2 + \omega_2) - (\Omega_1 + \omega_1). \tag{6.30}$$

Taking, as an example, $\Delta\Omega = \pi + 0.2$ and $\Delta\omega = 0.4$ we have

$$\begin{aligned} \Pi_{21} &= 0.4 - 2\arcsin\left(\sin\frac{\pi + 0.2}{2}\right) \\ &= 0.4 - 2 \times \frac{\pi - 0.2}{2} \\ &= \pi + 0.6. \end{aligned} \tag{6.31}$$

This is as expected from equation 6.30. However if the '+' sign is used instead of '−' then we have $\Pi_{21} = \pi + 0.2$. This is clearly not equal or related to $\Pi_{21} = \pi + 0.6$ which corresponds to $\Pi_{21} = \Delta\Omega + \Delta\omega$, the expected answer.

The reasoning behind this example is that the $2\arcsin(\sin(\Delta\Omega/2))$ directly outputs values of $\Delta\Omega \leq \pi$. However for $\Delta\Omega > \pi$ it outputs $2\pi - \Delta\Omega$. By multiplying this expression by -1 we have $\Delta\Omega - 2\pi$ or simply $\Delta\Omega$ making the form of equa-

tion 6.30 attainable.

6.2.4 Issue IV

There are several areas where D_N is vulnerable to problems with specific orbits or combinations of orbits. Problems arise if either of the following are true:

1. $a = 0$ causing division by zero of $1/a$ in $2 - 1/a - a(1 - e^2)$
2. $2 - 1/a - a(1 - e^2) < 0$

Condition 1 is unlikely to occur as an orbit with $a = 0$ is fully contained in the Sun. Due to the precision at which parameters in the AMOR data set are stored (see Appendix B) one does in practice obtain some orbits with $a = 0.00$. These occur only for $e = 6$ or $e = 60$ which are the preset maximum storage values for AMOR eccentricities at different stages of the data set history. Such orbits are so hyperbolic that it is impossible to define a reasonable value of a; these orbits are generally ignored in the current study as being of no interest in a study of Solar System meteoroid streams produced by comets.

Condition 2 does occur in a small number of orbits; the left hand side of this equation equals zero when

$$a = \frac{1 \pm e}{1 - e^2}. \tag{6.32}$$

This constraint is exactly that applied by the $q \leq r_\oplus$, $Q \geq r_\oplus$ conditions of equation 3.1. This equation assumes $r_\oplus = 1$ AU. Those orbits exhibiting Condition 2 exceed the limits applied by equation 6.32 mostly by small amounts. In fact they are entirely due to Aphelion distances in the range $0.975 < Q < 1.000$ AU in the AMOR data set. The problem stems from Öpik's original assumption of a planet on a circular orbit whereas due to the eccentricity of the Earth (≈ 0.016) the orbital radius varies slightly about 1 AU as discussed in Section 3.4. The solution here is to take the absolute value of the left hand side of Condition 2.

6.3 Characteristics of the D-criteria

In order to perform searches for members of a stream often a mean stream orbit is used. All orbits falling within a certain D-criterion value of this mean are then said to be members of the stream.

For example, typically when using the Southworth and Hawkins D-criterion, researchers will use a cutoff level of $D_{SH} = 0.10$ to find orbits in *very good* agreement with the mean orbit, this cutoff is generally extended up to a maximum of $D_{SH} = 0.25$ at which peripheral members of the stream are found. As an example Drummond (1981) uses limits of $D_{SH} = 0.25$ simultaneously with $D_D = 0.10$ to determine associations of meteoroids with mean stream orbits.

6.3.1 Sporadic Intrusion

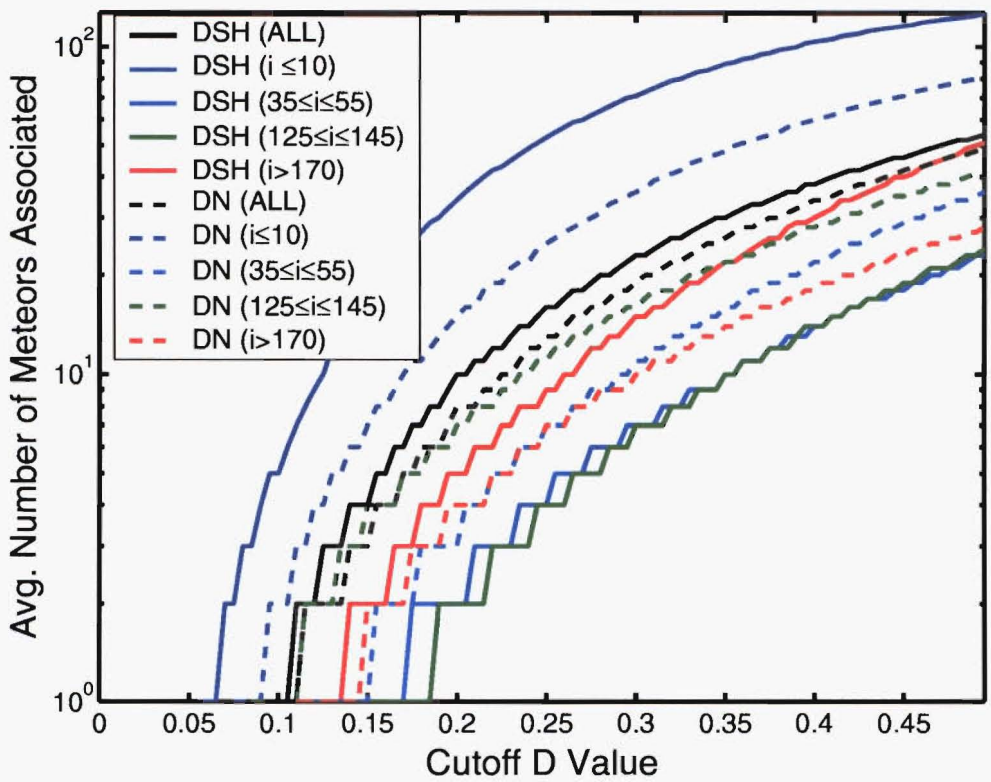

Figure 6.3: Intrusion of the Sporadic Background. The AMOR data set from the T1997 year is partitioned on the basis of inclination value. Orbits are selected at regular intervals from these regions and the number of associated meteoroids plotted as D-cutoff for association is increased. Intrusion is generally highest for very low inclination orbits.

It is difficult to get a feel for the relative qualities of the different D-criteria with respect to the inclusion of sporadics in streams found by direct stream searching simultaneously with regard to the retrieval of as much as possible of the original stream whose members have been simply spread out due to uncertainties in their orbital elements. The definition of a sporadic is obviously difficult—at some point the members of a shower will have such high uncertainties that many of them may be unrecognisable by any reasonable test as such. The data set from T1997 has been

partitioned into large-scale regions on the basis of orbital inclination (recall that the orbital parameter uncertainty generally increases with increasing inclination). Two of the dissimilarity functions, D_{SH} and D_N, have been chosen for the analysis as these represent quite different paradigms. Orbits in each inclination-defined region have been selected at set intervals from the data set to produce a subset containing 2,000 to 3,000 orbits in each region. In each of these partitions all of the subset members are compared to all of the orbits recorded the T1997 data set. The two dissimilarity values for each comparison are recorded. From these analyses Figure 6.3 is produced, this shows the average number of orbits retrieved in each region as the D-cutoff level is increased for a direct search.

The implicit assumption in this analysis is that only a small percentage of the overall AMOR meteoroid data set are shower members. Hence what is being presented is the likelihood of an orbit in a particular region being associated with other meteoroid orbits when in fact there is no real relationship, i.e. the likelihood of sporadic intrusion.

Referring to Figure 6.3, the first impression is that for both D_{SH} and D_N, the risk of sporadic intrusion is much greater at near-ecliptic ($i < 10°$) inclinations. Hence a lower level of D-cutoff is required in this region with D_{SH} showing itself to be systematically more prone to intrusion than D_N. D_{SH} is more prone to intrusion in this region for two reasons: this is by far the highest orbital density region and, also as i is near zero for this large number of orbits one of the two dimensions Ω and ω are lost as these angles are then measured approximately on the same plane, therefore effectively coalescing into a single entity, the longitude of perihelion (ϖ=$\Omega + \omega$)—with less parameters defining the orbital dissimilarity in D_{SH}, it becomes more probable for unrelated orbits to be declared similar. There are thus only really three independent elements defining orbits in this region: q, e and ϖ. Additionally q and e are linked directly to ω (equation 3.3) and therefore influence ϖ. The need for a low D-cutoff in this area is not as stringent as one might at first think as the uncertainties (and therefore spread induced by them on the orbits in this region) are also generally the lowest.

The retrograde equivalent to $i < 10°$ is $i > 170°$. This region only contains about 4% of the total T1997 data set and has relatively higher uncertainties than those for $i < 10°$. It is thus not surprising that the number of sporadics associated at any particular cutoff level should be smaller. At intermediate inclination regions in both retrograde and prograde regimes the differences between D_{SH} and D_N show

through. In both cases D_N appears to systematically associate a greater number of sporadics—the numbers retrieved in these regions are much lower than for the near-ecliptic D_{SH} case so the results are not so significant or potentially damaging. As will be discussed later in this section D_N is more robust with respect to spread caused by uncertainty than D_{SH}. The latter is well known for its ease of sporadic intrusion at low inclinations and its much harsher regime at higher inclinations while D_N is more even across the range of regions.

Finally a curve is presented on Figure 6.3 for a selection of orbits from the complete T1997 data set. This is biased upwards towards the low inclination curves but does indicate that despite the differences D_{SH} and D_N overall produce similar amounts of sporadic intrusion for a given cutoff level in the data set.

6.3.2 Significant D-criteria Values For Stream Retrieval By Monte Carlo Simulation

It is useful to establish typical D-criteria cutoff levels which may be used in the case of AMOR orbits to find streams whose orbits have been spread simply due to their uncertainties—spread by this mechanism is expected to be the dominant effect in data set with orbital perturbation and physical spread effects being of lesser importance. In order to accomplish this, the computer program `create_smeared_orbits.p` has been created. This produces a data set of orbits using Monte Carlo simulations where a single input orbit is chosen and a spectrum of input fundamental parameters, based on those of the chosen orbit, are used to simulate the possible range of results which might be obtained assuming a certain level of uncertainty in these parameters. The assumption of a Gaussian distribution in the fundamental parameters with standard deviations equivalent to their respective uncertainties is made (these uncertainties are taken from Table 5.1). In the current study for each input orbit, 5×10^4 simulated orbits have been produced by random selection of sets of the fundamental input parameters $(Lag_{12}, Lag_{13}, \psi)$ from their uncertainty defined Gaussian distributions. Additionally the uncertainty in position in the beam has been simulated by an azimuth angle distribution based on a 2σ wide Normal distribution. The meteor detection time has no uncertainty however a Gaussian distribution with a standard deviation of 1 Solar day has been used to simulate the spread in time of detection.

The 5×10^4 simulated meteor observations are processed by a modified version of `GetAzimuthOrbit` in order to produce output orbits. This procedure calculates

the azimuth angle of the meteor from time-lag measurements and then adds the beam uncertainty ΔA value to this angle. Likewise the time-spread is not used until the stage at which heliocentric components are being calculated as changing the date/time from that originally detected at the start of the procedure invalidates the meaning of the derived local frame velocities—these must be established at the original orbit date.

Meteor showers for study have been chosen from the stream data set discussed in Section D.1, some of these showers are well established while others are quite minor. The selection process is simple: any stream orbit which could demonstrate at least a single associated member, within $D_{SH} < 0.04$ of the mean orbit, in the AMOR data set is chosen. The result of this strategy is to produce 45 orbits which appeared at very similar times of year to each of 45 showers and had almost identical orbits. These similar orbits are listed in Table 6.2. Particularly of note in this table are the low prograde inclinations of the majority of the orbits—due to the detection probability it is more likely to find meteoroids on near-ecliptic orbits as earlier discussed. The fundamental detection parameters for each of these meteoroids were put through the process described above and 5×10^4 orbit simulations each thus produced.

The resultant orbit sets were compared in MATLAB using `dcrit_char.m`. In the case of each set, the progenitor orbit is assumed to be the mean orbit for the 5×10^4 simulated orbits. The dissimilarities between the parent and these orbits are determined for each of the four D-criteria functions discussed in Section 6.1. The data output are presented by showing the percentage of simulated orbits retrieved as the D-criterion cutoff is increased. Three representative levels have been chosen being those corresponding to 50%, 70% and 90%. Figure 6.4 presents the results for searches using D_{SH}, D_H, D_D and D_N respectively while Table 6.3 summarises the results from these figures. Additionally Figure 6.5 shows the full profiles returned from the Monte Carlo simulations for 5 of the 45 mean orbit based simulations in order to provide examples of the data on which the overall statistics are based.

Due to their functional similarity D_{SH} and D_H produce similar results—for low inclination streams D values of ≈ 0.10 retrieve 70% of the simulated orbits while D_D and D_N require only about two-thirds of this value to achieve a similar level of success. A higher cutoff is required for higher prograde inclinations with the difference in the eccentricity term of the D_H function causing a higher cutoff to be required than for D_{SH} at the 70% level. D_D and D_N again required lower values.

CSF	Shower	ID	$\lambda_\odot$	q(AU)	e	i	ω	Ω	α	δ	V_T	V_G	V_H	L_{12}	L_{13}	ψ
68	λ Virginids	960407:021035:067	17.1	0.311	0.861	4.5	119.3	197.1	207.3	-14.8	31.6	30.8	37.1	29.6	8.9	27.8
200	Nth α Virginid	960421:070405:093	31.0	0.386	0.844	7.6	290.3	31.0	220.3	-8.8	29.7	29.0	37.5	42.5	51.1	157.2
9	μ Virginids	960425:230117:039	35.6	0.482	0.840	10.5	278.2	35.6	221.2	-4.7	28.7	27.3	38.3	1.9	-27.6	36.7
10	α Scorpiids	960504:014629:038	43.5	0.217	0.890	2.1	131.8	223.4	239.9	-21.8	33.8	33.0	36.2	15.7	-0.4	21.4
14	η Aquarids	970504:075019:166	43.4	0.557	0.952	164.2	94.7	43.5	336.6	-1.9	64.8	65.4	41.0	12.6	-2.9	41.6
127	ϕ Ophiuchids	950507:040332:013	45.7	0.149	0.924	8.3	320.8	45.7	247.5	-18.1	36.2	35.8	36.2	31.2	19.0	22.4
72	θ Ophiuchids	960606:195118:026	75.9	0.399	0.818	5.0	110.5	255.9	264.7	-28.0	28.9	27.5	36.6	-52.0	-44.9	155.8
142	γ Pegasids	960609:062512:067	78.3	0.724	0.657	148.8	106.0	78.3	358.0	16.3	61.1	61.6	36.4	15.0	-6.1	59.9
261	GE0609	970612:015625:035	80.7	0.140	0.899	38.1	325.2	80.7	290.4	-6.9	36.4	35.8	33.3	16.6	-7.9	36.0
126	μ Sagittariids	950628:213359:005	96.3	0.664	0.744	4.5	259.2	96.3	270.3	-16.6	22.7	20.5	37.5	-16.9	-39.9	21.3
32	Sth δ Aquarids	950729:003448:121	125.0	0.074	0.948	26.7	154.8	305.0	341.4	-16.3	37.9	37.3	33.6	-7.3	-22.6	23.7
34	α Capricornids	950729:013903:127	125.1	0.568	0.766	7.4	270.9	125.1	305.6	-9.6	24.5	22.9	37.2	45.1	15.6	31.9
35	Sth ι Aquarids	960802:233312:026	130.5	0.189	0.917	7.1	134.5	310.5	334.0	-14.7	35.1	34.3	36.9	-9.1	-26.0	24.9
33	Nth δ Aquarids	970811:063402:098	138.2	0.068	0.964	18.1	334.2	138.2	346.7	-0.4	39.2	39.1	35.9	42.8	34.4	40.6
91	Nth δ Aquarids	950816:235402:050	143.2	0.087	0.963	18.8	329.6	143.2	349.0	1.5	39.8	39.3	37.1	1.4	-22.5	44.4
36	Nth ι Aquarids	950821:020809:061	147.2	0.272	0.847	5.7	306.5	147.2	344.0	-2.6	30.6	29.6	35.4	36.1	5.8	39.8
175	Aquarids Cetids	970822:231028:042	149.4	0.139	0.937	21.8	141.6	329.4	358.2	-10.4	37.6	36.9	36.8	-14.6	-30.1	27.7
186	Sth α Capric	970822:225614:006	149.4	0.645	0.620	5.5	86.9	329.4	333.3	-20.9	20.4	17.9	35.1	-6.2	-30.8	19.0
85	Nth ι Aquarids	960902:224653:028	160.3	0.324	0.835	3.6	299.4	160.3	353.4	0.2	29.8	28.5	36.2	-2.7	-32.4	42.0
39	Sth Piscids	950922:062710:042	178.4	0.424	0.793	2.2	107.8	358.4	7.3	0.7	26.6	25.6	36.5	57.3	56.8	31.7
42	κ Aquarids	950922:200454:015	178.9	0.811	0.752	1.8	236.4	178.9	338.6	-4.9	19.1	16.2	38.7	-18.6	-54.7	32.2
151	ζ ϵ Piscids	970923:011651:019	179.6	0.261	0.844	4.3	128.0	359.6	17.4	4.1	30.6	29.5	35.2	29.7	-5.9	46.3
167	α Leonids	950923:094812:048	179.5	0.101	0.954	18.7	32.7	179.5	157.6	16.1	39.6	39.2	36.9	19.5	-12.5	59.2
45	Day. Sextantids	970929:112404:086	185.9	0.140	0.855	22.3	209.9	5.9	152.1	-0.2	31.2	30.4	29.2	43.0	13.9	42.1
205	Sth ϵ Piscids	970928:004746:079	184.5	0.605	0.754	4.0	85.5	4.5	4.3	-4.3	23.2	21.4	37.6	42.5	4.3	37.1
159	Sth Arietids	971021:012309:015	207.2	0.337	0.834	6.4	117.0	27.2	39.7	9.9	29.6	28.5	36.7	39.2	-0.3	51.8

Table 6.2: Representative mean orbits corresponding to given showers. These orbits were used to create smeared orbit data sets. They are chosen as representative of the different showers after which they are named. They were selected by a very conservative D-criterion comparison against mean orbits contained in the common stream format data set file (Section D.1).

CSF	Shower	ID	$\lambda_\odot$	q(AU)	e	i	ω	Ω	α	δ	V_T	V_G	V_H	L_{12}	L_{13}	ψ
82	Sth Nth Taurids	961027:044050:086	213.6	0.352	0.845	3.9	114.2	33.6	43.9	13.3	29.5	28.7	37.4	63.7	39.2	61.5
43	Sth Taurids	961031:235355:015	218.4	0.378	0.791	4.9	113.8	38.4	49.0	13.4	27.8	26.4	36.0	24.6	-19.0	55.3
44	Nth Taurids	951108:233527:010	225.7	0.335	0.860	3.4	295.6	225.7	55.2	22.4	30.7	29.6	37.7	23.6	-19.5	65.1
198	σ Hydrids	951212:065115:104	259.3	0.226	0.993	124.5	123.1	79.3	126.2	2.1	57.4	58.1	42.1	30.2	19.6	46.2
196	Monocerotids	961213:023828:135	260.9	0.191	0.992	37.5	128.1	80.9	102.9	7.2	42.2	42.1	42.0	31.3	5.1	50.2
92	Geminids	950801:014030:103	128.0	0.091	0.944	27.2	151.0	307.9	342.7	-16.7	38.0	37.5	34.7	5.6	-11.8	25.9
214	GE1206	951216:001506:009	263.1	0.974	0.534	57.7	345.6	83.1	135.8	-62.9	34.0	33.1	37.1	-34.4	-16.0	150.8
171	β Capricornids	980214:100421:047	325.0	0.345	0.799	3.7	242.3	145.0	314.7	-20.5	28.5	27.2	35.8	-5.5	-23.8	20.1
219	GE0201	980213:062024:055	323.9	0.357	0.824	4.5	245.6	143.9	315.3	-21.0	29.5	28.1	36.9	-53.3	-47.5	150.8
224	GE0206	980215:025415:059	325.7	0.196	0.852	11.7	137.9	145.7	167.3	-1.9	32.1	31.3	33.6	37.4	8.8	40.6
226	GE0208	960215:062056:067	325.4	0.046	0.939	34.1	14.4	325.4	280.9	-14.1	33.6	32.6	24.9	-19.4	-33.8	21.9
156	upsilon_Leonids	980213:025209:003	323.7	0.277	0.842	4.8	304.9	323.7	163.1	10.9	31.2	30.4	36.0	46.0	9.9	53.2
170	β Capricornids	960216:113718:037	326.6	0.229	0.849	2.4	227.6	146.6	309.1	-20.3	31.2	30.3	34.8	19.4	1.1	22.8
83	Nth Virginids	960224:063215:105	334.5	0.233	0.899	4.6	308.0	334.5	173.7	5.7	34.1	33.7	37.5	51.1	41.3	54.5
242	GE0306	960317:214341:029	357.1	0.871	0.393	66.2	56.1	177.1	195.6	-72.9	36.3	35.7	34.1	-32.7	-9.9	143.1
150	α Aquarids	960319:100449:187	358.6	0.210	0.896	5.8	48.0	358.6	339.2	-5.2	33.7	32.9	36.6	10.7	-16.0	37.2
166	α Virginids	960316:051411:062	355.5	0.172	0.978	12.4	132.3	175.5	191.1	-10.7	39.8	39.8	40.9	37.1	29.7	25.2
240	GE0304	980317:141417:059	356.3	0.988	0.518	54.6	348.2	176.3	68.2	-82.4	32.1	31.2	36.8	-32.6	-3.4	140.2
237	GE0301	970319:121726:089	358.5	0.187	0.889	2.2	43.5	358.5	337.8	-8.0	33.2	32.5	35.4	34.1	10.5	34.5

Table 6.2: *continued*

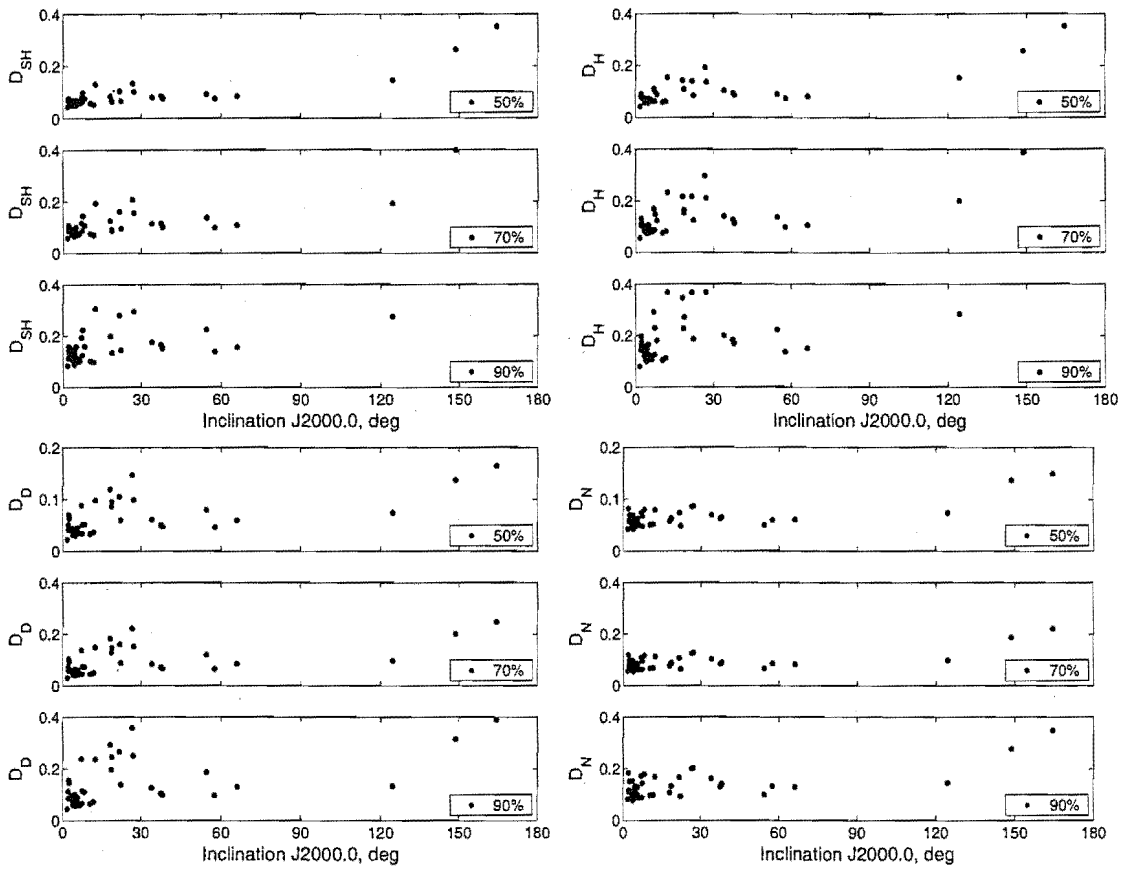

Figure 6.4: Retrieval of Monte Carlo simulations of representative stream orbits using different D-criteria. Results are given for cutoff levels corresponding to 50%, 70% and 90% of the original randomised set of 5×10^4 orbits for each of the 45 tested streams.

Few retrograde streams are listed but the expected behaviour is evident. It is well known that D_{SH}, and therefore also D_H, requires a large cutoff value in order to retrieve the stream for which a search is being made. D_{SH} and D_H require a cutoff value of 0.25 in order to retrieve 50% of the stream. The maximum dissimilarity allowed by the computer program in this search is 0.40. Insufficient orbits are retrieved within this constraint in order to provide a cutoff value at the 70% and 90% levels. Hence by performing a direct search against a mean using these D-criteria one expects only to retrieve at most 50% of the stream orbits. Both D_D and D_N appear to handle these orbits much better—they retrieve 70% of the orbits by a cutoff of 0.18.

It is interesting to reflect on the obviously different regimes shown in Table 6.3. D_{SH} appears to have particular problems retrieving higher inclination orbits: the dissimilarity for these is very high. As inclination angle increases so too does the speed as seen by AMOR; a speed increase implies an increase in orbital uncertainty (as discussed in Chapter 5) hence the large D values experienced for these high

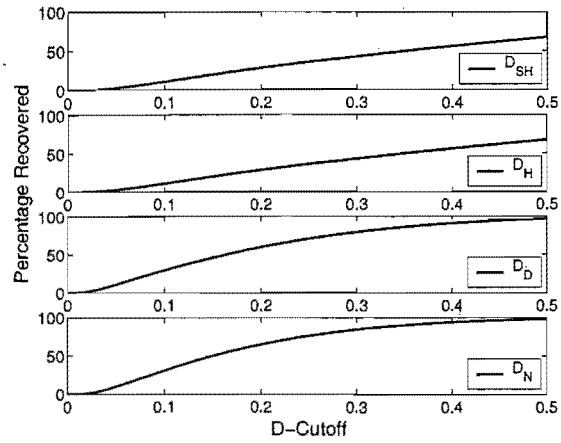

(a) η Aquarids

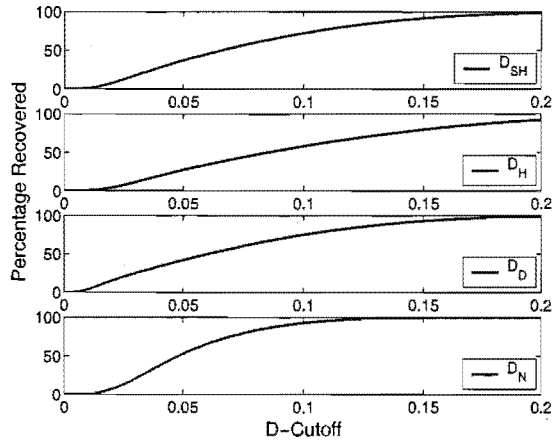

(b) Daytime Sextantids

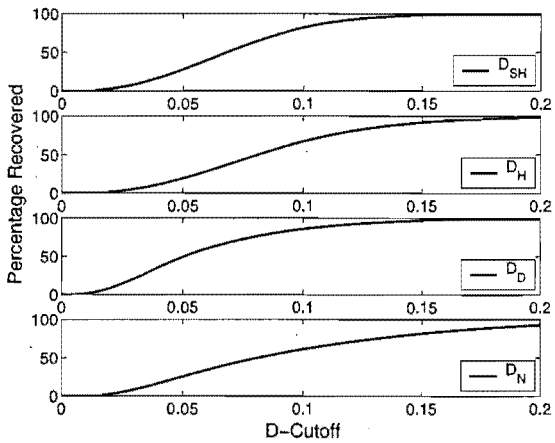

(c) α Scorpiids

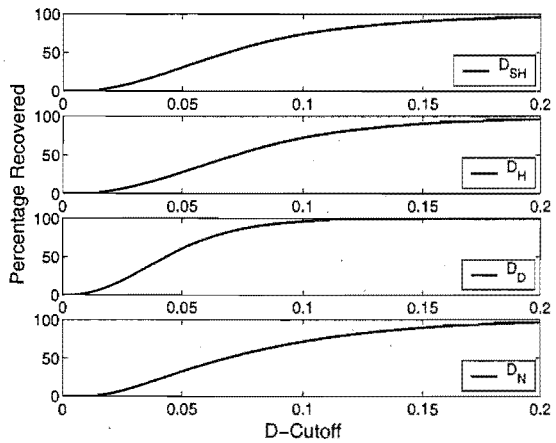

(d) β Capricornids

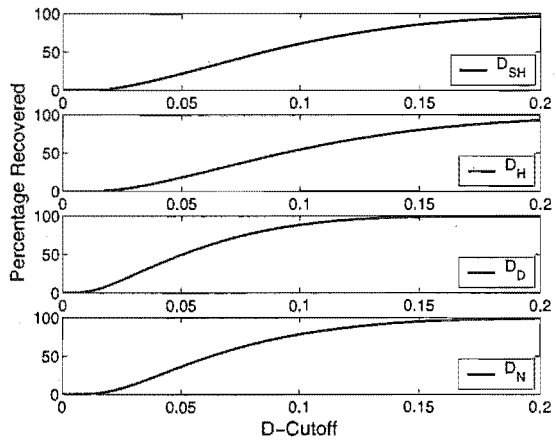

(e) Monocerotids

Figure 6.5: Selected profiles returned by the Monte Carlo simulation for five mean stream orbits. Note the particularly bad performance of the η Aquarids compared to prograde showers such as the Daytime Sextantids. Also note that apart from the η Aquarids and Daytime Sextantids the other showers do not occur significantly in the AMOR data set, as will be later shown, however they are still interesting to discuss here from a general retrieval point of view.

Regime	Amount Recovered	D_{SH}	D_H	D_D	D_N
$i < 10°$	50%	0.06	0.07	0.04	0.06
	70%	0.09	0.10	0.06	0.08
	90%	0.13	0.14	0.09	0.11
$10° \geq i < 90°$	50%	0.08	0.11	0.08	0.06
	70%	0.12	0.16	0.11	0.09
	90%	0.20	0.23	0.18	0.14
$i \geq 90°$	50%	0.25	0.25	0.12	0.12
	70%	-	-	0.18	0.17
	90%	-	-	0.28	0.26

Table 6.3: Summary of the performance of the D-criteria at retrieval of representative stream orbits. Here the results of the Monte Carlo simulation, shown in Figure 6.4, are summarised.

inclination orbits are explained. The uncertainty in the eccentricity of ETA (Halleyid) stream orbits is a rather large ≈ 0.3—this stream has an average inclination of $\approx 165°$. Eccentricity is one of several elements with very high uncertainties defining ETA orbits, hence the D-cutoff required to retrieve even a reasonable part of the shower is very large. Such a value of D is impractical as in addition to retrieving genuine spread-out stream orbits one would also include much of the general AMOR data set at such a high cutoff. D_{SH} is in many ways too sensitive to such differences in eccentricity, in particular, as relatively small changes in the velocity components may change the size and shape of the orbit drastically when it is near parabolic. D_N uses velocity components more directly and therefore is less troubled by such minor variations while D_D also achieves tolerance of large eccentricity value comparisons, in its calculation, by dividing the eccentricity differences by their sums.

At lower inclinations there is little difference between the different dissimilarity methods. It is wise when performing serial searches to keep the D-cutoff value as low as possible as orbits which are close in size and shape but differ in widely in longitude of ascending node may be found to be similar by the D-criteria. This is generally based on the similarity of longitude of perihelia ($\overline{\omega}$). It is quite reasonable that this should be so, from an orbital point of view. However in radar orbit data sets most of the orbits very close to the ecliptic have been randomised by planetary perturbations and no longer resemble their original orbits. The highest density is also found very near the ecliptic. It is thus very easy to add orbits into a stream which bear no real relationship given that the constraint on i has been removed and ω is derived from q and e and is therefore not independent. For near-ecliptic orbits then there are really only three independent quantities: q, e and Ω. This compares to the streams forming showers such as the SDA and ETA which have orbits at 15°–

25° off the ecliptic and therefore have four independent quantities defining them, thus increasing there chances of achieving distinction against the background. This argument is of course complicated by the very low uncertainties in the near-ecliptic orbits as compared to the these higher inclination streams.

6.4 Summary

D-criteria have been introduced which allow the association between two orbits to be calculated. While four criteria are discussed here only two of these, D_{SH} and D_N, will be used further in this study. It is impossible to continue using all four due to time constraints however this selection gives a good representation of the possibilities. D_{SH} has been preferred due to its historical standing: it continues to be the most used D-criterion and it becomes difficult to compare results if one does not have a common ground. D_N has been chosen as it represents a fresh way of looking at orbit association which has proved itself to be at least as good as D_{SH} at associating true stream members and disregarding sporadics as shown in the previous section.

The results obtained in Section 6.3.2 give useful guidelines for stream searching of the AMOR data set. They indicate the need for lower cutoff levels for association in near-ecliptic comparisons while showing the required minimum cutoff levels in order to achieve a large-scale retrieval of the stream members. It has been assumed throughout these studies, and will continue to be assumed, that the most important cause of apparent spread in the radar detected streams is not physical but instead measurement uncertainty driven. As will be seen in the major shower studies of Chapter 8, the observed spread is of the same order as that expected from the individual measurement uncertainties and it is virtually impossible to separate this uncertainty spread from the expected underlying physical spread.

Chapter 7

Searching for Stream Structure in a Radar Meteoroid Orbital Data Set

The large-scale structure of the AMOR data set has been described in Chapter 3. This structure was shown to be dominated by the detection biases inherent in the collection of data by an Earth-based radar system. While this study of these parameter distributions is in itself interesting it is important to determine any distinct smaller-scale structure. This is a very difficult problem. Radar meteoroid orbits have been shown in Chapter 5 to have relatively large uncertainties. The study of large-scale effects provides a robust picture due to the large number of meteors considered; in contrast when one attempts to probe for smaller-scale effects the number of orbits being considered is orders of magnitude smaller. This chapter applies various techniques to search for significant showers which constitute such small-scale structure in the data set.

We begin by reviewing the literature on the study of meteoroid stream structure in various data sets. A mixture of previously applied and new methods are then tested with varying degrees of success to determine the shower/stream structure of the AMOR data set. These methods are applicable not just to AMOR but to any (large) radar data set which is dominated by measurement uncertainty and by the presence of sporadic meteors.

7.1 Definition of Meteor Showers and Meteoroid Streams

A meteor shower is an event in which a number of meteors are seen emanating from a similar region of the sky with the originating bodies possessing a similar speed. Typically showers last for periods of between a few days and a month. A meteor shower is the manifestation of the impact of particles from a meteoroid stream on the Earth's atmosphere.

Because radar systems sample non-shower sporadic meteoroids for most of their operational time, meteor showers must stand out against this background both in

their intensity and their distinctness in the parameter spaces describing the meteor events. Either the radiant-speed-detection time system or an equivalent system utilising the orbital elements (as derived from measurements in the latter system) may be used to define meteor events and relate them back to the heliocentric orbits of the originating meteoroids. Under such systems the shower must stand out against the sporadic backgrounds and biases noted in Chapters 3 and 4. In practice this is taken to mean that (shower) meteors in the radiant space must occur over a limited region with an intensity greater than the sporadic source distribution which forms the background: wavelet enhancement is used to detect such occurrences in Section 7.7. Alternatively, in the orbital element space, meteoroids in a stream must have orbital elements which are much greater in density in a small region of the space than that expected due to the surrounding bias imposed background. Orbital element space is more prone to large uncertainty ranges in some of the elements, such as the argument of perihelion, in a data set of orbits than are the radiant coordinate parameters, hence generally the radiant position is a preferred method of detecting meteor showers and therefore meteoroid streams.

7.2 A Review of Past Meteoroid Stream Searches

Non-instrumentally based visual meteor shower observation techniques rely on the detection of an enhanced rate of meteors appearing to emerge from a small region of the sky called the "radiant". Surveys using a large number of volunteers have yielded results of scientific value, for example Jenniskens (1994) presents a 10 year study with an effective counting time of 4,482 hours of the activity (rate) curves of 50 major and minor showers. In these studies the meteor shower is defined in terms of radiant position and time of detection (α, δ, t_d).

Photographic and radar surveys offer the possibility of meteoroid speed determination. The meteor showers listed in works such as Lovell (1954) are defined on the basis of radiant position, geocentric velocity and time of detection $(\alpha, \delta, V_G, t_d)$. This system is sufficient to completely describe the shower: the heliocentric orbit of the meteoroid may be defined in terms of these parameters[1].

Southworth and Hawkins (1963) describe a search within 359 randomly selected meteoroid orbits photographed by Baker Super-Schmidt meteor cameras

[1]The geocentric system $(\alpha, \delta, V_G, t_d)$ is 4-dimensional while the heliocentric orbit is described by five parameters $(q, e, i, \omega, \Omega)$. However q, e and ω are linked by equation 3.3, leaving the orbit as a quasi-4 dimensional construct, which is completely defined by $(\alpha, \delta, V_G, t_d)$.

between the period 1954 to 1957. They find that previous searches which relied on geocentric quantities for classification were insufficient. They instead use these quantities to derive heliocentric orbits which are described by the five orbital elements $(q, e, i, \omega, \Omega_{1950})$. A method of inter-comparing orbits is required; to this end Southworth and Hawkins define a dissimilarity function called a D-criterion (equation 6.1). This function allows the calculation of the difference between two orbits using all five elements of the orbit. The assumption inherent in the D-criterion is that differences between orbits are caused by physical orbital differences with a negligible component due to measurement uncertainties—Southworth and Hawkins show that D_{SH} is related to the amount of energy it would take to perturb one orbit into the other. This assumption is reasonable in the case of photographic orbits which have very low uncertainties ($\approx 0.1°$ in angular elements).

Southworth and Hawkins define a meteoroid stream by two methods:

1. *Given a known mean stream orbit M, any orbit N is a member of the stream if $D(M, N) \leq D_m$ where D_m is an appropriate cutoff value.*

2. *Two meteoroid orbits A and B are associated if $D(A, B) \leq D_c$, where D_c is an appropriate association limit. A stream is defined as a group of meteoroid orbits where each orbit is associated with at least one other.*

The direct search approach (1) presupposes the knowledge of the correct mean orbit for the stream under consideration. It amounts to a search within a hypersphere of radius D_m in the D-criterion space centred on the mean. In this case the formulation of the D-criterion has a strong impact on the shape of streams discovered. The serial-association method (2) is in fact an implementation of the classical single-linkage hierarchical cluster analysis algorithm—providing a snapshot of the hierarchy at a single cutoff level, D_c. In contrast to the direct approach, this method allows a stream to define its own shape and does not require *a priori* knowledge of the stream structure of data set. A disadvantage is the possibility of the formation of long thin chains of orbits in the orbital element space should too large a cutoff value be used.

Southworth and Hawkins apply both techniques to their photographic data set. They find that cutoff levels set at 0.20, in both the direct and serial-association approaches, retrieve the streams they expect—this expectation being based on previous more rudimentary searches in the data. One should note that D_m and D_c are not necessarily linked together and applications to larger data sets would require

D_c to decrease. Assuming a four dimensional point distribution Southworth and Hawkins suggest that D_c should vary inversely as the fourth root of the sample size.

Lindblad (1971a,1971b) continues the work of Southworth and Hawkins. He extends their data set from 360 to 865 orbits; these observations are obtained from various precise photographic studies. He determines an appropriate cutoff level for single-linkage analysis of this data set as

$$D_{SH} = 0.20 \left(\frac{360}{865}\right)^{0.25} = 0.161, \tag{7.1}$$

which is based on the assumption that Southworth and Hawkins' suggested relationship between cutoff level and data set size, and their original cutoff level value itself, are correct.

Lindblad runs single-linkage searches at the 0.20, 0.15 and 0.10 cutoff levels on his data set. He finds that at the 0.20 level low inclination streams tend to form very long-lived pseudo-streams consisting of several well known streams: a stream is found extending from July to December including the α Capricornids, the χ Orionids, the Andromedids and the Nth. and Sth. Taurids; a similar stream is found featuring a combination of the Virginid stream with a number of sporadic meteors stretching from February to June. This effect illustrates a well known aspect of the single-linkage algorithm called "chaining" where very dissimilar data set members are linked together by intermediates forming in effect a long chain.

In order to remove these low inclination pseudo-streams Lindblad abandons the $D_{SH} = 0.20$ cutoff level, although it contains most of the known medium and higher inclination streams, and instead uses the more conservative 0.15 and 0.10 levels. He finds that the optimum of these levels is $D_{SH} = 0.15$ and this is used throughout the remainder of his study.

The approach of Southworth, Hawkins and Lindblad to cluster analysis, using the D_{SH} dissimilarity function, has been repeated in many studies since that time. Such stream searches have, almost exclusively, been performed on photographically derived orbit data sets—one of the few departures from this rule is that of Jopek (1993b) who uses his D_H adaptation of D_{SH} to search for TV derived meteor streams at a cutoff level, $D_H = 0.20$. He defines 23 streams comprising 30% of the 531 orbits. Most streams consist of ~ 5 orbits with a few larger streams of membership ~ 20. Due to the northerly latitude of the TV detectors (Ontario, Canada) the streams are almost exclusively of a northerly declination. The TV orbits used

by Jopek are published in Sarma and Jones (1985) and Hawkes et al. (1984). The uncertainties on these orbits vary greatly. Representative uncertainties according to Sarma and Jones (1985) are 2° in angular position and 0.8 $\mathrm{km\,s^{-1}}$ in velocity. The former uncertainty is obviously a typographical error; TV meteor radiant positions are commonly reported to have uncertainties which are an order of magnitude smaller than this (Hawkes et al. 1984): it is assumed that Sarma and Jones (1985) meant, therefore, to quote an uncertainty of 0.2°. This places the TV orbits on a par with photographic data sets and an order of magnitude lower in radiant position uncertainty than radar data sets. However, the number of TV meteors in recognisable showers is expected to be an order of magnitude lower than that for photographic meteors. This behaviour is in common with that found for radar meteors (Jopek 1993b): it happens because both TV and radar measurements probe dust populations much smaller in particle size than do photographic techniques[2].

Weiss (1960) using a radar system at Adelaide, Australia detects shower activity by changes in the meteor rate. By assuming that rate fluctuations in the sporadic background are essentially random events, he applies Poisson statistics to determine any significant fluctuations—such fluctuations are provisionally attributed to shower activity with range-time plots being used to confirm whether a shower is present. Nilsson (1964) surveys southern hemisphere radar meteor orbits obtained from the Adelaide radar in 1961. He notes that this survey is the first, in the southern hemisphere, in which individual orbits have been calculated. The data set consists of 2,200 orbits determined from meteors of limiting radio magnitude +6. It is estimated that 25% of the meteors in this survey were associated with showers. The search method adopted defines association between two orbits when[3]:

$$\begin{aligned} |1/a_1 - 1/a_2| &\leq 0.15\ \mathrm{AU}^{-1}, \\ |e_1 - e_2| &\leq 0.07, \\ |i_1 - i_2| &\leq 7^\circ, \\ \text{and} \qquad |\nu_1 - \nu_2| &\leq 7^\circ. \end{aligned} \tag{7.2}$$

The total range of the grouping must not exceed twice that of these limits. These conditions are assumed to cover the real spatial spread of shower orbits and the cen-

[2]Section 1.3 summarises the regimes in which the various meteor detection techniques operate.

[3]The longitude of the ascending node, Ω is not used by Nilsson (1964) nor by Kashcheev and Lebedinets (1967) to help define the stream. The Adelaide and Ukraine surveys respectively consisted of only 5–10 days of coverage per month. These months were analyzed separately effectively constraining Ω.

tral part of the measurement uncertainty induced spread. Nilsson (1964) appeared soon after Southworth and Hawkins (1963) and notes the similarity of D_{SH} to the conditions imposed by equation 7.2. The essential difference between these methods is the dependence on an idealized dispersive mechanism assumed by Southworth and Hawkins as compared to the assumption that most of the spread in radar detected streams is due to their uncertainties—there is an order of magnitude difference in the uncertainties between the two methods (Nilsson 1964). In Nilsson's study showers are accepted where they contain at least three orbits. There is a problem in the application of this method to a data set such as that provided by AMOR in that it is not clear how one prevents a grouping from growing to include all orbits through a *chaining* process, similar to that discussed under the serial-association method. For a small data set, such as that of Nilsson, the problem does not arise as there are natural boundaries in distribution in time which prevent *chaining* from proceeding too far: in the case of the near continuous AMOR data set this is not so and the result is quite unsatisfactory.

Kashcheev and Lebedinets (1967) also find the use of the D-criterion serial-association method to be inappropriate for radar meteor studies due to the large uncertainty derived scatter in their stream orbits. Their method involves partitioning the meteors for each month into overlapping groups according to their observed speeds. The radiants for these groups are "roughly" reduced to the middle of the observational period in order to remove the expected variation over time of the apparent radiant coordinates[4]. By studying relative enhancements in this $(\alpha, \delta, V_G, t_d)$ data space, regions of shower activity are noted. Meteors within these regions have their originating heliocentric orbits derived from such geocentric coordinates. All orbits are then compared with the mean stream orbit, i.e. that at the centre of the region, on the basis of similarities in the orbital elements: q, e, i and ω. Using known uncertainties in the orbital elements, meteors from adjacent months are declared to be associated with the stream if the following conditions are all met[2]:

$$
\begin{aligned}
|q - \overline{q}| &< 2\Delta q, \\
|e - \overline{e}| &< 2\Delta e, \\
|i - \overline{i}| &< 2\Delta \overline{i}, \\
\text{and} \qquad |\omega - \overline{\omega}| &< 2\Delta \omega. \qquad (7.3)
\end{aligned}
$$

[4]The radiant coordinates of the shower do not necessarily move at exactly the same rate as that of the Sun in ecliptic longitude hence such a reduction to the centre of the month must be in error in some cases although it is the best possible result which can be achieved.

Gartrell and Elford (1975) apply two techniques to search for streams within radar data from their multi-station continuous wave and pulse radar system in Adelaide, Australia. This system measured radio meteors down to a limiting magnitude, M_R=+8. They use a single-linkage search with cutoff levels at $D_{SH} = 0.10$ and 0.20 to search their 1,667 meteoroid orbit data set. They also apply a search in the form used by Nilsson by sorting on each orbital element in turn with the allowable differences for association set to ≈ 2 times the assumed measurement error. Using the single-linkage search they find 40% of orbits being associated with at least one other orbit and 30% of orbits being associated with two or more. Slightly fewer orbits are found to be grouped using the Nilsson approach but essentially the same groupings are retained.

Gartrell and Elford note in this study that while the data being used are of similar quality to that used by Nilsson (1964) benefit is found from using the D-criterion based single-linkage search. They find "...numerous streams of undoubted reality in which the dispersion greatly exceeds that due to measurement error alone...".

It is important to test the results of a stream search in order to discover the probability of chance association. Southworth and Hawkins (1963) in their original work perform such a check by randomising the values of Ω and i for meteors not originally classified as stream members. From a serial-association test on this "randomised" data set they determine that $\sim 50\%$ of the groupings formed are chance associations. Furthermore these chance associations were found in the most densely populated regions of phase space—this is to be expected as Chapter 3 has already shown that there are very strong biases on radar data sets many of which are also applicable to those determined photographically.

Baggaley and Galligan (1997) introduce the combination of the single-linkage method with a randomisation technique in order to determine a reasonable cutoff level. This technique involves determining the distribution in each of the orbital elements used by the D-criterion and creating pseudo-random data sets of orbits bearing the same large-scale distribution, but with all traces of shower activity removed. Several hundred such data sets are passed through the normal single-linkage analysis process and the point at which clusters larger than some minimum size (in this study $N \geq 5$) begin to appear is called the quasi-random level. This level is taken to be that at which groupings from the random background start to intrude on "real" groupings. Jopek and Froeschlé (1997) present a similar method which is more generalised to provide the probabilities of the intrusion of random

background orbits on groupings of a particular size at a particular cutoff level. Such randomisation methods have also been previously used in related fields such as those of asteroid cluster analysis using single-linkage (Zappalà et al. 1990, Zappalà et al. 1994, Zappalà et al. 1995).

There are two reasons why the present (thesis) author now disagrees with this method. Most low inclination streams are found under a single-linkage search at relatively low cutoff levels while one must venture to higher levels to retrieve showers such as the retrograde η Aquarids. In general higher inclination orbits have higher uncertainties, hence determining the probability of the existence of a stream at a particular level without reference to the area of the orbital element phase space to which one is referring is, in the author's opinion, erroneous. Balancing this statement, Jopek and Froeschlé (1997) work with photographic orbits which have much lower uncertainties than radar orbits, to which the present study is addressed. It is accepted that the proportion of photographic orbits which are well defined within streams is an order of magnitude higher than that for radar orbits while the uncertainty regimes also increase by an order of magnitude between these methods. Hence the randomisation method does remove much of the stream component in the case of photographic orbits but can do little to change the radar orbit local phase space density as there are so few stream meteors to begin with.

As discussed in Galligan and Baggaley (1998) it is likely that a randomisation technique will simply tell the interested party that the level at which clustering occurs is the level at which one should stop if one requires a low probability of random background orbit inclusion. This was the result found in the Galligan and Baggaley study and it is attributable to the predominant sporadic content of the radar data sets.

There are further problems in the production of pseudo-random data sets in that Baggaley and Galligan (1997), Jopek and Froeschlé (1997) and Valsecchi et al. (1999) all assume that the orbital elements are generally independent. The only exception made is for the very strong dependence, defined by equation 3.3, between q, e and ω. The histograms of the orbital elements in these studies are obtained and then the same number of orbits as in the original data set are recreated by randomly selecting parameter values within the large-scale distribution summarised by these histograms. In the case of D_{SH} usage this implies independence for q, e, i and Ω, with equation 3.3 being used to form an ω value from a (q, e) pair. Such a simplistic approach forms an unrealistic data set in several ways.There is a strong

bias towards certain regions of q-e space, as shown in Figure 3.8, however there is no strict condition similar to equation 3.3 governing this which could be applied. The solar longitude at detection directly defines the Ω value. There are frequent fluctuations in the rate of meteor detections by a radar system such as AMOR with sometimes interruptions of several days in temporal coverage hence randomising and reassigning Ω values to pseudo-orbits does not represent even the background orbit population expected. Finally, as shown in Chapter 4, there are very large-scale differences between the orbits which are detected at different times of day, due to the influence of the different sporadic source regions. The orbits obtained in pseudo-random data sets should contain recognition of all of these bias conditions: this is virtually an impossible task.

An entirely different approach was applied by Z. Sekanina (Sekanina 1970a, Sekanina 1970b, Sekanina 1973, Sekanina 1976) to the radar orbits obtained from the Harvard Radio Project in the 1960's. The data sets obtained from these surveys constituted the largest meteoroid orbit set then available until the advent of AMOR in 1990. Sekanina (1970a) introduces his stream searching method which was subsequently applied to 19,303 radar meteoroid orbits in his later papers. This method assumes that the sporadic meteor background has a different D-criterion distribution from meteoroid orbits in a stream. The procedure begins with an initial orbit and iterates the elements of the stream's mean orbit, weighting them with the addition of individual orbits from the data set, until the mean orbit converges. The model is based on a Maxwellian distribution in the stream orbits, i.e. the assumption is that, as D_{SH} has been shown to be a measure of energy difference between two orbits (Southworth and Hawkins 1963), one is measuring an energy distribution also for such a D_{SH} distribution. As Nilsson (1964) and others point out, a radar meteoroid orbit has a large measurement uncertainty and generally the spread in the parameters of a set of stream orbits detected in a shower will be due to this uncertainty and not to any physical spread, hence the Maxwellian approach is not valid.

Sekanina (1970a) sets out a method which involves no *a priori* knowledge of the shower content in the data set. However, owing to computer speed constraints Sekanina (1970b) and Sekanina (1973) use known meteor streams and objects respectively in order to initialise the search and thus bias the outcome. Sekanina (1976) attempts to provide a more unbiased search by using the original (single-linkage) computer program of Southworth and Hawkins (1963) to select initial show-

ers which are then used to seed his Maxwellian method. Sekanina notes the difficulty of extending this approach to large numbers of meteors. In total 275 streams are listed in Sekanina (1976), most of which had not been published previously and many of which are very small in size. It is questionable whether many of these associations are "real" or simply artifacts of the method.

7.3 The Current Study

The methods tested in the following sections begin with a search for obvious structure (i.e. major showers) in the data set which might be recognised by a large-scale increase in the rate of meteor detections over a small space of time. Following this a number of published showers are compared directly against the AMOR data set and a test of significance is attempted in order to determine whether the number of associations is statistically significant. A radiant-speed-time search ensues in which the question of detection of shower structure in the large-scale sporadic background is discussed with the help of wavelet transforms for image enhancement. This method allows one to apply some confidence intervals to test for significance. Finally the single-linkage algorithm is used to search for orbital structure; this method is shown, as predicted by Nilsson (1964), to be generally inappropriate for use in a radar data set.

It should be noted that when the author discusses a search for shower structure in the data set, it is implicit that such a search will determine the presence of streams in a data set. The detection of meteor showers is dependent on the presence of corresponding meteoroid streams. Some authors speak of a stream search in meteoroid orbit data while others speak of a search for meteor showers—these are equivalent statements.

7.4 Expected Shower Structure Within the AMOR Data Set

The most prominent shower structure expected in the AMOR data set are the so-called major showers. These are showers which have a medium to high rate and which have generally been observed for many years and by a variety of methods. Due to the southerly latitude of AMOR many of the major showers listed in various surveys do not apply in our analysis as their radiants do not appear high enough above the horizon—as shown in Figure 4.1 most meteors observed by AMOR are at declinations between $-30°$ and $5°$ with very few radiants at more northerly

declinations.

There are several sources to which one can refer for lists of the "known" meteor showers; these include Kronk (1988), the International Meteor Organisation[5] and older sources such as Cook (1973). For the purposes of major shower study these lists are virtually interchangeable: the newer Kronk (1988) will be used as a reference here.

According to Kronk the major showers which should be visible at such declinations are the η Aquarids ($\delta \approx 1°$) in May, the Southern δ Aquarids ($\delta \approx -17°$) in July/August, the α Capricornids ($\delta \approx -8°$), the ι Aquarids ($\delta \approx -6°$ and $\delta \approx -15°$ for north and south branches respectively) in early August and the Daytime Sextantids in September[6]. Other major showers such as the Leonids, Orionids and Geminids which are well studied in the northern hemisphere are at declinations too far north to be detectable by AMOR.

As Kronk notes, the ι Aquarids is a very diffuse shower—its active period lasts for $\sim$ 2 months hence recognition as a coherent stream is difficult. The radiant position of the SDA is close to that of the ι Aquarids and the active period of these showers are similar, as shown in Table 7.1. The SDA is by far the strongest of the showers detectable by AMOR: it is not expected that the ι Aquarids can be resolved from the SDA, when one takes into account the uncertainties and physical spread in the shower radiant centres.

Meteor Shower	CODE	Start	End	Maximum	$\lambda_{\odot}^{max}$	α_{max}	δ_{max}
η Aquarids	ETA	21/4	12/5	5/5	45.5°	337°	−1°
Sth. δ Aquarids	SDA	14/7	18/8	28–29/7	125°	339°	−17°
α Capricornids	CAP	15/7	11/9	1–2/8	129°	307°	−8°
Sth. ι Aquarids		1/7	18/9	6–7/8	133°	337°	−12°
Nth. ι Aquarids		11/8	10/9	25–26/8	152°	350°	0°
Daytime Sextantids	DSX	9/9	9/10	30/9–4/10	185°–190°	153°	−2°

Table 7.1: Expected major meteor showers in the AMOR data set. The active period of each shower is given in addition to representative maximum solar longitudes and radiant positions at those maxima. Data in this table are due to Kronk (1988) who compiles observations from many sources.

There are many more minor showers listed by Kronk and other surveys, including the plethora of minor radar orbit associations listed by Sekanina, as discussed in Section 7.2. These data sets are almost exclusively collected in the northern

[5]Internet Address: http://www.imo.net

[6]The four major showers are referred to, in this chapter and the next, by their abbreviations: η Aquarids (ETA), Southern δ Aquarids (SDA), α Capricornids (CAP) and Daytime Sextantids (DSX).

hemisphere and hence there is a northerly bias to their radiant declinations. Those showers are not listed and discussed in this section partly due to this bias and also due to the number of possible candidates listed in such surveys. Several data sets of stream orbits have been combined into a single computer readable file as described in Appendix D; this file is searched using the direct searching method in Section D in order to determine significant quantities of such stream members in the AMOR data set.

It is expected that it will be impossible to determine the presence of many such minor streams within the AMOR data set due to the overwhelming presence of the sporadic distribution as shown in Chapter 4; such showers must appear significantly against this background in order to be declared as "real" within the data set. Searches such as those of Sekanina do not establish the reality of streams listed: a search is simply made against a list of "expected" streams and any associations noted.

7.5 Shower Detection by Obvious Changes to Large-Scale Activity

Meteor showers are normally characterised by increases in meteor activity, in an area of orbital element space, over a short period of time typically a few days up to a month in duration. The simplest test then is to search for an increase in the meteor detection rate over the activity period of the showers known to have the highest yields. The meteor activity profiles for equinoctial years T1995–T1998 are shown in Figure 7.1, with the active periods of the three strongest showers expected as indicated.

The SDA is the strongest shower expected, during the activity period of this shower the rate curves do appear to increase slightly above normal. The ETA shower does not present a very distinct increase above normal. The DSX appear to form a very distinct peak in T1998, the only reason for this appearance is due to the radar having had technical difficulties and hence low rates at both sides of the peak. Similar artificially impressive peaks are often visible when the radar is not functioning properly, as for example in the case of the T1995 SDA period.

When one studies the rate per degree of solar longitude of the showers (as is done in Chapter 8) it is not surprising that one cannot see the showers. The highest rating shower, the SDA, has a peak of approximately 40 meteors per degree,

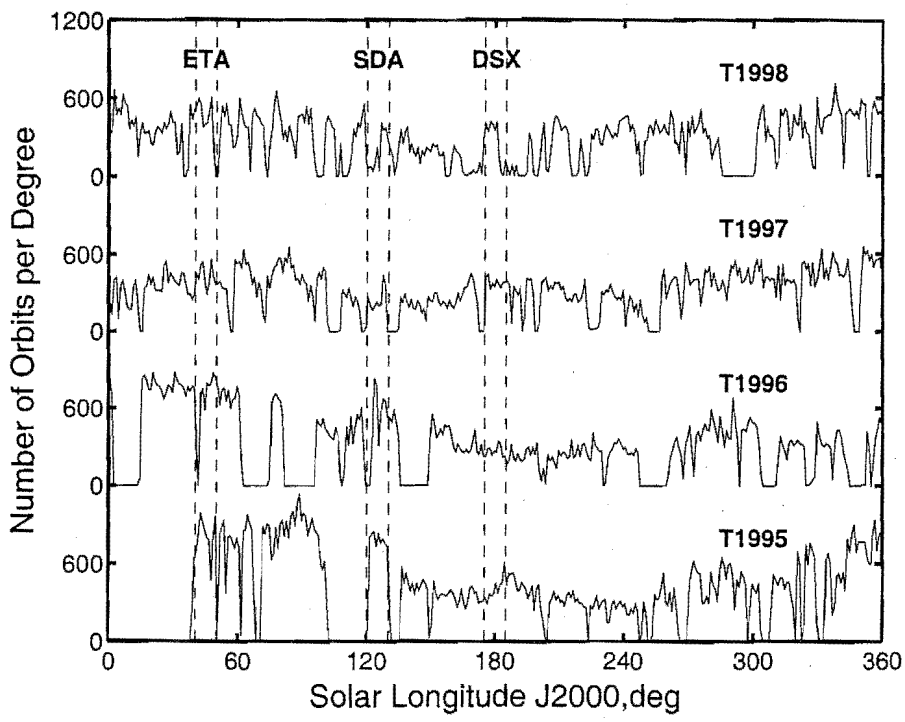

Figure 7.1: Activity curves for T1995–T1998. The regions of solar longitude, at which the three most prominent showers are expected, are marked.

while one can see from Figure 7.1, that the average background rate per degree is normally between 300 and 600. Hence, at the very peak of the shower, less than 10% of the meteors detected will be SDA; minor changes in the apparatus or atmosphere easily account for a comparable change in activity. The other two major showers discussed are even lower yielding and hence even less likely to present a detectable rate increase.

At this stage one forms the conclusion that detection of meteor showers by observation of the fluctuations in the daily activity rates of all meteors detected is not possible. Lovell (1954) demonstrates that this is not true for all radar surveys; a reprint of his original figure (Figure 184 in Lovell 1954) is shown in Figure 7.2 which indicates clearly delineated shower presence in several places. It is noted that Lovell's figure splits meteors into day and night detections, this would tend to raise the significance of showers against the background: unless a shower overlaps the day/night time boundary, the signal to noise ratio should approximately double compared with the no partitioning scenario. This time partition would implicitly tend to separate the sporadic source regions, with the helion source predominating during the day and the antihelion source predominating at night; the apex source would split fairly evenly between these regimes. Such a split of source regions

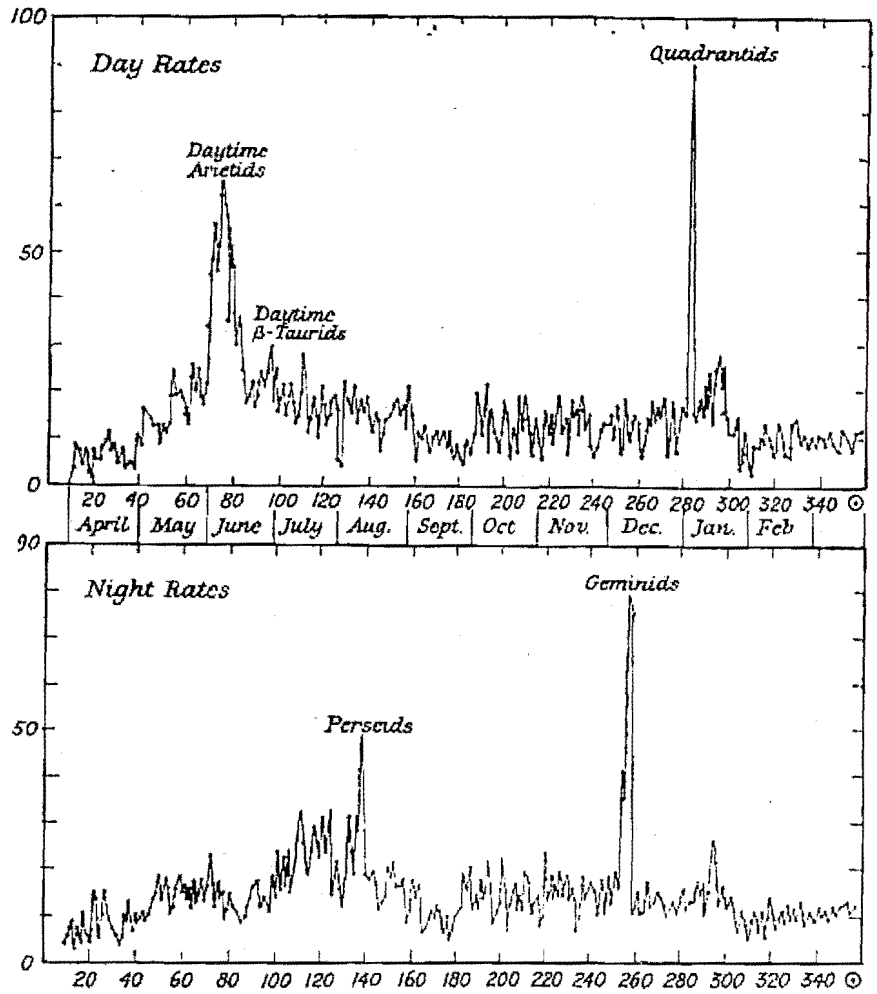

Figure 7.2: Detection of major meteor showers in the annual activity profiles of early radar surveys (limiting radio magnitude +9), after Lovell (1954) (originally Figure 184 in Lovell's book). The time-axis is measured in mean solar longitude while the dependent axis displays the number of meteor detections.

is highly favourable for increased shower detection: in the wavelet enhancement searches of Section 7.7 great value is found from partitioning by sporadic source region.

Figure 7.1, in the current study, does not use such a time partitioning noise reduction mechanism; the interested reader may well ask whether Lovell's partitioning, applied to AMOR data, could improve matters sufficiently for shower detection. In order to test this possibility, Figure 7.3 shows the same data as Figure 7.1 but here day/night partitioning has been applied. The partitioning yields activity profiles which are little better than that with no partitioning. The major shower periods show no more structure than that present in Figure 7.1. There is some promising increase at the time of the SDA in the nighttime graph, for example in

T1996: however, the feature is clearly not sufficient to declare a shower detection. This situation should be contrasted with that for the very clear Geminids peak in Figure 7.2. One should notice that most of the systematic increases and decreases in the AMOR rate are present in both the nighttime and daytime curves indicating the dominant sporadic nature of the detections.

It is interesting that such clear detections of a shower may occur for one radar survey and not for another, there must be some systematic difference between these to cause this. The difference lies in the magnitudes of the meteors detected. AMOR measures down to the very small +14 radio magnitude while early surveys, such as that shown, only measure down to about +9 (Lovell 1954, page 384); less shower structure is expected for smaller meteoroids explaining the ease of major shower detection in Figure 7.2. One should note the relative number of meteors quoted in Lovell's figure compared with that the Figure 7.3: the sporadic meteor rate in the latter is generally between 150 and 600 while that in the former is typically between 20 and 30 (apart from at showers). AMOR can be described here as an excellent detector of the sporadic background with major showers being a minor component of the total detected population, the reverse applies to data such as that in Figure 7.2. This provides a good argument for determination of meteoroid mass as part of the AMOR data reduction process—if the mass were known then the smaller meteoroids, i.e. those with appearing below radio magnitude +8 or +9, could be discarded for shower detection. This would improve not only the detection method of the current section but would also be expected to improve the outcome of methods discussed in later sections, such as single-linkage.

7.6 A Direct Search for Known Streams in AMOR Data

Section 7.2 notes previous direct search methods which have been made for known streams using a D-criterion as a measure of stream membership. Such a search is attempted here by comparing AMOR data from meteors recorded in the years 1995–1999 with the mean stream orbit data set of Appendix D.1 (note that the stream mean orbits are referred to in this study by an identification number preceded by CSF—common stream format data set member). As shown in previous chapters there are strong bias conditions on meteoroid detection by Earth and there are also relatively large uncertainties on the orbits determined by the radar method. It is therefore difficult to say, unless a stream is very strong, that it not simply an artifact of these considerations—if one searches amongst a $\sim 10^5$ orbit data set for a

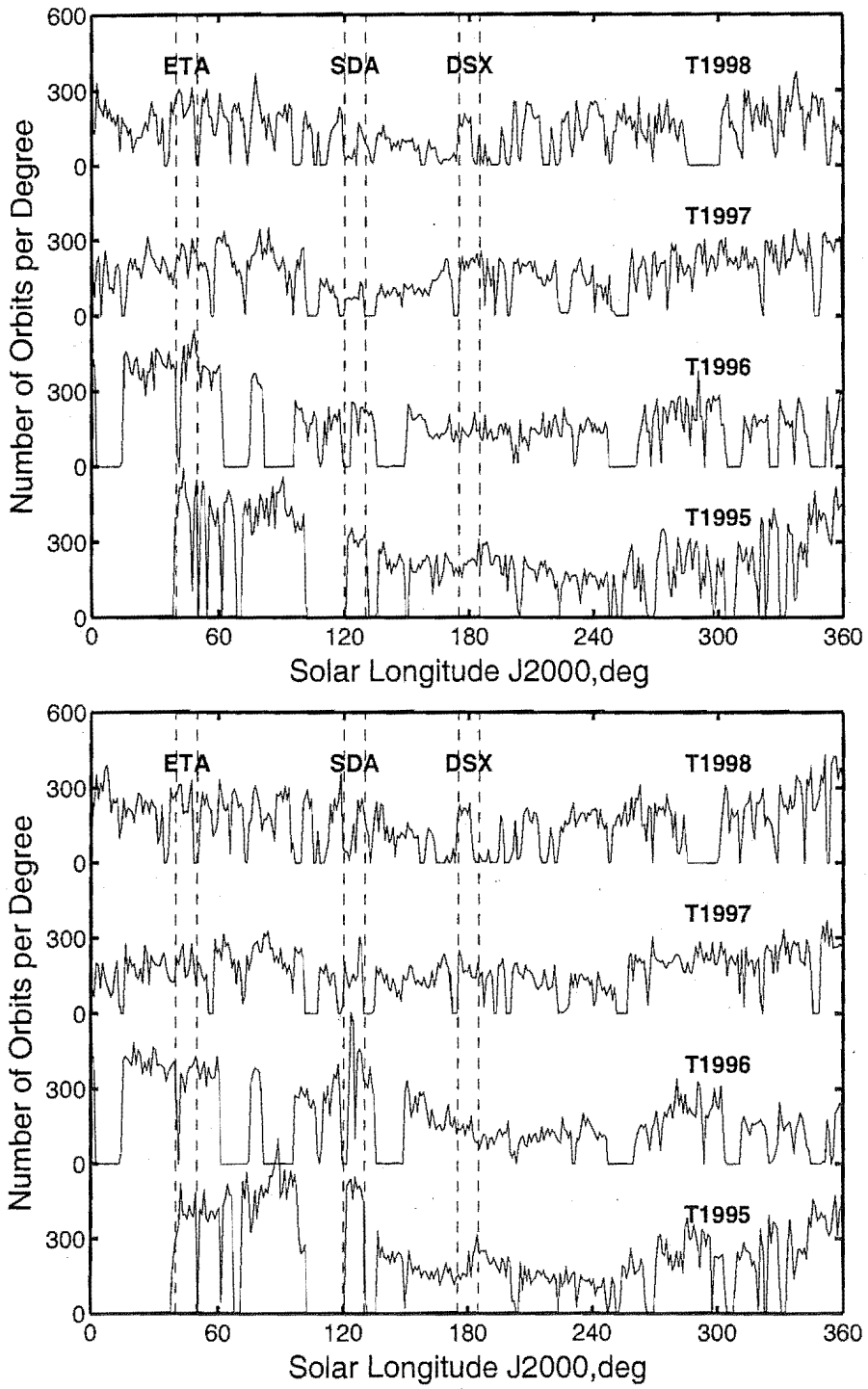

Figure 7.3: Activity curves for T1995–T1998. The regions of solar longitude, at which the three most prominent showers are expected, are marked. The meteor data are partitioned on the basis of the time of meteor occurrence; the upper curve shows daytime meteors (between 0600 and 1800 NZST) and the lower curve shows nighttime meteors (between 1800 and 0600 NZST).

particular stream it is very likely that a few meteors will almost exactly match that sought. It is clear then that some objective method must be found for determining a lower limit of stream strength at which one considers the stream "real".

A new method, which is applicable to any meteoroid orbit data set, is used to determine the significance of associations. It assumes that a shower does not last for a large proportion of a year and that due to the various bias effects on q, e and ω, identified in Chapter 3, shower associations occur purely due to a search in these high density regions. The null hypothesis which must be tested may be stated as:

The shower associations which one may infer by a direct comparison against a mean orbit are a result of the biased distribution in the orbital elements and have no astronomical significance.

The AMOR orbits are partitioned into equinoctial years and all orbits from each year are compared against each mean stream orbit using the dissimilarity function of Southworth and Hawkins (1963) at a wide variety of cutoff levels. At the same time a "box" in q, e and i space is rather arbitrarily assigned to contain all orbits for each year within a range of 0.2 AU, 0.2 and 10° centred at the orbital elements q, e and i of the mean orbit respectively. The aim here is to obtain the orbits of all meteoroids which are similar to the mean stream orbit apart from the temporal differences caused by the lack of use of the longitude of the ascending node. The argument of perihelion is also excluded, this parameter is defined by q and e via equation 3.3.

The orbits selected within the "box" are each used as reference orbits to directly search against using the same dissimilarity function and at the same cutoff levels as the original stream search is carried out at. Only orbits outside a 60° wide exclusion zone centred on the solar longitude at shower maximum are used in order to prevent the shower from removing its own significance: this of course does not work when the D-criterion chooses to associate with meteors at the other node of the shower—in such cases (apart from the Orionids) the shower is very minor so this is not significant. From this, an average number of associations per orbit at each cutoff level is established. This average is then compared with that obtained from the original direct search against the reference mean stream orbit. The null hypothesis is tested in this comparison: assuming Poisson random statistics then one can set a confidence level for rejection of the hypothesis. The 95% and 99% levels are used in the current study.

The Poisson distribution is defined by

$$P = \frac{\lambda^n}{n!} \exp(-\lambda), \tag{7.4}$$

where P is the probability of an event occurring n times over a certain time or spatial region whilst λ is the average number of times that such an event is expected to happen.

There are many periods of equipment down-time in systematic radar time-coverage as shown in Figure 3.1. Such lapses may lead to significant stream associations being rendered insignificant: however, in such cases it is impossible on the basis of the available data to determine otherwise. There is also a problem with endpoints in the equinoctial year data sets, where those showers occurring at solar longitudes near the 0°/360° equivalent point are biased due to their position. In order to provide an optimal background in each year those mean streams having $\overline{\lambda}_\odot \in (270°, 90°)$ are compared against data sets selected between autumnal rather than vernal equinoxes. These data sets have been labelled similarly to those used previously with the calendar year signifying that in which the first autumnal equinox occurred. There are four of these "years": A1995, A1996, A1997 and A1998. Streams having $\overline{\lambda}_\odot \in [90°, 270°]$ continue to be compared against the standard vernal equinox delimited years which have been used throughout this thesis: T1995, T1996, T1997, T1998 and T1999. Further details about these data files are given in Appendix D.

7.6.1 Results of the Direct Search

Appendix E presents tables showing the results from the direct search for significant streams within the data set. Here the search has been split into three sections: near-ecliptic ($i < 10°$), low inclination ($i \in [10°, 20°)$) and medium/high inclination ($i \geq 20°$). The D_{SH} based searches within these sets are shown, as performed at respective cutoff levels of 0.10, 0.15 and 0.20, in Tables E.1, E.2 and E.3 respectively. The reason for this partitioning of the reference mean orbits is due to the tendency of D_{SH} to associate unrelated orbits at a lower cutoff limit for lower inclination orbits. As noted in Section 6.3.2—in general due to the increased uncertainty in higher inclination orbit in combination with this low inclination sporadic association tendency it is necessary to use different cutoff levels. The imposition of these levels in the current study is at arbitrary positions with a conservative approach being

taken in order to ensure that only stream members are associated.

The near-ecliptic orbits (Table E.1) are the most populous; they also have the smallest average number of significant associations in comparison with the AMOR data set. This is not very surprising as in single-linkage style searches low inclination orbits are the first to form groupings: they also have generally the lowest uncertainties and also represent the most populous region in the AMOR data set. It is therefore relatively easier to form "streams" within this region than in others. This implies the presence in lists of orbits of some possible artifacts from such searches. Due to the low inclination of orbits in this region, there are likely to be very few coherent streams present as planetary perturbations on particles of the size range measured by AMOR are expected to act quickly to smooth-out any stream presence.

Of the significant streams, the CAP (CSF 88, 34 and 185) is detected at the 99% level in three years with T1997 and T1998 disappointing, perhaps due to the uneven coverage over the active times in the latter years. The Nth. ι Aquarids appear at the 99% level in T1995 using CSF 36 and also appear in T1996; however, this time using the CSF 85 stream definition. This change of definition is due to the change in time-coverage of the shower in the different years. In other years the lapses in time-coverage again cause the shower to appear insignificantly. The Sth. ι Aquarids which present normally a better target for detection do not appear significantly at all when using the CSF 80 definition. However this orbit, as listed by Jopek et al. (1998), has an inclination of 0° which leads to an ease of association of meteors well separated temporally; it also intermingles the southern and northern branches to further confuse the problem. The Sth. ι Aquarids do however appear significantly using definitions CSF 35 in T1996 and CSF 81 in T1995–T1998: only in T1999 does it remain insignificant, this is caused by the end of the data set occurring during the active period. It is interesting to note that CSF 81 which is the most significant stream for comparison is also that with the highest inclination (12.6°)—this underlines the ease with which orbits at lower inclinations are lost in the general background.

The only other shower having any significance in the near-ecliptic inclination regime is the κ Aquarids (CSF 42, 104 and 66). This shower only reaches a significant level in T1995. It occurs about the time of the autumnal equinox and has a low inclination of approximately 2°. The number of orbits in this shower is low in each year as shown in Table E.1 and although it is significant in one year the lack of

significance in other years does not allow further analysis.

We now look at the low inclination regime ($i \in [10°, 20°)$). The Sth. ι Aquarids (CSF 81) which appeared so significantly in the previous discussion is of course within this region. The Nth. δ Aquarids which one would expect to be significant is not detected here: this may be due to the similarity of the northern to the much stronger southern branch having caused a higher expectation value than would normally have been present.

Other showers having some significance are the omicron Serpentids and η Serpentids with the latter being significant in A1996 and A1998 and the former being significant in T1995. These showers have similar orbital elements (CSF 130 and 131) and occur at close times. However their crossover of the $\lambda_\odot = 90°$ point means that they are being compared against different yearly data sets: A1996 in this sense is the same year as T1995. These stream orbits tabulated by Jopek et al. (1998) do seem to be significant in the AMOR data set.

The strongest shower in the low inclination region appears to be the DSX (CSF 183) in the years T1995 and T1997 in which it is significant. Due to time-coverage problems in the other years this shower does not otherwise appear significantly. This illustrates the case of a shower which is clearly visible by several methods being impossible to confirm as significant if the shower period is not adequately covered.

The last shower which is significant in the data set is the β Capricornids. This daytime shower which appears a month before the vernal equinox appears significantly in A1998 only.

In the medium to high inclination regime there are a higher proportion of significant associations found in the AMOR data set. The first shower significantly associated in Table E.3 is the ETA. This major shower appears at the 99% level each year and its membership is generally greater than twice that expected randomly: there is no doubt as to the reality of this shower. Similarly the major SDA shower, in all its various definitions (CSF 32, 182, 93 and 202), generally achieves at least five times the expected value—this multiple falls to about three in T1999 where the data set finishes during the active period. The SDA is well above the 99% threshold in all years. A related shower, the so-called Aquarids-Cetids (CSF 175), as listed by Jopek et al. (1998) is also found to be significant in all years except T1999 where the data set does not cover the activity period. This mean orbit is really a version of the SDA biased towards a later mean $\lambda_\odot$ at detection: $\overline{\Omega} \approx 328°$ for CSF 175 while typically $\overline{\Omega} \approx 305°$ is that accepted for the SDA.

An interesting finding is the significance of the Orionids (CSF 199, 49, 275, 137 and 100) in all years—the declination of this shower is too northerly for the number of associated meteors in the AMOR data set. The Orionids has a similar orbit to the ETA. These showers are based on meteoroids sampled from the same stream but detected at opposite nodes: therefore the D-criterion in this case has correctly associated the ETA meteors with the Orionids. This case illustrates the difference between stream and shower detection: the meteors causing these showers share the same orbits however they have well-seperated dates of detection. The 60° wide exclusion zone around the time of the shower does not define these shower orbits as different when such a 180° change in detection area occurs.

A well known radar shower, the DSX is again found to be significant in T1995 and T1997. As discussed previously for this shower the time-coverage problems during the active time of this shower cause significance problems in other years.

While most of the other orbits listed are insignificant there appears to be two orbits GE0609 (CSF 261) and the ζ Cetids (CSF 181) which are significant in several years at about the same time of the year, $\lambda_\odot \approx 80°$. Both of these showers are quite similar in their orbital elements, as listed in Table D.1: they are also similar to the orbital elements of the SDA; but these are 1.5 months earlier and at the opposite nodes. This is a daylight shower, known as the omicron Cetids by Kronk (1988). This shower was detected at Jodrell Bank and by the Harvard Radio Meteor project. Lovell (1954) notes that 37 omicron Cetids meteors were detected at Jodrell bank between May 13 and May 23 in 1950 with a mean velocity of 36.7 ± 4.2 km s^{-1}. This shower appears to be one of the most significant non-major showers detected by AMOR; coupled with its daytime nature it becomes particularly interesting.

The other showers of interest, which appear significantly in several years, are GE1206 (CSF 214) and the Puppids (CSF 176). These showers occur over the same period and both share the properties of deep south declinations (−54.2° and −63.2°). Apart from a difference of 12.7° in inclination their orbits are very similar leading to the conclusion that the shower GE1206 listed by Gartrell and Elford (1975) was in fact the Puppids. The Puppids were seen by Nilsson (1964) where he noted that the group became more pronounced at fainter magnitudes in contrast to the ecliptic concentration of photographic meteors. Their high inclination and very low eccentricity (0.5) make this stream particularly unusual. Both showers occur at the 99% level in T1997 and T1998 while the Puppids occur at the 95% level in 1995 where GE1206 is again at 99%. time-coverage problems remove significance

in T1996 and T1999.

7.6.2 Summary of Significant Stream Detections

All of the streams predicted in Table 7.1 are found to be significant. Additionally streams such as the Puppids, ζ Cetids and the Serpentids are significant. It is interesting to note that on the whole the AMOR data set appears to be dominated by the major showers with, in general, little significance found for previously published (mostly photographic) minor showers. This is particularly true in the area where one is most likely to find streams—the near-ecliptic region. AMOR is a particularly sensitive detector and it would appear from this study that the showers detected by less sensitive equipment and therefore from larger particles are not present, in general, for AMOR. An alternative explanation, of course, is that many of the previously published streams may well be simply features of the large-scale bias in the observed distributions (as discussed in Section 3.4 and Chapter 4).

7.7 A Search for Radiant Source Enhancement

The heliocentric orbits of incoming meteoroids are described completely by radiant position, geocentric speed and time of detection of the resultant meteor[7]. A meteor shower is defined as a distinct grouping of orbits and therefore a search for a corresponding over-density in these observational parameters should enable any significant showers to be detected in any meteoroid orbit data set.

The observed geocentric parameters are chosen for the search (as opposed to the further refined orbital parameters) because of the impact of uncertainties on the elements of the orbit. Elements such as the argument of perihelion and eccentricity are often poorly defined: the form of their dependence on the heliocentric velocity components of the meteoroid can lead to particularly large uncertainties, as shown in Chapter 5. In contrast the radiant position angles are generally less affected by such problems: in particular, the declination angle uncertainty derives almost entirely from the small ($\approx 0.5°$) uncertainty in the echo elevation angle. The speed parameter carries much of the uncertainty associated with the geocentric measurements—typical uncertainties are $\approx 5\%$. By converting the radiant posi-

[7]Note that geocentric quantities should be corrected for the Earths' rotation, gravitational and zenith attraction, if they are used to directly represent the heliocentric orbit. AMOR performs these corrections, as discussed in Section 2.6. Other surveys should ensure that they are similarly compliant, i.e that these parameters as directly observed are not used without correction.

tion from the geocentric equatorial reference frame to the Sun-referenced geocentric ecliptic coordinate set of Section 2.6.1, the geocentric speed range is constrained, often quite severely, according to the λ_R position, as shown in Figure 4.10. Therefore the detailed use of the geocentric speed, as a shower detection mechanism, is rendered less important. In fact many radar systems such as the recent SKYiMET range (e.g. Arlt et al. (1999)) only comprehend the radiant position and detection time of the meteor with no knowledge of the actual incoming speed of the meteoroids. Such radar systems operate in a "forward-scatter" mode where showers are defined as a strong flux of meteors from a well-defined region of the radiant space.

It is expected that any significant shower in the AMOR data set should appear strongly in the 2-dimensional space defined by (λ_R, β) over a small time interval of up to $\sim 30°$ of mean solar longitude in a similar fashion to the forward-scatter radars. This time constraint is arrived at by noticing that the three major meteor showers appeared distinctly in Figures 4.6 and 4.5 against only one monthly radiant background: it is unlikely that a shower of lesser activity would thus extend distinctly over a longer period.

The aim of the current work is to search for the presence of other showers which are not strong enough to stand out against such monthly backgrounds but which might instead appear significantly against a background over a shorter time interval. A crude use of the geocentric speed is made in order to help distinguish weak showers against the background because the knowledge of speed at this stage is an obvious advantage over the forward-scatter systems. The geocentric speed distribution for the background resembles a Gaussian as shown in Figure 4.9 in the case of both prograde and retrograde orbits. In the current study these distributions have each been partitioned into three broad sections. These overlapping sections are defined by $V_G = 20 \pm 10$, 30 ± 10 and 40 ± 10 km s^{-1} for prograde and by $V_G = 50 \pm 10$, 60 ± 10 and 70 ± 10 km s^{-1} for retrograde meteoroids. A shower must have a speed distribution exceeding 10 km s^{-1} in width or near to the lower/upper boundaries in order to not be fully enclosed in one of the sections. A further analysis run is also completed in each case with no limitations being placed on speed in order to determine how important the knowledge of the speed is in order to detect shower structure.

A search of the combined data set from T1995–T1999 is performed based on the assumption that the occurrence of a shower is not a sporadic event only seen in one year. Such a search is inevitably biased due to equipment time-coverage

problems. It has been noted previously that there are large-scale fluctuations in the daily rate in the different years of AMOR coverage hence various combinations of years in which AMOR was inactive and those in which it was active could lead to the appearance of a large apparent "peak" over a day or two relative to the surrounding background. In order to test suspected shower maxima the individual years are also separately searched in order to see if there is any apparent structure at a similar time in these.

In order to discover any significant over-densities within the radiant space a method is used to enhance the structure. Two approaches are consider in the current study—the sliding window method and the wavelet transform. The sliding window has the advantage of speed and simplicity but it assumes a rigid shape and size to the shower radiant distribution (normally rectangular). Shower radiants are not rectangular and their radiant distribution does not generally lie parallel to the ecliptic, so the use of a rectangular window of the size expected due to uncertainties in the coordinates and situated parallel to the ecliptic is found to be inappropriate. This method is replaced by the wavelet transform enhancement method which, by contrast, assumes no particular shape to the shower radiant and imposes only a general size regime: it however has the disadvantages of slower speed and more complex operation, making 3-dimensional searches more difficult.

7.7.1 Structure Enhancement by Wavelet Transform

The wavelet transform is a popular tool which allows structure at various levels of an n-dimensional data set to be enhanced. By correlating an appropriate n-dimensional wavelet with the n-dimensional image under study, features at the scale-size of the wavelet are strongly enhanced relative to those at other scales. By varying the wavelet-scale a complete appreciation of the fine- and gross-scale structures present is gained. Bendjoya (1993) and Zappalà et al. (1995) use the wavelet enhancement method to search for asteroid families in three dimensions based on their orbital elements. Slezak et al. (1994), Damiani et al. (1996) and Freeman et al. (1996) apply wavelets to the detection of sources in galactic X-ray emission data. Skuljan (2000) searches for structure in stellar velocity distributions using wavelets.

The Choice of Wavelet Function

A suitable wavelet function must be chosen for the performance of a wavelet transform. The Mexican Hat wavelet[8] is most commonly used for the detection of over-densities in data sets (all of the references given above use this wavelet in their studies). This function, which is the second derivative of the well-known Gaussian function, is defined as

$$\psi(r/a) = (n - r^2/a^2)\exp(-r^2/2a^2), \tag{7.5}$$

where the n-dimensional radius r is given most generally by

$$r = \sqrt{\sum_{i=1}^{n} \frac{x_i^2}{\sigma_i^2}}. \tag{7.6}$$

The width (a) of the positive hyper-circle in the transform defines the scale at which the focus is placed. The coordinates are weighted relative to each other using the σ_i—for example in a two dimensional system if $(\sigma_x, \sigma_y) = (2, 1)$ then each increment in the y-ordinate is equivalent to two increments in the x-ordinate. Most often $\sigma_i = 1$ is used resulting in a symmetric function. Figure 7.4 shows both a typical symmetrical Mexican Hat and also the asymmetrical Mexican Hat described in the example. The great advantage of the Mexican hat in searching for

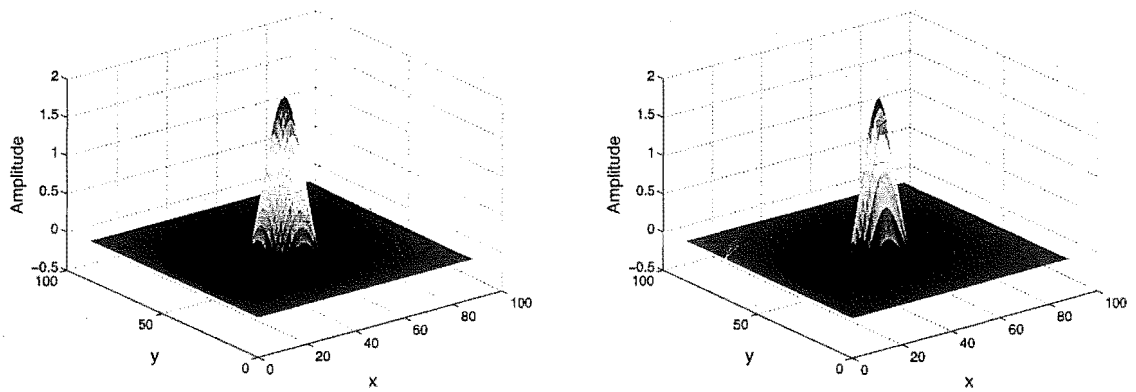

Figure 7.4: The standard symmetrical Mexican Hat function $(a, \sigma_x, \sigma_y) = (8, 1, 1)$ is shown on the left. This function is also shown on the right but here the y-ordinate has been compressed by a 2:1 ratio i.e. $(a, \sigma_x, \sigma_y) = (8, 2, 1)$.

over-densities is the negative annulus surrounding the positive core. The density of the space in the negative region exactly equals that in the positive region, therefore

[8]The Mexican Hat wavelet is also known as the Maar wavelet.

the wavelet transform of a uniform distribution will also be uniform as will that (approximately) for smaller/larger scale features. A feature in the image under study which appears at the scale of the Mexican hat, however, will be strongly enhanced in the transform.

The Wavelet Transform

The wavelet transform consists of the correlation of the function of the data set, $f(x, y)$ with the wavelet function, $\psi(x, y)$. In two dimensions this transform is defined as:

$$w(x,y) = \int_{-\infty}^{\infty}\int_{-\infty}^{\infty} f(\xi,\eta)\ \psi\left(\frac{\xi - x}{a}, \frac{\eta - y}{a}\right)\, d\xi\, d\eta, \tag{7.7}$$

where $w(x, y)$ are known as the wavelet transform coefficients (WTC).

The transform process would appear to be very time consuming due to the need to deal with all points in the data space. In practice, for speed of execution, the correlation is converted to a convolution and this evaluated in Fourier space. A 2-D histogram, $I(x, y)$, of the continuous $f(x, y)$ function is formed. Both this and a matching histogram of the wavelet function, ψ, are transformed by the Discrete Fourier Transform[9], $\mathcal{F}$. After multiplication of these transformed images has taken place in Fourier space the results are obtained in the spatial domain by inverse Fourier transform:

$$w(x,y) = \mathcal{F}^{-1}\{\mathcal{F}\{\psi\} \otimes \mathcal{F}\{I\}\}. \tag{7.8}$$

Initially, in the current study, a Mexican Hat with a 2:1 compression ratio in longitude:latitude was used. This was due to the higher uncertainty and the likely higher spread due to a larger daily motion in λ_R, relative to β. The natural coordinate system for an Earth-based observation system is the geocentric equatorial system. Coordinates in this system do not map directly onto coordinates of the geocentric ecliptic system used here. Uncertainties, and therefore spread, expected in the individual equatorial system parameters are distributed over both coordinates in the ecliptic system. In general, the spreads in λ_R and β are found to be similar with the source generally angled parallel to the ecliptic—as can be seen by comparing Figures 4.8 and 4.4. It does not make sense to provide a wavelet function which is biased on one coordinate over another under such conditions and therefore the standard symmetrical Mexican Hat wavelet is adopted and found to more sensibly

[9]A Fast Fourier transform (FFT) is used to obtain the Discrete Fourier Transform (DFT) in this study in order to provide sufficient computer execution speed. The only concession required to use the FFT is that the number of elements in each dimension must be a dyadic.

define the shower regions of the major showers.

Source Characterisation

Enhancing a source for ease of detection is the main purpose of the wavelet transform. Once such a source is discovered it is then necessary to determine characteristics such as the size, shape and strength[10] of the source.

If one assumes the source emission to be Gaussian in nature then the characterisation is straightforward using the wavelet transform; Appendix F presents the derivation and key results for such a case. The transform of a 2-D Gaussian source with spread σ, has a maximum in the spatially centred probe-size normalised $w(0,0)/a$ when the wavelet width (a) is equal to $\sqrt{3}\sigma$. This allows the source size to be estimated by variation of a. The central coefficient $w(0,0)$, for a fixed wavelet width, varies linearly with source strength, hence the relative strength of the source may be estimated from the size of this coefficient. Both of these tests are demonstrated clearly in Appendix F.

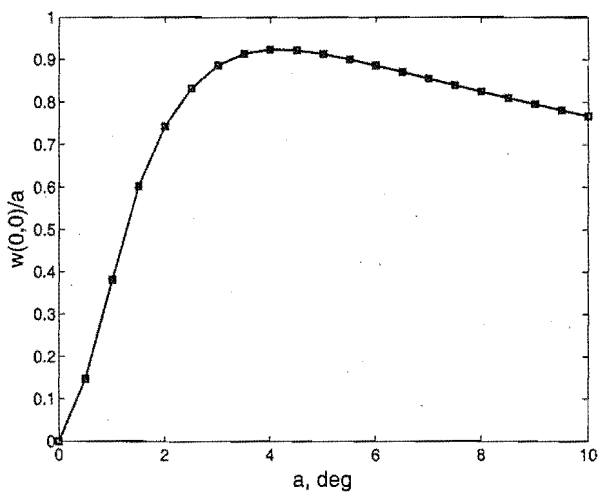

Figure 7.5: The variation in the probe-size normalised WTC at the spatial centre of the SDA shower as the probe-size is varied from $a = 0.5°$ to $10°$.

It is found that at the scale at which shower structure is expected in the AMOR data set, the change in $w(0,0)/a$ as a increases is insufficient to detect the size of the source. One may compare Figure 7.5, which shows a wavelet transform using various probe-sizes on the strongest source (the SDA) with the theoretical curve demonstrated in Figure F.2. It is obvious that the same effect is present in both

[10] "Source strength" within the context of the current study is taken to mean the number density of meteoroids within a defined source region over an appropriate period of time.

cases: however, as viewed by the wavelet transform, the range of widths used does not constitute a change of scale and therefore there is little change in $w(0,0)/a$. One is left with the knowledge that 2° to 6° appears to be the region most suited to searches for the source: however there is no strong maximum to give a more exact estimate as there was in the theoretical curve. In the current study a probe width of 3° has been used for all source detections: this was chosen qualitatively as it best fits the four major showers (which will be demonstrated in the next section). Such a value is also close to the radiant spread expected from two major showers, the Perseids and the δ Aquarids; Hawkes (1993) summarises (TV detected) radiant spreads for these showers of 3° and 3.5° respectively[11]. Smaller probes tend to result in badly defined sources while larger probes include many radiant pixels which are obviously outside the visible shower activity region. The probe-size chosen results in the best balance between these concerns, providing a relatively symmetrical source which stands out strongly from the background.

The measurement of source strength by central WTC is found to work well and the value of this coefficient is used as a gauge of strength in sliding window surveys of source time and speed characteristics. It is found that a $\lambda_\odot = 2°$ wide window stepping by 1° is appropriate, in order to determine the change with time of the stream strength. Using a smaller window may result in showers which lie on the borderline being cutoff: additionally, also in order to achieve a reasonably stable background distribution it is necessary to have at least this length of time. In contrast, too wide a window will cause problems as the shower is not necessarily stationary in the (λ_R, β) reference frame—it is shown later in this chapter and in the next that this is indeed true of most of the major showers to some extent.

Once the active time of the shower has been established the character of the shower is known in three of the four dimensions in which it exists. Detection and correction of any daily motion in the radiant can take place and the data from the period of the shower can be added together to enhance the structure under wavelet transform. Geocentric speed constitutes the fourth dimension to the shower. This parameter is broadly accounted for by the tri-level partitioning in which the search takes place but it now becomes necessary to use the speed in order to remove sporadic meteors which happen to occur within the source region[12].

[11] The radiant spreads in Hawkes (1993) are quoted from Jones and Sarma (1979) and Sarma and Jones (1980) for the Perseids and δ Aquarids respectively.

[12] A non-speed determining radar must assume at this point that all meteors within the radiant region belong to the shower.

The speed distribution within the radiant region is defined using another sliding window. The window width is 6 km s^{-1} which corresponds to an expected individual measurement uncertainty of 2 to 6 km s^{-1}. The window is moved in 1 km s^{-1} steps through the expected geocentric speed range. By experimentation with various window widths it is found that essentially the same speed curve is obtained in most cases. There is, of course, a tendency for curves to be slightly broadened by larger widths but this does not seriously change the measured spread of the curve.

7.7.2 A Search In Radiant-Speed Space

Using the wavelet transform enhancement method described in the previous sections a systematic search of the radiant space is performed. While 2° wide windows in solar longitude and 3° probe-sizes have been thought to be most appropriate, 6° wide time and probe-size windows are also used in order to detect more diffuse showers which might still stand out against the background. The data set is partitioned on the basis of the radiant regions in which meteors appear: antihelion, helion, prograde apex and retrograde apex. Within the first three regions there is a further partitioning based on geocentric speed with divisions set at 20 ± 10 km s^{-1}, 30 ± 10 km s^{-1}, 40 ± 10 km s^{-1} and all speeds. In the retrograde apex region these divisions are set at 50 ± 10 km s^{-1}, 60 ± 10 km s^{-1}, 70 ± 10 km s^{-1} and all speeds.

There are 64 permutations possible when combining all of these radiant regions—speed divisions, probe and time window sizes. For each of these permutations a wavelet transform is obtained centred at each degree of solar longitude, over the length of an equinoctial year, for the set of all meteors recorded in T1995–T1999. Appendix G shows the complete results from these 64 experimental runs: discussion here will frequently refer to figures in this appendix. For each run, four graphs are presented giving the radiant position of the maximum WTC, its amplitude and also that amplitude normalised to the total number of meteors (N_S) found within the period of time represented in the radiant region[13]. The value of N_S changes strongly according to source region and also in time due to daily changes in AMOR coverage over the five years of overlaid data: Figure 7.6 demonstrates these changes.

Only the strongest source feature in the wavelet transform for each solar longitude centre is studied, as the sporadic sources almost exclusively dominate the radiant regions (see for example Figure 4.4) and therefore any viable shower must

[13]The background activity normalised maximum WTC amplitude is frequently referred to as the "normalised amplitude" in the following discussions.

be stronger in amplitude than them. Using a wavelet probe-size of 3° tends to focus more on the size regime of "real" possible showers while the 6° probe averages over a larger region, taking increased notice of the sporadic background. The definition

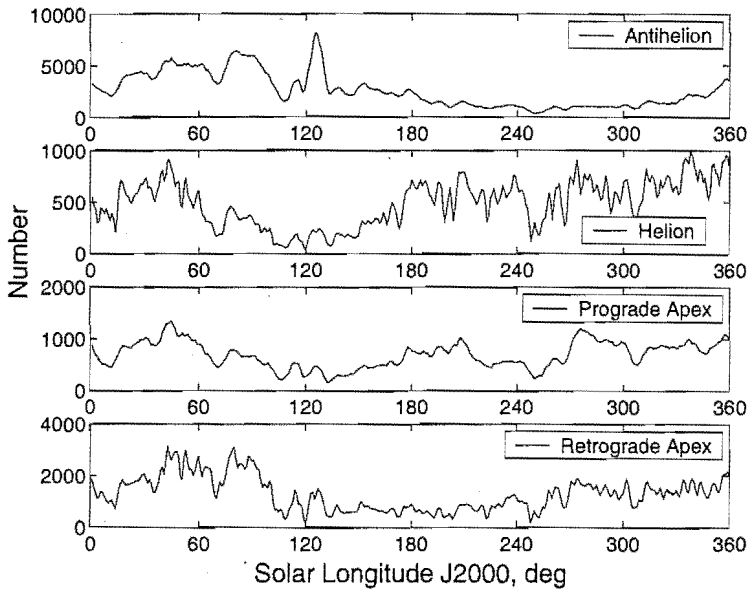

Figure 7.6: The daily number of meteors per sporadic source region (N_S). The data includes all meteors detected between T1995 and T1999.

of a meteor shower within the wavelet searching must rely on a strong change in longitude and/or latitude of the radiant and also an increase in the amplitude of the maximum WTC above the level expected due to white noise in the background level. The assumption of Gaussian noise in the amplitude is vindicated when one observes examples, such as Figure 7.7. Here one of the 64 runs, from the AH region, has been selected and a histogram formed of the normalised amplitudes over the virtual year. In this figure both the original normalised amplitude distribution and a "detrended" distribution are shown: the detrending is carried out by using a sliding median window from which the change in the background over time is obtained and this is then subtracted from the profile in order to place the profile on the same baseline (zero amplitude) due to the periodic nature of many of the radiant maximum WTC curves. The median window used is 60° in width—a size which is larger than any expected showers. (The median is used here rather than the mean in order to be as little affected by any strong showers as possible.)

The detrended distribution in Figure 7.7 is clearly Gaussian about 0, with a separated tail extending well beyond that suggested by symmetry with the negative side. This tail can be interpreted as "signal" while the Gaussian-like distribution close to 0 can be thought of as "noise". Determination of the standard deviation

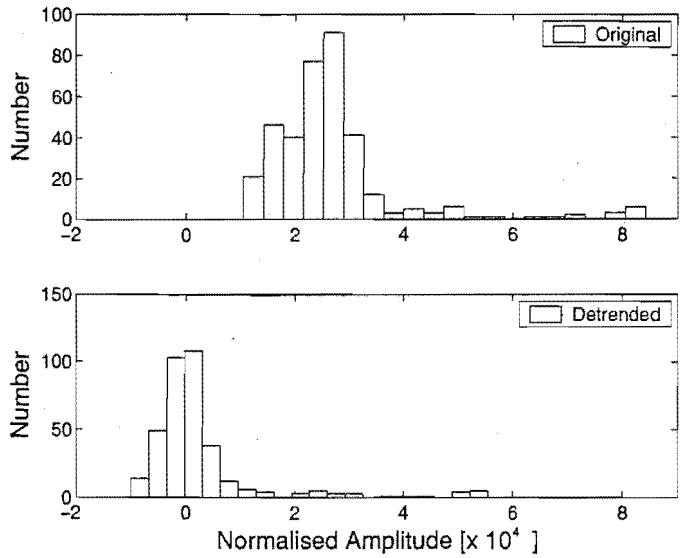

Figure 7.7: The distribution of normalised maximum wavelet amplitudes obtained for the AH region wavelet transforms of Figure G.1(k). These transforms use 3° probe and time window widths and include all meteoroids with speeds, $V_G = 40 \pm 10$ km s^{-1}. The upper graph shows the original distribution and the lower graph shows the detrended distribution from which the background "trend" in the data has been removed via a sliding median 60° wide window. The strongest amplitudes in these graphs are due to the SDA shower.

about the average value expected from such "noise" is difficult as any statistics taken of the virtual year's amplitude profile are prone to be biased due to relatively large signals (showers) in the data. A procedure has been developed to deal with such difficulties which assumes no *a priori* knowledge of the shower structure within the data set.

For each set of the 360 wavelet transforms obtained from one of the permutations of source direction etc. identified above, the following procedure is applied to the original maximum wavelet amplitude (w_{max}) and also to this in its background activity normalised form (w_{max}/N_S). A 60° wide median window is slid through the virtual year returning a view of the trend in the background. This trend is then subtracted from the original amplitude profiles to obtain detrended profiles, centred about 0—an example of this detrending process is shown in Figure 7.8. The standard deviations of these profiles are then determined and all data points at greater than 3σ above the 0 level are temporarily excluded in each case: this procedure removes outliers from the data set—such outliers are possible shower candidates and their removal provides an almost shower free background[14]. The standard deviation of the "shower-free" detrended profile is then taken and this is assumed to

[14]No background can ever be completely cleansed of a strong signal unless manual intervention is decided upon. This is also true of the detrending process using the sliding median window, there is always a remnant of the signal left in the profile.

correspond to the standard deviation of the noise distribution: of course this value is slightly higher than that due to noise alone due to some contamination from unremoved signal. This contamination cannot be avoided unless a more stringent shower removal level were used such as 2σ and such a level has the disadvantage of artificially causing a number of peaks to be considered significant if there is only pure noise present without any strongly outlying signals. Three and four times the

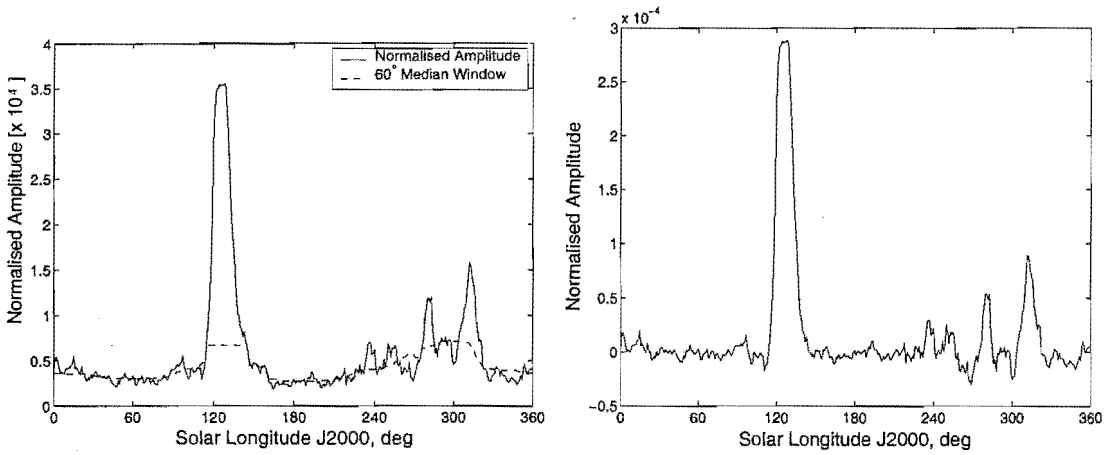

Figure 7.8: On the left a sample normalised amplitude profile is shown, from the AH region wavelet transforms of Figure G.1(k). It is obtained using 3° probe and time window widths, and includes all meteoroids with speeds in the range $V_G = 40 \pm 10$ km s^{-1}. The background average fit obtained using a 60° wide sliding median window is shown, note the slight bias in this background at the time of the largest peak corresponding to the SDA. The detrended profile resulting from the subtraction of this running average is shown on the right.

calculated noise standard deviation are added to the running background average obtained from the sliding 60° wide median window at each point on the amplitude profiles. These additions correspond to the 99% (3σ) and 99.99% (4σ) confidence levels respectively. The assumption here is that while the background trend may change, the spread about that trend is relatively static, with respect to a Gaussian noise distribution. Such an assumption is reasonably true for the normalised amplitudes which have a fairly homogeneous level of spread while it is not so true for the original amplitude profiles of Appendix G. There are "lulls" in activity in these profiles which correspond to the sporadic source being almost totally unobservable by AMOR, such events have correspondingly much lower spreads than their more active counterparts. This problem does not occur so much in the normalised profiles as the corresponding low N_S used in the ratio acts to "correct" the spread to "normal" levels. While this problem with the original profile is unfortunate, it is ignored as the normalised profile is the main interest. The confidence levels are simply attached to the original profiles with the knowledge that these may be too

harsh on the low activity regions.

While the significance of the normalised maximum amplitude in the wavelet transform is the primary measure of shower presence, a "steady-state" in the radiant position of the maximum over several days also assists in verification of the reality of a shower—this is especially true where the steady-state obtained differs markedly from that in the surrounding time period. In radiant position there is a pair of coordinates and steady-state is achieved when the position in both coordinates changes little over the period of the shower (apart from a systematic motion in λ_R attributed to daily motion). The radiant position of the maximum may differ from that of the surrounding period due to a large-scale change in the radiant position occupied and/or to the presence of a systematic motion in contrast to the surrounding random motion. The use of the radiant position must however be approached very cautiously. As shown in the following sections, an excellent steady-state in maximum radiant position can be obtained where there is no shower presence (according to the wavelet amplitude): this is particularly a feature of the retrograde apex region. The daily motion in the radiant position of the maximum is unpredictable and hence allowances cannot be made for it. There is also the problem where there may be two sporadic source regions active (as in the apex region for much of the time): then, the radiant position may toggle between these positions as the relative strengths of these sources change, thus emulating shower activity. Because of these reasons it is not possible to produce a mathematically sound definition of "steady-state" and the definition is inherently a subjective decision which changes with each application—only a small amount of weight may be attached to the motion of the maximum radiant position as an indicator of shower activity.

Analysis of Normalised Amplitude Profiles by Radiant Region

The four profiles corresponding to the $V_G = 20 \pm 10$ km s^{-1} partition of the AH region are shown in Figures G.1(a), G.1(b), G.1(c) and G.1(d). In the original amplitude profiles, using the 3° probe, there are clear local maxima over the period $\lambda_\odot \in [120°, 130°]$, in both cases appearing for several days above the 99.99% significance level. These peaks correspond to clear steady-state in both latitude and longitude over this period and are identified as corresponding to the CAP shower. The normalised amplitudes do not fare so well however: the peak is diminished to a single (99.99%) significant data point in normalised amplitude for the 2° wide time

window and it is below the 99% level for the 6° wide window. This is an unusual course of events and occurs due to the large-scale increase in meteor rate over this time acting to reduce the significance of the peak in question. There is little that can be done in this case for what is a rather weak shower, apart from realising that the significance of the ratio forming the normalised amplitude must be weighed against common sense provided in the form of the original amplitude profile, with support from the coherence of the corresponding longitude and latitude coordinates in such cases. It might be argued that division, in the ratio, by the total number of meteors in this period in the AH region unfairly biases the result due to the order of magnitude stronger SDA shower which is also present, at the same time, in a different speed partition.

Tests are made involving the removal of the SDA meteors from the background activity (N_S); the SDA shower is assumed to consist of the 2,413 meteors detected as shower members later in Section 8.4, these meteors are removed from N_S for the $\lambda_\odot$ bins in which they belong. Figure 7.9(a) shows the result of removing integer multiples (between 0 and 3) of 2,413 from N_S, for the search corresponding to that shown in Figure G.1(a) with parameters $(V_G, \Delta\lambda_\odot, a) = (20 \pm 10 \text{ km s}^{-1}, \pm 1°, 3°)$. One can see the improvement in the CAP normalised maximum WTC as one proceeds towards the highest multiple—as N_S is decreased the ratio w_{max}/N_S necessarily increases while the confidence levels simultaneously decrease. It is clear that either the SDA has been grossly underestimated or that the general background at the time of the shower conspires to remove the significance of the ratio—such a background being reduced as the SDA multiple increases. There appears to be a mixture of both cases here. As one can see from Figure 7.9(b) the reduction in the number of meteors occurring (mainly) over the $\lambda_\odot \in [120°, 130°]$ period seriously diminishes the background activity. This decrease is so marked that the second and third multiple subtraction sub-plots show an activity much lower than that expected from the surrounding time period. The radar system was more often actively observing over the central time-period than it was in the surrounding periods as evidenced by the large gaps in Figure 7.1; also the data ends at $\lambda_\odot = 128°$ in T1999. One should also note from study of the gross yearly activity curves of Section 7.5 that no conclusive annual proof for the existence of the SDA shower could be gleaned from these profiles, this implies that the SDA is not as dominant as would be implied by proceeding to the higher subtraction multiples of Figure 7.9(a).

The conclusion reached is that the CAP is a shower on the knife-edge of detection;

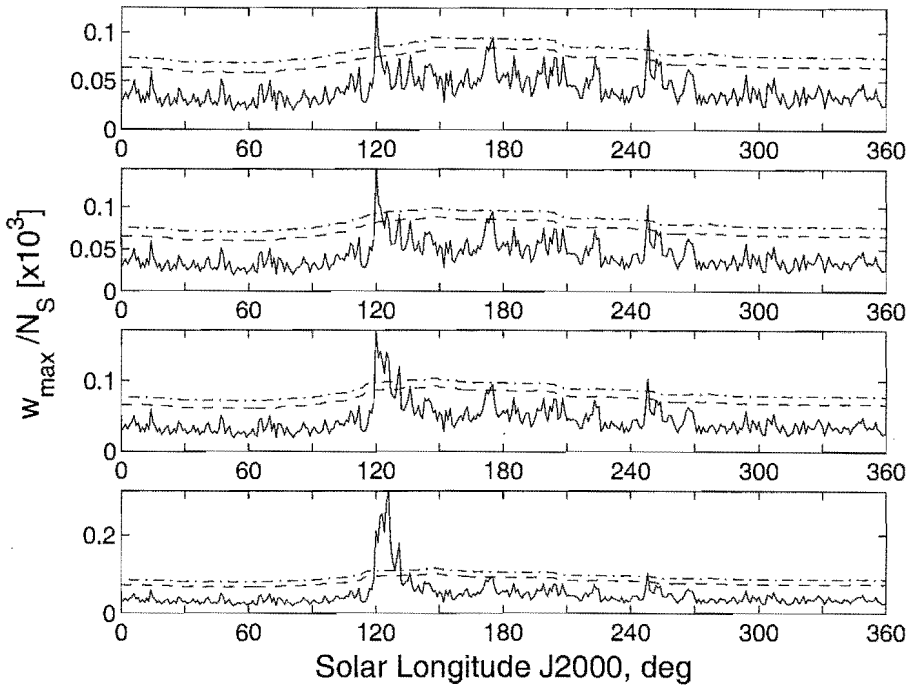

(a) Normalised Maximum WTC

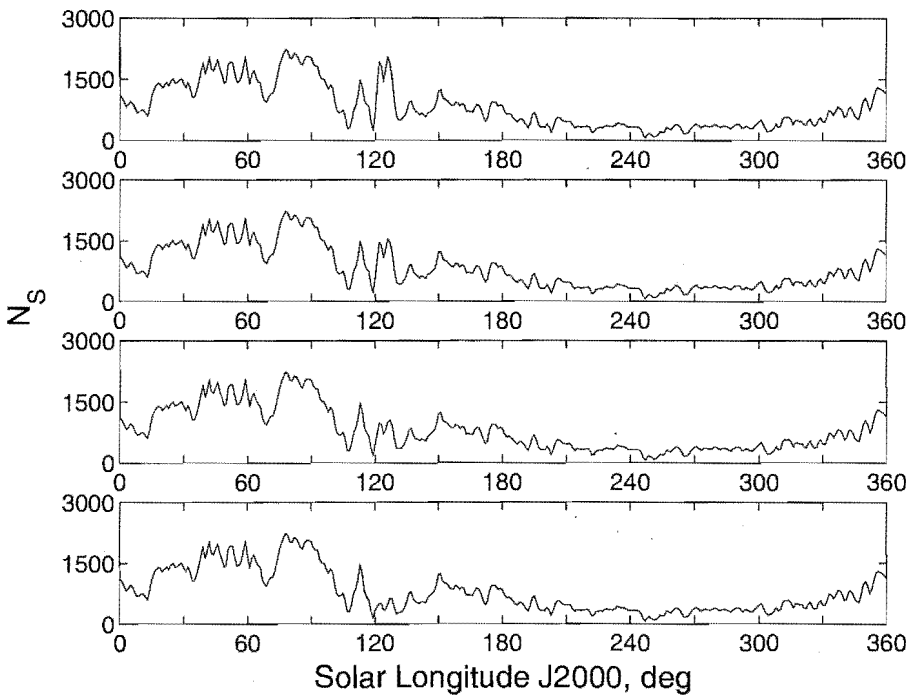

(b) Total Number of Meteors in the AH Region

Figure 7.9: A study into the effect of the removal of the SDA meteors from the background rate in order to increase the significance of the CAP which occur over the same time period. On the left the change in the normalised maximum WTC is shown as the subtraction multiple of the SDA shower strength (2,413 meteors) is increased in integer multiples from $\times 0$ at the top to $\times 3$ at the bottom; the corresponding change in N_S is shown on the right. These graphs correspond to the search shown in Figure G.1(a).

were it not for knowledge of the reality of this shower from other sources, one would have cause to doubt that reality given the representation in the AMOR data set. This shower represents a lower limit to that which might be detected distinctly by AMOR and is therefore useful in determining that minor showers which are sometimes published based on a few orbits (e.g. Gartrell and Elford (1975)) from other radar surveys will not be visible significantly using the AMOR radar, given that the total number of CAP meteoroids contained in the orbital data set used here is shown later in Section 8.5 to be ~ 300.

There are other peaks in Figures G.1(a) and G.1(c) which are also significant. These occur over the period $\lambda_\odot \in [170°, 180°]$ and also just after $\lambda_\odot = 250°$. The latter peak is not accompanied by any strong change in the radiant position and corresponds to a period of extremely low meteor rate in this region, as can be seen from the original amplitude profile, hence it is most likely a false detection; the former peak is more interesting as it is seen significantly in both the original and normalised amplitude profiles indicating its reality. This is considered a shower candidate, although the radiant position doesn't appear to achieve steady-state over this period.

Figures G.1(b) and G.1(d) show the corresponding results using the wider 6° probe. For the 2° time window the peak corresponding to the CAP and also that close to $\lambda_\odot \approx 180°$ are seen again at the 99% level attesting to their reality. The wider time window of Figure G.1(d) removes the significance of the CAP in the normalised profile while continuing that of that latter peak; the CAP peak is still visible in the corresponding radiant position change however. The original amplitude curve, in Figure G.1(d), corresponds closely to the gross rate curve of this region attesting to the fact that we are measuring mainly the sporadic background using this widest probe/time window combination. It is interesting to note the sudden change in the maximum radiant position at $\lambda_\odot \approx 200°$ towards near apex longitudes and latitudes (compare with later prograde apex curves). The boundaries of the AH region, as with the other regions, are of course somewhat artificial. In this case the central (near-ecliptic latitude) region falls in strength and the prograde apex region near the $\lambda_R = 240°$ boundary takes over as the strongest source. This period corresponds to the long low activity period, in the original amplitude of Figure G.1(d). This period is expected to begin at the autumnal equinox, but instead it starts later at $\lambda_\odot \approx 200°$, due to the fortuitous inclusion of the near-apex source. The strong radiant shift, seen at that time, is therefore not indicative of a shower presence.

We now turn our attention to the 30 ± 10 km s^{-1} partition, as shown in Figures G.1(e), G.1(f), G.1(g) and G.1(h). Using the 3° probe, significant peaks are evident over the period $\lambda_\odot \in [120°, 130°]$ at the 99.99% level and also at $\lambda_\odot \approx 255°$. The latter peak is clearly an artifact of the low activity at that time, as discussed for the previous partition; the former peak corresponds to the SDA meteor shower. The SDA peak is further verified by the strongly differentiated steady-state adopted by the radiant coordinates over this period. There is a daily motion in the longitude position which is clearly visible in the slope of the longitude line over this period, such motion defies efforts to define exactly what is meant by "steady-state" as discussed above. It is interesting to note also that the SDA peak in the original amplitude profile is much narrower in time than the corresponding normalised profile. This effect is caused by the AMOR system coverage being particularly weak just before $\lambda_\odot \approx 120°$ and just after $\lambda_\odot \approx 130°$. The usefulness of normalisation is obvious in realising the true active period, which lies over $\lambda_\odot \in [115°, 145°]$, of the shower.

A peak which just reached the 99% level using the smaller probe, at $\lambda_\odot \approx 315°$ is more clearly visible at the 6° probe size particularly when using the 6° wide time window of Figure G.1(h): here this peak is still weak though it almost reaches the 99.99% level. There is also a perceptible rise in the original amplitude profile although this is not significant above the surrounding background. This peak will be discussed in later speed partitions where it becomes more significant—here we are measuring the "tail" of the speed distribution of this possible shower source. Otherwise the 6° probe again reveals the peak in the $\lambda_\odot \in [120°, 130°]$ region corresponding to the SDA shower to be significant at the 99.99% level while continuing to show the artifact peak close to $\lambda_\odot \approx 255°$. As with other 6° probe-size runs the sporadic sources are strongly detected in general and this is evidenced by the smooth radiant position profiles, compared to those obtained using the smaller probe-size. The useful effect of the smooth profiles obtained using the 6° probe is that strong showers such as the SDA stand out more easily against the surrounding background due to the relative stability of the background over time.

The 40 ± 10 km s^{-1} partition as shown in Figures G.1(i), G.1(j), G.1(k) and G.1(l), shows the SDA peak once more, except this time it is much stronger (about twice the 99.99% level), this is evidence that average speed of the SDA is closer to the speed band defined by this partition. The artifact peak at $\lambda_\odot \approx 255°$ again appears to be significant while the previously identified peak at $\lambda_\odot \approx 315°$

appears at the 99.99% significance level when using the 2° time window with the 3° probe. This event corresponds to a peak in the original amplitude profile which just manages to make the 99% significance level, in combination with the coherence of the longitude/latitude positions over time: this indicates the reality of the shower occurrence. All probe/time window sizes show this peak to be significant at the 99.99% level or just below that and therefore it has been designated Peak A for further study as a shower candidate in Section 7.7.3.

Using the all speed partition, as shown in Figures G.1(m), G.1(n), G.1(o) and G.1(p), tells the same story as those partitions discussed above. The SDA is clearly present at the 99.99% level as is the peak at $\lambda_\odot \approx 315°$. No other peaks are significant.

Moving onto the HN source region, the 20 ± 10 km s^{-1} partition is shown in Figures G.2(a), G.2(b), G.2(c) and G.2(d). Using the 3° probe a 99.99% significant (in both original and normalised amplitude) shower is seen close after $\lambda_\odot \approx 180°$ for both the 2° and 6° time windows. This peak is identified with the DSX shower and is further characterised by a region of steady-state in the corresponding radiant position profiles. Several peaks are also visible using this probe about $\lambda_\odot \approx 120°$, these are discounted as artifacts due to corresponding very low activities in the background and also in the original amplitude profiles. The DSX appear under the larger probe also, although it falls below the 99% significance for the larger time window—this is probably due to the close appearance of a peak at $\lambda_\odot = 210°$, which is apparently an artifact as it occurs in no other profiles.

In all of this partition's profiles 99.99% significant peaks occur between $\lambda_\odot = 270°$ and 300°, these peaks are possible shower candidates and are therefore designated Peak B. On further investigation this source is found to be particularly long in λ_R suggesting the presence of a sporadically generated source. This is further confirmed by the broad activity structure which is very unstable with respect to probe and time window size, hence Peak B is ignored as an artifact.

The 30 ± 10 km s^{-1} partition is shown in Figures G.2(e), G.2(h), G.2(g) and G.2(h). In these profiles in addition to the previously discussed artifacts about $\lambda_\odot \approx 120°$, there are two peaks which both appear well above the 99.99% level in all cases. The DSX peak occurs at about twice the 99.99% confidence level and is much stronger than that seen in the 20 ± 10 km s^{-1} partition indicating that the average speed of its meteoroids is closer to 30 km s^{-1}. There is again a very visible steady-state in radiant position corresponding to this shower. The daily motion in

λ_R of the radiant centre of this shower is much smaller than that of the SDA, as evidenced by the slight slope to the longitude line during the shower activity. The DSX is seen to last from a few degrees prior to 180° until a few degrees after 190°, the size of this activity not changing markedly between the original and normalised amplitude curves (in marked difference to the SDA). It is obvious from the profiles that it is generally better to explore the DSX using a longer time window; this is due to the many gaps in coverage throughout the years during which AMOR was inoperative, in fact studying individual years particularly T1997 and T1998 can lead one to question whether the shower really exists exactly for this reason.

The other 99.99% significant peak present in this partition is the broad peak centred at $\lambda_\odot \approx 45°$. As shown in Figure G.2(g), this peak corresponds to a steady-state in radiant position at a very similar longitude and latitude to the DSX. The baseline (sporadic) longitude over the year does not appear to stray much from this $\lambda_R \approx 330°$ value, leading to questions as to the significance of this finding; the latitude, however, changes more markedly as the sporadic source oscillates first southwards in the first half of the year and then northwards of the ecliptic in the second half. There is some concern that this peak may be simply the result of the sporadic source passing in and out of the radar highest detection probability zone, due to the length of the shower's active period, particularly as the ends of the high significance region correspond to the latitude rising or falling well away from the optimum for detection ($\beta \approx -15°$). These reservations aside, this peak is designated as shower candidate Peak C and further studied in Section 7.7.3.

The 40 ± 10 km s^{-1} and all speed partitions tell the same stories as that above (Figures G.2(i), G.2(j), G.2(k) and G.2(l); Figures G.2(m), G.2(n), G.2(o) and G.2(p)). The DSX peak is again 99.99% significant but it is not as strong as in the 30 ± 10 km s^{-1} partition and this effectively constrains the average geocentric speed of this shower's meteoroids close to 30 km s^{-1}. Peak C is again present, in some cases more strongly in the 40 ± 10 km s^{-1} profiles than above. There are also the low activity level artifacts which are again ignored close to $\lambda_\odot \approx 120°$. Figure G.2(l), using the 6° probe, shows a particularly clear example of the sudden change in the relatively smooth longitude and latitude at the beginning and end of Peak C—this lends further evidence to the possibility that this is a long-lived shower. Meanwhile in the same figure an interesting, strongly differentiated, steady-state in radiant position on both coordinates, unaccompanied by a significant amplitude change, is evident centred about $\lambda_\odot = 270°$: this effect is also present to some degree in other

graphs. While this feature is not further studied here, it is worth bearing in mind for future studies of the data set. Apart from the lack of a significant amplitude peak it presents all the hallmarks of a meteor shower having both an appropriate activity time and the accompanying steady-state radiant position.

The apex region is now discussed. Meteors within this region are partitioned according to the orbital direction, prograde or retrograde, of their corresponding meteoroids. We discuss the prograde apex region first because this region is expected to be composed almost completely of noise due to the low activity of the region and further, the average latitude $\sim -50°$ from which the meteors appear in this region is not likely to include many meteoroids coming from the main meteoroid stream region, close to the ecliptic.

The geocentric speed partitioning on the prograde apex region follows that of the other prograde regions. The 20 ± 10 km s^{-1} partition is shown in Figures G.3(a), G.3(b), G.3(c) and G.3(d). The largest peaks, in general, correspond to the lowest level of the background over the same time period as seen in the HN region, $\lambda_\odot \in [60°, 180°]$. Such peaks as that appearing in the normalised amplitude at $\lambda_\odot = 120°$, in Figure G.3(a), are typical of these apparently artificial local maxima and are therefore ignored.

There are also peaks which appear between the 99% and 99.99% levels centred about $\lambda_\odot \approx 45°$. These correspond to some steady-state in the radiant position (e.g. Figure G.3(d)). Difficulty in reproducing this peak using different probe/time window sizes, in combination with the changing λ_R in some of the figures over the active period and the length of that period itself, leads to the conclusion that this peak is most likely simply a sporadic feature. The appearance of this source simultaneously to Peak C is unrelated, as these appear from quite different directions. Using the 6° probe with the 6° time window also yields a 99% significant peak at $\lambda_\odot \approx 200°$, in Figure G.3(d), with a corresponding steady-state in both radiant coordinates. Hence this peak is labelled shower candidate Peak D for further study. Upon such examination however, Peak D is found to not be strong and stable enough to support the notion so that it might correspond to a shower region.

There are also significant peaks in some of the prograde apex profiles at $\lambda_\odot \approx 255°$ and $\approx 310°$. These peaks correspond to particularly low activity in the background rate curve of this region, as shown in Figure 7.6. Although they cannot be discounted as there are slight corresponding peaks in the original amplitude curve, the fact that these peaks last as significant instances for only 1° leads to serious

doubts as to their reality.

In the 30 ± 10 km s^{-1} partition, shown in Figures G.3(e), G.3(f), G.3(g) and G.3(h), there are several apparently significant peaks about $\lambda_\odot \approx 120°$ in the normalised amplitudes of these profiles. As with similar peaks in the HN region these correspond to the lowest activity in the background, and also in the original amplitude profile: hence they are discounted as artifacts. The particularly convincing peak at this time, in Figure G.3(h), is designated Peak E to single it out for further study in an attempt to show that this region is indeed dominated by artifacts of the background rather than shower structure.

The 40 ± 10 km s^{-1} partition shown in Figures G.3(i), G.3(j), G.3(k) and G.3(l), presents very much the same picture as that above and also as that for the all speed partition shown in Figures G.3(m), G.3(n), G.3(o) and G.3(p). In these profiles Peak E in various forms is present above the 99.99% level in all cases with a particularly convincing version appearing in Figure G.3(l). This peak under further examination is found to extend over the AH/AX boundary. It is only present for the period of the very lowest background rate (see Figure 7.6), leading to the conclusion that this is simply an artifact of the normalisation ratio in the case of a very low activity background.

A significant peak structure, identified above as sporadic, is often seen about $\lambda_\odot \approx 45°$. There are also a number of peaks in the original amplitude distribution which appear above their 99.99% level close to $\lambda_\odot \approx 300°$ (e.g. Figure G.3(m)) and these peaks are rendered totally insignificant in the normalised amplitude profile as these are (correctly) seen to be artifacts of the changing background rate.

The retrograde apex data set is much more active than that selected for prograde orbits. This region is strongly dominated by sporadics: the true spatial distribution of orbits is strongly observationally biased (as previously discussed) due to the large geocentric speeds attained by retrograde orbiting meteoroids. Figure G.4 shows the various plots obtained from this region. The most notable feature of this series of plots is that the maximum WTC occurs invariably at $\lambda_R \approx 270°$ while the latitude generally follows a smooth curve in all speed ranges with $\beta \approx 0°$ for $\lambda_\odot \in [315°, 45°]$, a symmetrical fall from $\lambda_\odot \approx 45°$ towards $\beta \approx -30°$ at the autumnal equinox and then a rise upwards again as one approaches $\lambda_\odot \approx 315°$. In the lowest speed partition (50 ± 10 km s^{-1}), e.g. Figure G.4(c), the normalised amplitude of the wavelet transform rises to a stable height once the latitude moves south of the ecliptic. The increase in normalised wavelet amplitude with decreasing latitude

may at first appear unexpected. However, it is reasonable given the link between ecliptic latitude and orbital inclination: the peak of the observed retrograde orbit population is not at the ecliptic but instead at $i \approx 160°$, as shown in Figure 3.14, hence generally more southerly latitudes corresponding to this inclination bias will be observed more strongly. Only the near-ecliptic latitudes are visible by AMOR near the start and end of the equinoctial year as during this time the ecliptic radiant region is in the elevation centre of the northerly radar transmitted beam while the more southerly latitudes lie in the null region of the beam. As the ecliptic and celestial equator "part company" after the vernal equinox the near-ecliptic radiant region moves out of the beam and the more southerly latitudes enter. It is interesting to note the sharp step-function present between the near-ecliptic and southerly regimes in the apex maximum radiant positions. This may appear to be quite unphysical: however, it simply relates to the relative change in the strengths of the near-ecliptic source and southerly source because they both exist at $\lambda_\odot = 45°$, for example; however this is a turning point from which onwards the near-ecliptic source is weaker (but still visible) than the southerly source.

Looking now at the higher speed partitions of the retrograde apex region. The 60 ± 10 km s^{-1}, 70 ± 10 km s^{-1} and all speed partitions of Figure G.4, show strong peaks centred about $\lambda_\odot \approx 45°$. These peaks in amplitude and in normalised amplitude correspond to a 20° increase in the otherwise very stable 270° ecliptic longitude with respect to the Sun. The ecliptic latitude connected with this occurrence does not obviously change but it does become a little less variable than the surrounds, as can be seen in Figure G.4(f). This peak, designated Peak F, is identified with the ETA shower. One should note that although the radiant position of the shower may be particularly clearly differentiated when using the larger 6° wavelet probe, the corresponding normalised maximum amplitudes are in fact less significant in this case than in the case of 3° probe usage (e.g. Figure G.4(e)). This significance difference is attributed to the fact that while a larger probe will give extra stability to the radiant centre of a shower such as the ETA, it will also include a number of marginal outliers in the surround time periods when the ETA is not active and this will raise the background level in general resulting in a higher cutoff level for significance.

In the 50 ± 10 km s^{-1} partition the maximum amplitude during this time does not rise significantly above the background. There are some indications of the presence of this shower in the 50 ± 10 km s^{-1} partition due to the longitude varia-

tion (e.g. Figure G.4(a)) but without a significant amplitude this detection is not verified. These findings indicate that this shower is likely to have a higher speed centre probably between 60 and 70 $\mathrm{km\,s^{-1}}$. There is little (apart from a general understanding) which can be gleaned from the plots in Figure G.4: the bias is so strong towards the exact ecliptic longitude of the apex of the Earth's way that no other significant peaks in normalised amplitude, except the ETA, are detectable[15]. Bearing this problem in mind a rectangular block stretching through all latitudes and centred on the apex with longitudes within 7.5° of the apex have been "blanked out" in the wavelet transformed images; the figures have then been re-searched for significant structure: Figure G.5 shows the 16 resulting profiles. When using the large 6° probe it is evident that little has changed in the maximum coefficients found, apart from a change from 270° as the typical longitude to 277.5° in some cases and 262.5° in a small number of cases. The longitude of the maximum is effectively a Heaviside function of the latter two values: a typical example of this phenomena is shown in Figure G.5(d). The latitude variation is smooth in this class of profiles and corresponds to that seen in the corresponding profiles of Figure G.4. This is hardly surprising as the angle the Earth's velocity vector makes with the celestial equator must necessarily change over the period of observation. This shows the complete dominance of the apex region over all the surrounding parts of the profiles—indeed extending the blanking window further from the apex results in a similar phenomena occurring at the new window edge nearest the apex.

The smaller 3° probe produces a much less smooth radiant position variation, with random oscillations often between longitudes above and below the blanking window while the latitude generally follows the trend indicated in the smoother 6° curves: a typical example of this character is shown in Figure G.5(a). There are no significant amplitudes present in the 6° probe profiles apart from the previously identified ETA which once again make a strong showing in all partitions, apart from 50 ± 10 $\mathrm{km\,s^{-1}}$, on all four profiles for each instance: an example of this shower appears in Figure G.5(g), centred about $\lambda_\odot \approx 45°$. The smaller probe also finds the ETA significant in addition to a number of other peaks which appear above the 99.99% level, for example that at $\lambda_\odot = 75°$ in Figure G.5(a). Such peaks as this correspond to extremely low activity points in both the original amplitude and

[15]The significant peak appearing in various profiles (e.g. FigureG.4(j)) at $\lambda_\odot \approx 250°$ is not mentioned as a detection. This is almost definitely an artifact given that the same peak occurs in other radiant regions at the same time and corresponds to a very low activity in the background and original amplitude.

background rate profile (Figure 7.6) and therefore, as with similar "significant" peaks seen previously, these are ignored. That statement applies to all of the peaks appearing as significant, in the normalised profiles of Figure G.4, apart from the ETA peaks. This lack of shower structure in the amplitude profiles is backed up by the total lack of coherence in the 3° probe radiant position profiles over time and the obviously completely sporadic based profiles obtained using the 6° probe (again the ETA is excluded from this statement).

Single-Year Significant Peaks

Up to this point the T1995–T1999 data set, in its entirety, has been considered for shower detection. This assumes that showers are annual events and therefore that addition of several years of data, in a normalised form, will increase the signal to noise ratio when attempting to detect showers against the sporadic background. In this section the antihelion and helion radiant regions (the assumed main sources of prograde shower meteors) are examined to see whether year by year stream searching is viable and, if this is so, then whether any new showers appear under such a revised search strategy. Note that as this search is only intended as ancillary to the multi-year search, only the "all" geocentric speed partitions with the 3° wavelet probe are used in order to obtain an overall view of the data set; time window widths of both 2° and 6° are however used in each case.

Figures G.6 and G.7 display the AH and HN region single year searches respectively. The displays for each search are identically formed to those of the multi-year searches above, apart from the background number used to normalise the maximum WTC being set to 50 when it falls below this value—the intent of such an action is to avoid sharp speaks in the normalised profile for very low N_S and w_{max} values.

We examine first the AH region wavelet transform enhancement method results. The SDA shower shows up significantly in all years using both time windows. The length of shower coverage differs greatly between years. T1995 has a low level of coverage (Figure G.6(a)) while that of T1996 (Figure G.6(c)) is particularly good around the time of the shower. The 6° time window appears to serve little purpose here apart from smoothing the gaps in coverage in curves such as those of T1997 (Figure G.6(e)) to produce the more aesthetically pleasing Figure G.6(f). A common problem with the approach of using single equinoctial years is seen for T1999 where Figures G.6(i) and G.6(j) have a large gap after $\lambda_\odot \approx 130°$ due to the end of the data set having been reached: such a gap causes problems with

the significance level algorithm, which uses w_{max} values 30° in time each side of the point under consideration, hence the endpoints in this case are unbalanced in significance.

Apart from the strong SDA peaks in the AH graphs, which appear above the 99.99% significance level in all cases, there are few significant peaks in the T1995–T1999 graphs. An exception to this are peaks appearing centred about $\lambda_\odot \approx 315°$ in T1995 and T1997. These are significant at the 99.99% level for the 6° time window (Figures G.6(b) and G.6(f)) and more weakly and intermittently at the 99% level for the 3° window (Figures G.6(a) and G.6(e)) in these years. There are "hints" of these peaks in T1996 and T1998: but these these are mostly attributable to low background count rates—T1999 does not cover the time of this peak. The peak under discussion coincides with Peak A, as identified in Figure G.1(l) and this peak is discussed in a Section 7.7.3 so it will not be discussed further here. The interesting result gained from the single-year approach in this case is to show that such "shower" peaks can be highly significant in some years and not in others, raising the possibility that in some cases the multi-year approach is adding noise to the signal. A counter-argument here is easily made when looking at the profiles provided by the single- and multi- year approaches in Appendix G. It is clear that the single-year profiles are more prone to random fluctuation that the multi-year ones are—this is caused mainly by the low activity rates experienced at times whereas in the case of multi-year searches such fluctuations are smoothed out due to the background rate always being reasonably high—the minimum of $N_S = 50$ discussed earlier is used to help remove this problem from the single-year profiles.

The HN region, shown in Figure G.7, shows frequent fluctuations in its normalised maximum WTC. The DSX shower is strongly evident in most years. It generally presents stronger (generally 99.99% significant) peaks for the 6° time window than for the smaller 2° window where significance is often 99%. The DSX shower is relatively quite weak (against the background) and needs longer time integration to appear clearly. Apart from the DSX there are a number of sharp peaks present, particularly in the longer time window (e.g. at $\lambda_\odot \approx 120°$ in Figure G.7(b)), where system outages, or near outages, over some of the days covered result in an artificial and irrelevant significant peak being formed. Most such peaks in the 6° HN region profiles are attributable to this mechanism. The 2° time window profiles are characterised as containing mostly statistical fluctuations (noise), apart from the DSX which sometimes is not much above this noise level as can be seen in the

T1997 (Figure G.7(e)) profile for example. There is some sign of the presence of the Peak C (Figure G.2(j)) peak, identified earlier, in the single-year profiles particularly in T1996 where the 2° window has some significant peaks at $\lambda_\odot \approx 45°$, in both window sizes in T1998 and in the T1999 6° window profile. This peak is only just significant in these figures and leads to the concern that results obtained in the multi-year search, as shown for example in Figure G.2(j), may simply be an agglomeration of the effects of different time-coverage/background activity in the various years.

To summarise the findings of the single-year searching experiment: no showers are found which are not found in the multi-year searches discussed previously; very erratic profiles are often obtained due to the lower activity rates involved; shower profiles are less smooth than those obtained in multi-year analyses (this is not necessarily a problem as it reveals the true yearly make-up of the shower coverage/activity—such in-depth coverage can also be obtained from multi-year searches by using the profile provided to pinpoint the shower position and then to investigate activity profiles arising from meteor detections in that region over different years); a minimum background activity is needed in order to remove very large spikes arising from low activity. It appears that the multi-year searching method is sufficient and perhaps superior, especially given the low activity rates of AMOR yearly showers against the background, therefore further efforts are concentrated on this.

7.7.3 Characterisation of Significant Shower Structure

Four strong meteor sources have been shown to appear significantly in the data using the wavelet transform enhancement method. These are found at the locations expected for the major meteor showers—ETA, CAP, SDA and DSX. Other than the CAP, these showers appear strongly using a variety of probe and time window sizes and over a defined range of geocentric speeds: the CAP is much weaker and is barely significant above the background for most combinations of these parameters. The significance of these showers is generally detected by both an obvious change in the surrounding maximum wavelet position regime in combination with a strong increase in the normalised maximum WTC appearing well above the surrounding background.

In addition to these expected showers, a number of peaks (identified by designated letters in the normalised amplitude distributions shown in Appendix G),

have been investigated to determine the possibility that they are true astronomical events. Most of these have been dismissed as artifacts, however Peak A (Figure G.1(l)) and Peak C (Figure G.2(j)) have been identified as being potential shower candidates so they are investigated further in addition to the four major showers.

For each shower the motion, if any, in the geocentric ecliptic Sun-referenced frame is determined and removed. This removal is performed by reduction to some selected time (λ_c) during the shower period, the conventional epoch to use for λ_c is either the mean solar longitude of the shower meteors or the solar longitude at the peak of activity. The equation used to perform the reduction is

$$P_N = P - \frac{dP}{d\lambda_\odot}(\lambda_\odot - \lambda_\odot^c), \tag{7.9}$$

where P is any parameter containing daily motion (not limited to radiant position parameters), P_N is the motion-corrected parameter and $dP/d\lambda_\odot$ is the measured daily motion in P as obtained by linear fit.

Using the corrected data set the activity and speed profiles of the shower are determined (detailed discussion on these determinations is given in the first subsection below where showers are first studied in this fashion). The activity is given in two forms; the first being the directly observed rate and the second being a normalised rate, where the normalising parameter is the background rate in the particular radiant region under consideration as determined from Figure 7.6. Finally the wavelet transform, using the determined active period and speed profile of the shower, is shown next to the "raw" observed radiant distribution from which it derives. Each of the radiant regions is visited in turn, in the following sections, with a longer time being spent on the antihelion region where the methodology is discussed in-depth.

Prograde Meteoroids from the Antihelion Source Region

The antihelion region has been shown to have significant peaks in the normalised amplitude distributions corresponding to the major meteor showers: the SDA and the CAP, both of which are active over the period $\lambda_\odot \in [110°, 160°]$. There are also several other peaks which may be obtained from a survey of those in Figure G.1, most of these have been dismissed as artifacts in the data. A particularly strong peak having its activity centre shortly after $\lambda_\odot \approx 300°$ has been identified as a shower candidate. This peak, designated Peak A, is identified in Figure G.1(l). It

will be studied further in addition to the SDA and CAP below.

The radiant regions of the CAP and SDA are well separated from each other in longitude and latitude which contributes to the large ~ 20 km^{-1} difference between their average geocentric speeds. This speed difference explains why the CAP is able to be separated from the SDA in the 20 ± 10 km s^{-1} partition searches; the strength of these showers is decidedly different with the SDA being an order of magnitude stronger than the CAP hence detection of the latter by searching for the strongest source in each wavelet transform, with no speed discrimination, is not possible.

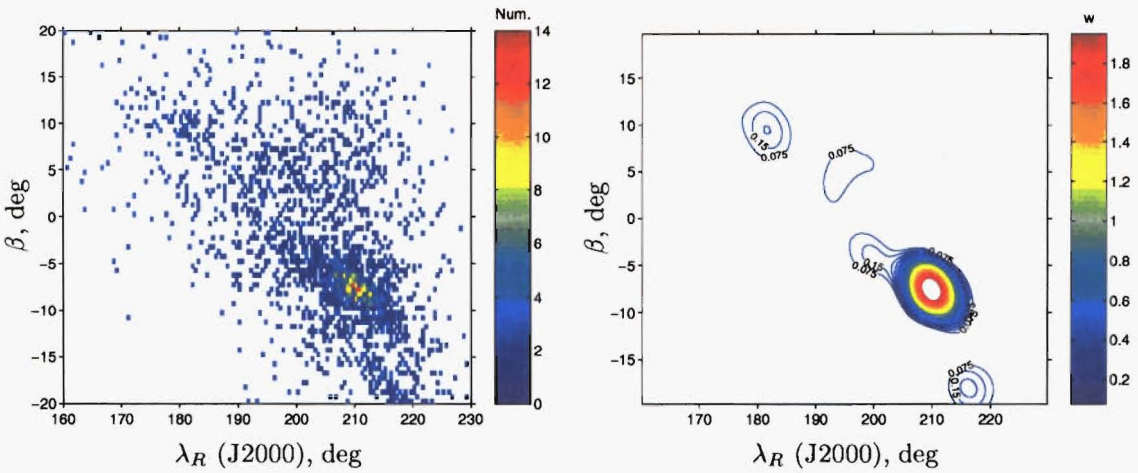

(a) Radiant Distribution

(b) Wavelet Transform

Figure 7.10: The original radiant distribution and the wavelet transform of that distribution in the AH region over the period $\lambda_\odot = 126° \pm 1°$ using an $a = 3°$ wavelet are shown. The meteors are unfiltered with respect to geocentric speed.

A wavelet transform of width $a = 3°$ in the AH region has been determined over the period in question. The SDA and CAP are at peak activity over the period $\lambda_\odot \in [120°, 130°]$. An example of the wavelet transform of a part of this period ($\lambda_\odot = 126° \pm 1°$) with no meteoroid speed filtering being applied, is shown in Figure 7.10. The SDA is clearly present in the wavelet transform (Figure 7.10(b)) as the very strong source centred at $\beta \approx -7°$. A weak sporadic source is present at mid-longitudes while at $\lambda_R \approx 180°$ the CAP shower is distinct. In addition to these sources another is identified at the lowest latitudes: this feature does not survive for a longer period of time and, as it is not very strong over the time it is active, is not therefore considered significant. This situation may be compared to the CAP which has similar strength in this instance but continues over several days.

As shown in Figure 4.10 there is a strong relationship between the meteoroid

speed and the location of the radiant. In order to better select the CAP and SDA regions for further study these showers are considered in the speed partitions shown to best suit them in Section 7.7.2—these are defined by $V_G = 20 \pm 10$ km s^{-1} and $V_G = 40 \pm 10$ km s^{-1} respectively. Within these partitions the wavelet transforms are obtained of radiant images, using a sliding window 2° wide in solar longitude in steps of 1°, in order to trace out the approximate length of time over which the showers are active with the showers' strength being gauged from the size of the maximum WTC in the respective regions. From this work it is found that the CAP is most active in $\lambda_\odot \in [120°, 130°]$ with a similar result for the SDA—although the latter is still clearly active over the wider region $\lambda_\odot \in [115°, 145°]$.

The CAP is on the borderline of detection in Figure 7.10. It is important to be able to bolster its significance by adding several days of data together. The unfortunate problem here is that the central radiant position of every shower experiences a daily motion: using the Sun-centred ecliptic longitude system should alleviate such a problem if it were simply due to the change in perspective as the Earth orbits the Sun. However, as previously noted, the motion is also linked to the physical structure and impact geometry of the stream; hence, while the motion is generally in the longitude parameter (parallel to the ecliptic) it is not expected to equal that of the Sun.

In order to determine the correction factor required, the position of the maximal WTC is studied as the solar longitude centre is moved in each of the two speed defined sets. It should be noted that the use of this method of daily motion analysis is crude at best (a more acceptable form of analysis is used in Chapter 8) but one must rely on the current technique here in order to work towards constraints on some of the degrees of freedom of the problem. Due to the strength of the SDA it is found that a $\lambda_\odot = 1°$ wide window is acceptable. A problem arises here as solar longitude is not a natural unit in which to measure meteor showers. It is possible inadvertently to place the boundary across a single day's apparition of the shower and in effect to diminish its true significance. This problem is exacerbated as the start of each "day's" apparition of the shower varies by 0.25° per year for the same "day". As five years of data have been used in the present study we do not attempt here to correct this problem and more elaborate methods are applied in Chapter 8.

The SDA window centre, shown in the upper row of Figure 7.11, moves from $\lambda_\odot = 114°$ to 145° in 1° steps. There is evidently a linear change in the longitude λ_R as $\lambda_\odot$ increases. A least-squares fit to the data in the region $\lambda_\odot = [115°, 135°]$

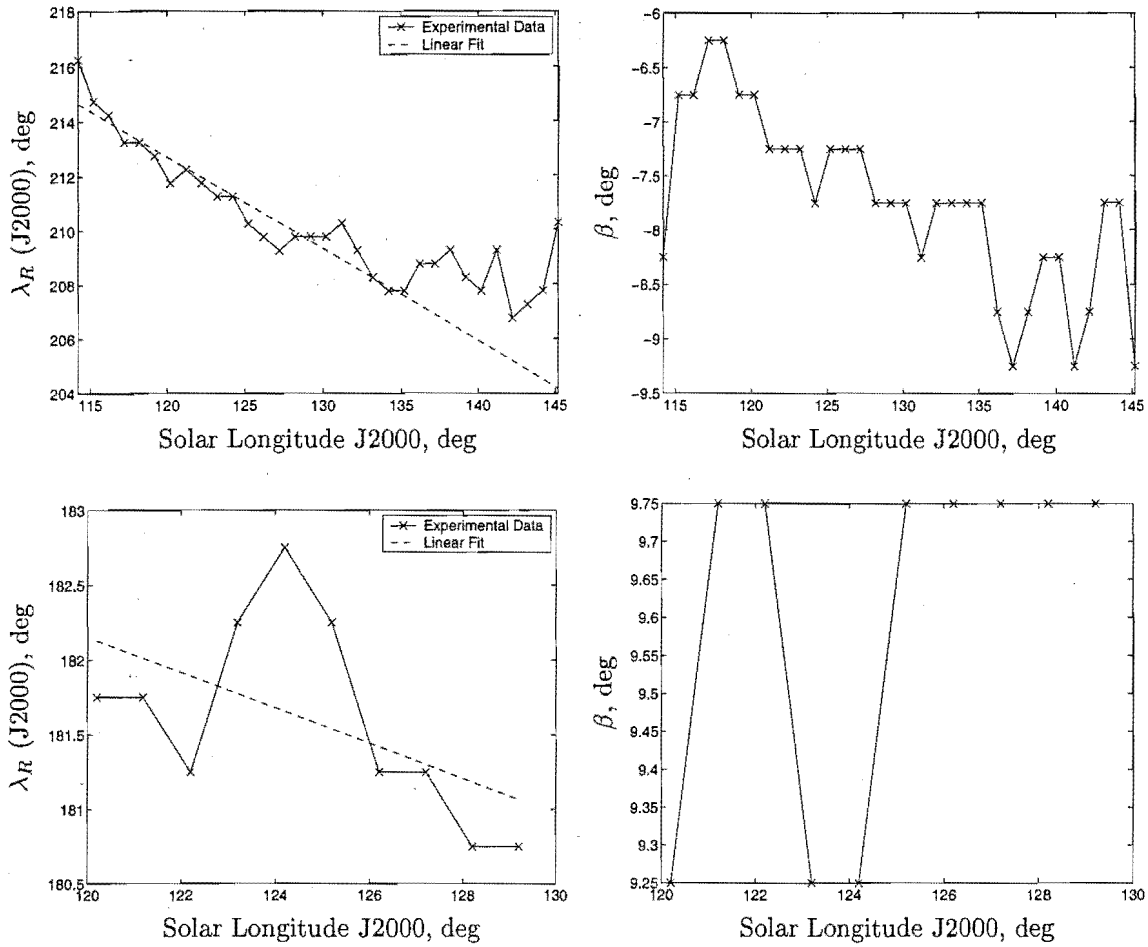

Figure 7.11: Daily motion of the SDA (upper row) and CAP (lower row) central radiant positions over their active periods.

yields the line shown on Figure 7.11. Data have been ignored in the later part of the shower activity as the low rate of shower meteor detection renders the wavelet transform relatively unstable. The daily motion obtained from this fit is given by

$$\lambda_R = -0.34\lambda_\odot + 252.3°. \tag{7.10}$$

The motion in the CAP radiant position over time is much less pronounced than that for the SDA as shown in Figure 7.11. The weakness of this shower makes the detection of daily radiant motion much more difficult—the best fit line for the motion, shown in the figure, is highly unstable and should be regarded as a vague guide only to the true motion. Using this linear fit the variation in radiant longitude over time is found to be $\sim 0.1°$ per degree of solar longitude with negligible change in ecliptic latitude. This motion is as expected from Cook (1973). The longitude variation over the maximum shower period of $\lambda_\odot \approx 20°$ is thought to be negligible

enough to be discounted in the current study as this motion does not exceed the uncertainty in longitude on the individual meteors.

The SDA meteoroid influx peaks in activity about $\lambda_\odot^c \approx 125°$. The value of λ_R, used previously, is thus corrected to compensate for the motion determined in equation 7.10 about this centre. Equation 7.9 is used to perform the reduction to the corrected longitude, λ_N. In the case of the CAP, whose daily motion is negligible, λ_N is set equal to λ_R.

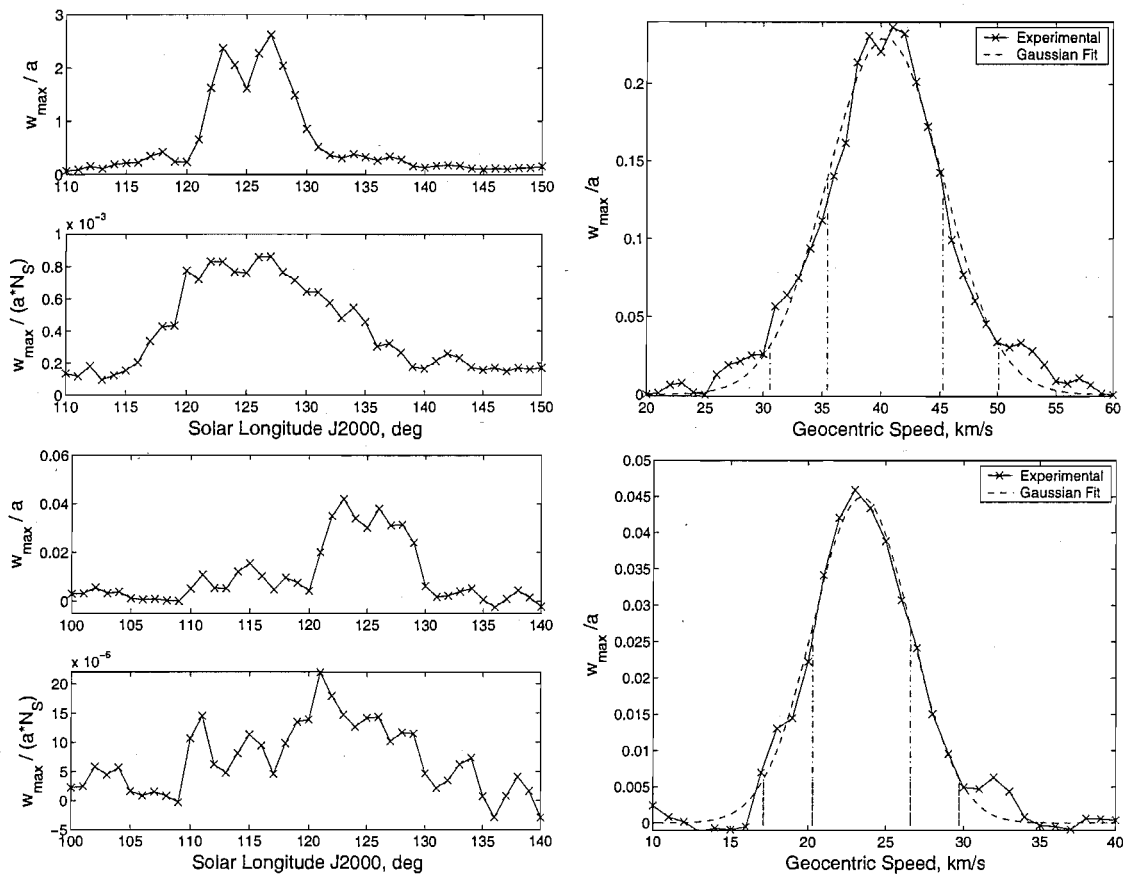

Figure 7.12: The distribution in speed and time of the SDA (upper row) and CAP (lower row) shower meteors. Both distributions are determined by moving window scans of the radiant region, with window widths of 2° and 2 km s^{-1} in time and speed respectively. The activity time profiles are given both for original (w_{max}/a) and for background normalised amplitudes ($w_{max}/(aN_S)$). The speed profile is fitted by a Gaussian curve with parameters $\overline{V}_G = 40.4$ km s^{-1} and $\sigma_V = 4.9$ km s^{-1} for the SDA; and $\overline{V}_G = 23.4$ km s^{-1} and $\sigma_V = 3.1$ km s^{-1} for the CAP. The first and second σ_V spacings from the mean are indicated in each case.

Using the adjusted radiant system for these showers it is now necessary to determine their activity and geocentric speed profiles accurately. The change in the maximum local WTC's over time for these showers is mapped using a sliding window in $\lambda_\odot$ with a width of 2°. The position of the coefficient in each case is held constant throughout the scan and fluctuations in its magnitude are attributed to the change

in shower strength.

Figure 7.12 shows the activity curves obtained for both showers: here both the observed activity curve and the curve normalised to the total number of meteors observed in the AH region for each data point are shown. The SDA is most active in the region $\lambda_{\odot} \in [120°, 132°]$ in the directly observed activity curve but the normalised curve clearly shows that this region extends over $\lambda_{\odot} \in [114°, 145°]$, the AMOR coverage on both sides of the central region is the cause of this difference. The CAP is found to again have highest activity in a similar region to the SDA—$\lambda_{\odot} \in [120°, 130°]$. The distinct activity of this shower extends over $\lambda_{\odot} \in [110°, 130°]$ according to the normalised curve; the exact ends of this activity are not clear as the centre of the normalised profile is not particularly strong and the rate tends to merge into the background. One should note that due to the 2° window widths employed these limits are perhaps 1° wider than they would have been with a smaller window.

As noted above, there is no obvious absolute cutoff for the end of a shower and the beginning of sporadic random noise. In this study this cutoff is defined to be the point in time at which the wavelet transform of the shower region does not show a visually distinct source at the appropriate position and at which the wavelet coefficient at the stationary pixel under analysis tends towards a relatively low level and appears to fluctuate randomly upwards and downwards. Perhaps Poisson statistics might be employed to resolve this issue. However, due to the motion of the background sporadic sources it is clear that the expectation value of the background will vary over the active period of these showers.

Using the determined active periods of these showers the distribution of geocentric speeds attained by the meteoroids within the shower region is studied. A sliding window 2 $\mathrm{km\,s^{-1}}$ in width is used for both showers with the period of time being fixed within the extended activity boundaries given above. The intensity of the stationary wavelet coefficient at the source centre is taken to imply a relative density of meteoroids with geocentric speeds within the window. The profiles for the SDA and CAP showers are both shown in Figure 7.12. It is clear that the profiles are approximately Gaussian and therefore a least-squares Gaussian fit has been attempted in each case.

The SDA region is found to have a mean speed of 40.4 $\mathrm{km\,s^{-1}}$ with a standard deviation of 4.9 $\mathrm{km\,s^{-1}}$. The CAP region has a mean speed of 23.4 $\mathrm{km\,s^{-1}}$ and standard deviation of 3.1 $\mathrm{km\,s^{-1}}$. These curves demonstrate the large difference

in speeds between the showers: shower radiant positions strongly influence the geocentric speed of the meteoroids detected. It is assumed that the shower mean speed is that determined for the shower region above and that the extent of the shower is within 1 or sometimes 2σ of that mean. It is possible that all meteors up to speeds of, for example, 3σ from each of the means are members of the shower, spread out simply by measurement uncertainties in the data. It is not possible in an exploratory technique to determine the individual distributions of the background and shower meteoroid speeds as these are too intermingled. However the region in which the clear bulk of the shower lies must be determined in order to prevent sporadic intrusion. Arbitrarily, in the current study a shower is defined as all meteoroids within the source region over the active period of the shower having speeds within 1σ of the shower region mean, where the mean and standard deviation are as determined above (this rule is broken for the ETA in Section 8.3.2 where 2σ must be used due to the very large uncertainties on this retrograde shower). In general, it is found for showers using the 1σ selection criterion in Chapter 8 that the spread expected in the speed distribution due to individual meteor measurement uncertainty is achieved, hence assuming that measurement uncertainties are large enough to mask any physical spread the current approach is vindicated. Recall from Section 1.1.1 that radar meteoroids typically leave the comet at speeds less than 1 $\mathrm{km\,s^{-1}}$. It is difficult to determine the distribution of speeds expected by the time the meteoroids impact the Earth but the ± 3 to ± 5 $\mathrm{km\,s^{-1}}$ at the 1σ level in all showers studied here allows for a reasonable spread over time in orbital speeds.

Now that the active times and speed regimes of the CAP and SDA have been established it is interesting to look at the showers as they appear both originally and under wavelet transform in these defined regions; Figure 7.13 depicts this for both showers. The SDA is clear by inspection of the original figure and more so in the wavelet transform. Note the strong negative region surrounding the positive SDA source—this "moat" is invaluable in providing a definite boundary to the source. The CAP due to its relative weakness does not enjoy such a strong surround. In order to separate this shower from the background it is necessary to define some level above zero at which an artificial "moat" might be formed; this will be discussed in Chapter 8.

Other interesting features to note in these wavelet transforms are the presence of minor structure. In the CAP figure there are clearly two sources at $\lambda_N \approx 200°$ and at low latitudes. This is the position at which the sporadic antihelion sources

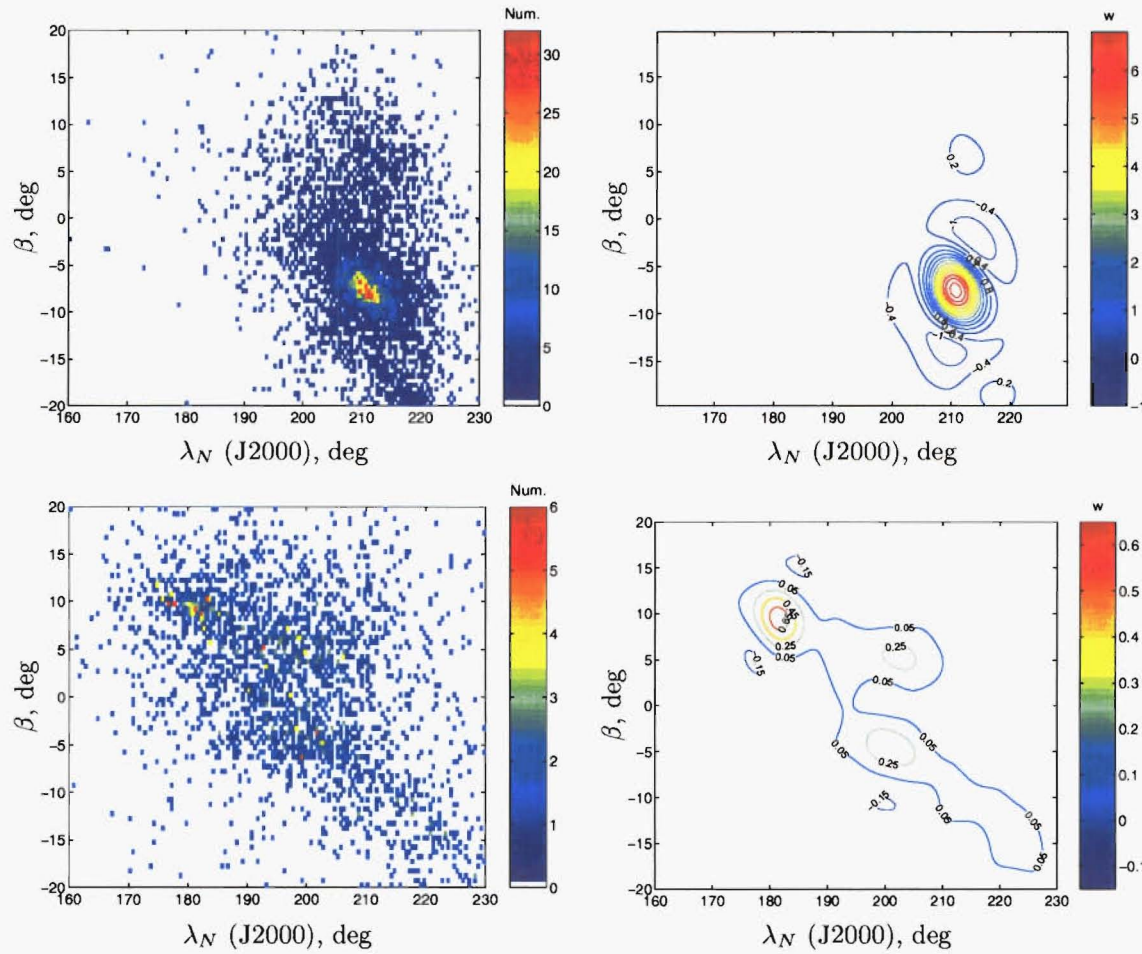

Figure 7.13: The wavelet transform of the SDA (upper row) and CAP (lower row) regions. Meteoroids are selected to have speeds within one standard deviation of the shower mean (see Figure 7.12) in each case and to have $\lambda_\odot \in [114°, 145°]$ for the SDA and $\lambda_\odot \in [110°, 130°]$ for CAP. The left column shows the original radiant distributions obtained by this selection while the column on the right shows the corresponding wavelet transforms.

occur and these sources are part of this complex. One may also note the strong effect of speed selection on density in radiant space. The centre of the wavelet transform for the SDA is found to be maximum at $(\lambda_N, \beta) = (210.8°, -7.2°)$ using all of the shower meteors with speeds within 1σ of the mean in the active period. This centre changes very slightly to $(\lambda_N, \beta) = (210.2°, -7.2°)$, if only the central activity period $\lambda_\odot \in [120°, 130°]$ is used, reflecting perhaps a small unaccounted for drift in the radiant which only manifests over longer time periods. While there is little difference between the central radiant positions the second value will be preferred as the majority of the meteoroids are included here and there is less time for any possible drift to occur. Normally, radiant positions are stated in geocentric equatorial coordinates, so we must translate this centre in order to compare it with published data on the shower.

The ecliptic longitude of the radiant is given by $210.2° + 125.0° = 335.2°$ with the ecliptic latitude not changing from $-7.2°$. This translates to give a right ascension, $\alpha = 339.5°$ and declination, $\delta = -16.3°$. Cook (1973) states $(\alpha, \delta) = (333.8°, -16.2°)$ at $\lambda^c_\odot = 125.0°$ with $V_G = 41.4$ km s^{-1}, these are generally in good agreement with the current study but the right ascension disagrees by 5.7°. Cook appears to have found an inaccurate mean due to the small sample of 13 photographic orbits available. Rendtel et al. (1995) find a mean radiant position from visual meteor observation which is much closer to that observed in the present study. In their working list of visual meteor showers they state a radiant position at shower maximum ($\lambda^c_\odot = 125°$) of $(\alpha, \delta) = (339°, -16°)$ with an average geocentric speed of 41 km s^{-1}. This also agrees with Kronk (1988) who gives identical details apart from his declination of $-17°$.

The centre of the wavelet transform for the CAP is found to be maximum at $(\lambda_N, \beta) = (181.8°, -9.2°)$ for all meteors within 1σ of the mean speed over the activity time of the shower. Narrowing the time interval down to the centre of the shower does not affect this value. In equatorial coordinates, for the time at the centre of the maximal region of the rate curve ($\lambda^c_\odot = 125°$), the mean radiant position is therefore given by $(\alpha, \delta) = (306.9°, -9.7°)$. This is close to the radiant location given by Cook (1973) of (307.7°, −9.8°) for a shower maximum of $\lambda^c_\odot = 127°$. Kronk (1988) and Rendtel et al. (1995) give similar positions of (306.7°, −8.3°) for a maximum at $\lambda^c_\odot = 128.6°$ and (307°, −10°) for a maximum at $\lambda^c_\odot = 127°$ respectively. If one adopts the radiant motion of Cook (noted earlier) then the differences between these published values and that of the current study are similar to the differences between each of the published studies (which are reasonably negligible).

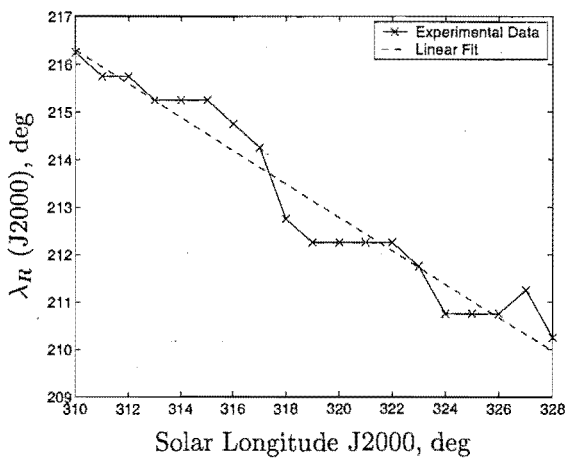

Figure 7.14: Daily motion of the Peak A radiant longitude over the active time of the shower.

Up to this point the SDA and CAP shower characteristics have been discussed; the technique considered therein is now applied to a possible new shower: Peak A (Figure G.1(l)). The ecliptic latitude of this peak is found to have a negligible motion over the active period while the longitude with respect to the Sun has a motion, shown in Figure 7.14 and fitted by a linear least-squares method, of

$$\lambda_R = -0.352\lambda_\odot + 325.4^\circ. \tag{7.11}$$

The daily motion in this case is equal to that determined for the SDA (equation 7.10). The shower is found to be centred at $\lambda_\odot^c \approx 316^\circ$ and hence the longitude motion is removed by reduction to this by equation 7.9. Using the corrected radiant position in this new reference frame, the activity and speed profiles are obtained as shown in Figure 7.15. As with the SDA and CAP, sliding windows are used in time (2° width) and speed (2 km s^{-1} width) to obtain these curves. The period over which the normalised amplitude appears to be above the general background level stretches over $\lambda_\odot \in [305^\circ, 320^\circ]$. The speed profile, as with the other AH region showers, is fitted by a Gaussian function. In this case a Gaussian does not provide nearly as good a fit as that obtained for the SDA and CAP (Figure 7.12): this difference may indicate that Peak A is caused by sporadic bias as opposed to being a true meteoroid stream however it may also simply relate to the small number of points which make up the source region.

In comparing Figure 7.15 to the activity profile of the CAP in Figure 7.12, one finds that this shower is slightly weaker at its most active than the CAP. Its duration is smaller than the other AH showers although this is increased from the directly observed rate when normalisation is added. The wavelet transform of this region over the period $\lambda_\odot = 313^\circ \pm 7^\circ$ is shown in Figure 7.16: here there is little doubt as to the definite radiant position of the source—however the sparse nature of the original image may lead to questions as to the astronomical reality of an associated meteoroid stream and this will be further discussed in Chapter 8.

Prograde Meteoroids from the Helion Source Region

Most meteor detections occur in the antihelion and (retrograde) apex regions. This is especially true for visual surveys where the helion region follows approximately the daily cycle of the Sun rendering detections within this region impossible: showers observed in the HN region are generally named with the prefix "Daytime" in order to

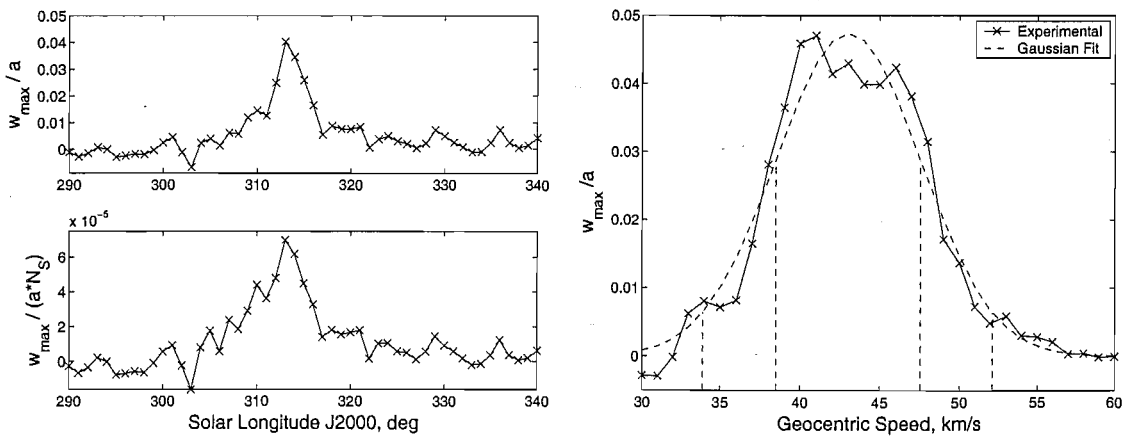

Figure 7.15: The distribution in speed and time of the Peak A meteors. Both distributions are determined by moving window scans of the radiant region. The activity (left) and speed (right) profiles use window widths of 2° and 2 km s^{-1} respectively. The activity profile is shown in the original (upper) and normalised (lower) amplitude cases. The speed profile is fitted by a Gaussian curve with parameters $\overline{V}_G = 43.0$ km s^{-1} and $\sigma_V = 4.6$ km s^{-1}.

remind observers of the impracticality of visual observation. A radar system remains operational 24 hours a day and so detection of daytime showers is possible. However radar surveys are also hampered to an extent during the day due to the problem of Sporadic-E interference which lowers the quality of meteor echo detections at times, often rendering them unusable for further reduction.

The HN region generally displays no significant activity in the AMOR data set. An exception to this rule is the DSX shower which occurs about $\lambda_\odot \approx 188°$ each year. This shower was only noticed with the advent of meteor radar systems. Similar techniques to those used for the AH region are again employed here to study this shower radiant. Additionally a possible shower identified in the wavelet enhancement search, designated Peak C, is also further studied to determine its astronomical reality.

The radiant position of the DSX is found to be at an ecliptic longitude with respect to the Sun of $\approx 330°$ and at an ecliptic latitude $\approx -10°$. The radiant exhibits a different style of daily motion from that of the SDA or CAP. A sliding window 2° wide is used to measure this motion, the resultant profile is shown in Figure 7.17. The strongest variation is in latitude as opposed to longitude, an unusual result as, generally, motion is predominantly parallel to the ecliptic. A linear fit to the latitude change is found to describe the motion well with

$$\beta = -0.28\lambda_\odot + 41°. \qquad (7.12)$$

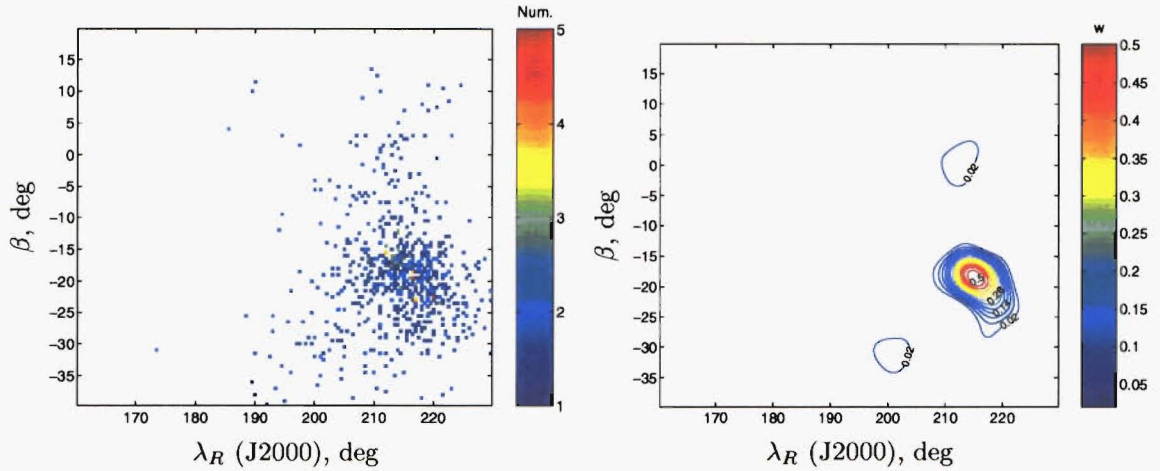

Figure 7.16: The wavelet transform of the Peak A region. Meteoroids are selected to have speeds within one standard deviation of the shower mean (see Figure 7.15) in each case and to have occurred within $\lambda_\odot \in [306°, 320°]$. On the left the original radiant distribution obtained by this selection is shown and on the right the corresponding wavelet transform is given.

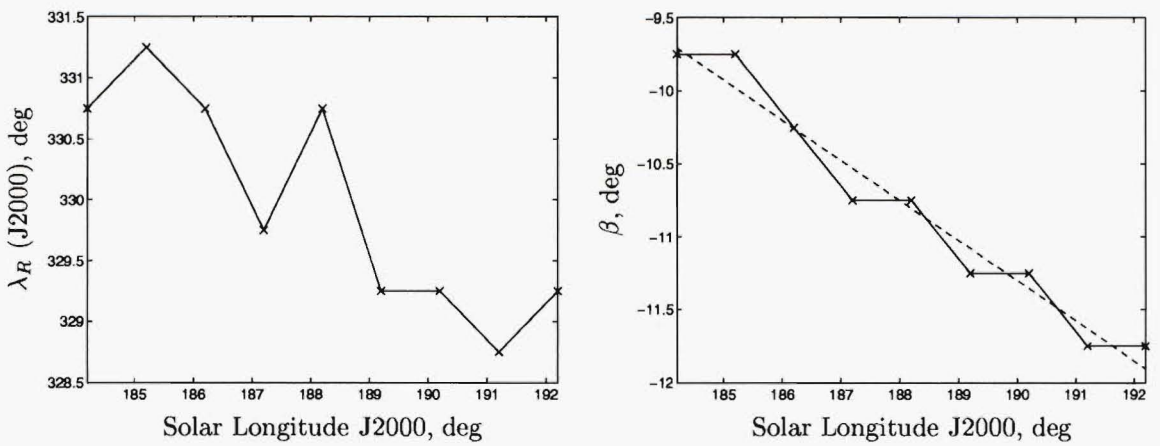

Figure 7.17: Daily motion of the DSX radiant over its central active period.

The longitude near the central active period of the shower (from $\lambda_\odot = 184°$ to 189°) shows variation in which no trend is clearly evident. Adding the positions from the later part of the shower from 189° onwards and viewing this together with the central period longitude positions suggests a decreasing linear trend. However, the later part of the shower is characterised by so few members that this apparent trend may simply be due to instability in the wavelet transform. Accordingly no adjustment has been made for longitude motion with only the ecliptic latitude being corrected by reduction to the time of the maximum ($\lambda^c_\odot = 187°$) using equation 7.9.

The change in strength of the shower over time is again found by studying the changes in the central WTC as a sliding window (2° width) is moved through the data in steps of 1°. The activity profile achieved using this method is shown in Figure 7.18; the shower active period is identified as $\lambda_\odot \in [178°, 192°]$. Due to a

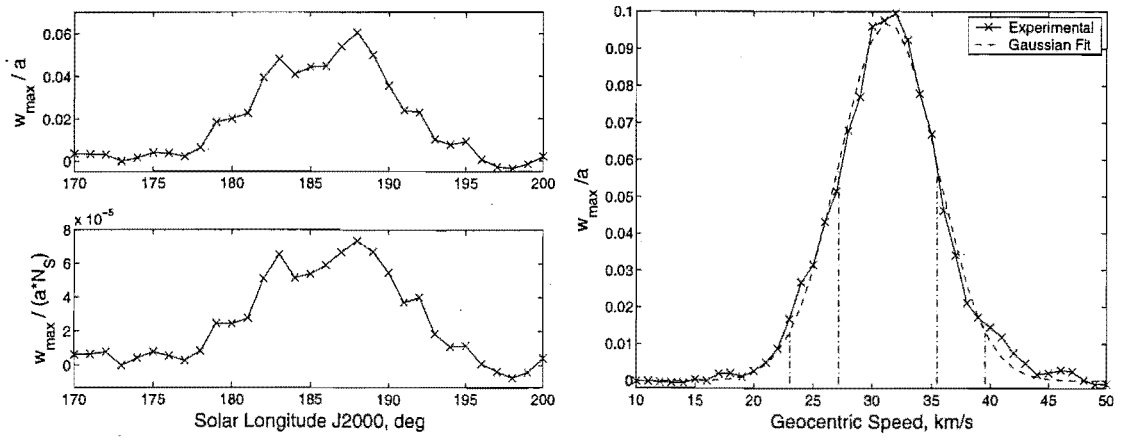

Figure 7.18: The distribution in speed and time of the DSX shower. A moving window scan of the radiant region is used with window widths of 2° and 2 km s^{-1} for the activity and geocentric speed profiles respectively. The activity profile is shown in the original (upper) and normalised (lower) amplitude cases. The Gaussian fit to the speed profile is defined by $\overline{V}_G = 31.3$ km s^{-1} with $\sigma_V = 4.1$ km s^{-1}. The first and second σ_V spacings from the mean are shown.

negligible change in the background over this period (see Figure 7.6) the normalised activity profile is virtually identical to that originally observed.

The geocentric speed distribution is also shown in Figure 7.18, as determined using a sliding window of width 2 km s^{-1} stepping by 1 km s^{-1} using all meteors from the established active period. This curve is fitted with a Gaussian and from this a mean speed of 31.3 km s^{-1} with a standard deviation of 4.1 km s^{-1} is obtained.

The active period and speed are in agreement with Cook (1973) who defines the shower as being active over $\lambda_\odot \in [179°, 190°]$ with a mean geocentric speed of 32.2 km s^{-1}. There is little agreement as to the exact time of the maximum with Cook stating $\lambda_\odot^c = 183.6$, Rendtel et al. (1995) stating 184.3° and Kronk (1988) stating the region of the maximum occurring between 185° and 190°. The current study agrees best with the results of Kronk. The DSX is known to be a rapidly evolving shower and most data up to now has been based on incomplete yearly surveys where determination of the maximum is difficult.

It is interesting once again to provide tangible evidence of the link between the geocentric speed and the ecliptic longitude. By using data on the longitude of the maximum WTC in the DSX during the sliding window speed search it is possible to show a direct change in the longitude of the maximum as one increases the speed at the centre of the window. This phenomenon, shown in Figure 7.19, implies that a selection based on geocentric speed will strongly change the profile of the shower. The current policy of choosing the central core of the shower based on the 1σ spread in speed is then to some extent defining the radiant region. This, of course, poses

the question as to which parameters to define rigidly within certain ranges for a shower and which to allow complete freedom.

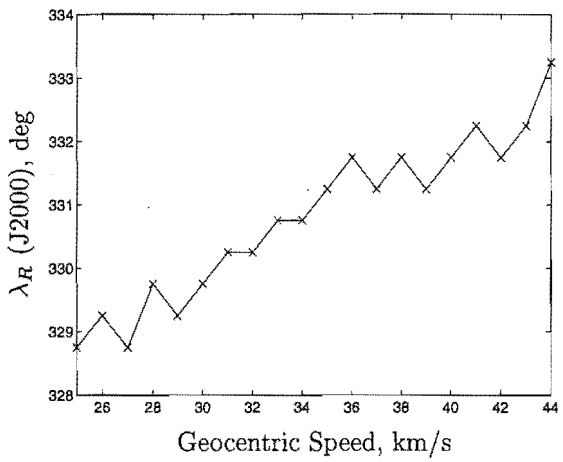

Figure 7.19: The change in position of the maximum WTC with change in geocentric speed within the DSX shower. Here the speed profiling performed in Fig 7.18 has yielded direct evidence of the longitude-speed link.

Using meteors from the active period, within the 1σ region in speed, yields the radiant distribution and its wavelet transform shown in Figure 7.20. The centre of the wavelet transform is found to occur at $(\lambda_R, \beta) = (330.2°, -11.2°)$ with the central solar longitude being 187°. This translates to an equatorial centre of $(\alpha, \delta) = (154.8°, -1.5°)$. Rendtel et al. (1995) quotes a maximum at $\lambda_\odot^c = 184.3°$ with a radiant centre $(\alpha, \delta) = (152°, 0°)$. When one translates this to the centre found in the current study it is found that each of the coordinates are within 1° of the Rendtel et al. values. Similar centres are found from other published sources.

Peak C (Figure G.2(j)) has been identified as a meteor shower candidate. This source appears separated by $\sim$ 140° of solar longitude from the DSX but has a radiant at an almost identical position in the ecliptic Sun-centred reference frame to the latter. The motion of the radiant position has been measured and found to be negligible in both longitude and latitude (as can be seen in Figure G.2(j)) hence the figures in this case are not displayed; this situation is the same as that encountered for the DSX.

The activity and speed profiles, as shown in Figure 7.21, have been obtained using identical methods to the DSX. The activity profile implies a lifetime for the shower of $\lambda_\odot \sim 50°$ centred about $\lambda_\odot^c = 45°$; the shower rate appears to rise and fall symmetrically from its peak gradually during this long period. It is still possible that this is a bona fide shower, however such a description appears more to confirm that this is simply the manifestation of the sporadic source bias in this region. It

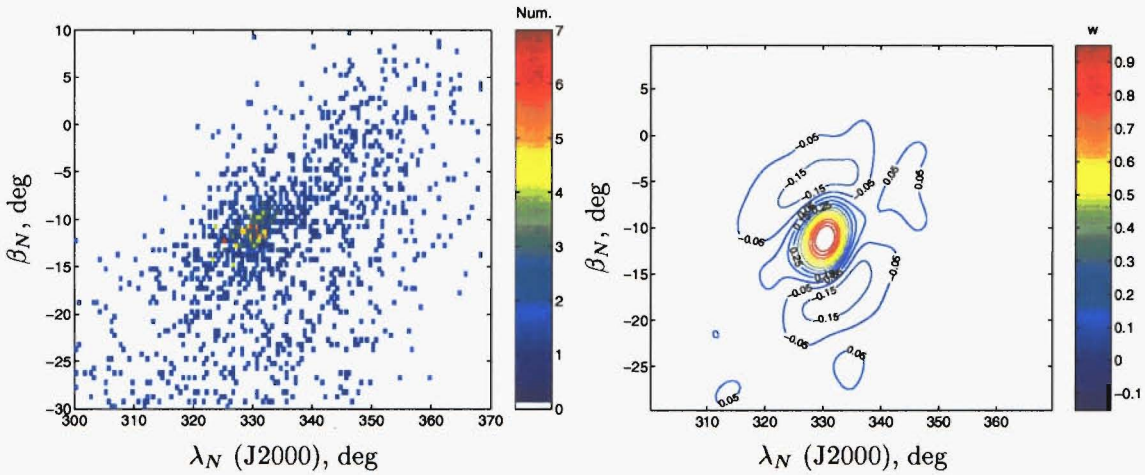

Figure 7.20: The wavelet transform of the DSX region. Meteoroids are selected to have speeds within one standard deviation of the shower mean (see Figure 7.18) and to have $\lambda_\odot \in [179°, 193°]$. On the left the original radiant distribution obtained by this selection is shown and on the right the corresponding wavelet transform.

is very difficult to prove or disprove the existence of a shower—there is the obvious case, where the density does not change over time; however, it is in the nature of both the sporadic source distributions and indeed the showers themselves to change position over time. One will never see a spatial density occurring statically over a year or even a few months. Whether Peak C is a true shower or not, its wavelet transform, using the 1σ region about the geocentric speed mean and a rather arbitrary $\lambda_\odot = 145° \pm 15°$, is shown in Figure 7.22; its orbital distribution is discussed in Chapter 8 for completeness.

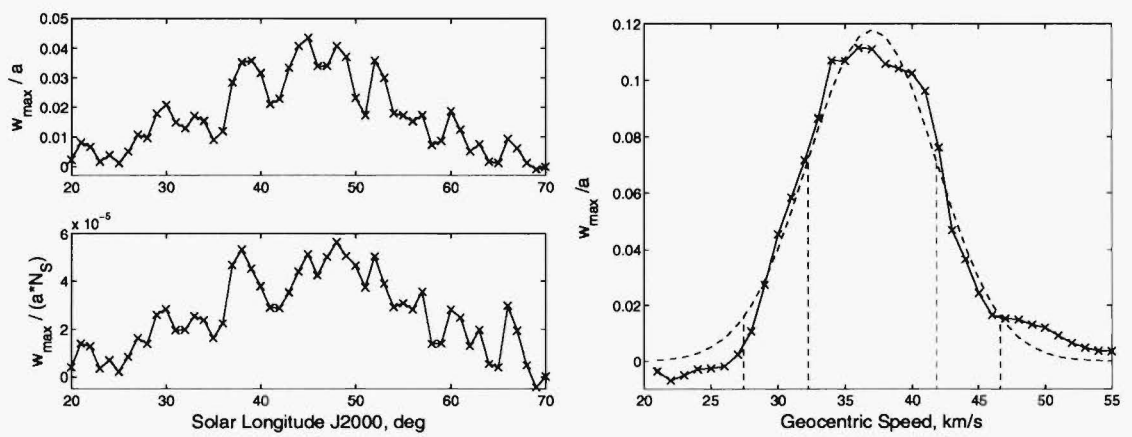

Figure 7.21: The distribution in speed and time of the Peak C region. Moving window scans of the radiant region are used with window widths of 2° and 2 km s^{-1} in solar longitude and geocentric speed respectively. The activity profile is shown in the original (upper) and normalised (lower) amplitude cases. The Gaussian fit to the speed curve is defined by $\overline{V}_G = 37.0$ km s^{-1} with $\sigma_V = 4.8$ km s^{-1}.

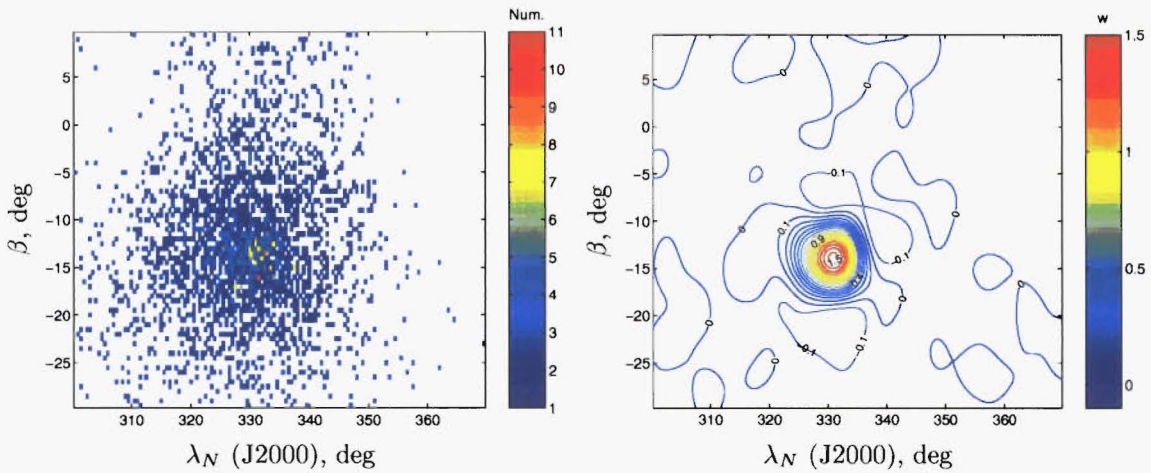

Figure 7.22: The wavelet transform of the Peak C region. Meteoroids are selected to have speeds within one standard deviation of the shower mean (see Figure 7.21) and to have $\lambda_\odot \in [30°, 60°]$. On the left the original radiant distribution obtained by this selection is shown and on the right the corresponding wavelet transform.

Retrograde Meteoroids from the Apex Source Region

The ETA is the only distinct shower found in the retrograde meteoroid population. As with most retrograde meteoroids, those from this shower appear at a radiant close to the apex of the Earth's way. As such the average speed of the shower members is much larger than those of the showers discussed already.

AMOR has built up an excellent record of this shower having been running at the time of the shower for 10 years. Methods similar to those used for the prograde showers are applied here. The only major change has been in the use of a smaller Mexican Hat width ($a = 2°$); the ETA source is characterised by a smaller spread in latitude with a larger spread in longitude. A smaller hat width is found to provide a wavelet transform which better fits the original source distribution. The coordinate system is first tested for stability over time with respect to the shower radiant centre. As shown in Figure 7.23 there is a systematic decrease in the longitude coordinate as the shower progresses with negligible change in latitude. A linear least-squares fit reveals a trend defined by

$$\lambda_R = -0.18\lambda_\odot + 302.4°. \tag{7.13}$$

The shower maxima occurs at $\lambda_\odot^c \approx 44°$, the ecliptic longitude of the radiant is therefore referred to the position of the mean radiant position at that time using equation 7.9 in order to remove the daily motion detected above.

The activity and geocentric speed profiles for the ETA are shown in Figure 7.24.

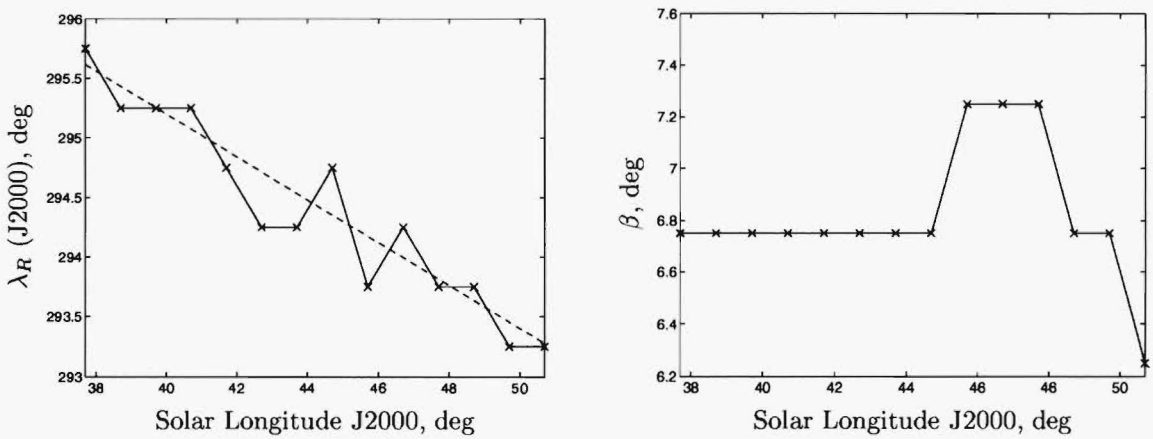

Figure 7.23: Daily motion of the ETA radiant over the central active period of the shower.

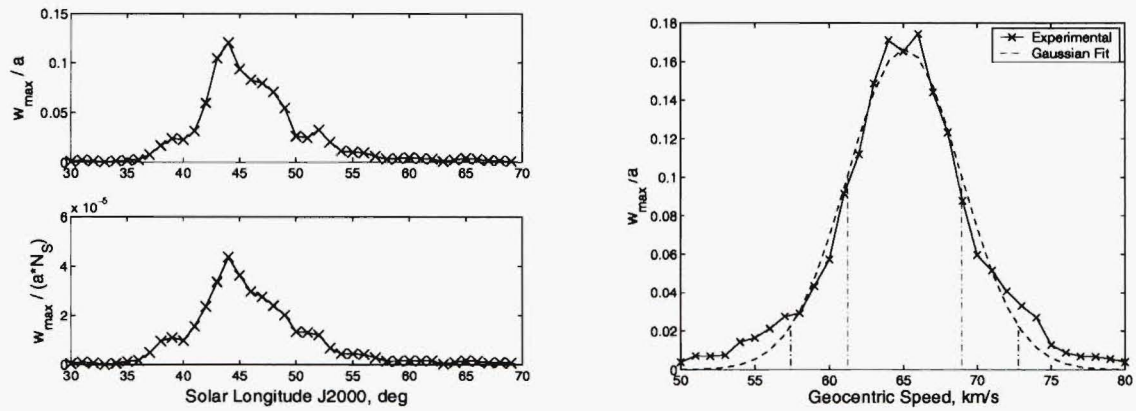

Figure 7.24: The distribution in speed and time of the ETA shower. Moving window scans of the radiant region are used to obtain the activity and speed profiles. Window widths of 2° and 2 km s^{-1} with units steps are used for these respective profiles. The activity profile is shown in the original (upper) and normalised (lower) amplitude cases. The Gaussian fit to the speed curve is defined by $\overline{V}_G = 65.1$ km s^{-1} with $\sigma_V = 3.8$ km s^{-1}.

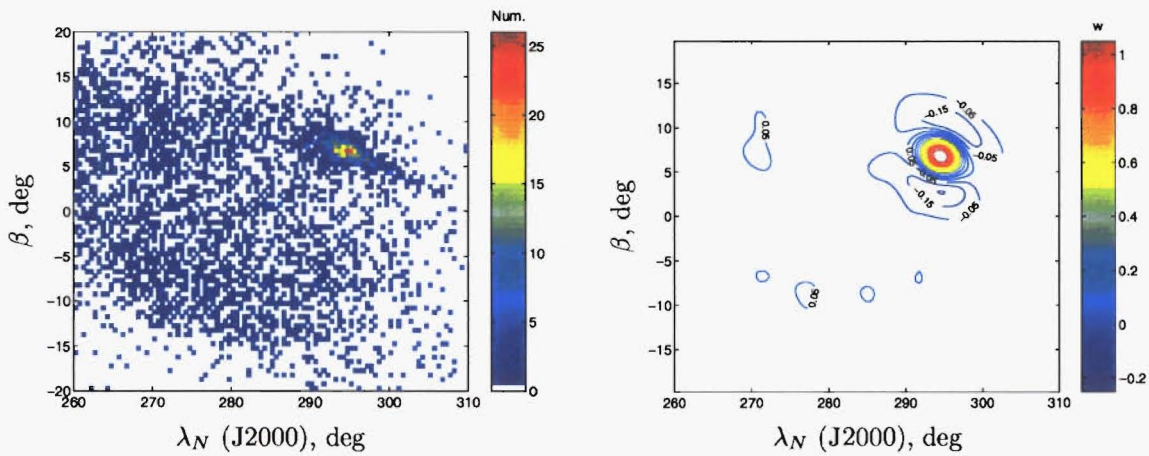

Figure 7.25: The wavelet transform of the ETA region. Meteoroids are selected to have speeds within one standard deviation of the shower mean (see Figure 7.24) and to have $\lambda_\odot \in [37°, 54°]$. On the left the original radiant distribution obtained by this selection is shown and on the right the corresponding wavelet transform.

These are obtained by similar methods to those discussed for previous showers. As can be seen in the figure the shower is most distinctly active over the period $\lambda_\odot \in [37°, 54°]$. Using meteors from this period a 2 $\mathrm{km\,s^{-1}}$ wide window in geocentric speed traces out the speed distribution. A Gaussian fit is found to describe the resultant curve well with an average speed 65.1 $\mathrm{km\,s^{-1}}$ and standard deviation 3.8 $\mathrm{km\,s^{-1}}$.

Using all retrograde meteoroids detected over the period of time in which the shower is distinct and by selecting based on those with speeds within 1σ of the mean, the resultant wavelet transform is presented in Figure 7.25. The narrow extent of the radiant of this shower can clearly be seen in this figure. There appears to be a large spread partially in longitude and also partially in latitude. Due to the speed of retrograde meteoroids the uncertainties in radiant position and speed are also quite large. This gives a large uncertainty, and therefore spread, in the natural equatorial coordinates—right ascension and declination. Most of the uncertainty in this reference frame occurs in the right ascension, as this is related relatively directly to speed, while the declination is mainly related to elevation angle which is unaffected by speed. When these coordinates are translated to the ecliptic reference frame the uncertainty induced spread does not remain predominantly in one coordinate, as with the equatorial system, instead the spread appears both in longitude and latitude.

The radiant is found to be centred at $(\lambda_N, \beta) = (294.2°, 6.8°)$ which translates to equatorial coordinates $(\alpha, \delta) = (337.3°, -2.2°)$, both referred to $\lambda^c_\odot = 44°$. This agrees well with Cook (1973) who suggests a radiant position of $(335.6°, -1.9°)$ on $\lambda^c_\odot = 42.4°$ with a geocentric speed of 65.5 $\mathrm{km\,s^{-1}}$. Rendtel et al. (1995) lists the shower maximum as occurring at $\lambda^c_\odot = 45.5°$ at a position $(338°, -1°)$ for visual showers; this is in particularly good agreement with the results of the present study.

7.7.4 Requirements of A Significant Shower

Based on the assumption of Gaussian sources in the radiant distributions (a reasonable physical assumption) and no background noise, a minimum source strength for significance in the diagrams shown in Appendix G may be calculated. This is performed by wavelet transforming randomly generated 2-D Gaussian weighted radiant distributions containing 10^5 simulated meteors. While such a large number of meteors are not normally available in a shower the wavelet transform is extremely stable under such conditions and the amplitude of the wavelet transform coefficients are

linearly proportional to the source strength and therefore the resulting coefficients can be scaled down to give that expected per meteor. Table 7.2 shows the maximum WTC's (w_{max}) resulting from the use of three different probe-sizes on Gaussian distributions with increasing standard deviations: note the general increase in coefficient with increasing probe-size and the opposite trend with increasing source spread.

Probe / Std. Dev.	1°	2°	3°	4°
3°	6.25	3.75	1.96	1.00
4.5°	7.05	5.47	3.77	2.45
6°	7.37	6.35	5.03	3.77

Table 7.2: The relationship of maximum WTC to probe and original source size. A range of these parameters are chosen and the corresponding maximum WTC per meteor for Gaussian simulated sources in each situation is given. Note all coefficients are in units of 10^{-3} per meteor.

The 3° wavelet probe has been found in the current study to be sufficient to find and define the major showers: such showers are thought to have a spread of approximately 3° and hence, according to Table 7.2, one expects about 2×10^{-3} per meteor from a typical shower in this regime. In the AH region for meteors with all speeds, a 3° probe and a 2° time window (Figure G.1(m)), one requires $\overline{w}_{max} = 0.2$ which implies a shower strength per time centre of $\sim$ 100; considering the five years over which the data is taken this indicates a minimum shower size of approximately 20; this scales proportionally for the corresponding 6° wide time window (Figure G.1(o)). The 6° probe when used for the 2° time window (Figure G.1(p)) yields $\sim$ 200 meteors per time centre or $\sim$ 40 meteors per day in order for detection. Comparing this to that required for the 3° probe used on the same Gaussian source, shows the value in using smaller probes, in that the shower strength required for a significant peak is halved.

The HN region generally requires only $\sim$ 50% of the meteors required in the AH region, in order to form a significant peak. For example in Figure G.2(m), a similar situation to the first case discussed for the AH region, one requires $\overline{w}_{max} = 0.1$, i.e. $\sim$ 50 meteors per time centre or no less that 10 per day per year for a significant peak. The retrograde AX region imposes a requirement halfway between that of the HN and AH while the prograde AX region requires only $\sim$ 50% of those in the HN region for a significant shower.

Great care must be taken when considering the above discussion as there are several points which indicate that the numbers of meteors required for significance are very much a lower limit. There is no background noise to the modelled Gaussian

source, if this had been present it would have acted to reduce the strength of the w_{max} with respect to a given source strength, hence the number of meteors required to reach the significance levels in Appendix G is underestimated. The curves used in the appendix relate to w_{max} rather than probe-size normalised w_{max} therefore their confidence levels are not as reliable, as discussed previously. Finally, if one is asking how many meteors per year must be found in a shower for detection to occur then, while it has been assumed that all five years are equally active here, this is generally not true due to the differences in meteor rate and radar system time-coverage over different years, as discussed in Chapter 3. It is likely that such assumptions will lead to the size of the shower required being grossly underestimated and the figures discussed are probably in error by at least 100%, if not more. It has been shown the weakest shower, which appears to be significant, is the CAP which appears in the AH region. This shower has $\sim$ 250 meteors over five years with a peak extending over $\sim$ 10 days, hence an average per day of $\sim$ 25 meteors. This agrees well with the modelling obtained above and points to the fact that the lower limit not be so far out as first thought. The size of such a shower also emphasises the point that the use of several years of data is better than a single year. The CAP typically has 40 to 50 meteors per year, such low numbers per day even given the reduced noise in its speed selected region of the AH population, would be almost impossible to detect as significant in any day of data.

In summary: the number of meteors listed above as a minimum for significance per shower per year are such that only those showers which are by definition major may be detected. The weak CAP major shower provides the lower limit to that which may be considered significant.

7.7.5 Summary of the Wavelet Enhancement Method Application

Wavelet enhancement has been shown to be a valuable tool for detecting the presence of showers against the background. While large-scale rate curve analysis was shown to fail in Section 7.5, the wavelet method is found to enhance structure in the radiant regions sufficient for its detection significantly. The four major showers are found using this method in addition to some other shower candidates. It is possible to relatively easily determine the significance of a shower peak using this approach.

7.8 Single-linkage Cluster Analysis

Single-linkage cluster analysis is a technique which has been used in many previous meteoroid stream searches. As discussed in Section 7.2, this method has been mainly used to search photographic data sets, where the uncertainty is an order of magnitude lower than for radar data sets. The following sections discuss the applicability of this method to searching the radar detected data sets, in particular that provided by AMOR, for streams/showers.

7.8.1 Theory

The single-linkage algorithm is a member of the hierarchical agglomerative class of cluster analysis algorithms. Such algorithms begin with N items (e.g. orbits) contained in N groupings. They progressively agglomerate these groupings until, ultimately, only one remains containing all N items. The rule governing this agglomeration is the defining characteristic of the particular algorithm. Single-linkage performs its agglomeration by joining the two entities which are closest to each other at each step—these entities may be single or groups of items. Where these entities are groupings of more than one item, the inter-group dissimilarity is based on the smallest dissimilarity between individual members of that entity and surrounding entities. Figure 7.26 shows a 2-D model example of the single-linkage grouping structure at a particular position in the hierarchy.

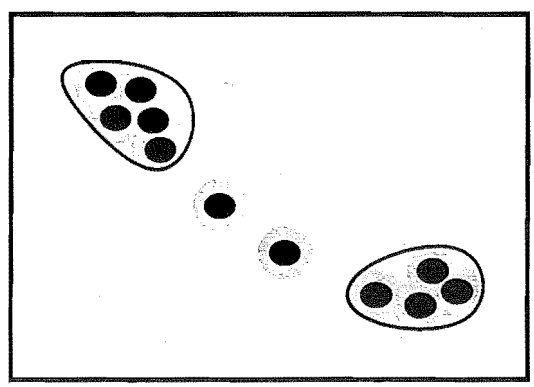

Figure 7.26: An example of the single-linkage process. The solid balls represent items, such as orbits, which in this case are for convenience assigned a 2-dimensional domain. The grey extended edges around these balls correspond to the cutoff level in the hierarchy at which the process is at. In this example any balls whose grey areas overlap are clustered together—at the stage shown there are two large groupings and two independent items in the centre. A higher cutoff level will cause these central items to merge, first with each other, and then to join the larger groupings together. Such a large scale agglomeration may lead to chaining, where homogeneous groupings are linked together by those on the margins to form a less homogeneous grouping.

The user must make two important decisions when using any of these agglomerative algorithms. Firstly, a suitable measure of dissimilarity between items must be defined, and secondly, a method of determining a cutoff level in the hierarchy at which meaningful groupings may be found must be specified.

For the cluster analysis of orbits the standard measures of dissimilarity are the so-called D-criteria as introduced in Chapter 6. Using these functions, at a particular level corresponding to the cutoff D_c, membership in a particular grouping is defined such that

$$\min(D(A,B)) < D_c, \tag{7.14}$$

where A and B are any individual orbits.

Certain facts are clear in such a process. As the cutoff level is increased the clusters become increasingly inhomogeneous. The highest quality clusters are those found in their final forms at low levels of the hierarchy. A cluster may be defined as highly compact and distinct against the background if it is found at such a level and it survives with little agglomeration until a much higher cutoff level. A lower quality cluster is one which is only found at higher levels of the hierarchy and quickly merges into the background as one proceeds to still higher levels—such clusters may be labelled as disperse and indistinct.

7.8.2 Implementation

Theoretically for N orbits the single-linkage algorithm must make $(N-1)$ complete passes through the inter-orbit dissimilarity matrix stored in memory. This is obviously time and memory consuming with the memory usage being given by $N(N-1)/2$ and the time usage given by $N^2(N-1)/2$—i.e. the process is $O(N^2)$ in memory and $O(N^3)$ in time. It is possible to extract the cluster analysis for a number of levels within the clustering hierarchy without performing a complete formal analysis—a useful feature of this algorithm is the independence of cutoff levels within the hierarchy. Therefore when searches such as those of Lindblad (1971a) were performed, only the clusters present at three cutoff levels at $D_{SH} = 0.10$, 0.15 and 0.20 were calculated for study.

The programs developed for the current study perform the discrete level cluster analysis in two steps. The data is first processed by a `C` program called `get_dissim.exe`. This program accepts input of a file of orbits, a particular dissimilarity function to use on these orbits and a maximum D value at which pairings should be accepted for further analysis. The program determines all or-

bital pairings satisfying this criteria and stores them in a specially compressed `*.wsr` output format file. This file effectively contains the dissimilarity matrix with only entries listed for pairings with suitably small dissimilarities. The `C` program `get_dissim2serial.exe` is then applied to the `*.wsr` file to determine the clustering hierarchy at each of a specified set of regularly spaced cutoff levels. This hierarchy is output to a `*.ser` file which contains a single large matrix representing it, where each column represents a cutoff level, each row a particular orbit and the particular numbers stored in each matrix location refer to the group number to which the orbit belongs (the group number is always the $(0..N-1)$ row number of the lowest number orbit in the grouping). A `*.des` description file contains a list of the cutoff levels to which each column of the clustering matrix refers. `MATLAB` routines are readily able to read the `*.ser` and `*.des` file pairs in order to further analyse the grouping structures contained therein.

7.8.3 Data Analysis

In the current study the dissimilarity functions D_{SH} and D_N, in particular, are tested in the application of single-linkage analysis to various data sets provided by AMOR. The application of these tests have already been partly discussed in Section 7.2, this section aims to give more in-depth information and some practical examples.

The use of randomisation tests, in an attempt to provide meaningful cutoff levels in the resulting agglomeration hierarchies, is found to be unsuccessful. These tests consist in producing a number of files, each containing pseudo-random orbits, which are based on the large-scale orbital parameter distributions in the original data set under study. In order to form each of these files, the distributions in each of the orbital elements q, e, i, ω and Ω, are determined from the original data set. The randomised orbits are then created, by making random selections from each of these parameter distributions, independently. Equation 3.3 is used to form a valid q given the randomly selected e and ω values (Baggaley and Galligan 1997). The assumption is that each of these randomised files, as produced by the `C` program `random_bin.c`, presents one possible instance of the background orbit population—with all effects of meteor showers being removed.

By running $\sim 10^2$ such files through the same cluster analysis process used for each corresponding original data set, a picture may be obtained of the level at which

clusters start to appear out of the sporadic (random) background[16]. Galligan and Baggaley (1998) discusses the results of the application of this method to data sets of $\sim 6 \times 10^4$ orbits. From data obtained in the years T1995 to T1998, eight data sets are formed each based on 180° of inter-equinox data in separate equinoctial years. Randomisation studies on these data (as described above) yield the result that the 95%/99% probability levels of background intrusion correspond well with the first appearance of structure in the original data set. Well-defined showers, such as the ETA, are therefore deemed to be structures appearing out of the random background with no statistical reality. The SDA, the largest shower detected in the AMOR data set and also having much lower individual orbit measurement uncertainties than the ETA, only begins its formation at the random-simulation determined cutoff level.

There are therefore two possibilities, either the randomisation method is too harsh in determining a significant cutoff level or the major showers known to be present within the AMOR data set are so weak that, while they may be detectable by "eye", they are marginal when it comes to statistically sound detection. Galligan and Baggaley (1998) assume the former and continue to develop new techniques, with no statistical basis, in order to provide a measure of relative significance. The first (ill-fated) method uses the percentage of orbits within any groupings at each cutoff level in order to line up the agglomerative hierarchies from several separate years of data. Relative cutoff levels, such as the 5% and 10% levels, are then used to compare grouping structure in the different searches—the assumption is that the relative cutoff level in the hierarchy is the same for similar data sets apart from a multiplier due to differences in their relative sizes; this in line with the assumption of Southworth and Hawkins (1963), as discussed in Section 7.2. This method is found to be wanting due to the lack of statistical basis to the cutoff level and also due to the totally different stream sizes/contents found in different years at the same relative level. In fact a general comment, emerging from work using the single-linkage algorithm on radar orbits, is that the agglomerative hierarchy is very often highly unstable—very minor changes in cutoff level often lead to disproportionately large changes in the stream structure obtained. Simulations have been performed

[16]It is desirable in a Monte Carlo-like simulation process to produce many more than $\sim 10^2$ randomised sample sets, especially given the 4-dimensional nature of the orbital data sets under study. Unfortunately each sample run takes 1-2 hours for the $\sim 6 \times 10^4$ orbits studied—this increases by a power-law relation for larger data sets. Hence it is impossible to increase the size of the sample sets. Studies such as Jopek et al. (1999) have no such problems as they are only dealing with a set of $\sim 10^3$ orbits and therefore can perform 10^3 randomised runs or more with no difficulty.

where an original data set has its orbits changed slightly within the bounds of the measurement uncertainty, retrieval of groupings similar to those originally obtained is by no means guaranteed and often the stronger showers are found to dwindle to the point of non-detectability.

Another single-linkage based method, tested more recently, involves taking several years of data and separately forming their agglomerative hierarchies. For each year's hierarchy, the computer program proceeds downwards from the highest agglomeration level. All groupings, of a suitable size, at each level, having a suitably small mean dissimilarity and range in mean solar longitude[17] are accepted. Appendix H lists a poster paper presented at the Asteroids, Comets and Meteors '99 conference where this method is more fully described. As noted therein the resulting stream/stream-fragment mean orbits from this process, for the several years of data, were combined using another pass of the cluster analysis process. The paper lists the major showers recovered by this method in addition to an unknown shower which appeared to be a reasonable candidate. This method, while more robust than a simple single-linkage algorithm, is also now rejected as the new showers found by it are not verifiable by other means: it is thought to be most likely producing large clusters made up of smaller individually insignificant clusters which in some cases occur at significantly different cutoff levels.

The decision therefore is that none of the single-linkage related search variants are suitable for radar meteoroid stream determination. The early result which showed by randomised simulation that in a set of half-year data sets no significant structure is present, appears in general to be vindicated. Exceptions to this are in the case of the major showers, which do appear visually in single-linkage searches and are supported by other methods and surveys. Due to the high "noise" level in the radar data sets it is assumed that these major showers are simply not strong enough to compete in a statistically sound test of the single-linkage algorithm. A substantial proportion of this noise is caused by the concentration of highly randomised orbits at low inclinations. Unfortunately one cannot simply remove such orbits as most of the major showers have members which, due to measurement uncertainty, often fall within the low inclination zone. Apart from this, the removal of the most populous portion of the orbital population in such an arbitrary way is difficult to justify if one assumes no *a priori* knowledge of the situation.

[17]Typically, the mean solar longitude range has a maximum set at 35°, in order to prevent chaining over large time intervals of orbits which are obviously unrelated.

7.8.4 Sample Results

Some results from single-linkage runs on three data sets are now presented in order to give examples of the types of results one expects from this method. These data sets cover the activity times of the four major showers, previously identified in the AMOR data set. The data files used are `95V99_110LS160_PR.ele`, `95V99_160LS210_PR.ele`, and `95V99_20LS70_RE.ele`. The first and second files are composed of prograde orbits recorded over $\lambda_\odot \in [110°, 160°)$ and $\lambda_\odot \in [160°, 210°)$ in T1995–T1999 respectively while the last file is composed of retrograde orbits recorded over $\lambda_\odot \in [20°, 70°)$ in the same years[18]. These time-frames/orbital orientations correspond to regions where the SDA and CAP; DSX; and finally ETA meteor showers are known to be active. Results, based on the analysis of these files, are presented for D_{SH} and in some cases for D_N—both functions produced similar results apart from the case of the ETA where higher uncertainties produce a scenario worthy of further discussion.

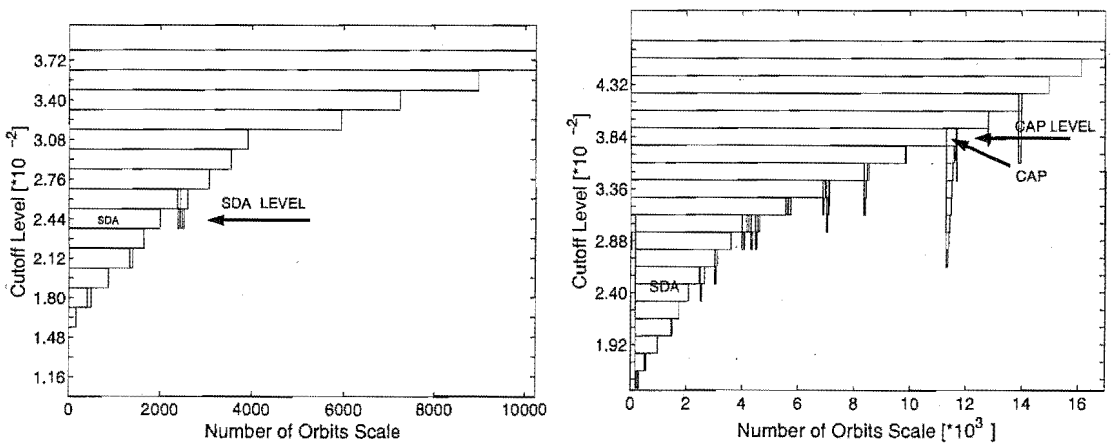

Figure 7.27: Dendrograms for the SDA (left) and CAP (right) showers obtained using D_{SH} for single-linkage cluster analysis on the data set contained in `95V99_110LS160_RE.ele`. The cutoff levels on these figures are set at D_{SH}=0.0252 and D_{SH}=0.0384 respectively. Only groupings of 40 orbits, or more, are shown.

Figure 7.27 shows dendrograms[19] corresponding to parts of the single-linkage

[18]Single-linkage searches on meteoroid orbits have generally been carried out, in the past, on data sets containing the complete range of orbital inclinations, i.e. both prograde and retrograde orbits. The examples presented here are of data sets which contain prograde or retrograde orbits exclusively. It is thought to be very improbable that streams will appear which cross over this boundary. Generally in the current study complete data sets were used but, for the sake of execution speed in the current examples, partitioning based on orbital direction has been performed.

[19]Dendrograms are convenient devices for graphical display of the hierarchical clustering process. They require input of a minimum size for grouping display and a cutoff level at which significant groupings are present. Parent groupings of those present at the cutoff level are shown at higher levels of agglomeration (and therefore D_c value) while, to continue the analogy, child groupings

hierarchy obtained for `95V99_110LS160_PR.ele`. Cutoff levels have been determined separately for the SDA and CAP searches in this data set. The method used to determine these levels is very simple: it is based on the assumption that meteor showers derive homogeneous groupings of similar orbits and that the mean intra-group dissimilarity is a good measure of this homogeneity. The agglomeration of the shower groupings are monitored until their mean D_{SH} exceeds 0.20—the level below this point is declared the cutoff level. The maximum $\overline{D}_{SH}$ reached under this regime is 0.199 for the SDA and 0.153 for the CAP. The reason for the lower CAP $\overline{D}_{SH}$ is clear from the corresponding dendrogram where the shower stalactite[20] merges into a $\sim 1.3 \times 10^4$ orbit grouping at the level above its cutoff.

		$\lambda_\odot$ deg	q AU	e	i deg	ω deg	Ω deg	V_H km s^{-1}	V_G km s^{-1}	α deg	δ deg	SIZE
	$\overline{x}$	125.7	0.079	0.951	27.5	153.5	305.8	38.5	35.1	340.9	-16.2	2144
SDA	s.d.	3.1	0.027	0.036	8.1	3.9	3.1	4.5	3.7	3.5	1.2	
(D_{SH})	s.e.	0.1	0.001	0.001	0.2	0.1	0.1	0.1	0.1	0.1	0.0	
	Unc.	0.0	0.021	0.025	9.3	3.4	0.0	3.2	2.5	2.8	1.2	
	$\overline{x}$	123.7	0.037	0.991	54.6	159.5	303.8	46.2	39.5	341.5	-16.5	84
SDA?	s.d.	1.9	0.010	0.012	2.8	2.4	1.9	3.0	3.3	2.7	0.9	
(D_{SH})	s.e.	0.2	0.001	0.001	0.3	0.3	0.2	0.3	0.4	0.3	0.1	
	Unc.	0.0	0.012	0.014	23.0	2.2	0.0	4.7	3.7	3.1	0.9	
	$\overline{x}$	123.5	0.544	0.733	7.0	275.9	123.5	22.5	36.2	306.4	-9.9	356
CAP	s.e.	5.2	0.045	0.074	1.7	6.1	5.2	2.2	1.6	4.5	2.4	
(D_{SH})	s.d.	0.3	0.002	0.004	0.1	0.3	0.3	0.1	0.1	0.2	0.1	
	Unc.	0.0	0.026	0.040	0.7	3.5	0.0	1.3	0.8	1.7	0.6	
	$\overline{x}$	45.5	0.528	0.914	165.1	89.2	45.5	64.2	39.8	338.7	-1.6	885
ETA	s.d.	4.4	0.082	0.119	2.1	12.4	4.4	2.9	2.7	3.8	1.6	
(D_{SH})	s.e.	0.1	0.003	0.004	0.1	0.4	0.1	0.1	0.1	0.1	0.1	
	Unc.	0.0	0.126	0.225	2.3	20.6	0.0	5.2	5.0	3.2	0.5	
	$\overline{x}$	45.4	0.541	0.951	165.4	91.4	45.5	64.8	40.4	338.5	-1.8	1119
ETA	s.d.	3.4	0.105	0.183	2.6	16.0	3.4	3.8	3.7	3.6	1.7	
(D_N)	s.e.	0.1	0.003	0.005	0.1	0.5	0.1	0.1	0.1	0.1	0.1	
	Unc.	0.0	0.123	0.247	2.4	20.2	0.0	5.3	5.1	3.3	0.5	
	$\overline{x}$	185.9	0.160	0.840	22.2	212.2	5.9	30.1	29.7	152.6	-1.0	845
DSX	s.d.	4.7	0.036	0.053	5.9	5.7	4.7	3.9	3.4	4.7	2.5	
(D_{SH})	s.e.	0.2	0.001	0.002	0.2	0.2	0.2	0.1	0.1	0.2	0.1	
	Unc.	0.0	0.017	0.020	3.0	2.5	0.0	1.4	1.1	2.1	0.5	

Table 7.3: Orbital statistics of the major meteor showers derived by single-linkage analysis. The four major meteor showers are shown here as obtained at cutoff levels described in the text. In each case the mean ($\overline{x}$), standard deviation (s.d.), standard error (s.e.) and the average individual orbit measurement uncertainty (Unc.) are shown for each parameter. Parameters having a circular angular nature are corrected where appropriate for endpoint ambiguity.

The two dendrogram figures of Figure 7.27 demonstrate many of the problems

are found at lower levels of agglomeration. Groupings cannot be shown on the dendrogram which are not related to those at the chosen significant cutoff level.

[20] As the groupings appear on dendrograms in a manner resembling a stalactite, they are named as such in this thesis.

which hinder use of the single-linkage method on the AMOR data set. The SDA, at its D_{SH}=0.0244 acceptance level, merge gradually into the background with no common sense cutoff point being visually present. The orbit set obtained for the SDA at this level, as shown in Table 7.3, has a spread (standard deviation) similar to that expected due to the individual stream orbit measurement uncertainties. This is in agreement with findings reported later in Chapter 8 and leads to the conclusion that any grouping partitions appearing at lower levels of this shower, as shown on the dendrogram, have no physical significance and that perhaps even a higher cutoff level might be desirable. Also shown in Table 7.3 is an 84 orbit group which appears at D_{SH}=0.0272 and then merges much higher in the hierarchy into a general SDA/background grouping. Such groupings show a particular problem with the use of D_{SH} in orbital analysis, the mean inclination on this group is double that of the SDA and therefore according to D_{SH} very different. Members of this group are believed to be outliers on the inclination distribution of the SDA occurring due to the large inclination angle uncertainties in this shower's orbits. The mean radiant, speed and detection solar longitudes of the main SDA grouping are very similar to this grouping further backing up the opinion that these are "real" SDA; however the height in the hierarchy at which this merges with the main SDA grouping is such that, if only the single-linkage hierarchy were considered, the association between these groupings could not be sensibly considered.

The CAP shower stalactite is quite different from the SDA. Its cutoff level, D_{SH}=0.0384, is very much higher than that of the SDA—its data set companion. Indeed at the stage of the CAP cutoff, the SDA has already been assimilated into a grouping of 1.2×10^4 orbits, clearly a grouping which is much too large and inhomogeneous to be called a shower. The reason for this difference in cutoff levels is due to the relative strength of the showers: the SDA has approximately 8 times as many orbits as the CAP. The CAP is the weakest shower detected in the wavelet probe searches, they also appear to set a limit on the size of shower which might be detected using the single-linkage method. It is clear that a weaker shower would simply not be able to be discerned when one notices the high cutoff level at which they are found and the small number of levels over which this shower's stalactite remains separated from the background. It is expected generally, that the probability of obtaining significant groupings at lower levels in a hierarchy is greater when one is searching for a smaller grouping rather than a larger grouping. The SDA is therefore more likely to be "real" astronomically than the CAP—any cutoff level generated by

a randomised simulation which did accept the SDA in the 95V99_110LS160_PR.ele data set would most likely ignore the CAP.

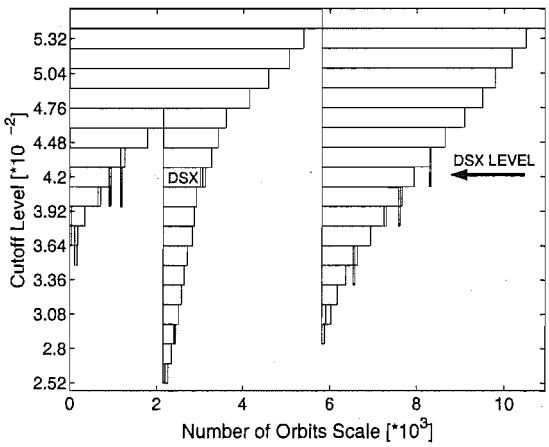

Figure 7.28: Dendrograms for the DSX shower obtained using D_{SH} in single-linkage cluster analysis on the data set contained in 95V99_160LS210_PR.ele. The cutoff level on this shower is set at D_{SH}=0.042. Only groupings of 40 orbits, or more, are shown.

The DSX is found in the D_{SH} based search of 95V99_160LS210_PR.ele. Again a mean D_{SH} maximum of 0.20 is set with the closest achieved being $\overline{D}_{SH}$=0.19. The corresponding dendrogram is shown in Figure 7.28 and the orbital statistics are shown in Table 7.3. The dendrogram shows the shower clearly detached at its cutoff level ($D_{SH} = 0.042$). An unrelated stalactite appears on this figure which appears to be larger at each level than the DSX—if one considers the DSX to be astronomically "real" then surely one should consider this to be "real". This provides an example of one of the major problems associated with stream searches in a large meteoroid orbit data set. The grouping in question is composed of low inclination ($i < 10°$) orbiting meteoroids. The detection of these "shower" meteoroids is spread over 50° of $\lambda_\odot$ in this 2,130 orbit grouping at the DSX cutoff level. One can pose the thesis that as this grouping is similar in size to the SDA and it appears at the same cutoff level as the DSX therefore it must be "real", assuming these showers are "real". This grouping is an example of "chaining"—a process whereby a series of unrelated items are linked together by intermediate items in order to define a serially associated, but not intra-associated, grouping. It contains orbits of meteors detected over the complete time-frame of the data set—a very long time for an astronomically "real" shower to last. The longitude of the ascending node, for all orbits, has negligible uncertainty and indeed for low inclination orbits combines with the argument of perihelion to produce a single parameter—the longitude of perihelion. It is therefore particularly easy to form a chain of orbits based on the

daily changes in $\lambda_\odot$ (and therefore Ω)—this is what is believed to have happened here. Such chains act to confuse randomisation techniques (like that considered earlier). The study of the original data sets leads to the combination of highly homogeneous groupings (showers) producing, in some cases, grossly inhomogeneous groupings for very small increases in cutoff level. Only very strong showers, outside the low inclination regime, can resist such effects. The example discussed above points out the futility of single-linkage algorithm use on large bias and the orbital uncertainties of radar meteoroid data sets: it is only possible to see the largest showers using this technique and it is not possible to prove whether these showers are statistically significant or not.

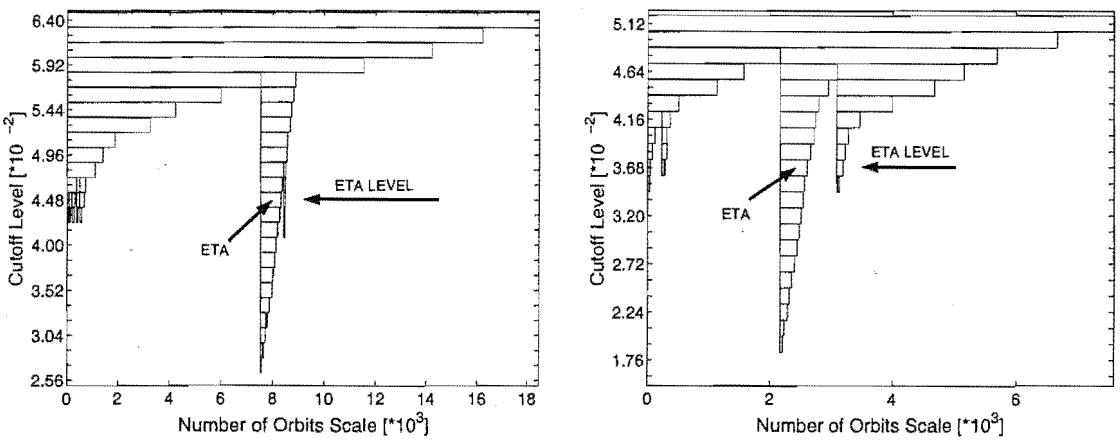

Figure 7.29: Dendrograms for the ETA shower obtained using D_{SH} (left) and D_N (right) for single-linkage cluster analysis on the data set contained in `95V99_20LS70_RE.ele`. The cutoff levels on these figures are set at D_{SH}=0.0480 and D_N=0.0368 respectively. Only groupings of 40 orbits, or more, are shown.

The above examples have been for prograde meteoroid streams. An example is now given of a retrograde stream: the ETA. This shower is clearly detected using both D_{SH} and D_N. The resulting hierarchies are shown in Figure 7.29 with the statistics of the groupings obtained listed in Table 7.3. Due to the large measurement uncertainty driven spread on this shower higher mean dissimilarities are used in order to include a reasonable proportion of the grouping: $\overline{D}_{SH}$=0.30 and $\overline{D}_N$=0.20 are used. The stalactite for the D_{SH} case appears to have the clearest delineation with only very minor showers present at the cutoff level apart from it. The D_N dendrogram is interesting for two reasons. Firstly the $\overline{D}_N$ required to retrieve a reasonable proportion of the grouping is more similar to that which is typically used to retrieve prograde showers, this compares with $\overline{D}_{SH}$ where a much higher value than usual is required due to the increased spread from uncertainties. D_N effectively

measures the compactness of radiant positions in addition to geocentric speed. The wavelet transform of the ETA region of Figure 7.25 clearly shows a highly compact region relative to such showers as the SDA (Figure 7.13). The geocentric speed is the major uncertainty laden parameter of the ETA due to its large size. The derived orbital elements almost all suffer from the speed uncertainty. This dispersal of the uncertainty appears to magnify its importance to D_{SH} while the shower's speed uncertainty does not change the response of D_N greatly as other showers have greater uncertainty in their radiant positions which partly compensates—in fact the number of stream orbits included in the grouping using D_N at its cutoff level (1,119) is much greater than that obtained at the very high cutoff required for D_{SH} where only 885 orbits are retrieved. The second reason for interest in the D_N dendrogram is the stalactite appearing to the right of the ETA stalactite representing a grouping of 259 meteors. By analogy with the SDA and CAP cutoff level difference, one might assume that such a grouping could be astronomically "real". This grouping, however, is a good example of a problem with retrograde orbits and the D_N. Due to the direct radiant region difference calculated by D_N the meteors appearing near to the apex of the Earth's way will have a tendency to form groupings under any analysis method using this dissimilarity function. The grouping identified here is found to be formed entirely from such meteors with an average ecliptic longitude with respect to the Sun of 271.2°. It is most likely therefore that this is a false detection which should be ignored. The same trend applies for other groupings at the cutoff level, hence the only clear shower in both dendrograms is the ETA.

7.8.5 Summary of the Single-Linkage Application

The single-linkage method is found to be poor as a detector of shower structure for meteor radar derived orbits. Determining an appropriate cutoff level in the hierarchy produced by this method is found to be difficult, with randomisation tests indicating that all structure found is simply an artifact of the background. The cutoff level is found to be unstable—a small step in the hierarchy may result in a large change in the grouping structure. It has been shown that the major showers are detectable using this method but one must be aware of their reality prior to the search and actively seek them out. Searching for showers smaller than the major showers is ruled out under this method.

Chapter 8

Properties of the Major Meteor Showers

Chapter 7 has shown that four major meteor showers are distinctly detectable within the AMOR data set using cluster analysis techniques developed there—the η Aquarids, Southern δ Aquarids, α Capricornids and Daytime Sextantids. In addition several peaks have been identified in the wavelet enhancement search for further investigation, two of these peaks being selected for study here. In the years T1995–T1999 the activity period of each of these showers has been covered by at least four of the years. Given such a large and continuous data set it is particularly interesting to study the showers to determine both their statistics from the 5 year collection period and to look at year to year variations in these statistics.

8.1 Shower Membership Criteria

The most direct method of defining shower membership is by radiant, speed and detection time data. Wavelet analysis, as described in Section 7.7, was used to enhance and study the major showers in these parameters. A question which is not often addressed in the literature is the method by which one can extract source members for further analysis from such wavelet transforms. Structure in a wavelet transform is defined by a region of positive wavelet transform coefficients (WTC) and the more over-dense the structure is in a particular region, the larger these coefficients are. By using the Mexican Hat wavelet these over-dense regions are clearly delineated by a surrounding "moat" of negative coefficients. It would seem a simple matter then of defining the edge of the shower region by the crossover points between positive and negative coefficients. However, due to surrounding minor structure the ideal of an absolutely delineated source is never realised: generally part of the boundary is definite while another part merges at a low positive level into the background. The straightforward method adopted in the current study has been to cutoff shower membership at 5%, or in some cases up to 10%, of the central maximum WTC of the shower. The appropriate cutoff, out of this range of values,

leads in all cases to an unambiguous definition of the shower. It also removes almost all traces of positive structure in the entire large-scale (e.g. helion) region of the shower showing that, assuming the rest of the sporadic source region in which the shower resides is an unrelated background, the cutoff criterion excludes any chance of background intrusion. It is obviously advantageous to use the lowest possible cutoff percentage in order to raise the number of shower meteors for what are, after all, relatively scant groupings from which to obtain meaningful statistics. It should be noted that the number of meteors retrieved prior to and after radiant daily motion correction differs in the case of all the showers discussed in this chapter, this is due to the inclusion in the original uncorrected wavelet transform of some non-shower meteors, those not following the expected daily motion are removed in the corrected wavelet transform image.

The wavelet probe-sizes used in the current study are 3° wide apart from that for the ETA for which a smaller 2° probe is used. It is indeed possible that the showers extend further in radiant space than such a probe will comprehend, for example Jones and Sarma (1979) note (from a survey of several other publications) that the Perseids has a sharply defined centre 3° wide surrounded by a diffuse component of width 10°–15°. Setting such measurements against the strength of the sporadic background encountered by the AMOR system implies that determination of the true extent of the diffuse component while simultaneously attempting to disallow non-shower members from contaminating the shower sample is virtually impossible; one should also note that the Perseid shower has a particularly diffuse radiant and that this diffusiveness represents an upper limit to that which is measurable. It is found that an increase in the size of the wavelet probe increases the average intra-orbital dissimilarity of the shower samples to unacceptable levels. A conservative approach is needed in order to be sure we are sampling the true shower population, hence the probe-sizes noted above are appropriate. It should be noted in the later shower analysis sections of this chapter that the spread in the radiant position approximately equals that expected according to the measurement uncertainties, hence one is recovering the shower diffusiveness expected from the measurement method.

8.2 A Problem of Definition in Orbital Statistics

Meteoroid stream orbit data sets are difficult to perform conventional statistical analysis on. Three different mechanisms are responsible for the spread in the data.

There is the obvious physical spread due to perturbations and initial cometary ejection conditions of the meteoroid bodies themselves; there are uncertainties which are of the same order as any physical spread in radar data sets and there is also a daily motion in many of the parameters over the period of the shower.

In the following sections unambiguous daily motion detected in several of the orbital parameters for the different showers is demonstrated. This is present most obviously in radiant position and longitude of the ascending node but there is also evidence, for some showers, in other parameters—particularly in q and ω. Normally motion in such other parameters is difficult to detect due to the relatively large uncertainties in radar meteor data, however the large numbers of shower members detected over five years by AMOR often allows a linear fit, as is the case in the particularly well defined daily motion of several of the SDA orbital parameters. The linear fit in the current study is obtained using the least-squares method on all orbital parameters. The assumption of a predominantly linear motion in these parameters is reasonable and easily demonstrated for radiant position coordinates. However, it is possible that for orbital elements, which derive indirectly from the radiant position, speed, and time, there may not be a strictly linear motion with $\lambda_{\odot}$. Because the daily motion in the orbital elements is generally small and often difficult to detect visually, the linear correction is favoured for the objectiveness it brings to the problem. Where the correction provides no visually changed results in the parameter distribution no harm is done and one must bear in mind that, owing to the non-uniform uncertainty regime, visual analysis does not comprehend all aspects of the problem. In the cases where the correction clearly removes obvious linear motion, as for the SDA q and ω discussed later in this chapter (Figure 8.13), an important service is more obviously rendered.

It is normal to state the radiant position, solar longitude and longitude of the ascending node of the shower referred to the time of maximum influx rate of the shower. This convention is adopted in the present study. As far as can be shown from the literature, the mean q, ω and other non-stationary parameters are simply obtained from the shower population with no correction for daily motion. Such a simplistic view of a non-stationary data set introduces errors when there is not a uniform (equipment related) coverage over the active period of the shower and/or the activity profile is asymmetric about the maximal rate point as will be shown, using the SDA as an example. A more convenient method for determining the true statistics of the shower is by reduction of the non-stationary parameters to a

reference time prior to the analysis and the time of the shower maximum rate is again used as this reference. It is found in the current study that the daily motion measured depends upon the choice of cutoff level in the wavelet transform to a small extent, i.e. the shower sample sizes are small enough that a minor change in the content affects the parameters measured. It is useful to obtain an estimate of the magnitude of this stability problem for comparison of daily motion values obtained in the current study with those from previous studies, bearing in mind that the other studies do not list uncertainties making comparisons difficult anyway.

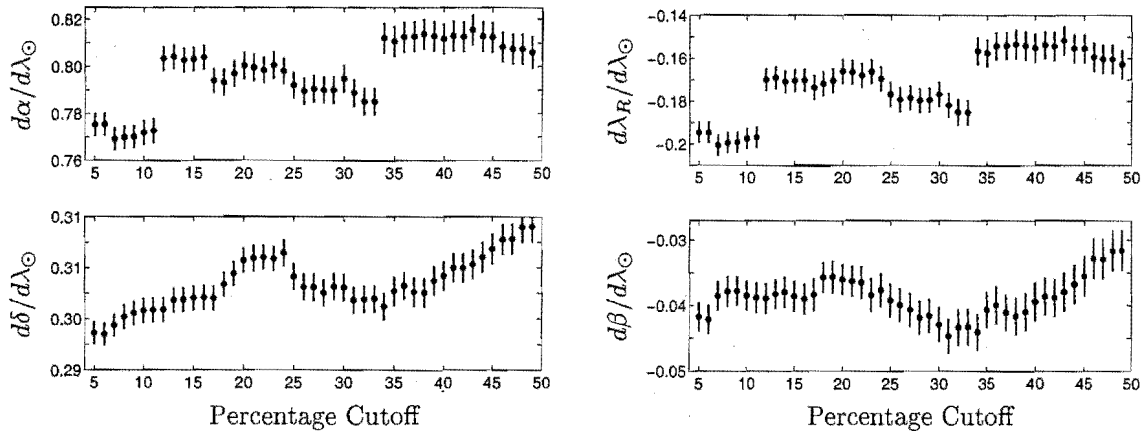

(a) Equatorial System (b) Ecliptic System

Figure 8.1: The stability of the SDA daily motion measurements in both the ecliptic and equatorial system coordinates is shown as the cutoff level in the wavelet transform is changed: this effectively changes the number of meteors selected and also changes the spread from the centre allowed in the original transform. Uncertainty bars are obtained from the uncertainty weighted least-squares fitting for the meteors corresponding to each 1% cutoff step in the sub-figures.

A cutoff level dependency in the measured radiant daily motion is seen even in the larger shower, the SDA which boast approximately 2×10^3 meteors. In an attempt to determine the extent to which this effect is felt, the cutoff level in this shower is varied between 5% and 50% of the maximum. This range is shown for both the ecliptic (Figure 8.1(b)) and equatorial (Figure 8.1(a)) coordinate daily motion; an approximately linear decrease over this range in the number of shower meteors is found. It is clear that the stability uncertainty exceeds that determined based on the data presented in each case, i.e. the choice of cutoff level has a strong influence on the "true" uncertainty determined in daily motion. From Figures 8.1(b) and Figures 8.1(a) a stability and measurement combined daily motion uncertainty of 0.02 in longitude, 0.005 in latitude, 0.02 in right ascension and 0.01 in declination

appear to be appropriate[1].

The stability/measurement combined estimated uncertainties determined above are adopted for all showers as it is more difficult to determine such parameters on the smaller showers. One should note that this stability problem may be overstated as generally one wishes to define the shower at the lowest cutoff level possible—by using motion values near 50% cutoff one is removing more than a third of the (assumed) shower members; the scatter in the latter is "real" according to that expected due to measurement uncertainty (as shown in later sections) hence one is effectively removing part of a valid sample when the sample is reasonably small even at the 5% level. The daily motions determined for the showers in the following sections are quoted with only the measurement uncertainty included owing to the desire to display the quality of the linear fit, with respect to the data in the form provided, used for correction in the current study. For comparisons with other studies the combined uncertainty determined here is preferred in order to encompass all possibilities presented from the current study.

In dealing with q and ω another problem arises. These parameters are linked into a relationship with the eccentricity (e) by a necessary condition for Earth impact (equation 3.3). The dilemma is whether to state a mean orbit which is clearly invalid for Earth impact due to the independent treatment of the q, e and ω distributions or instead to treat only two of the parameters independently and base the third on their outcome. In the current study the convention selected has been the independent treatment of all three parameters: therefore a given shower mean orbit may not give an Earth impacting solution as defined by equation 3.3 but it should generally be very close to giving such a solution.

The determination of representative uncertainties is another area which must be discussed. For a particular meteor shower the uncertainties on the individual shower members increase as the measured speed of the meteoroid increases. The uncertainties on the orbital elements are also related in a complex fashion to those in the fundamental parameters. Hence in parameters, such as the orbital elements, the Gaussian distribution which one normally expects to obtain for a large number

[1]As discussed in Section 2.6.1, "daily" motion measurements are given with respect to $\lambda_\odot$ rather than calendar day in the current study—hence the lack of units on the motions of angular parameters (which are measured in degrees unless stated otherwise) and their uncertainties. Published daily motion values used for comparison from Cook (1973) and Kronk (1988) were originally listed in units of degrees per day—in this chapter, these same motion magnitudes are given with no units for angular parameters or per degree for non-angular parameters, mindful of the negligable difference between the time-measurement regimes, to allow direct comparison with the motions in those parameters as determined here.

of random measurement uncertainties is not necessarily present—an arbitrary distribution which varies from parameter to parameter instead takes its place. As the showers change their apparent orientation over the period of activity the average speed of the shower and particularly certain components of the velocity will change thereby altering the uncertainty distribution: in many cases a percentage uncertainty on the elements is more constant across the range of parameter values than the absolute uncertainty. Due to the small number of meteors per day from each shower it is impossible to assign any kind of distribution. The difficulty then arises as to how one determines representative uncertainties for a particular shower. In order to obtain such figures the median of the uncertainties of the orbits detected in the shower has been chosen for each parameter. This assumes no particular distribution and has some obvious disadvantages but these cannot be avoided. As the measurement uncertainty in each parameter is normally quite large it is not generally possible to work out the underlying physical spread in the shower: parameter uncertainties must be a reasonable amount less than the spread in the shower in order to derive physical spread—a rare occasion in the current study. The radiant position parameters however have a more uniform uncertainty regime, particularly in the declination angle. These parameters also present approximately Gaussian observed distributions. Under these assumptions one can estimate the physical spread using

$$\sigma_o^2 = \sigma_u^2 + \sigma_p^2, \tag{8.1}$$

where σ_o^2 is the variance in the observed distribution and σ_u^2 and σ_p^2 are the variances expected from measurement uncertainty and from the underlying physical distribution respectively.

8.3 η Aquarids

The ETA is the only retrograde shower which is clearly visible against the sporadic background—the relative strength of this shower is demonstrated in Figure 7.25. It appears during the period from late-April to mid-May each year and is characterised by particularly fast apparent meteoroid speeds, as one would expect from retrograde meteoroids having radiants close to the apex of the Earth's way. This shower has been studied each year by AMOR since 1990, when the system began operation. While the ETA is visible in the northern hemisphere, their radiant is only above the horizon shortly before twilight. In contrast southern observers are

much better placed to observe it with the radiant being visible over approximately .0200–1300 NZST in New Zealand.

SURVEY	$\lambda_\odot$ deg	q AU	e	i deg	ω deg	Ω deg	V_H km s^{-1}	V_G km s^{-1}	α deg	δ deg	SIZE
C1973 P	43.1	0.560	0.958	163.5	95.2	43.1	-	65.5	336.8	-1.3	1
L1989 P	46.5	0.612	0.983	165.5	101.5	46.5	41.3	-	-	-	11
L1989 R	46.2	0.584	0.882	165.7	95.9	46.2	39.9	-	-	-	5
L1994 P	44.6	0.568	0.940	164.0	95.6	44.6	40.8	65.4	337.0	-1.5	17
L1994 TV	46.8	0.576	0.943	163.4	96.4	46.8	40.8	65.4	338.9	-0.4	6
L1994 P&TV	45.1	0.581	0.968	163.9	97.9	45.1	-	66.0	337.5	-1.2	23

Table 8.1: The mean orbital parameters of the ETA shower as determined in three different studies by Cook (1973), Lindblad (1989) and Lindblad et al. (1994) respectively. The angular parameters are referenced to the B1950.0 epoch in the original texts, they have been reduced by the author to the J2000.0 epoch in this table. Radiant positions are reduced to the central $\lambda_\odot^c$ in each case. The photographic and TV orbits from L1994 are not corrected for atmospheric deceleration whereas the combined mean orbit of these is corrected. Abbreviations used in this table for the type of observations are: P for photographic; R for radar and TV for TV meteor detections.

A number of studies have looked at the ETA in order to understand better its relationship to its twin shower, the Orionids, and also to its parent body, Comet Halley. Table 8.1 lists the mean stream orbits obtained from some of these studies. Cook (1973) does not state the number of orbits used to obtain his representative ETA mean orbit for inclusion in his working list of showers. It has since become known (Lindblad et al. 1994) that this "mean" orbit was obtained from a single photographic orbit (Harvard Super Schmidt meteor 11862). For several years in the literature this mean orbit was used to represent the ETA—such was the dearth of records of the shower, due to the lack of southern hemisphere observers. A larger sample of orbits was used by Lindblad (1989) where 11 photographic (comprising 7 Harvard Super Schmidt and 4 Nippon Meteor Society (NMS) small-camera orbits) and 5 radar measured orbits (Harvard Radio Meteor program) were studied. This sample was enlarged still further by Lindblad et al. (1994) with 17 precise photographic (comprising 1 precisely reduced Harvard and 16 NMS small-camera meteors) and 6 double station TV orbits being included.

It is interesting to reflect on the comments of Lindblad et al. (1994) who notes in his survey that: "The radio-determined orbits are, as a rule, of lower precision than the photographic data and will therefore not be discussed...". While this statement may be true for individual or small numbers of orbits, which are an order of magnitude higher in uncertainty than those derived from photographic methods, it is not true when one considers the corresponding order of magnitude increase in shower meteor rates provided by radar methods, as in the case of AMOR.

The determination of the physical spread in radar data parameters is of course hampered by such large uncertainties, however this problem has no bearing on the determination of statistical mean values, which is all Lindblad was interested in.

Taylor (1991) used the ETA in order to perform the original calibration check of AMOR. Using meteors detected over the period April 28th to the 18th of May in 1990 ($\lambda_\odot \in [37°, 57°]$) he defined the shower region by a rectangular box parallel to the ecliptic in equatorial radiant space; with reference to the daily motion of the shower described in Lindblad (1989), Taylor restricted the meteors accepted to the shower to appear within

$$\begin{aligned} 1.95\delta + 333.5° < \quad \alpha \quad < 1.95\delta + 349.0° \\ \text{and} \qquad\qquad\qquad\qquad\qquad\qquad\qquad\qquad\qquad (8.2) \\ -3.315\delta + 315.0° < \quad \alpha \quad < -3.315\delta + 354.0°. \end{aligned}$$

By inspection of the heliocentric speed distribution he determined that meteors falling within the above box should be also restricted in the speed dimension such that $V_H \in [34, 48]$ km s^{-1}. This step was taken in order to discriminate shower members from sporadic intruders.

In the current study the daily motion of the radiant is determined and the effects of this motion are subtracted from all retrograde meteoroids in the apex region over the time of the shower. This is inherently a better method than that of Taylor: the radiant box used in the latter does not take into account the possibility of random placement of a meteor in the box, in totally the wrong position for that meteoroid, given daily motion considerations in combination with the date of detection of the meteor.

The ETA shower is defined by the region of radiant space, which is highly positive and bordered by a negative region to each side, in the wavelet transform of Figure 7.25. In practice the border region does not always fall below zero on all sides as a small positive value may be found in some areas of the border due to a density spread in that direction, which is the case for the ETA. Figure 8.2 shows the outcome of selecting meteors in positive regions of the wavelet transform, firstly with no speed discrimination and then selecting only those within 1σ and 2σ of the determined shower region mean respectively[2]. It is clear from

[2]Note that the σ values in geocentric speed, used in the definition of the shower, are obtained from the distribution of shower and non-shower meteors in the radiant region in Section 7.7.3—as discussed there, the use of 1σ or 2σ cutoffs provide an arbitrary means to differentiate the

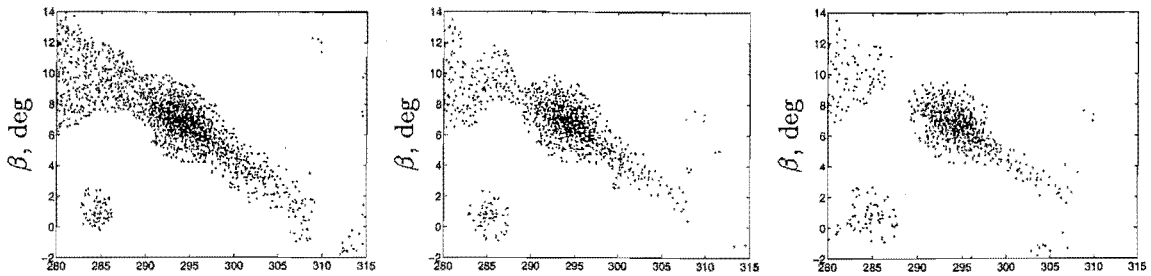

(a) All Speeds (b) V_G 2σ Criterion (c) V_G 1σ Criterion

Figure 8.2: The meteors within the positive regions of the retrograde apex region wavelet transform over the active period of the ETA shower. Use of geocentric speed discrimination is shown to better define the shower.

these graphs that knowledge of the centre of the speed distribution of the meteoroids under study does help refine the shower definition: the ETA is surrounded by large areas of white space except at the bottom right corner in the speed limited graphs. It is also clear that a WTC cutoff level slightly higher than zero is still necessary in order to define the grouping unambiguously; a level at 5% of the shower maximum has been found to perform excellently for this shower. As determined in Section 7.7.3, geocentric speed constrained at the 2σ speed criterion level lies within $V_G = 65.1 \pm 7.6$ km s^{-1} while the shower is taken exist over the period $\lambda_\odot \in [37°, 54°]$. Using these constraints the shower as shown in Figure 8.3(b), with an uncorrected centre at $(\lambda_R, \beta) = (294.2°, 6.8°)$, is relieved of all attached matter at this 5% level. In fact, as expected due to the strong detection bias there, apart from a latitudinally extended column at the exact longitude of the apex of the Earth's way nothing else in the entire apex radiant region appears at this cutoff level. By selecting within the radiant region highlighted in Figure 8.3(b) 1,018 meteors are detected, reduced to 942 after the daily motion is removed in the next section; this decrease is due to a change from an initial 5% cutoff to 8% following the daily motion correction—this increase is necessary in order to remove an artifact which develops on the periphery. The smaller cutoff is used initially in order to obtain the largest sample of possible shower members for the daily motion determination.

shower core from the (assumed) surrounding non-shower dominated background. In future uses throughout this chapter this speed selection from the mixed shower/background distribution shall be referred to in a similar fashion to "$n\sigma$ speed selection criterion" where n are the number of σ used.

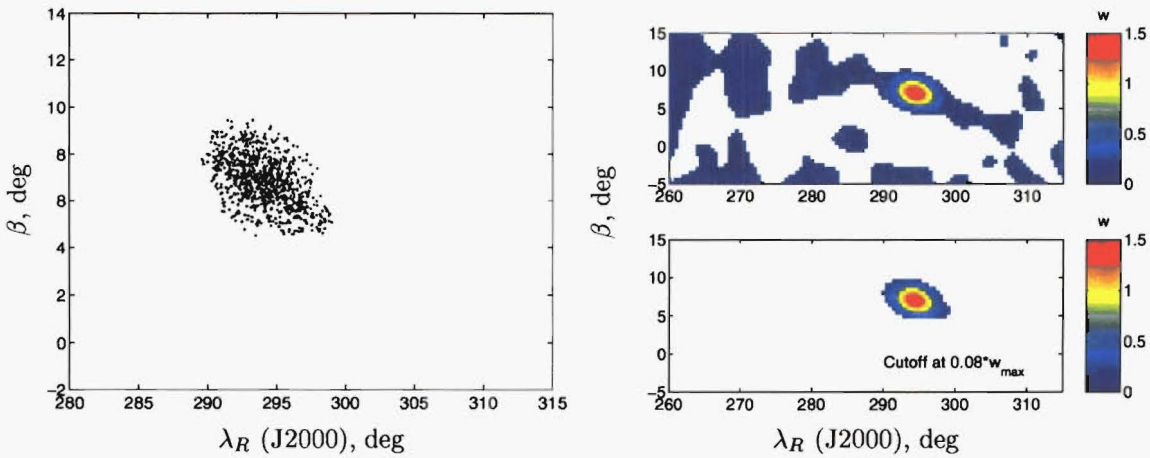

(a) Meteors Selected (b) Wavelet Transform

Figure 8.3: The retrograde apex region wavelet transform at the 1σ V_G criterion cutoff over the ETA shower active period. Meteors are selected which appear within the transform region defined by coefficients higher than 5% of the maximum WTC and with geocentric speeds constrained by the 1σ criterion.

8.3.1 Daily Motion of the Orbital Parameters

The daily motion in the orbital parameters occurs most obviously in the radiant position and the longitude of the ascending node. It is important to determine other parameters are similarly affected because the statistics of the shower in such parameters will be affected. The results of performing uncertainty weighted least-squares fitting on all orbital elements of the shower, selected at the 2σ V_G criterion cutoff level, are shown in Table 8.2. Minor daily motion of the mean parameters is seen for all of the orbital elements. Scatter plots for some of these parameters are shown in Figure 8.4(a), the fitted lines in some cases are not entirely convincing to the eye, however the respective daily motions are reasonably small and biased towards the period with highest activity. If the measured daily motion in the parameters were purely an artifact of the procedure, the corrections implied should not damage the data distributions overly, due to their small sizes; conversely where one has a fitted daily motion with a low uncertainty in that measurement it is important for completeness to include it.

The heliocentric and geocentric speeds both have uncertainties in their daily motion measurements which exceed the magnitude of that motion. It is likely that these parameters do experience some (minor) daily motion but measurement uncertainty precludes its determination. It is interesting to note that the fit in Figure 8.4(a) for the eccentricity motion appears to place the line very much lower

Parameter	$d/d\lambda_\odot$	Unit
q	$(5.2 \pm 0.9) \times 10^{-3}$	$\mathrm{AU\,deg^{-1}}$
e	$(-6 \pm 1) \times 10^{-3}$	$\mathrm{deg^{-1}}$
i	$(4 \pm 2) \times 10^{-2}$	-
ω	$(5 \pm 2) \times 10^{-1}$	-
V_G	$(-1 \pm 4) \times 10^{-2}$	$\mathrm{km\,s^{-1}\,deg^{-1}}$
V_H	$(-7 \pm 4) \times 10^{-2}$	$\mathrm{km\,s^{-1}\,deg^{-1}}$

Table 8.2: The daily motion of the ETA orbital parameters over the active period of the shower.

than one would expect. The reason for this is the changing nature of the uncertainty which increases steeply as one passes over into the hyperbolic region as shown in Figure 8.4(b).

In order to correct for the (minor) daily motion in the orbital parameters, they are referred to a central reference point. The reference used in Section 7.7.3 is $\lambda_\odot^c = 44°$; it is found, upon reflection, for reasons for which will become evident later in this chapter, that a more appropriate reference point is $\lambda_\odot^c = 46°$. Reduction to such a centre for each parameter experiencing daily motion is accomplished using equation 7.9.

While the daily motion of the ecliptic Sun-referenced geocentric radiant position has been measured using motion detected in the daily wavelet transforms of Chapter 7, it is rechecked here using all of the shower data points in order to give a more accurate result. Figure 8.5(a) shows a clear daily motion in Sun-referenced ecliptic longitude and apparently no daily motion in latitude. Weighted least-squares fits are in agreement with this observation, with slopes of -0.15 in longitude and a negligible 0.013 in latitude, being found:

$$\begin{aligned} \lambda_R &= (-1.5 \pm 0.2) \times 10^{-1}\lambda_\odot + (302° \pm 1°) \\ \text{and} \qquad & \qquad (8.3) \\ \beta &= (1.3 \pm 0.4) \times 10^{-2}\lambda_\odot + (6.3° \pm 0.2°). \end{aligned}$$

The use of the Sun-referenced system has, in this case, diminished the daily motion in longitude by $\sim 80\%$ but the residual -0.15 is still a significant amount which must be removed. This correction factor is in good agreement with the -0.18 slope determined in Figure 7.13 and this shows that the daily motion correction calculations of the previous chapter worked correctly: the value obtained here is in fact more valuable than that obtained previously, as obtaining a fit based on uncertainties in individual data points is inherently better than the approach of

Chapter 7 where a mean daily data point was used.

The radiant position and its daily motion are more normally quoted in the equatorial system. While the data provided from the ecliptic system above is obviously equivalent, the daily motion in right ascension and declination are given in this study for completeness. Figure 8.5(b) shows clear daily motion in both of these coordinates, corresponding to motion exactly parallel to the ecliptic, in agreement with Figure 8.5(a). The weighted least-squares fits in the equatorial parameters are defined by

$$\begin{aligned} \alpha &= (7.3 \pm 0.2) \times 10^{-1} \lambda_{\odot} + (305^{\circ} \pm 1^{\circ}) \\ \text{and} & \\ \delta &= (3.09 \pm 0.04) \times 10^{-1} \lambda_{\odot} - (15.6^{\circ} \pm 0.2^{\circ}). \end{aligned} \tag{8.4}$$

Correction to the $\lambda_{\odot}^{c} = 46^{\circ}$ centre for these coordinates is performed using the standard approach of equation 7.9. The calculated daily motion agrees well with the daily motion of 7.6×10^{-1} in right ascension quoted by Lindblad et al. (1994), however that in declination differs somewhat from Lindblad's quoted 4.22×10^{-1} motion. Lindblad only covers solar longitudes from 43° to 47° with 23 single data points, while the current study uses 942 points over a longer period, albeit with higher individual uncertainties. The declination angle uncertainty in the latter points is a uniformly small 0.5° due to the direct elevation angle uncertainty relationship. This uncertainty (while greater than the 0.1° expected for photographic meteors) is easily made up for by the data set size difference where the greater numbers of meteors in the AMOR shower data set provide a high quality declination daily motion estimate—as indicated by the very small uncertainty in the fitted motion of equation 8.4. The uncertainty in Lindblad's value is not known; one should also note that the exact shower selection will change the daily motion somewhat as discussed in Section 8.2 however the declination stability value (0.01) determined there is much smaller than the difference between Lindblad's motion and the current value. This declination motion difference is therefore considered to be due to the small number of data points used by Lindblad et al. (1994), with the AMOR measurements being preferred.

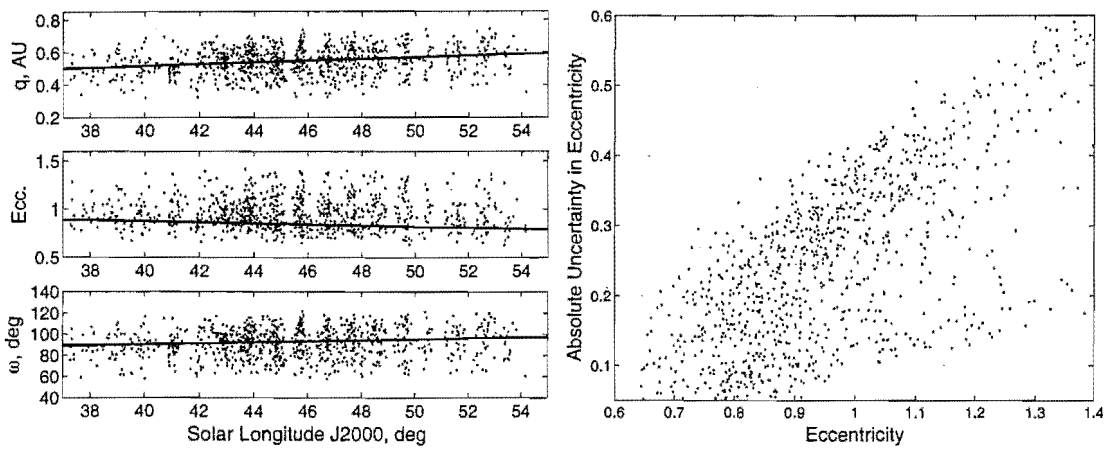

(a) Orbital Elements Daily Motion (b) Eccentricity Uncertainty Regime

Figure 8.4: Motion of the mean orbital parameters of the ETA over the period of the shower. A weighted least-squares linear fit for the daily motion of q, e and ω is provided. Due to increasing uncertainty with increasing e, as shown in Figure 8.4(b), the fit for e is strongly weighted towards lower values of eccentricity. Representative (median) uncertainties on the parameters shown are: 0.1 AU in q, 0.2 in e and 20° in ω.

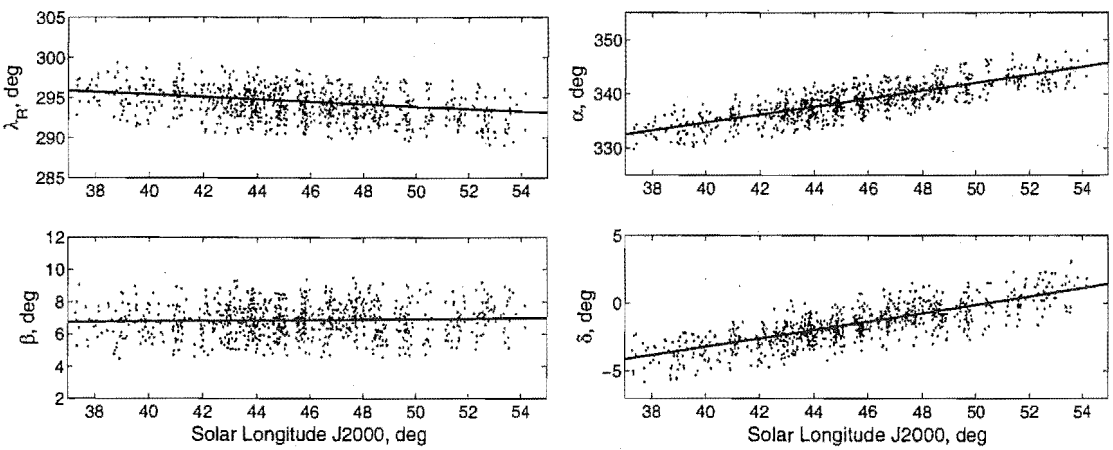

(a) Radiant Daily Motion (Ecliptic) (b) Radiant Daily Motion (Equatorial)

Figure 8.5: Daily motion in the radiant position of the ETA. Uncertainty weighted linear least-square fits are shown for this motion in the case of both the ecliptic and equatorial system.

8.3.2 Shower Statistics

Meteoroids are selected which appear within the wavelet transform region with coefficients greater than 8% of the local maximum coefficient value and speeds within the 1σ criterion determined in Figure 7.24. This leads to the 652 meteors shown in Figure 8.3(a) being included in the shower. The statistics of the corresponding meteoroid orbits are given in Table 8.3. The uncertainty in the individual orbital parameters is greater than the stream orbit distribution standard deviations which implies that the spread is totally dominated by uncertainties and that a substantial number of shower meteoroids are not being detected due to their level of dissimilarity with the mean stream orbit. One must ask whether the uncertainties are

YEAR		$\lambda_\odot$ deg	q AU	e	i deg	ω deg	Ω deg	V_H km s^{-1}	V_G km s^{-1}	α deg	δ deg	SIZE
ALL	$\overline{x}$	45.4	0.550	0.939	165.3	93.1	45.4	40.6	65.1	339.1	-1.5	652
	s.d.	3.7	0.057	0.098	1.9	8.6	3.7	2.0	2.1	1.7	0.8	
	s.e.	0.1	0.002	0.004	0.1	0.3	0.1	0.1	0.1	0.1	0.0	
	Unc.	0.0	0.136	0.254	2.2	21.8	0.0	5.6	5.7	3.0	0.5	

Table 8.3: Statistics of all ETA from T1995–T1999 at the 1σ V_G criterion level. All parameters experiencing daily motion, apart from $\lambda_\odot$ and Ω, are corrected to $\lambda_\odot^c = 46.0°$; all parameters are referred to the J2000.0 epoch. The medians of the parameter uncertainty distributions are used to provide representative values.

realistic in this table—if they are, then can something be done in order to include more shower meteoroids without contaminating the set with too much sporadic intrusion? The highest uncertainty, in the orbit determining parameters for the ETA, is that present in the speed measurements. This carries through to Table 8.3 where the spreads in the various speed parameters fall below those expected according to individual meteor speed measurement uncertainties—wide ranges in speed are necessary to retrieve all of the shower members due to these uncertainties. AMOR determines many angular quantities with a reasonably low uncertainty while speed related parameters such as shape and size generally have a much higher level of uncertainty.

Taylor, using his radiant box method, determines the statistics of the ETA shower, as shown in Table 8.4. The standard deviations in these distributions greatly exceed those in Table 8.3: they are similar to the expected spread due to uncertainties, as noted in Taylor's uncertainty analysis.

The differences between Tables 8.3 and 8.4 are due to the more stringent speed range allowed at the 1σ speed criterion level in the current study; Taylor uses $V_H = 41 \pm 7$ km s^{-1} as the speed constraint, which is approximately double that

allowed currently. A more liberal speed range most obviously affects the q, e and ω orbital elements which are, of course, linked together by equation 3.3. The shape and size of the orbit are defined by q and e and minor changes in speed, especially for streams such as that causing the ETA which is near the parabolic limit ($e = 1$), cause major changes in these parameters. Nowhere is this problem more evident

YEAR		$\lambda_\odot$ deg	q AU	e	i deg	ω deg	Ω deg	V_H km s^{-1}	V_G	α deg	δ deg	SIZE
1990	$\overline{x}$	46.5	0.566	0.969	165.8	95.4	46.5	41.0	-	-	-	361
	s.d.	4.1	0.118	0.171	2.8	16.7	4.1	3.3	-	-	-	
	s.e.	0.2	0.006	0.009	0.1	0.9	0.2	0.2	-	-	-	

Table 8.4: The orbital statistics of the 1990 apparition of the ETA shower detected using the radiant box method, after Taylor (1991); the original mean orbit was referred to B1950.0, this has been reduced to J2000.0 in the table above. Note that the AMOR system has been upgraded since this work from a single- to a dual-interferometer, hence better quality (lower uncertainty and less elevation angle ambiguity) results are achievable in the current study than at that time.

than in the use of D-criteria to study the ETA, as measured by AMOR. Often the mean D of a grouping is used to test whether the spread in the orbits is too great to be realistic in an astronomical sense: Lindblad (1971a) typically uses $\overline{D}_{SH}$ of between 0.10 and 0.20 for this purpose. Values of D_{SH} of 0.25 or D_D of 0.10 are regarded as an upper limit for stream membership in serial-searches by Drummond (1981). Using the 652 orbits obtained in the current study at the 1σ speed criterion cutoff yields $\overline{D}_{SH} = 0.24$, $\overline{D}_D = 0.11$ and $\overline{D}_N = 0.15$. These mean values are all at the maximum of the range at which orbital association would normally be accepted. This illustrates the problem in the use of D-criteria in this regard: it is clear that a liberalisation of the speed criterion cutoff to 2σ would allow many more true shower meteors to be recognised, however doing so will increase the mean D to very high, ordinarily unacceptable, levels.

YEAR		$\lambda_\odot$ deg	q AU	e	i deg	ω deg	Ω deg	V_H km s^{-1}	V_G	α deg	δ deg	SIZE
ALL	$\overline{x}$	45.6	0.545	0.953	165.1	91.9	45.6	40.5	65.0	339.0	-1.4	942
	s.d.	3.6	0.080	0.162	2.1	13.5	3.6	3.4	3.5	1.8	0.8	
	s.e.	0.1	0.003	0.005	0.1	0.4	0.1	0.1	0.1	0.1	0.0	
	Unc.	0.0	0.133	0.239	2.3	21.3	0.0	5.4	5.5	2.9	0.5	

Table 8.5: Statistics of all ETA from T1995–T1999 at the 2σ V_G criterion level. All parameters experiencing daily motion, apart from $\lambda_\odot$ and Ω, are corrected to $\lambda_\odot^c = 46.0°$; all parameters are referred to the J2000.0 epoch. The medians of the parameter uncertainty distributions are used to provide representative values.

Table 8.5 lists the statistics obtained using the 2σ speed cutoff criterion with Figure 8.6 displaying the corresponding histograms for reference. The spread in

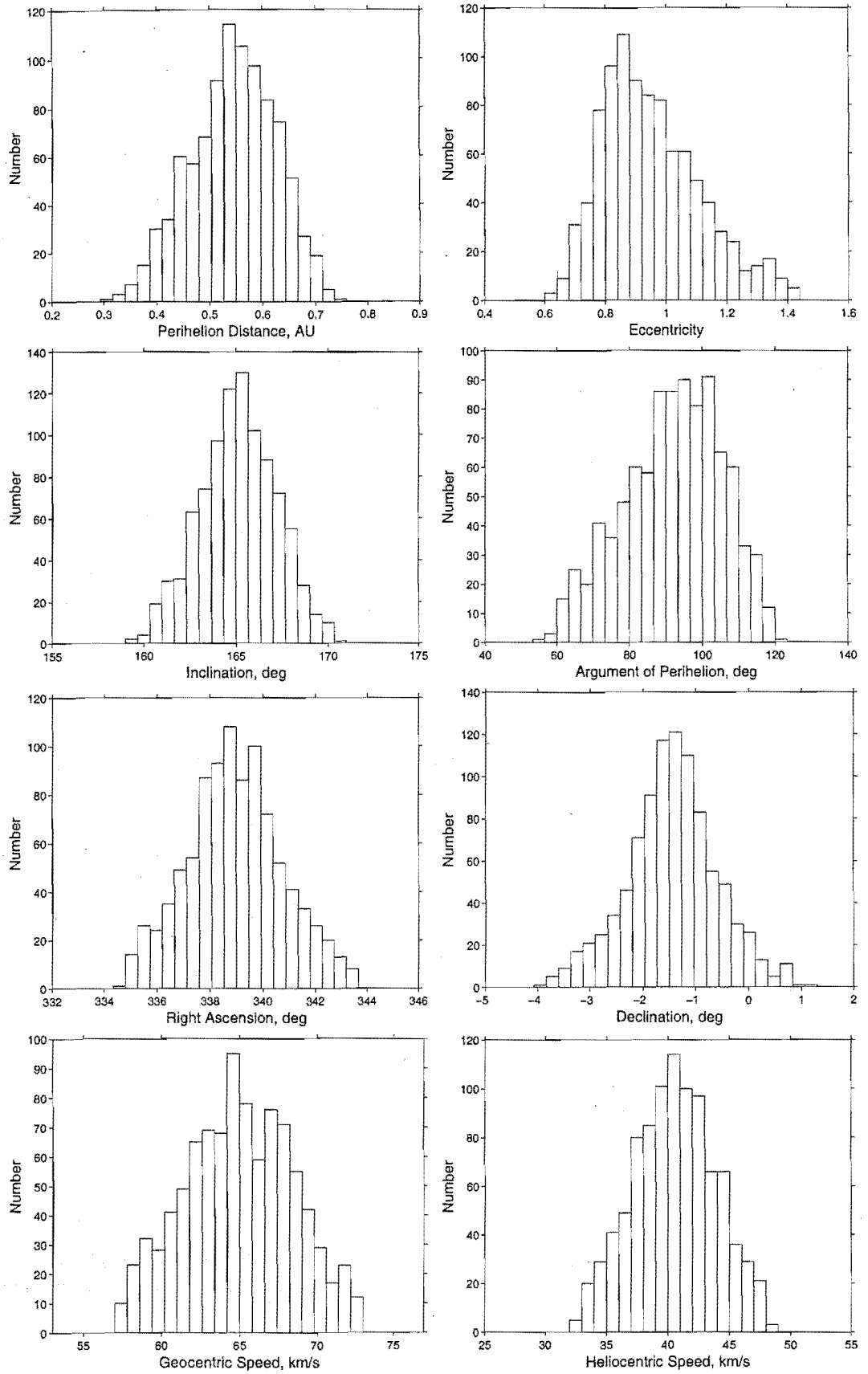

Figure 8.6: Histograms of the orbital parameters of the ETA shower for T1995–1999. The perihelion distance and radiant position coordinates are reduced to a centre at $\lambda_{\odot}^{c} = 46.0°$.

the shower distributions under this regime is found to bear greater similarity to that implied by the uncertainties and also to that obtained by Taylor (1991). As predicted, the mean D values increase dramatically with $\overline{D}_{SH} = 0.35$, $\overline{D}_D = 0.16$ and $\overline{D}_N = 0.19$, values much too high for a grouping of closely associated orbits by normal standards. Many ETA meteors are necessarily lost if normal orbit searching techniques are used—notice the increase from 652 to 942 orbits over five years when the 2σ speed criterion is used instead of 1σ. Retrograde streams must be treated as a special case, with higher cutoff levels in $\overline{D}$, speed-range etc. A problem implicit in this approach is that the wider one spreads the constraints, the more likely one is to associate unrelated meteors with a stream under study.

The spread in most parameter distributions in Table 8.5 is still smaller than their uncertainties would imply. The "full" distributions expected are not even being captured at the 2σ criterion level: some of the apex region background meteor detections, at this time, are shower meteors which are simply too far removed from the core to be recognised. The declination angle is the only parameter whose spread is greater than that implied by its 0.5° representative uncertainty. As the declination distribution is close to "Gaussian", as shown in Figure 8.6, one can therefore estimate the physical spread in this parameter using equation 8.1: this gives an expected physical standard deviation (σ_p) of 0.7°. More generally, the statistics of the ETA are clearly dominated by the uncertainty in the measured orbits. Secondary effects also present in the distributions are the physical spread in the orbit population and in some cases daily motion within the parameter: these effects are generally not resolvable.

In order to determine whether the shower appears to be changing in character over time, the mean parameter values are shown in Table 8.6, for each of the five years covered in the current study. A decrease in the number of shower orbits is evident in T1997 and T1998.

Statistics based on $\lambda_\odot$ and Ω are as much related to the time-coverage of the radar system, changes in equipment sensitivity, and atmospheric conditions, as they are to the distribution in time of shower meteor flux. As shown in Table 8.6, these parameters have mean values for all of the years, falling between 45° and 46°: this lies within the range expected from previous searches, as quoted in Table 8.1. In the yearly activity profiles of Figure 8.9, the background changes often over the period of the shower and the activity curve is far from symmetrical for most of the years. This asymmetry illustrates the importance of correction for daily motion:

YEAR		$\lambda_\odot$ deg	q AU	e	i deg	ω deg	Ω deg	V_H km s^{-1}	V_G km s^{-1}	α deg	δ deg	SIZE
1995	$\overline{x}$	46.0	0.536	0.928	165.6	90.2	46.0	40.0	64.5	339.0	-1.7	225
	s.d.	3.6	0.078	0.154	2.1	13.4	3.6	3.3	3.4	1.8	0.8	
	s.e.	0.2	0.005	0.010	0.1	0.9	0.2	0.2	0.2	0.1	0.1	
	Unc.	0.0	0.135	0.227	2.3	21.6	0.0	5.3	5.4	2.9	0.5	
1996	$\overline{x}$	46.0	0.552	1.007	165.4	94.4	46.0	41.5	65.9	339.4	-1.3	259
	s.d.	3.6	0.086	0.168	2.0	13.9	3.6	3.3	3.5	2.0	0.8	
	s.e.	0.2	0.005	0.010	0.1	0.9	0.2	0.2	0.2	0.1	0.1	
	Unc.	0.0	0.131	0.248	2.4	20.4	0.0	5.4	5.5	3.2	0.5	
1997	$\overline{x}$	45.4	0.550	0.941	165.0	92.3	45.4	40.3	64.9	338.7	-1.5	128
	s.d.	3.5	0.082	0.150	2.1	13.4	3.5	3.2	3.3	1.9	0.9	
	s.e.	0.3	0.007	0.013	0.2	1.2	0.3	0.3	0.3	0.2	0.1	
	Unc.	0.0	0.153	0.212	2.0	22.6	0.0	4.9	5.5	3.0	0.5	
1998	$\overline{x}$	44.9	0.527	0.908	164.3	88.4	44.9	39.6	64.0	338.8	-1.2	139
	s.d.	4.0	0.079	0.152	1.8	13.6	4.0	3.3	3.4	1.7	0.8	
	s.e.	0.3	0.007	0.013	0.2	1.2	0.3	0.3	0.3	0.1	0.1	
	Unc.	0.0	0.139	0.192	2.2	21.9	0.0	5.1	5.2	2.9	0.5	
1999	$\overline{x}$	45.0	0.554	0.948	164.9	93.0	45.0	40.5	65.1	338.7	-1.4	191
	s.d.	3.4	0.072	0.159	2.1	12.5	3.4	3.2	3.4	1.5	0.8	
	s.e.	0.2	0.005	0.012	0.1	0.9	0.2	0.2	0.2	0.1	0.1	
	Unc.	0.0	0.115	0.276	2.3	20.5	0.0	5.9	5.8	2.5	0.5	

Table 8.6: Mean orbital parameters of the ETA shower for each year between T1995 and T1999, at the 2σ V_G criterion level. Parameters experiencing a daily motion, apart from $\lambda_\odot$ and Ω, are corrected to $\lambda_\odot^c = 46°$; all parameters are referred to the J2000.0 epoch. The medians of the parameter uncertainty distributions are used to provide representative values.

a perfectly symmetric activity profile should implicitly remove any daily motion effects in the mean parameters, while an asymmetric curve will not.

The use of a Student's t-test to detect inter-annual changes in the means of observational orbit-defining parameters is introduced here. This test takes shower observations from a pair of years and, for a given confidence level, validates or negates the null hypothesis that "the means are the same"; the 95% confidence level is chosen to test this hypothesis here. Figure 8.7 shows this test performed for the ETA shower with observed years as summarised in Table 8.6; here five parameters are chosen for comparison, two pairs of which relate to the radiant position with the fifth parameter being the heliocentric speed. These parameters are chosen because any one of the radiant position pairs in conjunction with the speed and some representative time of detection for the shower define the mean shower orbit. The first five sub-figures in Figure 8.7 compare yearly means directly while the last sub-figure compares parameter means from each year against those means obtained from the combination of the five years of data (the latter is summarised in Table 8.5).

One would expect that the radiant position and speed defining parameters should have stable means from year to year as the form of these distributions is

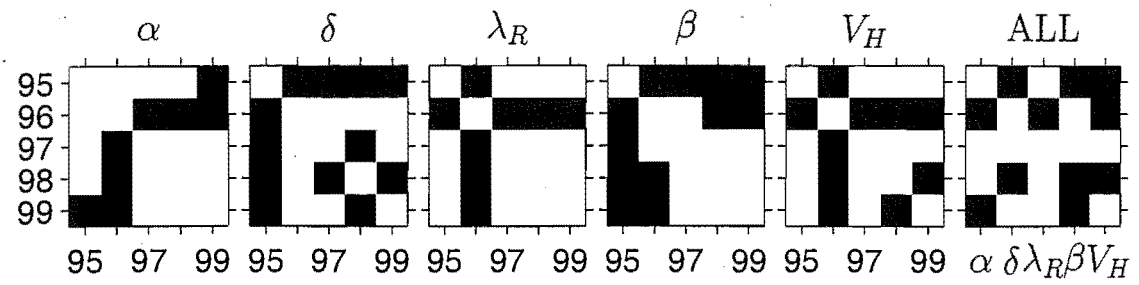

Figure 8.7: Student's t-test of inter-annual agreement of ETA parameter means. The means of five parameters for a series of years are inter-compared in the first five figures; the sixth "ALL" figure shows comparisons between these yearly means with the means obtained from all years of data combined. White squares signify agreement between parameter means at the 95% confidence level while black squares indicate disagreement. All parameters are corrected for daily motion.

imposed fairly directly by the shower membership criteria. However, study of the test results from Figure 8.7 indicate the instability of the ETA mean observed parameters. In particular, the T1995 and T1996 tend to disagree with each other and with other years on most parameters—if one were to remove these two years from the tests then almost complete agreement between the remaining years on all parameters tested is left. The shower mean radiant position may be said to be generally stable over T1997–T1999. Comparison of each year's parameter means against those from the combined shower mean indicates sporadic disagreement on several parameters from each year apart from T1997 where perfect agreement is reached with the mean of Table 8.5). This result indicates the inherent instability of the ETA observation—the individual and combined years means differ significantly but by a small magnitude in the observed parameters. Therefore observations in one year of the shower are not reliable to exactly predict those which will be obtained in subsequent years. The bias in most shower parameter distributions is shown in Table 8.6 to provide sample standard deviations which fall below those expected due to parameter measurement uncertainties. The instability introduced by this under-representation of the "true" distributions in combination with the expected physical inhomogeneity in the meteoroid stream itself act together to cause the disagreements, particularly between the combined and single-year means, in Figure 8.7.

The reason for the lack of inclusion in the Student's t-test of the orbital elements (q, e etc.) and geocentric speeds is the non-Gaussian character which these parameters often exhibit (e.g. e in Figure 8.6); the orbital elements are compared below to see if they appear to agree within standard error between years, however such a test is not statistically robust and the use of standard error, while the only option

here, becomes less valid as the parameter distributions stray from Gaussian. The mean inclination angle (whose uncertainty is particularly low) is constant within the standard error year after year. This parameter is expected to change little physically due to perturbations, so that in combination with low uncertainties, this makes for a robust distribution with little movement in the mean. The inclination differs by up to 1° from the mean published orbits of Table 8.1: the latter are made up from a smaller number of data points, although the individual points may have a lower uncertainty, the uncertainty in the mean must necessarily be increased, due to the low number of points. As the mean inclination angle changes little over five years separately and also in combination (Table 8.5), this parameter is shown to be reliable.

The perihelion distance, eccentricity and argument of perihelion experience the largest yearly changes in the current study, attributed to their large individual orbit uncertainties. Similarly in Table 8.1, one can see a wide range in these mean parameters, which were determined from particularly precise collections of individual orbits. As noted previously, the representative uncertainties on these parameters appear to exceed the measured spread in the AMOR data: this leads to poorly defined mean parameters. This is also true of heliocentric and geocentric speeds, where the measured spread is much smaller than that expected by orbital uncertainty, these values differ however by no more than 2 $\mathrm{km\,s^{-1}}$, from those measured in Table 8.1. From year to year the mean speeds differ from each other by a similar amount, with those in Table 8.5 giving the best agreement with the published mean speeds, a reasonable result given the larger number of orbits in this data set.

In directly comparing the mean orbit from all years obtained in the current study (Table 8.5) with those listed in Table 8.1, using the Southworth and Hawkins' D-criterion (D_{SH}) as a measure of dissimilarity, one finds satisfactory agreement with all of the published orbits. The best agreement is with Taylor (1991) at a very low D_{SH} of 0.05. This similarity confirms that the current method which differs from that used by Taylor, has achieved a similar result, from slightly modified AMOR equipment[3]. This gives confidence in the method, its implementation, and the quality of equipment calibration over time.

The highest dissimilarity is found for the Lindblad (1989) photographic mean with $D_{SH} = 0.16$—a rather large value considering that one is comparing stream

[3]The main modifications to the AMOR system since its original setup by Taylor are the addition of a dual-interferometer, to decrease elevation angle ambiguity, and the increase in transmitted radio power, in order to extend sensitivity to smaller dust particles.

means and not individual orbits from the stream searches: the difference mainly results from the unusually high ω value for Lindblad's mean, a value which is also in disagreement with other mean orbits shown in Table 8.1. In order of appearance in Table 8.1, the shower is found to have D_{SH} dissimilarities of 0.10, 0.16, 0.10, 0.08, 0.07 and 0.12 respectively. Note that here as in later inter- and intra- mean orbit comparisons, the mean parameters resulting from daily motion cleansed data sets are used[4]. This is in contrast to normal practice, particularly for small data samples (e.g. Table 8.1), where the means are based on distributions containing ingrained daily motion. The difference, for all showers surveyed in the current chapter, between comparisons of literature values with daily motion corrected and comparisons with non-daily motion corrected data sets is found to lead to changes of no more than 0.01 in D_{SH} for inter-mean and 0.02 for intra-mean comparisons—this is a negligible change compared with the dissimilarity magnitudes reached due to "real" differences.

One can also compare the shower determination with those provided by single-linkage analysis (D_{SH} determined stream in Table 7.3) and by the modified single-linkage analysis of Appendix H (Table H.1). It is found that agreement is good in both cases, with inter-mean orbit dissimilarities of $D_{SH} = 0.05$ for the former and $D_{SH} = 0.08$ for the latter (One should note that minor corrections have been made for daily motion in the wavelet determined mean orbit, which have not been made in the other cases). Incidentally, this comparison appears to show that the standard single-linkage algorithm provides stream means which agree better (with the wavelet approach) than do those obtained from the modified single-linkage method. This finding continues for the other three major showers lending credibility to the view (expressed in Section 7.8) that the modified method is including some unrelated sporadic groupings which have contaminated the resulting mean slightly.

8.3.3 Activity Profiles

Complementary to the tables of statistics, already presented, are the activity profiles for the shower and for the general non-shower retrograde population respectively. These are shown for each of the years covered in Figure 8.9. Here for each data point, corresponding to N meteor detections, a statistical uncertainty given by $\sqrt{N}$

[4]In the current study an inter-mean dissimilarity is defined as the dissimilarity between the means of two data set shower samples, this allows direct comparison of seperate data sets. In contrast the intra-mean dissimilarity is the mean dissimilarity between all members of a single data set shower sample, this gives a measure of the compactness of a shower.

has been assigned. This uncertainty allows one to decide if definite changes have occurred from point to point—changes which are outside those allowed uncertainty limits are judged to be important. In order to partition the data into 1° intervals, one must be mindful of the difference between the normal calendar day system and that based on mean solar longitude. The time of day, at which the shower radiant appears above the observer's horizon, corresponds to a particular range of solar longitude: this range will be less than 1° for each calendar day. One must split the data set in the gaps between such daily apparitions, in order to ensure artifacts are not introduced, where a data point might be composed of a null activity region in combination with a small part of two days observations to each side. It would appear to be a matter of determining a starting position in the centre of a gap in $\lambda_{\odot}$ and then of proceeding in 1° intervals from there. As shown in Figure 8.8, this procedure works well for T1995. However, applying the same procedure to T1997 results in positioning, not in gaps, but instead in the centre of daily distributions. The starting position must change, as shown in the figure, by approximately 0.25° per year. This yearly offset is due to the non-integer 365.25 days per Gregorian calendar year. As shown in Figure 8.8, this motion in the starting position has been applied to each year successively: the resultant daily boundary lines clearly mark the centre of the gaps in each year. The yearly activity profiles presented, therefore, use offset centres for each 1° position in order to accommodate this problem. If one were to add all of the years of data together, to obtain a representative activity profile, one would have difficulty in using $\lambda_{\odot}$ as a time measure: a calendar day counting time-frame (with the proper length of the year rather the compensatory leap year being used) in this case would actually be more appropriate. It is interesting that such concerns come up here since the mean solar longitude is normally used, in order to remove ambiguities associated with the use of the standard calendar year.

In order to demonstrate the problems that inappropriate bin centres in the data can cause, two sets of activity profiles are presented for this shower: one with a yearly changing offset (Figure 8.9) and the other with a fixed offset (0.2°) for all years (Figure 8.10). Good agreement, in the corresponding profiles, is present for the T1998 year. In T1998, the offset is similar to that required, while in T1996 where the fixed offset is insufficient with many of the peaks smoothed out in comparison to the corresponding floating offset profile. In T1995 at $\lambda_{\odot} \approx 51°$, the profile shows total equipment outage in the floating offset curve, while at the corresponding point on the constant offset profile there appears to be no change, in the average rate,

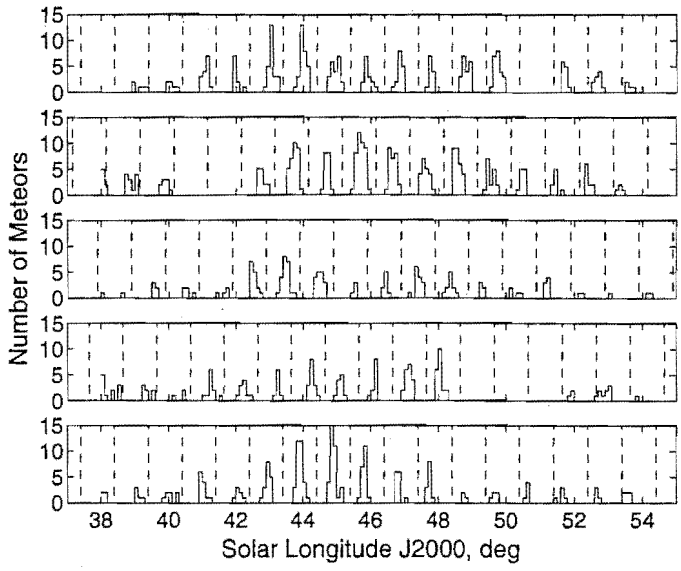

Figure 8.8: The relationship between solar longitude and detection time period for the ETA. The distribution shifts by approximately 0.25° per year. Appropriate cutoff points are shown at offsets from zero $\lambda_\odot$ of 0.4°, 0.15°, −0.1°, −0.35° and 0.4° for years T1995–T1999, shown from top to bottom respectively.

from that observed at the surrounding points. It is obvious on further examination of the floating offset curve, that the constant offset point has grabbed meteors from the surrounding points, in order to produce a common lower level over the surrounding points, in Figure 8.9. This problem may be seen in many other places when comparing these figures and the need for separate bin centre offsets for the different years becomes obvious; further discussions of shower activity in this section refer to the floating cutoff profiles of Figure 8.9. Because of the offset problem it is found to be very difficult to add together the activity profiles from several years in order to gain an "average" composite profile. The large differences between background activity in different days in different years is able to be accounted for in such composite profiles by normalisation of the shower rate but the problem then becomes how to merge different offset point data together. The resulting composite profile might combine the effects of data from up to 3° of solar longitude, the loss of positional resolution in the case of many of the low-yield showers studied here, including the ETA, would be profound; hence, it is judged impractical to form composite acivity profiles from several years.

There is seen to be a dramatic drop-off in the total number of ETA orbits archived in T1997 and T1998, with an upturn again in T1999, as noted earlier. Referring to Figure 8.9, the general retrograde meteor population does fall, but not by as much as the shower rate does in these years, partially indicating a change in sensitivity

of the radar system over this period but also that there was a real drop in the ETA shower activity.

The mean solar longitude and longitude of ascending node are always found to be in the region between 45° and 46°. There are generally no clear maxima for the shower, however a series of suggestive sub-peaks is shown. The obvious question is whether these are simply artifacts of the inoperative periods of the radar and its changing radar sensitivity, or instead that one is witnessing astronomically real phenomena.

In T1995 there are several peaks in the distribution. The only two which exceed the bounds allowed by statistical uncertainty are those appearing to peak at $\lambda_\odot = 43.9 \pm 1°$ and at $\lambda_\odot = 48.9°$. The second peak lasts for 1° and follows faithfully a strong increase in the background at the same time—this increase can therefore be attributed directly to a general data rate fluctuation. The first peak is stronger and lasts over 3°, the background appears to slightly decrease over this time, indicating the reality of the peak. It is found to be impossible to pinpoint the exact location of the centre, due to the overlapping of the error-bars from these three points, however it can be said that the global maximum does occur in the region bounded by $\lambda_\odot \in [42.4°, 45.4°]$. If one were to smooth the other peaks, a curve with a single maximum in this region and increasing slowly from each side, would seem to be the most likely underlying structure.

The T1996 curve has a peak which lasts at a constant level, within statistical uncertainties, over the region $\lambda_\odot \in [43.2°, 50.2°]$. There is no statistical evidence of any substructure within this region although there is a minor trend which appears to indicate an increase to a maximum at $\lambda_\odot = 46.7°$ from both sides.

T1997 presents a curve which appears to have two peaks, one centred at $\lambda_\odot = 43.4°$ and one at $\lambda_\odot = 47.4°$. Both of these peaks correspond to similar large-scale fluctuations in the background but little can be gleaned from this figure, apart from a general trend suggesting an increase towards a peak from 41.4° on the left and from 49.4° on the right. Therefore assuming there is, in reality, a single peak monotonically approached from both sides, this implies a shower maximum near 45°. One should note that the right hand peak should probably be a little lower relative to the left hand one, due to the difference in background counts in these two regions. The curve shown for T1998 is the most unusual. It appears that the shower peak is reached somewhere in the region $\lambda_\odot \in [44.8°, 49.8°]$. The strong decrease in background counts experienced about 45°, means that the shower particles in this

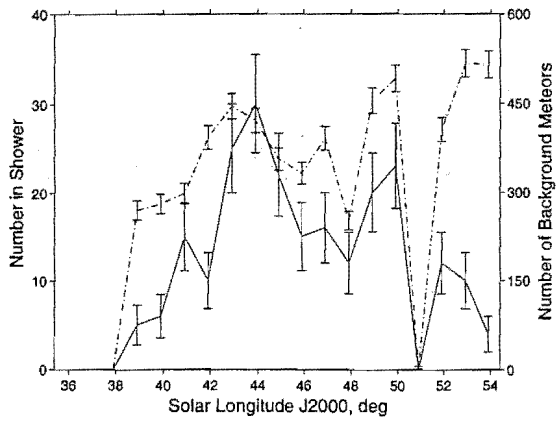

(a) T1995

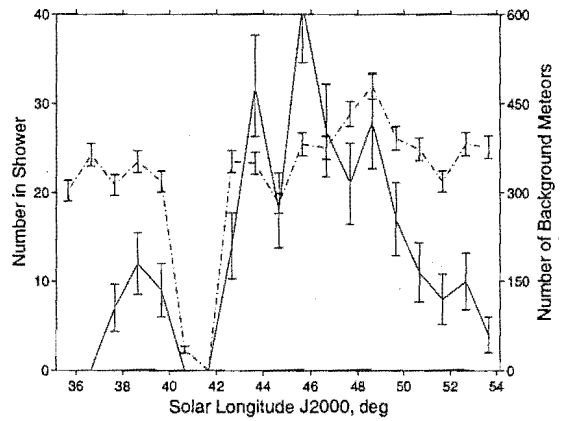

(b) T1996

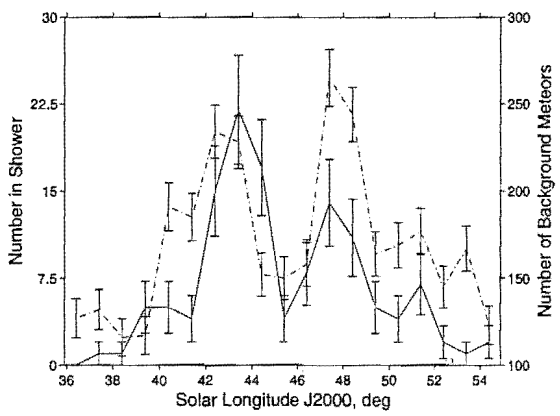

(c) T1997

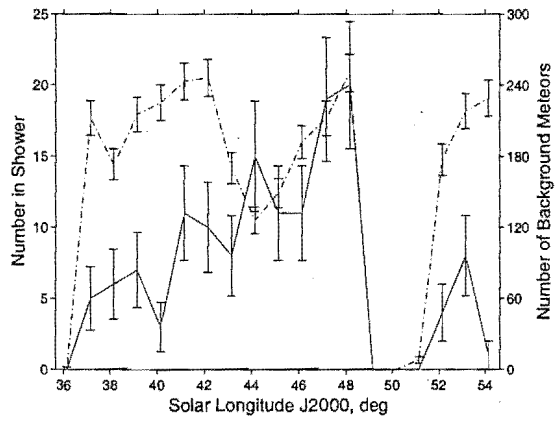

(d) T1998

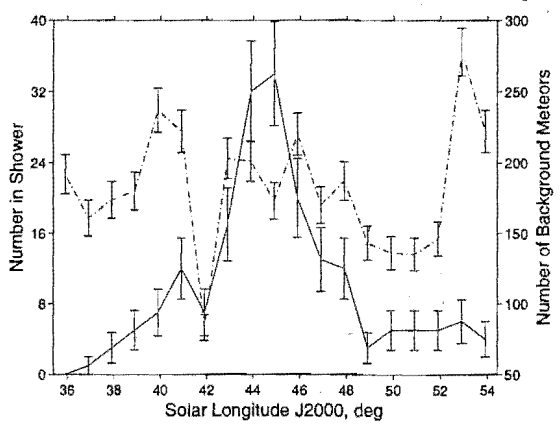

(e) T1999

Figure 8.9: The distribution in time of the ETA meteors for each year from T1995 to T1999. These distributions all use the separate shower centring which begins at $\lambda_\odot = 38° + \lambda_\odot^{off}$. Here $\lambda_\odot^{off}$ changes per year in order to best encapsulate the distribution resulting from the Earth's daily rotation; with reference to Figure 8.8, the centre offsets from zero used are: -0.10, -0.35, 0.40, 0.15 and -0.10 for years T1995–T1999 respectively. The change in shower rate per degree of solar longitude at these centres is shown as a solid line, while the change in the rate of all non-shower retrograde meteors over the same time-frame is shown as a dotted line. The statistical uncertainty, shown on each point, is given by $\sqrt{N}$. Note the use of two different y-axis systems for each graph.

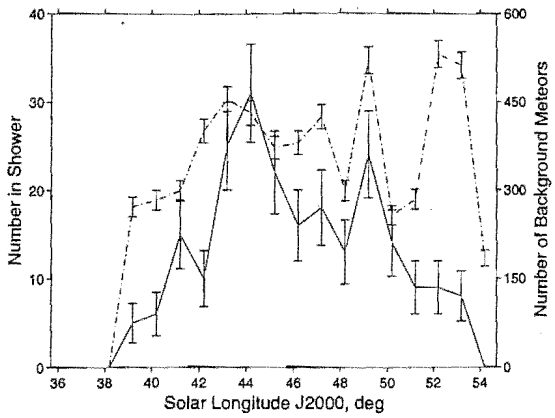

(a) T1995

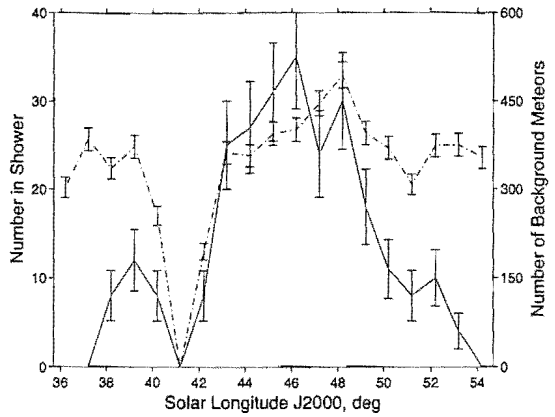

(b) T1996

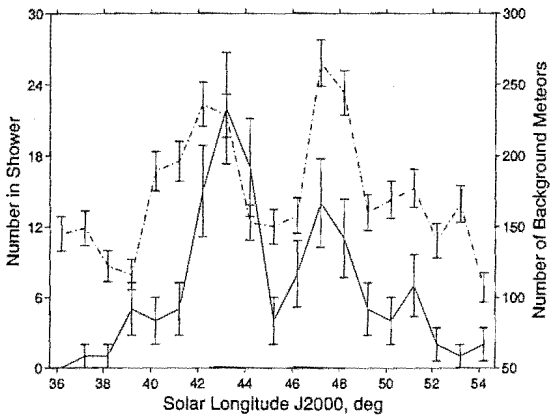

(c) T1997

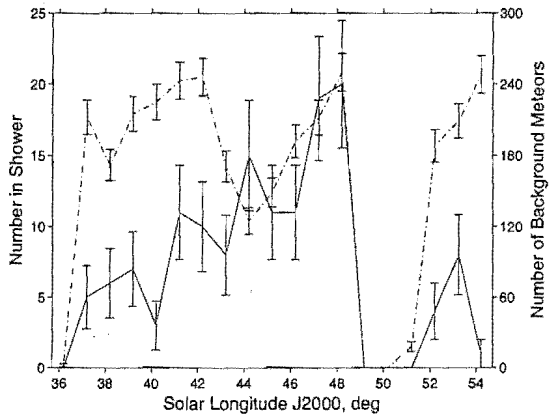

(d) T1998

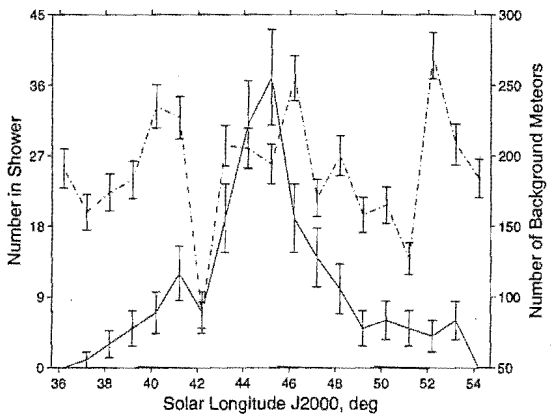

(e) T1999

Figure 8.10: The distribution in time of the ETA meteors for each year from T1995 to T1999. These distributions all use the same shower centring which begins at $\lambda_\odot = 38.2°$ and moves forward in 1° increments.The change in shower rate per degree of solar longitude is shown as a solid line while the change in the rate of all non-shower retrograde meteors over the same time-frame is shown as a dotted line. The statistical uncertainty, shown on each point, is given by $\sqrt{N}$. Note the use of two different y-axis systems for each graph.

region are underestimated and the apparent peak between 48° and 49° is likely to be a false maximum (as it occurs at the time of maximal background). AMOR was not operating for the last few days in T1998 further complicating interpretation. One should note, in both T1997 and T1998, the strong decrease in overall radar sensitivity compared with the previous years: this increases the chance of random noise having an influence on the shape of the profile.

The profile from T1999 is set against a constant background, with only a single 1° data point affected by AMOR inoperation. The resultant shower curve is particularly smooth and featureless with the rate increasing to a clear maximum between 43.9° and 45.9°. This is in contrast to curves, such as that for T1996, which appear to produce much broader maximum regions. There is indeed a general decline in the background count rate over the time of the shower, but this is hardly enough to have caused the very steep decrease after the maximum. It appears in T1999 that a particularly compact filament of the stream may have been detected. A physical interpretation of such a peak is that, it may be due to detection of a particularly new part of the stream, which has as yet had little time be perturbed. The parent body of the stream, Halley's Comet, approaches perihelion every 76 years and assuming the stream is replenished each time, it is quite possible that, in different years, meteoroids which were laid down in different passes might be detected. In fact, T1997 also shows a similar steep increase with the second peak being overemphasised, as explained earlier. It is very difficult to obtain conclusive evidence of such claims due to the instability of the background rate. An important project in the future would be to try and obtain highly stable, absolutely continuous operation of AMOR, throughout the full period of the shower. There are problems with this, at present, as we are near the maximum of the sunspot cycle and therefore experience much more interference on the radar system than previously.

When looking at Figure 8.9, it is interesting to note that in the discussion above, it has been assumed that the background bears no relation to the ETA shower. This is, at least to some extent, untrue. It is obvious that some of the background consists of bona fide members of the shower, as the discussions of uncertainty in the previous section show that the entire shower is not being selected at present. Should it be found that a major part of the background are in fact ETA meteors, then comparison against such a background can tell us nothing about the significance of shower peaks. Examples such as the peak at $\lambda_{\odot} = 47.6°$ appear to point to the truth of this argument, while the strongly differentiated peak against the pseudo-constant

background in T1999 argues oppositely. This is therefore an open question: perhaps with an increased PRF on the radar system the orbits would have sufficiently small uncertainties that it could be answered.

8.4 Southern δ Aquarids

The existence of the δ Aquarids has been known for some time. Originally it was thought that there was only a single branch of this shower to the south of the ecliptic, but more recently a northern branch has been detected. In the first radio observations of this shower, by McKinley (1954), both branches were recognised. He determined a mean in-atmosphere speed of 40.4 ± 0.1 km s^{-1} and a mean radiant position of $(\alpha, \delta) = (339° \pm 2°, -17° \pm 2°)$. He also noted two other similar radiant densities with the strongest being the northern branch located at $(340° \pm 5°, 0° \pm 5°)$. Both sessions of the Harvard Radio Meteor Project detect the δ Aquarids. Sekanina (1976), using his "statistical" search method, detects 70 meteors which he labels Southern δ Aquarids; he also detects the northern branch of this shower with 45 shower meteors. Nilsson (1964) also detects the SDA, however the northern branch does not appear to have been found in his data. Babadzhanov and Obrubov (1992b) show the δ Aquarids to be members of the meteoroid stream complex associated with comet 96P/Machholz.

Cook (1973), in his standard table of showers, lists a mean orbit for each of these showers, obtained from precise photographic records by McCrosky and Posen (1961). Mean orbital data obtained from this and other surveys is shown in Table 8.7. The orbits in this table are in close agreement with each other, but Cook's SDA right ascension value disagrees with most other sources, it is therefore ignored as discussed in Section 7.7.3. A typical value for the right ascension, as obtained from all other surveys, is 340°.

SURVEY	$\lambda_\odot$	q	e	i	ω	Ω	V_H	V_G	α	δ	SIZE
	deg	AU		deg	deg	deg	km s^{-1}		deg	deg	
S1976_S	126.4	0.069	0.958	28.2	155.4	306.4	33.9	38.2	342.5	-15.6	70
S1976_N	142.4	0.169	0.866	19.2	323.2	142.4	31.9	31.1	346.3	5.1	45
C1973_S	125.7	0.069	0.976	27.2	152.8	305.7	-	41.4	333.8	-16.3	-
C1973_N	139.7	0.07	0.97	20	332	139.7	-	42.3	339.6	-4.7	-
N1964_S	126.5	0.07	0.97	32.5	152.4	306.5	-	40.8	340.1	-17.0	48

Table 8.7: Mean orbital parameters of the δ Aquarids. The first two mean orbits are due to Sekanina (1976), gathered from data over the period 1961–1965; the second two are due to Cook (1973) and the last one is due to Nilsson (1964), from data collected in 1961. Note _N=northern and _S=southern branch. The original elements were referred to the mean epoch of B1950.0; these have been reduced to J2000.0 in this table for comparison with the AMOR data.

The table above, while by no means complete, gives a representative summary of the expected mean parameter values of the δ Aquarids. The δ Aquarids is a particularly interesting shower complex as it is strong, well defined and at the same time exhibits a peculiarly low perihelion distance which would be expected to cause the shower to undergo rapid perturbation. In the AMOR data only the southern branch of the shower is detected: while there are some meteors in the northern branch region these do not stand out sufficiently in order for detection to occur. The SDA complex is most active in the region of time $\lambda_{\odot} \in [120°,130°]$. It is the strongest shower detected by AMOR. The uncorrected radiant position centre is found to be located at $(\lambda_R, \beta) = (210.2°, -7.8°)$. As determined in Section 7.7.3, geocentric speed using the 1σ speed criterion level is defined by $V_G = 40.4 \pm 4.9$ km s^{-1}; the shower is taken to exist over the period $\lambda_{\odot} \in [114°, 145°]$.

The wavelet transform of part of the antihelion region under these definitions is shown in Figure 8.11(b). The SDA source is distinct with a surrounding negative region removing all links with the background. In order to ensure that the least dense regions of the SDA near the edges are as unaffected as possible by background intrusion, a 5% of the maximum WTC cutoff has been applied to Figure 8.11(b): the resultant wavelet transform is shown below the original. A scatter plot of all meteors found in this selected region, with speeds constrained by the 1σ speed criterion, is shown in Figure 8.11(a). This contains 2,405 meteors, in all, making this shower by far the strongest detected by AMOR.

8.4.1 Daily Motion of the Orbital Parameters

As with the ETA, there is daily motion in a number of the parameters. As the uncertainties on the parameters experiencing this motion are somewhat lower for the SDA, it is found to be possible to obtain acceptable linear fits to all elements of interest (recall that ω had such a large uncertainty for the ETA that a linear fit could not be found). The motion in q and ω is shown clearly in Figure 8.13(c); this is believed to be one of clearest examples of orbital element motion, shown thus far in the literature—due to the number of points involved, an excellent fit which is convincing to the eye is obtained. One may enquire of the reason for such a daily motion: it is easy to comprehend a radiant motion, but motion in the orbital elements themselves is more difficult to understand. For impact to occur on a number of different days, the measured heliocentric velocity components at impact must redistribute the overall speed. Figure 8.12 shows the Earth at two

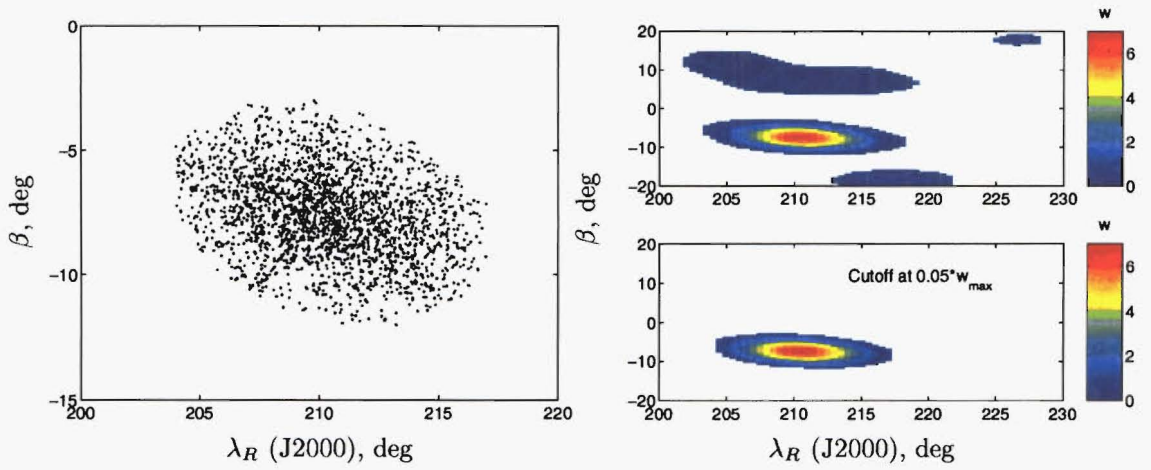

(a) Meteors Selected (b) Wavelet Transform

Figure 8.11: The antihelion region wavelet transform at the 1σ V_G criterion cutoff over the SDA shower active period. Meteors are selected which appear within the transform region defined by coefficients higher than 5% of the maximum WTC and with corresponding geocentric meteoroid speeds constrained by the 1σ criterion.

positions labelled 1 and 2 in its orbit about the Sun with a meteoroid stream shown based on the assumption of $i = 0°$. Using the coordinate system described in Section 2.5.2, the change in the velocity component distribution in the **x** and **y** directions, assuming a constant heliocentric meteoroid speed, is obvious between positions 1 and 2. Should the orbit have a non-zero inclination then there will be an additional component into or out of the page in Figure 8.12. The orbital elements are based on the radial and angular velocity which are defined by $V_r = -V_y$ and $V_\nu^2 = V_x^2 + V_z^2$ respectively. As neither of these measures contain all three velocity components, the changes over time will affect both V_r and V_ν, which due to their relation to the orbital parameter (p) via equation 2.6 and to the true anomaly (ν) via equation 2.7, will in turn affect q, e, a, ω which rely on these parameters (equations 2.9, 2.10 and 2.11). The inclination angle may also be affected as it is defined directly in terms of V_z and V_x (equation 2.13): it is unlikely for this angle to change by much as, generally, the motion is in both V_x and V_z with little overall change in their ratio. The eccentricity is not normally observed to experience much change but this may be simply due to the large uncertainties in eccentricity, for most showers, which would act to preclude measurement of such a motion. By performing weighted least-squares linear fits to the data the daily motion values for all orbital elements are obtained as listed in Table 8.8 and as illustrated, for selected parameters, in Figure 8.13.

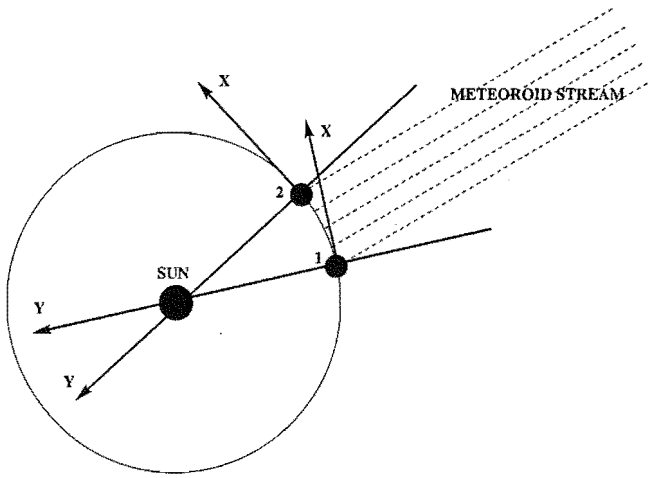

Figure 8.12: Model of stream detection on Earth. Here the Earth is shown at two positions (1 and 2) passing through a wide meteoroid stream (shown here parallel to the ecliptic).

Parameter	$d/d\lambda_\odot$	Unit
q	$(2.04 \pm 0.04) \times 10^{-3}$	$\mathrm{AU\,deg^{-1}}$
e	$(-3.1 \pm 0.7) \times 10^{-4}$	$\mathrm{deg^{-1}}$
i	$(-2.1 \pm 0.2) \times 10^{-1}$	-
ω	$(-4.24 \pm 0.08) \times 10^{-1}$	-
V_G	$(-1 \pm 1) \times 10^{-2}$	$\mathrm{km\,s^{-1}\,deg^{-1}}$
V_H	$(9.5 \pm 0.6) \times 10^{-2}$	$\mathrm{km\,s^{-1}\,deg^{-1}}$

Table 8.8: The daily motion of the orbital parameters of the SDA shower meteoroids over the active period of the shower.

The daily motion in q, ω and i (see Figure 8.13 for visual confirmation) is large enough to be significant while that in speed and e is unimportant. The V_G daily motion is found to be both minor and of a similar magnitude to the measurement uncertainty, this is not so for V_H where the magnitude of the daily motion is an order of magnitude larger and therefore much more reliable relative to the uncertainty. The eccentricity daily motion is very small, however for consistency, eccentricity and all of the other parameters are corrected for daily motion. Correction to the central $\lambda_\odot^c = 125°$ point (approximately the centre of the region of maximum rate of the shower) is made for each parameter, P, using the approach of equation 7.9, with $dP/d\lambda_\odot$ as listed in Table 8.8.

Correction of the radiant position for daily motion reveals 2,413 meteors to be shower members at the 5% cutoff level. It is useful to review the wavelet-determined daily radiant motion of Section 7.7.3 using these data. Figures 8.13(a) and 8.13(b) show this motion in the case of both the ecliptic and equatorial coordinate systems respectively. As with the ETA, the motion in position is in both coordinates in the

case of the equatorial system and in only one coordinate for the ecliptic system. The motion in the ecliptic system, obtained by weighted least-squares fitting, is described by

$$\begin{aligned} \lambda_R &= (-1.95 \pm 0.05) \times 10^{-1} \lambda_\odot + (234.7^\circ \pm 0.6^\circ) \\ \text{and} & \\ \beta &= (-4.2 \pm 0.2) \times 10^{-2} \lambda_\odot - (2.3^\circ \pm 0.3^\circ). \end{aligned} \tag{8.5}$$

The equatorial coordinates, more commonly used, have a motion defined by

$$\begin{aligned} \alpha &= (7.31 \pm 0.05) \times 10^{-1} \lambda_\odot + (248.9^\circ \pm 0.6^\circ) \\ \text{and} & \\ \delta &= (2.61 \pm 0.02) \times 10^{-1} \lambda_\odot - (48.9^\circ \pm 0.3^\circ). \end{aligned} \tag{8.6}$$

The longitudinal motion is significantly different (assuming the 0.02 unit-less stability value determined in Section 8.2) from that for equation 7.10, where a daily motion of -0.34 was observed. The present method is inherently better due to its inclusion of measurement uncertainties and a greater number of points and is therefore preferred; it is easy to imagine how the fit obtained from Figure 7.11 might change if any of its data points were to shift by a small amount. The measured motion is closer to that of Cook (1973), where the daily radiant motion of the SDA is given as $+0.8$ in right ascension and $+0.18$ in declination. Two more recent standard sources for meteor shower information, Rendtel et al. (1995) and Kronk (1988), each state a radiant motion of $+0.9$ in right ascension and $+0.4$ in declination. While the daily motion shown in equation 8.6 significantly differs from these published values, assuming the stability/measurement uncertainties of Section 8.2, the disagreement is no worse than that between these values themselves. Cook's radiant motion is obtained from 13 meteors, Rendtel and Kronk obtain their motion from a (presumably) small number of photographic meteors; the AMOR data is obtained from approximately 2×10^3 meteors hence it is more likely that the present data is more accurate, at least for radar meteors.

8.4.2 Statistics

The statistics of the 2,413 SDA meteors recorded from T1995 to T1999 are given in Table 8.9; the histograms of the various parameters are shown in Figure 8.15 for ref-

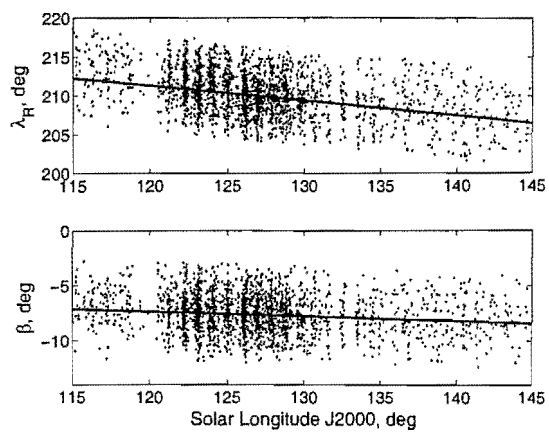

(a) Radiant Daily Motion (Ecliptic)

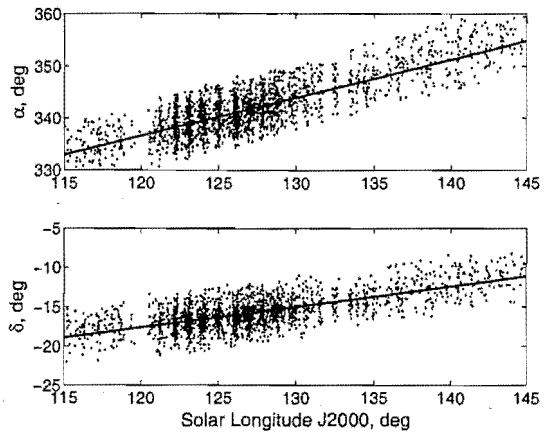

(b) Radiant Daily Motion (Equatorial)

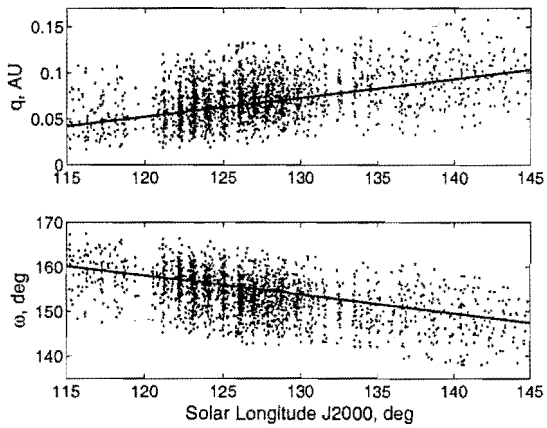

(c) Daily Motion in q and ω

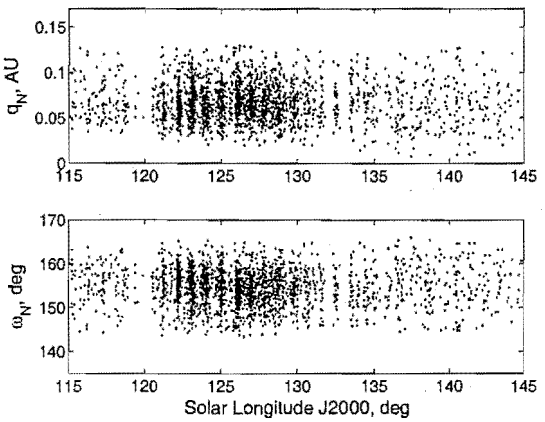

(d) Reduction of q and ω to $\lambda_\odot^c = 125°$

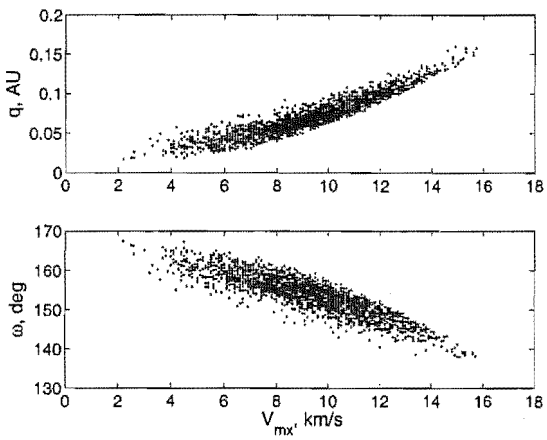

(e) The link between q, ω and V_x

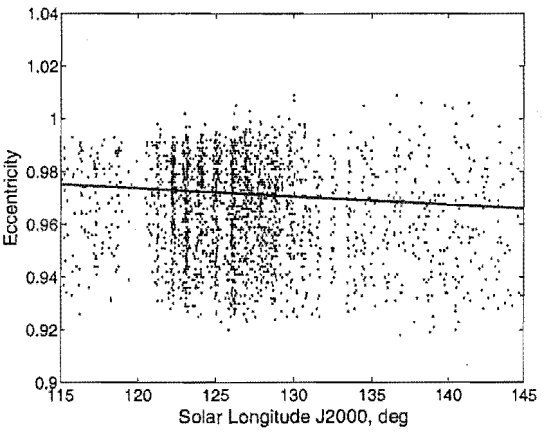

(f) Minor Daily Motion in Eccentricity

Figure 8.13: Motion of the mean orbital parameters of the SDA over the period of the shower. Note that the fitted lines do not appear to be correctly centred, in some cases, due to the increased uncertainties at higher q and lower ω respectively biasing the fitting routine. The median Δq is 0.014 AU for $q_N < 0.07$ AU and 0.019 AU for $q_N > 0.07$ AU; the median $\Delta\omega$ is 3.2° for $\omega_N < 155°$ and 2.2° for $\omega_N > 155°$. The median uncertainties in the radiant position coordinates are 2.5° in λ_R; 0.6° in β; 2.5° in α and 0.6° in δ.

YEAR		$\lambda_\odot$ deg	q AU	e	i deg	ω deg	Ω deg	V_H km s^{-1}	V_G km s^{-1}	α deg	δ deg	SIZE
ALL	$\overline{x}$	127.2	0.067	0.966	30.8	154.5	307.2	36.0	40.2	340.4	-16.3	2,413
	s.d.	5.8	0.021	0.018	9.8	4.1	5.8	2.3	2.7	2.9	1.5	
	s.e.	0.1	0.000	0.000	0.2	0.1	0.1	0.0	0.1	0.1	0.0	
	Unc.	0.0	0.015	0.023	9.0	2.8	0.0	2.7	3.4	2.5	0.6	

Table 8.9: Statistics of all SDA from T1995–T1999 at the 1σ V_G criterion level. The parameters experiencing a daily motion, apart from $\lambda_\odot$ and Ω, are corrected to $\lambda_\odot^c = 125°$; all parameters are referred to the J2000.0 epoch. The medians of the individual uncertainty distributions are used to provide representative values.

erence. The spread in the various parameters is shown to slightly exceed their uncertainties. This compares with the opposite situation, in the case of the ETA, where the uncertainties are so large that is impossible to retrieve the whole shower distinctly from the background. Of particular note here, are the large spread/uncertainty in i, in contrast to much smaller amounts in the other elements. For most shower observations the inclination is found to be the most stable element, both physically and observationally, while ω is found often to have uncertainties exceeding 10°. The reason for this unexpected result for the SDA lies in the fundamental heliocentric velocity components, which are used to define ω and i. The inclination angle is defined in equation 2.13 with respect to V_x and V_z; the uncertainty in i (in degrees) follows from this:

$$\Delta i = \left(\frac{180°}{\pi}\right)\left(\frac{(V_z/V_x)}{1+(V_z/V_x)^2}\right)\sqrt{\left(\frac{\Delta V_x}{V_x}\right)^2+\left(\frac{\Delta V_z}{V_z}\right)^2}. \qquad (8.7)$$

The median V_z/V_x ratios for ETA and SDA are 0.27 and 0.56 respectively. Representative (median) percentage uncertainties for the ETA are given by 18% for V_x and 17% for V_z, while those for the SDA are given by 18% for V_x and 16% for V_z. Inserting these values into equation 8.7 yields inclination uncertainties of 10° and 4° for the SDA and the ETA respectively. These values are in good agreement with the representative uncertainties in this parameter as given in Tables 8.3 and 8.9.

ETA meteors would normally be expected to have much greater uncertainties in all elements due to their high geocentric speed. However, in the case of inclination they have a small uncertainty owing to the large magnitude of $V_x \approx -30$ km s^{-1} relative to $V_z \approx -8$ km s^{-1} which leads to a comparatively small V_z/V_x ratio. In contrast both velocity components are small and of similar size for the SDA ($V_x \approx 9$ km s^{-1} and $V_z \approx 5$ km s^{-1}) yielding a larger ratio and thence a higher uncertainty. Note that the percentage uncertainties in the velocity components

are very similar for the SDA and ETA even though the former have lower absolute uncertainties, due to the lower speeds. This unusual case, in which the ETA is better defined than a prograde stream, does not continue for uncertainties calculated on most other elements (q and ω particularly are not susceptible to small speed components): in these cases the smaller the speed component, the better, as the uncertainty in the measurement will also be less due to longer time-lags between stations.

It is unfortunate that the inclination angle should be so ill-defined for a shower which is in most other respects defined reasonably accurately by AMOR. This angle is normally expected to be the most physically stable element, while others such as shape and size parameters are rapidly perturbed by the planets. This presents a good case for increasing the pulse repetition frequency of the AMOR transmitter: an increased PRF will lead to more accurate time-lag measurements and therefore lower uncertainties in the heliocentric velocity components.

The mean dissimilarities of the SDA (as identified in Table 8.9) are given by $\overline{D}_{SH} = 0.26$, $\overline{D}_D = 0.21$ and $\overline{D}_N = 0.21$. These values are all rather high, although lower than those of the ETA, because of the large uncertainty-based spread in the normally tightly distributed inclination angle. It is not useful to proceed to 2σ speed criterion levels, as was done in the case of the ETA, as the uncertainties are already similar to the spread and the mean dissimilarity functions argue against further increase. Figure 8.15 also argues against any loosening of the geocentric speed constraints; the distribution in the latter parameter is found to be relatively "flat", it is likely that many more sporadic meteors, than in the case of the ETA (which have a definite distribution peak), would be added at increased speed range.

On comparison of the mean combined-year stream orbit of Table 8.9 with the published mean orbits of Table 8.7, one obtains good agreement. Using the Southworth and Hawkins' D-criterion to facilitate this comparison, D_{SH} values of 0.05, 0.08, 0.06 are obtained with the SDA orbits listed (in that order). The closest means are those obtained by Sekanina (1976) from 70 radar orbits and Nilsson (1964) from 48 radar orbits. The mean orbit of Cook (1973) also gives very satisfactory agreement, the small increase in dissimilarity being mainly due to the (minor) lower inclination and argument of perihelion values compared with those obtained by AMOR. Comparison of the current mean stream orbit against those obtained using the single-linkage (Table 7.3) and modified single-linkage method (Table H.4 1995 mean) yields good agreement, with dissimilarities of 0.07 and 0.08 found respec-

tively. Note that the latter dissimilarity is actually lower than that for the ETA shower comparison: it appears the SDA is marginally more method-dependent than is the ETA.

YEAR		$\lambda_\odot$ deg	q AU	e	i deg	ω deg	Ω deg	V_H km s^{-1}	V_G km s^{-1}	α deg	δ deg	SIZE
1995	$\overline{x}$	127.9	0.065	0.968	32.2	154.9	307.9	36.2	40.5	340.7	-16.3	763
	s.d.	6.2	0.021	0.018	10.1	4.2	6.2	2.3	2.7	2.9	1.5	
	s.e.	0.2	0.001	0.001	0.4	0.2	0.2	0.1	0.1	0.1	0.1	
	Unc.	0.0	0.017	0.023	10.9	3.1	0.0	2.6	3.6	2.5	0.6	
1996	$\overline{x}$	126.4	0.068	0.966	30.7	154.3	306.4	36.1	40.2	340.2	-16.4	743
	s.d.	4.6	0.020	0.018	9.5	4.0	4.6	2.3	2.7	2.8	1.4	
	s.e.	0.2	0.001	0.001	0.3	0.1	0.2	0.1	0.1	0.1	0.0	
	Unc.	0.0	0.014	0.023	9.1	2.7	0.0	3.0	3.4	2.8	0.7	
1997	$\overline{x}$	127.6	0.069	0.963	28.7	154.5	307.6	35.7	39.6	340.2	-16.1	266
	s.d.	6.6	0.021	0.018	8.6	4.1	6.6	2.2	2.6	2.7	1.5	
	s.e.	0.4	0.001	0.001	0.5	0.2	0.4	0.1	0.2	0.2	0.1	
	Unc.	0.0	0.015	0.022	7.1	2.5	0.0	2.6	3.3	2.3	0.6	
1998	$\overline{x}$	129.1	0.068	0.964	30.6	154.6	309.1	35.8	39.9	340.5	-16.3	367
	s.d.	7.4	0.023	0.019	10.0	4.3	7.4	2.3	2.8	2.9	1.6	
	s.e.	0.4	0.001	0.001	0.5	0.2	0.4	0.1	0.1	0.2	0.1	
	Unc.	0.0	0.016	0.023	7.4	2.7	0.0	2.7	3.1	2.3	0.7	
1999	$\overline{x}$	124.1	0.069	0.965	29.7	154.2	304.1	36.1	40.1	340.0	-16.2	274
	s.d.	1.8	0.021	0.018	10.0	4.1	1.8	2.2	2.8	2.7	1.5	
	s.e.	0.1	0.001	0.001	0.6	0.2	0.1	0.1	0.2	0.2	0.1	
	Unc.	0.0	0.016	0.023	9.1	2.7	0.0	2.8	3.5	2.5	0.6	

Table 8.10: Statistics of all SDA from T1995–T1999 (individual years) at the 1σ V_G criterion level are presented. All parameters experiencing a daily motion, apart from $\lambda_\odot$ and Ω, are corrected to a centre at $\lambda_\odot^c = 125.0°$; all parameters are referred to the J2000.0 epoch. The medians of the individual uncertainty distributions are used to provide representative values.

If one examines each year separately one finds, as has already been found for the ETA, that the numbers of meteors both in the background and in the shower are lowest in T1997–98. As shown in Table 8.10 the total number of shower members recorded in these two years is actually less than that recorded in either T1995 or T1996. The mean orbital parameters show differences within standard errors from year to year in T1995–98 apart from the mean longitude of the ascending node and the Sun which show variations mainly related to AMOR system operation. Most of the parameters show a spread consistent with the individual measurement uncertainties listed. But, as with the ETA, the spread in the declination angle clearly exceeds that expected from measurement uncertainties.

The observed radiant position and heliocentric speed parameter means are compared using the Student's t-test, as discussed in Section 8.3.2. The results from this test are shown in Figure 8.14. In the α and δ parameters it is seen that only T1995 differs significantly from other years while in δ and β disagreements between T1997

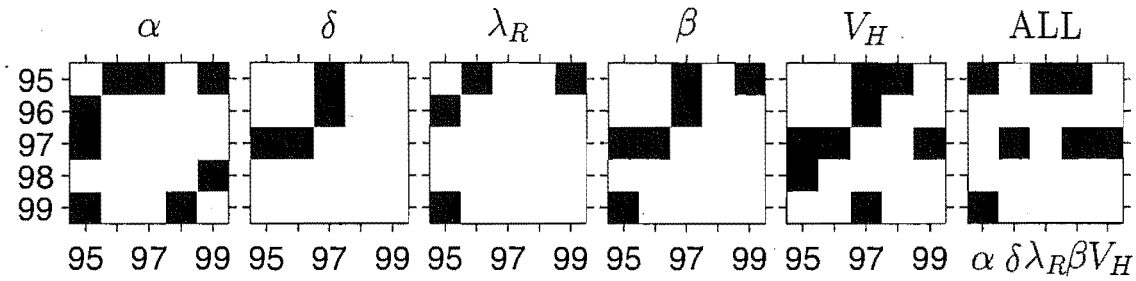

Figure 8.14: Student's t-test of inter-annual agreement of SDA parameter means. The means of five parameters for a series of years are inter-compared in the first five figures; the sixth "ALL" figure shows comparisons between these yearly means with the means obtained from all years of data combined. White squares signify agreement between parameter means at the 95% confidence level while black squares indicate disagreement. All parameters are corrected for daily motion.

and the T1995 and T1996 pair are the only major points of note. In heliocentric speed only the T1997 mean, with a particularly low mean value of 35.7 $\mathrm{km\,s^{-1}}$, is found to be disagreeable to most other years with a particularly low mean value of 35.7 $\mathrm{km\,s^{-1}}$. In the combined mean comparison with the single-year means T1996, T1998 and T1999 can be seen to agree well while those from T1995 and T1997 disagree on several parameters each. As with the ETA tests of Figure 8.7, it is apparent that many of the years present annually repeatable mean parameter values while some parameters in some years (e.g. T1995 α) differ significantly from those of other years. Again the instances of significant differences between the yearly means and those obtained from the combined years raises concerns as to the level to which the "exact" shower mean can be known. It is apparent from Table 8.10 that the SDA shower as defined has a spread approximately equal to that expected from measurement uncertainty hence the instability explanation used for the ETA cannot be used here; additionally the number of meteors detected in the SDA shower is the highest for any AMOR shower, therefore instability due to a small sample argument may not be used either.

It would appear then that in the yearly comparisons in which significant differences have been noted above there must be a "real" physical difference between some shower apparitions. This explanation is quite plausible due to the random and unique character of each meteor observation. There is however an alternative explanation which is equally plausible; it has been assumed that the daily motion obtained for the combined data set is valid for each year and that the measurement of this motion is accurate—if either of these assumptions were wrong, even by a small amount, then the small changes in radiant and speed parameters would easily be explained by minor changes in coverage of shower period in the different years.

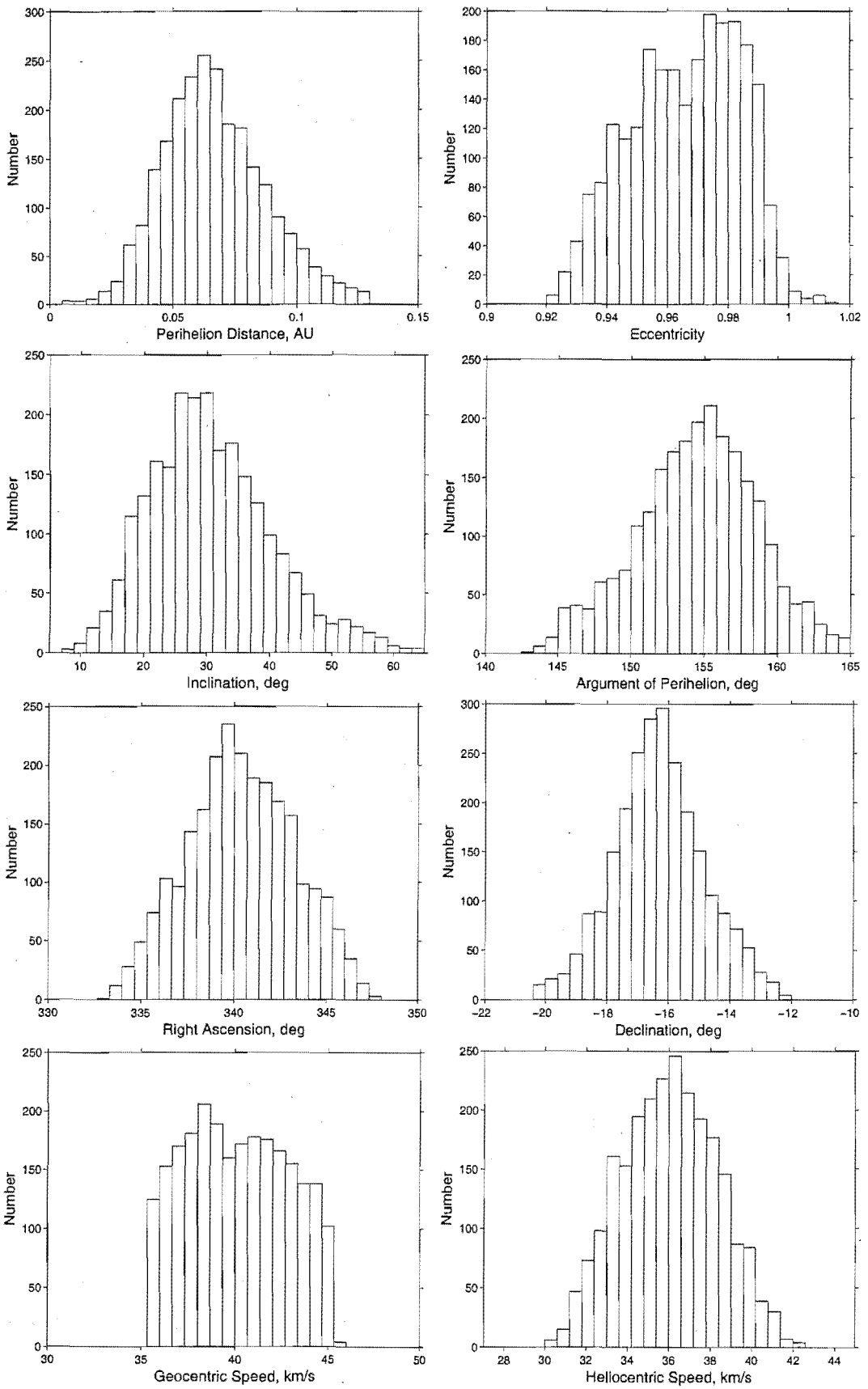

Figure 8.15: Histograms of the orbital parameters of the SDA shower for T1995–T1999. Note that the daily motion corrected values of q and ω have been used to produce "stationary" distributions in these elements.

Almost all of the SDA meteors share a common declination uncertainty of 0.6° and, as shown in Figure 8.15, the distribution in this parameter is a smooth "Gaussian". Hence, by using equation 8.1, one can calculate the physical spread in the data, to be $\sigma_p = 1.4°$; i.e. in this case most of the measured spread is due to the physical spread and not to the uncertainty. Applying this approach, to the argument of perihelion, which is in a similar position, leads to a physical spread of $\sigma_p = 3°$. In order to encompass the likely spread in the speed distributions however, due to uncertainty it is apparent that a wider geocentric speed range would need to be allowed. This has not been attempted, as noted previously, for fear of including outliers in the orbital population.

An Example of the Importance of Daily Motion Correction

YEAR		$\lambda_\odot$ deg	q AU	e	i deg	ω deg	Ω deg	V_H km s^{-1}	V_G km s^{-1}	α deg	δ deg	SIZE
EARLY	$\overline{x}$	123.0	0.062	0.967	32.1	155.7	303.0	35.8	40.4	339.0	-16.7	778
	s.e.	0.0	0.001	0.001	0.4	0.1	0.0	0.1	0.1	0.1	0.1	
LATER	$\overline{x}$	127.3	0.073	0.966	29.8	153.1	307.3	36.5	40.3	341.8	-15.9	996
	s.e.	0.0	0.001	0.001	0.3	0.1	0.0	0.1	0.1	0.1	0.0	

Table 8.11: A demonstration of the dependence of shower statistics on the time-coverage of the survey. Statistics of the two sets of T1995–T1999 measured SDA orbits which are based on the original single set which has been split into an early shower segment ($\lambda_\odot \in [120°, 125°)$) and a later segment ($\lambda_\odot \in [125°, 130°]$). Parameters experiencing daily motion are not corrected to remove this.

Due to the correction for parameter daily motion, annual differences in q and ω, which can show up in uncorrected data sets due to uneven time-coverage, do not appear in Table 8.10. In particular, T1999 which boasted a truncated shower period due to the termination of the data set, had a clearly lower perihelion distance and a higher argument of perihelion than for other years, until this was corrected. It is interesting to see the effect this time dependence can have on the data and to this end the full five year data set has been split into two subsets about the time of shower maximum: one subset is based on meteors detected from $\lambda_\odot \in [120°, 125°)$ and the other is based on those from $\lambda_\odot \in [125°, 130°]$. The statistics of these subsets are presented in Table 8.11. Here the changes in q, ω and i are different within the bounds imposed by standard errors: there is also a clear increase in heliocentric speed which is expected to change slightly over time and, of course, the uncorrected radiant position makes its well known daily motion during this time hence the change in α and δ. The slightly disturbing fact is that most observing

programs have lower stream orbit detection rates than AMOR. This is particularly true of radar observations, which have already been noted to have significantly large uncertainties. Many of the early programs only had their systems active for a few hours per week due to data reduction constraints; when one combines such "holes" in the shower coverage with the uncertainties in the data the quality of the mean orbit as published, is degraded.

8.4.3 Activity Profiles

As with the ETA, it proves interesting to look at the shower activity profiles of the SDA. A careful selection of daily cutoff points must again be made, in order to avoid the introduction of artifacts into these curves. Figure 8.16 shows the determined points with bin edges offset from zero by 0.6°, 0.35°, +0.1°, −0.15° and 0.6° for years T1995–T1999 respectively. This scheme generally works well, however in the later period of the shower, in some years, one can see the boundaries cutting into the middle of some daily distributions. This is unavoidable, with a solar longitude based system, and relates to the time the shower spends above the horizon changing over the month-period of the shower. This problem is also related to the difference in range between the 360° solar longitude and the 365/366 day year so that one should really increment $\lambda_\odot$ by $\approx 0.98°$ rather than by 1°, especially over extended periods, to prevent an accumulation of offset. It is judged in the current study that the concerns mentioned previously and the difficulty in defining an absolute offset at the start are more likely to blame for the centring problem. The SDA is more difficult in this regard than the ETA as the latter has a very narrowly defined daily time-span of activity due to its apex source direction, while the antihelion region from which the SDA emerges, spends more time above the horizon therefore making minor boundary changes potentially more difficult to deal with.

The activity profiles for the SDA are shown in Figure 8.17. As with the ETA these curves benefitted greatly from the use of correct bin centres for the different years. There is an obvious peak in most of the graphs over the period $\lambda_\odot \in [120°, 130°]$; in many cases this peak is accentuated by equipment non-operation in the period; surrounding this, AMOR appears to have had "difficulties" in operation between 115° and 120° and over the period between 130° and 135° in most years—these gaps in the data set are due to the emphasis on coverage over the most active period of the SDA with maintenance schedules being suspended for execution in the times immediately preceding and/or succeeding this period. The background rate is

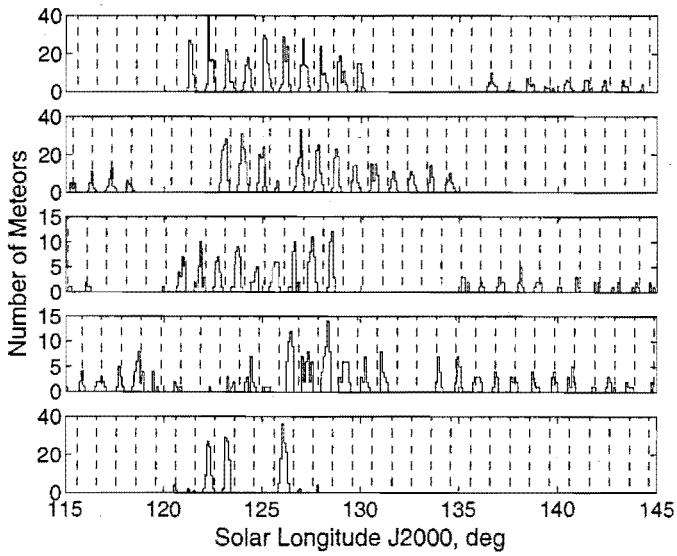

Figure 8.16: The relationship between solar longitude and detection time period for the SDA. The distribution shifts by $\approx 0.25°$ per year. Appropriate cutoff points are shown at offsets from zero $\lambda_\odot$ of 0.6°, 0.35°, +0.1°, −0.15° and 0.6°, for years T1995–T1999 shown from top to bottom respectively.

provided from all prograde meteoroids unidentified as SDA appearing between 2300 and 0600 NZST, a period corresponding to the time range of the shower detection.

The T1995 activity profile is almost a square wave over $\lambda_\odot \in [120.1°, 131.1°]$. There is a decline at the 123.1° and 124.1° points which corresponds to a smaller general background decline; the proportionally larger impact on the shower population is attributed to the spike at 121.1° which artificially raises the level of the shower in the vicinity. There appear to be two average levels in $\lambda_\odot \in [120°, 130°]$, one operating at approximately 75 and the other at 50 meteors per degree. The lower points do tend to follow the background but as discussed these are rather stronger than one would expect.

In T1996 the curve is well defined with a reasonably steady background. One could imagine a smooth curve rising to a peak at $\lambda_\odot \approx 125°$ and falling to a background level at $\pm 10°$ here. The data support a reasonably flat plateau from 122° to 129° and then falling from 130° onwards; no firm conclusions can be reached based on the earlier part. T1997 presents the major part of the shower over $\lambda_\odot \in [120.6°, 129.6°]$ with equipment non-operation for 5° after that. The shower and background rates, as previously noted, are very low in T1997 and T1998: on average they are about one-half or one-third of those in T1995–T1996. Over the period $\lambda_\odot \in [120.6°, 124.6°]$, there are no fluctuations in rate outside the bounds allowed by statistical uncertainties; at $\lambda_\odot = 125.6°$ the rate decreases outside statistical

uncertainty bounds from the previous bin centre, this occurrence corresponds to an increase in the background rate. The activity decrease is small so that additional years of data are needed to confirm if there is anything physically happening: most other years show no such fluctuation at this solar longitude. There is also a clear peak in the data at 128.6° but this follows the background distribution exactly and hence is defined as an artifact of the radar sensitivity change. The various peaks occurring after 135° are also judged uninteresting according both to their close adherence to the background trends and to their overlapping error bars.

The activity profile in T1998 appears at first to be interesting as there is only a strong peak from 125.4° to 130.4°. Such an occurrence obviously has implications for orbital statistics, when parameters experiencing a daily motion are not corrected, as discussed previously and demonstrated in Table 8.11. The background shows large-scale fluctuations which fit much of the shower structure seen. The periods $\lambda_{\odot} \in [119.8°, 125.9°]$ and $\lambda_{\odot} \in [132.9°, 134.9°]$ show unstable or non-operation of the radar, with a very low background count generally being achieved. In the 3° period in which the peak occurs, it appears that the $\lambda_{\odot} = 126.9°$ shower amplitude, is overstated due to a large background increase. The next two points, in this region, show a plateau which rises above the limits expected by degree-point statistical uncertainties. The later solar longitudes from $\lambda_{\odot} = 135°$ onwards do not show interesting structure with an average rate of approximately six per degree.

The coverage in T1999 is so sparse that little can be said about it. There are only 3° of solar longitude over which the radar was active. One can notice here though that over these points the rate has increased appreciably on the downward trend of T1998–T1999. In fact the $\lambda_{\odot} = 126.1°$ count-rate is the highest in any graph and it is entirely possible that if the coverage were better, this might have been the highest rate shower detection of the past five years.

In summary, one can easily determine the region of the maximum rate from these graphs as lying in $\lambda_{\odot} \in [120°, 130°]$. Due to coverage difficulties and sensitivity changes, it is difficult to determine the shape of the activity profile from these data. Most "spikes" in the data are found to be artifacts of the background. The data from T1996 presents the possibility of fitting a smooth curve extending $\pm 10°$ from the centre. T1995 and T1997 would support this model. T1999 would fit within the model however there are so few points, that any model would fit such data. T1998 is more unusual partly due to the large fluctuations in background rate so this would support the model proposed: however the curve would fit better if extended across

the whole time series shown.

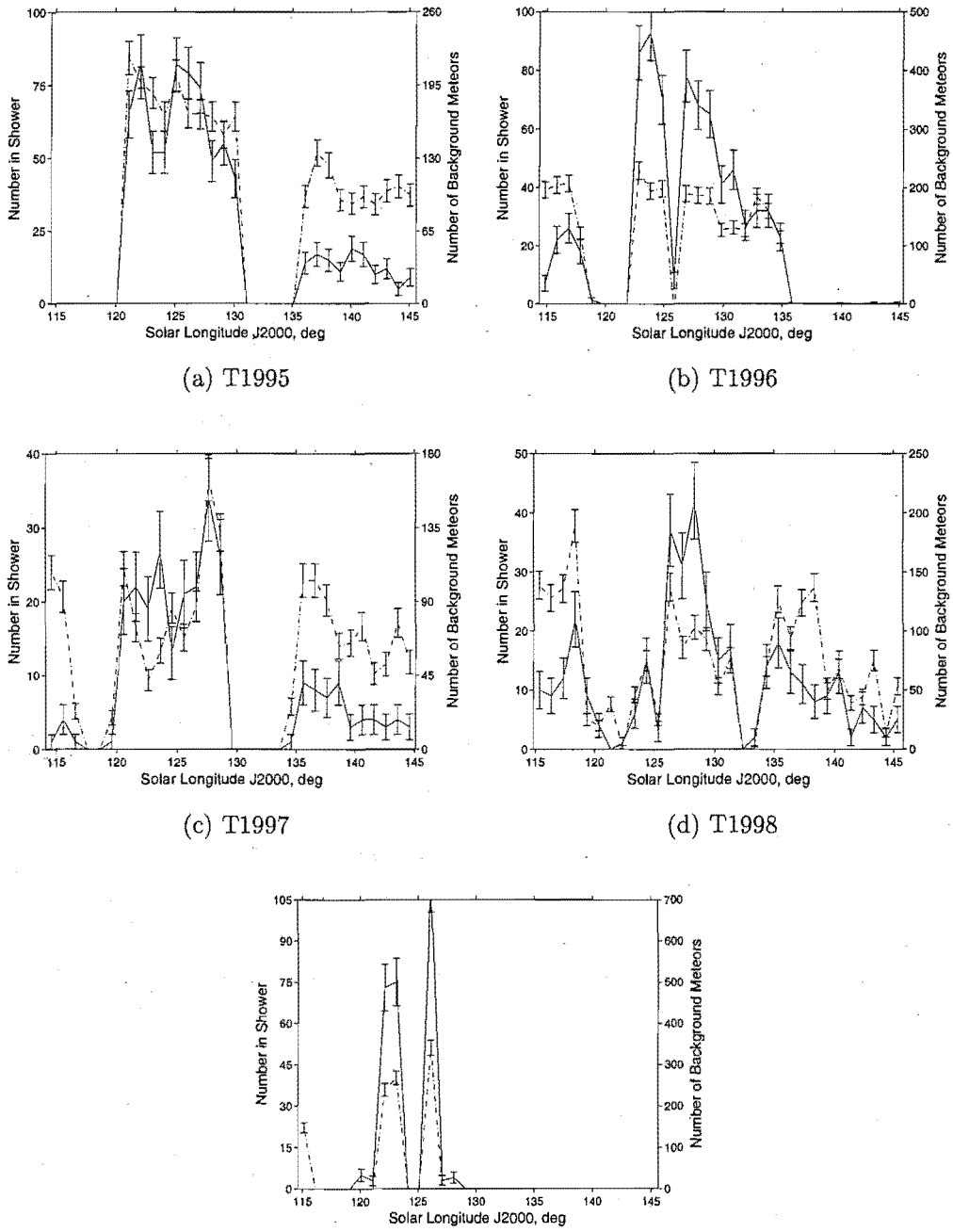

(a) T1995 (b) T1996

(c) T1997 (d) T1998

(e) T1999

Figure 8.17: The distribution in time of the SDA meteors for each year from T1995 to T1999. Bin centres offset from 0 by 0.10, −0.15, −0.40, 0.35 and 0.10 in solar longitude are used for the years T1995–T1999 as per Figure 8.16. The change in shower rate per degree of solar longitude is shown as a solid line while the change in the rate of all non-shower retrograde meteors over the same time-frame is shown as a dotted line. The statistical uncertainty, shown on each point, is given by $\sqrt{N}$. Note the use of two different y-axis systems for each graph.

8.5 α Capricornids

The CAP shower is active at the same time as the SDA, but in a different region of the antihelion source area. According to Kronk (1988) it is believed that this shower was originally discovered visually in 1871 in Hungary. It has been well known since that time. The short-period comet 45P/Honda-Mrkos-Pajdušáková is believed to be the parent body of this shower (Ceplecha et al. 1998).

As Cook (1973) notes, it is generally impossible to distinguish visually between the CAP and the SDA, as their radiant positions are simply too close together. Therefore many meteors identified as CAP may in fact be SDA and vice versa. The latter is an order of magnitude higher in activity than the former so it is most likely that it will dominate. Kronk (1988) presents three different possible streams

SURVEY	$\lambda_\odot$ deg	q AU	e	i deg	ω deg	Ω deg	V_H km s^{-1}	V_G km s^{-1}	α deg	δ deg	SIZE
KI	129.3	0.497	0.785	7.8	266.5	129.3	-	-	-	-	17
KII	142.6	0.582	0.780	1.1	268.1	142.6	-	-	-	-	5
KIII	122.9	0.573	0.723	5.4	272.2	122.9	-	-	-	-	7
W1960	127.7	0.59	0.77	7	269	127.7	-	22.8	307.7	-9.8	-
S1973	147.5	0.630	0.659	0.9	267.2	147.5	35.6	18.8	327.1	-11.7	20
S1976	137.3	0.620	1.920	6.1	267.9	137.3	35.8	19.7	315.5	-6.9	44

Table 8.12: Mean orbits of the CAP as published by Kronk (1988) (first three), Weiss (1960) (fourth entry), Sekanina (1973) (fifth entry) and Sekanina (1976) (last entry). Originally the elements were referred to the mean epoch of B1950.0; they have been reduced to J2000.0 for comparison with the AMOR data in this table.

determined from various photographic data sets: these differ mainly in the longitude of the ascending node of the shower, but also, in particular, on the inclination angle value which falls as low as 1.1° in one stream and is as high as 7.8° in another. The Harvard Radio Meteor Project also detected this shower during its two sessions (Sekanina 1973 and 1976 respectively): the orbital elements, as shown in Table 8.12, differ markedly between the sessions with the inclination angle once again having a particularly large range. It is interesting to note the changes in the shower mean orbits between the different surveys: it is possible that the shower structure differs between the photographic and radar sized parts of the stream structure. However the orbit provided by Weiss (1960), obtained from the Adelaide radar system, agrees much more closely with the photographic mean orbits than with the Harvard radar orbits—thereby nullifying this point to some extent. The CAP inherently exhibits low uncertainties on the orbits, including those given by the Radio Meteor Project—hence orbital uncertainties may not be blamed for such differences.

The CAP is defined by very slow meteors which appear from a region very close to the exact antihelion position. It occurs at the same time as the SDA shower but is separated sufficiently in speed and radiant position to be distinguishable. This is unlike the case of the ι Aquarids which is indistinct in the SDA region. The radiant position of the CAP is found in Section 7.7.3 to be $(\lambda_N, \beta) = (181.8°, -9.2°)$, as referred to the centre of the active period $\lambda_\odot \in [107°, 131°]$. The geocentric speed using the 1σ cutoff criterion is found to be defined by $V_G = 23.4 \pm 3.1$ km s^{-1}. Under these constraints the wavelet transform of the central core of the shower is obtained, as shown in Figure 7.13. The wavelet transform of the shower region is again shown in Figure 8.18(b) but here a cutoff level set at 12% of the maximum WTC is used to separate the shower clearly from the surrounding background. This separation, while clear, is not as globally distinct as that in other showers discussed in this chapter—where the use of such a high cutoff level would remove almost all traces of the background from the figure.

There are 263 shower meteors within the selected region between T1995–T1999, i.e. on average approximately 40–50 per year. The distribution in radiant of these points is shown in Figure 8.18(a) with an uncorrected centre at $(\lambda_R, \beta) = (181.8°, -9.2°)$. This shower is the weakest of any of the showers clearly detected by AMOR and as such presents a lower limit to the shower strength needed for detection.

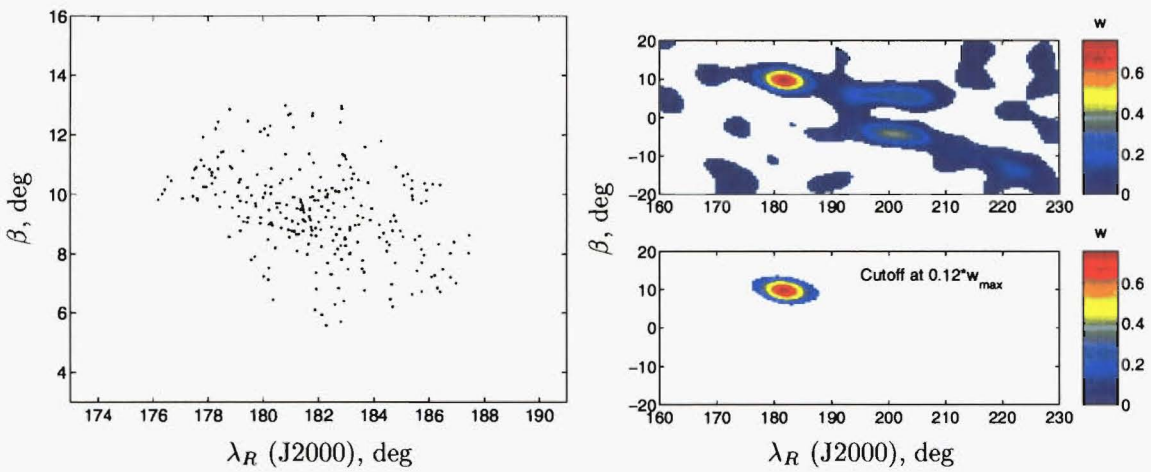

(a) Meteors Selected

(b) Wavelet Transform

Figure 8.18: The antihelion region wavelet transform at the 1σ V_G criterion cutoff over the CAP shower active period. Meteors are selected which appear within the transform region defined by coefficients higher than 12% of the maximum WTC and with corresponding geocentric meteoroid speeds constrained by the 1σ criterion.

8.5.1 Daily Motion of the Orbital Parameters

As with other showers, some of the parameters of the CAP experience a daily motion. A weighted least-squares fit has been made for the longitudinal motion of the parameters listed in Table 8.13. It is evident that this motion in some cases is so small that the uncertainty in the fit renders measurement impossible. The ω, i and speed parameters experience this problem and they are therefore assumed to have no daily motion. The minor motion in q and e is corrected for, although this is expected to make little difference to the distribution statistics.

Parameter	$d/d\lambda_\odot$	Unit
q	$(1.4 \pm 0.2) \times 10^{-3}$	$\mathrm{AU\,deg^{-1}}$
e	$(-5 \pm 5) \times 10^{-4}$	$\mathrm{deg^{-1}}$
i	$(-1.55 \pm 0.08) \times 10^{-1}$	-
ω	$(2 \pm 3) \times 10^{-2}$	-
V_G	$(0 \pm 1) \times 10^{-2}$	$\mathrm{km\,s^{-1}\,deg^{-1}}$
V_H	$(9 \pm 8) \times 10^{-3}$	$\mathrm{km\,s^{-1}\,deg^{-1}}$

Table 8.13: The daily motion of the CAP orbital parameters over the active period of the shower.

The motion of the radiant longitude detected in most showers is pronounced (such as those discussed above) and generally differs by a perceivable amount in longitude from that of the Sun and so the λ_R coordinate is non-stationary. For the CAP, in Section 7.7.3, the motion in the Sun-referenced longitude coordinate was found to be small and impossible to measure exactly. Here using all points in the data, an attempt is made again to verify the size of the daily motion. The results of a weighted least-squares fit yield the following equations for the ecliptic Sun-referenced coordinate motion:

$$\begin{aligned} \lambda_R &= (-3 \pm 2) \times 10^{-2}\lambda_\odot + (186^\circ \pm 2^\circ) \\ \text{and} & \\ \beta &= (3.4 \pm 0.7) \times 10^{-2}\lambda_\odot + (5.2^\circ \pm 0.8^\circ). \end{aligned} \tag{8.8}$$

The ecliptic longitude and latitude coordinates, therefore, have negligible motion, especially when the stability concerns (0.02 in $d\lambda_R/d\lambda_\odot$ and 0.01 in $d\beta/d\lambda_\odot$) discussed in Section 8.2, hence no correction is required in the data. This implies that the CAP radiant moves parallel to the ecliptic at the same rate as the Sun appears to move due to the Earth's motion. The lack of radiant motion in this coordinate system is evident in Figure 8.19(a). The equatorial coordinates do, of

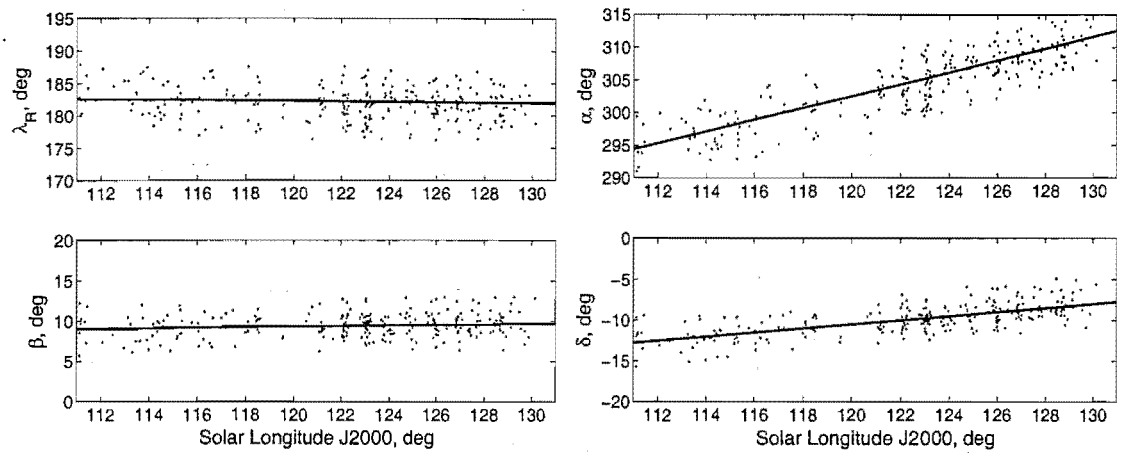

(a) Radiant Daily Motion (Ecliptic) (b) Radiant Daily Motion (Equatorial)

Figure 8.19: Daily motion in the radiant position of the CAP. Weighted linear least-square fits are shown for this motion, in the case of both the ecliptic and equatorial radiant positions. Median individual point uncertainties on the parameters shown are 1.5° in ecliptic longitude, 0.5° in latitude, 1.5° in right ascension and 0.5° in declination.

course, experience a daily motion which is found to be described by

$$\begin{aligned} \alpha &= (9.1 \pm 0.2) \times 10^{-1}\lambda_{\odot} + (194^{\circ} \pm 2^{\circ}) \\ \text{and} & \\ \delta &= (2.52 \pm 0.06) \times 10^{-1}\lambda_{\odot} - (40.7^{\circ} \pm 0.8^{\circ}). \end{aligned} \tag{8.9}$$

Coordinates identified above as experiencing a daily motion are reduced, using equation 7.9, to the common time-centre $\lambda_{\odot} = 125°$. Notice that e, ω and the speed parameter daily motions are all small and have uncertainty measurements greater than their magnitudes, it is difficult to say whether these parameters experience any true daily motion; conversely q and i appear to have acceptably measured motions.

Comparison of the measured radiant motion with Cook (1973), who states daily motions of +0.9 and +0.3 in α and δ respectively, reveals close agreement in δ and agreement within uncertainties in α. The small difference in δ motion is easily explained by the unknown uncertainty in Cook's measurements and the likely 0.01 (unit-less) stability/measurement uncertainty expected in this parameter.

8.5.2 Statistics

After correction for daily motion, 269 meteors are found at the 12% cutoff level; their yearly statistics are shown in Table 8.14. The CAP presents an excellent example

YEAR		$\lambda_\odot$ deg	q AU	e	i deg	ω deg	Ω deg	V_H km s^{-1}	V_G km s^{-1}	α deg	δ deg	SIZE
ALL	$\overline{x}$	122.3	0.550	0.768	7.7	273.3	122.3	37.0	23.4	306.7	-9.3	269
	s.d.	5.2	0.036	0.059	1.2	5.3	5.2	1.3	1.7	2.7	1.3	
	s.e.	0.3	0.002	0.004	0.1	0.3	0.3	0.1	0.1	0.2	0.1	
	Unc.	0.0	0.026	0.044	0.7	3.1	0.0	1.0	1.3	1.5	0.5	
1995	$\overline{x}$	125.0	0.543	0.771	7.6	274.0	125.0	37.0	23.5	307.1	-9.5	66
	s.d.	2.6	0.034	0.051	1.1	4.7	2.6	1.1	1.5	2.4	1.2	
	s.e.	0.3	0.004	0.006	0.1	0.6	0.3	0.1	0.2	0.3	0.2	
	Unc.	0.0	0.026	0.044	0.6	3.1	0.0	0.9	1.4	1.6	0.5	
1996	$\overline{x}$	121.5	0.554	0.764	7.8	273.1	121.5	37.0	23.2	306.5	-9.1	80
	s.d.	6.0	0.037	0.065	1.1	5.5	6.0	1.4	1.7	2.7	1.2	
	s.e.	0.7	0.004	0.007	0.1	0.6	0.7	0.2	0.2	0.3	0.1	
	Unc.	0.0	0.026	0.043	0.7	3.3	0.0	1.0	1.3	1.6	0.5	
1997	$\overline{x}$	121.1	0.553	0.764	7.7	273.2	121.2	37.0	23.3	306.6	-9.1	31
	s.d.	6.8	0.042	0.065	1.4	5.8	6.8	1.4	2.0	2.9	1.6	
	s.e.	1.2	0.008	0.012	0.3	1.0	1.2	0.3	0.4	0.5	0.3	
	Unc.	0.0	0.024	0.044	0.7	2.9	0.0	0.9	1.4	1.4	0.5	
1998	$\overline{x}$	120.5	0.548	0.756	7.7	274.3	120.5	36.7	23.2	307.1	-9.1	31
	s.d.	5.2	0.038	0.057	1.4	5.7	5.2	1.3	1.6	2.9	1.6	
	s.e.	0.9	0.007	0.010	0.3	1.0	0.9	0.2	0.3	0.5	0.3	
	Unc.	0.0	0.024	0.043	0.7	3.0	0.0	1.0	1.4	1.5	0.5	
1999	$\overline{x}$	121.9	0.553	0.781	7.7	272.5	121.9	37.3	23.7	306.3	-9.4	61
	s.d.	4.2	0.034	0.058	1.2	5.2	4.2	1.3	1.6	2.6	1.3	
	s.e.	0.5	0.004	0.007	0.2	0.7	0.5	0.2	0.2	0.3	0.2	
	Unc.	0.0	0.026	0.047	0.7	3.3	0.0	1.0	1.4	1.6	0.5	

Table 8.14: Statistics of all CAP from T1995–T1999 (individual and combined sets) at the 1σ V_G criterion level are presented. All parameters experiencing a daily motion, apart from $\lambda_\odot$ and Ω, are corrected to a centre at $\lambda_\odot^c = 125.0°$; all parameters are referred to the J2000 epoch. The medians of the individual uncertainty distributions are used to provide representative values.

of the difference a small geocentric speed ($V_G \approx 20$ km s^{-1} as compared to $V_G \approx 40$ km s^{-1} for the SDA) can make on the uncertainties in the various measured orbital parameters. All of the parameter distributions have standard deviations which exceed those expected simply due to the individual uncertainties in the meteors. It is perhaps this nature which allows the detection of such a weak shower. The orbits from each year agree very well with each other: there are no differences within the bounds of the standard errors on the parameters. A Student's t-test applied, as discussed in Section 8.3.2, to the observational parameters of this shower yields the results shown in Figure 8.20. In contrast with similar tests performed for the ETA and SDA, there are very few (three) significant differences between the shower parameter means of different years. There are no significant differences between the means from each year and those obtained from the combinations of all years; this indicates the complete interchangeability of shower mean data from different years.

There is no need to allow the speed range to proceed beyond the 1σ speed

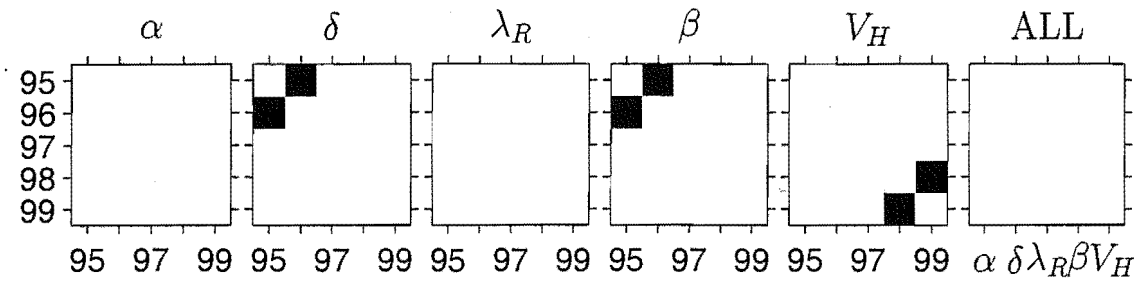

Figure 8.20: Student's t-test of inter-annual agreement of CAP parameter means. The means of five parameters for a series of years are inter-compared in the first five figures; the sixth "ALL" figure shows comparisons between these yearly means with the means obtained from all years of data combined. White squares signify agreement between parameter means at the 95% confidence level while black squares indicate disagreement. All parameters are corrected for daily motion.

criterion level assumed in this survey, it is found from Table 8.14 that the spread in the speed distribution of the shower is contained within the bounds expected due to uncertainties on the meteors. The range of geocentric speeds allowed is greater than 20% of the mean speed, this is judged as more than sufficient an allowance to make. The mean dissimilarities are reasonably low for this shower with $\overline{D}_{SH} = 0.15$, $\overline{D}_D = 0.08$ and $\overline{D}_N = 0.19$. Such values are expected for low inclination low uncertainty streams where the inclination plays only a small role in determining the average dissimilarity. The relatively high value of $\overline{D}_N$ turns out to be partly due to the correction for daily motion. Uncorrected radiant coordinates for these same meteors produce a more reasonable $\overline{D}_N$ of 0.15, owing to the daily motion in the radiant position assumed in equation 6.15 having occasional incompatibilities with that found for some showers.

The histograms of the parameters shown in Table 8.14 are displayed in Figure 8.21; many of these are approximately "Gaussian" in nature and so equation 8.1 may be used to estimate the physical spread in some of these elements. In particular the physical standard deviation in i is expected to be about 1.0° while that in radiant position is given by 2.2° in right ascension and 1.2° in declination. The inclination angle is expected to have a small natural spread as, for a near-ecliptic stream such as this, perturbations would quickly remove the on-ecliptic component of the distribution. The published values given in Table 8.12 show a wide range of orbital parameters. The photographic orbits KI and KIII and the radar orbit W1960 agree best with the AMOR mean orbit for all years (Table 8.14) with dissimilarities $D_{SH} = 0.06$, 0.06 and 0.05 respectively. These are followed by photographic orbit KII at $D_{SH} = 0.24$, a very high value for association of near-ecliptic stream orbits. Finally the radar orbits of Sekanina are not in acceptable agreement with

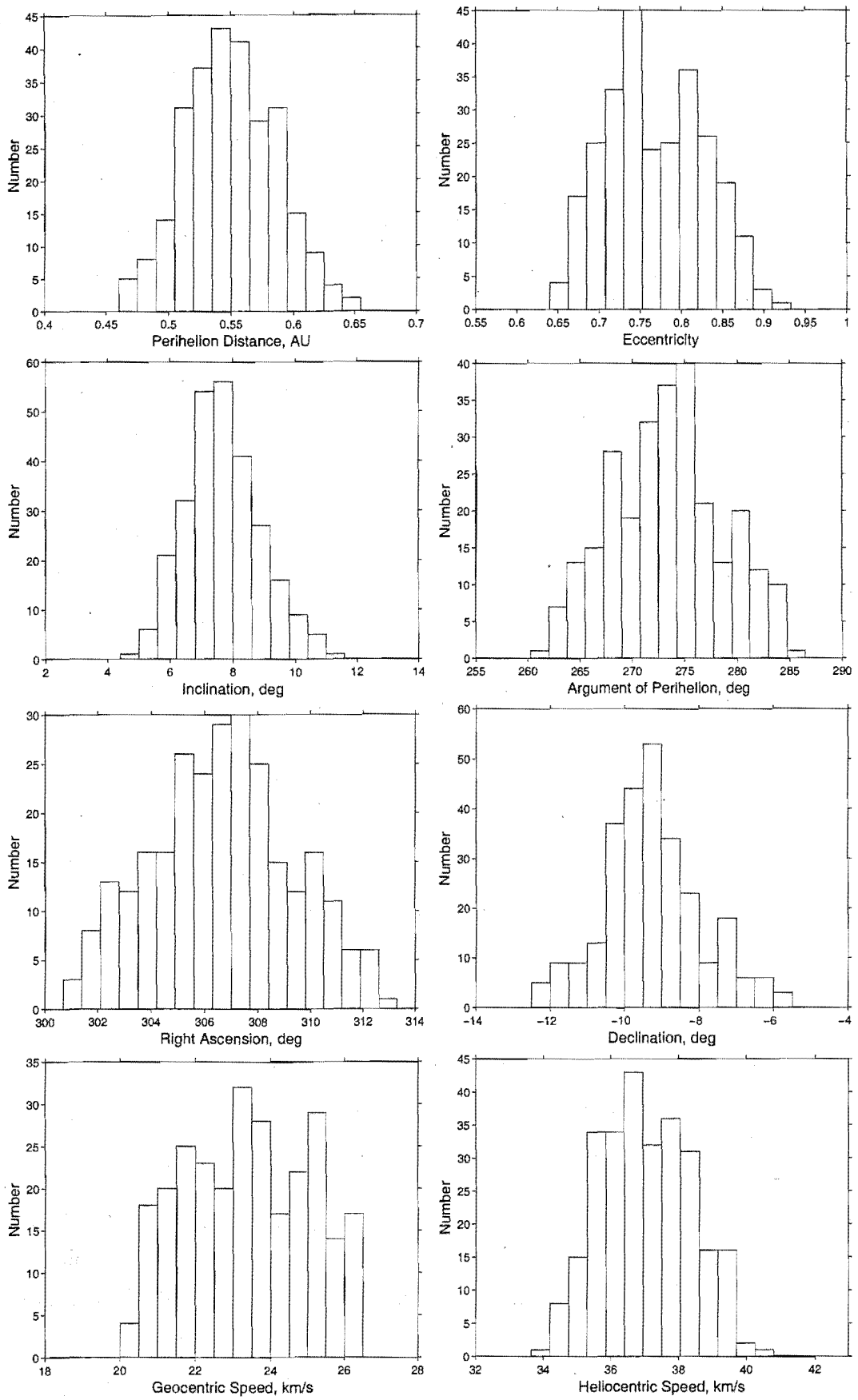

Figure 8.21: Histograms of the orbital parameters of the CAP shower for T1995–T1999. Note that the daily motion corrected values of q and ω have been used to produce "stationary" distributions in these elements.

that determined by AMOR—$D_{SH} = 0.30$ is obtained on comparison with S1973 and an extreme $D_{SH} = 1.18$ with S1976. Sekanina's mean orbits are biased towards late mean solar longitudes. S1973 and S1976 appear to be internally inconsistent in key parameters, such as eccentricity and inclination (assuming they're measuring the same shower). The strongly hyperbolic eccentricity listed for S1976 is the cause of the unacceptable D_{SH} above. This parameter is so much above what might be expected that it is possible that a transcription error was present originally. Little weight is attached to the lack of agreement between these mean orbits and that obtained in the current study.

The single-linkage method determines an CAP mean orbit, shown in Table 7.3, which is as similar to the wavelet derived orbit as are those of Weiss (1960) and Kronk (1988): the D_{SH} dissimilarity between these mean orbits is 0.06.

8.5.3 Activity Profiles

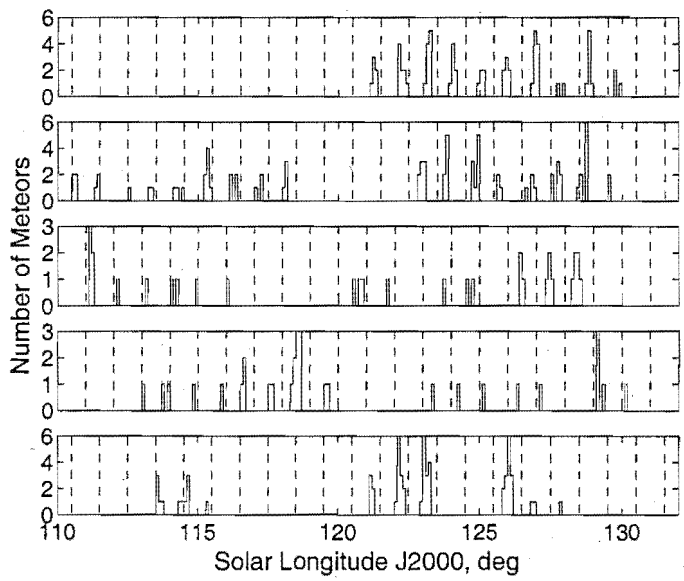

Figure 8.22: The relationship between solar longitude and detection time period for the CAP. The distribution shifts by an average of approximately 0.25° per year. Appropriate cutoff points are shown at offsets from zero $\lambda_\odot$ of 0.5°, 0.5°, +1°, +1° and +0.5°, for years T1995–T1999 shown from top to bottom respectively.

This shower suffers from the general decline of the AMOR detected rate in T1997–T1998. Its strength is weak in general, however in these years the shower falls to half its normal strength, leaving only about 25 orbits over 30° of solar longitude to form the shower. Figure 8.23 shows shower activity profiles for each year, partitioning of points in these profiles is performed with reference to Figure 8.22.

The first impression one gains from the activity profiles is the fragile nature of this shower, for example T1998 has a typical shower count rate of one meteor per degree of $\lambda_\odot$, with a single very large peak at the single $\lambda_\odot = 118°$ point. It is clear that if this shower had not be been selected based on all of the available data, but instead on a search of each year individually, then T1998 would have been declared a year in which the CAP was not seen. It is indeed possible from the T1998 curve that there was a single short outburst in T1998 followed by equipment non-operation for 3° which may have covered a time of continuing maxima. However after this there appears to be a total falloff in the shower strength, even given the reasonable strength of the background.

T1995, T1996 and T1999 present stronger evidence for a shower with obvious peaks in the region $\lambda_\odot \in [120°, 130°]$—the same time at which the peak of the SDA is found. In these curves a number of sudden declines in activity are evident: these can be correlated with changes in the background rate, apart from that at $\lambda_\odot = 128°$ in T1995 which is small but outside that expected due to statistical uncertainty—lack of corroboration with other years dismisses this decline as an artifact. T1997 is interesting in the activity in the period from $\lambda_\odot = 125°$ onwards increases, as with years such as T1995, however here the increase corresponds to a two-fold increase in the background. From these yearly profiles one cannot in fact determine the region of an exact peak in the data; $\lambda_\odot = 125°$ is used as an arbitrary centre for reduction of components experiencing daily motion—this is done more for comparison with other surveys rather than due to the structure present in the activity profiles. For example in T1996 if the background rate in the first half of the graph were the same as that in the later half the shower rate could be approximately even across the whole graph. T1998 and T1999 due to lack of data and major fluctuations in the background add to this problem; for example T1999 appears to have a symmetric peak in the region $\lambda_\odot \in [120°, 130°]$, however this peak exactly follows the background and therefore may be regarded as totally background induced.

The various published orbits in Table 8.12 seem to point to a wide range of shower maxima. Kronk (1988) notes that the maximum of the shower "seems" to occur during $\lambda_\odot = 128.6°$. A range of peaks appear in the table between $\lambda_\odot = 122.2°$ and 146.8°. The data only supports a distinguishable shower presence over the period $\lambda_\odot \in [110°, 130°]$ with a changing peak structure in different years. This period encompasses orbits KI, KIII and radar orbit W1960. It does appear that,

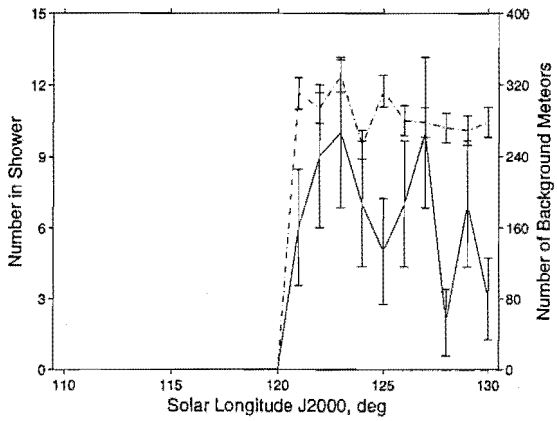

(a) T1995

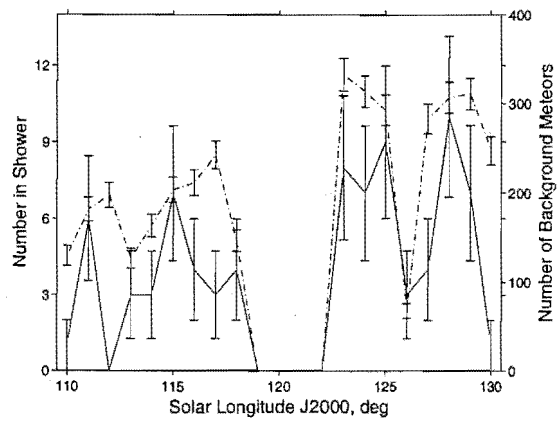

(b) T1996

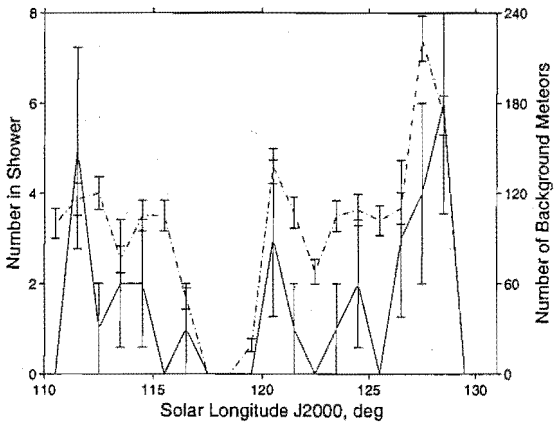

(c) T1997

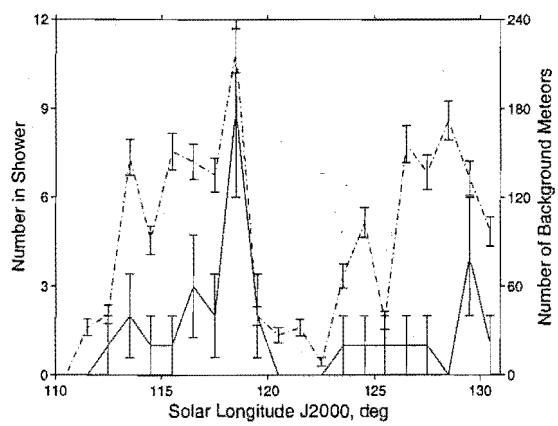

(d) T1998

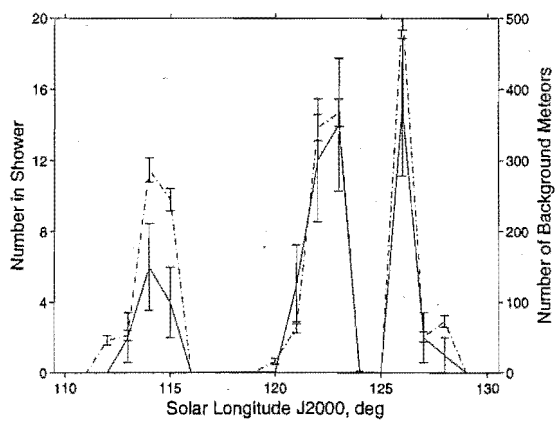

(e) T1999

Figure 8.23: The distribution in time of the CAP meteors for each year from T1995 to T1999. These distributions all use separate shower centring were $\lambda_{\odot}^{off}$ changes per year in order to best encapsulate the distribution resulting from the Earth's daily rotation; with reference to Figure 8.22 the centre offsets used are: 0°, 0°, 0.5°, 0.5° and 0° for years T1995–T1999 respectively. The change in shower rate per degree of solar longitude at these centres is shown as a solid line, while the change in the rate of all non-shower retrograde meteors over the same time-frame is shown as a dotted line. The statistical uncertainty, shown on each point, is given by $N/\sqrt{N}$. Note the use of two different y-axis systems for each graph.

on average, the AMOR peak occurs earlier than that expected from most of the tabulated orbits though many of these (e.g. those of Sekanina) suffer from large gaps in the data coverage which may have biased the finding of the maxima. Additionally the AMOR coverage of the shower period in different years is "patchy" which adds a further layer of complexity.

In summary, from the activity profiles presented in Figure 8.23, little can be learned. Such low rates make it difficult to determine the period over which the shower is distinct. Unfortunately adding the years of data together does not overly improve matters as there are such differences between the profiles in each year that artifacts will be readily introduced into the data.

8.6 Daytime Sextantids

The DSX is the only shower which is evident in the helion region in the AMOR data set. Due to its daytime nature this shower was only discovered when radars were first used for meteor research. A. Weiss in an Australian radio meteor survey at Adelaide, was the first to notice this shower in 1957. Weiss (1960) notes the discovery of a shower he calls the Sextantids-Leonids. The radiant position was not well defined because of the method used: it was estimated at $(\alpha, \delta) = (155° \pm 8°, 0° \pm 10°)$. Peak activity in that study, of about 30 echoes hr^{-1}, persisted from September 29th to October 3rd. No trace of activity was found in data from previous years obtained from the same site, indicating the possible periodic nature of the shower. Using similar equipment, again at the Adelaide site, Nilsson followed this up in 1961 with a survey between September 21st to 29th. According to Nilsson (1963), he detected 9 members of the stream, with a mean radiant position $(\alpha, \delta) = (151.7° \pm 0.9°, -0.1° \pm 1.5°)$ at a mean $\lambda_{\odot}^{c} = 183.6°$. The mean geocentric speed for these meteors was found at 32.2 ± 0.6 $\mathrm{km\,s}^{-1}$. Nilsson (1964) predicts an orbital period of between 1.2 and 1.3 years for the dense part of the shower, at that time detected by their magnitude +6 radar equipment. This, he notes, is consistent with the observation of the shower on only two occasions, separated by four years[5].

The 2nd session of the Harvard Radio Meteor Project also detected the DSX, although 9 meteors associated with the shower were only detected at the tail end of the activity profile, from October 7th to 9th, due to earlier equipment opera-

[5]According to Nilsson (1964) the DSX is more fully covered in Nilsson (1963). However the latter reference is incorrect. Searching for other articles by Nilsson between 1960 and 1970 does not reveal an appropriate paper although a short article on an unrelated shower, the Scorpiids, is found in the supposed volume of the Observatory in which Nilsson (1963) is supposed to appear.

YEAR	$\lambda_\odot$ deg	q AU	e	i deg	ω deg	Ω deg	V_H km s^{-1}	V_G km s^{-1}	α deg	δ deg	SIZE
N1964	184.3	0.146	0.87	21.8	213.2	4.3		32.2	151.7	-0.1	9
S1976	195.8	0.172	0.816	31.1	212.3	15.8	28.5	29.7	157.4	-8.6	9

Table 8.15: Mean orbits of the DSX are given by Nilsson (1964) and Sekanina (1976), from surveys carried out by radar in 1961 and 1969 respectively. Originally the elements were referred to the mean epoch of B1950.0; they have been reduced to J2000.0 for comparison with the AMOR data in this table.

tion (Sekanina 1976). Table 8.15 presents a summary of the published orbits of the DSX. In compiling his standard list of stream orbits, Cook (1973) appears to use the orbit of Nilsson (1964). Since that time, to the author's knowledge, little work has been done on the DSX shower apart from a variety of amateur studies of meteor activity rate and radiant position, by members of the Dutch and International Meteor Organisations (IMO). The IMO list only mean radiant position/time with $(\alpha, \delta, \lambda_\odot^c) = (152°, 0°, 184.3°)$ and they define the shower as medium strength (Rendtel et al. 1995). Ohtsuka et al. (1997) publish a study of radiant positions and activity using a forward scatter radar. This has disadvantages of inability to measure meteoroid orbits and requires assumptions that all meteors in a certain region of the sky are due to the shower.

Because of the lack of published information on the DSX, the present study is particularly valuable: as can be seen from the historical summary, above, generally radiant flux measurements, in addition to a few low yield meteoroid orbit analyses, have been performed.

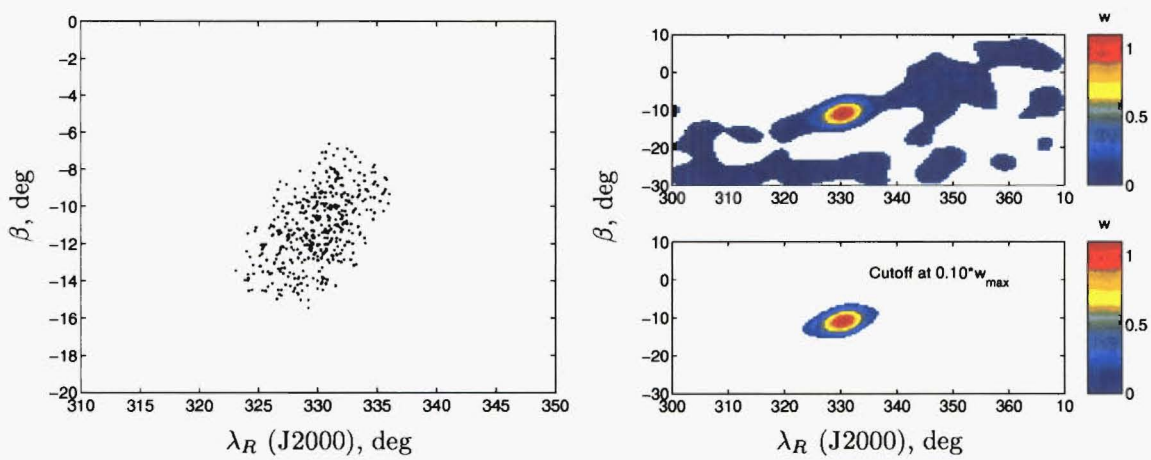

(a) Meteors Selected (b) Wavelet Transform

Figure 8.24: Helion region meteors selected by the 10% of the maximum wavelet coefficient cutoff method with speed constrained by the 1σ V_G criterion cutoff for the DSX shower.

According to the wavelet transform information of Section 7.7.3, the central radiant position is found at $(\lambda_N, \beta) = (330.2°, -11.2°)$ as referred to the centre of the active period. It is found there that the geocentric speed distribution at the 1σ criterion cutoff is defined by $V_G = 31.3 \pm 4.1$ km s^{-1}; the shower is found to be most active over the period $\lambda_\odot \in [178°, 193°]$, with the reference for daily motion corrections thus being chosen at $\lambda_\odot^c = 187°$. Using these definitions of the shower and a 1σ speed criterion spread, about the mean, a wavelet transform reveals the region of the shower. As with the previous showers a cutoff level must be chosen at which to define the unambiguous shower region with respect to the background. In the current study 10% of the maximum WTC has been chosen for this purpose. As shown in Figure 8.24(b), such a cutoff level effectively removes any background from the surrounding region and distinctly defines the shower source region. The 414 meteors in this region using the 1σ V_G criterion cutoff, are shown in Figure 8.24(a) with an uncorrected centre at $(\lambda_R, \beta) = (330.2°, -11.2°)$.

8.6.1 Daily Motion of the Orbital Parameters

As with the showers already covered, the DSX experience a daily motion in a number of its parameters. While the SDA showed strong motion in q, ω and i orbital parameters, such motion is not found to be present significantly in the case of the DSX. In fact none of the orbital parameters, apart from the obvious $\lambda_\odot$, Ω and the radiant position, experience very much daily motion at all. Weighted linear least-squares fits to the data yield rates of change over time as shown in Table 8.16. Here the change in q and V_G are obviously negligible, over the period, while the changes in the other parameters are small, but included for completeness. The

Parameter	$d/d\lambda_\odot$	Unit
q	$(-4 \pm 2) \times 10^{-4}$	AU deg^{-1}
e	$(-1.0 \pm 0.3) \times 10^{-3}$	deg^{-1}
i	$(2.4 \pm 0.4) \times 10^{-1}$	-
ω	$(-1.9 \pm 0.3) \times 10^{-1}$	-
V_G	$(-9 \pm 2) \times 10^{-2}$	km s^{-1} deg^{-1}
V_H	$(-7 \pm 1) \times 10^{-2}$	km s^{-1} deg^{-1}

Table 8.16: The daily motion of the orbital parameters of the DSX over the active period of the shower.

radiant motion, under the Sun-referenced ecliptic system, was found to be small in Section 7.7.3, this is verified here by the least-squares fits. A slight slope in the case of the Sun-referenced longitude of -0.08 and a larger, but still minor slope, in

the latitude of -0.10 are found. These linear fits are shown in Figure 8.25(a) and defined by

$$\begin{aligned} \lambda_R &= (-8 \pm 2) \times 10^{-2}\lambda_\odot + (346^\circ \pm 4^\circ) \\ \text{and} & \\ \beta &= (-9.8 \pm 0.6) \times 10^{-2}\lambda_\odot + (7^\circ \pm 1^\circ). \end{aligned} \tag{8.10}$$

The longitude motion is negligible especially if one considers the likely stability-based uncertainty given in Section 8.2, the radiant appears to experience almost exactly the same daily motion in longitude, as the Sun. This is perhaps not surprising, given that it appears in the same "helion" region as the Sun. The daily motion in latitude differs from that quoted in the original wavelet analysis (equation 7.12). This difference is not large and it is expected that the least-squares fit should yield a better estimate of the true radiant motion; therefore a motion of -0.1 has been adopted for the DSX study in this chapter. The minor change in longitude motion and those notified in Table 8.16, including those judged negligible, have also been corrected for. Note that the measured motions in Table 8.16, while small in magnitude, generally have magnitudes exceeding their measurement uncertainty by a reasonable margin. This situation may be compared to previous showers where several parameters had uncertainties in excess of the magnitude measured implying the possibility of no daily motion at all. Again for completeness the daily motion in equatorial coordinates is fitted as shown in Figure 8.25(b). Here the least-squares fits are defined by

$$\begin{aligned} \alpha &= (8.4 \pm 0.2) \times 10^{-1}\lambda_\odot - (1^\circ \pm 4^\circ) \\ \text{and} & \\ \delta &= (-4.25 \pm 0.06) \times 10^{-1}\lambda_\odot + (78^\circ \pm 1^\circ). \end{aligned} \tag{8.11}$$

8.6.2 Statistics

Using the defined region of the shower, with corrections being applied to the various parameters to counter daily motion as listed in Section 8.6.1, the shower is now explored. After correction for daily motion 410 meteors are selected at the 10% cutoff level. Table 8.17 lists the statistics for the corresponding orbital parameters, complementary histograms are shown in Figure 8.26. The number of DSX meteors detected per year is rather small, justifying the "medium" strength assigned to it

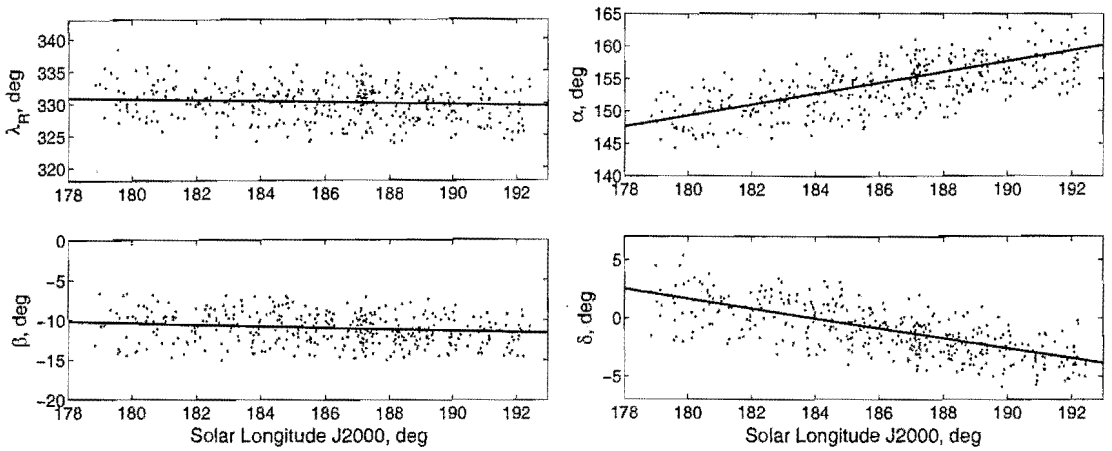

(a) Radiant Daily Motion (Ecliptic)

(b) Radiant Daily Motion (Equatorial)

Figure 8.25: Daily motion in the radiant position of the DSX. Weighted linear least-square fits are shown for this motion in the case of both the ecliptic and equatorial radiant positions. Median individual point uncertainties on the parameters shown are 2° in ecliptic longitude, 0.5° in latitude, 2° in right ascension and 0.5° in declination.

by the International Meteor Organisation.

The 1σ V_G criterion cutoff level used for meteor selection is not extended to 2σ, as was done for the ETA, because at the 1σ level the spread is found to be commensurate with the uncertainties and the mean D are acceptable. The mean dissimilarities of the 410 meteoroid orbits are $\overline{D}_{SH} = 0.16$, $\overline{D}_D = 0.11$ and $\overline{D}_N = 0.16$; such values are lower than the maximum which can be accepted, apart from $\overline{D}_D$ which is at Drummond's (1981) limit. The helion region sporadic source starts to contribute unrelated meteors if the 1σ speed criterion range is exceeded. The DSX is observationally a weak major shower, this may be partly caused by its daytime transit, where radar detection can be hampered by Sporadic-E interference—the helion region itself is noted to be weaker than its antihelion counterpart, indicating the weakness may not be simply a function of the meteoroid density in the stream.

Comparison of the mean orbit for all years (Table 8.17) with the published mean orbits of Table 8.15 shows very good agreement—the mean of Nilsson (1964) has a dissimilarity of only $D_{SH} = 0.03$; that of Sekanina (1976) is much more dissimilar with a close to unacceptable value of $D_{SH} = 0.21$, this is caused by the $\approx 10°$ difference between Sekanina's orbit and that obtained by AMOR—the inclination of the latter is more in line with that generally expected for the DSX, it is possible that a typographic mistake in Sekanina's table may have led to such a difference. Comparison with the single-linkage (Table 7.3) and modified single-

linkage (Table H.2) results give excellent agreement: associations of $D_{SH} = 0.025$ and $D_{SH} = 0.026$ are found respectively. Such low dissimilarities indicate that the determined orbit is effectively method independent.

YEAR		$\lambda_\odot$ deg	q AU	e	i deg	ω deg	Ω deg	V_H km s^{-1}	V_G km s^{-1}	α deg	δ deg	SIZE
ALL	$\overline{x}$	186.1	0.151	0.855	23.1	212.5	6.1	30.4	31.2	154.5	-1.5	410
	s.d.	3.5	0.025	0.030	5.0	3.5	3.5	1.7	2.2	2.8	1.5	
	s.e.	0.2	0.001	0.001	0.2	0.2	0.2	0.1	0.1	0.1	0.1	
	Unc.	0.0	0.023	0.023	3.9	3.0	0.0	1.5	1.6	2.7	0.5	
1995	$\overline{x}$	186.8	0.149	0.855	22.7	212.0	6.8	30.2	31.1	154.3	-1.2	155
	s.d.	3.2	0.026	0.031	4.9	3.5	3.2	1.7	2.3	2.9	1.3	
	s.e.	0.3	0.002	0.002	0.4	0.3	0.3	0.1	0.2	0.2	0.1	
	Unc.	0.0	0.022	0.023	3.9	3.0	0.0	1.6	1.6	2.9	0.5	
1996	$\overline{x}$	186.2	0.159	0.851	23.1	213.6	6.2	30.6	31.1	154.9	-2.0	86
	s.d.	3.4	0.026	0.032	4.9	3.6	3.4	1.8	2.3	2.8	1.4	
	s.e.	0.4	0.003	0.003	0.5	0.4	0.4	0.2	0.2	0.3	0.1	
	Unc.	0.0	0.023	0.023	3.8	3.3	0.0	1.5	1.7	2.7	0.5	
1997	$\overline{x}$	185.8	0.149	0.857	23.4	212.2	5.8	30.4	31.3	154.4	-1.5	128
	s.d.	3.5	0.023	0.029	5.1	3.4	3.5	1.7	2.2	2.7	1.7	
	s.e.	0.3	0.002	0.003	0.5	0.3	0.3	0.2	0.2	0.2	0.1	
	Unc.	0.0	0.023	0.023	4.0	3.0	0.0	1.4	1.6	2.7	0.5	
1998	$\overline{x}$	184.0	0.149	0.859	23.5	212.5	4.0	30.7	31.4	154.9	-1.6	41
	s.d.	3.4	0.022	0.027	5.1	3.0	3.4	1.5	2.1	2.5	1.6	
	s.e.	0.5	0.003	0.004	0.8	0.5	0.5	0.2	0.3	0.4	0.3	
	Unc.	0.0	0.022	0.023	3.9	2.8	0.0	1.5	1.7	2.3	0.5	

Table 8.17: Statistics of the DSX stream as recorded between T1995 and T1998. All parameters experiencing a daily motion, apart from $\lambda_\odot$ and Ω, have been corrected to $\lambda_\odot^c = 187.0°$; all parameters are referred to the J2000.0 epoch. The medians of the individual uncertainty distributions are used to provide representative values.

Cursory study of Table 8.17 appears to suggest that there is a strong cycle to the shower every two years, which would tie in well with the suggestion of Nilsson (1964). Here T1995 and T1997 are particularly strong while T1996 is weak and T1998 is very weak; the radar system was undergoing an upgrade at the time in T1999, so no data is available. In general the mean orbital elements do not change from year to year within standard errors. The distributions in the orbital parameters are generally "Gaussian", as shown in Figure 8.26, hence the use of standard error is acceptable. The exceptional year is T1996 where q, e and ω are all different by up to three standard errors. These differences are actually quite small as the standard errors are small. Based on only four years of data, with a small number of orbits per year, one must conclude that it is most likely, that this difference is simply a statistical anomaly. Radar observations over several subsequent years are needed to confirm this statement.

There are no other differences in orbital elements between the four years of

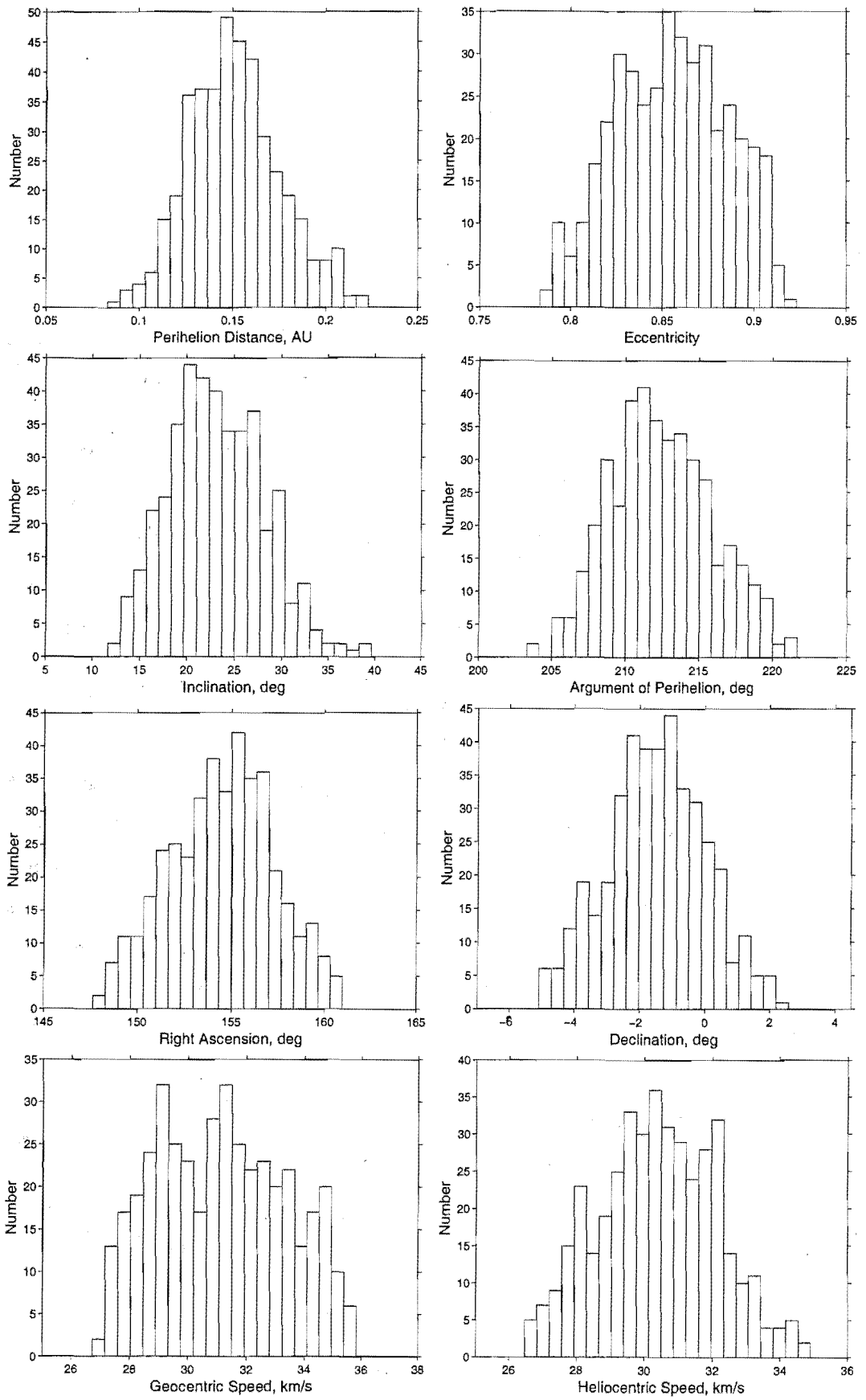

Figure 8.26: Histograms of the orbital parameters of the DSX shower for T1995–1998. All parameters are reduced for daily motion to a centre at $\lambda_{\odot}^{c} = 187.0°$.

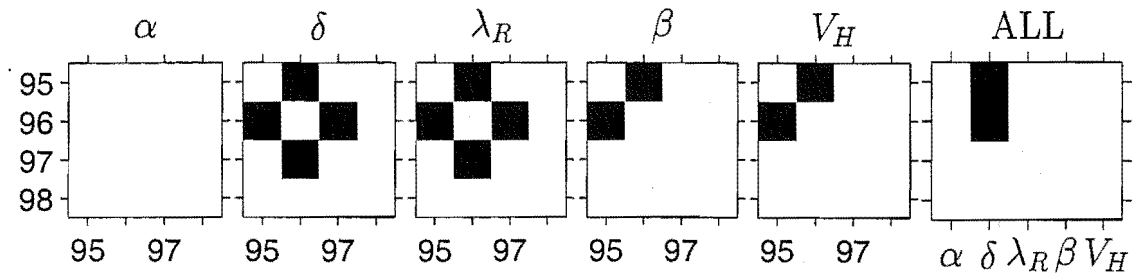

Figure 8.27: Student's t-test of inter-annual agreement of DSX parameter means. The means of five parameters for a series of years are inter-compared in the first five figures; the sixth "ALL" figure shows comparisons between these yearly means with the means obtained from all years of data combined. White squares signify agreement between parameter means at the 95% confidence level while black squares indicate disagreement. All parameters are corrected for daily motion.

data, apart from a slight change in mean radiant position in T1996. The mean radiant position and speed are particularly well defined in general and differ little over the years. A Student's t-test applied, as discussed in Section 8.3.2, to the observational parameters of this shower yields the results shown in Figure 8.27. Apart from a general disagreement in mean δ and λ_R between T1995 and T1996 and between T1996 and T1997, in addition to a disagreement between the latter pair in the mean β and V_H, there are no significant differences between the mean parameters for each year—it is of note that the mean α boasts complete agreement in all yearly comparisons, which might not be expected due to the disagreements in λ_R. Comparison of the parameter means from individual years with those from the combined yearly means yields excellent agreement with δ in T1995 and T1996 being the only significant disagreements; the mean δ in these years were at the higher and lower regions of the range of mean values in the four years surveyed. This lack of disagreement with the combined years mean indicates that the DSX, with the exceptions noted previously, provide shower-defining parameter means which are the same from year to year.

The measurement uncertainty ascribed to each orbital parameter is similar to the spread found in its shower distribution. This indicates that the detectable region of the shower is defined almost entirely by the uncertainties in measurement. The parameters having the larger spread, with respect to the uncertainty in the individual orbits are the inclination and declination angles, this corresponds to a similar spread in β ($\sigma_\beta = 1.8°, \Delta\beta = 0.5°$). A large spread in i will of course create a spread in β and therefore δ, the root cause of the spread is therefore the inclination angle, which is the real astronomically important parameter. By using equation 8.1 and noting the approximately "Gaussian" profiles of these parameters

in Figure 8.26, an estimate of the physical spread is gained. This yields physical standard deviations of 3.1° in inclination and 1.4° in declination. The estimated spread in inclination may not be overly relied upon—the measurement uncertainty in this parameter increases as the inclination angle increases.

8.6.3 Activity Profiles

In order to answer the question of the apparent two year period, it is necessary to study the rate curves from each year separately. Because of the inconstant mapping of the solar longitude of detection to time of day, it is necessary to vary slightly the positions of the bins each year. With reference to Figure 8.28, it is found that the best offsets on the zero $\lambda_\odot$ position for the edges of the 1° wide bins, are 0.8°, 0.55°, 0.3° and 0.05°, for T1995–T1998 respectively. The activity profiles shown in Figure 8.29 are obtained using these offsets. For each shower curve there is provided also a background curve which is determined from the rate of all prograde orbits detected over the shower time-frame, from 0400 and 1600 NZST. All prograde orbit detections could be included in this background but this would also include those detected later with no Sporadic-E interference present (e.g. close to midnight); owing to its radiant position the DSX experience the latter condition strongly therefore it is important that the background reflects this.

In T1995 the background (prograde) meteoroid rate is very changeable from a minimum of $\sim$ 150 up to maximum of $\sim$ 250 per day. There appears to be a broad peak in the background, from $\lambda_\odot \approx 184°$ to the end of the shower. The shower rate has a structure, with a slow increase towards a broad peak, then a slow decay. The ascent to the maximum is generally featureless with small fluctuations occurring within the uncertainty bars. The activity profile seen in T1997 is similar with a broad featureless peak. The background in this case is more uniform than for T1995; against such a background the activity profile is also smoother, indicating that most of the minor fluctuations seen in T1995, are aspects of an irregular meteor detection sensitivity. The lack of data at the $\lambda_\odot = 187.9°$ point is caused by an equipment malfunction; this is followed by a background which decreases, as the shower rate gradually decreases. This implies a link between the background and the shower, or a gradual decline in general meteor detection rate.

The activity profiles obtained in T1996 and T1998 are apparently more interesting, than for the other years, as they exhibit multiple statistically distinct "spikes" in activity. T1998 exhibits three peaks rising above that expected due to statistical

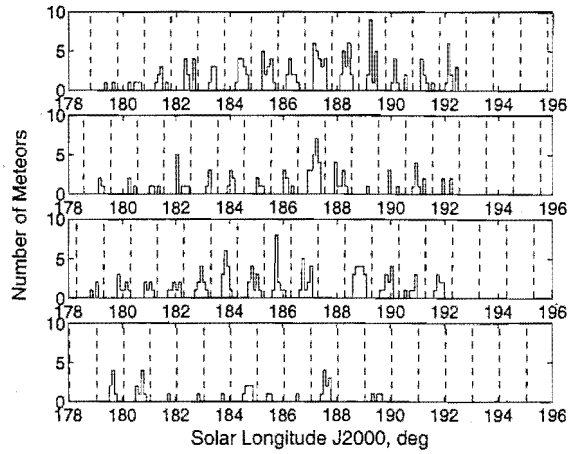

Figure 8.28: The relationship between solar longitude and detection time period for the DSX. The distribution shifts by approximately 0.25° per year. Appropriate cutoff points are shown at offsets from zero $\lambda_\odot$ of 0.8°, 0.55°, 0.3° and 0.05° for years T1995–T1998, shown from top to bottom respectively.

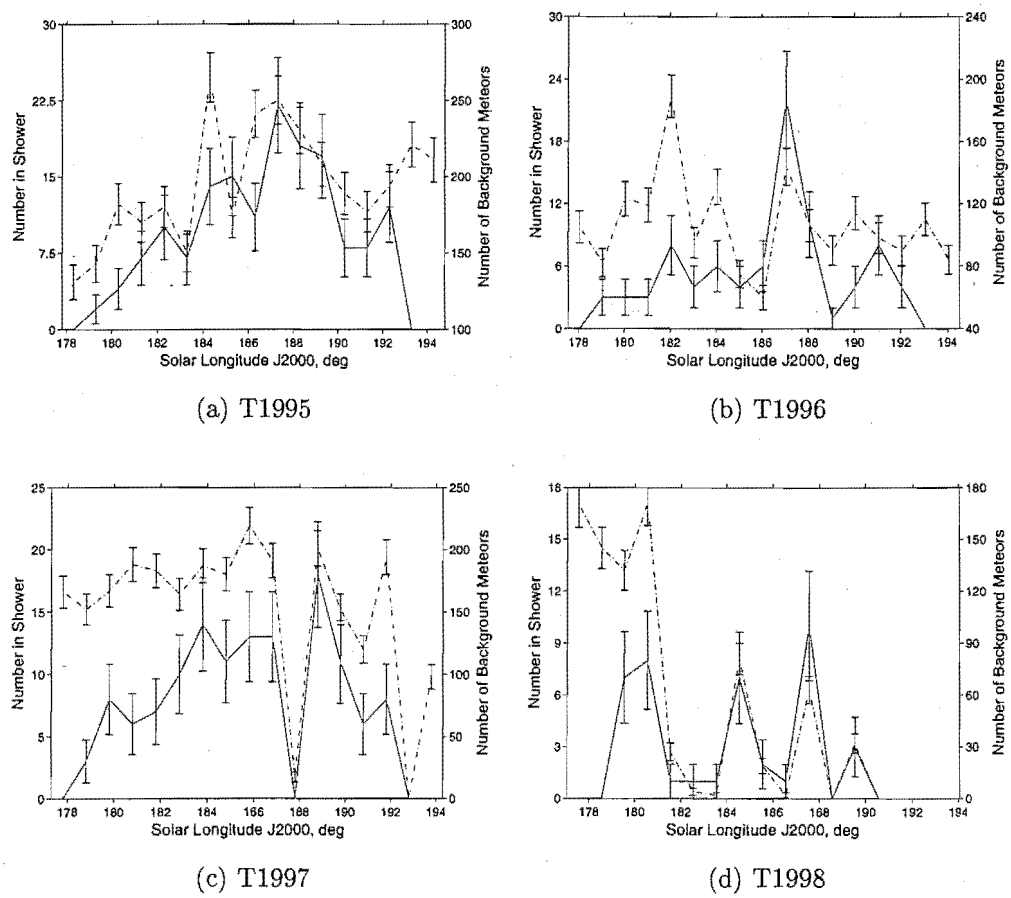

Figure 8.29: The distribution in time of the DSX meteors for each year from T1995 to T1998. The change in shower rate per degree of solar longitude (offset from zero by 0.3°, 0.05°, −0.2° and −0.45° for T1995–T1998 respectively) is shown as a solid line, while the change in the rate of all non-shower prograde meteors between 0400–1600 NZST is shown as a dotted line. The statistical uncertainty, shown on each point, is given by $N/\sqrt{N}$. Note the use of two different y-axis systems for each graph.

uncertainty at $\lambda_\odot \approx 180°$, 184.7° and 187.7°. It is noted that these peaks follow exactly changes in background distributions at the corresponding times; i.e. the peaks are artifacts of system operational coverage. The T1998 background rate is unusually low and this is also reflected in the size of the shower peaks. If one could remove the frequent system outages, one could reasonably assume that a similar distribution to that obtained in T1995 and T1997, would be obtained.

Moving on to T1996, one notes a background local maximum rising above that expected due to statistical uncertainty at 182.1°; this corresponds to a modest increase in the shower rate. Otherwise the shower rate contains a flat peak, with a very strong feature at only one point in the distribution. At 187.1° the rate rises to ~ 22 from the ~ 6 surrounding average level. Correspondingly the background also experiences a peak at this point. It appears, however, that the shower peak is real to an extent, as a similarly sized background peak at 184.1° does not see any great change in the shower rate. Due to the decrease in background rate over 185°–186°, it is difficult to say how long the shower peak should last. It does appear, though, to be stronger and much shorter lived than in previous years.

There is no evidence from the activity curves, presented here, that there is a 2 year cycle in DSX detection. If one were searching year by year for a shower one would probably not consider T1998 to display a credible shower at all and T1996 would also be under suspicion if it were not for the very strong peak at 187.1° in that year. The low rates in T1996 and T1998 are explained, to some extent, by instrument fluctuations in both time and sensitivity of coverage. On average the background rate in T1996 is approximately half that in either T1995 or T1997. In T1998, after $\lambda_\odot = 180.7°$, the background rate is $\sim 30\%$ of the latter years. In order to accurately identify the yearly changes in the character of the DSXit is important to gather several more years of data, using AMOR. All care must be taken to have the system running, in as stable a fashion as possible, over the active time of the shower. An explanation is also needed, and a future solution determined, for the large-scale changes in the background rate recorded by AMOR in years such as T1998.

8.7 Peak A Shower Candidate

Peak A (Figure G.1(l)) is identified as a shower candidate in Section 7.7. This enhancement in radiant-speed-time space occurs in the antihelion radiant region at $\lambda_\odot \approx 315°$. The wavelet transform, over its identified active period, is shown in

Figure 8.30(b). As determined in Section 7.7.3, the geocentric speed 1σ criterion cutoff is defined by $V_G = 43.0 \pm 4.6$ km s^{-1} while the shower is found to be active over $\lambda_\odot \in [305°, 320°]$. Meteors detected within the region, defined by a cutoff at 10% of the maximum positive WTC and satisfying these speed and time constraints are deemed shower meteors—these are shown in Figure 8.30(a). The uncorrected centre of the distribution shown is at $(\lambda_R, \beta) = (215.2°, -18.2°)$; 331 meteors are selected about this centre at the 10% cutoff level.

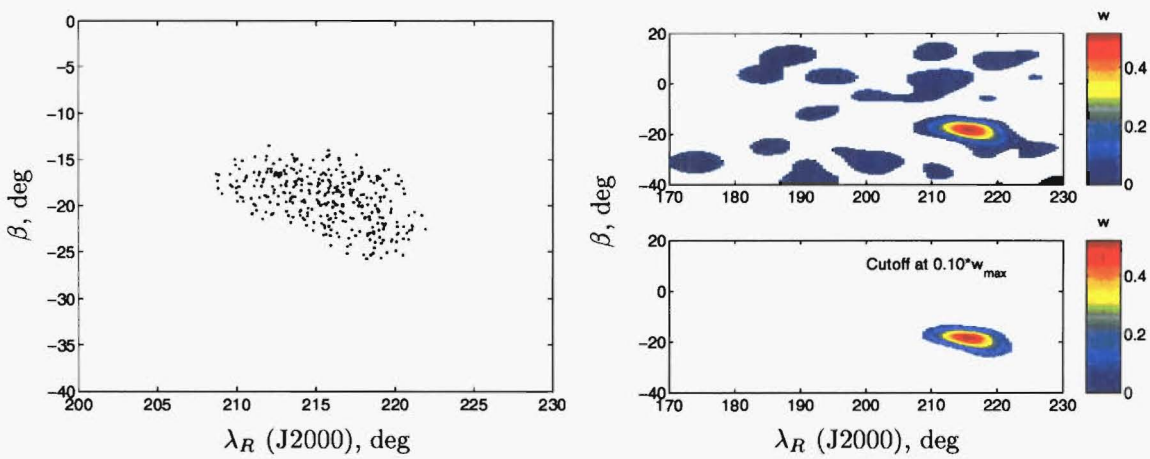

(a) Meteors Selected (b) Wavelet Transform

Figure 8.30: The antihelion region wavelet transform for Peak A. Meteors are selected by the 10% of the maximum WTC cutoff method and with speeds constrained by the 1σ criterion cutoff.

8.7.1 Daily Motion of the Orbital Parameters

The motion of the radiant was previously crudely measured, as shown in Figure 7.14. In this section, each parameter has its motion determined using the standard uncertainty weighted least-squares method, on the set of 331 shower meteor data points.

The daily motion in the radiant coordinates is shown in Figures 8.31(a) and 8.31(b) for ecliptic and equatorial systems respectively. The motion in the ecliptic system is defined by

$$\begin{aligned} \lambda_R &= (-2.3 \pm 0.3) \times 10^{-1} \lambda_\odot + (290° \pm 10°) \\ \text{and} \qquad & \qquad (8.12) \\ \beta &= (1.1 \pm 0.1) \times 10^{-1} \lambda_\odot - (52° \pm 3°). \end{aligned}$$

Clearly, as with most showers, the motion is predominantly parallel to the ecliptic.

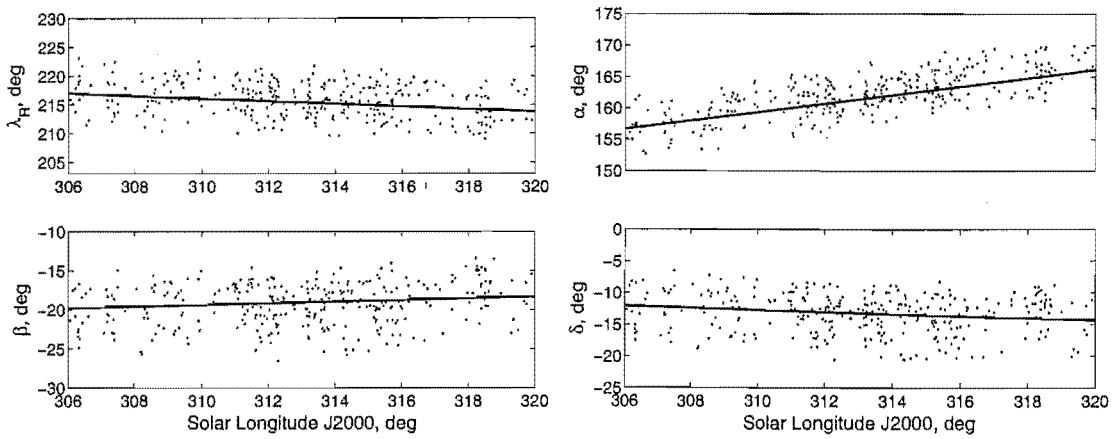

(a) Radiant Daily Motion (Ecliptic)

(b) Radiant Daily Motion (Equatorial)

Figure 8.31: Daily motion in the radiant position of the Peak A meteors. Weighted linear least-square fits are shown for this motion in the case of both the ecliptic and equatorial radiant positions. Median individual point uncertainties on the parameters shown are 2.9° in ecliptic longitude, 0.6° in latitude, 2.9° in right ascension and 0.6° in declination.

The equatorial system has a motion defined by

$$\begin{aligned} \alpha &= (6.8 \pm 0.3) \times 10^{-1} \lambda_{\odot} - (50^{\circ} \pm 10^{\circ}) \\ \text{and} & \qquad (8.13) \\ \delta &= (-1.6 \pm 0.1) \times 10^{-1} \lambda_{\odot} + (38^{\circ} \pm 3^{\circ}). \end{aligned}$$

It is found that $d\lambda_R/d\lambda_{\odot}$ differs from that determined using the WTC of Equation 7.11 by ≈ 0.1, this is believed to another example of the approximate nature of the daily motion results obtained using the daily WTC maximum position in the previous chapter—such measurements while useful to remove some daily motion have proved to be crude and unreliable in the current study, but they are necessary as "initial guesses" in order to obtain speed and activity time information.

Parameter	$d/d\lambda_{\odot}$	Unit
q	$(0 \pm 3) \times 10^{-4}$	$\mathrm{AU\,deg^{-1}}$
e	$(1.2 \pm 0.4) \times 10^{-3}$	$\mathrm{deg^{-1}}$
i	$(3.2 \pm 0.9) \times 10^{-1}$	-
ω	$(-8.5 \pm 0.7) \times 10^{-1}$	-
V_G	$(-4 \pm 5) \times 10^{-2}$	$\mathrm{km\,s^{-1}\,deg^{-1}}$
V_H	$(2 \pm 3) \times 10^{-2}$	$\mathrm{km\,s^{-1}\,deg^{-1}}$

Table 8.18: Daily motion of the Peak A shower orbital parameters over its active period.

There are small measured daily motions on the other orbital parameters, which

are listed in Table 8.18. The uncertainty in the daily motion of the speed exceeds the measured motion, it is possible that there is no real motion for these parameters. The motion in q, e and i is almost negligible, these motions are applied in the statistics section regardless. Each parameter, P, is reduced to the $\lambda_{\odot}^{c} = 313°$ centre using the approach of equation 7.9, with $dP/d\lambda_{\odot}$ as given in Table 8.18.

8.7.2 Shower Statistics

All meteors selected within the wavelet transform enhanced region, identified in Figure 8.30(b), have the daily motion corrections of the previous section applied. 327 meteors remain at the 10% level after the application of these corrections. Mean dissimilarities are measured at $\overline{D}_{SH} = 0.23$, $\overline{D}_{D} = 0.16$ and $\overline{D}_{N} = 0.18$. It is difficult to determine from these whether this is a true association—they are all around the upper limit at which we might accept this as a shower, however mitigating factors include the large uncertainty/spread in both inclination and argument of perihelion.

YEAR		$\lambda_{\odot}$ deg	q AU	e	i deg	ω deg	Ω deg	V_H km s^{-1}	V_G km s^{-1}	α deg	δ deg	SIZE
ALL	$\overline{x}$	313.1	0.143	0.920	64.3	141.9	133.1	36.1	42.7	162.1	-13.3	327
	s.d.	3.5	0.032	0.034	7.8	5.3	3.5	2.4	2.6	2.3	3.1	
	s.e.	0.2	0.002	0.002	0.4	0.3	0.2	0.1	0.1	0.1	0.2	
	Unc.	0.0	0.027	0.029	8.3	6.0	0.0	3.0	3.5	3.0	0.6	
1995	$\overline{x}$	313.1	0.136	0.927	65.2	142.7	133.1	36.2	43.1	162.4	-12.8	71
	s.d.	2.5	0.033	0.031	7.9	6.0	2.5	2.6	2.6	2.6	3.0	
	s.e.	0.3	0.004	0.004	0.9	0.7	0.3	0.3	0.3	0.3	0.4	
	Unc.	0.0	0.025	0.027	9.8	5.8	0.0	2.9	3.6	3.0	0.6	
1996	$\overline{x}$	315.3	0.139	0.911	64.1	142.5	135.3	35.3	41.9	162.6	-13.7	28
	s.d.	2.6	0.030	0.037	6.6	4.7	2.6	2.6	2.7	2.2	3.0	
	s.e.	0.5	0.006	0.007	1.3	0.9	0.5	0.5	0.5	0.4	0.6	
	Unc.	0.0	0.019	0.027	7.8	5.7	0.0	3.1	3.5	2.3	0.5	
1997	$\overline{x}$	312.7	0.142	0.920	63.9	142.3	132.7	36.0	42.6	162.0	-13.2	105
	s.d.	3.6	0.032	0.033	7.6	5.4	3.6	2.3	2.5	2.3	3.0	
	s.e.	0.4	0.003	0.003	0.7	0.5	0.4	0.2	0.2	0.2	0.3	
	Unc.	0.0	0.029	0.029	7.1	6.1	0.0	3.1	3.4	3.2	0.8	
1998	$\overline{x}$	313.0	0.149	0.918	64.1	141.0	133.0	36.2	42.7	161.8	-13.6	123
	s.d.	3.8	0.030	0.034	8.3	4.9	3.8	2.4	2.7	2.2	3.1	
	s.e.	0.3	0.003	0.003	0.7	0.4	0.3	0.2	0.2	0.2	0.3	
	Unc.	0.0	0.028	0.031	8.6	6.1	0.0	3.0	3.6	2.9	0.6	

Table 8.19: Mean orbital parameters of the Peak A meteoroids for each year between T1995 and T1998 selected at the 1σ V_G criterion level. Radiant parameters experiencing a daily motion are corrected to a centre at $\lambda_{\odot}^{c} = 313°$; all parameters are corrected to the J2000 epoch. The medians of the individual uncertainty distributions are used to provide representative values.

Distributions with statistics as listed in Table 8.19 are obtained from the selected meteors. The orbit population is, not unusually, characterised by q and e

values which are within the highest density region (as shown in Figure 3.8). The inclination angle is larger than the major showers which have been discussed thus far; this angle has a high uncertainty. As with other showers measured by AMOR, the uncertainty orbital parameters meets, or exceeds, the standard deviation in the data. This implies that the statistical spread is entirely attributable to measurement uncertainty. Application of the Student's t-test, as discussed in Section 8.3.2, to this shower's observational parameters yields the results shown in Figure 8.32. Apart from disagreement between the mean β for T1995 and T1999 there are no other significant disagreements in any of the parameters. The parameter means obtained from the combination of data from all years agree at the 95% confidence level with those obtained from each year's data individually. The means of this shower in these observational parameters may therefore be determined from any year's observations and applied globally to later years with confidence.

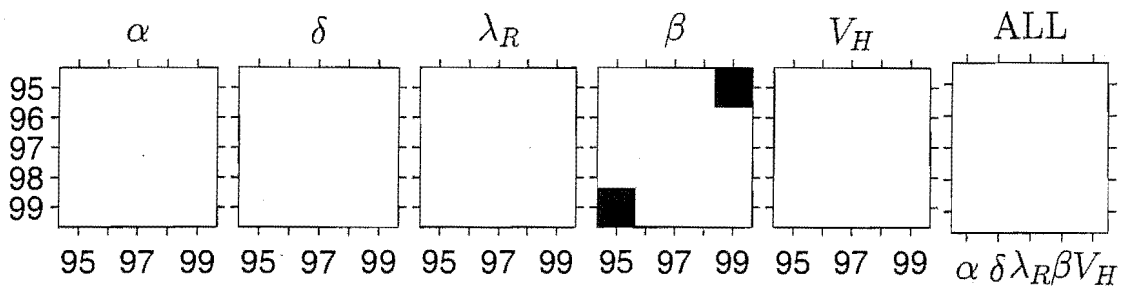

Figure 8.32: Student's t-test of inter-annual agreement of Peak A parameter means. The means of five parameters for a series of years are inter-compared in the first five figures; the sixth "ALL" figure shows comparisons between these yearly means with the means obtained from all years of data combined. White squares signify agreement between parameter means at the 95% confidence level while black squares indicate disagreement. All parameters are corrected for daily motion.

This "shower" does not appear in the catalogues of Cook (1973), Kronk (1988) or Rendtel et al. (1995). It does not appear in the previous radar specific surveys of Gartrell and Elford (1975) and Nilsson (1964). It is observed by AMOR to have a stable medium strength in all years, apart from in T1996, when the radar equipment was inoperative for much of the active period. Due to this strength one would expect the shower existence to be in the literature, if it had been seen before. It is impossible to absolutely prove or disprove the existence of a shower but this appears to be one of the more likely candidates for astronomical reality, especially given its repetitious nature year after year.

8.8 Peak C Shower Candidate

As with Peak A of the previous section, Peak C (Figure G.2(j)) is also found within the wavelet enhancement searches of Section 7.7. As determined in Section 7.7.3, the geocentric speed at the 1σ cutoff criterion is defined by $V_G = 37.0 \pm 4.8$ km s^{-1}; the shower is found to be active over $\lambda_\odot \in [130°, 160°]$. The wavelet transform of the shower region under these constraints is shown in Figure 8.33(b). The 948 meteors selected under the 10% of the maximum positive WTC rule are shown in Figure 8.33(a) with an uncorrected centre at $(\lambda_R, \beta) = (330.8°, -13.8°)$.

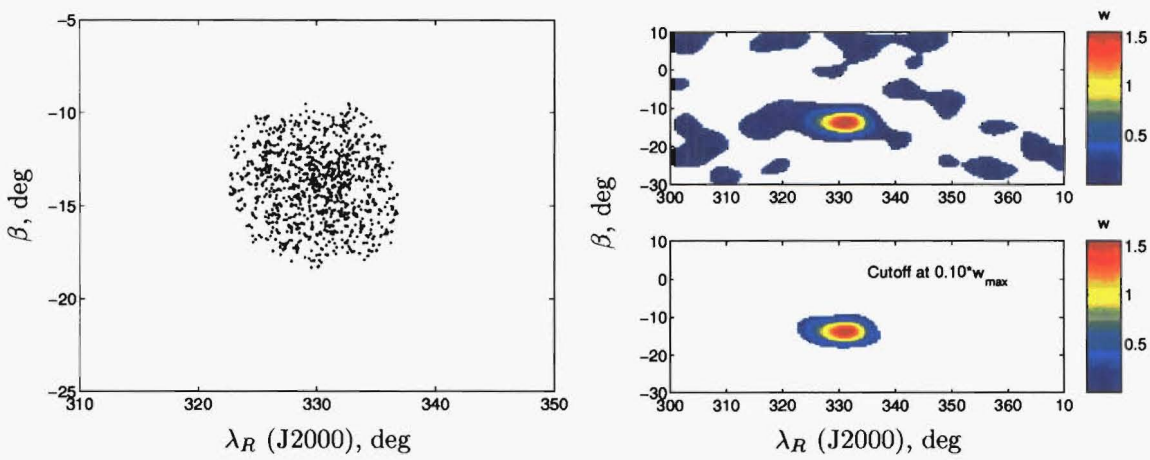

(a) Meteors Selected (b) Wavelet Transform

Figure 8.33: The helion region wavelet transform for Peak C. Meteors are selected by the 10% of the maximum WTC cutoff method with speeds constrained by the 1σ criterion cutoff.

8.8.1 Daily Motion of the Orbital Parameters

Parameter	$d/d\lambda_\odot$	Unit
q	$(-7.6 \pm 0.8) \times 10^{-4}$	AU deg^{-1}
e	$(2.5 \pm 0.8) \times 10^{-4}$	deg^{-1}
i	$(-4 \pm 1) \times 10^{-2}$	-
ω	$(-1.2 \pm 0.1) \times 10^{-1}$	-
V_G	$(1.9 \pm 0.8) \times 10^{-2}$	km s^{-1} deg^{-1}
V_H	$(-2 \pm 5) \times 10^{-3}$	km s^{-1} deg^{-1}

Table 8.20: Daily motion of the Peak C shower orbital parameters over the active period of the shower.

The orbital parameters experience a daily motion. This motion is pronounced in the radiant coordinates, as shown in Figures 8.34(a) and 8.34(b), for ecliptic

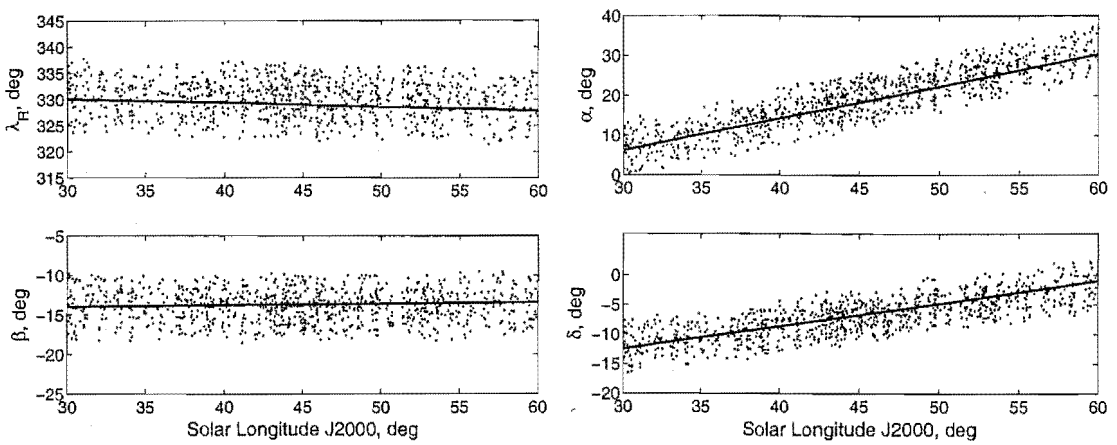

(a) Radiant Daily Motion (Ecliptic) (b) Radiant Daily Motion (Equatorial)

Figure 8.34: Daily motion in the radiant position of the Peak C meteors. Weighted linear least-square fits are shown for this motion in the case of both the ecliptic and equatorial radiant positions. Median individual point uncertainties on the parameters shown are 2.3° in ecliptic longitude, 0.5° in latitude, 2.3° in right ascension and 0.5° in declination.

and equatorial systems respectively. The uncertainty weighted linear fit performed allows this motion to be determined. The fits are visually very bad for the ecliptic longitude and right ascension coordinates, this is due to the large uncertainties and the particular central density profiles of these showers. Setting the data point uncertainties to 0 is found to provide a fit which is much more visually appealing. However, the algorithm, using the data point uncertainties, takes a more objective approach than the human eye and this is preferred. The motion in the ecliptic radiant position is defined by

$$\begin{aligned} \lambda_R &= (-7.6 \pm 0.8) \times 10^{-2} \lambda_\odot + (332.3^\circ \pm 0.3^\circ) \\ \text{and} & \qquad (8.14) \\ \beta &= (1.9 \pm 0.2) \times 10^{-2} \lambda_\odot - (14.5^\circ \pm 0.1^\circ), \end{aligned}$$

while that in the equatorial coordinates is given by

$$\begin{aligned} \alpha &= (8.04 \pm 0.08) \times 10^{-1} \lambda_\odot - (17.9^\circ \pm 0.3^\circ) \\ \text{and} & \qquad (8.15) \\ \delta &= (3.82 \pm 0.02) \times 10^{-1} \lambda_\odot - (23.9^\circ \pm 0.1^\circ). \end{aligned}$$

The daily motion in the other parameters is generally very small, as shown in

Table 8.20. V_H has an uncertainty exceeding its measured daily motion, otherwise most parameters motion magnitudes exceed their uncertainties by a reasonable margin. These minor motions in each parameter, P, are removed from the orbits detected in the shower by reducing all orbits to $\lambda_{\odot}^{c} = 45°$, using equation 7.9.

8.8.2 Shower Statistics

The statistics of the 970 meteors selected at the 10% cutoff level after correction are now discussed. It was suspected, in Section 7.7, that Peak C is simply a product of the background sporadic bias distribution. The mean dissimilarities of this shower's originating meteoroid orbits are at the upper level for association: $\overline{D}_{SH} = 0.27$, $\overline{D}_{D} = 0.19$ and $\overline{D}_{N} = 0.27$. Such levels of dissimilarity indicate that it is unlikely that all of the meteors collected are members of the same shower especially given the low uncertainties on the orbital parameters compared to those of the ETA(recall that the ETA was forgiven its high mean dissimilarities on the basis of high orbital parameter measurement uncertainties). Nevertheless the Peak C shower is now explored further to determine its character.

$\lambda_{\odot}$ deg	q AU	e	i deg	ω deg	Ω deg	V_H km s^{-1}	V_G km s^{-1}	α deg	δ deg	SIZE
48.6	0.122	0.925	32.6	213.9	228.6	34.7	36.6	22.1	-3.7	11

Table 8.21: The mean orbit of the omicron Cetids as given by Sekanina (1976). All elements are referred to the J2000.0 epoch.

This shower cannot be detected visually, as it is seen within the helion region, hence one must rely on other radar surveys for corroboration. Nilsson (1964) and Gartrell and Elford (1975) do not list this shower from their Adelaide radar data; there appears to be a general dearth of showers listed for the April/May month even though the latter survey was active until June. Sekanina (1976), however, does find a very similar shower, named the omicron Cetids, in the Harvard Radio Project data. The omicron Cetids as noted previously, was seen in Jodrell Bank surveys (Lovell 1954). It is also listed as a medium strength radar shower in Rendtel et al. (1995). The orbital elements of this shower are listed in Table 8.21. Comparison using D_{SH} between the current mean orbit (based on 970 meteors in Table 8.22) and Sekanina's mean omicron Cetids orbit yields a dissimilarity of 0.09, a value clearly indicating excellent agreement.

The strength and stability of this "shower" over the years appear to define it as a fairly major shower within the AMOR data set. One must bear in mind

YEAR		$\lambda_\odot$ deg	q AU	e	i deg	ω deg	Ω deg	V_H km s^{-1}	V_G km s^{-1}	α deg	δ deg	SIZE
ALL	$\overline{x}$	45.0	0.133	0.916	37.1	214.9	225.0	34.4	36.5	19.0	-7.0	970
	s.d.	7.9	0.035	0.029	7.5	6.0	7.9	2.3	2.6	3.3	2.1	
	s.e.	0.3	0.001	0.001	0.2	0.2	0.3	0.1	0.1	0.1	0.1	
	Unc.	0.0	0.025	0.024	3.8	4.6	0.0	1.9	2.2	2.4	0.5	
1995	$\overline{x}$	48.9	0.132	0.915	38.0	214.1	228.9	34.1	36.4	19.0	-7.2	207
	s.d.	6.1	0.035	0.028	7.5	6.1	6.1	2.4	2.6	3.3	2.1	
	s.e.	0.4	0.002	0.002	0.5	0.4	0.4	0.2	0.2	0.2	0.1	
	Unc.	0.0	0.024	0.023	3.8	4.3	0.0	1.8	2.2	2.3	0.5	
1996	$\overline{x}$	43.5	0.136	0.918	37.1	215.8	223.5	34.8	36.8	19.4	-7.0	310
	s.d.	8.3	0.036	0.029	7.6	6.2	8.3	2.3	2.6	3.3	2.1	
	s.e.	0.5	0.002	0.002	0.4	0.3	0.5	0.1	0.2	0.2	0.1	
	Unc.	0.0	0.024	0.025	3.8	4.4	0.0	2.0	2.3	2.2	0.5	
1997	$\overline{x}$	44.2	0.131	0.915	36.9	214.3	224.2	34.2	36.4	18.7	-7.0	128
	s.d.	7.1	0.036	0.029	7.3	6.0	7.1	2.2	2.6	3.3	1.9	
	s.e.	0.6	0.003	0.003	0.6	0.5	0.6	0.2	0.2	0.3	0.2	
	Unc.	0.0	0.030	0.025	4.1	4.4	0.0	1.3	2.0	2.3	0.5	
1998	$\overline{x}$	46.3	0.136	0.914	36.5	215.3	226.3	34.4	36.3	19.4	-6.9	177
	s.d.	7.8	0.034	0.028	7.5	5.7	7.8	2.3	2.6	3.3	2.2	
	s.e.	0.6	0.003	0.002	0.6	0.4	0.6	0.2	0.2	0.2	0.2	
	Unc.	0.0	0.024	0.024	3.4	4.7	0.0	1.9	2.2	2.5	0.5	
1999	$\overline{x}$	41.6	0.126	0.918	36.8	214.0	221.6	34.3	36.6	18.3	-7.0	148
	s.d.	7.8	0.034	0.029	7.7	5.9	7.8	2.4	2.6	3.3	2.3	
	s.e.	0.6	0.003	0.002	0.6	0.5	0.6	0.2	0.2	0.3	0.2	
	Unc.	0.0	0.026	0.024	3.6	5.2	0.0	2.1	2.2	2.6	0.5	

Table 8.22: Mean orbital parameters of the Peak C meteoroids for each year between T1995 and T1999 selected at the 1σ V_G criterion level. Radiant parameters experiencing a daily motion are corrected to $\lambda^c_\odot = 45°$; all parameters are referred to the J2000.0 epoch. The medians of the individual uncertainty distributions are used to provide representative values.

that this shower is spread fairly evenly over a relatively long period of time, as shown in Figure 7.15. The daily activity is in fact much lower than for any shower surveyed, apart from that associated with Peak A and the CAP. The standard deviations in right ascension and inclination are particularly interesting: they are considerably larger than those seen for the major shower surveys and they also exceed the standard deviation expected, due to measurement uncertainty, by a large amount as shown in Table 8.22. When considered with the approximately "Gaussian" character of these parameters, one may use equation 8.1 to estimate the physical spread in the radiant position. A physical spread of 2.3° in right ascension and 2.0° in declination is obtained, using the statistics of the 970 meteors from all years. Similarly for the inclination angle, a physical spread of 6.5° is obtained—such a large spread in inclination is particularly worrying, if one wishes to define Peak C as a shower. Generally the inclination physical spread is very small (e.g. 3.0° for the DSX) in streams, as this parameter is reasonably stable with respect to

planetary perturbations.

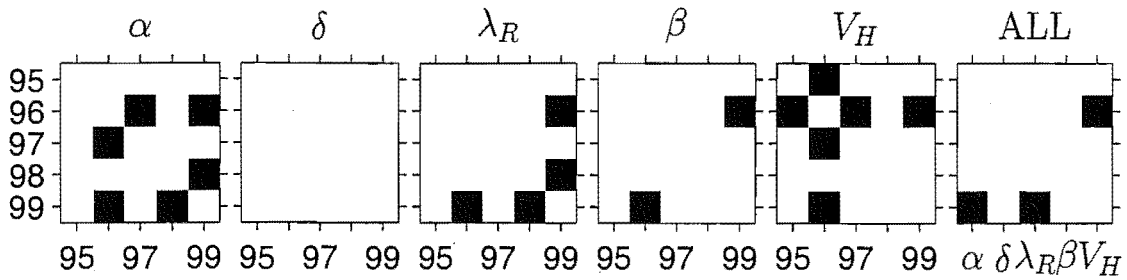

Figure 8.35: Student's t-test of inter-annual agreement of Peak C parameter means. The means of five parameters for a series of years are inter-compared in the first five figures; the sixth "ALL" figure shows comparisons between these yearly means with the means obtained from all years of data combined. White squares signify agreement between parameter means at the 95% confidence level while black squares indicate disagreement. All parameters are corrected for daily motion.

Inter-year comparison of the observational parameter means is performed by means of the Student's t-test as discussed in Section 8.3.2—the results of these comparisons are shown in Figure 8.35. The latitudinally based paremeters δ and β are found to have generally similar means in all years. Meanwhile α shows disagreements between three pairs of yearly means; λ shows complete agreement between years if the T1999 year is removed. Heliocentric speed agrees on all years apart from T1996. Generally the comparisons between the combined year means and the single-year means in the last subfigure show good agreement—if T1999 were to be removed this situation improves to almost perfection. From these results it appears that the T1999 result may be anomalous on several of the parameters, it is possible that a physical difference in the composition of the detected stream presence in that year modified the parameter distributions; the T1996 mean speed while significantly different than other years differs by a rather small magnitude as shown in Table 8.22. In general, bearing these concerns in mind, the Peak C mean observed parameters are found to be stable and repeatable between years with minor fluctuations in the magnitude of these means being expected occassionally.

The reality of this shower is an open question; the difference between a long lived shower and a sporadic source is very difficult to determine. While previous authors tabulate such a shower, it may be that they simply sampled the helion source region, at the same position as this shower, and found some apparent structure there. As with the "shower" associated with Peak A, that associated with Peak C is simply tabulated and analysed here.

8.9 Direct Searches for Peak A and C Meteors

A direct significance test of the mean orbits of the 327 Peak A meteors from Table 8.19 and the 970 Peak C meteors from Table 8.22 is performed in the fashion described in Section 7.6. The result of comparisons against each of four (vernal equinox centred) equinoctial years, using the dissimilarity measure D_{SH} with a cut-off at 0.20, is shown in Table 8.23. Both showers are shown to be significant at 99% levels or above; A1998 is not a fair comparison with Peak A due to the large time-coverage gap over the shower activity region, as shown in Figure 3.1. From these tests it is clear that these showers are distinct and significant, this finding however does not preclude their being simply convenient manifestations of the sporadic background—as discussed in the previous sections there is no method by which to absolutely differentiate a sufficiently long-lived shower from the observation of a strong and distinct sporadic biased source. The fact that an independent method, based on different parameter sets from the original search, backs up the presence of these showers does however lend the maximum support possible to their reality.

	Peak A			Peak C		
Year	N_S	N_E	Confidence level	N_S	N_E	Confidence level
A1995	77	30	99.99%	284	152	99.99%
A1996	33	18	99.99%	129	66	99.99%
A1997	42	27	99%	177	82	99.99%
A1998	26	23	-	130	79	99.99%

Table 8.23: Test of the significance of the Peak A and C showers by direct comparison.

Chapter 9

Conclusions

The thesis has surveyed a number of aspects of the structure of the data set provided by the AMOR meteoroid orbit radar system in the period 1995 to 1999. Results show the data set to be composed predominantly of sporadic meteors with only four major meteor showers being definitely detected by multiple methods. The η Aquarids, Southern δ Aquarids, Daytime Sextantids and α Capricornids, over the five years surveyed, comprised $\sim 4\times10^3$ out of the $\sim 5.3\times10^5$ orbits in the data set. While the shower content could easily have been raised if observation time had been continuous (particularly during the Daytime Sextantids period) the fact remains that less than 1% of the total meteoroid orbit population appeared within recognisable shower configurations. This is to be expected when one considers that AMOR is one of the most sensitive meteor radars ever built; meteoroids near the limiting dust particle size of 40 μm are expected to be removed from coherent streams and merged into the sporadic background expeditiously. Undoubtedly many of the so-called sporadic meteors in the current study were members either of undetected minor streams or simply of major stream meteoroids which were spread by uncertainty and by perturbations from the defined stream core. The latter possibility was demonstrated in Chapter 8; there it was shown that the spread in the stream populations did not exceed that expected due to measurement uncertainty in some cases, particularly the η Aquarids. The lack of coherent shower structure found within the AMOR data set implies that AMOR is, in general, a poor determiner of distinguishable past cometary orbital paths and activities. Fewer than ten showers (only four definite) were found within the data set while Hughes (1993) notes that all 135 short-period comets known at the time had associated streams.

Chapter 3 has shown the very strong biasing effects which act on the observed population of meteoroids. It was found that the retrograde orbit population, which appears strongly in the AMOR data set, is of negligible significance astronomically compared with the prograde population. The retrograde region was found to be biased almost wholly towards perihelion/aphelion distances of $\approx$ 1 AU while its

eccentricity distribution was slightly biased towards higher e values. The prograde population was found to be highly biased towards near-parabolic eccentricities ($e > 0.7$) in combination with low perihelion distances ($q < 0.4$ AU). These values are typical of those expected of cometary orbits while those for retrograde orbits are simply a function of the Earth observation bias. Corrections were applied to the observed orbital parameter distributions, these removed the strong retrograde $q \approx 1$ AU and $Q \approx 1$ AU biases. The inclination distribution, which was shown to have a strong peak for $i < 10°$ and a secondary smaller peak at $i \approx 160°$, had both of these reduced, once corrected; the retrograde region ($i > 90°$) was, of course, almost completely removed by this correction. While the near-ecliptic region ($i < 10°$) was reduced greatly there was a corresponding increase in observed meteors for $i \in (10°, 90°)$; a uniform decrease in meteor detections over the latter region was obtained, as opposed to the sharp drop-off seen previously.

The radiant distribution of meteors, as seen by AMOR, was shown in Chapter 4 to appear within strongly defined regions, often termed sporadic sources. Three such sources were found to be present in the data: the helion, antihelion and apex sources. These were shown to have a seasonal variation in their ecliptic latitudes which was explained as being entirely due to the motion of the Earth in its orbit—the declination range seen by the radar remains constant over the year but the ecliptic latitude to which this declination refers changes daily. It was shown that as the observed helion/antihelion sources moved further from the ecliptic plane ($\beta = 0°$) they became weaker; this was attributed to the highest density of dust being expected close to this plane. The apex source was found to be composed almost entirely of retrograde meteors; the importance of this region was accentuated by the geocentric speeds reached here as most of the Earth's orbital speed added directly to that of the incoming meteoroid. A small number of prograde meteors were found in the apex region, these occurred at far-south latitudes ($\beta < -50°$) and corresponded to meteoroids on medium to high prograde inclinations ($i > 40°$).

Both static and seasonal orbital distributions, within the sporadic source regions, were explored. As expected, it was found that the helion and antihelion sources sample similar orbit populations. However, there was a difference in the activity of these sources; this was attributed to atmospheric/radar related influences such as Sporadic-E interference, as there is no astronomical reason that these regions should differ. The orbital populations in the source regions were found to vary strongly with season. For example, in the second season ($\lambda_\odot \in (90°, 180°]$) most

orbits in the antihelion region were found close to the ecliptic ($i < 20°$) while in the third season ($\lambda_\odot \in (180°, 270°]$) there was an almost uniform distribution up to $i = 60°$ followed by a gradual decline. Similar obvious differences were present between other seasons and in other orbital parameters; these were attributed to the motion of the sporadic source regions in ecliptic latitude. It was noted that an annual distribution in a particular parameter will contain features related to the continuity of the data set.

A strong link between the geocentric speed and radiant position was shown in Chapter 4. For certain radiant regions the range of speeds allowed was found to be severely constrained. This link was exploited in Chapter 7 to partially justify the use of large-scale geocentric speed partitioning when searching for showers in radiant-speed-time space. It is an open question whether the use of geocentric or heliocentric speed would have been more appropriate in the current study. As can be seen from the histograms of geocentric speed there was a relatively flat distribution found for most of the showers (e.g. Figure 8.21) in this parameter. Taylor (1991) used the heliocentric speed in order better to define the η Aquarids, noting its more peaked distribution, and this approach is clearly vindicated here. In future surveys more weight might be applied to the use of V_H over V_G but balancing this, V_G has been found in the current study to provide reliable shower definition and it also has the particular distinction of having a direct relationship to the radiant position (Figure 4.10).

The measurement uncertainties on AMOR orbits were derived and discussed in Chapter 5. The application of automated algorithms to the systematic derivation of uncertainties in individual AMOR orbits has not been previously accomplished. The information this adds to the data set was important in providing both representative uncertainties on the parameters in a stream and in summarising the quality of the data set as a whole. Two methods for determining individual orbit uncertainties were introduced. A Monte Carlo simulation technique involving the perturbation of the fundamental measured parameters 5×10^4 times for each orbit, under Gaussian weighting according to the assumed uncertainties in these parameters, was used to provide output distributions, where the spread in each parameter was taken to be that parameter's uncertainty. This method had the disadvantage that it took $\sim$ 1 week of computer time (on a 500 MHz Digital Alpha computer) to produce results for $\sim 1 \times 10^5$ meteors. A second new method using classical analytical error methods was introduced. This was found to execute at a very fast speed, producing

a complete set of uncertainties for the 5.3×10^5 orbits under study in ~ 5 minutes. The results of these two methods were compared and found to be in agreement, hence the analytic method was chosen due to its execution speed advantage. Using this method, representative uncertainties were derived for each orbital parameter of importance in the current study.

It was shown that the uncertainty in most parameters increased as the geocentric speed and inclination increased (a link was shown between V_G and i): this is expected as the faster the meteoroid, the smaller the time-lag measurements and thus the larger the percentage uncertainty in those measurements. Partitioning the data on the basis of geocentric speed or inclination was found to provide appropriate representative uncertainties for the distinct regimes present. For example, in the prograde ($i \leq 45°$) partition the perihelion distance uncertainty was 0.03 AU while in the equivalent retrograde partition ($i \geq 135°$) this uncertainty rose to 0.22 AU. The uncertainty in heliocentric velocity components was also found to increase with increasing inclination and such an increase leads directly to higher uncertainties in all orbital elements. The inclination parameter itself was not affected in quite the same manner, as it is determined in terms of a fraction of two of the heliocentric velocity components. The declination and ecliptic latitude of the radiant were found to be the parameters with lowest uncertainties because they are almost directly linked to the elevation angle which was assumed to have a fixed uncertainty of 0.5°. The argument of perihelion was found to be the angle with the highest uncertainty, particularly for retrograde orbits. Previous assumptions based on a uniform 2° uncertainty in this parameter were found upon closer analysis to be too low; the lowest representative uncertainty was 5° in the $i \leq 45°$ partition and the highest was 50° in the $i \geq 135°$ partition. The inclination parameter was also assumed originally to have a uniform 2° uncertainty; this, more detailed, study reveals that this was only true in the $i \leq 45°$ partition while it has between double and quadruple this value in other partitions.

The inter-orbital dissimilarity functions (D-criteria) were discussed in Chapter 6. In order to determine the characteristics of these functions, in relation to the retrieval of streams within the AMOR data set. A series of simulations was performed. AMOR-detected meteors were selected which had similar orbits to those of published streams. Their fundamental parameters were perturbed by their expected Gaussian uncertainties, many times, thus building up a simulated stream spread entirely by measurement uncertainty. This follows the lead of the uncertainty analysis (above)

with each meteor providing 5×10^4 perturbed samples. By gradually increasing the cutoff level for comparison of these distributions against the original published stream means, the responses of the D-criteria were determined. It was found in the near-ecliptic ($i < 10°$) region that to retrieve 70% of a "stream's" orbits D-criteria values of D_{SH}=0.09, $D_H = 0.1$, $D_D = 0.06$ and $D_N = 0.08$ were required. Generally the required D_{SH} and D_H cutoff levels were higher than the corresponding D_D and D_N levels. To retrieve 70% of the $i \in (10°, 90°)$ population, D_{SH}=0.12, $D_H = 0.16$, $D_D = 0.11$ and $D_N = 0.09$ were required. Similarly for the retrograde population $D_D = 0.18$ and $D_N = 0.17$ were required—in this case D_{SH} and D_H both reached 0.25 at the 50% retrieval level and were not able to retrieve further due to the maximum value set in the program (generally in other surveys, using the standard D_{SH} measure, 0.25 was taken as an extreme level for association). It was found, when studying retrograde streams, such as the η Aquarids, that even at $D_{SH} = 0.50$ less than 70% of the stream was retrieved. In other prograde partitions discussed the cutoff level required for 70% stream retrieval was also close to the maximum level used for stream retrieval in other surveys. One must remember that it is not possible to use a very high cutoff level because of the danger of sporadic intrusion. It was found that the maximum cutoff level which may be used was dynamic depending on the region of inclination space under consideration, that it was found to be most likely that in a stream search of AMOR data some orbits will be lost from the stream simply due to measurement uncertainty spread and it was shown that the D-criteria were effectively measuring uncertainty spread and not energy spread for which they were originally designed—this was in agreement with the comments of Nilsson (1964).

A number of systematic meteor shower search methods were discussed in Chapter 7. This is believed to be one of the most complete surveys of the various techniques to date. Some of the more promising of these methods, including a new adaptation of an old method and the use of an entirely new method, were tested and their applicability discussed. It was found that meteor showers were not directly visible in the overall daily activity profiles over the year, i.e. even the major showers are a second-order effect compared to the large-scale sporadic background distribution. This is an important finding as it shows that one must use very focussed methods in order to detect any showers through the observation-bias and uncertainty-spread background—showers detected by such methods must therefore be strongly concentrated in local regions of the orbit-describing space. Searches were made of both

orbital element space and radiant-speed-time (geocentric) space for such showers (when one combines time of detection ($\lambda_{\odot}$) (which has negligible uncertainty) and geocentric speed with the radiant position one completes the definition for a valid orbit). Using Poisson statistics, assuming a constant time-coverage on average in each year of the data set, it was shown that the direct searching method against a reference orbit was apt to declare orbits as stream members even when there was no significance, in the time dimension, to this result. Data sets exhibiting strong observation bias, such as that provided by AMOR, generally always associate a few meteors given any representative "stream" orbit with which they are compared. This new adaptation of a previously well-used method has taken the important step of adding a significance test in order to lower the risk of false stream association. This method verifies the presence of the four major showers (listed above) and also points to the significance of the Puppids, ζ Cetids and the Serpentids minor showers in the AMOR data set. These minor showers were not verified by other methods, where no *a priori* knowledge of particular stream structure was assumed, leading to an open question as to their presence in the AMOR data set. The small number of streams found to be significantly present was placed in perspective when one realised that the reference data set searched against had $\sim 10^2$ unique streams in it (the complete data set had 277 streams present, however several of these were repetitions with minor variations). The application of a wavelet enhancement technique to T1995–T1999 data, using a Mexican Hat wavelet in radiant-speed-time space, also showed a low level of stream content. Wavelet enhancement has not been applied previously in meteor stream searching (few studies of the radiant-speed-time space were systematically performed in the past). This method was found to be robust and efficient, the large number of meteors in the data set not affecting the execution speed of the algorithm. An important feature of this technique is that it does not need *a priori* knowledge about the data set structure: it was found to be possible to apply a significance test to the shower candidate peaks within the time series in order to identify significant increases in local (normalised) meteor activity. This compares with the single-linkage technique which was often, in the past, used at a fixed cutoff level derived in a subjective manner (as discussed in Section 7.2). From these considerations, the wavelet enhancement search technique is recommended for future stream searches.

The wavelet enhancement search revealed the four major showers significantly in the data in addition to a number of other promising amplitude peaks. Most of

the latter were later determined to be artifacts. Two peaks labelled Peak A and Peak C in Section 7.7.2 were considered further in Chapter 8 together with the major showers for further analysis. Finally discussion, with some practical examples, of the use of the single-linkage algorithm on the AMOR data set was given. After extensive testing it was found that this method, while revealing the four major showers within the data set, generally tended to group together sporadic meteors into shower-like clusters. It was difficult to define a shower under this method. The only reason that the Daytime Sextantids were considered a shower, as compared with a larger grouping appearing at a similar level of the clustering hierarchy, was that this was known to be a shower by other methods. It was found, when using a randomisation technique to determine a cutoff level with a given statistical significance, that all of the shower structure found by the single-linkage method was formed from the random background. This result explains the stability problems associated with this method. Clearly, single-linkage was found to be unsatisfactory for use in an unbiased search of a radar data set such as that provided by AMOR where no *a priori* knowledge of shower structure is assumed.

The only undoubted showers, in the AMOR data set, are the four major showers: the Southern δ Aquarids, α Capricornids, Daytime Sextantids and the η Aquarids. These showers were shown to be significant, while the few other showers seen significantly under the direct search and wavelet enhancement methods were not repeatable by any other method. Peak A and C meteors, as found using the wavelet enhancement search, were also seen significantly in a direct search using the mean orbits of Table 8.19 and 8.22. They did not appear in the original direct searches of Section 7.6 as they were not listed in the surveys comprising the data set used (which was predominated by northern hemisphere biased shower declination). The large number of streams detected by Sekanina (1976), in which a similar shower (omicron Cetids) to Peak C was seen, were not included in the direct search. It was noted that both Peak A and Peak C were active for times of a long enough duration that it is entirely possible that they were simply products of the appearance of the sporadic sources at optimal positions within the AMOR radar beam illumination.

In addition to its use in the search for stream structure, the wavelet enhancement method was also found to be successful in defining the shapes of the meteor showers found within the AMOR data set. The orbital character of the η Aquarids, α Capricornids, Southern δ Aquarids and Daytime Sextantids was demonstrated, in addition to that of two shower candidates labelled Peak A and Peak C, in Chap-

ter 8. There is no mention in the literature of a shower similar to Peak A while Peak C was found (above) to have a very similar orbit to that of the Sekanina's omicron Cetids. The spread in all the orbital parameters in each of the showers was shown to be approximately that expected due to measurement uncertainty in the individual orbits. In the case of the η Aquarids this spread under represented that expected while for the α Capricornids it exceeded it. A summary of the mean orbital parameters (corrected for daily motion) determined for these showers is shown in Table 9.1.

SHOWER	$\lambda_\odot$	q	e	i	ω	Ω	V_H	V_G	α	δ	SIZE
	deg	AU		deg	deg	deg	km s^{-1}		deg	deg	
ETA	45.6	0.545	0.953	165.1	91.9	45.6	40.5	65.0	339.0	-1.4	942
SDA	127.2	0.067	0.966	30.8	154.5	307.2	36.0	40.2	340.4	-16.3	2,413
CAP	122.3	0.550	0.768	7.7	273.3	122.3	37.0	23.4	306.7	-9.3	269
DSX	186.1	0.151	0.855	23.1	212.5	6.1	30.4	31.2	154.5	-1.5	410
Peak A	313.1	0.143	0.920	64.3	141.9	133.1	36.1	42.7	162.1	-13.3	327
Peak C	45.0	0.133	0.916	37.1	214.9	225.0	34.4	36.5	19.0	-7.0	970

Table 9.1: A summary of the mean orbits of the major showers. These orbits were determined from T1995–T1999 data. They have been corrected for daily motion in those parameters experiencing such with corrections being made to centres at the solar longitude/longitude of the ascending node given; all parameters are referred to the mean epoch J2000. The showers are denoted by their acronyms: η Aquarids (ETA), Southern δ Aquarids (SDA), α Capricornids (CAP) and Daytime Sextantids (DSX). In addition to the major showers the two possible showers discussed in the text are also shown.

The daily motion in the orbital parameters was well demonstrated for the radiant position in all cases (as summarised in Table 9.2). A large longitudinal daily motion for the η Aquarids and Southern δ Aquarids relative to their latitudinal motion was noted. Relatively minor longitudinal and latitudinal daily motions were shown to be experienced by the α Capricornids. Daily motions in other parameters were also measured in the current study, a particularly convincing example was that in q, i and ω for the Southern δ Aquarids as displayed in Figure 8.13.

	η Aquarids	Southern δ Aquarids	Daytime Sextantids	α Capricornids
$(\lambda - \lambda_\odot)$	-0.15	-0.20	-0.08	-0.03
β	0.01	-0.04	-0.10	0.03

Table 9.2: A summary of the daily motion detected in the major showers.

The activity profiles of the major showers in each year were investigated. It was shown that the fluctuations in these generally mirrored similar variation in the background activity profiles indicating a lack of astronomical reality to most of these instances. There were large changes in the background character, within and

between years of AMOR data, which hampered these investigations. The shape of profiles such as the SDA changed markedly with year: only a general determination of the period of activity of the shower could be gained from such profiles.

It was necessary to combine several years data in order to detect the weak α Capricornids shower; this shower in particular has been shown to exhibit very changeable activity over time between different years. The use of a fixed radiant distribution, provided by the wavelet distribution over the five years surveyed, assumed that the distribution does not change noticeably per year. This approach is vindicated if one explores the tabulated published stream radiant and orbit information where the radiant and speed vary little between surveys while the orbital parameters may vary by much larger amounts (e.g. α Capricornids in Table 8.12). Radiant coordinates were found generally to experience lower uncertainties, making detection by radiant enhancement an important technique. It must be recognised that the use of a fixed radiant position over several years does place limits on the orbital distributions themselves which one expects to find; variations in the distributions within the geocentric speed, defined radiant region and time of detection, will of course act to offset much of this predetermination.

Chapter 10

Future Work

The wavelet transform has been shown to be effective as an enhancing tool for the observed radiant distribution in order to determine areas of over-density. It has the advantage of not requiring foreknowledge of the shape of this over-density. In the current study only a 2-D wavelet is applied to what is in fact a 4-D problem. It is envisaged that a refinement of the technique would be to use a 3-D Mexican Hat wavelet with the third dimension being in the geocentric speed: this would allow for a more precise definition of the shower and would give the chance for detection of weaker structure. It is not appropriate to use a wavelet transform including a time dimension because this parameter is strongly biased by changes in system time-coverage and sensitivity especially when several years of data are combined (as in the current study). The method of normalisation against the background rate for a single or multiple years of data used in the current study is the only solution to remove this time bias. It is impossible to include such a weighting system in a 4-D wavelet transform.

The single-linkage method, from which there had been hopes for an automatic and statistically sound method of stream detection, has been shown to be unworthy of further development for AMOR meteoroid orbit study. The problems with this technique include difficulty in the definition of significant shower structure, the instability of the clustering hierarchy and the problems associated with "chaining".

From the point of view of future data set improvement, the most important task is the increase in the pulse repetition frequency of the radar—such an increase will immediately decrease the time-lag uncertainty thereby causing all speed related parameters to be known more accurately. With this improvement the retrieval of a greater percentage of the η Aquarids shower, much of which currently merges into the background owing to large speed uncertainties, should be possible. A reliable method of determining mass might also be of benefit to the detection of showers. Meteoroids of larger mass are generally expected within distinguishable showers and therefore removal of the smallest meteoroids should remove some of the

"noise" from the data set when searching for such showers. The determination of mass involves knowledge of the amplitude of the returned radar signal, assumptions about the composition of the meteoroid and the properties of the meteor train. It is therefore not an easy task. The use of cutoff masses for shower searches have the added problem that streams have different distributions in meteoroid mass: the η Aquarids, for example, is known to have a distribution biased towards smaller meteoroids. As the meteoroids for different streams derive from different comets, it is also unsatisfactory to assume that all such meteoroids have similar compositions. This is still an interesting problem and will be the subject of future research.

The author believes that the most important future work for AMOR is that involving the study of gross-scale distributions of Solar System dust. It has been shown that all showers, except for the most major showers, are imperceptible against the sporadic background. Therefore the most important work must be in further studying these sporadics, with corrections for bias in the observation, to determine "true" dust orbit populations. Work has been initiated in the current study in this direction, with the earlier chapters being devoted to discussion of the large-scale statistics in, and bias corrections applicable to, the AMOR data set. AMOR has recently been upgraded: it now includes an orthogonal array system to transmit and receive in both the North-South and East-West directions. At the time of the current study only the former was available. The new system should provide greater coverage of the overall "all-sky" meteor population. The orbital distributions obtained, after correction for bias, are to be used in conjunction with those derived from other dust experiments (e.g. the detector aboard the Galileo spacecraft) to provide a "global" model of the Solar System dust population.

Chapter 11

Acknowledgements

I would like to thank my supervisor Prof. Jack Baggaley for his help, encouragement and the sharing of his meteor expertise, during my years at Canterbury. I would also like to thank Dr Grahame Fraser, Dr Bob Bennett, Dr Bryan Lawrence, Dr Don Grainger, Dr Mike Reid and Dr Steve Marsh: I have benefitted through their critical and helpful discussions over the time of my doctoral study.

I would like to thank the atmospheric research group at Canterbury for their help and support, I hope I gave as much as I got! Thanks to Graeme Plank for his technical support in keeping AMOR running so there was a large data set to analyse.

I wish to thank Dr Jovan Skuljan for his helpful discussions of the wavelet analysis method and for access to his pre-publication thesis and some original computer code for comparison with that being used in the current study.

I acknowledge and thank the University of Canterbury for its provision of facilities and its support through a Doctoral Scholarship during my time here. Thanks also to the Claude McCarthy Fellowship which funded my travel to the "Asteroids, Comets and Meteors '99" conference at Cornell University to present some results from this research; the Vatican Observatory for supporting my attendance at their summer school in 1997; the New Zealand Meteorological Society for their support in my attendance at their 1999 conference; the Marsden Fund for support to attend the "Dust in the Solar System and Other Planetary Systems" conference at the University of Kent at Canterbury, England and finally the Physics and Astronomy Department at the University of Canterbury for their financial help in these attendances.

Jack Baggaley, Bob Bennett, Janine Galligan and Steve Marsh are gratefully acknowledged for their stamina in the proof reading of this thesis.

Thank-you to my family for their help and support during my years of university study. Finally and most importantly a special acknowledgement to my wife, Janine, for all of her help, support and patience, through the inevitable ups and downs of this research project.

Appendix A

Glossary

A number of acronyms are used in the current study in order to make the reading less terse. There are also several mathematical symbols which appear often in the text. Table A.1, over-leaf, summarises these.

Note that the various radiant position defining coordinates used in the current study are corrected for the Earths' rotation, gravitational and zenith attraction, as discussed in Section 2.6.

Grouping	Symbol	Meaning
Date coverage	TYYYY	Equinoctial year starting at YYYY vernal equinox
	AYYYY	Equinoctial year starting at YYYY autumnal equinox
Meteor showers	ETA	η Aquarids
	SDA	Southern δ Aquarids
	CAP	α Capricornids
	DSX	Daytime Sextantids
Sporadic source regions	AH	Antihelion
	HN	Helion
	AX	Apex of the Earth's way
Dissimilarity functions	D_{SH}	Southworth and Hawkins (1963)
	D_D	Drummond (1979)
	D_H	Jopek (1993a)
	D_N	Valsecchi et al. (1999)
Orbital elements	a	Semi-major axis length
	q	Perihelion distance
	Q	Aphelion distance
	e	Eccentricity
	ω	Argument of perihelion
	Ω	Longitude of the ascending node
Speeds	V_A	Atmospheric speed
	V_G, $\mathbf{V}_G$	Geocentric speed and velocity
	V_H, $\mathbf{V}_H$	Heliocentric speed and velocity
	V_x, V_y, V_z	Heliocentric velocity components
	V_E, $\mathbf{V}_E$	Orbital speed and velocity of Earth
Radiant coordinates	α, δ	Right ascension and declination
	λ, β	Ecliptic longitude and latitude
	$\lambda_\odot$	Mean solar ecliptic longitude
	$\lambda_\odot^c$	$\lambda_\odot$ at centre of activity/mean $\lambda_\odot$ of shower
	λ_R	Ecliptic longitude w.r.t. $\lambda_\odot$ ($\lambda_R = \lambda - \lambda_\odot$)
	λ_N	λ_R corrected to $\lambda_\odot^c$ for daily motion
	β_N	β corrected to $\lambda_\odot^c$ for daily motion
	P_N	any parameter, P, corrected to $\lambda_\odot^c$ for daily motion
Wavelet transform terms	WTC	Wavelet transform coefficient
	$w(x, y)$	Wavelet coefficient at spatial coordinates (x, y)
	w_{max}	Maximum wavelet coefficient
	w_{max}/a	w_{max} normalised to probe-size (a)
	w_{max}/N_S	w_{max} normalised to background activity (N_S)
	a	Wavelet prove size
	N_S	Total number of meteors in a given source region
Miscellaneous	NZST	New Zealand Standard Time (GMT+12^h)
	PRF	Pulse Repetition Frequency (Radar)

Table A.1: Thesis glossary.

Appendix B

AMOR Orbit Catalogue Files

In the past ten years there have been near to $\sim 10^6$ high quality meteoroid orbits reduced. This appendix shows the three formats of file which have been used over the years (1990–1999) to record these data. For the interested reader these tables provide an insight to the wide variety of parameters which are recorded for each meteoroid used for orbit analysis. A reference is also available here as to any anomalies present in the `YYMMDD.amr` data files.

B.1 The Three Orbit File Formats

In each case there is a small SiteData record which contains the various fundamental parameters measured at each of the sites. These parameters are first-order reduced results—higher-order reductions are stored in the main body of the `AMORData` records.

For each parameter the identifier, symbol, unit, storage multiplier, Pascal storage data type, number of bytes used, record ending byte and description are given. Three data types are used: 'T' is a signed two-byte word, 'W' is an unsigned two-byte word and 'B' is an unsigned byte. These parameters are stored under DOS Turbo Pascal or VMS DEC Pascal. The extraction program `amr2asc.exe` (see Section C.1) used to read `YYMMDD.amr` files for this project is written in `C` and compiled in `gcc` under Linux on an Intel Pentium computer. For two-byte integers Linux uses the reverse storage coding to that used under DOS/VMS, hence to read such a number `amr2asc.exe` reads two bytes, reverses them and then recombines them into a two-byte integer.

AMORData							
Year,Month,Day				B	3	3	date in NZST
Hour,Min,Sec				B	3	6	time in NZST
Number				B	1	7	Sequential number in Metstore
PersTime		sec		B	1	8	Duration of a persistant
ReductionCode				B	1	9	
SpareCode				B	1	10	
Home,Nutt,Spit				ASD	42	52	14 bytes per site (3 sites)
Lag12		pulses	10	T	2	54	Lags between Home and Nutt
Lag13		pulses	10	T	2	56	Lags between Home and Spit
							N.B: Lag23 = Lag13 - Lag12
AvTin,AvTos			10	W	4	60	Average of locked phases
Phase			10	W	2	62	Relative phase angle, Home
Elev	ψ		10	W	2	64	Elevation angle of the meteor
AvFresVel		km s^{-1}	10	W	2	66	Average Fresnel velocity
AtmosDecel		km s^{-2}	10	T	2	68	Fresnel deceleration
Vx,Vy,Vz		km s^{-1}	10	T	6	74	Observed velocity components
Azimuth			10	W	2	76	Azimuth angle of velocity
Zenith			10	W	2	78	Zenith angle of meteor trail
Speed			10	W	2	80	Calculated speed of the meteor
RightAsc	α		10	W	2	82	R.A. of the corrected radiant
Declin	δ		10	T	2	84	Declination, corrected radiant
SpeedGeo			10	W	2	86	Corrected geocentric speed
Vmx,Vmy,Vmz		km s^{-1}	10	T	6	92	Heliocentric velocity components
		+y to vernal equi +x to increasing longit.+z to north					
SpeedHelio	V_H	km s^{-1}	10	W	2	94	Heliocentric speed
LongAsc1950	Ω_{1950}	deg	100	W	2	96	at mean equinox of 1950.0
Inclin	i	deg	100	W	2	98	Inclination of the orbit
Perihel	ω	deg	100	T	2	100	Argument of perihelion
Ecc	e		100	W	2	102	Eccentricity of the orbit
SemiMajor	a	AU	100	T	2	104	Semi-major axis
PeriDist	q	AU	100	W	2	106	Perihelion distance
PeriLong	λ	radians	1000	T	2	108	Ecliptic longitude and latitude
PeriLat	β	radians	1000	T	2	110	of perihelion
AMORSiteData (ASD)							
Noise				B	1	1	Noise from detection routine
Max				B	1	2	Maximum amplitude, smoothed
Imax				B	1	3	Index location of maximum
NumHalfCycles				S	1	4	Num. Fresnel half oscillations
Range		km		W	2	6	Range to the meteor trail
Rise		pulses		B	1	7	Echo profile rise time
Decay		pulses		B	1	8	Exponential decay time
DiffHeight		km	10	W	2	10	Diffusion height
Altitude		km	10	W	2	12	Geometric altitude
Velocity		km s^{-1}	10	W	2	14	Fresnel velocity

Table B.1: AMORData record format used from 1990–1992.

AMORData93							
Year,Month,Day				B	3	3	date in NZST
Hour,Min,Sec				B	3	6	time in NZST
Number				B	1	7	Sequential number in Metstore
PersTime		sec		B	1	8	Duration of a persistant
Home,Nutt,Spit				S93	60	68	
Lag12		pulses	10	T	2	70	Lags between Home and Nutt
Lag13		pulses	10	T	2	72	Lags between Home and Spit
							Lag23 = Lag13 - Lag12
AvTin,AvTos			10	W	4	76	Average of locked phases
Phase			10	W	2	78	Relative phase angle, Home
Elev	ψ		10	W	2	80	Elevation angle of the meteor
AvFresVel		km s^{-1}	10	W	2	82	Average Fresnel velocity
NotUsed2				W	2	84	not used in 1993/4 reductions
AtmosDecel		km s^{-2}	10	T	2	86	Fresnel deceleration
Vx,Vy,Vz			10	T	6	92	Observed velocity components
Azimuth			10	W	2	94	Azimuth angle of velocity
Zenith			10	W	2	96	Zenith angle of meteor trail
Speed			10	W	2	98	Calculated speed of the meteor
RightAsc	α		10	W	2	100	R.A. of the corrected radiant
Declin	δ		10	T	2	102	Declination, corrected radiant
SpeedGeo			10	W	2	104	Corrected geocentric speed
Vmx,Vmy,Vmz			10	T	6	110	Heliocentric velocity components
SpeedHelio	V_H	km s^{-1}	10	W	2	112	Heliocentric speed
LongAsc1950	Ω_{1950}	deg	100	W	2	114	at mean equinox of 1950.0
Inclin	i	deg	100	W	2	116	Inclination of the orbit
Perihel	ω	deg	100	T	2	118	Argument of perihelion
Ecc	e		100	W	2	120	Eccentricity of the orbit
SemiMajor	a	AU	100	T	2	122	Semi-major axis
PeriDist	q	AU	100	W	2	124	Perihelion distance
PeriLong	λ	radians	1000	T	2	126	Ecliptic longitude and latitude
PeriLat	β	radians	1000	T	2	128	of perihelion
SiteData93 (S93)							
Noise				B	1	1	Noise from detection routine
Max				B	1	2	Maximum amplitude, smoothed
Islope				B	1	3	index of max slope
Imax				B	1	4	Index location of maximum
NumHalfCycles				S	1	5	Num. Fresnel half oscillations
Range		km		W	2	7	Range to the meteor trail
Duration				B	1	8	Use for echo duration
Rise		pulses	8	B	1	9	Echo profile rise time
Decay		pulses		B	1	10	Exponential decay time
TauErr				B	1	11	Fractional uncertain in decay
DiffHeight		km	10	W	2	13	Diffusion height
Altitude		km	10	W	2	15	Geometric altitude
Velocity		km s^{-1}	10	W	2	17	Fresnel velocity
Vris				W	2	19	speed from echo rise-times
NotUsed1				B	1	20	not used in 1993/4 reductions

Table B.2: `AMORData93` record format used from 1993–1994.

AMORData95							
Year,Month,Day				B	3	3	date in NZST
Hour,Min,Sec				B	3	6	time in NZST
Number				B	1	7	Sequential number in Metstore
PersTime		sec		B	1	8	Duration of a persistant
Home,Nutt,Spit				S95	63	71	
Lag12		pulses	10	T	2	73	Lags between Home and Nutt
Lag13		pulses	10	T	2	75	Lags between Home and Spit
							Lag23 = Lag13 - Lag12
Phase14	λ_{14}			W	2	77	Angle antennas 1-4 separ 3.0λ
Phase15	λ_{15}			W	2	79	Angle antennas 1-5 separ 11.5λ
ErrPhase14				B	1	80	Uncert in Phase14
ErrPhase15				B	1	81	Uncert in Phase15
Elev	ψ		10	W	2	83	Elevation angle of the meteor
							from these phases
AvFresVel		km s^{-1}	10	W	2	85	Average Fresnel velocity
AtmosDecel		km s^{-2}	10	B	1	86	Fresnel deceleration
Vx,Vy,Vz			10	T	6	92	Observed velocity components
Azimuth			10	W	2	94	Azimuth angle of velocity
Zenith			10	W	2	96	Zenith angle of meteor trail
Speed			10	W	2	98	Calculated speed of the meteor
RightAsc	α		10	W	2	100	R.A. of the corrected radiant
Declin	δ		10	T	2	102	Declination, corrected radiant
SpeedGeo			10	W	2	104	Corrected geocentric speed
Vmx,Vmy,Vmz			10	T	6	110	Heliocentric velocity components
SpeedHelio	V_H	km s^{-1}	10	W	2	112	Heliocentric speed
LongAsc1950	Ω_{1950}	deg	100	W	2	114	at mean equinox of 1950.0
Inclin	i	deg	100	W	2	116	Inclination of the orbit
Perihel	ω	deg	100	T	2	118	argument of perihelion
Ecc	e		1000	W	2	120	Eccentricity of the orbit
SemiMajor	a	AU	100	T	2	122	Semi-major axis
PeriDist	q	AU	1000	W	2	124	Perihelion distance
PeriLong	λ	radians	1000	T	2	126	Ecliptic longitude and latitude
PeriLat	β	radians	1000	T	2	128	of perihelion
SiteData95 (S95)							
Noise				B	1	1	Noise from detection routine
Max				B	1	2	Maximum amplitude, smoothed
Islope				W	2	4	accurate index of max slope
Imax				B	1	5	Index location of maximum
NumHalfCycles				S	1	6	Num. Fresnel half oscillations
Range		km		W	2	8	Range to the meteor trail
Duration				B	1	9	Use for echo duration
Rise		pulses	8	B	1	10	Echo profile rise time
Tau		pulses		W	2	12	Exponential decay time
TauErr				B	1	13	Fractional uncertain in decay
DiffHeight		km	10	W	2	15	Diffusion height
Altitude		km	10	W	2	17	Geometric altitude
Velocity		km s^{-1}	10	W	2	19	Fresnel velocity
Vris		km s^{-1}	?	W	2	21	speed from echo rise-times

Table B.3: `AMORData95` record format used from 1995 onwards.

Appendix C

Summary of Developed Program Code

This appendix presents some of the many C and MATLAB programs and functions which have been developed in the course of the current study. Almost all software including dendrogram drawing routines, the single-linkage package, the wavelet package etc. have been written by this study's author. Programs such as `random_bin.c` are not presented here as they are $\sim$ 20 pages in length, otherwise most of the important programs used for single-linkage, wavelet enhancement searching and direct mean stream searching are listed in addition to functional definitions for the D-criteria.

C.1 Data Retrieval

Data are stored in `YYMMDD.amr` files by VAX Pascal reduction programs. A C program, `amr2asc.exe`, is used to read the data back. This program can filter orbits based on orbital inclination, eccentricity and also automatically filters the files for several anomalies which have occurred from time to time in the data reduction process. The calling syntax for the program is:

`amr2asc.exe` *Source_Directory Start_YYMMDD End_YYMMDD Output_File*,

where the *Source_Directory* is searched for data files from *Start_YYMMDD*, up to and including, *End_YYMMDD*; after filtering of the data set output orbits are written to *Output_File*. Additional commands may be added to the end of this sequence, these set conditions for selection of particular meteors based on:

`--sl` $\lambda_{\odot}^{i}$ $\lambda_{\odot}^{f}$	a period of time measured in $\lambda_{\odot}$,
`--ve` yr^{i} yr^{f}	a (4 digit) inter-vernal equinoctial year range,
`--ae` yr^{i} yr^{f}	a (4 digit) inter-autumnal equinoctial year range,

and/or

`--mode` n	an output format to use (default=1).

The program allows filtering to be performed via the `filter_orbit` function. This typically removes orbit records with no orbital element information recorded, may limit orbits according to orbital direction (prograde, retrograde, etc.) and also may limit orbits according to their degree of eccentricity (e.g. removes very hyperbolic orbits). In principle `filter_orbit` can perform any type of filtering which may be specified in program code. In some cases orbital element record files contain faulty or repeated orbits—the scanning procedure removes such instances also.

C.2 Data Input

The program amr2asc.exe produces orbital element (*.ele) files in a standard format for reading into C and MATLAB. In C the function used to read such files is called read_orbit_ele_file. From a specified file which has been opened for reading, an array of orbit_elements structures is returned, which are defined by:

```
struct orbit_elements {
  char name_id[18];
  short MMDD_start,MMDD_end,MMDD_mean; /* only used for csf */
  short EqYr;                          /* 4 digit equinoctial year */
  short Epoch;
  double PeriDist,Ecc,Inc,ArgPeri,LongAsc1950,RightAsc,Declin,
    SpeedHelio,SpeedGeo,Speed,EcLong,EcLat,SemiMajor,
    Mjd,DayNum,DecTime,SolarLong,
    Vmx,Vmy,Vmz,Vgx,Vgy,Vgz;
  short at_asc_node,post_peri;
};
```

The read_orbit_ele_file C procedure is used to read in orbital element files. It can take several different versions of such files as input. The main files are the standard AMOR orbital element *.ele files, for which an orbit_file_type '1' is entered, and the mean stream orbit data file from the common stream format data set of Appendix D, for which a '2' is entered.

```
struct orbit_elements *read_orbit_ele_file(FILE *fin,
                        int orbit_file_type,int *num_orbits) {
  /* by David Galligan 1998-2000 */
  int stream_size,stream_source;
  double LA2000,RA2000,DEC2000,dummy1=0.0,dummy2=0.0;
  double *VG_comp;
  int clump_num;
  int index=0;
#define orbit_string_len 1500
  int n_orb_init=300000;
  char nullstring[200]="";
  char orbit_string[orbit_string_len]="";
  char orbit_date[7]="";
  char orbit_time[7]="";
  char orbit_seqnum[3]="";
  struct orbit_elements *orbits;
  /* send help if fin==NULL sent + return code -1 */
  if (!fin) {
    warning_msgf("read_orbit_ele_file","Returning_Information");
    printf("____read_orbit_ele_file_file_type_numbers:_\n");
    printf("______1:_*.ele_file_(standard)\n");
    printf("______2:_*.csf_file_(common_stream_format)\n");
    printf("______3:_*.mel_file_(gb_dcrit_cols_style)\n");
    return(orbits);
  }
  /* rewind input file */
  fseek(fin,0L,0);
  /* malloc space for velocity component matrix */
  VG_comp=malloc_dvector(3);
  /* malloc place for orbits */
```

```
orbits=(struct orbit_elements*)
          malloc(n_orb_init*sizeof(struct orbit_elements));
printf("%d\n",n_orb_init*sizeof(struct orbit_elements));
if (!orbits)
  error_msg("orbits malloc error in read_orbit_ele_file");
/* ignore header */
fgets(nullstring,200,fin);
fgets(nullstring,200,fin);
fgets(nullstring,200,fin);
/* read in orbits */
while (!(feof(fin))) {
  fgets(orbit_string,orbit_string_len,fin);
  if (!feof(fin)) {
    if (orbit_file_type==1) {
      sscanf(orbit_string,"%s %s %s %hd %lf %lf %lf %lf %lf "
               "%lf %lf %lf %lf %lf %lf %lf %lf %lf %lf %lf "
               "%lf %*f %*f %*f %*f %*f %*d %lf %lf %hd %hd",
         orbit_date,                orbit_time,
         orbit_seqnum,              &orbits[index].EqYr,
         &orbits[index].Mjd,        &orbits[index].SemiMajor,
         &orbits[index].PeriDist,   &orbits[index].Ecc,
         &orbits[index].Inc,        &orbits[index].ArgPeri,
         &orbits[index].LongAsc1950,&orbits[index].EcLong,
         &orbits[index].EcLat,      &orbits[index].RightAsc,
         &orbits[index].Declin,     &orbits[index].SpeedGeo,
         &orbits[index].SpeedHelio, &orbits[index].Speed,
         &orbits[index].Vmx,        &orbits[index].Vmy,
         &orbits[index].Vmz,        &orbits[index].SolarLong,
         &orbits[index].DayNum,     &orbits[index].at_asc_node,
         &orbits[index].post_peri);
      /* unique orbit identifier 990221 DPG*/
      sprintf(orbits[index].name_id,"%s %s %3s",
              orbit_date,orbit_time,orbit_seqnum);
    }
    else if (orbit_file_type==2) {
      /* extract orbit information for "csf_str"  string */
      sscanf(orbit_string,"%*d %s %d %hd %hd %hd %d %lf %lf "
                   "%lf %lf %lf %lf %lf %lf %lf %lf %lf %hd %d",
         orbits[index].name_id, &clump_num,
         &orbits[index].MMDD_start,&orbits[index].MMDD_end,
         &orbits[index].MMDD_mean, &stream_source,
         &orbits[index].SemiMajor, &orbits[index].PeriDist,
         &orbits[index].Ecc,       &orbits[index].Inc,
         &orbits[index].ArgPeri,   &orbits[index].LongAsc1950,
         &orbits[index].RightAsc,  &orbits[index].Declin,
         &orbits[index].SpeedGeo,  &orbits[index].SolarLong,
         &orbits[index].at_asc_node,&stream_size);
      /* reduce from 1950 to 2000 */
      ReducePresentTo2000(JD1950,
                          orbits[index].RightAsc,
                          orbits[index].Declin,
                          dummy1,orbits[index].LongAsc1950,
                          &RA2000,&DEC2000,
                          &dummy2,&LA2000);
      orbits[index].RightAsc=RA2000;
```

```
        orbits[index].Declin=DEC2000;
        orbits[index].LongAsc1950=LA2000;
        if (orbits[index].at_asc_node)
          orbits[index].SolarLong=LA2000;
        else
          orbits[index].SolarLong=fmod(LA2000+180.0,360.0);
      }
      else if (orbit_file_type==3) {
        /* gb_dcrit_cols (matlab) style orbit *.mel file */
        sscanf(orbit_string,"%lf_%lf_%lf_%lf_%lf_%lf_%lf_%lf_"
                            "%lf_%lf_%lf_%lf_%hd_%hd",
           &orbits[index].PeriDist,    &orbits[index].Ecc,
           &orbits[index].Inc,         &orbits[index].ArgPeri,
           &orbits[index].LongAsc1950, &orbits[index].EcLong,
           &orbits[index].EcLat,       &orbits[index].SemiMajor,
           &orbits[index].SolarLong,   &orbits[index].SpeedGeo,
           &orbits[index].RightAsc,    &orbits[index].Declin,
           &orbits[index].at_asc_node, &orbits[index].post_peri);
      }
      else
        error_msgf("read_orbit_ele_file",
                   "Wrong_orbit_file_type_entered");
      /* change to radians */
      orbits[index].Inc*=deg2rad;
      orbits[index].ArgPeri*=deg2rad;
      orbits[index].LongAsc1950*=deg2rad;
      orbits[index].SolarLong*=deg2rad;
      orbits[index].RightAsc*=deg2rad;
      orbits[index].Declin*=deg2rad;
      /* Which Epoch are elements for? */
      orbits[index].Epoch=2000;

      /* calculate VG components (Opik 1951 Type System) */
      calc_VG_components(orbits[index],VG_comp);
      orbits[index].Vgx=VG_comp[0];
      orbits[index].Vgy=VG_comp[1];
      orbits[index].Vgz=VG_comp[2];
      ++index;
      if (index==(n_orb_init-1)) {
        n_orb_init+=50000;
        printf("B%d\n",n_orb_init);
        orbits=resize_orbits_array(orbits,n_orb_init);
      }
    }
  }
  *num_orbits=index;
  /* realloc matrices/vectors */
  orbits=resize_orbits_array(orbits,*num_orbits);
  free((double *) VG_comp);
  return(orbits); /* returns number of orbits read */
}
```

C.3 *D*-criteria

The *D*-criteria discussed in Chapter 6 and used in Chapter 7 for direct and associative stream searching are defined in a number of C functions. These all have the same input syntax with two orbits entered in the `(struct) orbit_elements` form as the first two parameters and a maximum D value entered as the third parameter. These functions are now listed with the Southworth and Hawkins (1963) *D*-criterion being calculated by `dissim_DSH`, that of Drummond (1981) by `dissim_DD` and that of Valsecchi et al. (1999) by `dissim_DN`. The *D*-criterion of Jopek (1993a) is determined by `dissim_DJ`—it is not listed here due to its similarity to `dissim_DSH`.

```
double dissim_DSH(struct orbit_elements x,
                  struct orbit_elements x1,
                  double d_max_stop) {
  /* by David Galligan 1996-2000 */
  double Dsqred, cosI_2, BigI1, BigPi, diff_LongAsc, diff_ArgPeri,
         sum_Inc, sqr_diff_Ecc, sqr_diff_PeriDist, dissim,
         sqr_d_max_stop, cos_fract;
  double local_eps = 2e-16; /* fine eps for cos(I/2)~=0 */
  double local_eps_2 = 1e-4;/* coarse eps for sum_i~=pi test */
  /* basic reusable combinations */
  sqr_d_max_stop=pow2(d_max_stop);
  sqr_diff_Ecc=pow2(x.Ecc-x1.Ecc);
  sqr_diff_PeriDist=pow2(x.PeriDist-x1.PeriDist);
  /* primary check against set max. dissim. size (d_max_stop) */
  if ((sqr_diff_Ecc<=sqr_d_max_stop) &&
      (sqr_diff_PeriDist<=sqr_d_max_stop)) {
    diff_LongAsc=x.LongAsc1950-x1.LongAsc1950;
    diff_ArgPeri=x.ArgPeri-x1.ArgPeri;
    sum_Inc=(x.Inc+x1.Inc);
    BigI1=pow2(2*sin(0.5*(x.Inc-x1.Inc)))+sin(x.Inc)*sin(x1.Inc)
          *pow2(2*sin(0.5*diff_LongAsc));
    if (BigI1>4.01)
      error_msgf("dissim_DSH","1-0.25*BigI1_negative");
    else if (BigI1>4.0) BigI1=4.0;
    cosI_2=sqrt_sf(1-0.25*BigI1);
    /* check for near zero cos(I/2) */
    if ((fabs(cosI_2)<local_eps)) {
      if ((fabs(pi_val-sum_Inc)<local_eps_2)) /* coarse eps */
        cos_fract=1.0;
      else {
        /* error if misunderstood cos(I/2)=0 conditions */
        fprintf(stderr,
                "Param: i1=%20.17f, i2=%20.17f, dLA=%19.16f\n",
                x.Inc, x1.Inc, diff_LongAsc);
        error_msgf("dissim_DSH","div. by 0 w/out sum_Inc=180");
      }
    }
    else cos_fract=cos(0.5*sum_Inc)/cosI_2;
    if (fabs(diff_LongAsc)>pi_val)
      BigPi=diff_ArgPeri
            -2*asin_protect(cos_fract*sin(0.5*diff_LongAsc));
    else
      BigPi=diff_ArgPeri
```

```
                +2*asin_protect(cos_fract*sin(0.5*diff_LongAsc));
    Dsqred=sqr_diff_Ecc+sqr_diff_PeriDist+BigI1+
           pow2((x.Ecc+x1.Ecc)*sin(0.5*BigPi));
    dissim=sqrt_sf(Dsqred);
    if (dissim>d_max_stop) dissim=999.0;
    return(dissim);
  }
  /* return 999.0 for dissimilarity > d_max_stop */
  else return(999.0);
}

double dissim_DD(struct orbit_elements x,struct orbit_elements x1,
                 double d_max_stop)
{
  /* by David Galligan 1996-2000 */
  double Dsqred,BigI,Theta,diff_Ecc,sum_Ecc,diff_LongAsc,
         diff_EcLong,dissim,sqr_frac_PeriDist,sqr_frac_Ecc,
         sqr_d_max_stop;
  double local_eps = 2e-16;
  diff_Ecc=x.Ecc-x1.Ecc;  sum_Ecc=x.Ecc+x1.Ecc;
  /* protect against division by zero */
  if (fabs(x.PeriDist+x1.PeriDist)<local_eps)
    sqr_frac_PeriDist=0.0;
  else
    sqr_frac_PeriDist=pow2((x.PeriDist-x1.PeriDist)
                           /(x.PeriDist+x1.PeriDist));
  if (fabs(sum_Ecc)<local_eps)
    sqr_frac_Ecc=0.0;
  else
    sqr_frac_Ecc=pow2((diff_Ecc)/(sum_Ecc));
  /* test whether to bother continuing */
  sqr_d_max_stop=pow2(d_max_stop);
  if ((sqr_frac_Ecc<sqr_d_max_stop)
   && (sqr_frac_PeriDist<sqr_d_max_stop)) {
    diff_LongAsc=x.LongAsc1950-x1.LongAsc1950;
    diff_EcLong=x.EcLong-x1.EcLong;
    BigI=acos_protect(cos(x.Inc)*cos(x1.Inc)
                      +sin(x.Inc)*sin(x1.Inc)*cos(diff_LongAsc));
    Theta=acos_protect(sin(x.EcLat)*sin(x1.EcLat)
                       +cos(x.EcLat)*cos(x1.EcLat)*cos(diff_EcLong));
    Dsqred=sqr_frac_Ecc+sqr_frac_PeriDist+pow2(recip_pi*BigI)
           +pow2(0.5*recip_pi*sum_Ecc*Theta);
    dissim=sqrt_sf(Dsqred);
    /* return 999.0 for dissimilarity > d_max_stop */
    if (dissim>d_max_stop) dissim=999.0;
    return(dissim);
  }
  else
    return(999.0);
}


void calc_VG_components(struct orbit_elements x,double *Out31) {
  /* by David Galligan 1999-2000 */
  /* Used by dissim_DN for Opik VG component calculation.
```

```
      Calculates VG components relative to Earth Velocity
      All components are J2000.0 and all angles are in radians */
  int row;
  double rot_xz[3][3];
  double Vg_comp[3];
  double Earth_EPS,sin_EPS,cos_EPS,LE,sin_LE,cos_LE;
  double speed_Earth=29.7; /* Average Earth Speed [km/s] */
  /* Obliquity of Earth orbit for J2000.0 (Boulet)
     (23.0+26/60+21.448/3600)*deg2rad; */
  Earth_EPS=0.40909280;
  sin_EPS=sin(Earth_EPS);
  cos_EPS=cos(Earth_EPS);
  /* Terrestial Longitude J2000.0 */
  LE=x.SolarLong-pi_val;
  sin_LE=sin(LE);
  cos_LE=cos(LE);
  /* Rotation Matrix */
  rot_xz[0][0]=cos_LE;          rot_xz[0][1]=sin_LE*cos_EPS;
  rot_xz[0][2]=sin_LE*sin_EPS;  rot_xz[1][0]=-sin_LE;
  rot_xz[1][1]=cos_LE*cos_EPS;  rot_xz[1][2]=cos_LE*sin_EPS;
  rot_xz[2][0]=0.0;             rot_xz[2][1]=-sin_EPS;
  rot_xz[2][2]=cos_EPS;
  /* Vg components before rotation */
  Vg_comp[0]=-(x.SpeedGeo/speed_Earth)*cos(x.Declin)
              *cos(x.RightAsc);
  Vg_comp[1]=-(x.SpeedGeo/speed_Earth)*cos(x.Declin)
              *sin(x.RightAsc);
  Vg_comp[2]=-(x.SpeedGeo/speed_Earth)*sin(x.Declin);
  /* Rotate Vg components */
  for (row=0; row<3; row++)
    Out31[row]=rot_xz[row][0]*Vg_comp[0]
      +rot_xz[row][1]*Vg_comp[1]
      +rot_xz[row][2]*Vg_comp[2];
}


double dissim_DN_fast(struct orbit_elements x1,
                      struct orbit_elements x2,
                      double d_max_stop) {
  /* by David Galligan 1999-2000 */
  /* service function for dissim_DN...provides core algorithm */
  double w1=1.0,w2=1.0,w3=1.0;
  double LS1,Vg1,phi1,cos_theta1,
         LS2,Vg2,phi2,cos_theta2,
         d_phi_A,d_phi_B,d_lambda_A,d_lambda_B,d_zeta,
         dissim,sqr_diff_Vg,sqr_diff_cos_theta;
  double speed_Earth=29.7; /* Average Earth Speed [km/s] */
  Vg1=x1.SpeedGeo/speed_Earth;
  Vg2=x2.SpeedGeo/speed_Earth;
  /* primary comparison */
  sqr_diff_Vg=pow2(Vg2-Vg1);
  /* primary check against set maximum dissim. (d_max_stop) */
  if (sqr_diff_Vg<=d_max_stop) {
    /* orbit 1B */
    LS1=x1.SolarLong;
```

```
    phi1=atan2(x1.Vgx,x1.Vgz);/* atan2 to correct quadrant */
    cos_theta1=x1.Vgy/Vg1;
    /* orbit 2B */
    LS2=x2.SolarLong;
    phi2=atan2(x2.Vgx,x2.Vgz);/* atan2 to correct quadrant */
    cos_theta2=x2.Vgy/Vg2;
    /* final comparison */
    sqr_diff_cos_theta=w1*pow2(cos_theta2-cos_theta1);
    /* secondary check against set maximum dissim. */
    if (sqr_diff_cos_theta<=d_max_stop) {
      d_phi_A=2*sin((phi2-phi1)/2);
      d_phi_B=2*sin((pi_val+phi2-phi1)/2);
      d_lambda_A=2*sin((LS2-LS1)/2);
      d_lambda_B=2*sin((pi_val+LS2-LS1)/2);
      d_zeta=DMIN(w2*pow2(d_phi_A)+w3*pow2(d_lambda_A),
                  w2*pow2(d_phi_B)+w3*pow2(d_lambda_B));
      dissim=sqrt_sf(sqr_diff_Vg+sqr_diff_cos_theta+d_zeta);
    }
    /* return 999.0 for dissimilarity > d_max_stop */
    else dissim=999.0;
  }
  else dissim=999.0;
  if (dissim>d_max_stop) dissim=999.0;
  return dissim;
}

double dissim_DN(struct orbit_elements x1,
                 struct orbit_elements x2,
                 double d_max_stop) {
  /* by David Galligan 1999-2000 */
  /* obtains geocentric velocity components and then turns
     over to dissim_DN_fast to do dissimilarity calculation */
  double dissim,*VG_comp;
  /* calculate VG components (Opik 1951 Type System) */
  VG_comp=malloc_dvector(3);
  calc_VG_components(x1,VG_comp);
  x1.Vgx=VG_comp[0]; x1.Vgy=VG_comp[1]; x1.Vgz=VG_comp[2];
  calc_VG_components(x2,VG_comp);
  x2.Vgx=VG_comp[0]; x2.Vgy=VG_comp[1]; x2.Vgz=VG_comp[2];
  free((double *) VG_comp);
  dissim=dissim_DN_fast(x1,x2,d_max_stop);
  return(dissim);
}
```

In MATLAB programs the C dissimilarity functions listed above are called directly to ensure that exactly the same form of the function is applied in both environments. An equally important reason for calling these functions from a C gateway "Mex" function is in order to obtain the extra speed offered by C in calculating a large number of dissimilarities. MATLAB suffers an enormous loss of speed when multiple nested `for` loops are used in the code. Due to the memory overheads when dealing with a large-sized orbit data set it is impossible to use native MATLAB alternatives to remove the necessity for `for` loops—an external call to C is found in many cases to be the only feasible option in the current study.

The C to MATLAB crossover function `calc_dissim_mex` is implemented in the program `calc_dissim_mex.c`. The program consists of a gateway function `mexFunction` which transfers variables back and forth between MATLAB and C. This function calls the algorithmic function `find_dissims` which calculates the inter-orbital dissimilarity between every orbit in the input matrix up to a cutoff level defined by an input maximum dissimilarity. The output dissimilarity matrix consists of '-1' in the lower triangular region and in any locations whose dissimilarity is above the cutoff level; the dissimilarities for the requested dissimilarity function are contained in the upper triangular region. The called function `dissim_function` chooses between the various dissimilarity functions, by number, shown above.

```
/* calc_dissim_mex.c
   by David Galligan 1998-2000 */
#include "math.h"
#include "mex.h"
#include "genutils.h"
#include "meteors.h"
#include "numbers_def.h"
/* Input Arguments */
#define orbits_in      prhs[0]
#define dissim_num_in  prhs[1]
#define d_max_stop     999.0
/* Output Arguments */
#define dissims_out    plhs[0]
/* Prototypes */
void find_dissims(double *orbits,int num_orbits,double *dissims,
                  int dissim_func_num);
void find_dissims(double *orbits,int num_orbits,double *dissims,
                  int dissim_func_num) {
  struct orbit_elements orb1,orb2;
  int i,j;
  /* Firstly fill dissim matrix with -1 at each point. This
     makes it easier to pick out the upper triang real dissims
     from the lower triang which I don't bother filling. */
  for (i=0; i<num_orbits;i++)
    for (j=0; j<num_orbits;j++)
      dissims[ind2d(i,j,num_orbits)]=-1.0;
  /* Now fill upper triangle with real dissims */
  for (i=0; i<(num_orbits-1);i++) {
    orb1=read_incoming_dcrit_orbits(orbits,i,num_orbits);
    for (j=i+1; j<num_orbits;j++) {
      orb2=read_incoming_dcrit_orbits(orbits,j,num_orbits);
      dissims[ind2d(i,j,num_orbits)]=
          dissim_function(orb1,orb2,d_max_stop,dissim_func_num);
    }
  }
return;
}
void mexFunction(
                 int nlhs,       mxArray *plhs[],
                 int nrhs, const mxArray *prhs[]
                 ) {
  double *dissims,*orbits;
  int num_orbits;
```

```
  int dissim_func_num;
  double (*dissim_func)();
  /* Check for proper number of arguments and columns */
  if (nrhs != 2 || mxGetN(orbits_in)!=17)
    mexErrMsgTxt(
       "A matrix of orbits with columns in the form given by"
       "dcrit_cols is required followed by the number of the"
       "dissimilarity function to use. Angles are entered in"
       "degrees");
  /* Sort out values of interest */
  num_orbits = (int) mxGetM(orbits_in);
  dissim_func_num=(int) mxGetScalar(dissim_num_in);
  /* Create matrices for the return argument */
  dissims_out=mxCreateDoubleMatrix(num_orbits,num_orbits,mxREAL);
  /* Assign pointers to the various parameters */
  orbits=mxGetPr(orbits_in);
  dissims=mxGetPr(dissims_out);
  /* calculate dissimilarities */
  find_dissims(orbits,num_orbits,dissims,dissim_func_num);
  return;
}
```

The C to MATLAB crossover function `calc_dissim_2grps_mex` is implemented in the program `calc_dissim_2grps_mex.c`. This function accepts the input of two orbital data sets, a dissimilarity function identification number and a maximum dissimilarity cutoff. The algorithmic function `find_dissims` calculates the dissimilarity between each of the orbits in the first data set and each of those in the second data set. The inter-data set dissimilarity rectangular matrix is output.

```
/* calc_dissim_2grps_mex.c
   by David Galligan 1998-2000 */
#include "math.h"
#include "mex.h"
#include "genutils.h"
#include "meteors.h"
#include "numbers_def.h"
/* Input Arguments */
#define orbits_in1      prhs[0]
#define orbits_in2      prhs[1]
#define dissim_num_in   prhs[2]
#define d_max_stop_in   prhs[3]
/* Output Arguments */
#define dissims_out     plhs[0]
void find_dissims(double *orbits1,double *orbits2,int n_orbits1,
                  int n_orbits2,double *dissims,
                  double d_max_stop,int dissim_func_num);
void find_dissims(double *orbits1,double *orbits2,int n_orbits1,
                  int n_orbits2,double *dissims,
                  double d_max_stop,int dissim_func_num) {
  struct orbit_elements orb1,orb2;
  int i,j;
  for (i=0; i<(n_orbits1);i++) {
    orb1=read_incoming_dcrit_orbits(orbits1,i,n_orbits1);
    for (j=0; j<n_orbits2;j++) {
      orb2=read_incoming_dcrit_orbits(orbits2,j,n_orbits2);
```

```
            dissims[ind2d(i,j,n_orbits1)]=
              dissim_function(orb1,orb2,d_max_stop,dissim_func_num);
        }
    }
    return;
}

void mexFunction(
                    int nlhs,       mxArray *plhs[],
                    int nrhs, const mxArray *prhs[]
                    ) {
    double *dissims,*orbits1,*orbits2;
    int n_orbits1,n_orbits2;
    int dissim_func_num;
    double d_max_stop;
    double (*dissim_func)();
    /* Check for proper number of arguments and columns */
    if (nrhs != 4 || mxGetN(orbits_in1)!=17 || mxGetN(orbits_in2)!=17)
      mexErrMsgTxt(
          "Two matrices of orbits with columns in the form given "
          "by dcrit_cols are required followed by the number of "
          "the dissimilarity function to use and then the maximum "
          "dissimilarity value. Angles are entered in degrees");
    /* Sort out values of interest */
    n_orbits1 = (int) mxGetM(orbits_in1);
    n_orbits2 = (int) mxGetM(orbits_in2);
    dissim_func_num=(int) mxGetScalar(dissim_num_in);
    d_max_stop=mxGetScalar(d_max_stop_in);
    /* Create matrices for the return argument */
    dissims_out=mxCreateDoubleMatrix(n_orbits1,n_orbits2,mxREAL);
    /* Assign pointers to the various parameters */
    orbits1=mxGetPr(orbits_in1);
    orbits2=mxGetPr(orbits_in2);
    dissims=mxGetPr(dissims_out);
    find_dissims(orbits1,orbits2,n_orbits1,n_orbits2,dissims,
                 d_max_stop,dissim_func_num);

    return;
}
```

C.4 Single-Linkage Cluster Analysis

The single-linkage searches of Section 7.8 are performed by a 2 step process. In the first step the dissimilarity matrix up to a limiting maximum dissimilarity is calculated. This is carried out by the C stand-alone `get_dissim.c` program, the calling syntax of which is:

`get_dissim.exe` *infile outfile d_max orbit_file_type dissim_func_num*,

where *infile* is normally a `*.ele` standard orbital element file; *outfile* is the base filename for 3 output files comprising: a binary compressed format `*.wsr` file containing the dissimilarity matrix in linear form, a text `*.wds` file containing a machine-readable description of the contents of the latter and a log-file containing details of the program run; the integer *orbit_file_type* corresponds to the type of input orbital

element file, as passed to the function `read_orbit_ele_file`, and finally the integer *dissim_func_num* corresponds to the dissimilarity function required.

```
/* get_dissim.c
   by David Galligan 1997-2000 */
/* This is an efficient serial_search component. It produces a
   binary file containing two orbit ids and the dissimilarity
   between them for all orbit-pairs whose dissimilarities are
   less than an input D_max.                                    */
#include <stdio.h>
#include <math.h>
#include <stdlib.h>
#include <string.h>
#include <time.h>
#include "meteors.h"
#include "genutils.h"
#include "numbers_def.h"
/* definitions */
#define max_orbits_start     300000
#define version_womble "990812"
/* globals */
#define FOUT_BUFFER_SIZE 1000000
char fout_buffer[FOUT_BUFFER_SIZE];
/* prototypes */
int analyse_dissims(FILE *fout,
                    struct orbit_elements *orbit_matrix,
                    double d_max,orbit_id_type num_orbits,
                    double (*dissim_func)());
/* Main program block begins */
int main(int argc, char *argv[])
{
  /* Assign variables */
  struct orbit_elements *orbit_matrix;
  int orbit_file_type; /* =1 for *.ele 2 for *.elem input */
  int dissim_func_num=1;/* num. of dissim funcn(default:DSH) */
  FILE *fin,*fhead,*fout;
  double (*dissim_func)();
  orbit_id_type num_orbits=0;
  double d_max;
  char BUILD_VERSION_STR[7]="";
  char header_filename[300]="",serial_filename[300]="";
  char dissim_name[30]="";
#ifndef BUILD_VERSION
  BUILD_VERSION_STR="NOTDEF";
#else
  padzero(BUILD_VERSION,6,BUILD_VERSION_STR);
#endif
  /* Program block begins */
  printf("Serial_search_program_V4.0_(Womble).___"
         "Build_Version_%s.__Machine:_%s\n",BUILD_VERSION_STR,
         getenv("ALIAS_ACTIVE"));
  printf("Run_Date:_");
  fflush(stdout); system("date");
  printf("VERSIONS:_womble_%s_meteors_%s_genutils_%s_"
         "numbers_def_%s.\n",version_womble,version_meteors,
          version_genutils,version_numbers_def);
```

```
if (argc<5) {
  printf("Max Orbits Storable: %d. Orbit id type size: %ld.\n",
         max_orbits_storable,(long)sizeof(orbit_id_type));
  printf("Enter parameters vis: infile outfile d_max "
         "orbit_file_type (dissim_func_num)\n");
  error_msg("Invalid number of parameters entered");
}
/* open input orbital element file */
fin=fopen(argv[1],"r");
if (!fin) error_msg("Input file not openable");
/* assign output filenames */
sprintf(header_filename,"%s.wds",argv[2]);
sprintf(serial_filename,"%s.wsr",argv[2]);
/* read in run parameters */
sscanf(argv[3],"%lf",&d_max);
sscanf(argv[4],"%d",&orbit_file_type);
if (argc==6) {
  sscanf(argv[5],"%d",&dissim_func_num);
}
/* determine dissimilarity function to use */
switch (dissim_func_num) {
case 1:
  dissim_func=dissim_DSH;
  sprintf(dissim_name,"%s","DSH");
  break;
case 2:
  dissim_func=dissim_DJ;
  sprintf(dissim_name,"%s","DJ");
  break;
case 3:
  dissim_func=dissim_DD;
  sprintf(dissim_name,"%s","DD");
  break;
case 4:
  dissim_func=dissim_DN_fast;
  sprintf(dissim_name,"%s","DN");
  break;
case 5:
  dissim_func=dissim_DV;
  sprintf(dissim_name,"%s","DV");
  break;
default:
  error_msg("Incorrect dissimilarity function entered");
}
/* Allocate space for orbit storage matrix */
orbit_matrix=(struct orbit_elements*)
        malloc(max_orbits_start*sizeof(struct orbit_elements));
if (!orbit_matrix)
  error_msg("Memory alloc error: orbit_matrix");
/* read in orbital elements for orbits */
printf("Reading orbits...");
orbit_matrix=read_orbit_ele_file(fin,orbit_file_type,&num_orbits);
fclose(fin);
printf("%d orbits read\n",num_orbits);
/* write header file */
```

```
  fhead=fopen(header_filename,"w");
  if (!fout) error_msg("Output header file not openable");
  fprintf(fhead,"program version date: %s\n",BUILD_VERSION_STR);
  fprintf(fhead,"distance function:    %s\n",dissim_name);
  fprintf(fhead,"machine used:         %s\n",getenv("ALIAS_ACTIVE"));
  fprintf(fhead,"orbit file:           %s\n",argv[1]);
  fprintf(fhead,"num orbits:           %d\n",num_orbits);
  fprintf(fhead,"set d max lim:        %f\n",d_max);
  /* open output serial file */
  fclose(fhead);
  fout=fopen(serial_filename,"w");
  if (!fout) error_msg("Output binary file not openable");
  setvbuf(fout,fout_buffer,_IOFBF,FOUT_BUFFER_SIZE);
  /* analyse clustering */
  analyse_dissims(fout,orbit_matrix,d_max,num_orbits,dissim_func);
  fclose(fout);
  return(0);
}

int analyse_dissims(FILE *fout,
                    struct orbit_elements *orbit_matrix,
                    double d_max,orbit_id_type num_orbits,
                    double (*dissim_func)()) {
  /* Intelligent output only outputs row number each time it
     changes. A -1 is used in order to signal row break. */
  boolean first_this_row=1;
  int num_accept=0,num_millions=0;
  long total_doable; /* in millions */
  long num_done=0L;
  long num_millions_done=0L;
  long five_perc_total_doable;
  int num_five_perc_done=0L;
  orbit_id_type row=0,col=0,change_row_sym=-1;
  float dissim;
  total_doable=(long) (num_orbits/1000)*((num_orbits-1)/1000)/2;
  five_perc_total_doable=(long) total_doable/20L;
  while (row<num_orbits-1) {
    first_this_row=1;
    col=row+1;
    while (col<num_orbits) {
      num_done++;
      if (num_done==1000000) {
        num_done=0;
        num_millions_done++;
      }
      if (num_millions_done>=five_perc_total_doable) {
        num_millions_done=0L; /* zero for next five percent run */
        num_five_perc_done++;
        printf("%3d%% OF THE WAY THROUGH\n",num_five_perc_done*5);
        fflush(stdout);
      }
      dissim=(float)(*dissim_func)
                  (orbit_matrix[row],orbit_matrix[col],d_max);
      if (dissim<d_max) {
        ++num_accept;
```

```
        if (num_accept==1000000) {
          num_accept=0;
          num_millions++;
          printf("NUM_MILLIONS_%d\n",num_millions);
          fflush(stdout);
        }
        if (first_this_row) {
          fwrite(&row,sizeof(orbit_id_type),1,fout);
          first_this_row=0;
        }
        fwrite(&col,sizeof(orbit_id_type),1,fout);
        fwrite(&dissim,sizeof(float),1,fout);
      }
      col++;
    }
    /* signal row change if we've done anything on the current row */
    if (!first_this_row)
      fwrite(&change_row_sym,sizeof(orbit_id_type),1,fout);
    row++;
  }
  return(0);
}
```

Once the `*.wsr,*.wds` set of files have been formed using `get_dissim.c` it is then necessary to translate the output dissimilarity matrix into a single-linkage hierarchy. The `C` program `get_dissim2serial.c` performs this task for a given regularly spaced set of cutoff levels in the hierarchy. The call syntax for this program is:

`get_dissim2serial.exe` *infile outfile D_min D_max D_inc OPT:max_levels_per_run*,

where *infile* corresponds to the filename (without file-type) of a pair of `get_dissim.c` output files; *outfile* is the filename (without file-type) which is to be assigned to the output pair of files representing the linkage hierarchy—this set is comprised of a `*.ser` binary file containing a rectangular matrix representing the hierarchy and a `*.des` text file containing a computer readable description of the contents of the latter; `D_min`, `D_max` and `D_inc` define the required cutoff levels (with automatic correction, if possible, in the program when these values do not make sense); finally `max_levels_per_run` defines the maximum number of levels to process in each pass of the program, the ideal is to calculate all levels in 1 pass—this is the fastest method if sufficient computer memory is available, however, generally for the large data sets used in the current study more than 1 pass is required.

The $(N \times M)$ matrix contained in the `*.ser` files has each row representing a single orbit and each column a cutoff level in the hierarchy, matrix locations contain the grouping number to which the orbit belongs—the grouping number is defined by the lowest orbit number $(0..N-1)$ contained therein.

Once the (`*.ser, *.des`) pair has been created they can be read easily into `MATLAB` using a gateway `C` function to load either a single level or a set of levels. From there on a series of `MATLAB` and `C` programs and functions, not shown here, are used to manipulate the part of the hierarchy entered and to provide figures such as the dendrograms of Section 7.8.

```
/* get_dissim2serial.c
   by David Galligan 1997-2000 */
```

```
/* This is the second part of the single-linkage hierarchy
   calculation program suite.
   Form of input file is row,col,dissim(float) in binary
   Form of output file is a rectangular matrix in binary */
#include <stdio.h>
#include <stdlib.h>
#include <math.h>
#include "meteors.h"
#include "genutils.h"
#include "fast_serial_lib.h"
/* structure to output details after a *.wds file is read */
struct wds_details_struct {
  char version_date[7];
  char dissim_func[20];
  char machine_used[50];
  char orbit_file[400];
  orbit_id_type num_orbits;
  float dissim_max;
};
#define version_womble2serial "990526"
/* user set values */
#define set_max_levels_at_time   100   /* solely memory dependent */
#define checksum_divisor   1000
#define diag_mode          FALSE   /* diagnostics */
/* alternative diagnostics + diag_level */
#define want_diag          FALSE
#define diag_level         100
/* prototypes */
struct wds_details_struct read_wds_file(char *wds_filename);
int write_header_file(FILE *fhead,char *version_date,
                      char *dissim_func,char *machine_used,
                      char *orbit_file,orbit_id_type num_orbits,
                      int num_levels,float d_min,float d_max,
                      float d_inc,float *d_cuts);
orbit_id_type **cut_up_hierarchy(char *cluster_filename,
                                 float *d_cuts,float d_inc,
                                 orbit_id_type num_orbits,
                                 int num_levels);
/* main program block begins */
int main(int argc,char *argv[]) {
  /* variables */
  int max_levels_at_time;
  int i,lev,num_levels,run,num_runs;
  int curr_start_lev,curr_end_lev,curr_num_lev;
  int error_code;
  orbit_id_type j,num_orbits;
  orbit_id_type **curr_groups;
  long checksum_a,checksum_b;
  float D_cut_init,D_cut_final,D_cut_inc;
  float *D_cuts,*curr_d_cuts;
  struct wds_details_struct wds_details;
  FILE *fout,*fchksum,*fhead;
  char input_run_base[300]="",input_des_base[300]="";
  char output_run_base[300]="",output_chk_base[300]="",
       output_des_base[300]="";
```

```
  char BUILD_VERSION_STR[7]="";
#ifndef BUILD_VERSION
  BUILD_VERSION_STR="NOTDEF";
#else
  padzero(BUILD_VERSION,6,BUILD_VERSION_STR);
#endif
  /* check for correct number of parameters */
  if (argc!=6 && argc!=7) {
    printf("Get_Dissim2Serial_Converter.__Build_Version_%s._"
           "Machine:_%s\n",BUILD_VERSION_STR,getenv("ALIAS_ACTIVE"));
    printf("VERSIONS:_Get_Dissim2serial_%s_meteors_%s_genutils_%s_"
           "numbers_def_%s\n",version_womble2serial,version_meteors,
           version_genutils,version_numbers_def);
    printf("\n");
    printf("Enter_Input_File_Base,_Output_File_Base,_"
           "D_min,D_max,_D_inc_OPT:max_levels_per_run\n");
    error_msg("Incorrect_number_of_parameters_for_womble2serial");
  }
  /* assign filenames */
  sprintf(input_run_base,"%s.wsr",argv[1]);
  sprintf(input_des_base,"%s.wds",argv[1]);
  sprintf(output_run_base,"%s.ser",argv[2]);
  sprintf(output_chk_base,"%s.chk",argv[2]);
  sprintf(output_des_base,"%s.des",argv[2]);
  sscanf(argv[3],"%f",&D_cut_init);
  sscanf(argv[4],"%f",&D_cut_final);
  sscanf(argv[5],"%f",&D_cut_inc);
  if (argc==7)
    sscanf(argv[6],"%d",&max_levels_at_time);
  else
    max_levels_at_time=set_max_levels_at_time;
  /* read womble run description file */
  wds_details=read_wds_file(input_des_base);
  num_orbits=wds_details.num_orbits;
  /* work out cut levels */
  num_levels=1+(int) floor((D_cut_final-D_cut_init)/D_cut_inc);
  if (num_levels<=0)
    error_msg("Zero_or_negative_cutoff_levels_requested");
  D_cuts=malloc(num_levels*sizeof(float));
  curr_d_cuts=malloc(num_levels*sizeof(float));
  if (!D_cuts || !curr_d_cuts)
    error_msg("Memory_alloc_error:_d_cuts");
  /* calculate cutoff levels */
  for (lev=0; lev<num_levels; ++lev)
    D_cuts[lev]=D_cut_init+lev*D_cut_inc;
  if (D_cuts[num_levels-1]>wds_details.dissim_max)
    error_msg("run_does_not_extend_to_your_max._cutoff_level");
  /* write normal header file */
  /* open file */
  fhead=fopen(output_des_base,"w");
  if(!fhead) error_msg("Cannot_open_des_file");
  write_header_file(fhead,wds_details.version_date,
                    wds_details.dissim_func,
                    wds_details.machine_used,wds_details.orbit_file,
                    wds_details.num_orbits,num_levels,D_cut_init,
```

```
                    D_cut_final,D_cut_inc,D_cuts);
  fclose(fhead);
  /* open output serial file */
  fout=fopen(output_run_base,"w");
  fchksum=fopen(output_chk_base,"w");
  if (!fout || !fchksum)
    error_msg("Unable to open output serial search files");
  num_runs=ceil((float) num_levels/max_levels_at_time);
/* tell the user the state of play */
/* summary of fileio */
  printf("CONVERTING WOMBLE OUTPUT TO FAST SERIAL OUTPUT:\n");
  printf("  INPUT: %s\n",input_run_base);
  printf("  INPUT: %s\n",input_des_base);
  printf("  OUTPT: %s\n",output_run_base);
  printf("  OUTPT: %s\n",output_chk_base);
  printf("  OUTPT: %s\n",output_des_base);
  /* summary of quantities */
  write_header_file(stdout,wds_details.version_date,
                    wds_details.dissim_func,
                    wds_details.machine_used,wds_details.orbit_file,
                    wds_details.num_orbits,num_levels,D_cut_init,
                    D_cut_final,D_cut_inc,D_cuts);
  printf("  MAX_LEV_PER_RUN: %d. NUM_RUNS_REQUIRED: %d.\n",
         max_levels_at_time,num_runs);
  printf("  MAX_CORE_MEMORY_REQUIRED_APPROX. %d_MB\n",
        (int) (max_levels_at_time*num_orbits
              *sizeof(orbit_id_type)*3/1000000));
  for (run=0; run<num_runs; run++) {
    curr_start_lev=run*max_levels_at_time;
    curr_end_lev=curr_start_lev+max_levels_at_time-1;
    if (curr_end_lev>=num_levels) curr_end_lev=num_levels-1;
    curr_num_lev=curr_end_lev-curr_start_lev+1;
    for (lev=curr_start_lev; lev<=curr_end_lev; lev++)
      curr_d_cuts[lev-curr_start_lev]=D_cuts[lev];
    printf("  RUN: %d_START_LEV: %d_END_LEV: %d.\n",
           run,curr_start_lev,curr_end_lev);
    curr_groups=cut_up_hierarchy(input_run_base,curr_d_cuts,
                                 D_cut_inc,num_orbits,curr_num_lev);
    /* write out grouping structure to current point in 1..n form */
    for (i=0; i<curr_num_lev; ++i) {
      checksum_a=0L; checksum_b=0L;
      for (j=0; j<num_orbits; ++j) {
        ++curr_groups[i][j]; /* change to 1..n */
        /* integer div and mod completely describe number */
        /* integer div */
        checksum_a+=(long) curr_groups[i][j]/checksum_divisor;
        /* integer mod */
        checksum_b+=(long) curr_groups[i][j] % checksum_divisor;
      }
      error_code=
       fwrite(curr_groups[i],sizeof(orbit_id_type),num_orbits,fout);
      if (error_code!=num_orbits)
        error_msg("write_out_groups-group_structure_not_written");
      fprintf(fchksum,"%d_%ld_%ld_%d\n",
              (run*max_levels_at_time)+i+1,
```

```
                checksum_a,checksum_b,checksum_divisor);
      }
      /* free curr_groups for next run */
      for (i=0; i<curr_num_lev; ++i)
         free((orbit_id_type *) curr_groups[i]);
   }
   fclose(fchksum); fclose(fout);
   return(0);
}

orbit_id_type **cut_up_hierarchy(char *cluster_filename,
            float *d_cuts,float d_inc,orbit_id_type num_orbits,
            int num_levels) {
   /* variables */
   boolean first_time=1;
   int lev,first_lev;
   int error_code,err_code1,err_code2,err_code3;
   orbit_id_type orb,row,col,current_row,new_grp_id,old_grp_id;

   orbit_id_type first_val,num_orbits_in_grp;
   orbit_id_type *orbits_in_grp;
   orbit_id_type **link_groups,**groups,**end_groups;
   long counter=0L, num_million_pairs=0L;
   float dissim;
   FILE *fcluster;
   /* open file */
   fcluster=fopen(cluster_filename,"r");
   if (!fcluster) error_msg("cannot_open_cluster_filename");
   /* allocate and initialise groups */
   end_groups=
      (orbit_id_type **) malloc(num_levels*sizeof(orbit_id_type*));
   link_groups=
      (orbit_id_type **) malloc(num_levels*sizeof(orbit_id_type*));
   groups=
      (orbit_id_type **) malloc(num_levels*sizeof(orbit_id_type*));
   for (lev=0; lev<num_levels; ++lev) {
     groups[lev]=
        (orbit_id_type *) malloc(num_orbits*sizeof(orbit_id_type));
     link_groups[lev]=
        (orbit_id_type *)malloc(num_orbits*sizeof(orbit_id_type));
     end_groups[lev]=
        (orbit_id_type *)malloc(num_orbits*sizeof(orbit_id_type));
   if (!groups[lev] || !link_groups[lev] || !end_groups[lev])
       error_msg("Malloc_error:groups/link_groups/end_groups");
     for (orb=0; orb<num_orbits; orb++) {
       groups[lev][orb]=orb; /* 0..n-1 */
       link_groups[lev][orb]=orb;
       end_groups[lev][orb]=orb;
     }
   }
   orbits_in_grp=malloc(num_orbits*sizeof(orbit_id_type));
   if (!orbits_in_grp) error_msg("Malloc_Problem:_orbits_in_grp");
   /* go through each pairing and establish grouping structure */
   /* row and col at present are assumed to be 0..n-1 */
   while (!feof(fcluster)) {
```

```
err_code1=fread(&first_val,sizeof(orbit_id_type),1,fcluster);
/* check for row change symbol-if so reread to get row number */
if (first_time) {
  row=first_val;
  err_code2=fread(&col,sizeof(orbit_id_type),1,fcluster);
  err_code3=fread(&dissim,sizeof(float),1,fcluster);
  current_row=row;
  first_time=0;
}
else if (err_code1>0 && first_val==-1) {
  err_code1=fread(&row,sizeof(orbit_id_type),1,fcluster);
  err_code2=fread(&col,sizeof(orbit_id_type),1,fcluster);
  err_code3=fread(&dissim,sizeof(float),1,fcluster);
  current_row=row;
  if (diag_mode) printf("ROW_BREAK_DETECT\n");
}
/* not changing row */
else {
  row=current_row;
  col=first_val;
  err_code3=fread(&dissim,sizeof(float),1,fcluster);
}
if (err_code1>0 && err_code2>0 && err_code3>0) {
  if (diag_mode) printf("%d_%d_%6.4f\n",row,col,dissim);
  counter++;
  if (counter==1000000L) {
    counter=0L;
    num_million_pairs++;
    printf("__NOW_AT_%3ld_MILLION_PAIRS\n",num_million_pairs);
  }
  /* assume uniformly spread levels */
  first_lev=(int) ceil((dissim-d_cuts[0])/d_inc);
  if (first_lev<0) first_lev=0;
  for (lev=first_lev; lev<num_levels; ++lev) {
    if (dissim<d_cuts[lev]) {
      /* if they're not in the same grp already grp them
         together...the lowest orbit id in the group becomes
         the new group id */
      if (groups[lev][row]!=groups[lev][col]) {
        new_grp_id=imin(groups[lev][row],groups[lev][col]);
        old_grp_id=imax(groups[lev][row],groups[lev][col]);
        if (diag_mode)
          printf("1ST_LEV_%d,_LEV:_%d_D_MAX:_%6.4f_"
                 "MERGE_GRPS:_%d_%d\n",first_lev,lev,
               d_cuts[lev],old_grp_id,new_grp_id);
        /* bind groups together */
        error_code=bind_groups2(new_grp_id,old_grp_id,
                                lev,link_groups,end_groups);
        if (error_code) error_msg("Binding_of_groups_failed");
        if (want_diag && lev==diag_level) {
          printf("LEV:_%d_DISSIM_%f_ROW:_%d_COL_%d__"
                 "BIND_GRPS:_%d_and_%d\n",
                 lev,d_cuts[lev],row,col,old_grp_id,new_grp_id);
          display_group("___OLD__",old_grp_id,lev,link_groups,
                        num_levels);
```

```
                display_group("___NEW__",new_grp_id,lev,link_groups,
                              num_levels);
              }
              /* update group ids */
              num_orbits_in_grp=
                 search_group(old_grp_id,lev,link_groups,
                              orbits_in_grp,num_levels);
              for (orb=0; orb<num_orbits_in_grp; orb++) {
                if (want_diag && lev==diag_level)
                  printf("UPDATE:_OLD_ID_%d_TO_NEW_ID_%d\n",
                         orbits_in_grp[orb],new_grp_id);
                groups[lev][orbits_in_grp[orb]]=new_grp_id;
              }
            }
          }
        }
      }
    }
  }
  fclose(fcluster);
  /* clear link_groups and end_groups */
  for (lev=0; lev<num_levels; ++lev) {
    free((orbit_id_type *) link_groups[lev]);
    free((orbit_id_type *) end_groups[lev]);
  }
  return groups;
}


struct wds_details_struct read_wds_file(char *wds_filename) {
  struct wds_details_struct wds_details;
  FILE *wds_file;
  /* open file */
  wds_file=fopen(wds_filename,"r");
  if(!wds_file) error_msg("Cannot_open_wds_file");
  /* read description therein */
  fscanf(wds_file,"%*s_%s",wds_details.version_date);
  fscanf(wds_file,"%*s_%s",wds_details.dissim_func);
  fscanf(wds_file,"%*s_%s",wds_details.machine_used);
  fscanf(wds_file,"%*s_%s",wds_details.orbit_file);
  fscanf(wds_file,"%*s_%d",&wds_details.num_orbits);
  fscanf(wds_file,"%*s_%f",&wds_details.dissim_max);
  /* close file */
  fclose(wds_file);
  return wds_details;
}

int write_header_file(FILE *fhead,char *version_date,
                      char *dissim_func,
                      char *machine_used,char *orbit_file,
                      orbit_id_type num_orbits,int num_levels,
                      float d_min,float d_max,float d_inc,float *d_cuts) {
   /* output header information */
  fprintf(fhead,"Serial_Search_Run_Output_File\n");
  fprintf(fhead,"quick_scan:_%s_%d_%d_%f_%f_%f_%f\n",version_date,
          num_orbits,num_levels,d_min,d_max,
```

```
        d_inc, d_cuts[num_levels-1]);
  fprintf(fhead,"program_version_date:␣%s\n",version_date);
  fprintf(fhead,"distance_function:␣␣␣␣%s\n",dissim_func);
  fprintf(fhead,"machine_used:␣␣␣␣␣␣␣␣␣%s\n",machine_used);
  fprintf(fhead,"orbit_file:␣␣␣␣␣␣␣␣␣␣␣%s\n",orbit_file);
  fprintf(fhead,"num_orbits:␣␣␣␣␣␣␣␣␣␣␣%d\n",num_orbits);
  fprintf(fhead,"num_levels:␣␣␣␣␣␣␣␣␣␣␣%d\n",num_levels);
  fprintf(fhead,"req_d_min:␣␣␣␣␣␣␣␣␣␣␣␣%f\n",d_min);
  fprintf(fhead,"req_d_max:␣␣␣␣␣␣␣␣␣␣␣␣%f\n",d_max);
  fprintf(fhead,"req_d_inc:␣␣␣␣␣␣␣␣␣␣␣␣%f\n",d_inc);
  fprintf(fhead,"set_d_max:␣␣␣␣␣␣␣␣␣␣␣␣%f\n",d_cuts[num_levels-1]);
  fprintf(fhead,"\n");
  return(0);
}
```

An example of the calculation of a single-linkage hierarchy using the above programs is given for the case of the prograde orbit file `95V99_110LS160_PR.ele`, as used in Section 7.8.4. The description files created by the single-linkage analysis on this file, obtained from `get_dissim.c` and `get_dissim2serial.c`, are shown below.

```
distance_function:    DSH
machine_used:         bardeen
orbit_file:           amor_data/95V99_110_160LS_PR.ele
num_orbits:           38380
set_d_max_lim:        0.100000
```

File: `95V99_110_160LS_PR_DSH.wds` produced by `get_dissim.c`.

```
Serial_Search_Run_Output_File
quick_scan: 000323 38380 250 0.000400 0.100000 0.000400 0.100000
program_version_date: 000323
distance_function:    DSH
machine_used:         bardeen
orbit_file:           amor_data/95V99_110_160LS_PR.ele
num_orbits:           38380
num_levels:           250
req_d_min:            0.000400
req_d_max:            0.100000
req_d_inc:            0.000400
set_d_max:            0.100000
```

File: `95V99_110_160LS_PR_DSH.des` produced by `get_dissim2serial.c`.

C.5 Direct Search

The direct search based on Poisson statistics of Section 7.6 is performed using 3 inter-woven programs. To perform the search a `MATLAB` script `direct_search.m`) is used as a frontend program while most of the core processing is performed by the `C` gateway function `mxDirectSearch`. This gateway function calculates the

mean number of associations for the type of orbit under consideration throughout the year; this value is then used in the Poisson statistics of the third script, `understand_direct_search.m`, to determine if the number of associations to the stream under study are attributable to random chance or not. The latter script receives an output file from `direct_search.m` as its input—this allows various methods to be tested without having to perform the long searching process each time.

```
/* mxDirectSearch.c
   by David Galligan 2000 */
#include "math.h"
#include "mex.h"
#include "genutils.h"
#include "meteors.h"
#include "numbers_def.h"
#define orbits_in1      prhs[0]
#define orbits_in2      prhs[1]
#define mean_assoc_out  plhs[0]
#define num_bins 25
void mexFunction(
                 int nlhs,       mxArray *plhs[],
                 int nrhs, const mxArray *prhs[]
                 ) {
  double d_stop=0.26;
  struct orbit_elements orb1,orb2;
  double dissim,*orbits1,*orbits2,*mean_assoc;
  int orb_num1,orb_num2,n_orbits1,n_orbits2;
  int div_num,divn;
  n_orbits1 = (int) mxGetM(orbits_in1);
  n_orbits2 = (int) mxGetM(orbits_in2);
  orbits1=mxGetPr(orbits_in1);
  orbits2=mxGetPr(orbits_in2);
  mean_assoc_out=mxCreateDoubleMatrix(num_bins,1,mxREAL);
  mean_assoc=mxGetPr(mean_assoc_out);
  for (divn=0; divn<num_bins; divn++) {
    mean_assoc[divn]=0.0;
  }
  for (orb_num2=0; orb_num2<n_orbits2; orb_num2++) {
    orb2=read_incoming_dcrit_orbits(orbits2,orb_num2,n_orbits2);
    for (orb_num1=0; orb_num1<n_orbits1; orb_num1++) {
      orb1=read_incoming_dcrit_orbits(orbits1,orb_num1,n_orbits1);
      dissim=dissim_function(orb1,orb2,d_stop,1);
      div_num=(int) floor(dissim/0.01);
      for (divn=div_num; divn<num_bins; divn++)
        mean_assoc[divn]=mean_assoc[divn]+1.0;
    }
  }
  /* return means --- note remove self-agreements */
  for (divn=0; divn<num_bins; divn++)
    mean_assoc[divn]=(mean_assoc[divn]-n_orbits2)/(1.0*n_orbits2);
}
```

```
% direct_search.m
% by David Galligan 2000
% check significance of search against csf
```

```
global CSFParCol
init_rad_search; % read in T1995--T1999 AMOR orbits
peridist=orbits(:,OrbParCol.PeriDist);
ecc=orbits(:,OrbParCol.Ecc);
inc=orbits(:,OrbParCol.Inc);
[csf_data,csf_names]=read_csf;
% presets
q_pm=0.1; ecc_pm=0.1; inc_pm=5;
num_csf_streams=size(csf_data,1);
for csf_num=1:num_csf_streams
  if csf_data(csf_num,CSFParCol.Declin)<30
    c_peridist=csf_data(csf_num,CSFParCol.PeriDist);
    c_ecc=csf_data(csf_num,CSFParCol.Ecc);
    c_inc=csf_data(csf_num,CSFParCol.Inc);
    for yr=1995:1999
      yr,
      ind=find(eq_yr==yr &...
        peridist>=(c_peridist-q_pm) & ...
        peridist<=(c_peridist+q_pm) & ...
        ecc>=(c_ecc-ecc_pm) & ecc<=(c_ecc+ecc_pm) & ...
        inc>=(c_inc-inc_pm) & inc<=(c_inc+inc_pm));
      allind=find(eq_yr==yr &  inc>=(c_inc-35) & inc<=(c_inc+35));
      length(ind), length(allind)
      [mean_num_DSH]=...
        mxDirectSearch(orbits(allind,dcrit_cols),...
                       orbits(ind,dcrit_cols));
    end
  else
    fprintf(1,'Ignored CSF: %d\n',csf_num);
  end
end
```

```
% understand_direct_search.m
% by David Galligan 2000
% read in run files from direct search (C version) and analyse
global main_data_disk CSFParCol dcrit_cols
ddisk=main_data_disk; % output directory
bin_cuts=0.05:0.05:0.25;
[csf_data,csf_names]=read_csf;
csf_used=zeros(size(csf_data,1),1);
cdata=zeros(size(csf_data,1),19); % combined data for output
cdata(:,1)=csf_data(:,CSFParCol.SolarLong);
cdata(:,3)=csf_data(:,CSFParCol.Inc);
cdata(:,4)=csf_data(:,CSFParCol.Declin);
for yr=1995:1999
  eval(sprintf('dsh=load(''%sdirect_%dV.txt'');',ddisk,yr));
  for row=1:size(dsh,1)
    csf_num=dsh(row,1);
    csf_used(csf_num)=1;
```

```
      csf_inc=csf_data(csf_num,CSFParCol.Inc);
      if csf_inc<=10
        cols=[9 4];
      elseif csf_inc>10 & csf_inc<=20
        cols=[10 5];
      else
        cols=[11 6];
      end
      cdata(csf_num,(3*(yr-1994)+2:3*(yr-1994)+3))=dsh(row,cols);
      cdata(csf_num,2)=-4;
    end
  end
  for yr=1995:1998
    eval(sprintf('dsh=load(''%sdirect_%dA.txt'');',ddisk,yr));
    for row=1:size(dsh,1)
      csf_num=dsh(row,1);
      csf_used(csf_num)=1;
      csf_inc=csf_data(csf_num,CSFParCol.Inc);
      if csf_inc<=10
        cols=[9 5];
      elseif csf_inc>10 & csf_inc<=20
        cols=[10 5];
      else
        cols=[11 7];
      end
      cdata(csf_num,(3*(yr-1994)+2:3*(yr-1994)+3))=dsh(row,cols);
      cdata(csf_num,2)=-5;
    end
  end
  for csf=1:size(csf_data,1)
    csf
    for yr_ind=1:5
      found=cdata(csf,3*yr_ind+2);
      expect=cdata(csf,3*yr_ind+3);
      if expect==0
        expect=1;
      end
      poiss_min95p=poissinv(0.95,expect);
      poiss_min99p=poissinv(0.99,expect);
      if found>=poiss_min99p
        cdata(csf,3*yr_ind+4)=-1;
      elseif found>=poiss_min95p
        cdata(csf,3*yr_ind+4)=-2;
      else
        cdata(csf,3*yr_ind+4)=-3;
      end
    end
  end
  % Low Inclination
```

```
ind=find(csf_data(:,CSFParCol.Inc)<=10);
[sl,ind2]=sort(csf_data(ind,CSFParCol.SolarLong));
ind3=ind(ind2);
for csf=ind3'
  if csf_used(csf)
    fprintf(3,'%3d&%s&%5.1f&%d&%5.1f&%5.1f&%4d&%4d&%2d&%4d&%4d'...
            '&%2d&%4d&%4d&%2d&%4d&%4d&%2d&%4d&%4d&%2d\\\\\n',...
            csf,csf_names(csf,:),cdata(csf,:));
  end
end
fprintf(1,'-----------------------------------------------------------\n');
% Medium Inclination
ind=find(csf_data(:,CSFParCol.Inc)>10 ...
      & csf_data(:,CSFParCol.Inc)<=20);
[sl,ind2]=sort(csf_data(ind,CSFParCol.SolarLong));
ind3=ind(ind2);
for csf=ind3'
  if csf_used(csf)
    fprintf(3,'%3d&%s&%5.1f&%d&%5.1f&%5.1f&%4d&%4d&%2d&%4d&%4d&'...
            '%2d&%4d&%4d&%2d&%4d&%4d&%2d&%4d&%4d&%2d\\\\\n',...
            csf,csf_names(csf,:),cdata(csf,:));
  end
end
fprintf(1,'-----------------------------------------------------------\n');
% High Inclination
ind=find(csf_data(:,CSFParCol.Inc)>=20);
[sl,ind2]=sort(csf_data(ind,CSFParCol.SolarLong));
ind3=ind(ind2);
for csf=ind3'
  if csf_used(csf)
    fprintf(3,'%3d&%s&%5.1f&%d&%5.1f&%5.1f&%4d&%4d&%2d&%4d&%4d&'...
            '%2d&%4d&%4d&%2d&%4d&%4d&%2d&%4d&%4d&%2d\\\\\n',...
            csf,csf_names(csf,:),cdata(csf,:));
  end
end
```

C.6 Mexican Hat Wavelet Transforms

The Mexican Hat wavelet is defined in Section 7.7.1. The functions used to calculate the 1-D and 2-D versions of this wavelet are programmed in MATLAB; `mexhat1d` and `mexhat2d` perform these calculations respectively.

```
function hatval=mexhat1d(n_elt,width)
% by David Galligan 1999-2000
x=(1-n_elt/2):(n_elt-1)-n_elt/2;
rad=((x.^2)./(width^2));
hatval=(1-rad).*exp(-rad/2);
```

```
function hatval=mexhat2d(n_rows,n_cols,width)
% by David Galligan 1999-2000
[x,y]=meshgrid((1-n_rows/2):(n_rows-1)-n_rows/2, ...
                (1-n_cols/2):(n_cols-1)-n_cols/2);
rad=((x.^2)./((width*2)^2)+(y.^2)./(width^2));
hatval=(2-rad).*exp(-rad/2);
```

The 2-D Mexican Hat wavelet transform is performed in MATLAB using the `mexhat_transform` function. It performs the convolution in frequency space, for speed, using a Fast Fourier transform (FFT) to change domains and the corresponding inverse function to return to the spatial domain. The FFT requires that the 2-D matrix entered have a dyadic number of elements hence the image entered is padded with zeroes to the nearest dyadic, after a specified margin of zeros have also been added to the image (such a margin is used to remove problems associated with the assumption that the image is periodic). The transformed image produced is subsequently normalised to remove the scaling effects imposed by the Fourier transform.

Due to the time taken to calculate the transform of the original Mexican Hat function, and the fact that this function is normally used many times without change, `mexhat_transform` allows the option of entering a pre-calculated transformed Mexican Hat—it calculates this each time if not provided.

```
function [out_im,hat_ft]= ...
      mexhat_transform(image_matrix,hat_width,margin,hat_ft)
% by David Galligan 1999-2000
% always enter a square image of any size necessary but must be
% even num of pixels
size_initX=size(image_matrix,1);
size_initY=size(image_matrix,2);

size_final=2^(ceil(log2(max([size_initX size_initY])+margin*2)));
im_mat=zeros(size_final,size_final);
% new image always has even number of cells in both directions
% is inital size even??
if rem(size_initX,2)==0
  % exact centre
  cnr_locX=(size_final/2-size_initX/2)+(1:size_initX);
else
  % 1 back from exact centre
  cnr_locX=floor(size_final/2-size_initX/2)+(1:size_initX);
end
if rem(size_initY,2)==0
  % exact centre
  cnr_locY=(size_final/2-size_initY/2)+(1:size_initY);
else
  % 1 back from exact centre
  cnr_locY=floor(size_final/2-size_initY/2)+(1:size_initY);
end
% create images in time space
im_mat(cnr_locX,cnr_locY)=image_matrix;
```

```
if nargin==3
  hat_im=mexhat2d(size_final,size_final,hat_width);
  % pad hat image with a column and a row of zeros
  hat_im=[hat_im; zeros(1,size_final-1)];
  hat_im=[hat_im zeros(size_final,1)];
end
% move images to frequency space
im_ft=fft2(im_mat);
if nargin==3
  hat_ft=fft2(ifftshift(hat_im));
end
% perform convolution and return result in time space
conv_im=(real((2/size_final)*ifft2(im_ft.*hat_ft)));
% output final image
out_im=conv_im(cnr_locX-1,cnr_locY-1);
```

The wavelet enhancement based searches systematically performed in the current study use the `final_systematic_search.m` script or a variant of this. This script searches based on source direction (AH=antihelion, HN=helion, AX=prograde apex, RAX=retrograde apex) as set in the *mode* variable; geocentric speed partitioned with centre *vg_cnr* and half-range *vg_pm*; probe-size, as measured in the units of half a degree, in *probe_size* and finally time-window size as defined in units of mean solar longitude in *sl_pm*.

The output of the search run is written from this script to an `*.mdt` file. This file contains all details of the search and compressed versions of the wavelet transforms—using MATLAB to store such transformed images, directly, uses twice as much disk space as the current method. This is an important problem as these files are usually $\sim 10^2$ megabytes in size.

```
% final_systematic_search.m
% by David Galligan 1999-2000
% final version of systematic search using wavelet enhancement
init_rad_search % inputs T1995-T1999 AMOR orbits
% begin user selection
global main_data_disk
vg_pm=10; % half-width of speed partition
want_drawing=0;
output_dir=main_data_disk;
for mode={'AH','HN','AX'}
  for yr_sel=-1 % set to 4 digit year for single-year search
    for probe_size=6:6:12 % in units of half a degree
      % change speed centres for RAX mode
      for vg_cnr=[20 30 40 5000] % 5000 means all speeds
        for sl_pm=1:2:3
          % automatically assign *.mdt filename
          if vg_cnr==5000
            output_file=sprintf('%s%s_SPDAL_P%d_S%d_Y%d.mdt',
                output_dir,mode{:},probe_size/2,sl_pm,yr_sel);
          else
```

```
    output_file=sprintf('%s%s_SPD%d_P%d_S%d_Y%d.mdt',
          output_dir,mode{:},vg_cnr,probe_size/2,...
          sl_pm,yr_sel);
end
% cycle the 0 deg endpoint by 90 deg in order to mode
% active region to centre of angular range
eclong(find(eclong<90))=eclong(find(eclong<90))+90;
% initialisations
maxX=[]; maxY=[];
frame_num=0; num_frames=360;
% select source direction
switch mode{:},
  case 'AH',
    use_ind=find(eclong>=150 & eclong<=240 & inclin<90);
  case 'HN',
    use_ind=find(eclong>=300 & eclong<=390 & inclin<90);
  case 'AX',
    use_ind=find(eclong>240 & eclong<300 & inclin<90);
  case 'RAX',
    use_ind=find(eclong>220 & eclong<320 & inclin>=90);
end;
if yr_sel>1989
 use_ind=use_ind(find(eq_yr(use_ind)==yr_sel));
end
fout=fopen(output_file,'w');
counter=[];
for sl_cnr=1:360
  min_sl=sl_cnr-sl_pm;
  max_sl=sl_cnr+sl_pm;
  if min_sl<0
    curr_ind=use_ind(find((sl(use_ind)<=(max_sl))...
                        | (sl(use_ind)>=(360+min_sl))));
  elseif max_sl>360
    curr_ind=use_ind(find((sl(use_ind)<=(max_sl-360))...
                        | (sl(use_ind)>=min_sl)));
  else
    curr_ind=use_ind(find(sl(use_ind)>=(sl_cnr-sl_pm)...
                        & sl(use_ind)<=(sl_cnr+sl_pm)));
  end
  num_all_spd=length(curr_ind);
  if vg_cnr<5000
    curr_ind=curr_ind(...
      find(spdgeo(curr_ind)>=(vg_cnr-vg_pm)...
        & spdgeo(curr_ind)<=(vg_cnr+vg_pm)));
  end
  num_sel_spd=length(curr_ind);
  frame_num=frame_num+1
  % choose source direction
  switch mode{:},
```

```
    case 'AH',
      [src_im,cnrX,cnrY,bin_ind]=...
          bin2d(eclong(curr_ind),150,240,180,...
                eclat(curr_ind),-90,30,240);
    case 'HN',
      [src_im,cnrX,cnrY,bin_ind]=...
          bin2d(eclong(curr_ind),300,390,180,...
                eclat(curr_ind),-90,30,240);
    case 'AX',
      [src_im,cnrX,cnrY,bin_ind]=...
          bin2d(eclong(curr_ind),240,300,120,...
                eclat(curr_ind),-90,30,240);
    case 'RAX',
      [src_im,cnrX,cnrY,bin_ind]=...
          bin2d(eclong(curr_ind),240,300,120,...
                eclat(curr_ind),-50,30,160);
   otherwise,
      error('Unknown_Region')
  end
  % note that bin2d is a 2-D binning function defined by
  % the author due to the lack of such a function in Matlab
  if frame_num==1
    fwrite(fout,uint32(num_frames),'uint32');
    fwrite(fout,uint32(length(cnrX)),'uint32');
    fwrite(fout,uint32(length(cnrY)),'uint32');
    fwrite(fout,uint32(probe_size),'uint32');
    fwrite(fout,cnrX,'float32');
    fwrite(fout,cnrY,'float32');
    fwrite(fout,sl_pm,'float32');
    [out_im,hat_ft]=...
       mexhat_transform(src_im,probe_size,180);
  else
    [out_im,hat_ft]=...
       mexhat_transform(src_im,probe_size,180,hat_ft);
  end
  % output drawing
  if want_drawing
    pcolor_ext(cnrX,cnrY,out_im);
    shading flat
    colorbar
    pause
  end
  out_im_str=sprintf('out_im%d',frame_num);
  src_im_str=sprintf('src_im%d',frame_num);
  % write out wavelet transform to *.mdt file in 32 bit
  % floating form rather than the ridiculously precise
  % 64 bit form normally forced by Matlab
  fwrite(fout,out_im,'float32');
  fwrite(fout,uint8(src_im),'uint8');
```

```
            fwrite(fout,num_all_spd,'uint32');
            fwrite(fout,num_sel_spd,'uint32');
          end
          eval(sprintf('!gzip_%s',output_file))
        end
      end
    end
    fclose(fout)
  end
end
```

Appendix D

Data Set Files Used

D.1 Common Stream Format Mean Orbit Data Set

In order to easily perform computerised searches in which a given orbit is compared to many known shower orbits simultaneously a data set has been assembled of representative stream orbits. This data set, contained in a computer readable file called `stream_library.csf`, comprises the results of several stream searches over the past decades as gleaned the published literature. Several of the showers in this data set are not visible by AMOR due to their northerly declinations however they have been included for completeness as at the time of compilation it was not certain which cutoff declination would be used.

There are six published sources from which the mean orbits are drawn, the reference numbers in Table D.1 correspond to these. Source 1 is from the standard list of meteor showers of Cook (1973), this includes all of the major and also many minor showers. Sources 2 and 3 are from the serial-association searches in precise photographic data sets by Lindblad (1971a,1971b). Source 4 is from a serial-association search of 3,675 radar meteoroid orbits by Jopek et al. (1998) while Source 5 is similarly from a search of 865 photographic orbits—the latter are same orbits surveyed by Lindblad (1971a) using a slightly different technique. Source 6 is from a survey of radar meteoroid orbits detected by Adelaide radar system as given in Gartrell and Elford (1975). Many of the 277 orbits within the data set are slightly different variants of the same stream's orbit. The inclusion of such repetition, which is particularly significant in Lindblad (1971a) and Jopek et al. (1998), is deemed to be useful as often the difference between the different mean orbits will be great enough to make some difference to a search process.

In some cases the solar longitude for the mean/maximum of the shower is not given in the original data sets. In these cases this parameter has been calculated based on the longitude of the ascending node and the active dates (limits of activity, mean, or date of maximum) of the shower.

CSF	Shower	Ref.	Start	End	Peak	$\lambda_\odot$ deg	q AU	e	i deg	ω deg	Ω deg	α deg	δ deg	V_G km s^{-1}	Num.
1	Quadrantids	1	1/1	4/1	3/1	283.4	0.977	0.683	72.5	170.0	283.4	230.5	48.3	41.5	-
2	δ Canerids	1	13/1	21/1	16/1	296.7	0.450	0.800	0.0	283.0	296.7	126.7	19.8	28.0	-
3	Virginids	1	3/2	15/4		350.7	0.260	0.900	3.0	304.0	350.7	186.6	-0.3	35.0	-
4	δ Leonids	1	5/2	19/3	26/2	338.7	0.640	0.750	6.0	259.0	338.7	159.7	18.7	23.0	-
5	Camelopardalids	1	14/3	7/4		359.7	0.974	0.352	8.2	185.0	359.7	119.9	68.2	6.8	-
6	σ Leonids	1	21/3	13/5	17/4	28.7	0.750	0.660	1.0	248.0	28.7	195.6	-5.3	20.0	-
7	δ Draconids	1	28/3	17/4		14.4	0.996	0.640	37.5	171.1	14.4	281.0	68.1	26.7	-
8	κ Serpentids	1	1/4	7/4		14.7	0.450	1.000	64.0	275.0	14.7	230.6	17.8	45.0	-
9	μ Virginids	1	1/4	12/5	25/4	35.7	0.480	0.830	10.0	280.0	35.7	221.7	-5.2	29.0	-
10	α Scorpiids	1	11/4	12/5	3/5	42.7	0.210	0.900	3.0	134.0	222.7	240.7	-22.1	35.0	-
11	α Bootids	1	14/4	12/5	28/4	36.7	0.750	0.710	18.0	247.0	36.7	218.6	18.8	20.0	-
12	ϕ Bootids	1	16/4	12/5	1/5	40.7	0.950	0.240	19.0	226.0	40.7	240.3	50.9	12.0	-
13	April Lyrids	1	20/4	23/4	22/4	32.4	0.919	0.968	79.0	214.3	32.4	271.9	33.6	47.6	-
14	η Aquarids	1	21/4	12/5	3/5	43.1	0.560	0.958	163.5	95.2	43.1	336.2	-1.6	65.5	-
15	τ Herculids	1	19/5	14/6	3/6	72.7	0.970	0.630	19.0	204.0	72.7	228.5	38.8	15.0	-
16	χ Scorpiids	1	27/5	20/6	5/6	74.7	0.680	0.770	6.0	257.0	74.7	247.7	-13.1	21.0	-
17	Daytime Arietids	1	29/5	19/6	7/6	77.7	0.090	0.940	21.0	29.0	77.7	44.7	23.2	37.0	-
18	Daytime ζ Perseids	1	1/6	17/6	7/6	78.7	0.340	0.790	0.0	59.0	78.7	62.7	23.1	27.0	-
19	Librids(a)	1	8/6	9/6	8/6	78.9	0.880	0.650	4.0	46.0	258.9	228.0	-28.5	16.0	-
20	Librids(b)	1	8/6	9/6	8/6	78.9	0.850	0.920	5.0	49.0	258.9	228.0	-28.5	16.0	-
21	Sagittariids	1	8/6	16/6	11/6	80.7	0.100	1.000	99.0	142.0	260.7	304.8	-34.8	52.0	-
22	θ Ophiuchids	1	8/6	16/6	13/6	82.7	0.460	0.840	4.0	101.0	262.7	267.8	-28.0	26.7	-
23	June Lyrids(a)	1	11/6	21/6	16/6	85.2	0.830	0.670	44.0	237.0	85.2	278.4	35.0	31.0	-
24	June Lyrids(b)	1	11/6	21/6	16/6	85.2	0.840	0.920	50.0	231.0	85.2	278.4	35.0	31.0	-

Table D.1: The mean stream orbit data set as obtained from several sources for use as a reference in determining stream associations. The units for each quantity are shown with the avtivity dates for the shower being given in the form day/month. All angular elements are given with respect to the Epoch J2000.0 (most of the original data sets are given with respect to B1950.0). Where possible the number of orbits used to originally determine the mean is shown. The derivation of these stream orbits is described in more detail in the text.

CSF	Shower	Ref.	Start	End	Peak	$\lambda_\odot$ deg	q AU	e	i deg	ω deg	Ω deg	α deg	δ deg	V_G km s^{-1}	Num.
25	Daytime β Taurids	1	24/6	6/7	29/6	97.1	0.340	0.850	6.0	246.0	277.1	86.7	19.0	30.0	-
26	Corvids(a)	1	25/6	30/6	26/6	95.6	1.013	0.600	3.0	7.6	275.6	192.6	-19.4	10.0	-
27	Corvids(b)	1	25/6	30/6	26/6	95.6	1.012	0.900	4.0	7.9	275.6	192.6	-19.4	10.0	-
28	June Bootids	1	28/6	28/6	28/6	98.7	1.020	0.690	18.0	180.0	98.7	219.4	48.8	13.9	-
29	July Phoenicids(a)	1	3/7	18/7	14/7	110.3	0.960	0.620	82.0	31.0	290.3	31.6	-47.7	47.0	-
30	July Phoenicids(b)	1	3/7	18/7	14/7	110.3	0.970	1.000	87.0	24.0	290.3	31.6	-47.7	47.0	-
31	o Draconids	1	7/7	24/7	16/7	113.7	1.010	1.000	43.0	190.0	113.7	271.2	59.0	28.6	-
32	Sth δ Aquarids	1	21/7	29/8	29/7	125.7	0.069	0.976	27.2	152.8	305.7	333.8	-16.3	41.4	-
33	Nth δ Aquarids	1	14/7	25/8	12/8	139.7	0.070	0.970	20.0	332.0	139.7	339.6	-4.7	42.3	-
34	α Capricornids	1	15/7	10/8	30/7	127.7	0.590	0.770	7.0	269.0	127.7	307.7	-9.8	22.8	-
35	Sth ι Aquarids	1	15/7	25/8	5/8	131.7	0.208	0.912	6.9	131.8	311.7	334.0	-14.5	33.8	-
36	Nth ι Aquarids	1	15/7	20/9	20/8	147.7	0.260	0.840	5.0	308.0	147.7	327.7	-5.8	31.2	-
37	Perseids	1	23/7	23/8	12/8	139.7	0.953	0.965	113.8	151.5	139.7	47.2	57.6	59.4	-
38	κ Cygnids	1	9/8	6/10	18/8	145.7	0.990	0.680	38.0	194.0	145.7	286.2	59.1	24.8	-
39	Sth Piscids	1	31/8	2/11	20/9	177.7	0.420	0.820	2.0	107.0	357.7	6.6	0.3	26.3	-
40	Nth Piscids	1	25/9	19/10	12/10	199.7	0.400	0.800	3.0	291.0	199.7	26.7	14.2	29.0	-
41	Aurigids	1	1/9	1/9	1/9	158.6	0.802	1.000	146.4	121.5	158.6	85.5	42.0	66.3	-
42	κ Aquarids	1	11/9	28/9	21/9	178.7	0.810	0.740	2.0	236.0	178.7	338.6	-4.7	16.0	-
43	Sth Taurids	1	15/9	26/11	3/11	220.7	0.375	0.806	5.2	113.2	40.7	51.2	13.8	27.0	-
44	Nth Taurids	1	19/9	1/12	13/11	230.7	0.359	0.861	2.4	292.3	230.7	59.0	22.4	29.2	-
45	Daytime Sextantids	1	24/9	5/10	29/9	184.3	0.160	0.870	22.0	213.0	4.3	152.6	-0.2	32.2	-
46	An Andromedids(a)	1	25/9	12/11	3/10	190.7	0.580	0.820	4.0	267.0	190.7	5.6	8.3	23.2	-
47	An Andromedids(b)	1	25/9	12/11	3/10	228.7	0.790	0.760	12.0	238.0	228.7	20.7	34.3	18.2	-
48	Andromedids	1	27/11	27/11	27/11	247.7	0.860	0.760	13.0	222.0	247.7	25.8	44.3	16.5	-
49	Orionids	1	2/10	7/11	21/10	208.7	0.571	0.962	163.9	82.5	28.7	95.2	15.8	66.4	-
50	October Draconids	1	9/10	9/10	9/10	197.0	0.996	0.717	30.7	171.8	197.0	262.4	54.1	20.4	-
51	ϵ Geminids	1	14/10	27/10	19/10	209.7	0.770	0.970	173.0	237.0	209.7	104.8	26.9	69.4	-
52	Leo Minorids	1	22/10	24/10	24/10	211.7	0.650	0.990	124.0	106.0	211.7	162.7	36.7	61.8	-
53	Pegasids	1	29/10	12/11	12/11	230.7	0.970	0.750	8.0	196.0	230.7	335.6	21.3	11.2	-

Table D.1: *continued.*

CSF	Shower	Ref.	Start	End	Peak	$\lambda_\odot$ deg	q AU	e	i deg	ω deg	Ω deg	α deg	δ deg	V_G km s^{-1}	Num.
54	Leonids	1	14/11	20/11	17/11	235.2	0.985	0.915	162.6	172.5	235.2	153.0	22.0	70.7	-
55	Monocerotids	1	27/11	17/12	10/12	258.3	0.140	0.997	24.8	135.8	78.3	100.5	14.0	42.4	-
56	σ Hydrids	1	3/12	15/12	11/12	259.7	0.244	0.992	125.5	120.7	79.7	127.2	1.4	58.4	-
57	Nth χ Orionids	1	4/12	15/12	10/12	258.7	0.470	0.790	2.0	281.0	258.7	84.8	26.0	25.2	-
58	Sth χOrionids	1	7/12	14/12	11/12	259.7	0.470	0.780	7.0	101.0	79.7	85.7	16.0	25.5	-
59	Geminids	1	4/12	16/12	14/12	261.7	0.142	0.896	23.6	324.3	261.7	113.1	32.4	34.4	-
60	Dec. Phoenicids(a)	1	5/12	5/12	5/12	253.7	0.980	0.680	16.0	0.0	73.7	15.5	-54.7	12.7	-
61	Dec. Phoenicids(b)	1	5/12	5/12	5/12	254.7	0.990	0.670	13.0	359.0	74.7	15.6	-44.7	11.7	-
62	δ Arietids	1	8/12	14/12		258.3	0.838	0.605	1.8	232.8	258.3	52.7	22.2	13.2	-
63	Coma Berenicids	1	12/12	23/1		282.7	0.580	1.000	134.0	258.0	282.7	175.7	24.7	65.0	-
64	Ursids	1	17/12	24/12	22/12	271.4	0.939	0.850	53.6	205.9	271.4	217.1	75.7	33.4	-
65	Cyclids	2	10/4	19/10		52.8	0.922	0.087	1.9	83.0	52.8	61.8	28.1	-	6
66	κ Aquarids	2	18/9	12/10		186.6	0.867	0.705	2.1	229.2	186.6	314.7	-2.8	19.0	4
67	ρ Geminids	2	15/1	27/1		302.1	0.771	0.710	3.5	243.4	302.1	110.8	28.9	-	6
68	λ Virginids	2	23/3	22/4		17.5	0.322	0.861	2.8	119.4	197.5	208.7	-14.2	32.0	7
69	θ Librids	2	23/5	7/6		71.2	0.755	0.713	3.3	249.1	71.2	238.7	-14.1	21.0	4
70	ϵ Piscids	2	2/10	12/10		195.5	0.550	0.749	0.7	274.0	195.5	15.6	7.3	26.0	6
71	ψ Ur Major	2	27/2	21/4		7.2	0.940	0.489	8.0	212.1	7.2	162.7	42.7	-	4
72	θ Ophiuchids	2	21/5	16/6		77.7	0.430	0.839	4.4	108.7	257.7	265.8	-27.0	-	6
73	θ Cetids	2	27/9	12/11		208.4	0.788	0.528	5.5	68.2	28.4	21.6	-4.7	18.0	4
74	σ Leonids	2	18/3	14/6		32.5	0.812	0.683	3.1	239.7	32.5	195.6	0.7	-	27
75	α Pegasids	2	11/11	12/11		230.3	0.997	0.697	7.5	199.0	230.3	344.6	22.3	-	4
76	ω Ur Major	2	21/5	5/6		67.0	1.017	0.653	16.7	170.5	67.0	174.7	66.7	-	5
77	τ Herculids	2	1/6	24/6		81.5	0.986	0.660	20.7	203.6	81.5	236.4	40.8	-	8
78	Nth δ Arietids	3	8/12	2/1		263.3	0.857	0.634	2.1	228.0	263.3	54.7	25.2	17.0	14
79	Sth Virginids	3	12/3	27/3		357.1	0.431	0.783	0.3	287.0	357.1	185.6	-2.3	28.0	3
80	Sth ι Aquarids	3	19/7	6/8		124.7	0.266	0.925	0.0	121.5	304.7	320.7	-14.8	35.0	4
81	Sth ι Aquarids	3	5/8	22/8		142.5	0.119	0.959	12.6	143.9	322.5	348.7	-9.7	41.0	8
82	Sth Nth Taurids	3	19/9	21/11		209.4	0.330	0.828	3.3	118.8	29.4	40.7	13.2	31.0	91
83	Nth Virginids	3	18/2	12/3		334.5	0.234	0.912	3.5	308.0	334.5	173.6	4.7	36.0	4
84	Nth χ Orionids	3	4/12	13/12		259.0	0.472	0.787	2.5	281.0	259.0	83.8	26.0	28.0	4

Table D.1: *continued.*

CSF	Shower	Ref.	Start	End	Peak	$\lambda_\odot$ deg	q AU	e	i deg	ω deg	Ω deg	α deg	δ deg	V_G km s^{-1}	Num.
85	Nth ι Aquarids	3	21/8	20/9		162.1	0.326	0.830	4.0	299.7	162.1	354.6	1.3	31.0	3
86	Piscids	3	31/8	2/11		190.8	0.525	0.808	1.5	273.6	190.8	10.6	6.3	27.0	33
87	Pegasids	3	29/10	12/11		227.7	0.966	0.718	6.8	200.2	227.7	344.6	19.3	16.0	5
88	α Capricornids	3	15/7	10/8		126.1	0.592	0.760	7.1	267.9	126.1	304.7	-9.8	25.0	18
89	α Capricornids	3	4/8	9/8		134.1	0.497	0.807	8.7	279.0	134.1	317.7	-6.8	28.0	3
90	Sth χ Orionids	3	7/12	14/12		259.8	0.471	0.790	6.9	100.6	79.8	85.7	16.0	28.0	8
91	Nth δ Aquarids	3	5/8	25/8		141.2	0.085	0.956	20.7	330.8	141.2	347.6	1.3	40.0	9
92	Geminids	3	4/12	16/12		260.9	0.140	0.902	23.2	324.2	260.9	111.8	31.9	37.0	77
93	Sth δ Aquarids	3	21/7	8/8		127.8	0.074	0.972	28.4	151.6	307.8	340.7	-15.7	43.0	13
94	Draconids	3	9/10	9/10		196.7	0.999	0.700	25.0	177.0	196.7	276.3	49.0	21.0	2
95	Quadrantids	3	2/1	3/1		283.5	0.974	0.618	72.4	170.5	283.5	229.4	48.8	42.0	17
96	Lyrids	3	21/4	22/4		32.3	0.879	0.956	78.6	217.2	32.3	271.5	34.0	47.0	5
97	Hyper Perseids	3	9/8	13/8		139.3	0.958	1.065	113.0	153.4	139.3	281.4	-	-	11
98	Perseids	3	8/8	15/8		139.4	0.934	0.920	113.2	147.9	139.4	47.0	57.2	60.0	20
99	σ Hydrids	3	13/12	15/12		262.7	0.230	0.980	125.0	124.0	82.7	129.6	0.8	59.0	2
100	Orionids	3	16/10	7/11		209.9	0.570	0.931	163.9	83.4	29.9	95.7	16.0	67.0	23
101	Hyper Orionids	3	14/10	29/10		208.7	0.617	1.135	164.1	75.0	28.7	281.4	-	-	21
102	ϵGeminids	3	16/10	27/10		208.2	0.770	0.940	173.0	236.7	208.2	102.8	26.9	70.0	4
103	σ Leonids	3	21/3	13/5		28.9	0.753	0.663	0.7	247.5	28.9	195.6	-5.3	20.0	19
104	κAquarids	3	11/9	28/9		178.7	0.814	0.744	1.8	235.6	178.7	338.6	-4.7	20.0	5
105	μ Ophiuchids	3	10/8	10/8		137.7	0.980	0.595	2.5	204.5	137.7	267.7	-14.0	15.0	2
106	Nth λ Virgin	3	4/4	15/4		20.2	0.343	0.870	2.0	295.0	20.2	210.7	-10.2	32.0	2
107	Sth λ Virgin	3	5/5	6/5		45.2	0.686	0.895	3.5	72.0	225.2	210.7	-18.2	25.0	2
108	ρ Geminids	3	15/1	23/1		298.4	0.708	0.673	5.0	252.3	298.4	112.8	30.9	21.0	3
109	θ Ophiuchids	3	4/6	16/6		78.7	0.405	0.852	4.7	108.0	258.7	266.8	-28.0	30.0	4
110	Sth χ Geminids	3	23/1	7/2		311.2	0.693	0.710	4.0	72.0	131.2	122.7	12.9	21.0	2
111	χ Scorpiids	3	27/5	20/6		74.6	0.679	0.767	6.0	256.7	74.6	246.7	-12.1	23.0	11
112	θ Cetids	3	19/10	21/10		207.7	0.783	0.555	8.5	67.0	27.7	22.6	-10.7	19.0	2
113	Nth χ Geminids	3	19/1	21/1		300.7	0.595	0.675	9.5	268.5	300.7	127.8	33.8	23.0	2
114	ω Ur Major	3	7/5	5/6		60.0	0.998	0.740	12.3	186.7	60.0	184.6	46.7	16.0	3

Table D.1: *continued.*

CSF	Shower	Ref.	Start	End	Peak	$\lambda_\odot$ deg	q AU	e	i deg	ω deg	Ω deg	α deg	δ deg	V_G km s^{-1}	Num.
115	ψ Ur Major	3	10/4	13/4		22.2	0.984	0.455	14.0	203.0	22.2	188.6	58.7	15.0	2
116	θ Herculids	3	6/8	9/8		135.7	1.005	0.667	16.7	194.3	135.7	260.5	30.0	18.0	3
117	τ Herculids	3	19/5	14/6		72.6	0.970	0.633	18.6	204.2	72.6	228.5	39.8	18.0	14
118	ϕ Bootids	3	16/4	12/5		41.2	0.949	0.237	19.3	225.8	41.2	240.3	50.9	16.0	6
119	α Bootids	3	14/4	12/5		36.9	0.753	0.706	18.0	246.9	36.9	218.6	18.8	23.0	8
120	γ Bootids	3	13/4	15/4		24.7	0.818	0.775	27.0	235.5	24.7	215.5	35.8	25.0	2
121	δ Leonids	3	5/2	19/3		338.8	0.643	0.747	6.2	259.0	338.8	159.7	18.7	23.0	24
122	δ Cancrids	3	13/1	21/1		297.1	0.448	0.800	0.3	282.6	297.1	126.7	19.8	28.0	7
123	Piscids	3	25/9	19/10		199.8	0.399	0.797	3.4	290.8	199.8	26.7	14.2	29.0	9
124	α Scorpiids	3	9/5	12/5		50.2	0.212	0.905	3.5	132.0	230.2	247.8	-24.1	35.0	2
125	α Scorpiids	3	11/4	5/5		37.0	0.189	0.893	2.3	136.7	217.0	235.7	-21.2	34.0	3
126	μ Sagittariids	3	22/6	6/7		96.0	0.680	0.757	5.5	257.5	96.0	268.7	-15.0	23.0	4
127	ϕ Ophiuchids	3	3/5	8/5		44.7	0.133	0.937	10.0	322.0	44.7	247.7	-18.1	38.0	3
128	α Triangulids	3	7/11	12/11		228.2	0.784	0.757	9.7	238.0	228.2	22.7	30.3	21.0	4
129	μ Virginids	3	13/4	12/5		35.7	0.477	0.831	9.9	280.0	35.7	221.7	-5.2	29.0	7
130	o Serpentids	3	9/6	25/6		86.5	0.430	0.847	13.0	284.2	86.5	274.7	-11.0	30.0	4
131	η Serpentids	3	25/6	3/7		97.7	0.606	0.715	15.5	268.5	97.7	278.7	-2.0	25.0	2
132	α Lyrids	3	4/8	13/8		135.4	0.958	0.720	29.7	207.7	135.4	282.4	42.1	23.0	3
133	ζ Draconids	3	20/8	25/8		150.2	1.015	0.640	33.0	183.5	150.2	269.2	59.0	24.0	2
134	Lyncids	3	27/9	28/9		185.2	0.770	0.990	136.5	152.5	185.2	110.9	47.9	66.0	2
135	ζ Arietids	3	13/8	25/8		146.7	0.973	0.945	172.5	19.5	326.7	49.7	14.2	71.0	2
136	η Aquarids	4	13/4	13/4		22.7	0.410	0.860	132.0	74.0	22.7	319.6	4.2	58.0	1
137	Orionids	4	16/10	30/10		208.7	0.550	0.860	158.0	88.0	28.7	95.7	13.0	64.0	25
138	ω Sagittariids	4	10/6	17/6		81.7	0.060	0.950	40.0	158.0	261.7	301.8	-29.9	39.0	5
139	β Librids	4	14/12	15/12		261.7	0.090	0.940	39.0	29.0	261.7	230.7	-7.2	40.0	4
140	ψ Piscids	4	11/6	13/6		81.7	0.300	0.870	147.0	59.0	81.7	16.7	20.3	58.0	3
141	υ Hydrids	4	5/12	16/12		259.7	0.280	0.970	122.0	117.0	79.7	128.6	-1.2	57.0	12
142	γ Pegasids	4	9/6	15/6		80.7	0.740	0.640	149.0	108.0	80.7	0.6	17.3	62.0	7
143	γ Sextantids	4	14/12	16/12		262.7	0.680	0.540	139.0	83.0	82.7	150.6	-9.2	59.0	2

Table D.1: *continued.*

CSF	Shower	Ref.	Start	End	Peak	$\lambda_\odot$ deg	q AU	e	i deg	ω deg	Ω deg	α deg	δ deg	V_G km s^{-1}	Num.
144	η Opiuchids	4	12/2	19/2		326.7	0.580	0.730	143.0	91.0	326.7	258.7	-6.1	61.0	4
145	υ Cetids	4	17/8	20/8		145.7	0.640	0.750	144.0	82.0	325.7	38.6	-2.8	61.0	2
146	Arietids	4	8/6	18/6		82.7	0.160	0.920	22.0	37.0	82.7	53.7	22.2	36.0	160
147	Geminids	4	5/12	17/12		264.7	0.190	0.890	17.0	352.0	264.7	105.8	23.9	34.0	127
148	Ophiuchids	4	8/6	19/6		83.7	0.470	0.780	4.0	100.0	263.7	268.8	-24.0	25.0	25
149	Scorpiids	4	5/12	15/12		249.7	0.470	0.760	4.0	234.0	69.7	248.8	-23.1	24.0	13
150	α Aquarids	4	12/3	22/3		358.7	0.230	0.890	5.0	46.0	358.7	339.7	-6.7	32.0	16
151	ζ ϵ Piscids	4	22/9	29/9		182.7	0.290	0.860	5.0	125.0	2.7	17.7	7.3	30.0	49
152	α Cancrids	4	17/1	23/1		296.7	0.310	0.820	5.0	5.0	296.7	137.7	15.8	29.0	11
153	β Geminids	4	23/7	1/8		214.7	0.270	0.850	5.0	148.0	214.7	109.7	20.9	31.0	6
154	ϵ Arietids	4	19/5	28/5		63.7	0.360	0.820	6.0	65.0	63.7	46.7	21.2	28.0	35
155	Sth Taurids	4	16/11	24/11		237.7	0.450	0.790	5.0	107.0	57.7	61.7	19.1	25.0	28
156	υ Leonids	4	10/2	17/2		328.7	0.310	0.830	5.0	301.0	328.7	163.7	9.7	30.0	13
157	α Cancrids	4	17/8	24/8		144.7	0.320	0.870	9.0	242.0	324.7	133.7	10.8	32.0	6
158	δ Piscids	4	12/4	30/4		26.7	0.350	0.820	9.0	63.0	26.7	9.6	11.3	28.0	12
159	Sth Arietids	4	16/10	31/10		208.7	0.340	0.830	6.0	115.0	28.7	40.7	12.2	28.0	121
160	κ Cancrids	4	21/1	23/1		301.7	0.200	0.930	6.0	131.0	121.7	141.7	11.8	36.0	2
161	ϵ ρ Geminids	4	24/7	28/7		122.7	0.240	0.900	10.0	52.0	122.7	107.8	27.9	33.0	4
162	σ Sagittariids	4	12/6	19/6		81.7	0.240	0.890	10.0	128.0	261.7	283.8	-26.9	32.0	22
163	γ Librids	4	7/12	15/12		257.7	0.260	0.880	9.0	49.0	257.7	239.7	-18.1	32.0	7
164	γ Sextantids	4	12/2	19/2		326.7	0.440	0.880	19.0	101.0	146.7	150.6	-6.2	30.0	10
165	κ Leonids	4	17/8	22/8		146.7	0.430	0.790	12.0	72.0	146.7	143.7	26.8	27.0	3
166	α Virginids	4	14/3	22/3		358.7	0.140	0.970	12.0	130.0	178.7	199.7	-9.3	39.0	10
167	α Leonids	4	23/9	29/9		183.7	0.090	0.970	18.0	29.0	183.7	159.7	12.7	41.0	15
168	ω Sagittariids	4	12/2	16/2		325.7	0.140	0.900	20.0	216.0	145.7	301.8	-28.9	34.0	2
169	β Capricornids	4	12/2	19/2		327.7	0.170	0.930	13.0	43.0	327.7	305.7	-12.8	37.0	3
170	β Capricornids	4	12/2	16/2		331.7	0.230	0.860	4.0	222.0	151.7	309.7	-20.8	31.0	3
171	β Capricornids	4	12/2	16/2		324.7	0.340	0.820	5.0	242.0	144.7	314.7	-20.8	28.0	6
172	α Aquarids	4	16/8	20/8		145.7	0.340	0.800	9.0	297.0	145.7	338.6	-1.7	27.0	6
173	λ Aquarids	4	18/8	20/8		142.7	0.220	0.900	4.0	340.0	142.7	345.6	-5.7	33.0	5
174	ω Piscids	4	16/8	24/8		148.7	0.130	0.940	27.0	323.0	148.7	351.6	7.3	37.0	9

Table D.1: *continued.*

CSF	Shower	Ref.	Start	End	Peak	$\lambda_\odot$ deg	q AU	e	i deg	ω deg	Ω deg	α deg	δ deg	V_G km s^{-1}	Num.
175	Aquarids-Cetids	4	18/8	24/8		147.7	0.130	0.930	22.0	144.0	327.7	357.6	-10.7	36.0	5
176	Puppids	4	8/12	17/12		259.7	0.970	0.500	70.0	347.0	79.7	142.4	-54.2	39.0	16
177	Carinids	4	18/1	23/1		300.7	0.980	0.540	75.0	4.0	120.7	163.5	-62.3	41.0	6
178	Chamaeleonids	4	11/2	17/2		325.7	0.940	0.600	75.0	338.0	145.7	208.3	-78.2	42.0	33
179	λ Octantids	4	12/3	23/3		357.7	0.950	0.640	72.0	337.0	177.7	328.8	-82.8	40.0	25
180	α Arietids	4	20/5	28/5		63.7	0.150	0.950	11.0	41.0	63.7	37.7	20.2	37.0	8
181	ζ Cetids	4	8/6	19/6		81.7	0.150	0.890	45.0	325.0	81.7	292.7	-4.9	37.0	19
182	δ Aquarids	4	22/7	6/8		125.7	0.080	0.960	33.0	152.0	305.7	340.7	-16.7	40.0	99
183	Sextantids	4	2/9	29/9		183.7	0.130	0.880	19.0	211.0	3.7	152.6	2.8	32.0	14
184	Lyrids	5	21/4	23/4		32.7	0.920	0.990	80.0	214.0	32.7	272.5	33.0	47.0	5
185	Nth α Capric	5	24/7	22/8		134.7	0.580	0.780	6.0	268.0	134.7	314.7	-8.8	23.0	-
186	Sth α Capric	5	22/8	22/8		149.7	0.630	0.620	4.0	89.0	329.7	333.7	-17.8	18.0	-
187	Perseids	5	4/8	21/8		139.7	0.950	0.950	113.0	150.0	139.7	48.0	58.2	59.0	30
188	κ Cygnids	5	19/8	22/8		147.7	0.980	0.760	39.0	202.0	147.7	289.2	56.1	25.0	4
189	ϵ Geminids	5	11/10	22/10		203.7	0.810	0.960	174.0	231.0	203.7	100.8	25.9	70.0	-
190	Nth Taurids	5	16/9	15/11		213.7	0.320	0.850	3.0	299.0	213.7	44.7	19.2	30.0	-
191	Sth Taurids	5	17/9	21/11		207.7	0.340	0.820	6.0	118.0	27.7	40.7	10.2	28.0	-
192	Quadrantids	5	2/1	4/1		282.7	0.980	0.680	72.0	171.0	282.7	230.4	48.8	41.0	14
193	Geminids	5	7/12	14/12		261.7	0.140	0.900	24.0	324.0	261.7	112.8	31.9	35.0	51
194	Nth χ Orionids	5	9/12	30/12		265.7	0.380	0.830	3.0	291.0	265.7	97.8	26.0	28.0	-
195	Sth χ Orionids	5	4/12	14/12		257.7	0.510	0.790	5.0	96.0	77.7	80.7	17.0	25.0	-
196	Monocerotids	5	10/12	15/12		260.7	0.180	1.000	37.0	129.0	80.7	103.7	7.9	43.0	-
197	Leonids	5	15/11	20/11		235.7	0.980	0.920	162.0	173.0	235.7	153.7	21.8	71.0	5
198	σ Hydrids	5	4/12	15/12		258.7	0.240	0.980	126.0	122.0	78.7	127.6	1.8	58.0	3
199	Orionids	5	19/10	24/10		209.7	0.570	0.970	165.0	83.0	29.7	96.7	16.0	66.0	20
200	Nth α Virginid	5	4/4	12/5		34.7	0.410	0.830	8.0	288.0	34.7	222.7	-8.2	28.0	11
201	Sth α Virginid	5	2/4	24/4		18.7	0.320	0.870	7.0	118.0	198.7	208.7	-17.2	31.0	-
202	Sth δ Aquarid	5	21/7	8/8		128.7	0.080	0.970	27.0	151.0	308.7	340.7	-15.7	41.0	-
203	Nth δ Aquarid	5	5/8	25/8		142.7	0.100	0.950	21.0	328.0	142.7	347.6	2.3	38.0	-
204	Nth ϵ Piscids	5	19/9	13/10		190.7	0.580	0.760	5.0	268.0	190.7	6.6	10.3	22.0	-

Table D.1: *continued.*

CSF	Shower	Ref.	Start	End	Peak	$\lambda_\odot$ deg	q AU	e	i deg	ω deg	Ω deg	α deg	δ deg	V_G km s^{-1}	Num.
205	Sth ϵ Piscids	5	14/9	9/10		185.7	0.610	0.730	4.0	85.0	5.7	4.6	-4.7	21.0	-
206	Draconids	5	9/10	9/10		196.7	1.000	0.700	25.0	177.0	196.7	271.3	47.0	17.0	2
207	Cyclids	5	19/10	19/10		206.7	0.830	0.120	3.0	119.0	26.7	50.6	-6.8	3.0	2
208	α Pegasids	5	12/11	12/11		230.7	0.970	0.680	7.0	200.0	230.7	342.6	22.3	11.0	2
209	GE1201	6			13/12	261.7	0.090	0.930	2.0	331.0	261.7	111.8	22.9	38.0	4
210	GE1202	6			14/12	262.7	0.330	0.850	7.1	117.0	82.7	95.7	18.0	32.0	6
211	GE1203	6			14/12	262.7	0.740	0.770	9.4	65.0	82.7	71.7	5.1	23.0	3
212	GE1204	6			12/12	260.7	0.500	0.830	20.4	95.0	80.7	88.7	2.0	30.0	5
213	GE1205 Geminids	6			14/12	261.7	0.130	0.900	18.2	327.0	261.7	112.8	29.9	36.0	20
214	GE1206	6			15/12	262.7	0.970	0.560	57.3	344.0	82.7	135.3	-63.2	35.0	7
215	GE1207 Monocer	6			13/12	261.7	0.980	0.160	69.5	0.0	81.7	141.5	-43.2	37.0	6
216	GE1208	6			13/12	262.7	0.980	0.080	74.5	1.0	82.7	145.5	-45.2	39.0	3
217	GE1209	6			13/12	262.7	0.190	0.980	39.9	130.0	82.7	106.7	5.9	42.0	3
218	GE0101	6			22/1	302.7	0.980	0.640	74.3	7.0	122.7	160.5	-63.3	43.0	3
219	GE0201	6			13/2	324.7	0.360	0.820	4.5	246.0	144.7	316.7	-20.8	31.0	3
220	GE0202	6			15/2	327.7	0.270	0.850	0.1	125.0	147.7	164.6	5.7	32.0	6
221	GE0203	6			14/2	325.7	0.600	0.870	18.0	98.0	325.7	320.6	7.2	29.0	3
222	GE0204	6			15/2	326.7	0.190	0.900	7.8	315.0	326.7	169.6	8.7	35.0	3
223	GE0205	6			12/2	323.7	0.610	0.690	8.1	86.0	143.7	148.7	24.8	24.0	5
224	GE0206	6			14/2	325.7	0.200	0.860	12.2	137.0	145.7	167.6	-2.3	33.0	3
225	GE0207	6			14/2	325.7	0.230	0.850	20.4	313.0	325.7	174.6	15.7	33.0	4
226	GE0208	6			14/2	326.7	0.040	0.960	33.6	13.0	326.7	284.7	-15.9	37.0	3
227	GE0209	6			12/2	323.7	0.860	0.930	49.9	43.0	143.7	133.4	-50.2	35.0	3
228	GE0210	6			14/2	325.7	0.980	0.890	47.2	12.0	145.7	110.1	-65.1	32.0	3
229	GE0211	6			13/2	325.7	0.980	0.670	48.4	354.0	145.7	98.5	-76.0	31.0	5
230	GE0212	6			14/2	326.7	0.990	0.250	54.1	3.0	146.7	155.1	-77.3	31.0	3
231	GE0213	6			14/2	325.7	0.930	0.600	62.0	33.0	145.7	152.4	-65.2	37.0	9
232	GE0214	6			14/2	325.7	0.930	0.440	61.9	340.0	145.7	179.6	-83.3	36.0	47
233	GE0215	6			13/2	324.7	0.950	0.930	70.2	330.0	144.7	254.5	-86.1	44.0	4
234	GE0216	6			12/2	323.7	0.980	0.560	118.0	171.0	323.7	241.6	14.9	59.0	5

Table D.1: *continued.*

CSF	Shower	Ref.	Start	End	Peak	$\lambda_\odot$ deg	q AU	e	i deg	ω deg	Ω deg	α deg	δ deg	V_G km s^{-1}	Num.
235	GE0217	6			13/2	323.7	0.460	0.430	141.5	322.0	323.7	225.6	0.8	54.0	3
236	GE0218	6			14/2	324.7	0.820	0.620	2.1	299.0	144.7	346.7	-23.7	18.0	11
237	GE0301	6			19/3	359.7	0.180	0.890	1.8	42.0	359.7	338.7	-7.7	35.0	7
238	GE0302	6			19/3	358.7	0.750	0.910	7.3	62.0	178.7	159.6	-5.3	23.0	3
239	GE0303	6			19/3	358.7	0.230	0.860	19.4	312.0	358.7	203.6	2.7	33.0	5
240	GE0304	6			18/3	358.7	0.980	0.530	55.3	347.0	178.7	50.3	-80.8	34.0	11
241	GE0305	6			19/3	358.7	0.980	0.870	58.3	346.0	178.7	49.6	-77.8	38.0	10
242	GE0306	6			18/3	357.7	0.880	0.410	65.7	57.0	177.7	195.9	-74.3	37.0	5
243	GE0307	6			19/3	359.7	0.650	0.650	57.3	83.0	179.7	184.7	-58.3	36.0	3
244	GE0308	6			17/3	357.7	0.930	1.000	61.9	28.0	177.7	154.2	-73.3	40.0	3
245	GE0309	6			19/3	358.7	0.760	0.900	59.3	58.0	178.7	173.6	-60.3	40.0	3
246	GE0310	6			17/3	357.7	0.950	0.670	73.6	332.0	177.7	333.3	-78.8	43.0	4
247	GE0311	6			19/3	359.7	0.930	0.340	85.2	317.0	179.7	298.4	-71.9	45.0	3
248	GE0312	6			19/3	358.7	0.940	0.620	92.8	29.0	178.7	242.4	-71.1	50.0	7
249	GE0313	6			21/3	1.7	0.990	0.760	95.9	353.0	181.7	282.5	-71.9	53.0	4
250	GE0314	6			19/3	358.7	0.980	0.620	121.6	13.0	178.7	263.1	-56.0	60.0	6
251	GE0315	6			20/3	359.7	0.660	0.430	137.4	97.0	179.7	250.9	-43.1	57.0	3
252	GE0316	6			19/3	359.7	0.420	0.930	141.8	282.0	359.7	240.7	-4.1	62.0	4
253	GE0601	6			11/6	80.7	0.520	0.770	1.3	97.0	260.7	262.8	-25.0	26.0	4
254	GE0602	6			10/6	79.7	0.930	0.680	14.0	216.0	79.7	234.6	19.8	18.0	3
255	GE0603	6			13/6	82.7	0.040	0.980	2.4	18.0	82.7	47.7	18.2	42.0	3
256	GE0604	6			11/6	81.7	0.020	0.990	18.0	14.0	81.7	44.7	19.2	43.0	9
257	GE0605 Arietids	6			11/6	81.7	0.080	0.960	17.4	28.0	81.7	49.7	23.2	41.0	32
258	GE0606	6			11/6	80.7	0.020	0.990	30.9	11.0	80.7	39.7	19.2	43.0	4
259	GE0607	6			12/6	81.7	0.060	0.960	38.2	203.0	261.7	48.7	9.2	41.0	6
260	GE0608	6			10/6	79.7	0.110	0.900	33.5	152.0	259.7	297.8	-33.9	35.0	4
261	GE0609	6			11/6	80.7	0.150	0.900	39.5	324.0	80.7	289.7	-5.9	38.0	13
262	GE0610	6			9/6	79.7	0.370	0.860	43.3	292.0	79.7	280.6	6.0	37.0	4
263	GE0611	6			10/6	80.7	0.140	0.840	66.3	333.0	80.7	303.6	3.2	37.0	5
264	GE0612	6			11/6	81.7	0.120	0.920	65.3	214.0	261.7	47.6	-1.8	43.0	6

Table D.1: *continued.*

CSF	Shower	Ref.	Start	End	Peak	$\lambda_\odot$ deg	q AU	e	i deg	ω deg	Ω deg	α deg	δ deg	V_G km s^{-1}	Num.
265	GE0613	6			11/6	80.7	0.290	0.960	68.1	297.0	80.7	290.6	5.1	46.0	3
266	GE0614	6			12/6	81.7	0.900	0.810	171.0	317.0	261.7	4.6	-3.7	68.0	3
267	GE0615	6			11/6	80.7	0.270	0.590	145.3	6.0	80.7	349.6	10.3	48.0	3
268	GE0616	6			13/6	80.7	0.420	0.980	166.4	280.0	80.7	323.7	-8.8	65.0	4
269	GE0617	6			11/6	80.7	0.990	0.790	177.7	165.0	80.7	354.6	-0.7	69.0	8
270	GE0618	6			13/6	82.7	0.510	0.890	177.8	266.0	262.7	16.6	6.3	65.0	3
271	GE1001	6			16/10	203.7	0.470	0.900	8.2	96.0	23.7	28.6	3.2	31.0	3
272	GE1002	6			17/10	204.7	0.430	0.860	8.9	104.0	24.7	32.7	4.2	31.0	3
273	GE1003	6			17/10	203.7	0.920	0.850	138.2	34.0	23.7	101.6	-0.1	66.0	3
274	GE1004	6			17/10	203.7	0.510	0.840	145.0	94.0	23.7	87.7	8.0	63.0	4
275	GE1005	6			17/10	204.7	0.650	0.850	161.8	76.0	24.7	94.7	14.0	67.0	6
276	GE1006	6			17/10	203.7	0.990	0.580	171.6	352.0	23.7	115.7	16.9	68.0	3
277	GE1008	6			17/10	204.7	0.630	1.260	147.7	70.0	24.7	87.7	8.0	71.0	7

Table D.1: *continued.*

D.2 AMOR Data Sets Used

The AMOR data set from the vernal equinox of 1995 to the end of July 1999 is used throughout this study. The inter-vernal equinoctial year is used as opposed to the normal calendar year (Section 3.1). Each of these years is denoted `TYYYY`, with `YYYY` corresponding to the calendar year in which the initial vernal equinox occurs. Data files are generally named according to the following conventions. For a single equinoctial year `TYYYY.ele` is used. For multiple years `Y1VY2.ele` is used where `Y1` and `Y2` are the two digit calendar years identifying the first and last equinoctial years respectively. The file `95V99.ele` contains the entire data set under consideration—it should be noted that although this implies a full year, only the first third of T1999 is actually included in this file, due to the data set cutoff for this thesis study having been reached at that time. Segments of an equinoctial year are measured out according to the longitude of the Sun at the start and end of the period selected; the file obtained from such data is named `YYYYVS1LS2` where `S1` and `S2` are the solar longitudes of the end-points. In some cases files limited to only prograde or retrograde orbits have been constructed, such files bear the labels '_PR' and '_RE' respectively.

In the case of the direct search of the mean orbit data set (Section 7.6) years stretching between autumnal equinoxes have also been used. There are only four such years labelled `A1995`, `A1996`, `A1997` and `A1998`. `A1998` is missing the last part due to the end of the data set having been reached as for `T1999` above.

Table D.2 shows the files used in various parts of the present study. The different uses to which these files have been put have been assigned numbers so that the interested reader may cross-reference these with sections/chapters in the thesis. Files labelled I are used for overall data set statistics, e.g. Figure 3.1; II are used for the gross rate increase tests of Section 7.5; III are used for wavelet analysis searches in Chapters 7 and 8; IV are used for sporadic source analysis in Chapter 4; V are used in the orbital element distribution discussions of Section 3.5; VI are used for uncertainty analysis in Chapter 5; VII are used for direct searches in Section 7.6; VIII are used for tests of single-linkage analysis in Section 7.8; IX are used for tests of sporadic intrusion in Section 6.3.1; and finally X are used to show the level of D-criteria suitable for stream retrieval in Section 6.3.2.

Datafile	Size	Use
90V99.ele	877,609	I
95V97.ele	376,718	V
95V98.ele	431,509	VI,IX,X
95V99.ele	531,334	II,III,IV
1995V.ele	145,414	III
1996V.ele	114,405	III
1997V.ele	116,899	III,V,IX
1998V.ele	104,344	III
1999V.ele	50,272	III
1995A.ele	140,040	VII
1996A.ele	100,323	VII
1997A.ele	115,098	VII
1998A.ele	101,418	VII
95V99_110LS160_PR.ele	38,380	VIII
95V99_160LS210_PR.ele	38,031	VIII
95V99_20LS70_RE.ele	53,280	VIII

Table D.2: AMOR orbital element files used in the various sub-studies within this thesis. The different uses to which these files have been put are indicated by Roman numerals, these numbers correspond to those described in the text.

Appendix E

Results of Direct Mean Stream Searches

This appendix lists tables of results for the direct searches of the AMOR data sets in separated years from 1995–1999 as described in Section 7.6. The data set is split into three sections: near-ecliptic ($i < 10°$), low inclination ($i \in [10°, 20°)$) and medium/high inclination ($i \geq 20°$). The D_{SH} based searches within these sets are shown as performed at respective cutoff levels of 0.10, 0.15 and 0.20 in Tables E.1, E.2 and E.3 respectively.

The number of associations which might be randomly expected for each stream given in the mean stream file (Section D.1) is listed as N_E while the number found to be associated with a stream from the mean orbit data set is given as N_S. If N_S is sufficiently greater than the expectation value (N_E) then there is a strong likelihood that the stream is not part of the random background; using Poisson statistics these numbers are tested against each other at the 95% and 99% levels respectively. The "CL" column in the tables contains nothing if the association is at less than the 95% level, "✗" if it is between 95% and 99% and "✓" if it is greater than or equal to the 99% level.

The "Set" column contains "A" where a virtual year stretching between autumnal equinoxes has been used and a "V" where a similar year between vernal equinoxes has been used. The calendar year label refers to that in which the equinoctial year begins.

CSF	Shower	$\lambda_\odot$ (deg)	Set	i (deg)	δ (deg)	1995			1996			1997			1998			1999		
						N_S	N_E	CL	N_S	N_E	CL	N_S	N_E	CL	N_S	N_E	CL	N_S	N_E	CL
68	λ Virginids	17.5	A	2.8	-14.2	33	183		27	127		35	179		58	192				
201	Sth α Virginids	18.7	A	7.0	-17.2	14	146		16	101		17	140		31	154				
106	Nth λ Virginids	20.2	A	2.0	-10.2	45	181		20	121		33	173		50	188				
158	δ Piscids	26.7	A	9.0	11.3	0	132		1	96		0	122		0	131				
6	σ Leonids	28.7	A	1.0	-5.3	39	66		18	63		16	55		13	40				
103	σ Leonids	28.9	A	0.7	-5.3	39	65		16	62		16	55		11	40				
74	σ Leonids	32.5	A	3.1	0.7	26	41		7	38		7	33		10	26				
200	Nth α Virginids	34.7	A	8.0	-8.2	37	133		24	87		17	112		40	126				
9	μ Virginids	35.7	A	10.0	-5.2	18	89		7	58		12	71		26	80				
129	μ Virginids	35.7	A	9.9	-5.2	18	91		8	59		13	72		28	82				
125	α Scorpiids	37.0	A	2.3	-21.2	72	192		38	127		55	182		70	206				
10	α Scorpiids	42.7	A	3.0	-22.1	58	195		25	126		39	178		45	201				
127	ϕ Ophiuchids	44.7	A	10.0	-18.1	58	114		22	69		37	99		59	118				
107	Sth λ Virginids	45.2	A	3.5	-18.2	9	39		5	26		2	27		2	24				
124	α Scorpiids	50.2	A	3.5	-24.1	53	197		23	119		30	174		40	199				
65	Cyclids	52.8	A	1.9	28.1	2	15		4	25		5	14		3	13				
154	ϵ Arietids	63.7	A	6.0	21.2	3	190		4	120		5	152		2	167				
69	θ Librids	71.2	A	3.3	-14.1	9	67		9	52		13	49		8	38				
111	χ Scorpiids	74.6	A	6.0	-12.1	3	74		4	54		9	55		13	47				
16	χ Scorpiids	74.7	A	6.0	-13.1	3	73		4	54		10	54		11	46				
72	θ Ophiuchids	77.7	A	4.4	-27.0	17	168		25	102		18	129		14	150				
18	Day. ζ Perseids	78.7	A	0.0	23.1	8	243		4	170		5	215		2	226				
109	θ Ophiuchids	78.7	A	4.7	-28.0	15	169		19	105		17	133		11	154				
19	Librids(a)	78.9	A	4.0	-28.5	1	33		6	28		2	24		1	17				
20	Librids(b)	78.9	A	5.0	-28.5	0	10		0	5		0	5		0	6				
253	GE0601	80.7	A	1.3	-25.0	15	170		20	112		18	135		20	139				
162	σ Sagittariids	81.7	A	10.0	-26.9	3	134		6	83		7	115		5	135				

Table E.1: Direct search by comparison against near-ecliptic mean stream orbits. Here mean orbits with $i < 10°$ from the `stream_library.csf` data set are compared against all AMOR orbits from the `95V99.ele` data set. Comparison is by D_{SH} with a moderate cutoff level of 0.10 being used.

CSF	Shower	$\lambda_\odot$ (deg)	Set	i (deg)	δ (deg)	1995			1996			1997			1998			1999		
						N_S	N_E	CL	N_S	N_E	CL	N_S	N_E	CL	N_S	N_E	CL	N_S	N_E	CL
22	θ Ophiuchids	82.7	A	4.0	-28.0	22	155		23	95		23	118		12	136				
255	GE0603	82.7	A	2.4	18.2	27	151		8	84		9	142		8	155				
148	Ophiuchids	83.7	A	4.0	-24.0	27	172		26	117		38	138		18	149				
26	Corvids(a)	95.6	V	3.0	-19.4	1	2		1	2		1	2		1	1		1	2	
27	Corvids(b)	95.6	V	4.0	-19.4	0	0		2	0		1	0		0	0				
126	μ Sagittariids	96.0	V	5.5	-15.0	12	15		3	14		9	13		5	10		8	10	
25	Day. β Taurids	97.1	V	6.0	19.0	3	41		0	31		0	30		2	29		1	41	
161	ϵ ρ Geminids	122.7	V	10.0	27.9	0	33		1	25		0	22		0	23		0	39	
80	Sth ι Aquarids	124.7	V	0.0	-14.8	26	50		35	37		13	37		9	37		25	43	
88	α Capricornids	126.1	V	7.1	-9.8	36	20	✓	36	17	✓	14	16		14	14		27	16	✓
34	α Capricornids	127.7	V	7.0	-9.8	48	20	✓	46	17	✓	15	15		15	14		26	16	✓
35	Sth ι Aquarids	131.7	V	6.9	-14.5	49	40		56	32	✓	29	30		33	31		20	42	
89	α Capricornids	134.1	V	8.7	-6.8	13	22		19	18		12	15		16	14		8	21	
185	Nth α Capricornids	134.7	V	6.0	-8.8	40	22	✓	32	19	✓	15	16		15	15		14	17	
105	μ Ophiuchids	137.7	V	2.5	-14.0	1	2		3	2		0	2		2	1		0	2	
173	λ Aquarids	142.7	V	4.0	-5.7	15	49		14	39		9	37		9	38		0	46	
157	α Cancrids	144.7	V	9.0	10.8	0	33		1	25		1	22		0	23		0	36	
172	α Aquarids	145.7	V	9.0	-1.7	33	35		17	27		5	24		9	24		0	37	
36	Nth ι Aquarids	147.7	V	5.0	-5.8	87	52	✓	36	41		44	40		50	39	✗	0	47	
186	Sth α Capricornids	149.7	V	4.0	-17.8	22	24		17	24		30	24		15	19		0	17	
85	Nth ι Aquarids	162.1	V	4.0	1.3	61	51		59	40	✓	38	39		23	38		5	43	
39	Sth Piscids	177.7	V	2.0	0.3	37	41		30	33		29	33		14	30		3	33	
42	κ Aquarids	178.7	V	2.0	-4.7	15	7	✓	8	7		4	6		2	4		0	5	
104	κ Aquarids	178.7	V	1.8	-4.7	15	7	✓	7	7		4	6		2	4		0	5	
151	ζ ϵ Piscids	182.7	V	5.0	7.3	50	51		11	41		28	38		32	37		0	45	
205	Sth ϵ Piscids	185.7	V	4.0	-4.7	30	24		9	21		22	19		7	17		1	17	
66	κ Aquarids	186.6	V	2.1	-2.8	10	6	✗	6	6		5	5		1	3		0	4	
46	Andromedids(a)	190.7	V	4.0	8.3	14	22		4	16		10	15		4	14		2	16	

Table E.1: *continued.*

CSF	Shower	$\lambda_\odot$ (deg)	Set	i (deg)	δ (deg)	1995			1996			1997			1998			1999		
						N_S	N_E	CL	N_S	N_E	CL	N_S	N_E	CL	N_S	N_E	CL	N_S	N_E	CL
204	Nth ϵ Piscids	190.7	V	5.0	10.3	13	25		8	20		16	19		3	17		3	18	
86	Piscids	190.8	V	1.5	6.3	13	29		13	23		13	22		5	20		3	21	
70	ϵ Piscids	195.5	V	0.7	7.3	7	32		15	24		11	26		4	23		1	21	
40	Nth Piscids	199.7	V	3.0	14.2	7	44		3	35		2	35		1	32		1	36	
123	Piscids	199.8	V	3.4	14.2	7	44		4	35		3	35		1	31		1	36	
271	GE1001	203.7	V	8.2	3.2	6	18		1	13		1	10		3	10		0	17	
272	GE1002	204.7	V	8.9	4.2	5	24		5	18		3	15		7	14		0	24	
207	Cyclids	206.7	V	3.0	-6.8	1	5		2	4		4	5		0	3		1	4	
112	θ Cetids	207.7	V	8.5	-10.7	2	8		3	6		7	7		5	5		0	5	
191	Sth Taurids	207.7	V	6.0	10.2	12	47		8	37		14	34		17	32		0	41	
73	θ Cetids	208.4	V	5.5	-4.7	4	11		6	10		9	12		4	7		0	6	
159	Sth Arietids	208.7	V	6.0	12.2	14	46		7	36		16	33		20	31		0	41	
82	Sth Nth Taurids	209.4	V	3.3	13.2	8	52		7	41		5	39		6	37		0	43	
190	Nth Taurids	213.7	V	3.0	19.2	5	51		2	41		1	38		3	36		2	43	
153	β Geminids	214.7	V	5.0	20.9	44	52		21	42		18	39		22	37		28	46	
43	Sth Taurids	220.7	V	5.2	13.8	5	45		8	35		5	34		3	31		0	38	
87	Pegasids	227.7	V	6.8	19.3	0	1		2	2		0	1		1	1		0	1	
75	α Pegasids	230.3	V	7.5	22.3	0	1		0	1		0	1		1	0		0	1	
44	Nth Taurids	230.7	V	2.4	22.4	4	46		0	36		2	33		3	31		1	37	
53	Pegasids	230.7	V	8.0	21.3	0	1		0	1		0	1		1	0		0	1	
208	α Pegasids	230.7	V	7.0	22.3	0	2		2	2		0	1		1	1		0	2	
155	Sth Taurids	237.7	V	5.0	19.1	1	37		0	29		1	28		1	26		0	30	
149	Scorpiids	249.7	V	4.0	-23.1	16	38		32	30		25	30		28	27		15	28	
163	γ Librids	257.7	V	9.0	-18.1	16	39		3	30		5	26		14	26		0	41	
195	Sth χ Orionids	257.7	V	5.0	17.0	1	31		0	25		1	23		0	22		0	23	
62	δ Arietids	258.3	V	1.8	22.2	3	10		0	9		1	11		1	6		0	6	
57	Nth χ Orionids	258.7	V	2.0	26.0	3	38		1	29		1	30		0	28		0	28	
84	Nth χ Orionids	259.0	V	2.5	26.0	3	37		0	29		0	29		0	27		0	28	
58	Sth χ Orionids	259.7	V	7.0	16.0	0	31		0	25		1	22		0	21		0	27	
90	Sth χ Orionids	259.8	V	6.9	16.0	0	31		0	24		1	22		0	21		0	26	

Table E.1: *continued.*

CSF	Shower	$\lambda_\odot$	Set	i	δ	1995			1996			1997			1998			1999		
		(deg)		(deg)	(deg)	N_S	N_E	CL	N_S	N_E	CL	N_S	N_E	CL	N_S	N_E	CL	N_S	N_E	CL
209	GE1201	261.7	V	2.0	22.9	10	42		4	35		4	34		4	36		0	40	
210	GE1202	262.7	V	7.1	18.0	1	42		0	32		2	28		2	28		0	39	
211	GE1203	262.7	V	9.4	5.1	3	6		0	4		1	5		3	3		0	5	
78	Nth δ Arietids	263.3	V	2.1	25.2	3	8		0	8		2	9		1	5		0	5	
194	Nth χ Orionids	265.7	V	3.0	26.0	0	45		1	35		1	33		0	33		0	37	
2	δ Canerids	296.7	A	0.0	19.8	3	199		3	135		1	153		0	182				
152	α Cancrids	296.7	A	5.0	15.8	14	207		12	149		8	180		23	208				
122	δ Cancrids	297.1	A	0.3	19.8	3	199		3	134		1	153		0	181				
160	κ Cancrids	301.7	A	6.0	11.8	1	168		1	109		2	146		0	183				
67	ρ Geminids	302.1	A	3.5	28.9	0	57		0	48		1	44		0	36				
110	Sth χ Geminids	311.2	A	4.0	12.9	0	88		1	69		1	65		1	61				
223	GE0205	323.7	A	8.1	24.8	6	93		3	75		7	78		6	79				
171	β Capricornids	324.7	A	5.0	-20.8	22	182		17	142		43	157		33	186				
219	GE0201	324.7	A	4.5	-20.8	29	179		22	140		40	154		35	182				
236	GE0218	324.7	A	2.1	-23.7	15	53		5	54		6	44		8	33				
222	GE0204	326.7	A	7.8	8.7	4	142		3	102		4	122		6	158				
220	GE0202	327.7	A	0.1	5.7	49	212		26	161		35	190		50	214				
156	υ Leonids	328.7	A	5.0	9.7	15	184		4	141		10	160		13	187				
170	β Capricornids	331.7	A	4.0	-20.8	41	186		30	136		54	163		49	190				
83	Nth Virginids	334.5	A	3.5	4.7	22	175		7	118		13	149		14	181				
4	δ Leonids	338.7	A	6.0	18.7	0	88		1	67		2	68		0	67				
121	δ Leonids	338.8	A	6.2	18.7	0	86		1	67		2	66		0	67				
3	Virginids	350.7	A	3.0	-0.3	28	180		10	121		20	157		42	185				
79	Sth Virginids	357.1	A	0.3	-2.3	71	185		29	136		42	162		67	157				
150	α Aquarids	358.7	A	5.0	-6.7	62	175		29	115		32	156		23	176				
238	GE0302	358.7	A	7.3	-5.3	1	18		2	13		0	11		1	11				
237	GE0301	359.7	A	1.8	-7.7	74	190		65	118		64	165		72	186				

Table E.1: *continued.*

CSF	Shower	$\lambda_\odot$ (deg)	Set	i (deg)	δ (deg)	1995			1996			1997			1998			1999		
						N_S	N_E	CL	N_S	N_E	CL	N_S	N_E	CL	N_S	N_E	CL	N_S	N_E	CL
11	α Bootids	36.7	A	18.0	18.8	2	8		1	5		0	7		1	9				
119	α Bootids	36.9	A	18.0	18.8	2	8		1	5		0	7		1	9				
180	α Arietids	63.7	A	11.0	20.2	5	114		0	63		1	93		1	110				
254	GE0602	79.7	A	14.0	19.8	1	6		2	4		1	4		4	3				
256	GE0604	81.7	A	18.0	19.2	3	100		1	52		2	60		0	62				
257	GE0605 Arietids	81.7	A	17.4	23.2	2	99		1	54		1	66		4	68				
130	o Serpentids	86.5	A	13.0	-11.0	36	68		63	41	✓	54	46		108	68	✓			
131	η Serpentids	97.7	V	15.5	-2.0	58	36	✓	21	24		22	26		23	22		38	31	
116	θ Herculids	135.7	V	16.7	30.0	1	8		1	4		0	5		0	3		0	1	
33	Nth δ Aquarids	139.7	V	20.0	-4.7	51	96		36	118		20	57		34	57		4	74	
81	Sth ι Aquarids	142.5	V	12.6	-9.7	163	104	✓	127	96	✓	87	73	✓	117	79	✓	21	114	
165	κ Leonids	146.7	V	12.0	26.8	3	95		2	78		0	66		4	64		0	109	
167	α Leonids	183.7	V	18.0	12.7	7	95		2	104		1	59		3	63		0	81	
183	Sextantids	183.7	V	19.0	2.8	180	98	✓	86	103		138	61	✓	48	65		0	85	
60	Dec. Phoenicids(a)	253.7	V	16.0	-54.7	1	7		3	5		2	4		3	3		0	1	
61	Dec. Phoenicids(b)	254.7	V	13.0	-44.7	2	6		2	5		1	4		3	3		0	3	
213	GE1205 Geminids	261.7	V	18.2	29.9	0	102		0	104		3	66		1	67		0	88	
147	Geminids	264.7	V	17.0	23.9	0	106		0	100		0	71		0	72		0	106	
168	ω Sagittariids	325.7	A	20.0	-28.9	18	108		9	58		16	65		13	66				
221	GE0203	325.7	A	18.0	7.2	4	14		2	7		3	9		3	12				
224	GE0206	325.7	A	12.2	-2.3	56	116		33	83		51	92		49	126				
164	γ Sextantids	326.7	A	19.0	-6.2	12	23		3	17		10	17		14	23				
169	β Capricornids	327.7	A	13.0	-12.8	104	103		37	72		103	78	✓	104	109				
166	α Virginids	358.7	A	12.0	-9.3	66	93		20	58		56	73		85	86				
239	GE0303	358.7	A	19.4	2.7	27	71		12	52		22	56		40	60				

Table E.2: Direct search by comparison against low inclination mean stream orbits. Here mean orbits with $i \in [10°, 20°)$ from the `stream_library.csf` data set are compared against all AMOR orbits from the `95V99.ele` data set. Comparison is by D_{SH} with a medium cutoff level of 0.15 being used.

CSF	Shower	$\lambda_\odot$ (deg)	Set	i (deg)	δ (deg)	1995			1996			1997			1998			1999		
						N_S	N_E	CL	N_S	N_E	CL	N_S	N_E	CL	N_S	N_E	CL	N_S	N_E	CL
249	GE0313	1.7	A	95.9	-71.9	3	9		0	4		5	7		1	4				
8	κ Serpentids	14.7	A	64.0	17.8	0	22		0	11		0	16		0	25				
136	η Aquarids	22.7	A	132.0	4.2	9	25		0	13		2	20		2	18				
14	η Aquarids	43.1	A	163.5	-1.6	147	54	✓	72	25	✓	80	41	✓	110	46	✓			
17	Day. Arietids	77.7	A	21.0	23.2	7	418		4	227		7	285		6	271				
260	GE0608	79.7	A	33.5	-33.9	21	317		51	152		48	185		37	151				
262	GE0610	79.7	A	43.3	6.0	1	57		7	35		11	44		9	41				
21	Sagittariids	80.7	A	99.0	-34.8	0	17		0	25		0	18		0	14				
142	γ Pegasids	80.7	A	149.0	17.3	2	76		1	34		0	55		1	62				
258	GE0606	80.7	A	30.9	19.2	2	385		4	163		4	208		7	176				
261	GE0609	80.7	A	39.5	-5.9	60	227		133	103	✓	123	135		221	110	✓			
263	GE0611	80.7	A	66.3	3.2	27	55		25	36		22	60		45	47				
265	GE0613	80.7	A	68.1	5.1	3	36		0	25		1	30		1	27				
267	GE0615	80.7	A	145.3	10.3	0	90		4	94		6	112		6	97				
268	GE0616	80.7	A	166.4	-8.8	12	96		15	41		14	48		19	59				
269	GE0617	80.7	A	177.7	-0.7	31	119		21	49		23	85		28	89				
138	ω Sagittariids	81.7	A	40.0	-29.9	13	240		38	98		34	127		32	109				
140	ψ Piscids	81.7	A	147.0	20.3	0	54		1	34		0	50		0	50				
181	ζ Cetids	81.7	A	45.0	-4.9	65	155		125	75	✓	119	93	✓	217	88	✓			
259	GE0607	81.7	A	38.2	9.2	31	266		22	108		27	146		32	121				
264	GE0612	81.7	A	65.3	-1.8	7	64		11	34		6	60		6	52				
266	GE0614	81.7	A	171.0	-3.7	17	101		23	44		20	72		22	83				
146	Arietids	82.7	A	22.0	22.2	1	420		3	239		3	291		6	277				
270	GE0618	82.7	A	177.8	6.3	9	64		4	33		8	45		9	48				
29	July Phoenicids(a)	110.3	V	82.0	-47.7	0	10		12	8		12	11		8	7		4	4	
30	July Phoenicids(b)	110.3	V	87.0	-47.7	0	3		4	4		4	2		1	1		0	0	

Table E.3: Direct search by comparison against medium/high inclination mean stream orbits. Here mean orbits with $i \geq 20°$ from the `stream_library.csf` data set are compared against all AMOR orbits from the `95V99.ele` data set. Comparison is by D_{SH} with a medium cutoff level of 0.20 being used.

CSF	Shower	$\lambda_\odot$ (deg)	Set	i (deg)	δ (deg)	1995			1996			1997			1998			1999		
						N_S	N_E	CL	N_S	N_E	CL	N_S	N_E	CL	N_S	N_E	CL	N_S	N_E	CL
32	Sth δ Aquarids	125.7	V	27.2	-16.3	732	134	✓	872	134	✓	347	82	✓	433	78	✓	346	114	✓
182	δ Aquarids	125.7	V	33.0	-16.7	685	130	✓	800	123	✓	289	68	✓	377	70	✓	292	101	✓
93	Sth δ Aquarids	127.8	V	28.4	-15.7	752	162	✓	863	162	✓	344	90	✓	427	83	✓	334	141	✓
202	Sth δ Aquarid	128.7	V	27.0	-15.7	762	171	✓	872	179	✓	366	100	✓	455	92	✓	341	145	✓
33	Nth δ Aquarids	139.7	V	20.0	-4.7	51	96		36	118		20	57		34	57		4	74	
91	Nth δ Aquarids	141.2	V	20.7	1.3	121	210		82	245		36	133		72	138		13	175	
203	Nth δ Aquarid	142.7	V	21.0	2.3	117	215		84	241		38	132		68	138		14	175	
145	υ Cetids	145.7	V	144.0	-2.8	43	27	✓	19	17		13	13		15	14		0	18	
135	ζ Arietids	146.7	V	172.5	14.2	10	38		5	40		2	19		5	25		3	30	
175	Aquarids-Cetids	147.7	V	22.0	-10.7	413	224	✓	295	247	✓	212	134	✓	276	140	✓	13	174	
174	ω Piscids	148.7	V	27.0	7.3	58	212		37	253		17	114		38	121		0	148	
45	Day. Sextantids	184.3	V	22.0	-0.2	402	221	✓	198	234		273	139	✓	95	148		0	185	
189	ϵ Geminids	203.7	V	174.0	25.9	3	31		1	26		0	16		1	20		2	19	
273	GE1003	203.7	V	138.2	-0.1	15	23		3	13		8	7		11	9		0	12	
274	GE1004	203.7	V	145.0	8.0	5	24		8	15		4	12		6	13		4	12	
276	GE1006	203.7	V	171.6	16.9	4	78		8	65		1	44		3	48		0	59	
275	GE1005	204.7	V	161.8	14.0	59	45	✗	59	38	✓	37	22	✓	36	27	✗	51	38	-2
277	GE1008	204.7	V	147.7	8.0	0	4		1	5		0	2		0	2		0	3	
102	ϵ Geminids	208.2	V	173.0	26.9	4	30		3	25		1	14		2	18		4	19	
49	Orionids	208.7	V	163.9	15.8	99	54	✓	127	63	✓	70	30	✓	63	32	✓	96	49	✓
137	Orionids	208.7	V	158.0	13.0	19	41		50	31	✓	20	21		23	25		30	33	
51	ϵ Geminids	209.7	V	173.0	26.9	3	27		3	25		2	13		1	16		1	18	
199	Orionids	209.7	V	165.0	16.0	105	55	✓	134	63	✓	66	30	✓	66	32	✓	102	49	✓
100	Orionids	209.9	V	163.9	16.0	106	55	✓	127	63	✓	72	30	✓	71	34	✓	103	50	✓
54	Leonids	235.2	V	162.6	22.0	1	43		0	34		0	19		1	19		0	30	
197	Leonids	235.7	V	162.0	21.8	1	43		0	33		0	19		1	18		0	30	

Table E.3: *continued.*

CSF	Shower	$\lambda_\odot$ (deg)	Set	i (deg)	δ (deg)	1995 N_S	1995 N_E	1995 CL	1996 N_S	1996 N_E	1996 CL	1997 N_S	1997 N_E	1997 CL	1998 N_S	1998 N_E	1998 CL	1999 N_S	1999 N_E	1999 CL
55	Monocerotids	258.3	V	24.8	14.0	6	235		5	277		14	119		8	133		0	154	
198	σ Hydrids	258.7	V	126.0	1.8	8	8		2	6		7	5		2	5		0	4	
56	σ Hydrids	259.7	V	125.5	1.4	6	7		2	6		5	5		2	4		0	3	
141	υ Hydrids	259.7	V	122.0	-1.2	7	6		1	5		3	4		3	3		0	3	
176	Puppids	259.7	V	70.0	-54.2	22	15	✗	9	10		36	17	✓	39	14	✓	0	7	
196	Monocerotids	260.7	V	37.0	7.9	5	135		4	124		5	61		7	74		0	104	
212	GE1204	260.7	V	20.4	2.0	8	75		6	52		14	48		23	40		0	78	
139	β Librids	261.7	V	39.0	-7.2	19	165		14	156		27	62		32	76		0	99	
215	GE1207 Monocerotids	261.7	V	69.5	-43.2	16	20		6	18		13	17		17	15		0	14	
99	σ Hydrids	262.7	V	125.0	0.8	7	8		3	6		6	6		4	5		0	4	
143	γ Sextantids	262.7	V	139.0	-9.2	15	34		13	17		25	16	✗	29	19	✗	0	18	
214	GE1206	262.7	V	57.3	-63.2	36	19	✓	18	13		27	17	✓	45	16	✓	0	9	
216	GE1208	262.7	V	74.5	-45.2	15	16		6	17		10	16		5	13		0	13	
217	GE1209	262.7	V	39.9	5.9	6	119		3	92		7	55		6	57		0	100	
63	Coma Berenicids	282.7	A	134.0	24.7	1	16		0	8		0	10		0	11				
177	Carinids	300.7	A	75.0	-62.3	13	37		9	30		35	39		5	31				
218	GE0101	302.7	A	74.3	-63.3	11	30		14	27		26	35		4	27				
227	GE0209	323.7	A	49.9	-50.2	1	10		1	10		2	8		0	8				
234	GE0216	323.7	A	118.0	14.9	2	40		0	30		0	24		0	24				
235	GE0217	323.7	A	141.5	0.8	12	74		5	91		13	107		17	107				
233	GE0215	324.7	A	70.2	-86.1	4	11		4	11		3	12		1	9				
168	ω Sagittariids	325.7	A	20.0	-28.9	18	108		9	58		16	65		13	66				
178	Chamaeleonids	325.7	A	75.0	-78.2	15	28		9	26		21	37		18	21				
225	GE0207	325.7	A	20.4	15.7	10	396		1	282		11	297		5	349				
228	GE0210	325.7	A	47.2	-65.1	3	21		4	19		10	16		1	14				
229	GE0211	325.7	A	48.4	-76.0	22	46		7	38		15	44		22	42				
231	GE0213	325.7	A	62.0	-65.2	21	36		6	33		25	40		23	37				
232	GE0214	325.7	A	61.9	-83.3	24	47		11	39		15	51		17	47				
144	η Opiuchids	326.7	A	143.0	-6.1	43	55		7	33		21	39		14	42				
226	GE0208	326.7	A	33.6	-15.9	42	365		25	158		51	198		47	177				

Table E.3: *continued.*

CSF	Shower	$\lambda_\odot$ (deg)	Set	i (deg)	δ (deg)	1995			1996			1997			1998			1999		
						N_S	N_E	CL	N_S	N_E	CL	N_S	N_E	CL	N_S	N_E	CL	N_S	N_E	CL
230	GE0212	326.7	A	54.1	-77.3	37	63		18	51		35	61		24	51				
179	λ Octantids	357.7	A	72.0	-82.8	23	30		8	29		7	39		12	29				
242	GE0306	357.7	A	65.7	-74.3	22	47		11	36		20	48		28	44				
244	GE0308	357.7	A	61.9	-73.3	5	9		0	8		6	9		5	6				
246	GE0310	357.7	A	73.6	-78.8	18	28		10	26		8	37		7	27				
240	GE0304	358.7	A	55.3	-80.8	20	50		18	44		21	53		18	51				
241	GE0305	358.7	A	58.3	-77.8	6	19		6	16		6	17		3	14				
245	GE0309	358.7	A	59.3	-60.3	3	9		3	8		9	8		14	9				
248	GE0312	358.7	A	92.8	-71.1	2	11		2	7		3	12		2	7				
250	GE0314	358.7	A	121.6	-56.0	1	42		6	30		7	26		3	23				
243	GE0307	359.7	A	57.3	-58.3	13	23		6	22		21	28		16	27				
247	GE0311	359.7	A	85.2	-71.9	11	20		4	14		6	22		4	16				
251	GE0315	359.7	A	137.4	-43.1	7	54		6	47		5	59		9	57				
252	GE0316	359.7	A	141.8	-4.1	6	31		4	18		11	23		12	20				

Table E.3: *continued.*

Appendix F

Source Characterisation by Wavelet Analysis

If one assumes a Gaussian source then the Mexican Hat wavelet transform allows the determination of its size and emission rate. This wavelet transform has a strong maximum at the centre of the spatial source. The size of the wavelet transform coefficient ($w(r = 0, a)$) at the centre is also related to the width of the Mexican Hat used. There is an optimal width (a) which is related to the standard deviation (σ) of the Gaussian source distribution under study.

In one dimension the wavelet transform coefficients for the convolution of a Gaussian[1] source and a Mexican Hat wavelet are given by

$$w(x,a) = \int_{\eta=-\infty}^{\eta=+\infty} \exp\left(\frac{-\eta^2}{2\sigma^2}\right)\left(1 - \frac{(x-\eta)^2}{a^2}\right)\exp\left(-\frac{(x-\eta)^2}{2a^2}\right) d\eta. \qquad \text{(F.1)}$$

Taking the wavelet transform coefficient at the centre of the spatial distribution ($x = 0$), yields

$$w(x = 0, a) = \frac{1}{(1 + \sigma^2/a^2)^{1.5}}. \qquad \text{(F.2)}$$

This centre is at an extrema when the first derivative is zero, i.e.

$$\frac{d(w(0,a)/a)}{da} = \frac{a(a^2 - 2\sigma^2)}{(a^2 + \sigma^2)^{2.5}}. \qquad \text{(F.3)}$$

Solving for w'=0 yields $a = 0, \pm\sqrt{2}\sigma$. In the context of the current problem the maximum wavelet transform coefficient at the spatial centre is given by $a = \sqrt{2}\sigma$. By using a Monte Carlo simulated Gaussian source this result is shown to occur practically as shown in Figure F.1.

If in two dimensions one has a Gaussian source with different standard deviations in the coordinates then the wavelet transform coefficients for its correlation with a

[1]The amplitude information has been removed from the Gaussian sources as it is unnecessary and simply cancels out.

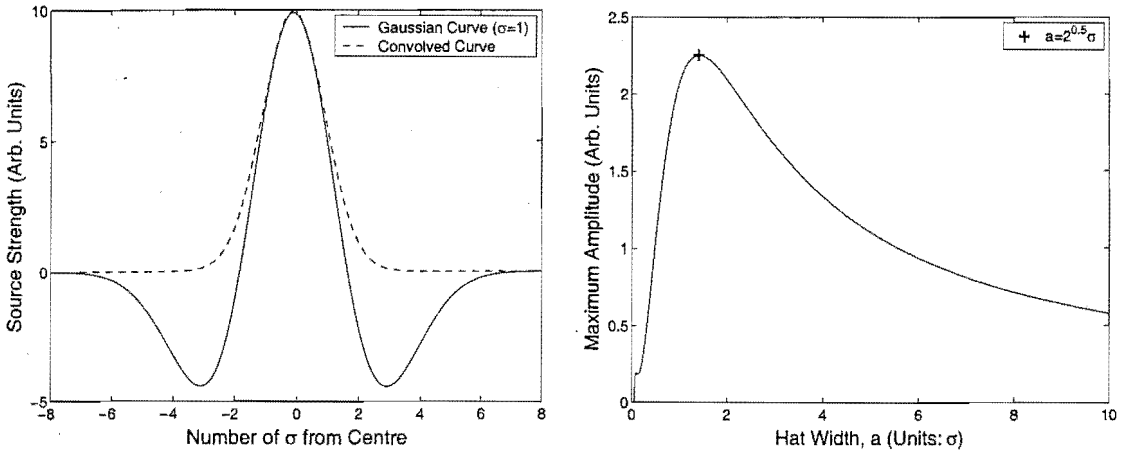

Figure F.1: Optimal one dimensional Mexican Hat wavelet transforms. On the left a theoretical Gaussian distribution function is shown along with the function which results upon the correlation of this Gaussian with the optimal ($a = \sqrt{2}\sigma$) Mexican Hat function. On the right the change in strength of the central wavelet coefficient ($w(x = 0)$) of in the correlation of a Mexican Hat with a simulated Gaussian function is shown as the hat width (a) is varied.

two dimensional Mexican Hat are given by

$$w(x, y, \sigma_\eta, \sigma_\zeta, a_\eta, a_\zeta) = \int_{\eta=-\infty}^{\eta=+\infty} \int_{\zeta=-\infty}^{\zeta=+\infty} \exp\left(\frac{-\eta^2}{2\sigma_\eta^2} - \frac{\zeta^2}{2\sigma_\zeta^2}\right)\left(2 - \frac{(x-\eta)^2}{a_\eta^2} - \frac{(y-\zeta)^2}{a_\zeta^2}\right)\cdots \exp\left(\frac{-(x-\eta)^2}{2a_\eta^2} - \frac{(y-\zeta)^2}{2a_\zeta^2}\right) d\eta\, d\zeta. \quad \text{(F.4)}$$

For $k > 0$ one can write $\sigma = \sigma_x = k\sigma_y$. The shape of the Mexican Hat is optimal if it fits the shape of the Gaussian therefore one should also set the width $a = a_\eta = k a_\zeta$. The wavelet coefficient at the spatial centre is then given by

$$w(x = 0, y = 0, a, \sigma) = \int_{\eta=-\infty}^{\eta=+\infty} \int_{\zeta=-\infty}^{\zeta=+\infty} \exp\left(\frac{-\eta^2}{2k^2\sigma^2} - \frac{\zeta^2}{2\sigma^2}\right)\left(2 - \frac{\eta^2}{k^2a^2} - \frac{\zeta^2}{a^2}\right)\cdots \exp\left(\frac{-\eta^2}{2k^2a^2} - \frac{\zeta^2}{2a^2}\right) d\eta\, d\zeta \quad \text{(F.5)}$$

$$= \frac{4\pi k\sigma^2}{(1 + \sigma^2/a^2)^2}. \quad \text{(F.6)}$$

The derivative of this function is

$$\frac{d(w(0, 0, a)/a)}{da} = -4a^2\sigma^2 k\pi \frac{a^2 - 3\sigma^2}{(a^2 + \sigma^2)^2}. \quad \text{(F.7)}$$

Solving for $w' = 0$ yields the width: $a = 0, \pm\sqrt{3}\sigma$. The optimal width is therefore $a = \sqrt{3}\sigma$ where a and σ may change in value for each coordinate direction. Figure F.2 demonstrates the practical truth of this finding for a simulated 2-D Gaussian source. The source size may now be estimated by fitting a series of different wavelet

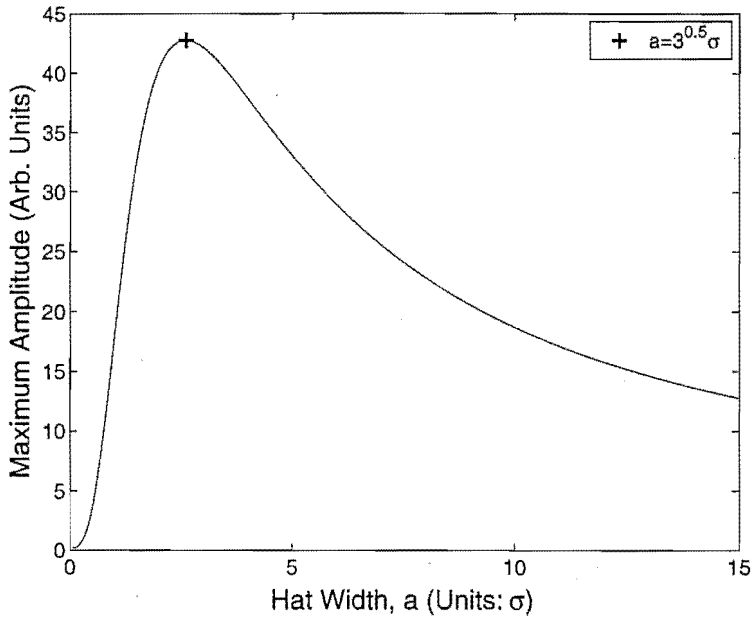

Figure F.2: Optimal two dimensional Mexican Hat wavelet transforms. Here a simulated 2-D Gaussian with $\sigma_x = 3$ and $\sigma_y = 1.5$ is fitted by correlation of a series of Mexican Hat functions of varying widths. The optimal width is shown to be that for $a_y = \sqrt{3}\sigma_y$ where $a_x = (\sigma_x/\sigma_y)a_y$.

widths and determining that which is optimal. The source strength may also be estimated as the amplitude of the central wavelet coefficient increases linearly with source strength. If one knows $w(x = 0, y = 0)$ for a particular source strength using a particular wavelet width then it is in principle possible to estimate the source strength for any other sources/wavelet widths.

Appendix G

Results of Radiant Space Searches

This appendix contains the results of searches of radiant-speed-time space using the wavelet transform to enhance features. Only the strongest feature in each day is shown. A full description of the method and analysis are contained in Section 7.7.

The radiant space, for all orbits from the `95V99.ele` file (see Table D.2), is divided into four regions: prograde antihelion (Figure G.1), prograde helion (Figure G.2), prograde apex (Figure G.3), and retrograde apex (Figures G.4 and G.5). These are further partitioned based on geocentric speed with the prograde regions having boundaries defined by: $20\pm10\,\mathrm{km\,s^{-1}}$, $30\pm10\,\mathrm{km\,s^{-1}}$, $40\pm10\,\mathrm{km\,s^{-1}}$ and also all speeds; the retrograde apex region uses instead $50\pm10\,\mathrm{km\,s^{-1}}$, $60\pm10\,\mathrm{km\,s^{-1}}$, $70\pm10\,\mathrm{km\,s^{-1}}$ and all speeds. Additionally two wavelet probe-sizes ($a = 3°$ and $6°$) and two time window widths ($2°$ and $6°$) are used for each partition.

The antihelion and helion source regions for each individual equinoctial year from T1995 to T1999 have been analysed separately, as shown in Figures G.6 and G.7 respectively. Only the all speed partition with a fixed $3°$ wide wavelet probe for two time window size partitions of $2°$ and $6°$ have been used for these single year searches.

For each amplitude profile the 99% and 99.99% confidence levels are given based on the assumption that these profiles are purely the product of a Gaussian white noise generator. The 99% level is the lower dashed line in each case while the other is a dot-dashed line and it sits above. These lines although not coloured should be obvious in the graphs as apart from the amplitude profiles themselves.

Several shower candidate peaks are labelled with alphabetic letters for reference, the major showers are also labelled with their acronyms. Each of these labellings is only made on one of the figures with the strongest profile for the peak in order to major them easily distinguishable.

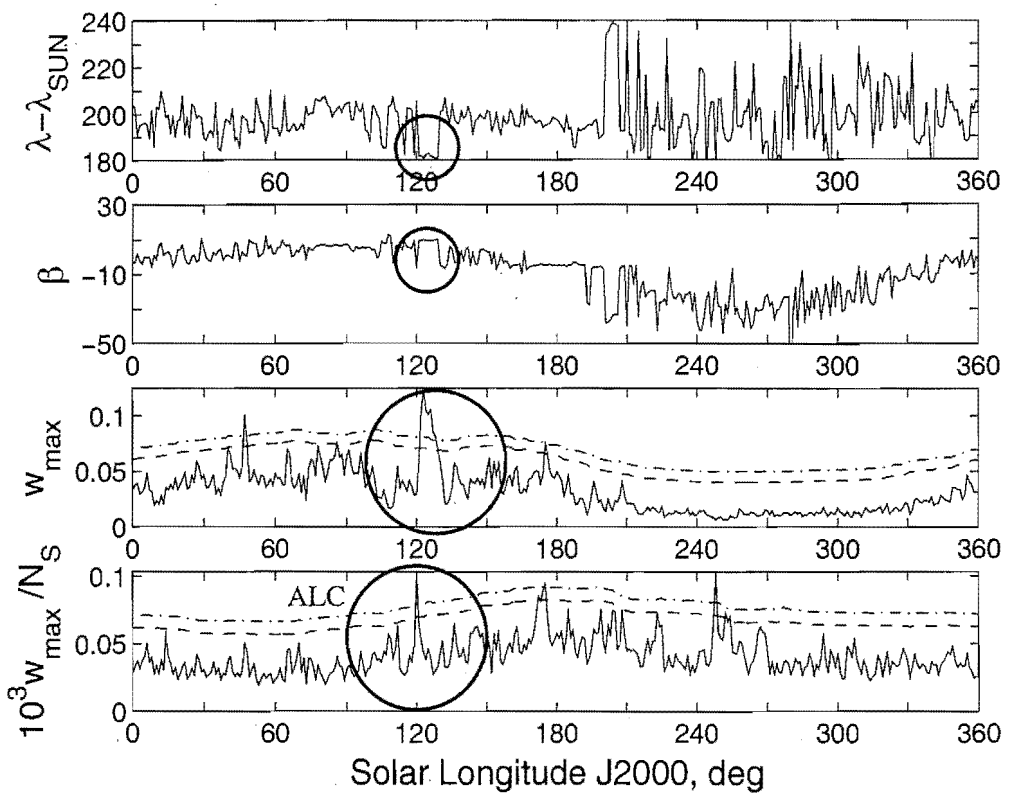

(a) Antihelion Region. $(V_G, \Delta\lambda_\odot, a) = (20 \pm 10\ \mathrm{km\,s^{-1}}, \pm 1°, 3°)$.

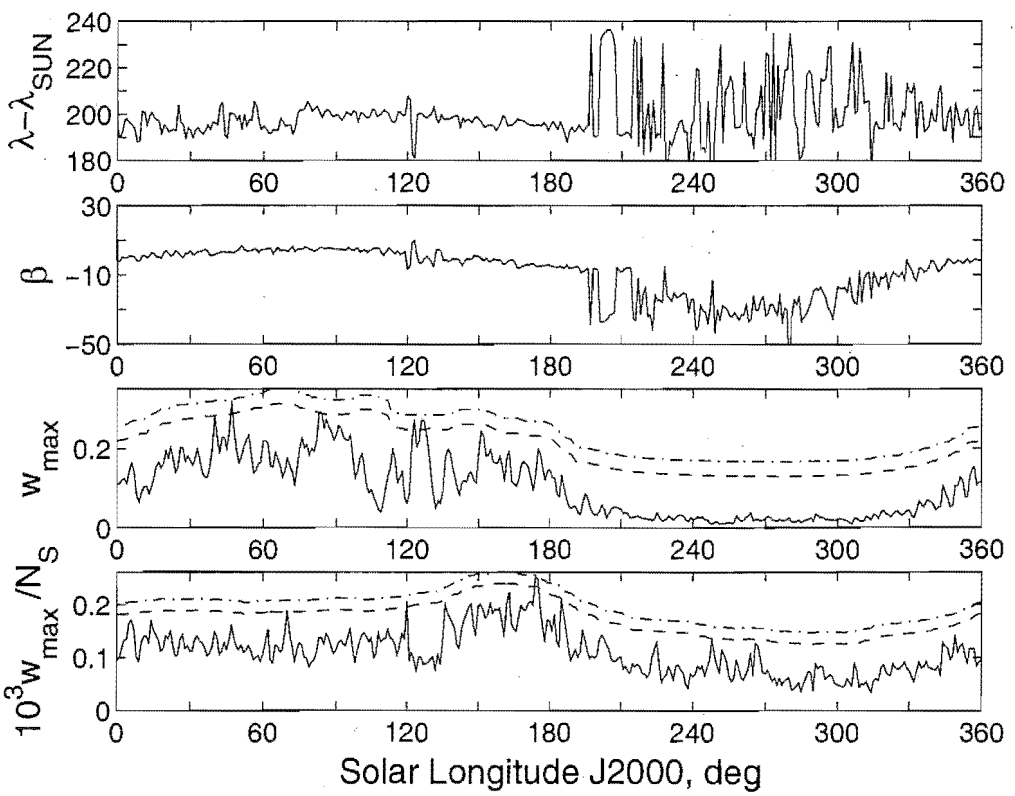

(b) Antihelion Region. $(V_G, \Delta\lambda_\odot, a) = (20 \pm 10\ \mathrm{km\,s^{-1}}, \pm 1°, 6°)$.

Figure G.1: A wavelet transform enhanced search of the antihelion region using two wavelet scales (a), two time windows ($\Delta\lambda_\odot$) and four speed (V_G) partitions in all possible combinations.

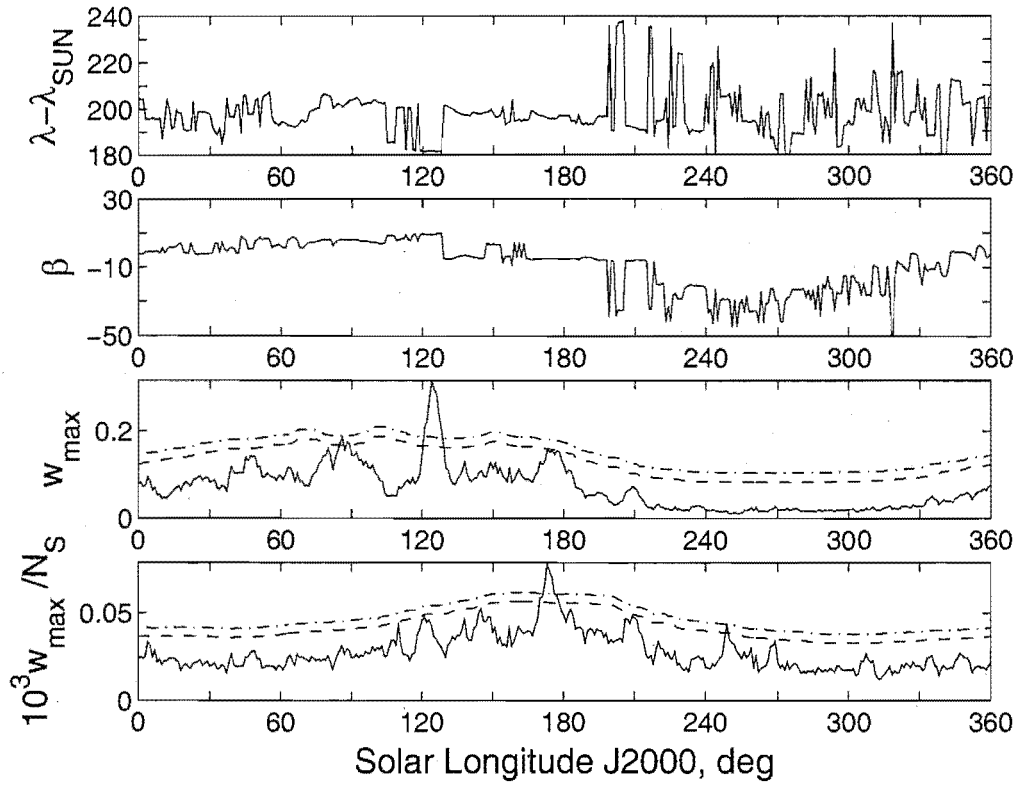

(c) Antihelion Region. $(V_G, \Delta\lambda_\odot, a) = (20 \pm 10\ \mathrm{km\,s^{-1}}, \pm 3°, 3°)$.

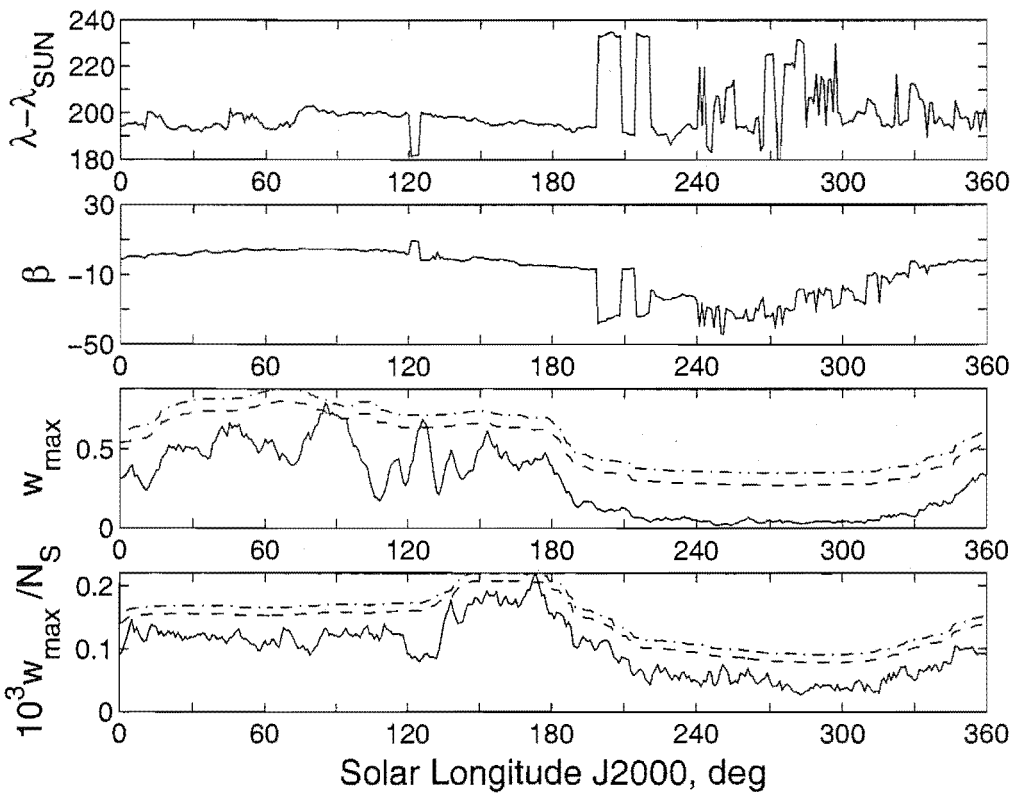

(d) Antihelion Region. $(V_G, \Delta\lambda_\odot, a) = (20 \pm 10\ \mathrm{km\,s^{-1}}, \pm 3°, 6°)$.

Figure G.1: *continued.*

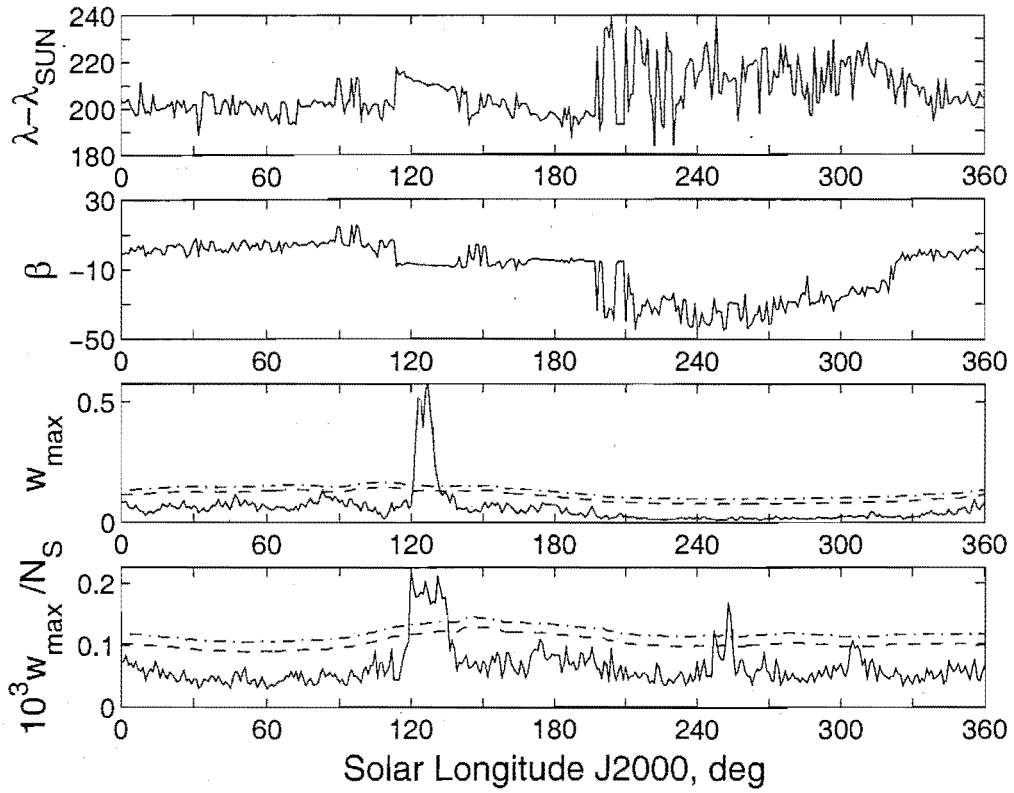

(e) Antihelion Region. $(V_G, \Delta\lambda_\odot, a) = (30 \pm 10\ \mathrm{km\,s^{-1}}, \pm 1°, 3°)$.

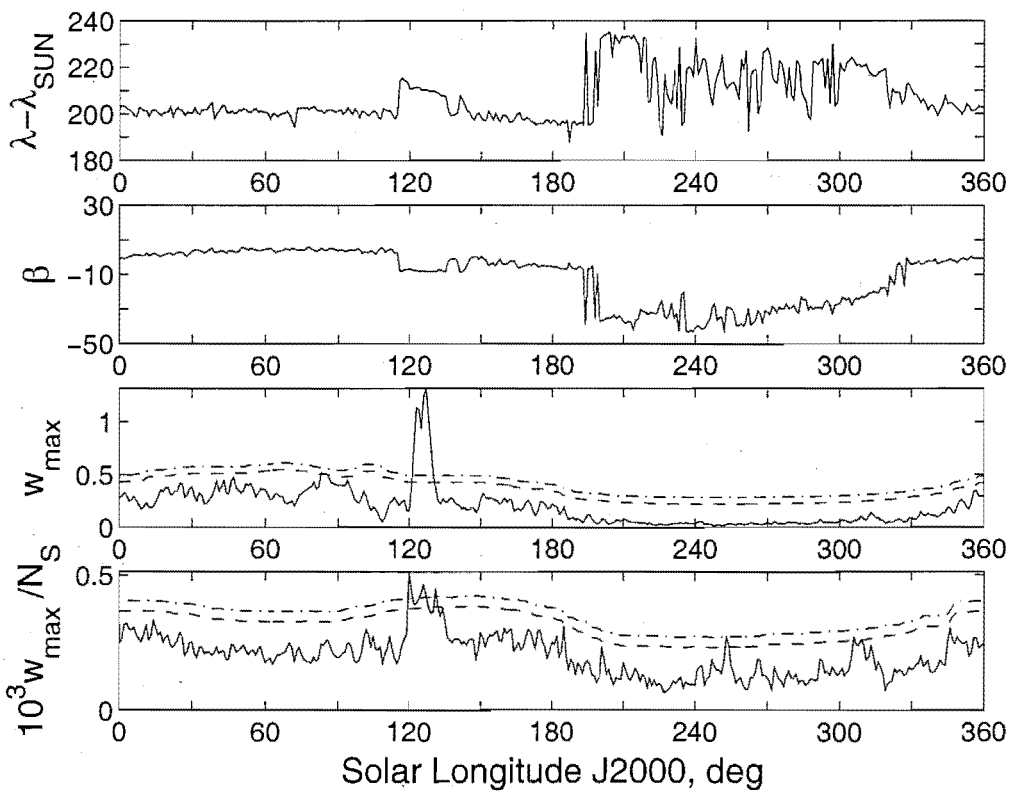

(f) Antihelion Region. $(V_G, \Delta\lambda_\odot, a) = (30 \pm 10\ \mathrm{km\,s^{-1}}, \pm 1°, 6°)$.

Figure G.1: *continued.*

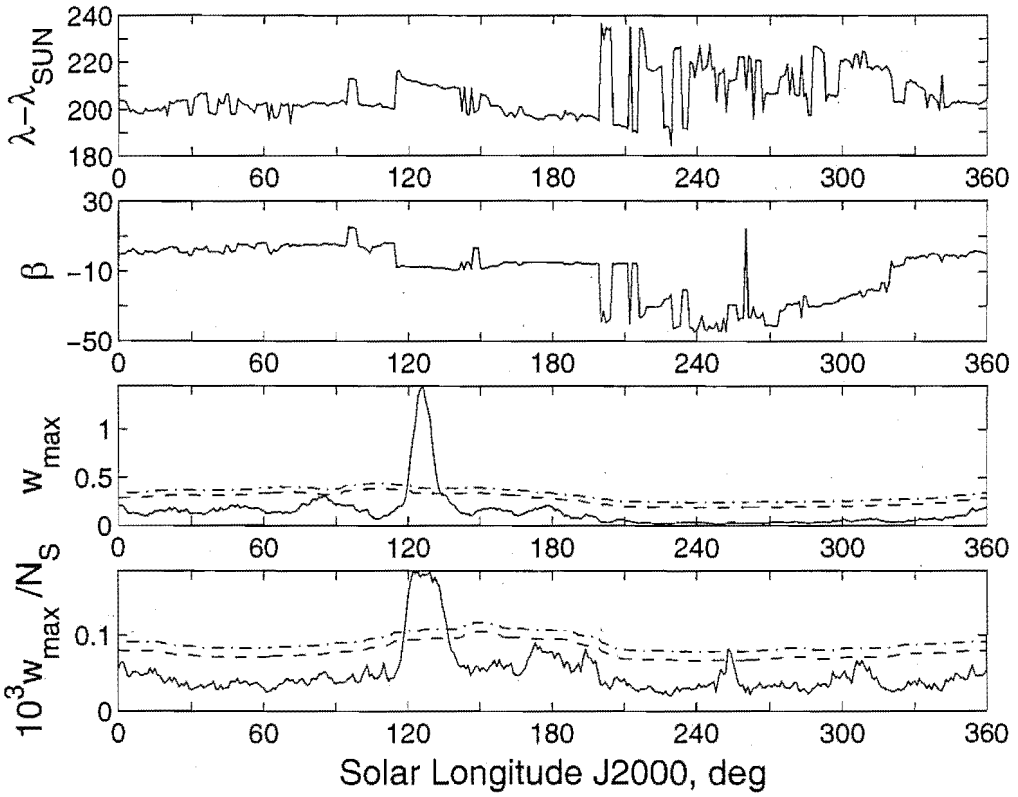

(g) Antihelion Region. $(V_G, \Delta\lambda_\odot, a) = (30 \pm 10\ \mathrm{km\,s^{-1}}, \pm 3°, 3°)$.

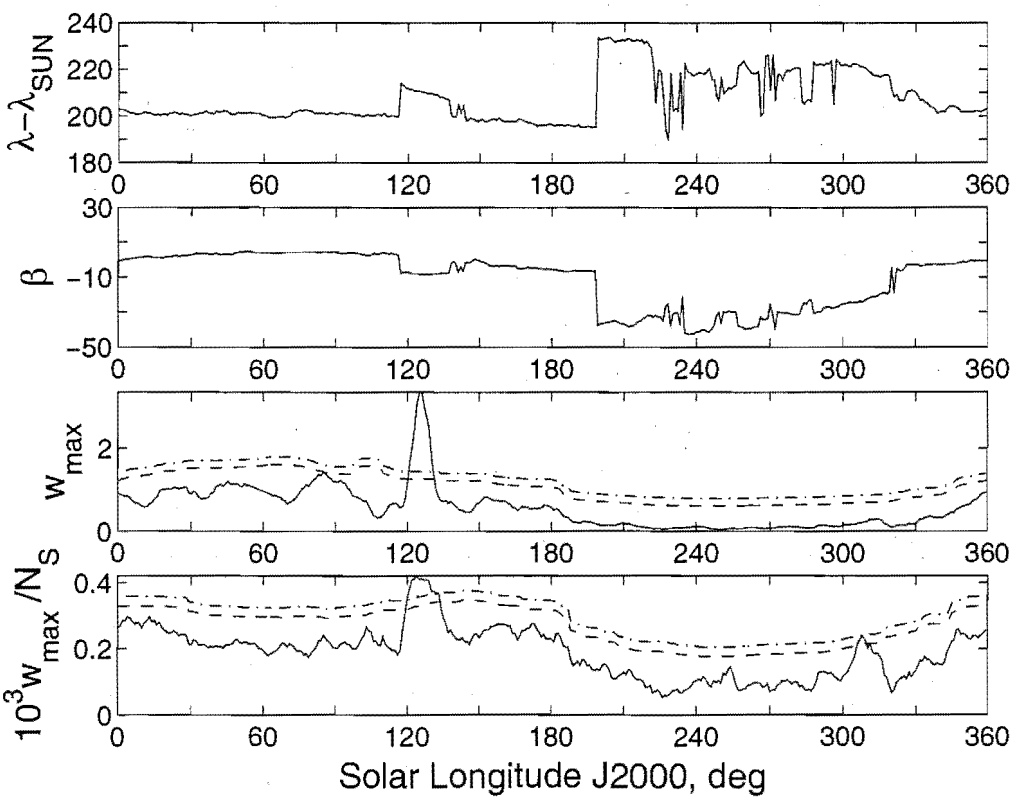

(h) Antihelion Region. $(V_G, \Delta\lambda_\odot, a) = (30 \pm 10\ \mathrm{km\,s^{-1}}, \pm 3°, 6°)$.

Figure G.1: *continued.*

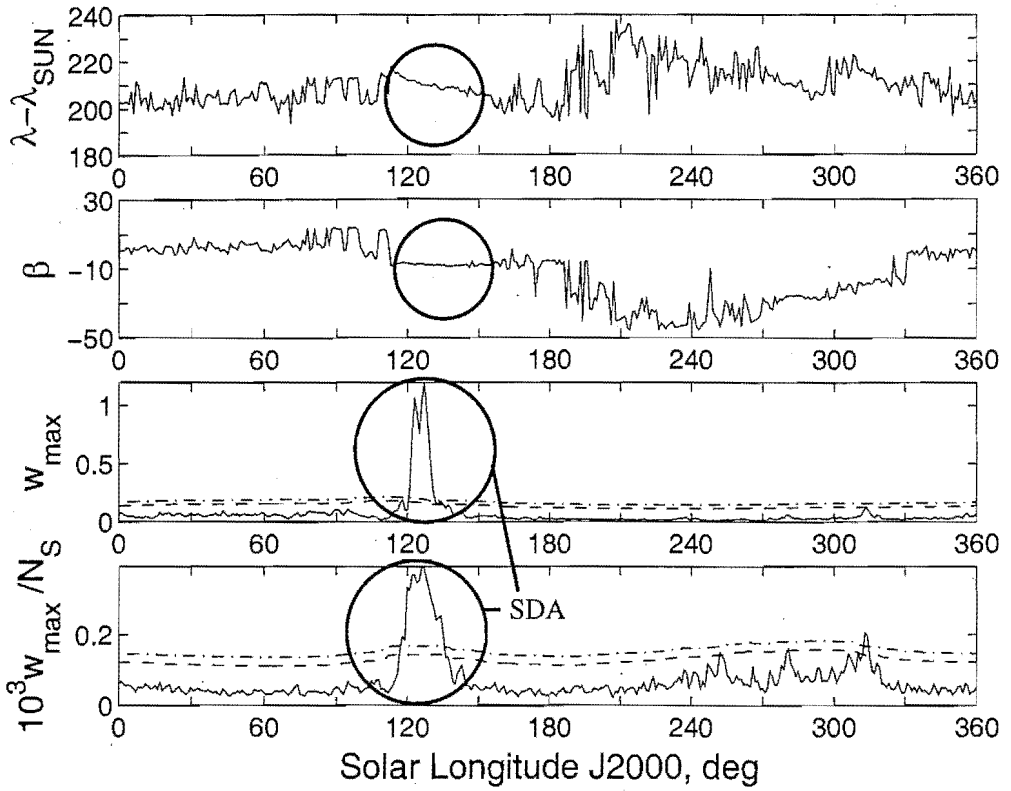

(i) Antihelion Region. $(V_G, \Delta\lambda_\odot, a) = (40 \pm 10\ \mathrm{km\,s^{-1}}, \pm 1°, 3°)$.

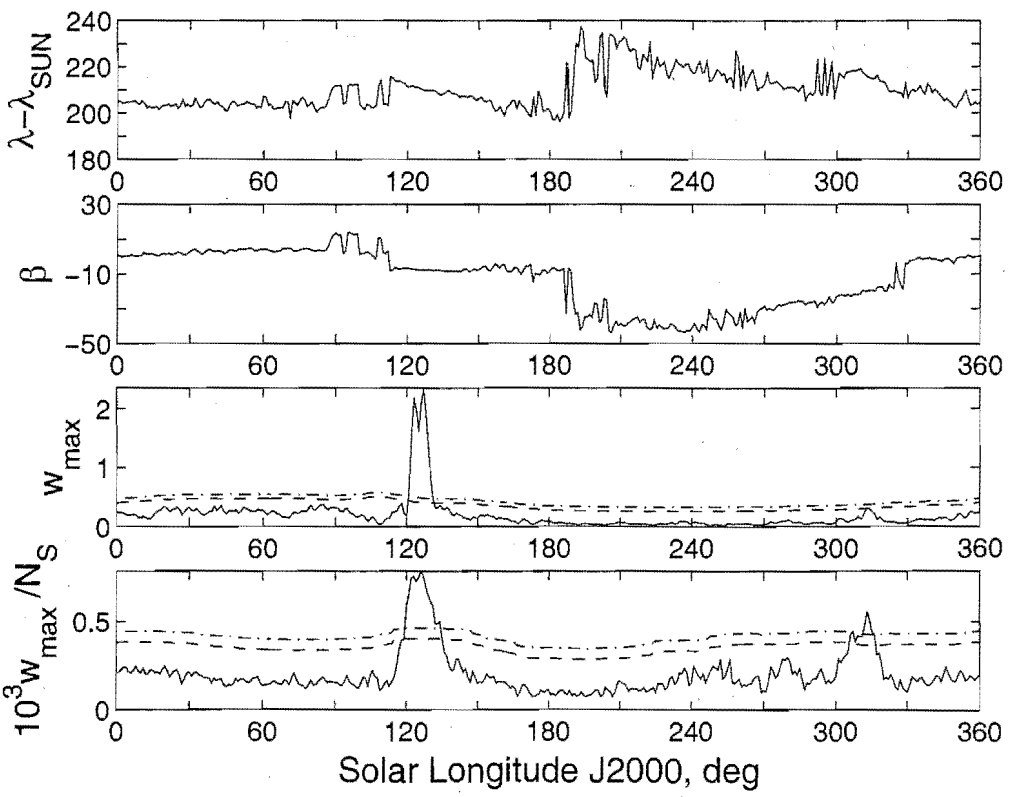

(j) Antihelion Region. $(V_G, \Delta\lambda_\odot, a) = (40 \pm 10\ \mathrm{km\,s^{-1}}, \pm 1°, 6°)$.

Figure G.1: *continued.*

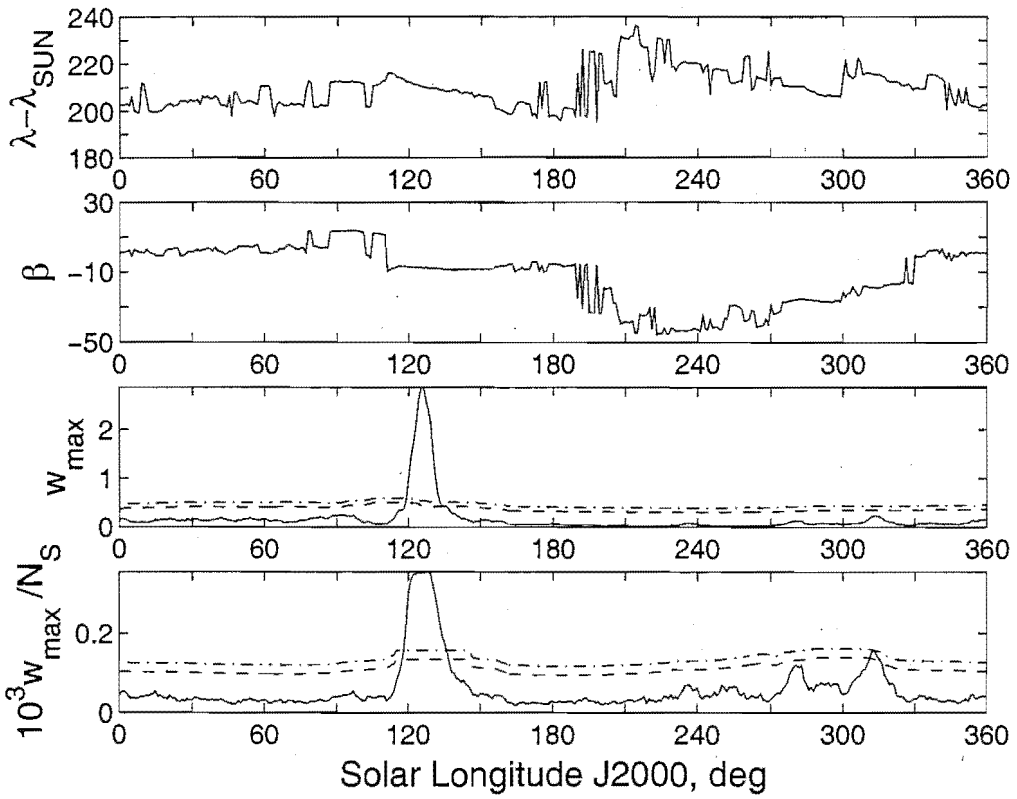

(k) Antihelion Region. $(V_G, \Delta\lambda_\odot, a) = (40 \pm 10\ \mathrm{km\,s^{-1}}, \pm 3°, 3°)$.

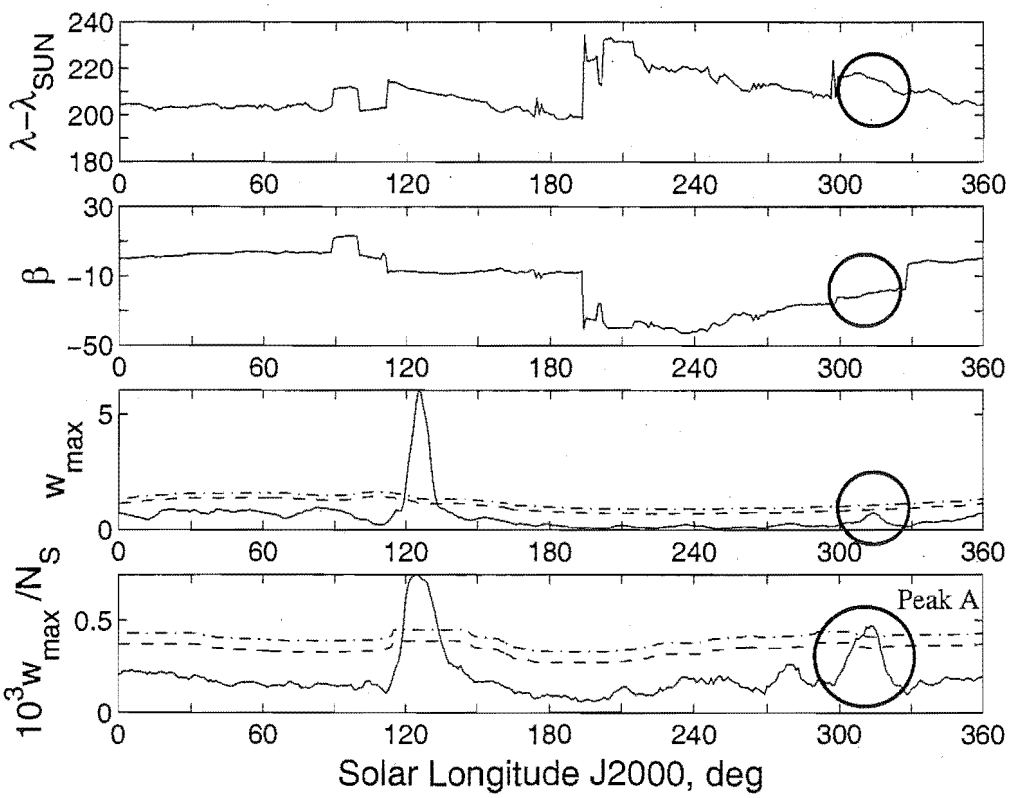

(l) Antihelion Region. $(V_G, \Delta\lambda_\odot, a) = (40 \pm 10\ \mathrm{km\,s^{-1}}, \pm 3°, 6°)$.

Figure G.1: *continued.*

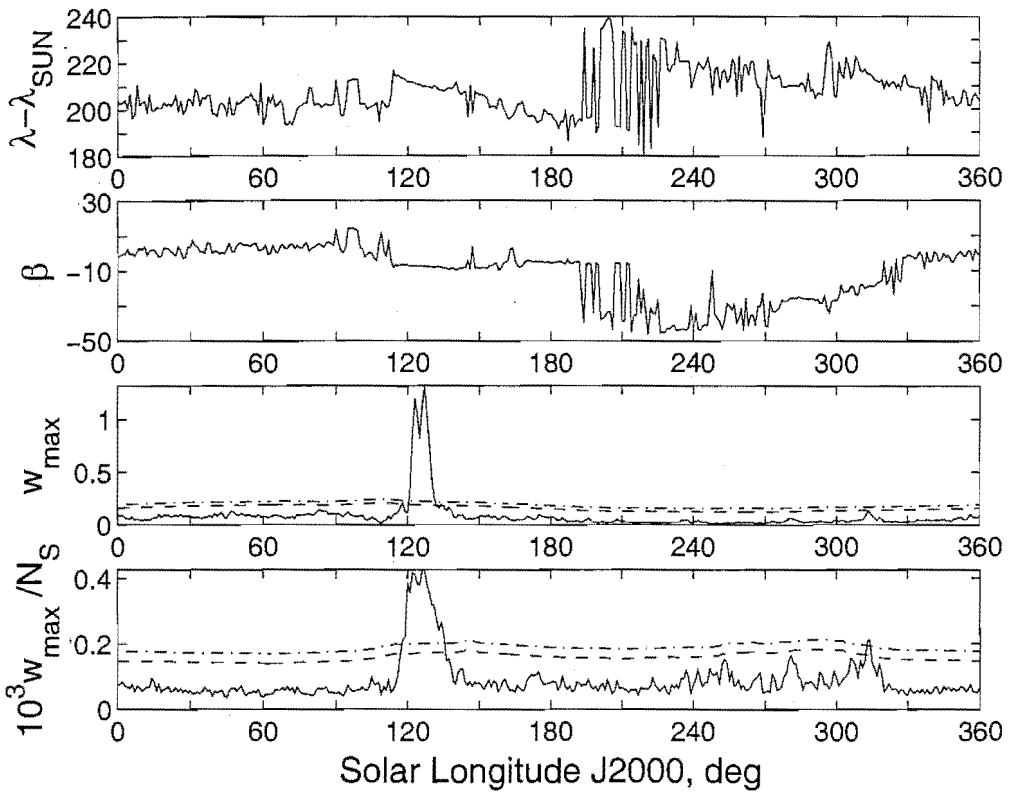

(m) Antihelion Region. $(V_G, \Delta\lambda_\odot, a) = ([0, \infty)\ \mathrm{km\,s^{-1}}, \pm 1°, 3°)$.

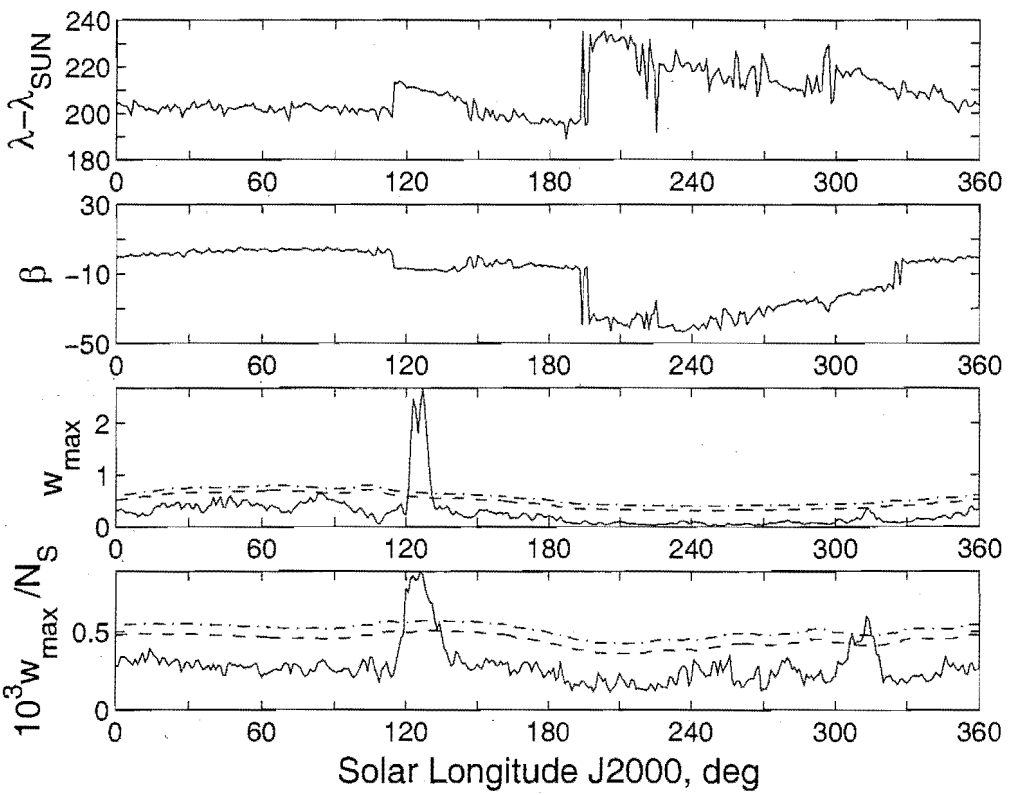

(n) Antihelion Region. $(V_G, \Delta\lambda_\odot, a) = ([0, \infty), \pm 1°, 6°)$.

Figure G.1: *continued.*

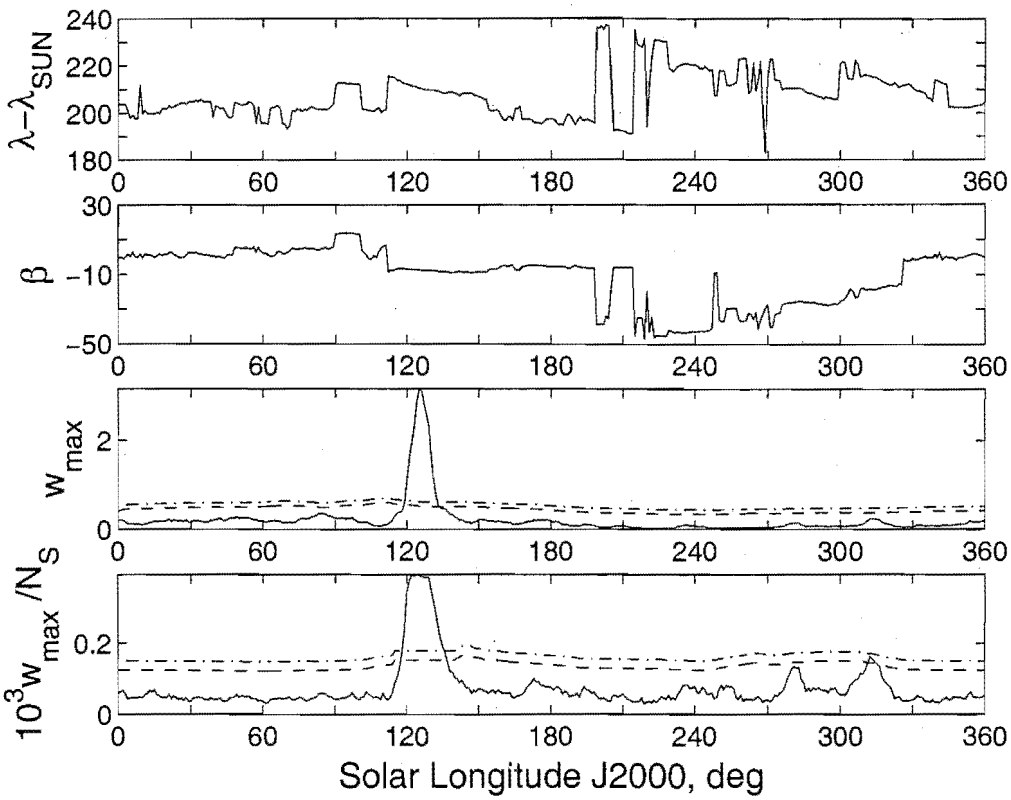

(o) Antihelion Region. $(V_G, \Delta\lambda_\odot, a) = ([0,\infty)\ \mathrm{km\,s^{-1}}, \pm 3°, 3°)$.

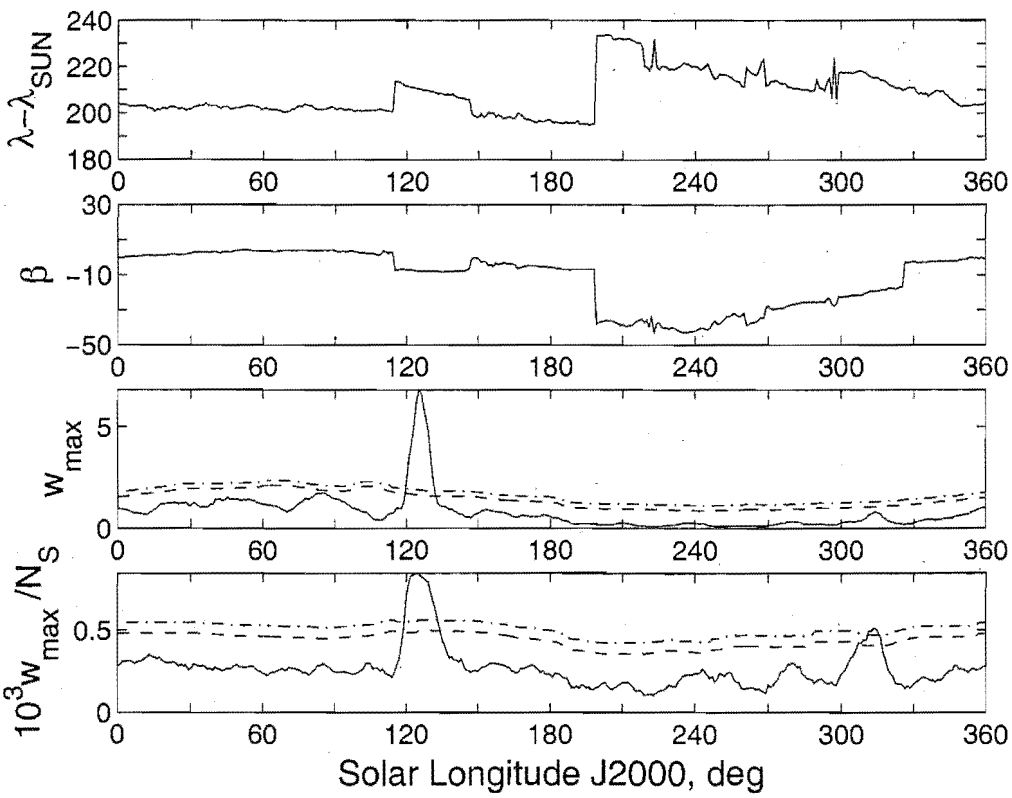

(p) Antihelion Region. $(V_G, \Delta\lambda_\odot, a) = ([0,\infty)\ \mathrm{km\,s^{-1}}, \pm 3°, 6°)$.

Figure G.1: *continued.*

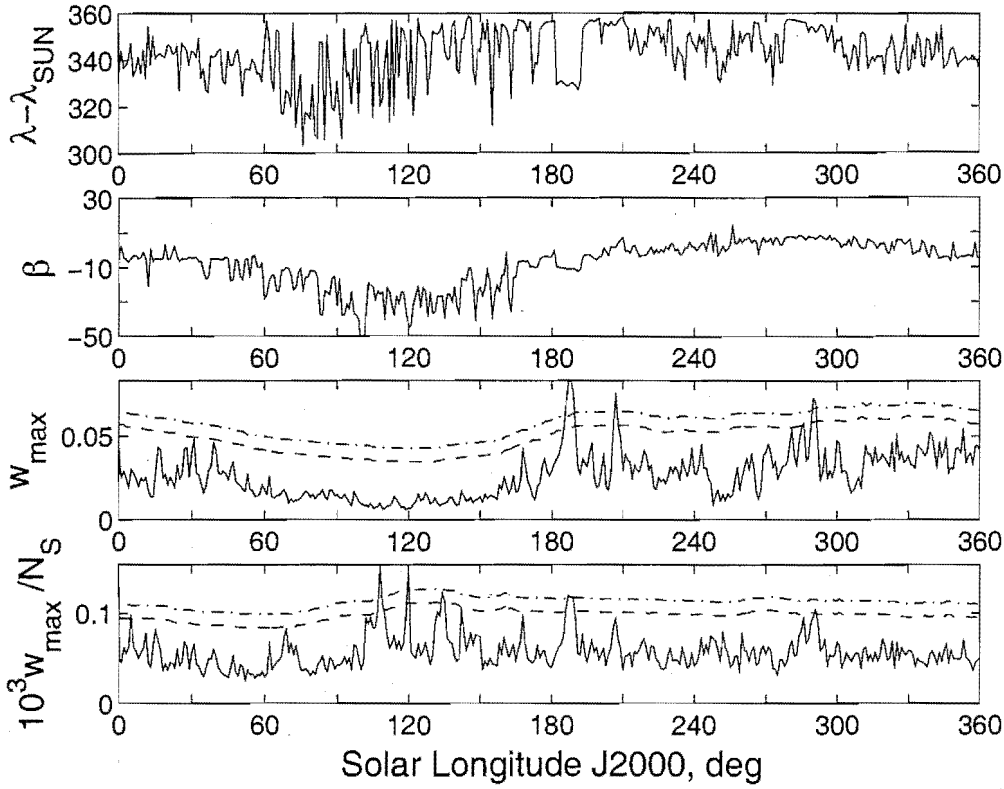

(a) Helion Region. $(V_G, \Delta\lambda_\odot, a) = (20 \pm 10\ \mathrm{km\,s^{-1}}, \pm 1°, 3°)$.

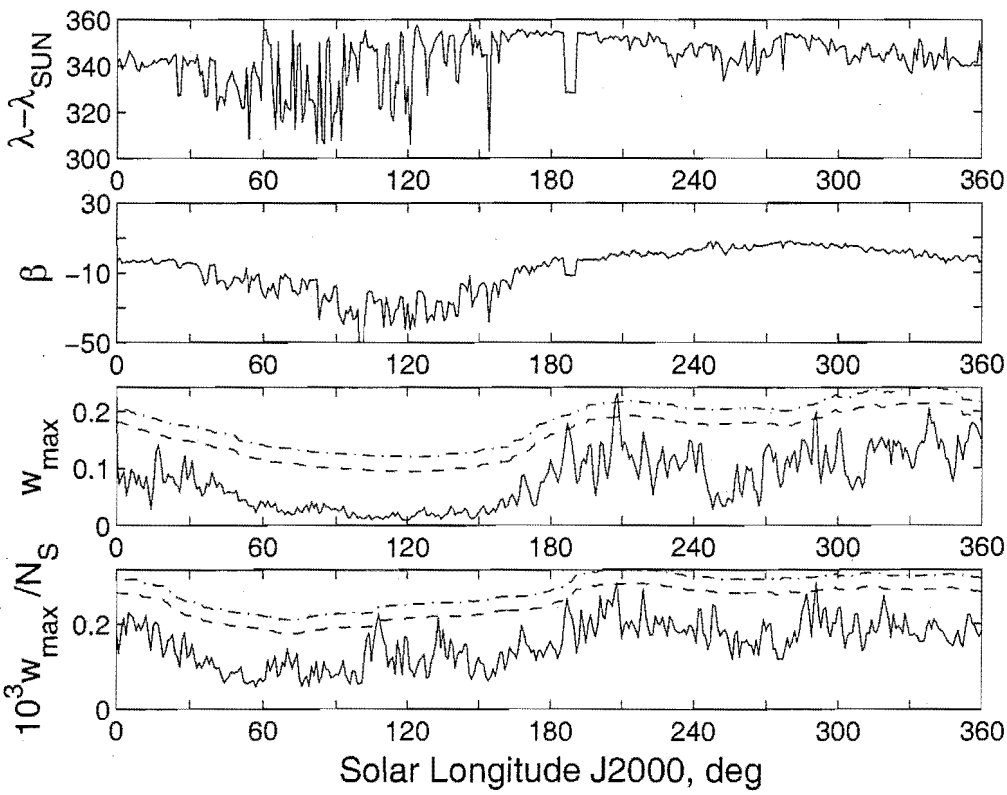

(b) Helion Region. $(V_G, \Delta\lambda_\odot, a) = (20 \pm 10\ \mathrm{km\,s^{-1}}, \pm 1°, 6°)$.

Figure G.2: A wavelet transform enhanced search of the helion region using two wavelet scales (a), two time windows ($\Delta\lambda_\odot$) and four speed (V_G) partitions in all possible combinations.

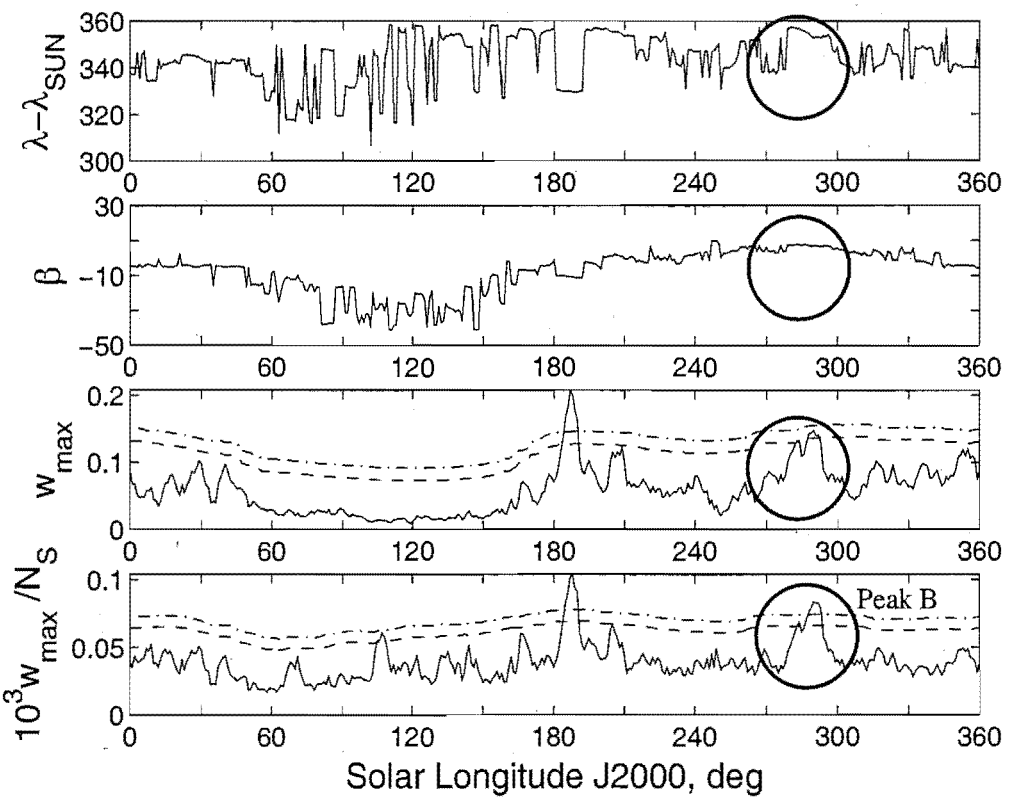

(c) Helion Region. $(V_G, \Delta\lambda_\odot, a) = (20 \pm 10\ \mathrm{km\,s^{-1}}, \pm 3°, 3°)$.

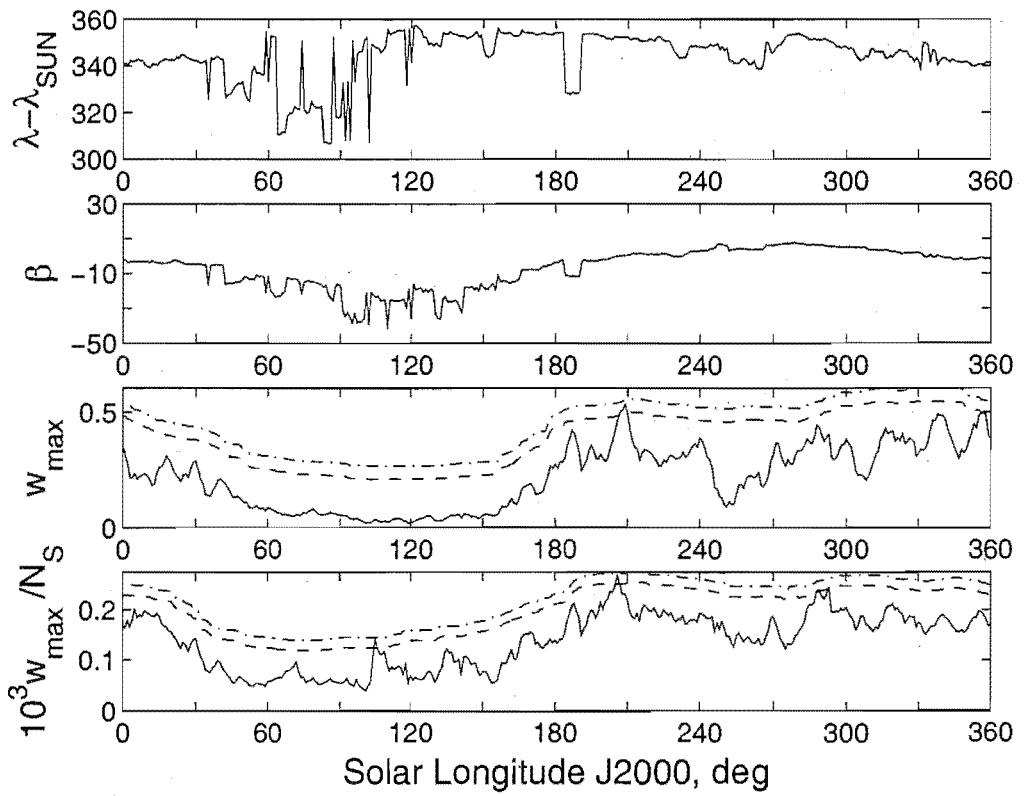

(d) Helion Region. $(V_G, \Delta\lambda_\odot, a) = (20 \pm 10\ \mathrm{km\,s^{-1}}, \pm 3°, 6°)$.

Figure G.2: *continued.*

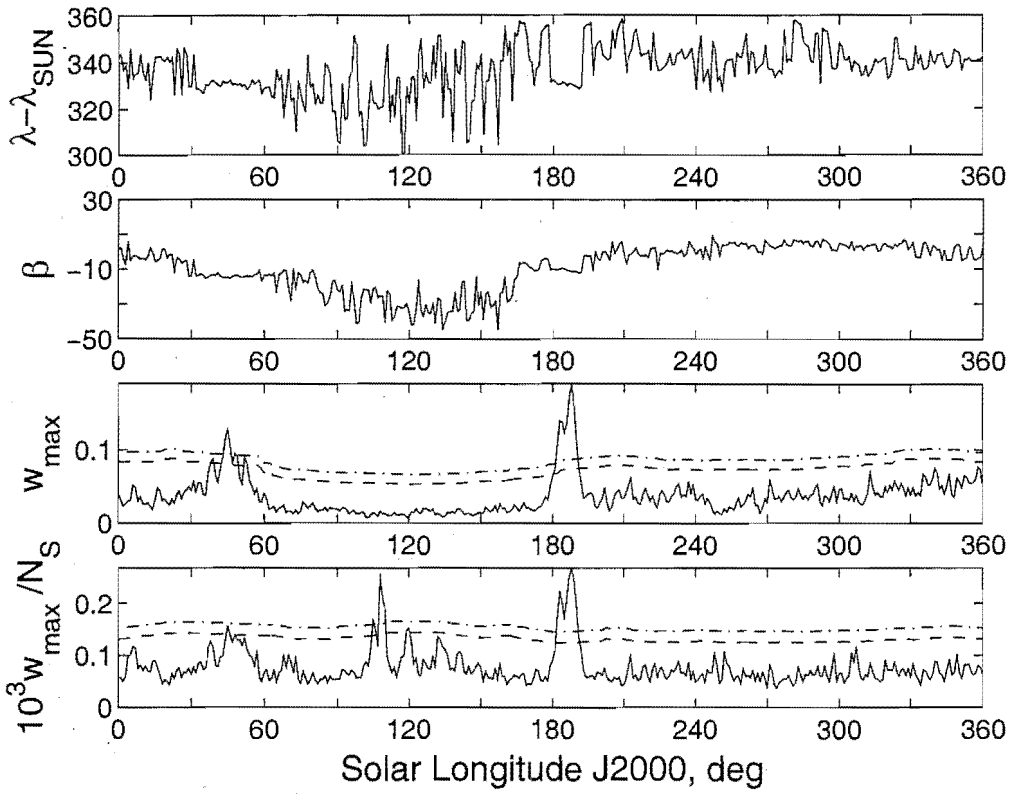

(e) Helion Region. $(V_G, \Delta\lambda_\odot, a) = (30 \pm 10\ \mathrm{km\,s^{-1}}, \pm 1°, 3°)$.

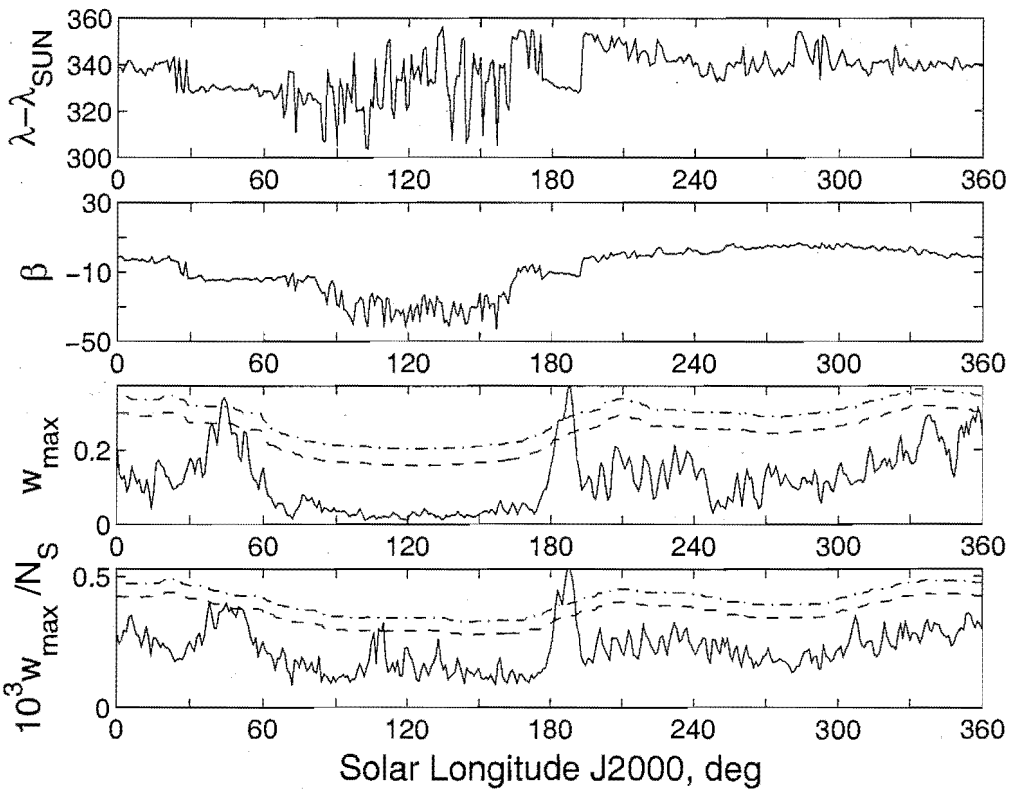

(f) Helion Region. $(V_G, \Delta\lambda_\odot, a) = (30 \pm 10\ \mathrm{km\,s^{-1}}, \pm 1°, 6°)$.

Figure G.2: *continued.*

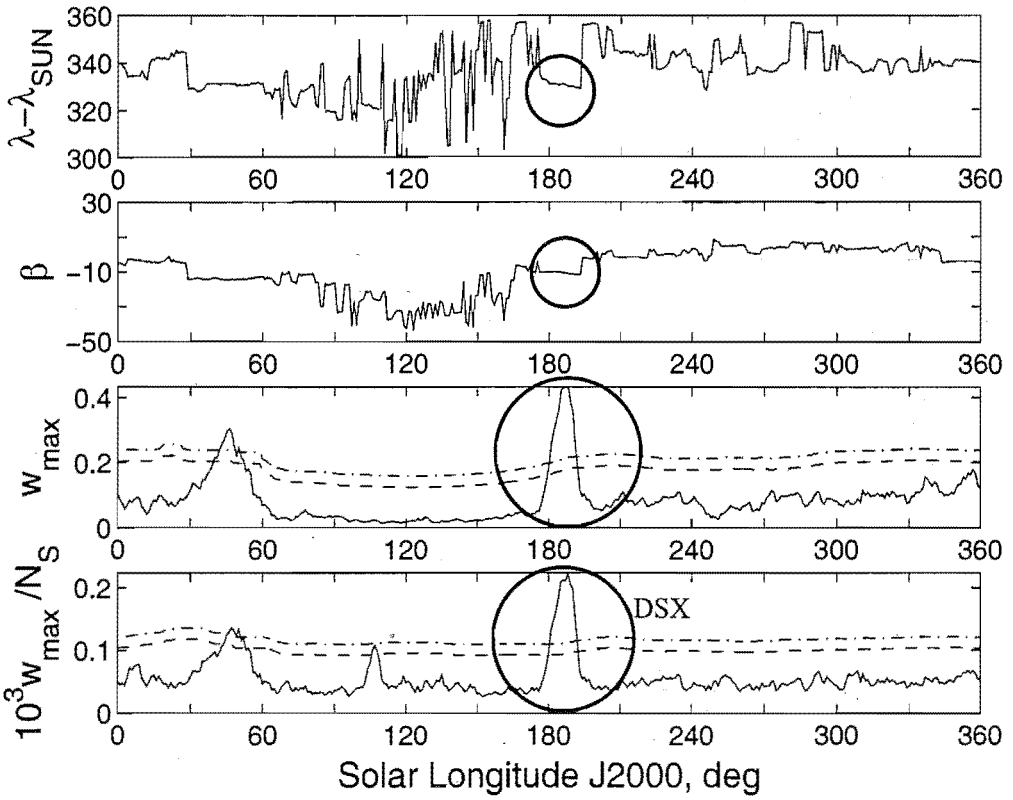

(g) Helion Region. $(V_G, \Delta\lambda_\odot, a) = (30 \pm 10\ \mathrm{km\,s^{-1}}, \pm 3°, 3°)$.

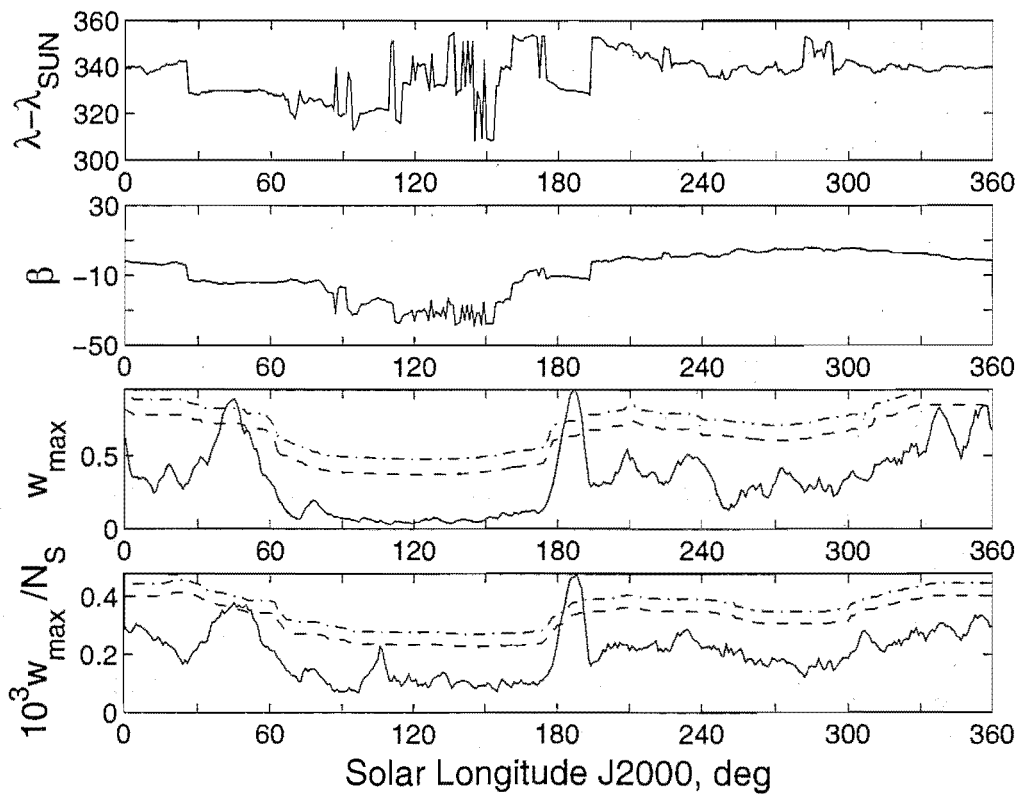

(h) Helion Region. $(V_G, \Delta\lambda_\odot, a) = (30 \pm 10\ \mathrm{km\,s^{-1}}, \pm 3°, 6°)$.

Figure G.2: *continued.*

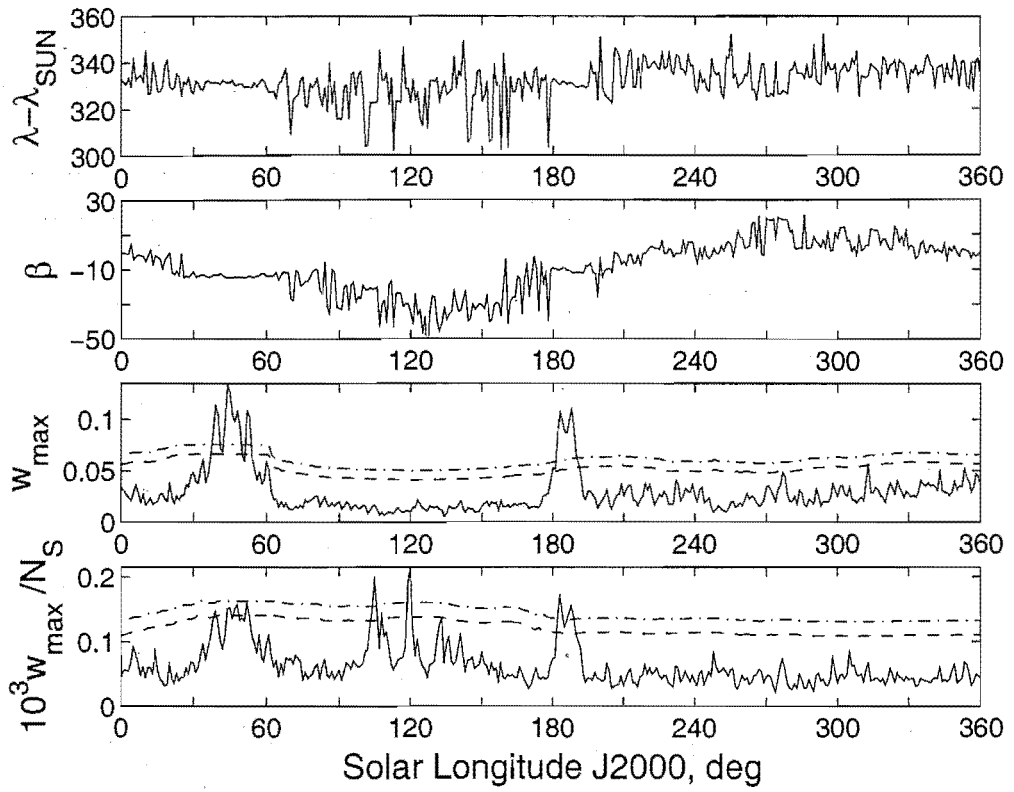

(i) Helion Region. $(V_G, \Delta\lambda_\odot, a) = (40 \pm 10\ \mathrm{km\,s^{-1}}, \pm 1°, 3°)$.

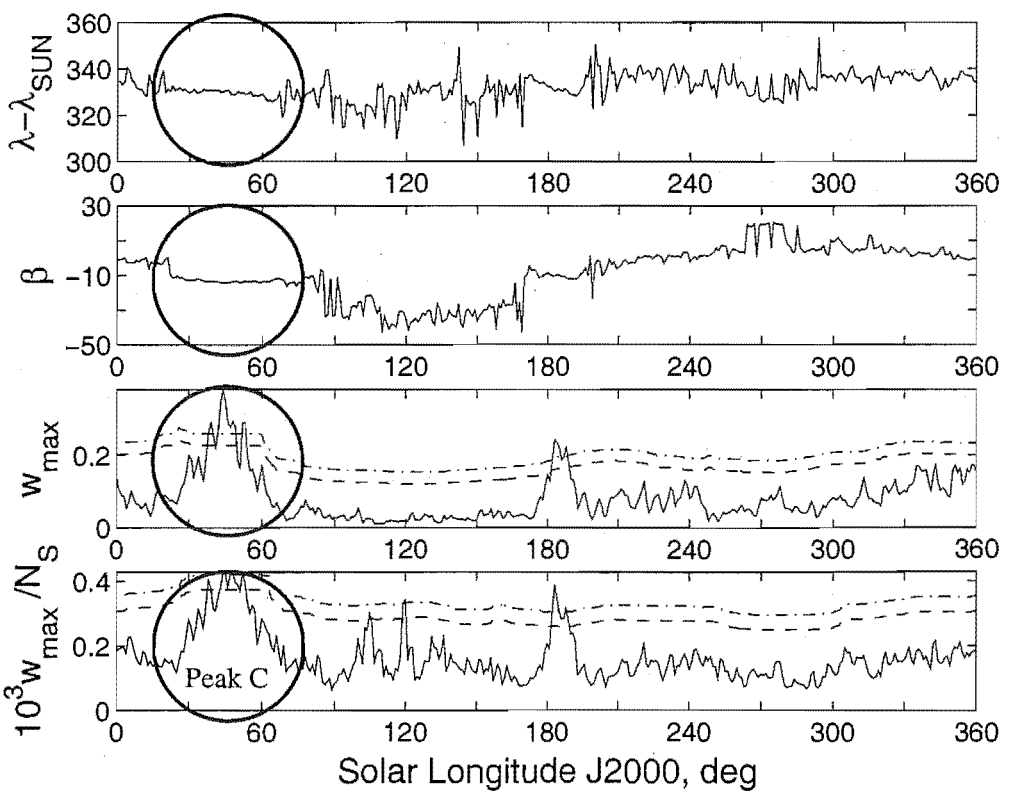

(j) Helion Region. $(V_G, \Delta\lambda_\odot, a) = (40 \pm 10\ \mathrm{km\,s^{-1}}, \pm 1°, 6°)$.

Figure G.2: *continued.*

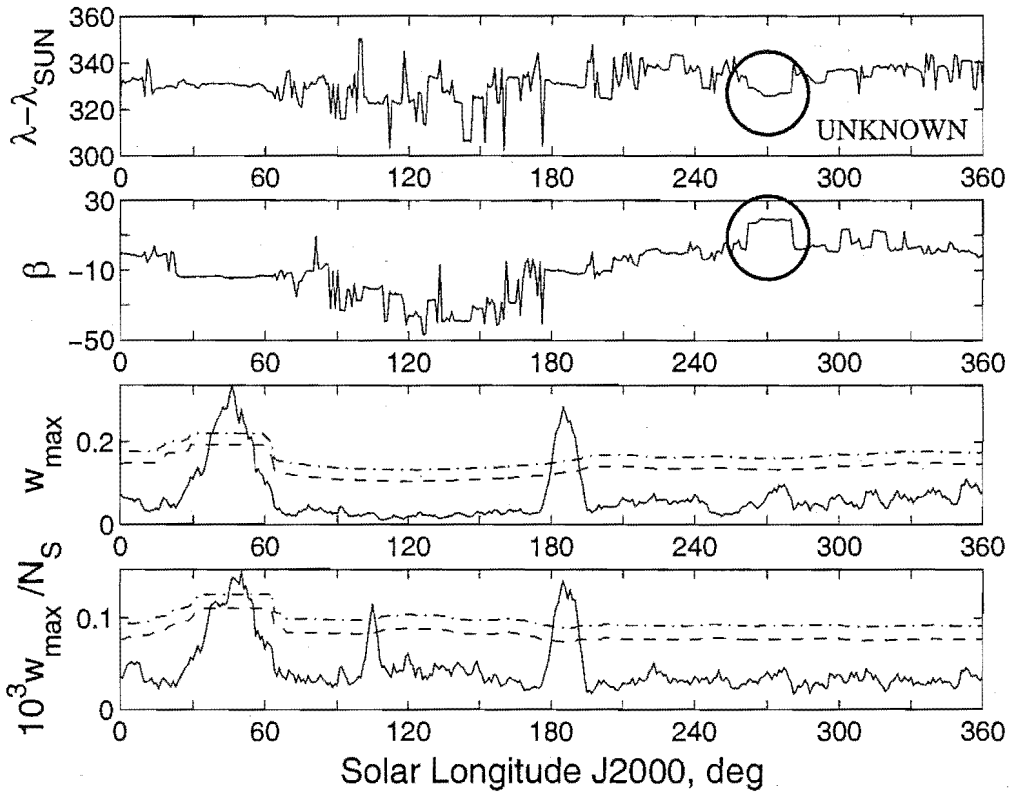

(k) Helion Region. $(V_G, \Delta\lambda_\odot, a) = (40 \pm 10\ \mathrm{km\,s^{-1}}, \pm 3°, 3°)$.

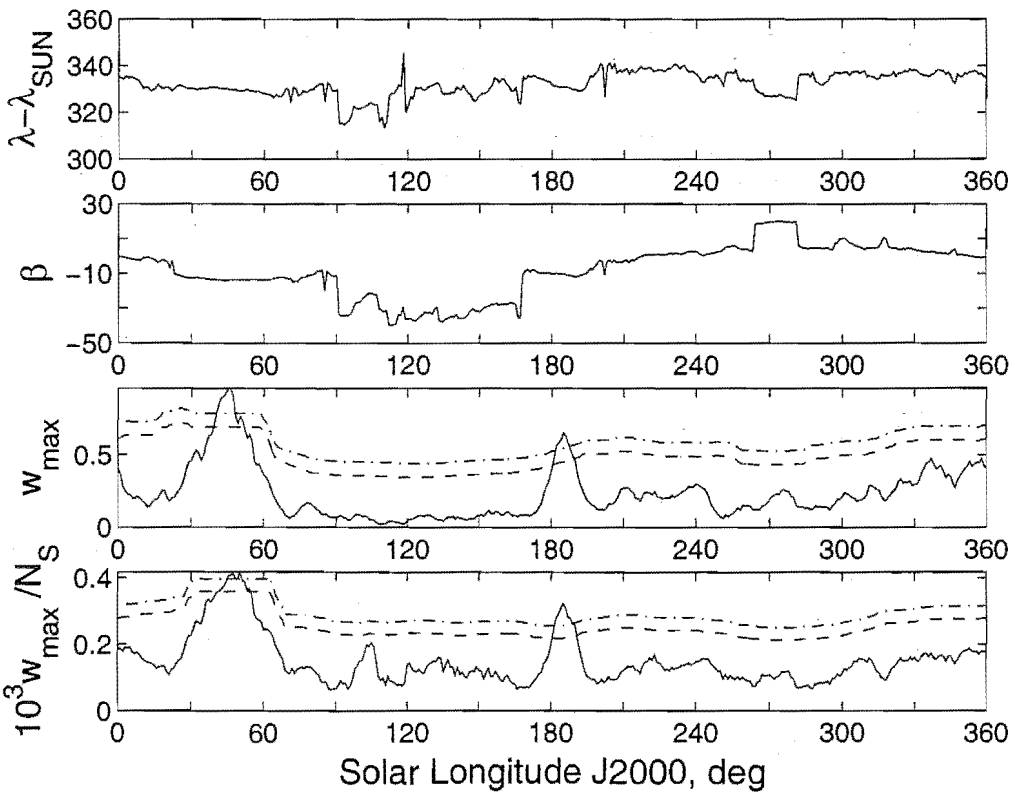

(l) Helion Region. $(V_G, \Delta\lambda_\odot, a) = (40 \pm 10\ \mathrm{km\,s^{-1}}, \pm 3°, 6°)$.

Figure G.2: *continued.*

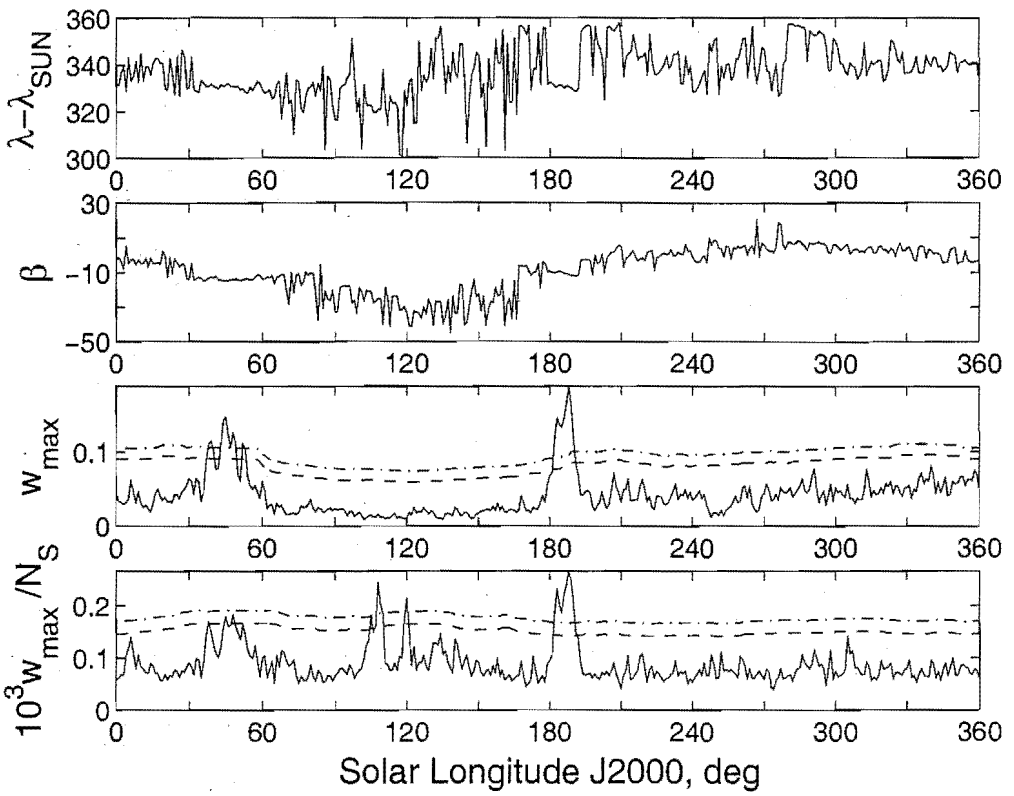

(m) Helion Region. $(V_G, \Delta\lambda_\odot, a) = ([0, \infty)\ \mathrm{km\,s^{-1}}, \pm 1°, 3°)$.

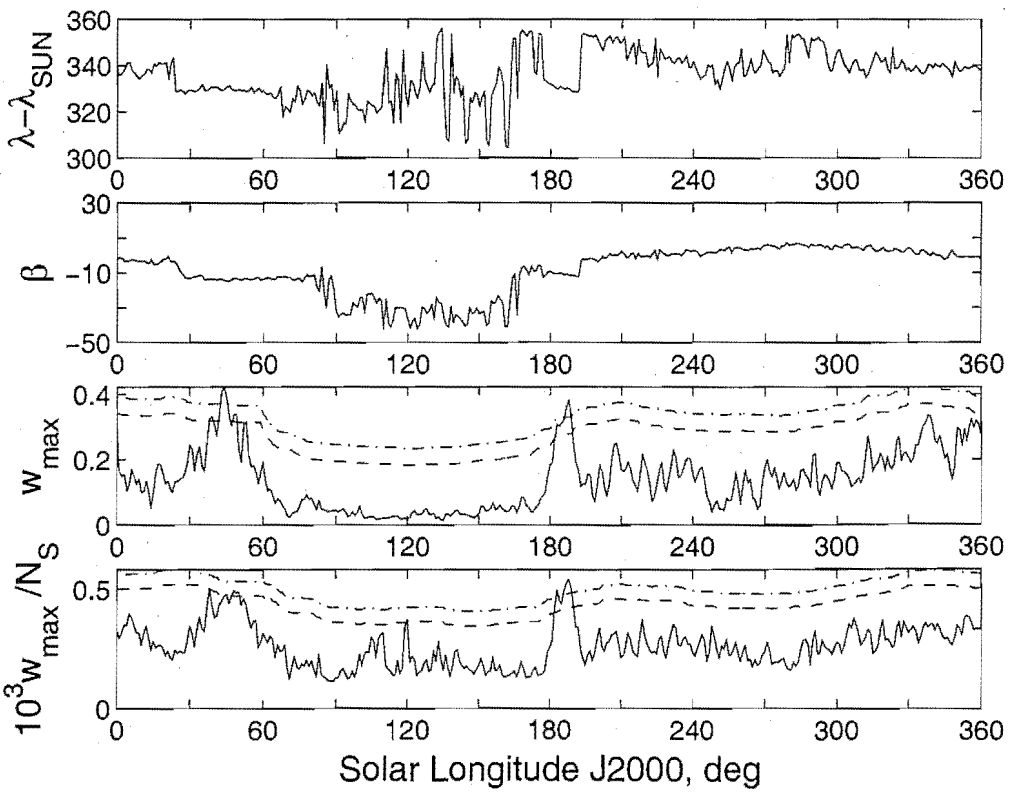

(n) Helion Region. $(V_G, \Delta\lambda_\odot, a) = ([0, \infty)\ \mathrm{km\,s^{-1}}, \pm 1°, 6°)$.

Figure G.2: *continued.*

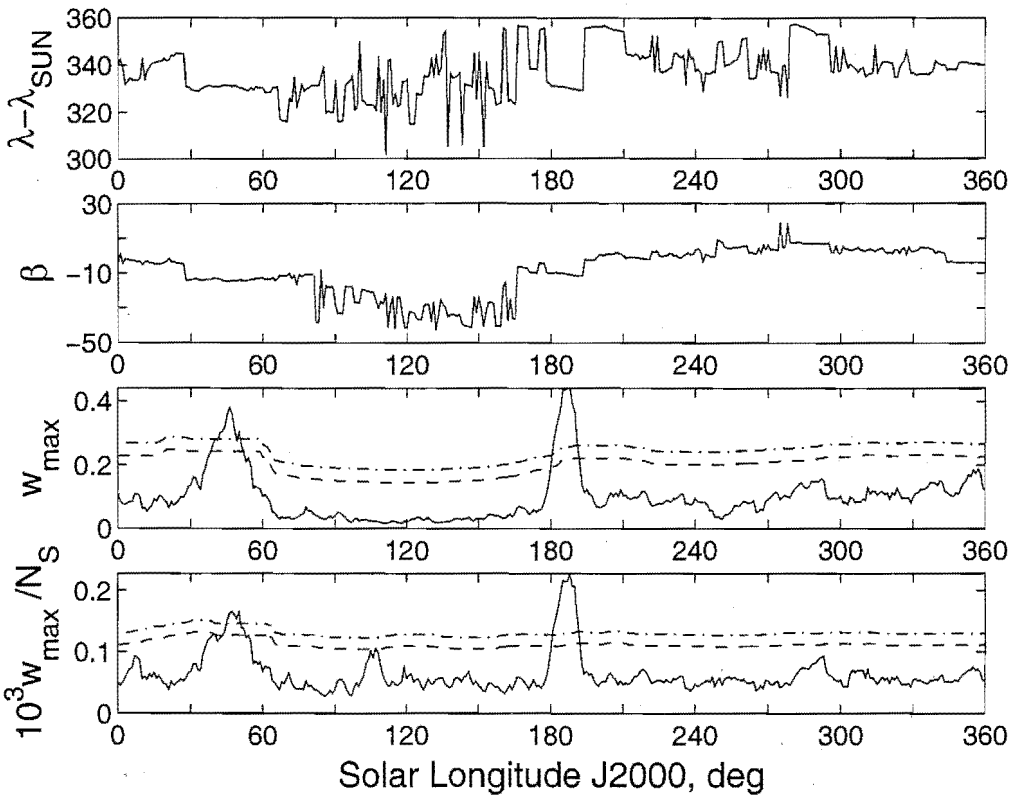

(o) Helion Region. $(V_G, \Delta\lambda_\odot, a) = ([0, \infty)\ \mathrm{km\,s^{-1}}, \pm 3°, 3°)$.

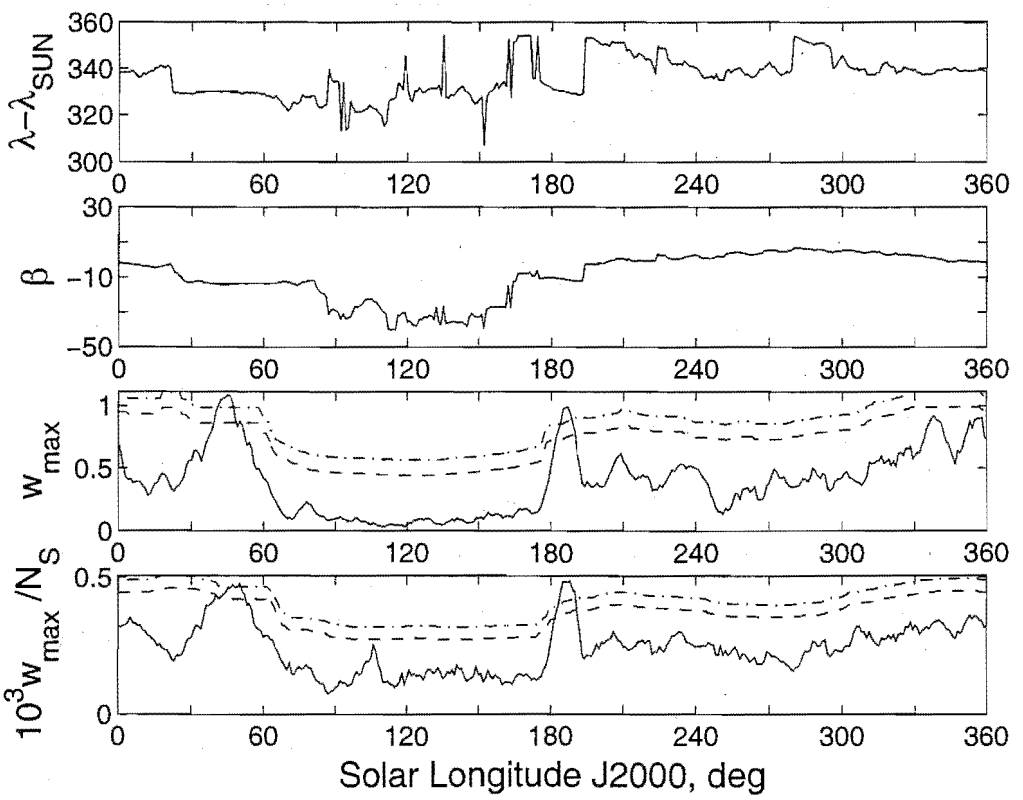

(p) Helion Region. $(V_G, \Delta\lambda_\odot, a) = ([0, \infty)\ \mathrm{km\,s^{-1}}, \pm 3°, 6°)$.

Figure G.2: *continued.*

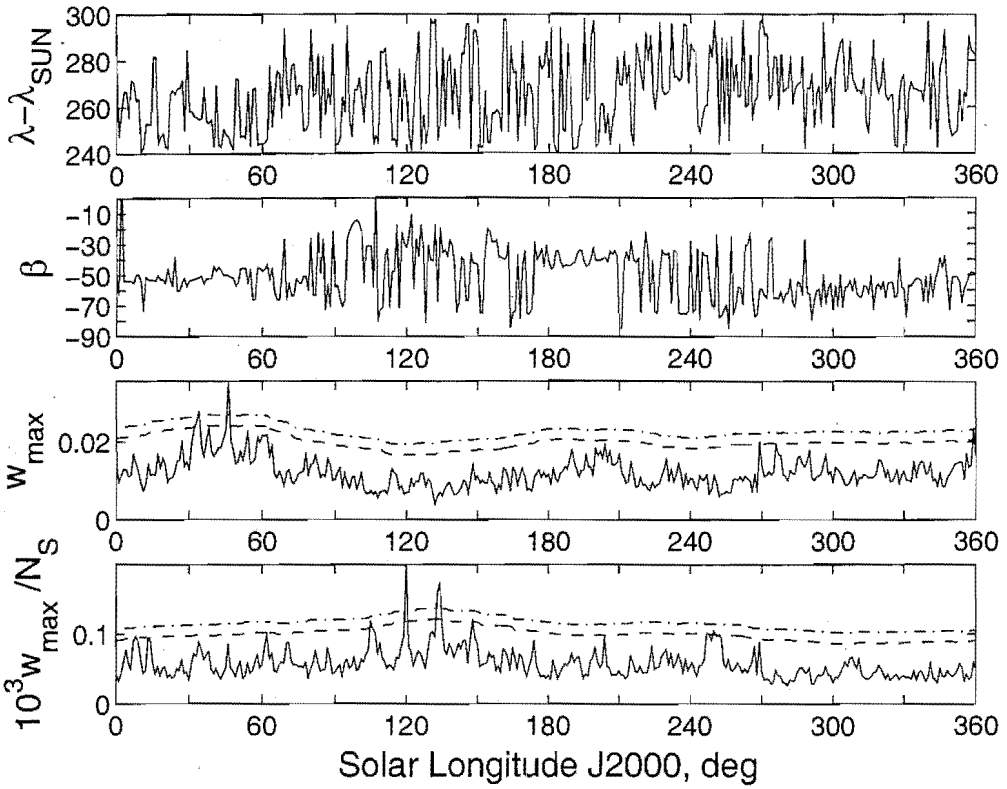

(a) Prograde Apex Region. $(V_G, \Delta\lambda_\odot, a) = (20 \pm 10\ \mathrm{km\,s^{-1}}, \pm 1°, 3°)$.

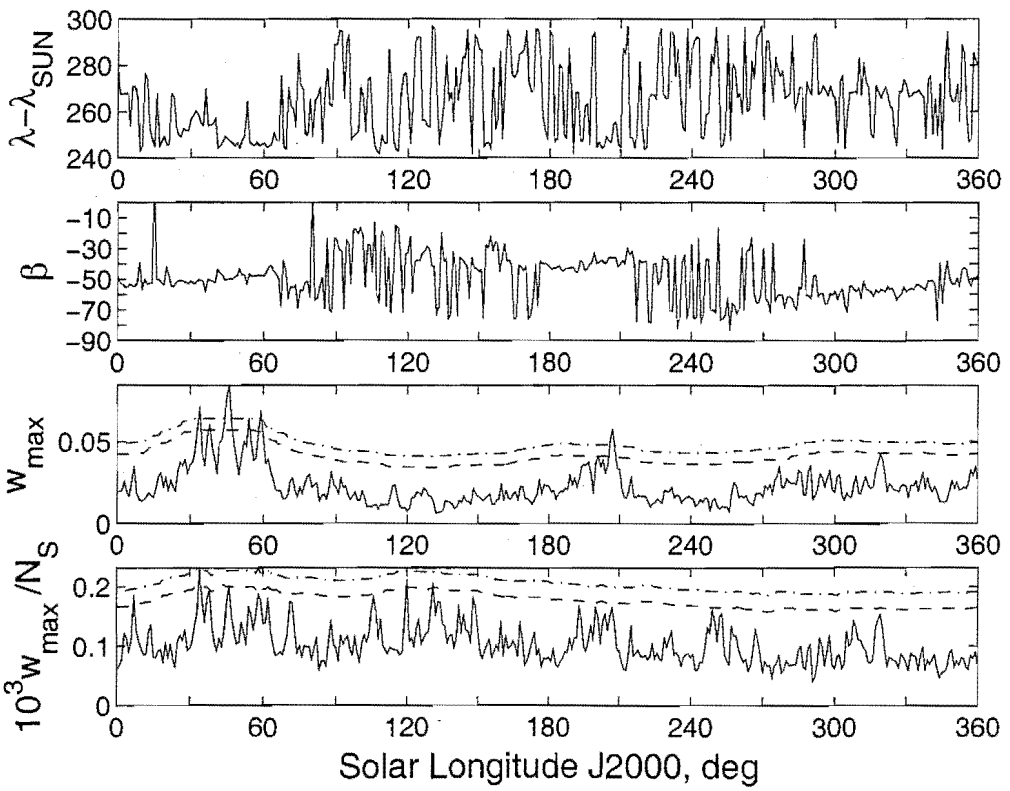

(b) Prograde Apex Region. $(V_G, \Delta\lambda_\odot, a) = (20 \pm 10\ \mathrm{km\,s^{-1}}, \pm 1°, 6°)$.

Figure G.3: A wavelet transform enhanced search of the prograde apex region using two wavelet scales (a), two time windows ($\Delta\lambda_\odot$) and four speed (V_G) partitions in all possible combinations.

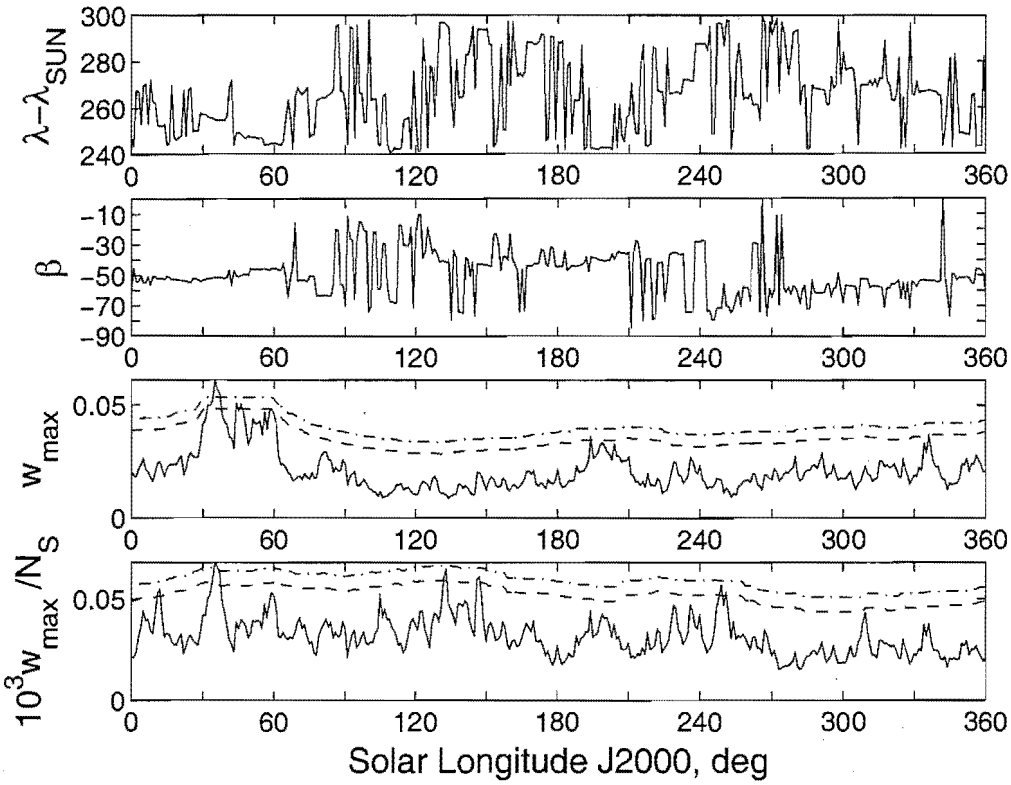

(c) Prograde Apex Region. $(V_G, \Delta\lambda_\odot, a) = (20 \pm 10\ \mathrm{km\,s^{-1}}, \pm 3°, 3°)$.

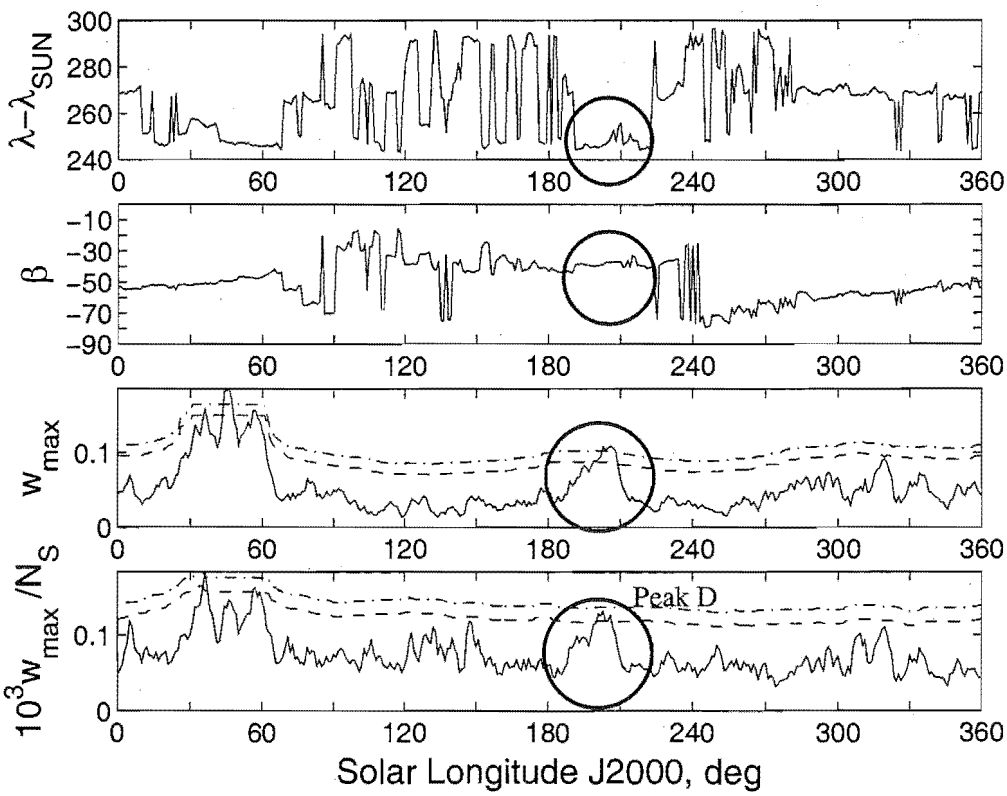

(d) Prograde Apex Region. $(V_G, \Delta\lambda_\odot, a) = (20 \pm 10\ \mathrm{km\,s^{-1}}, \pm 3°, 6°)$.

Figure G.3: *continued.*

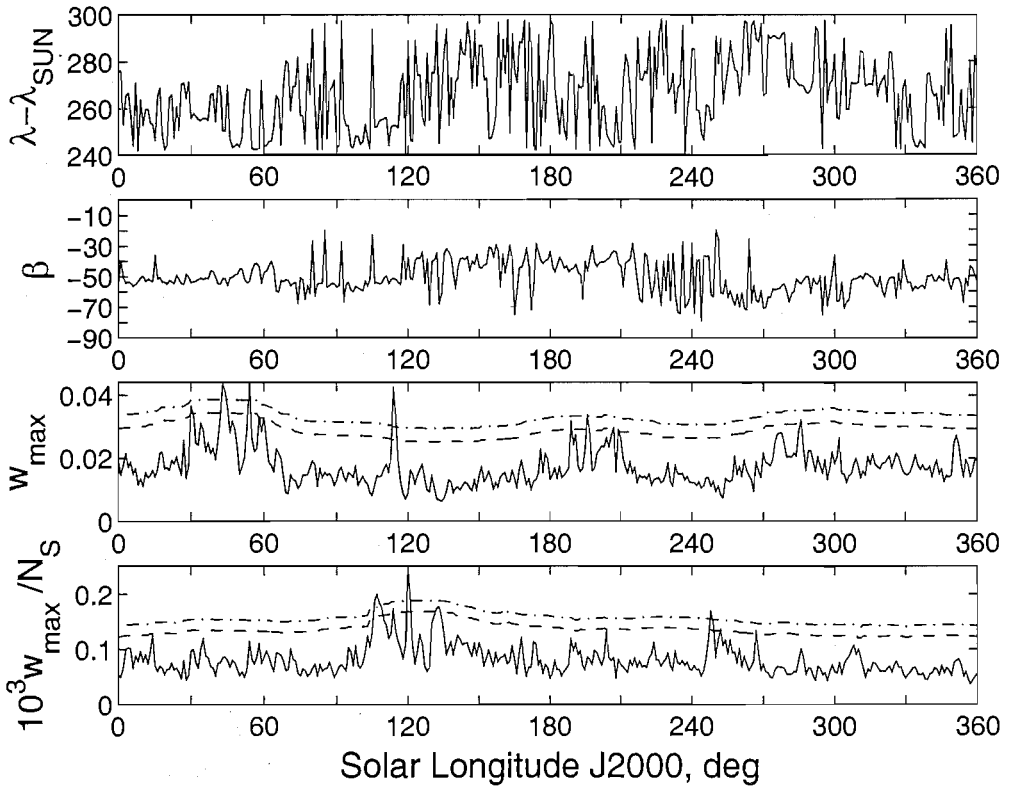

(e) Prograde Apex Region. $(V_G, \Delta\lambda_\odot, a) = (30 \pm 10\ \mathrm{km\,s^{-1}}, \pm 1°, 3°)$.

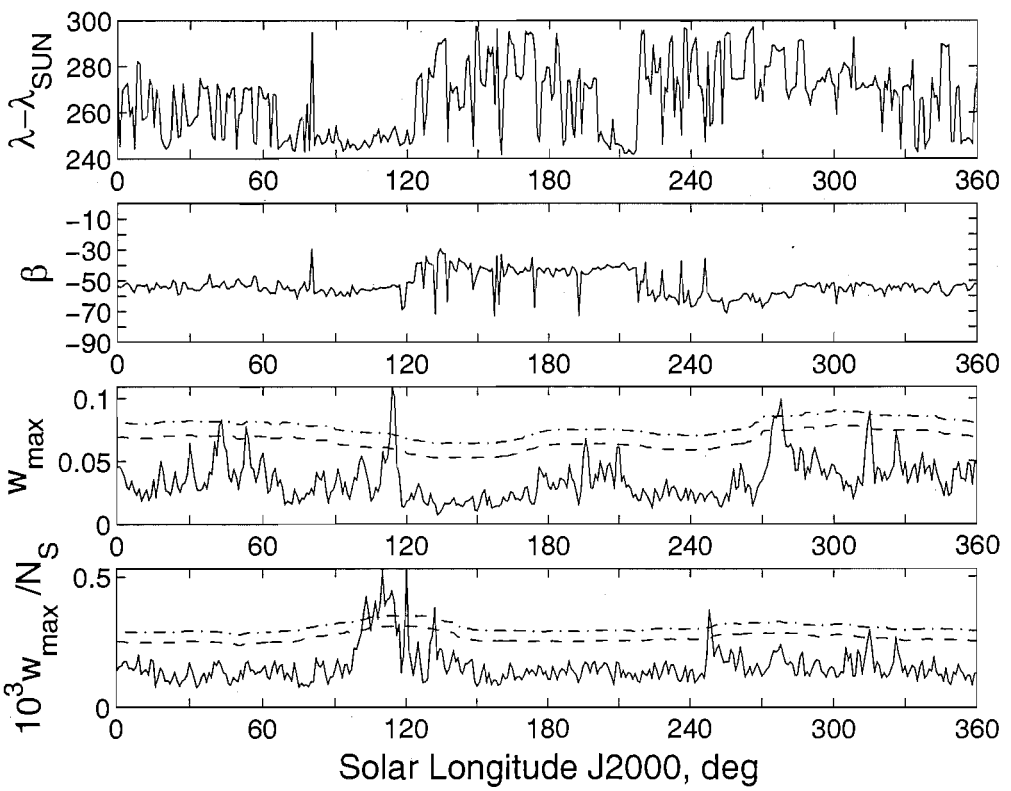

(f) Prograde Apex Region. $(V_G, \Delta\lambda_\odot, a) = (30 \pm 10\ \mathrm{km\,s^{-1}}, \pm 1°, 6°)$.

Figure G.3: *continued.*

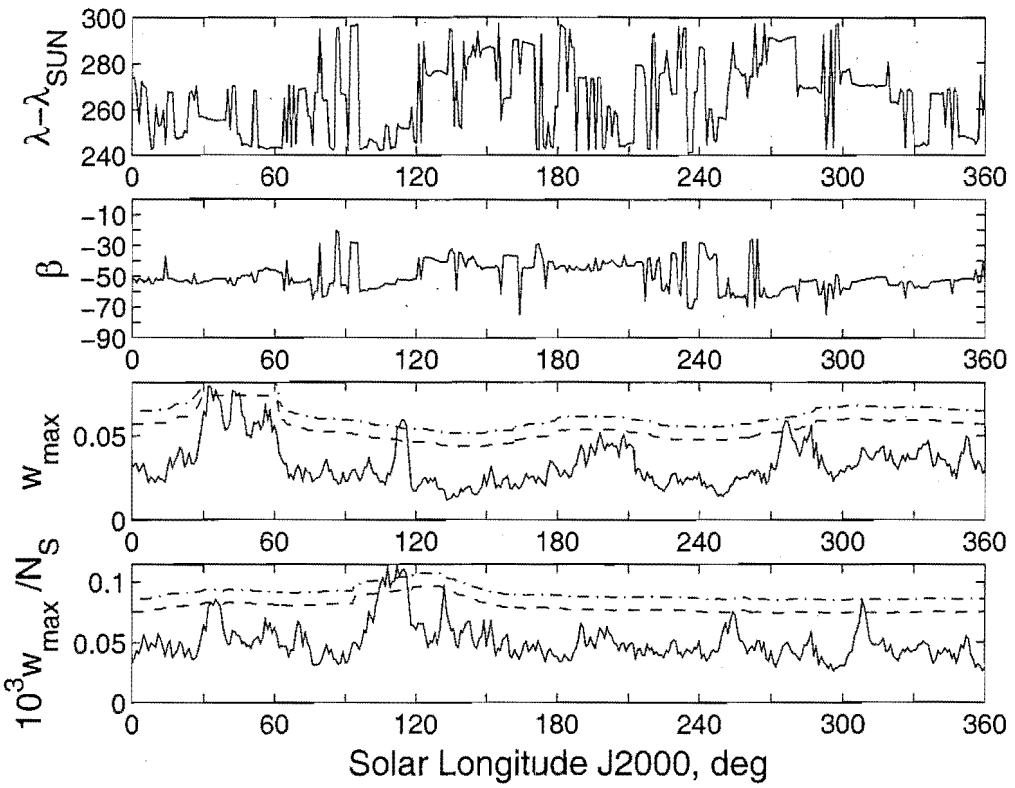

(g) Prograde Apex Region. $(V_G, \Delta\lambda_\odot, a) = (30 \pm 10\ \mathrm{km\,s^{-1}}, \pm 3°, 3°)$.

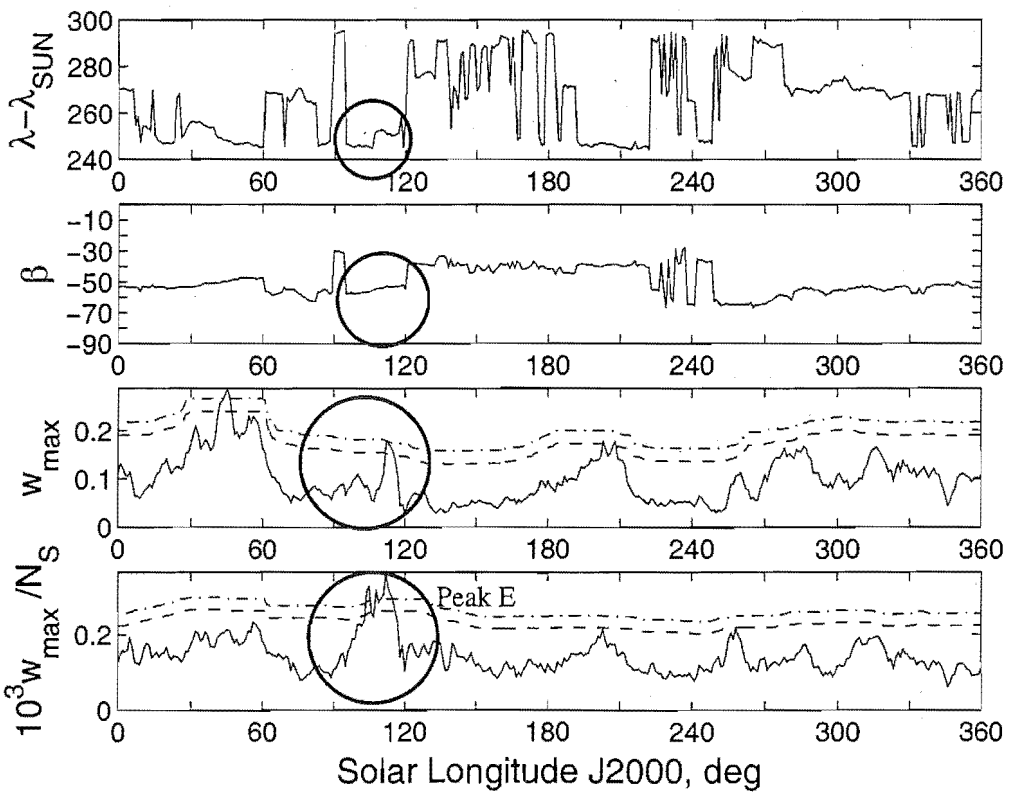

(h) Prograde Apex Region. $(V_G, \Delta\lambda_\odot, a) = (30 \pm 10\ \mathrm{km\,s^{-1}}, \pm 3°, 6°)$.

Figure G.3: *continued.*

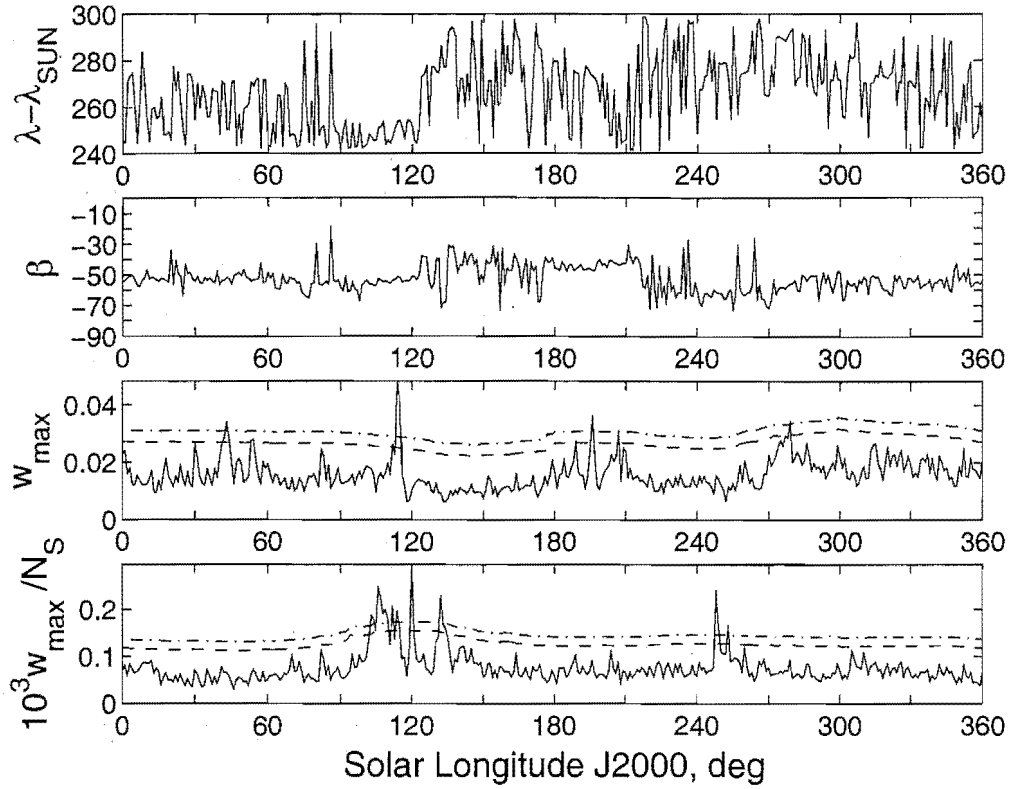

(i) Prograde Apex Region. $(V_G, \Delta\lambda_\odot, a) = (40 \pm 10\ \mathrm{km\,s^{-1}}, \pm 1°, 3°)$.

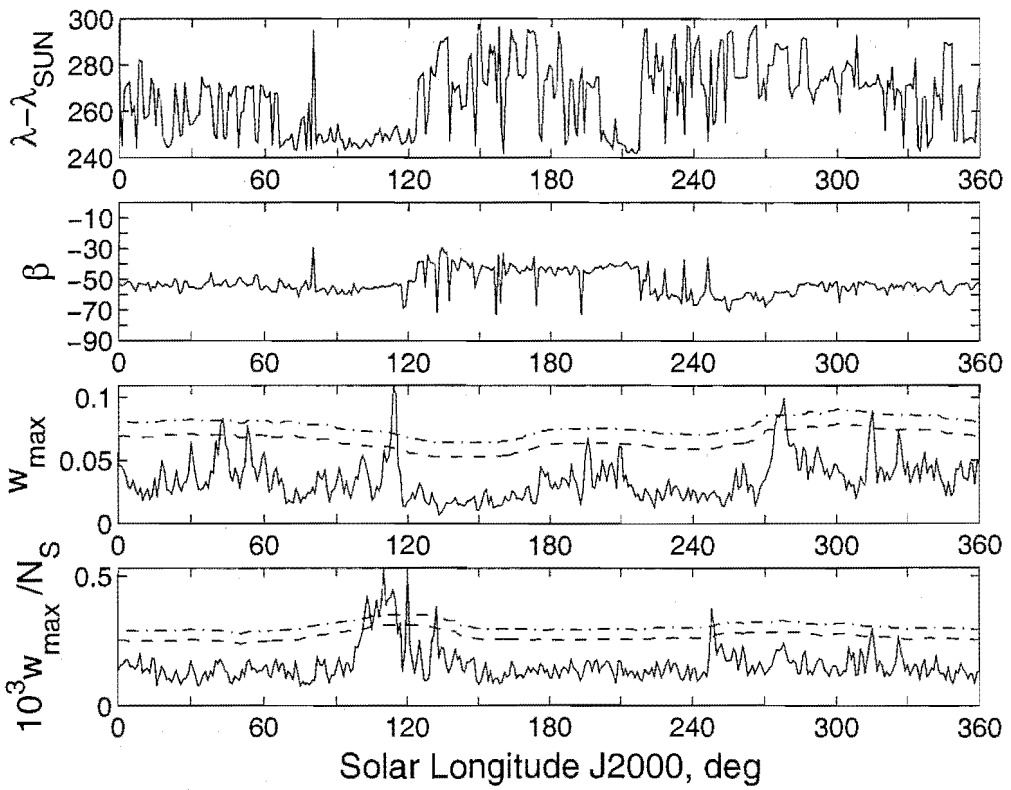

(j) Prograde Apex Region. $(V_G, \Delta\lambda_\odot, a) = (40 \pm 10\ \mathrm{km\,s^{-1}}, \pm 1°, 6°)$.

Figure G.3: *continued.*

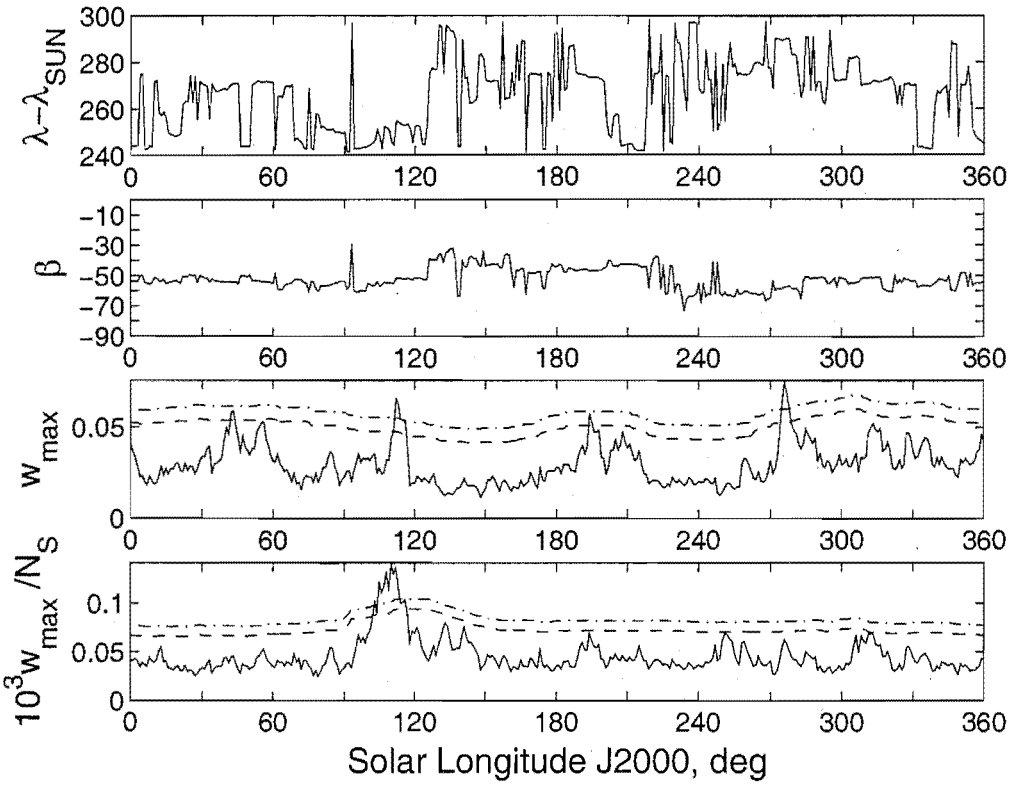

(k) Prograde Apex Region. $(V_G, \Delta\lambda_\odot, a) = (40 \pm 10\ \mathrm{km\,s^{-1}}, \pm 3°, 3°)$.

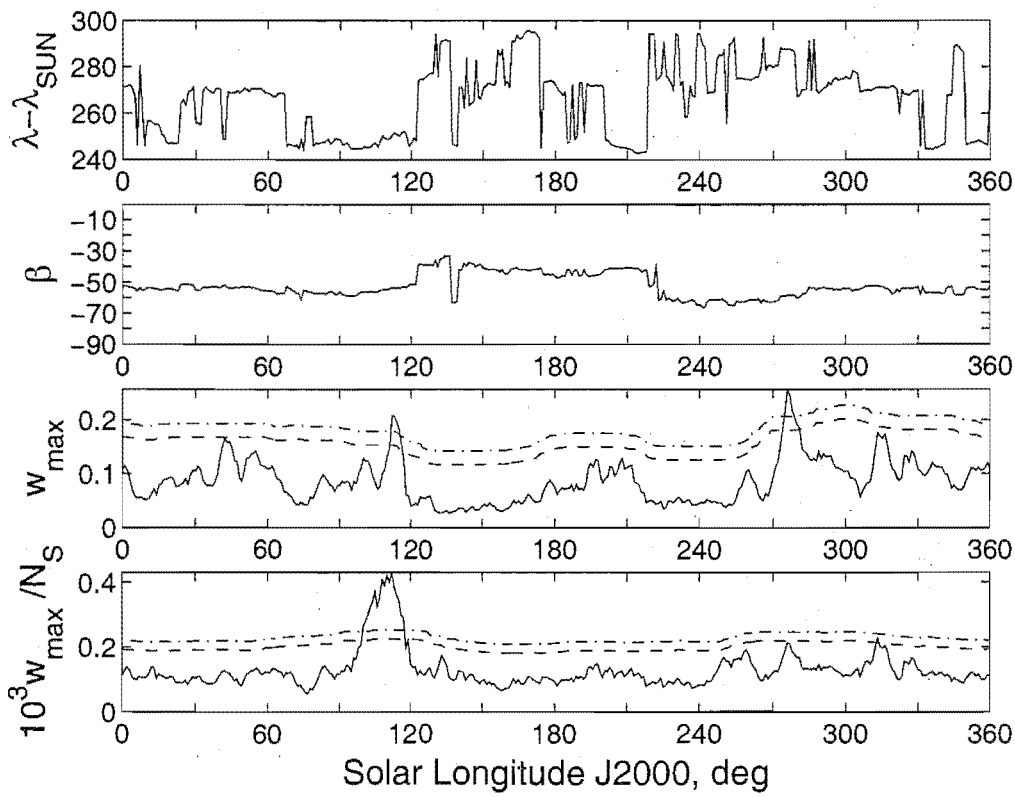

(l) Prograde Apex Region. $(V_G, \Delta\lambda_\odot, a) = (40 \pm 10\ \mathrm{km\,s^{-1}}, \pm 3°, 6°)$.

Figure G.3: *continued.*

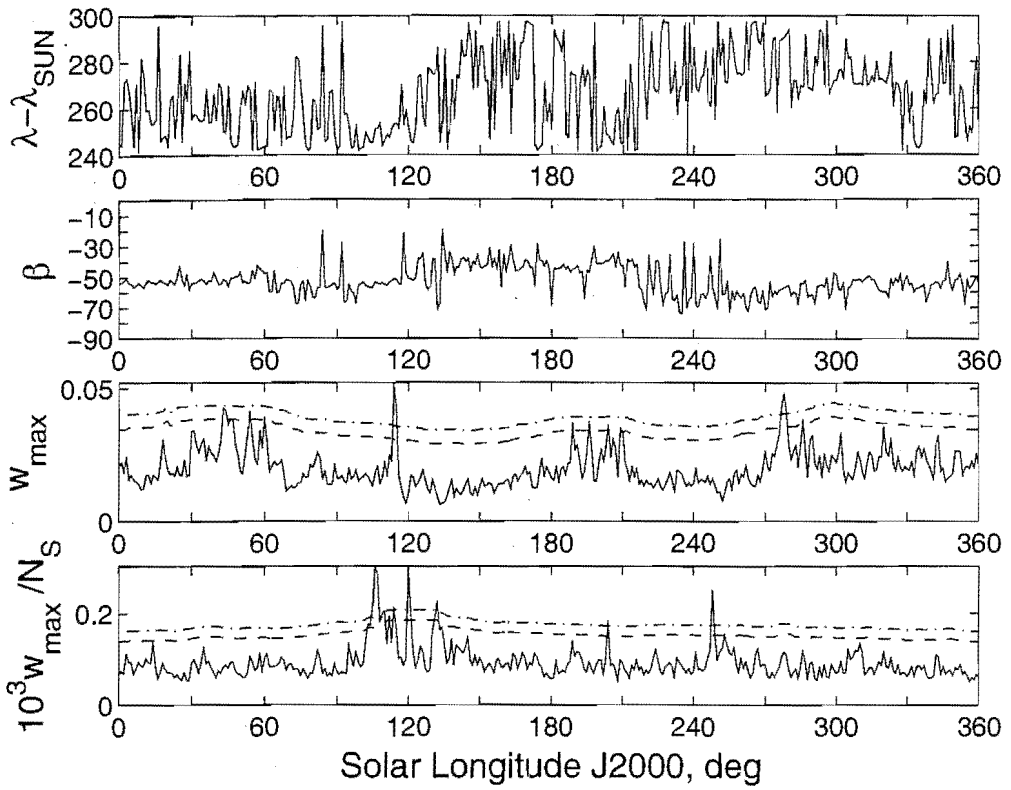

(m) Prograde Apex Region. $(V_G, \Delta\lambda_\odot, a) = ([0, \infty)\ \mathrm{km\,s^{-1}}, \pm 1°, 3°)$.

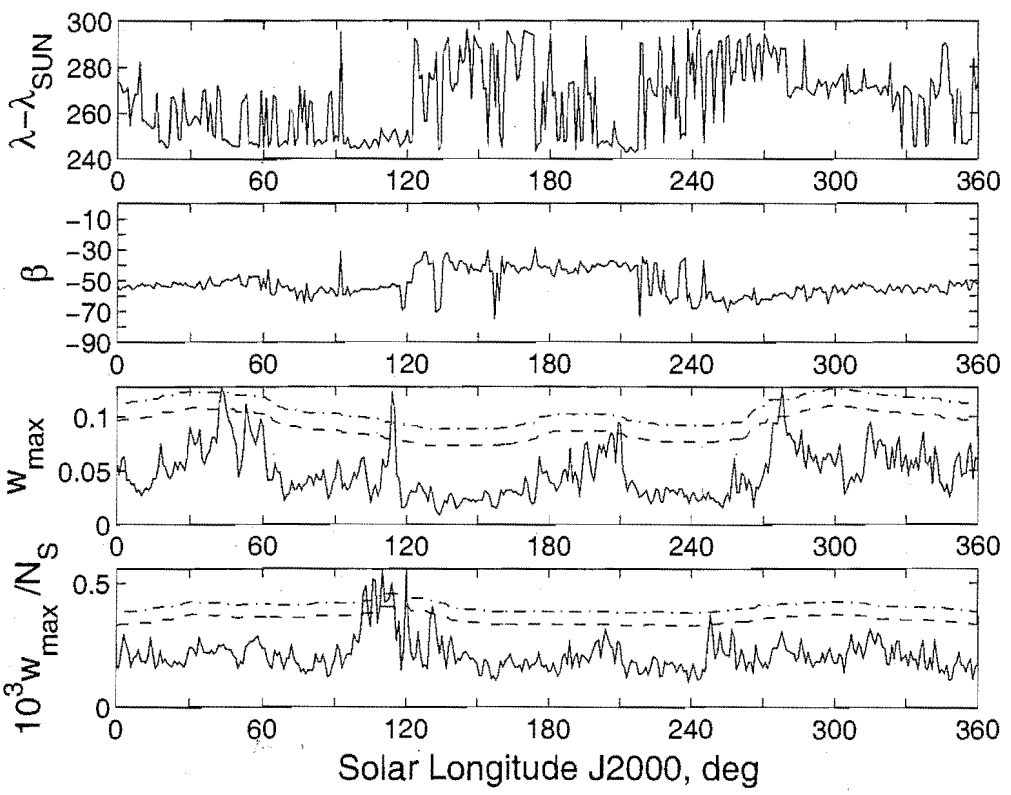

(n) Prograde Apex Region. $(V_G, \Delta\lambda_\odot, a) = ([0, \infty)\ \mathrm{km\,s^{-1}}, \pm 1°, 6°)$.

Figure G.3: *continued.*

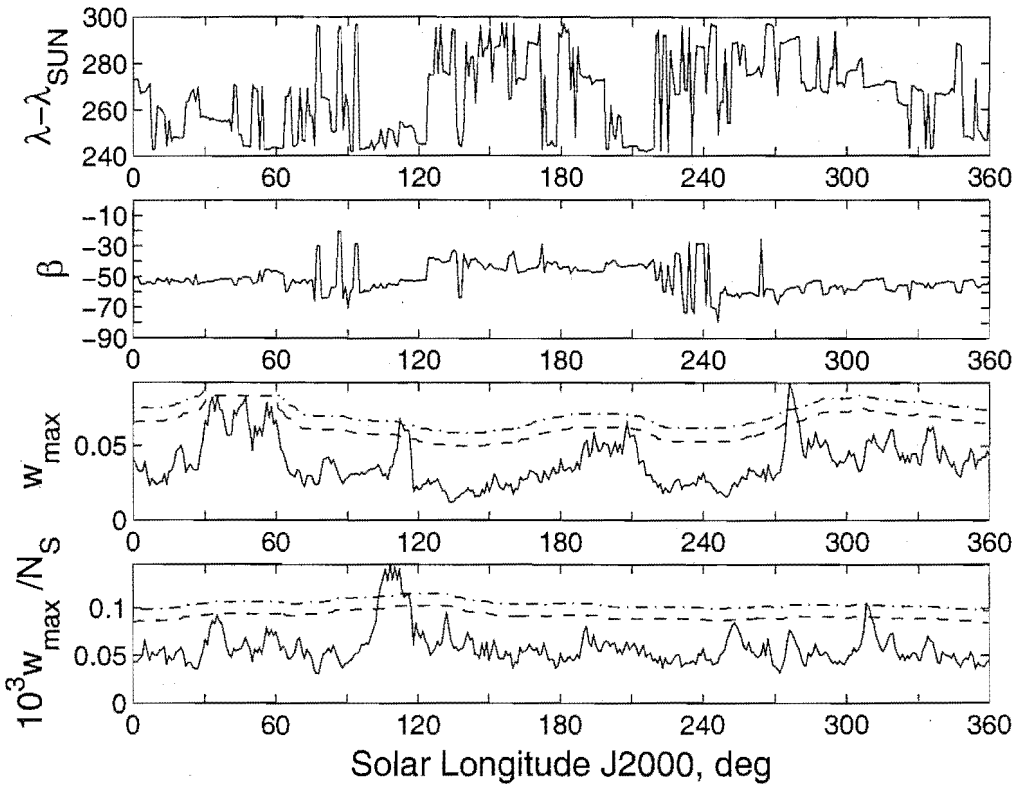

(o) Prograde Apex Region. $(V_G, \Delta\lambda_\odot, a) = ([0, \infty)\ \mathrm{km\,s^{-1}}, \pm 3°, 3°)$.

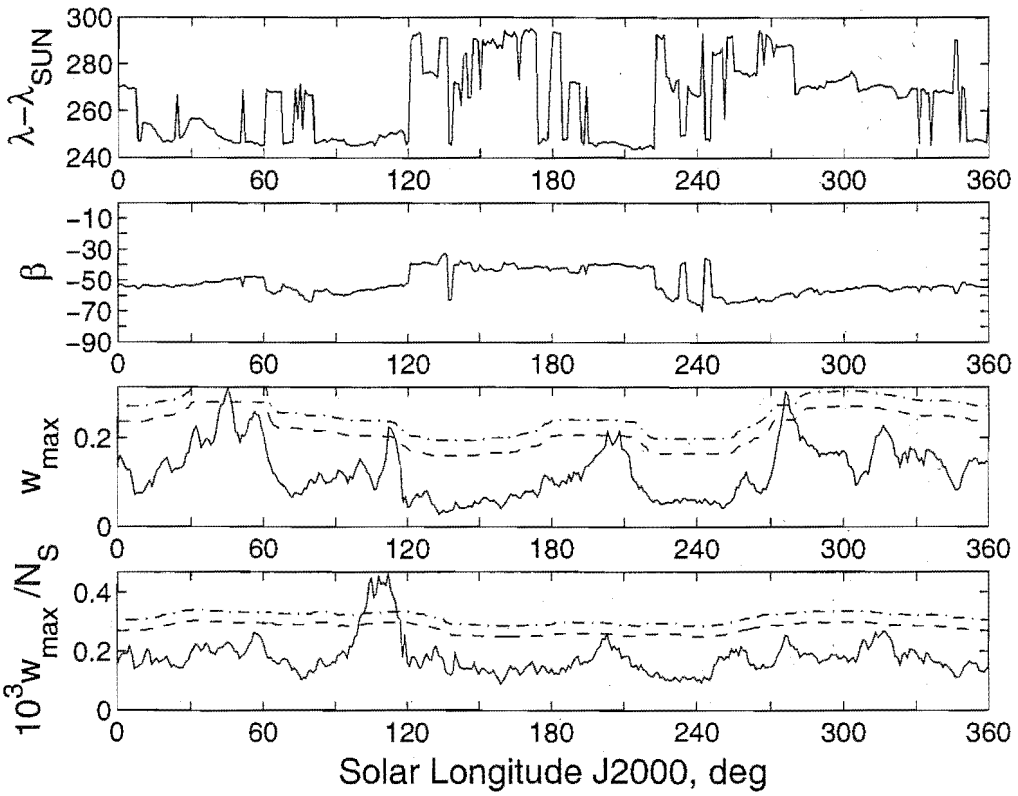

(p) Prograde Apex Region. $(V_G, \Delta\lambda_\odot, a) = ([0, \infty)\ \mathrm{km\,s^{-1}}, \pm 3°, 6°)$.

Figure G.3: *continued.*

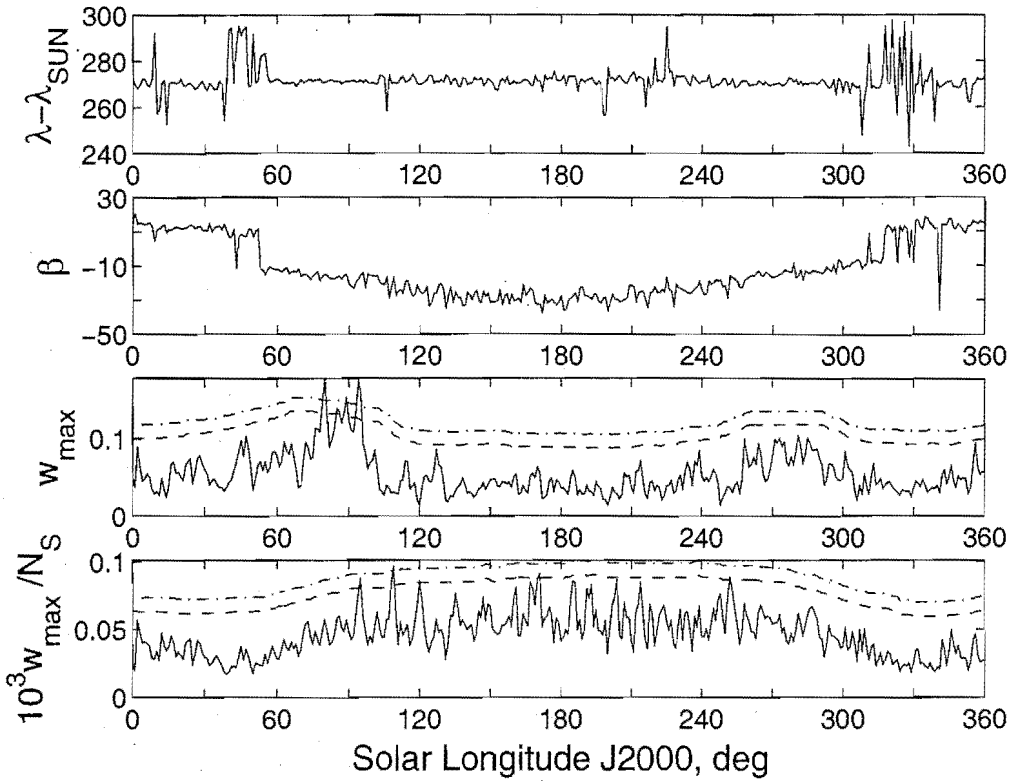

(a) Retrograde Apex Region. $(V_G, \Delta\lambda_\odot, a) = (50 \pm 10\ \mathrm{km\,s^{-1}}, \pm 1°, 3°)$.

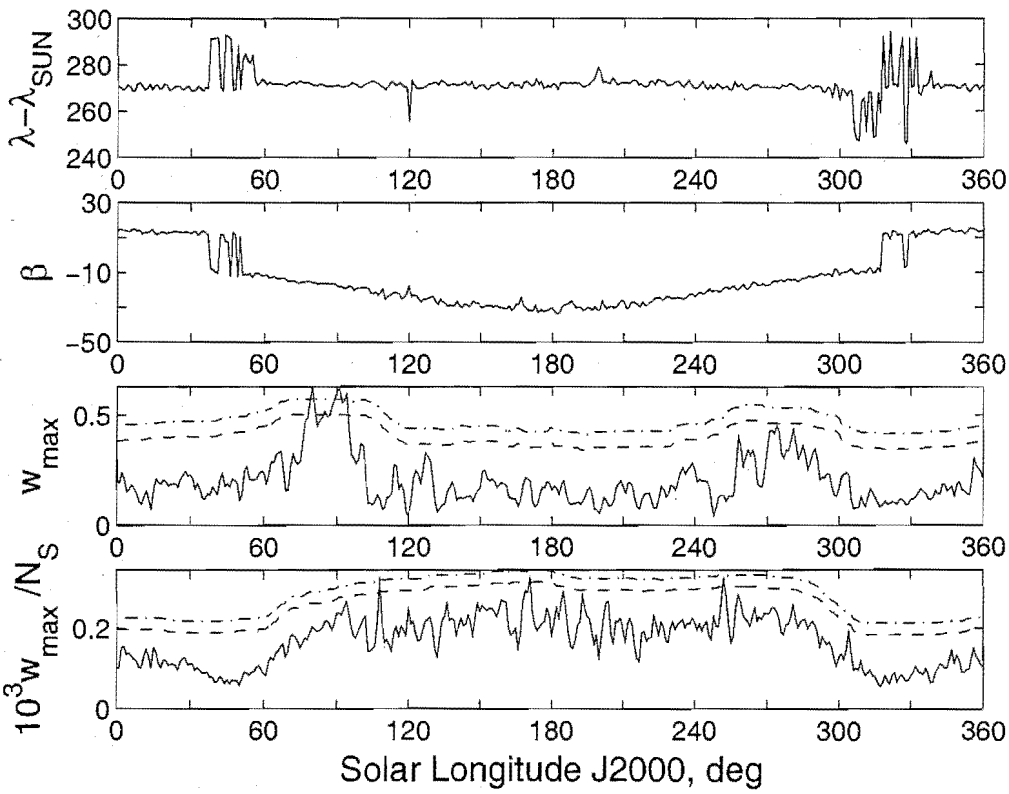

(b) Retrograde Apex Region. $(V_G, \Delta\lambda_\odot, a) = (50 \pm 10\ \mathrm{km\,s^{-1}}, \pm 1°, 6°)$.

Figure G.4: A wavelet transform enhanced search of the retrograde apex region using two wavelet scales (a), two time windows ($\Delta\lambda_\odot$) and four speed (V_G) partitions in all possible combinations.

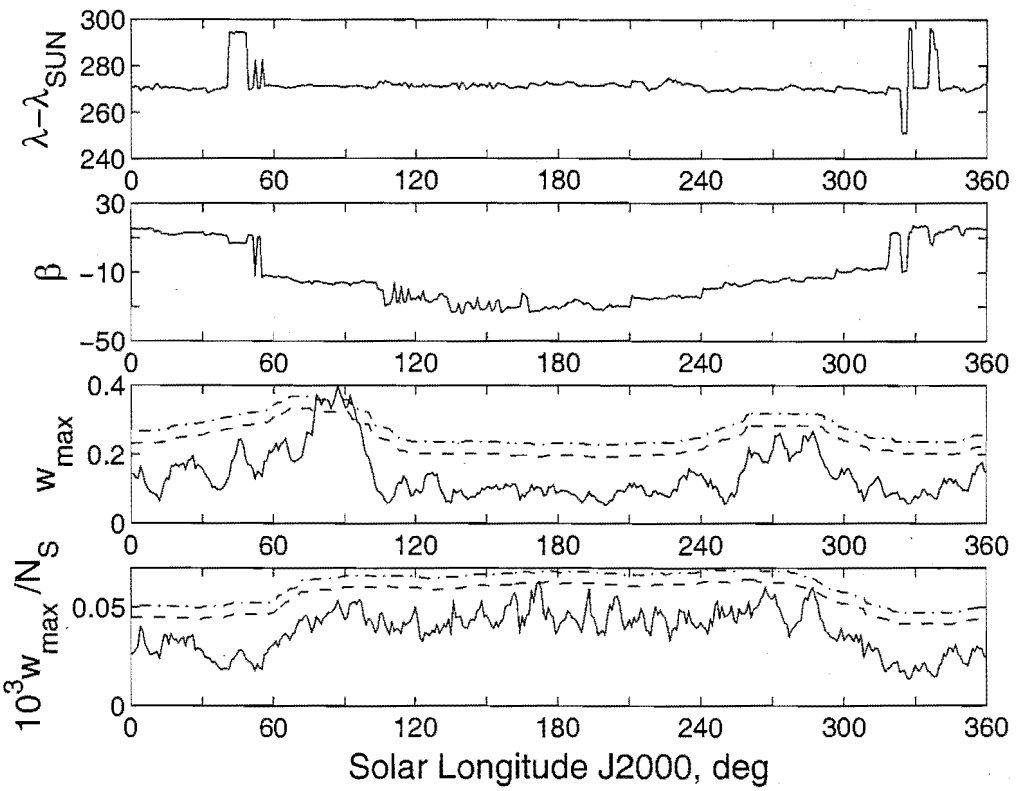

(c) Retrograde Apex Region. $(V_G, \Delta\lambda_\odot, a) = (50 \pm 10\ \mathrm{km\,s^{-1}}, \pm 3°, 3°)$.

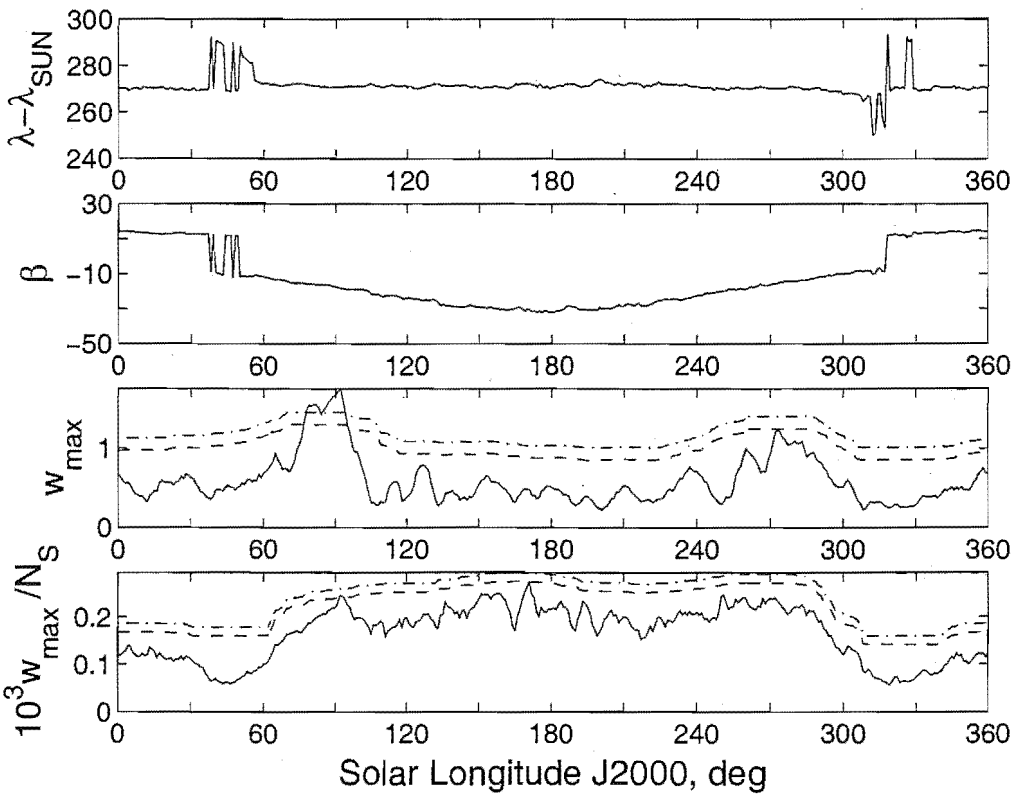

(d) Retrograde Apex Region. $(V_G, \Delta\lambda_\odot, a) = (50 \pm 10\ \mathrm{km\,s^{-1}}, \pm 3°, 6°)$.

Figure G.4: *continued.*

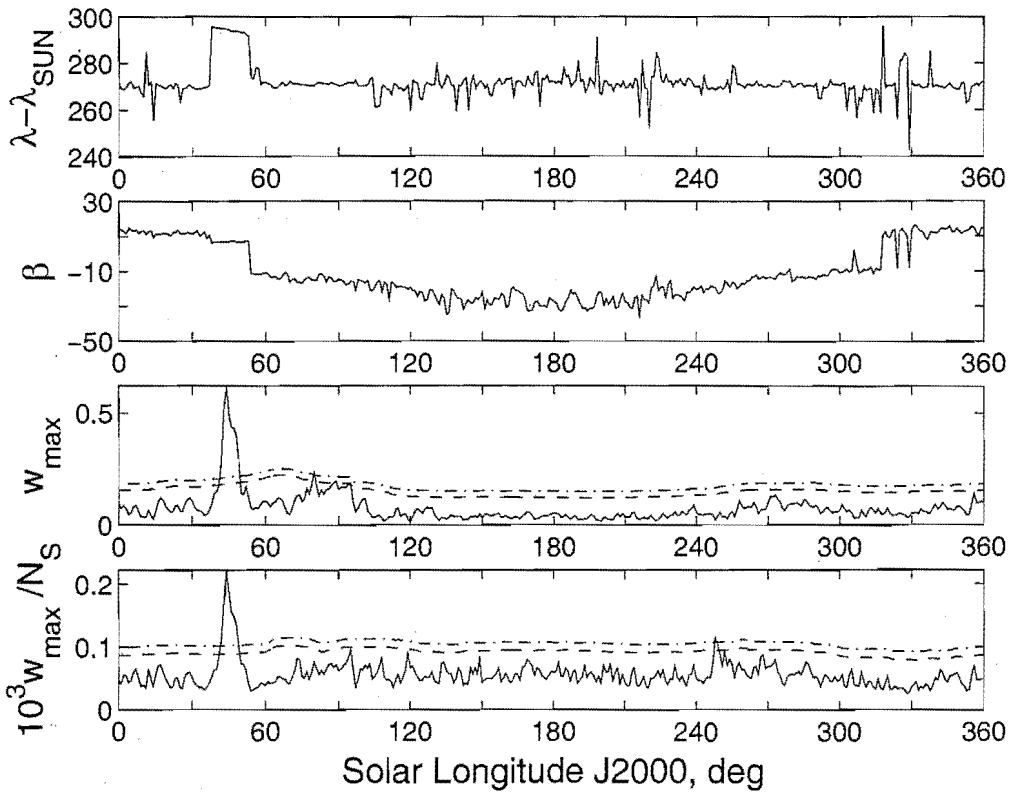

(e) Retrograde Apex Region. $(V_G, \Delta\lambda_\odot, a) = (60 \pm 10\ \mathrm{km\,s^{-1}}, \pm 1°, 3°)$.

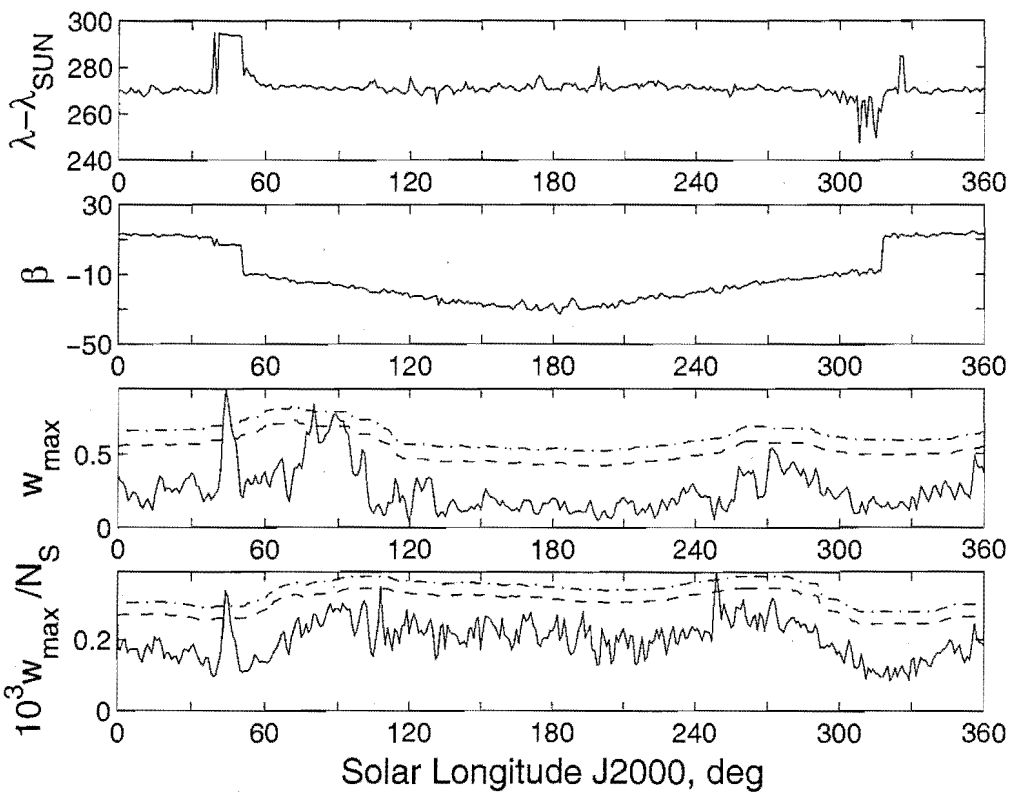

(f) Retrograde Apex Region. $(V_G, \Delta\lambda_\odot, a) = (60 \pm 10\ \mathrm{km\,s^{-1}}, \pm 1°, 6°)$.

Figure G.4: *continued.*

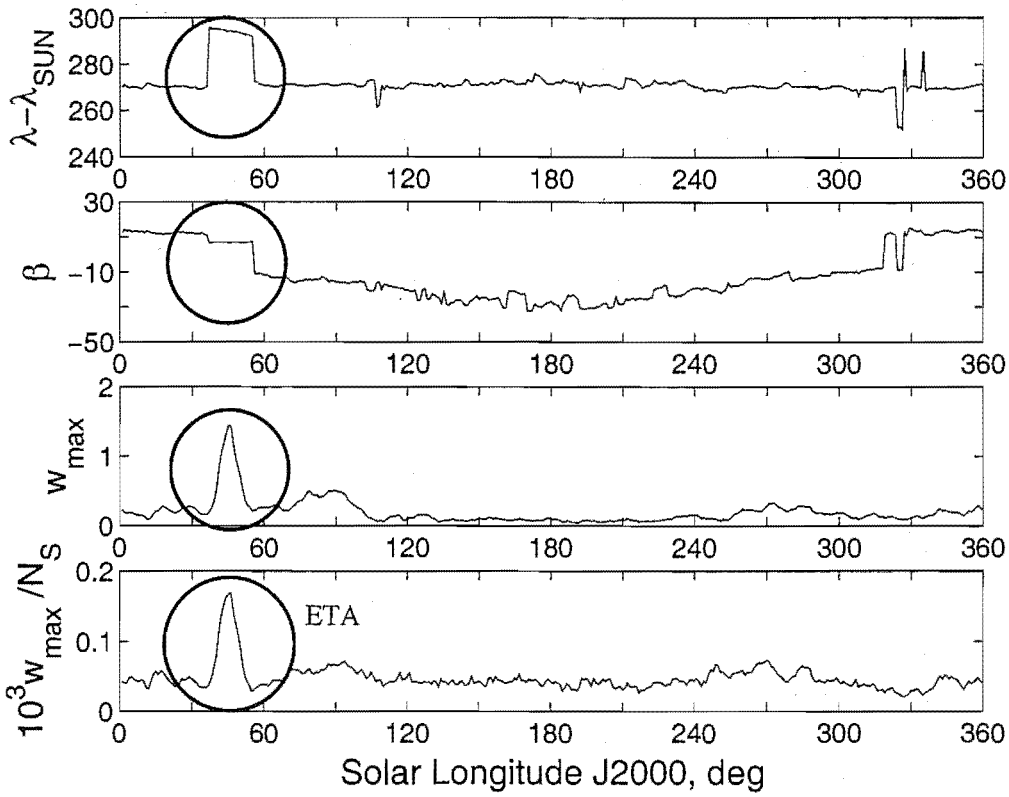

(g) Retrograde Apex Region. $(V_G, \Delta\lambda_\odot, a) = (60 \pm 10\ \mathrm{km\,s^{-1}}, \pm 3°, 3°)$.

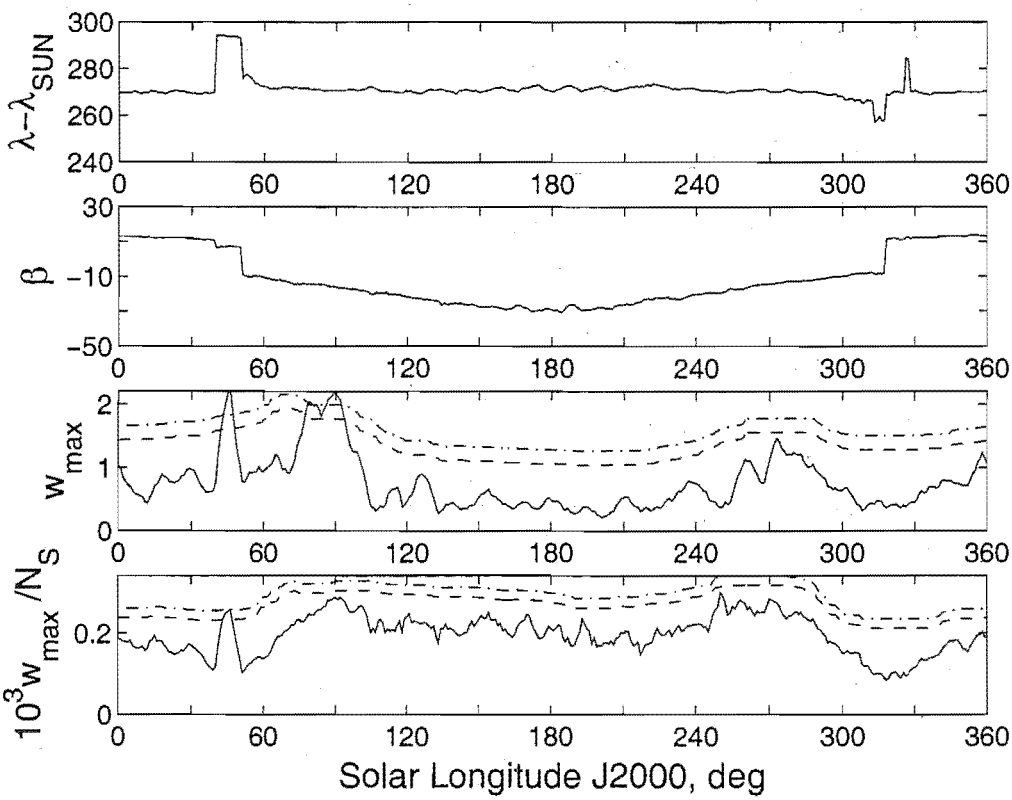

(h) Retrograde Apex Region. $(V_G, \Delta\lambda_\odot, a) = (60 \pm 10\ \mathrm{km\,s^{-1}}, \pm 3°, 6°)$.

Figure G.4: *continued.*

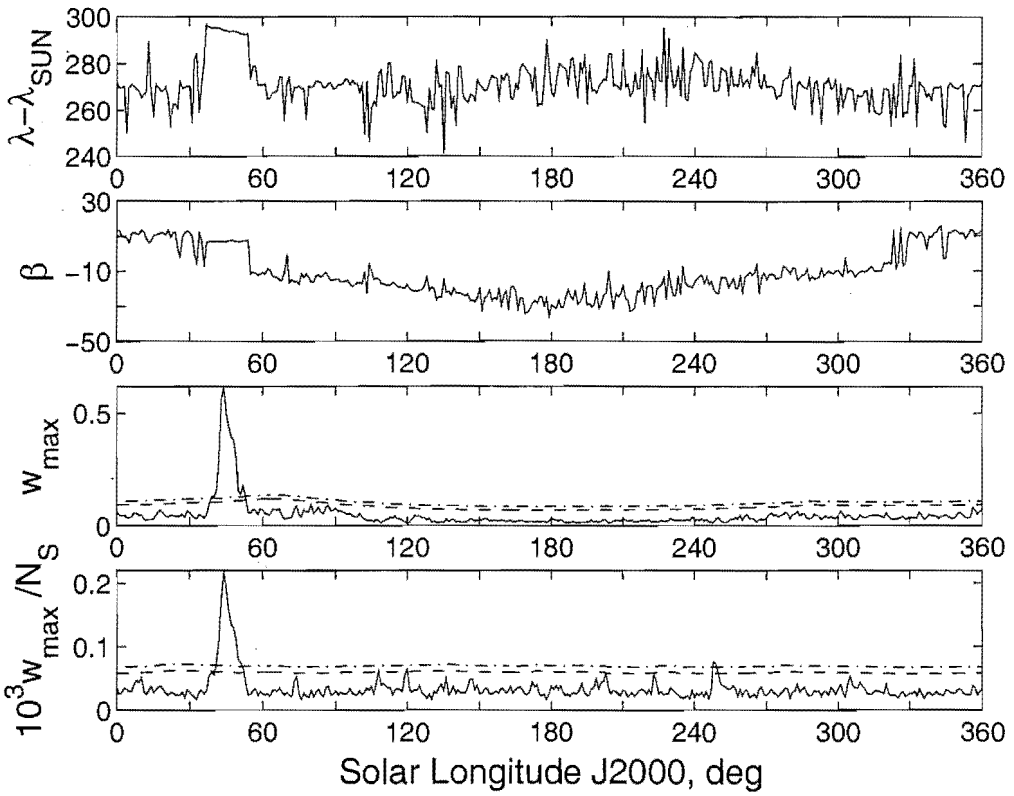

(i) Retrograde Apex Region. $(V_G, \Delta\lambda_\odot, a) = (70 \pm 10\ \mathrm{km\,s^{-1}}, \pm 1°, 3°)$.

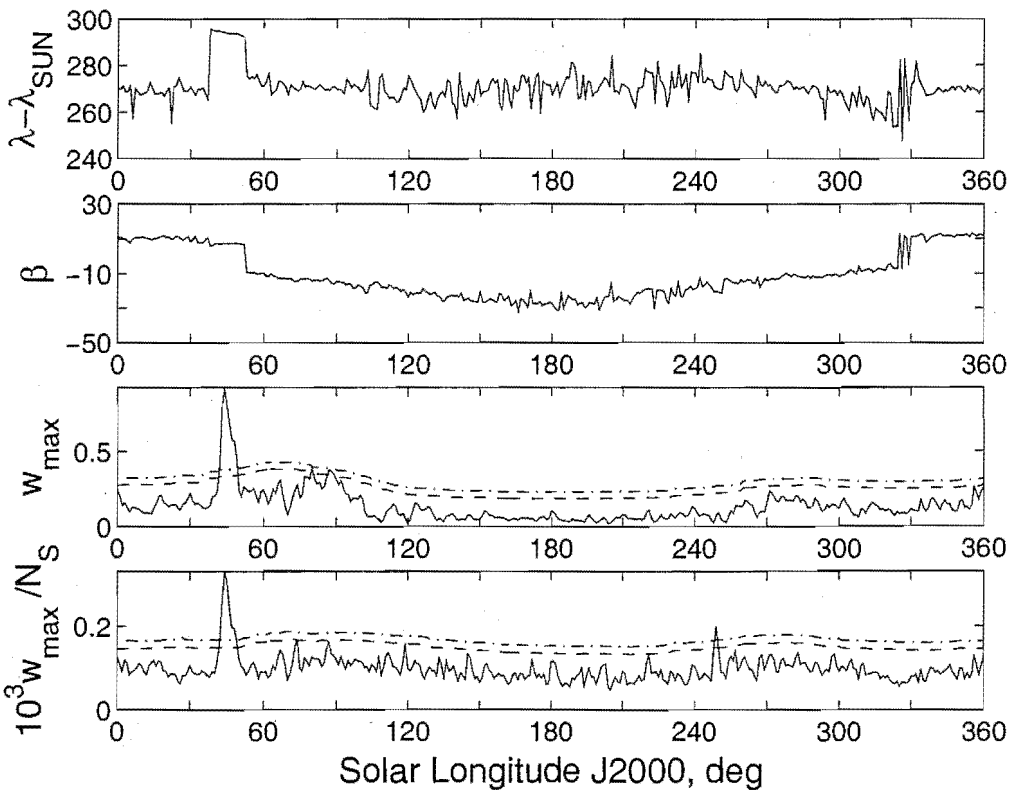

(j) Retrograde Apex Region. $(V_G, \Delta\lambda_\odot, a) = (70 \pm 10\ \mathrm{km\,s^{-1}}, \pm 1°, 6°)$.

Figure G.4: *continued.*

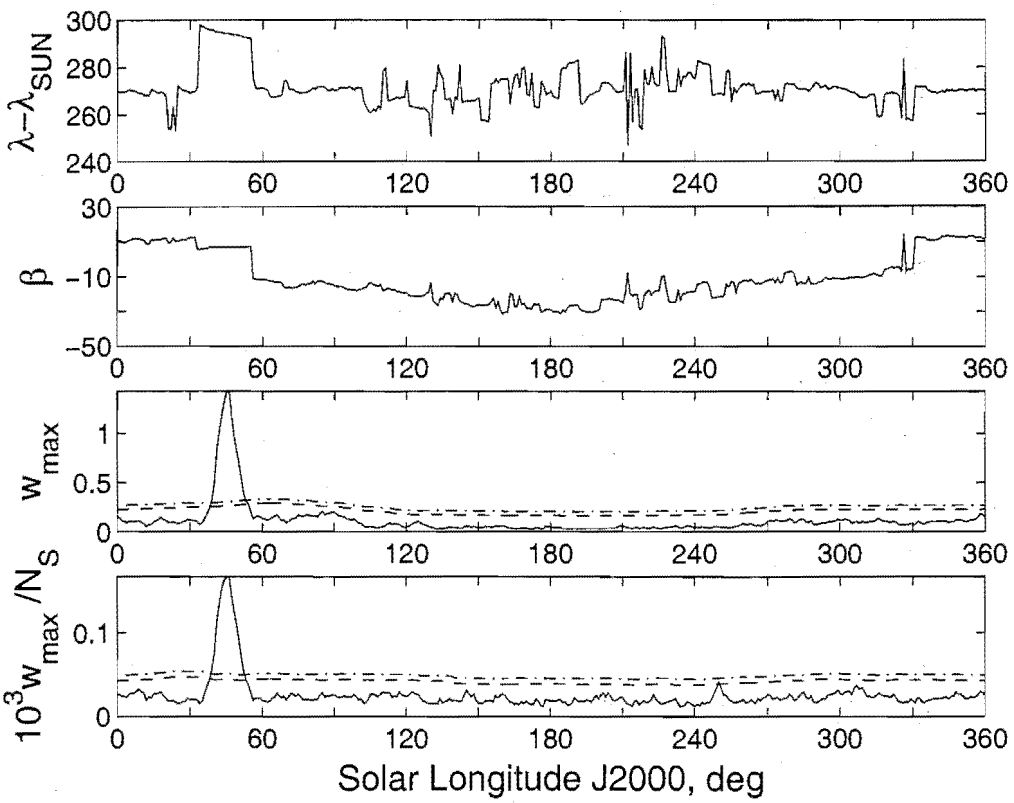

(k) Retrograde Apex Region. $(V_G, \Delta\lambda_\odot, a) = (70 \pm 10\ \mathrm{km\,s^{-1}}, \pm 3°, 3°)$.

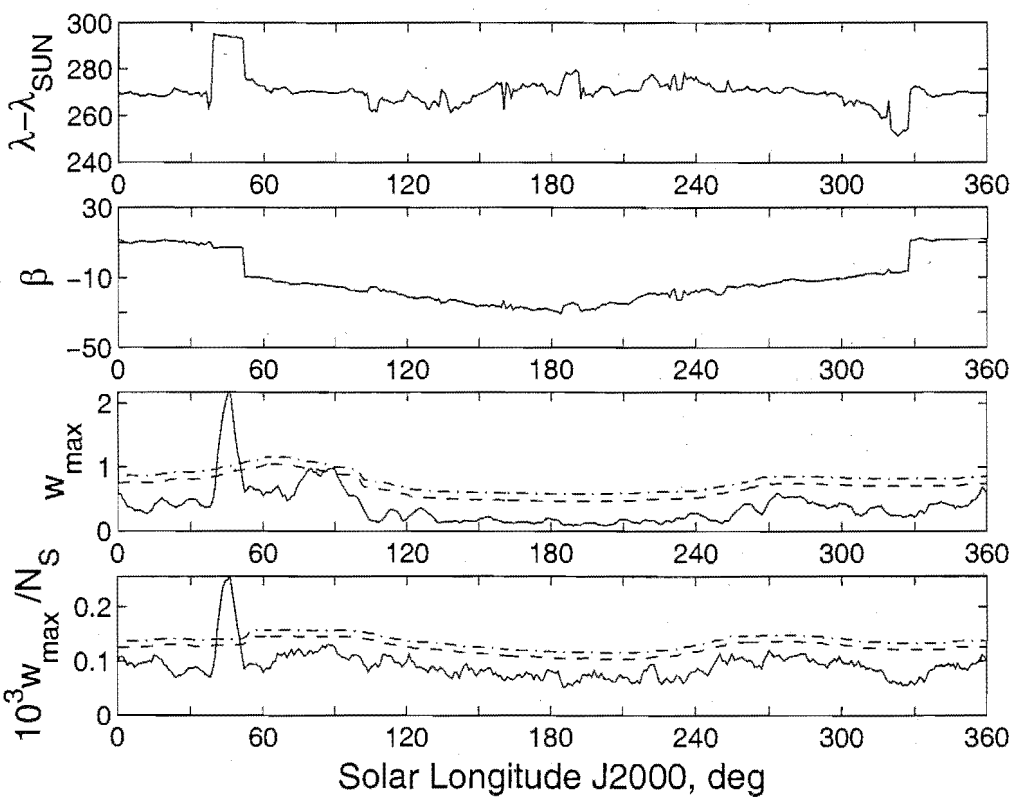

(l) Retrograde Apex Region. $(V_G, \Delta\lambda_\odot, a) = (70 \pm 10\ \mathrm{km\,s^{-1}}, \pm 3°, 6°)$.

Figure G.4: *continued.*

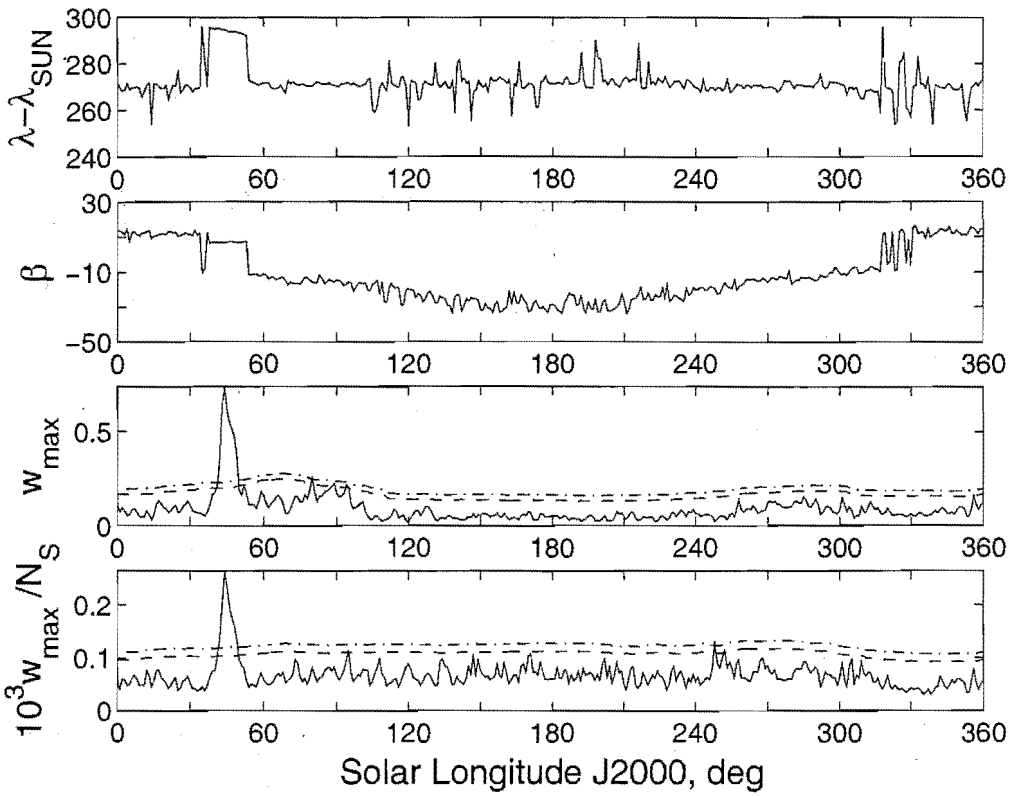

(m) Retrograde Apex Region. $(V_G, \Delta\lambda_\odot, a) = ([0, \infty)\ \mathrm{km\,s^{-1}}, \pm 1°, 3°)$.

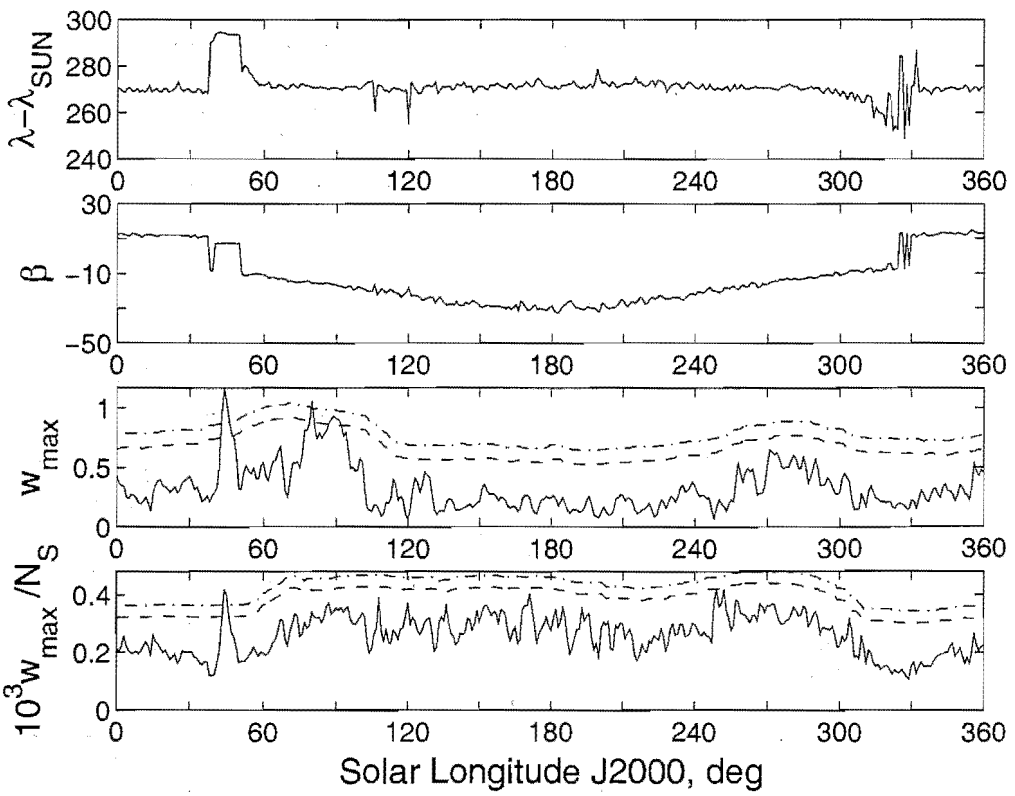

(n) Retrograde Apex Region. $(V_G, \Delta\lambda_\odot, a) = ([0, \infty)\ \mathrm{km\,s^{-1}}, \pm 1°, 6°)$.

Figure G.4: *continued.*

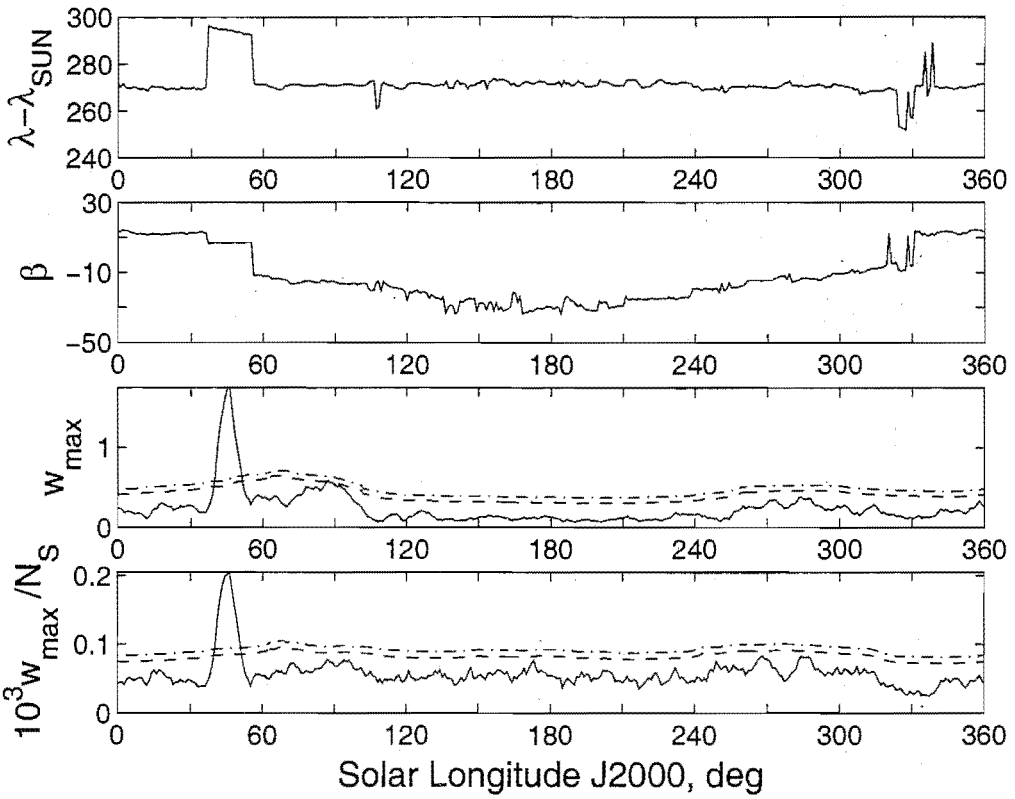

(o) Retrograde Apex Region. $(V_G, \Delta\lambda_\odot, a) = ([0, \infty)\ \mathrm{km\,s^{-1}}, \pm 3°, 3°)$.

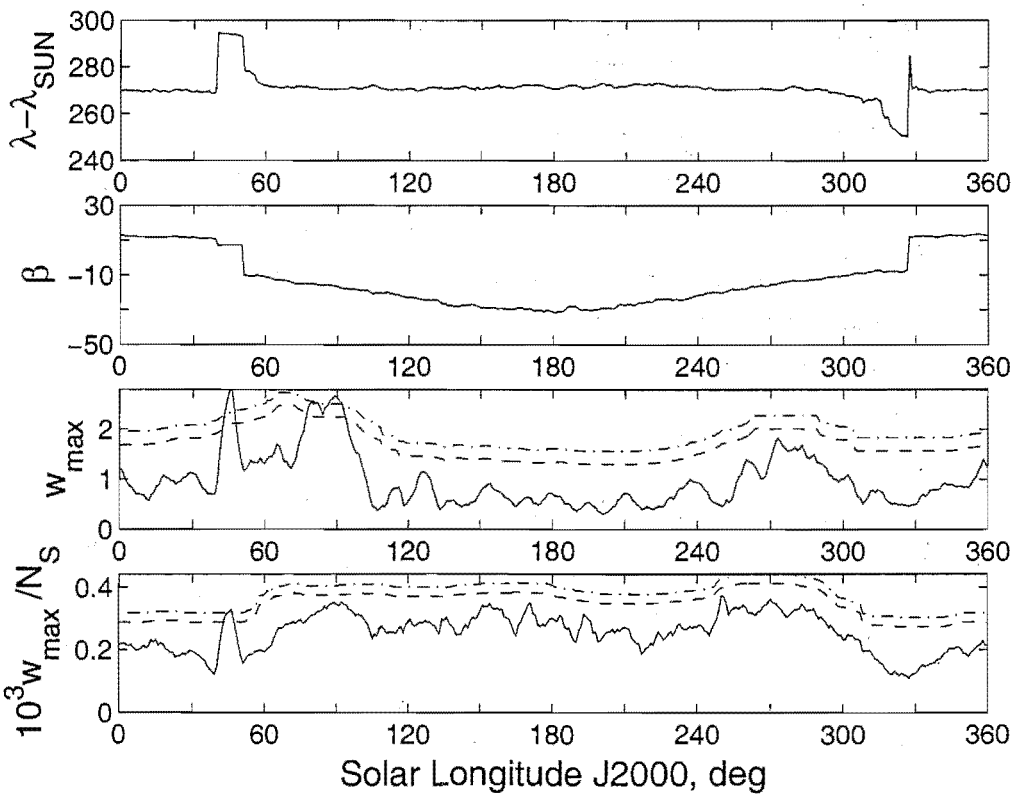

(p) Retrograde Apex Region. $(V_G, \Delta\lambda_\odot, a) = ([0, \infty)\ \mathrm{km\,s^{-1}}, \pm 3°, 6°)$.

Figure G.4: *continued.*

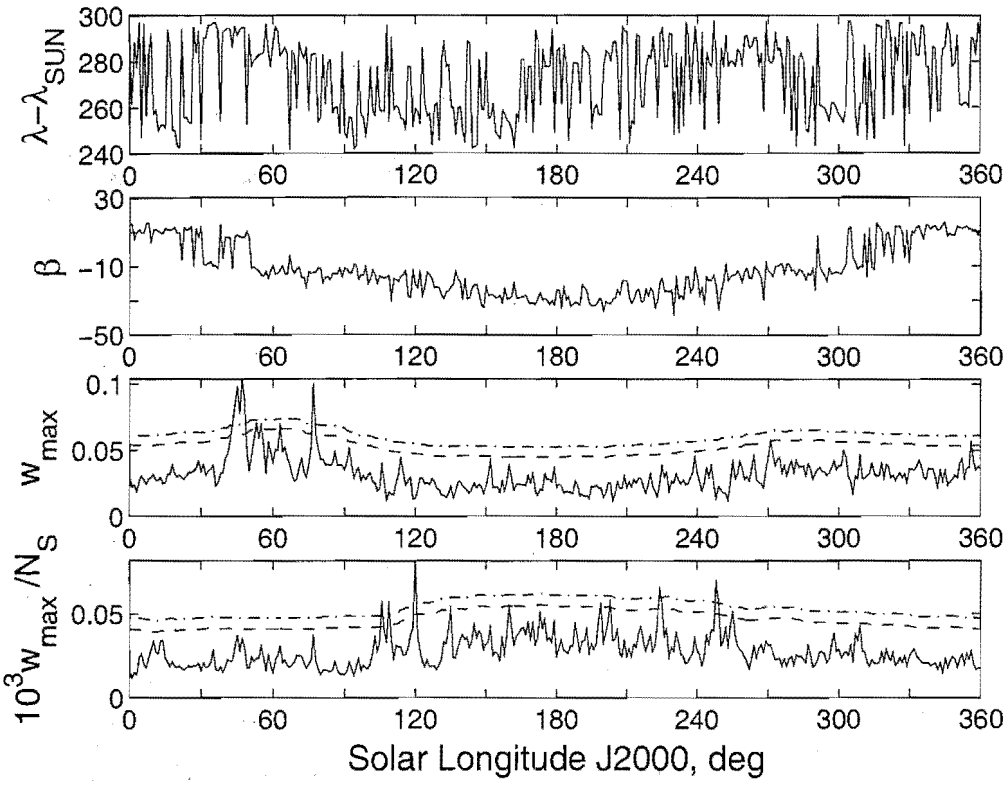

(a) Retrograde Apex Region (Blanked). $(V_G, \Delta\lambda_\odot, a) = (50 \pm 10\ \mathrm{km\,s^{-1}}, \pm 1°, 3°)$.

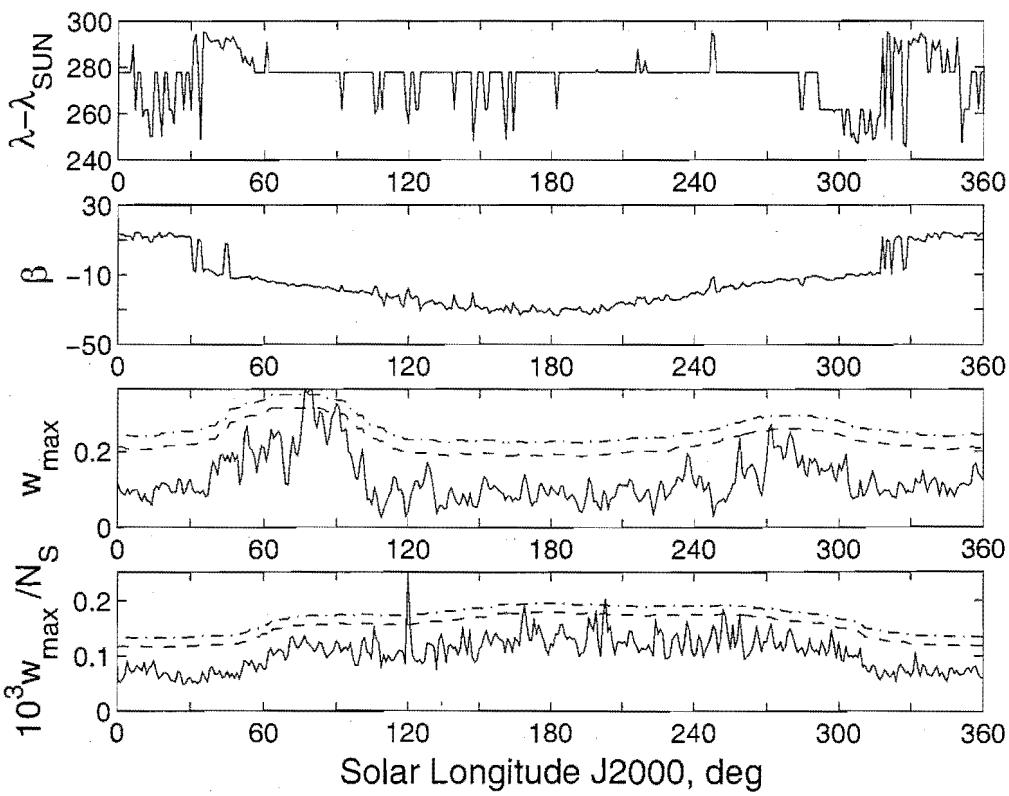

(b) Retrograde Apex Region (Blanked). $(V_G, \Delta\lambda_\odot, a) = (50 \pm 10\ \mathrm{km\,s^{-1}}, \pm 1°, 6°)$.

Figure G.5: A wavelet transform enhanced search of the retrograde apex region, with blanked direct apex longitude over $(\lambda - \lambda_\odot) = 270° \pm 7.5°$, using two wavelet scales (a), two time windows $(\Delta\lambda_\odot)$ and four speed (V_G) partitions in all possible combinations.

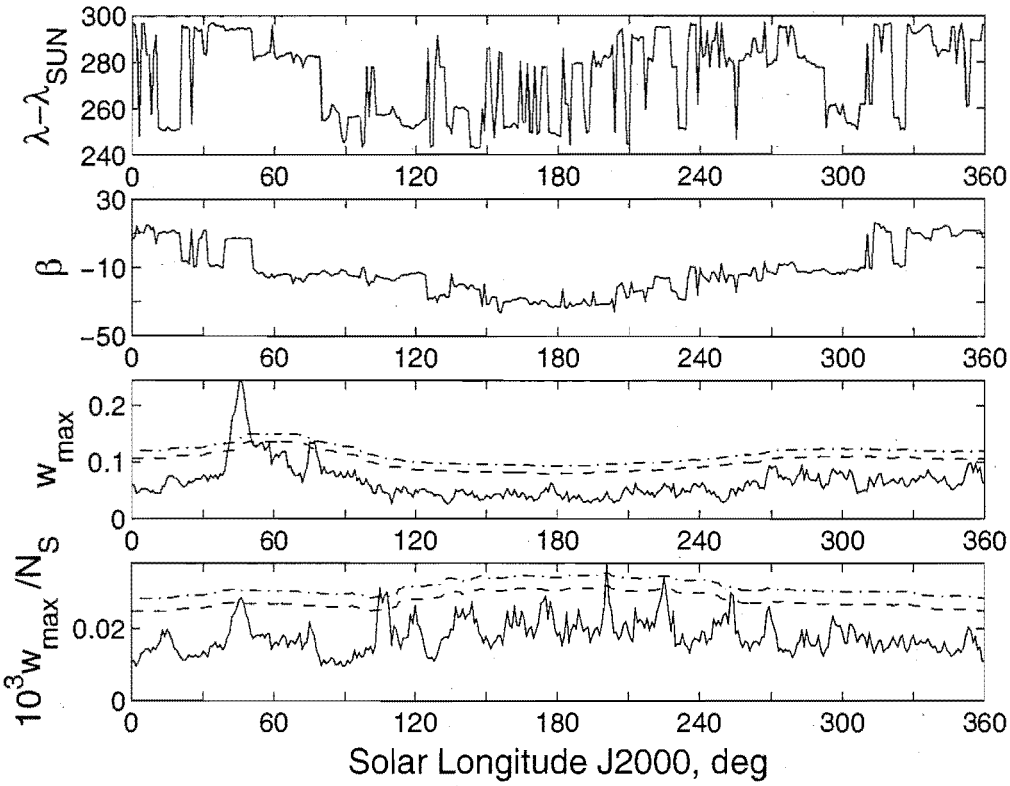

(c) Retrograde Apex Region (Blanked). $(V_G, \Delta\lambda_\odot, a) = (50 \pm 10\ \mathrm{km\,s^{-1}}, \pm 3°, 3°)$.

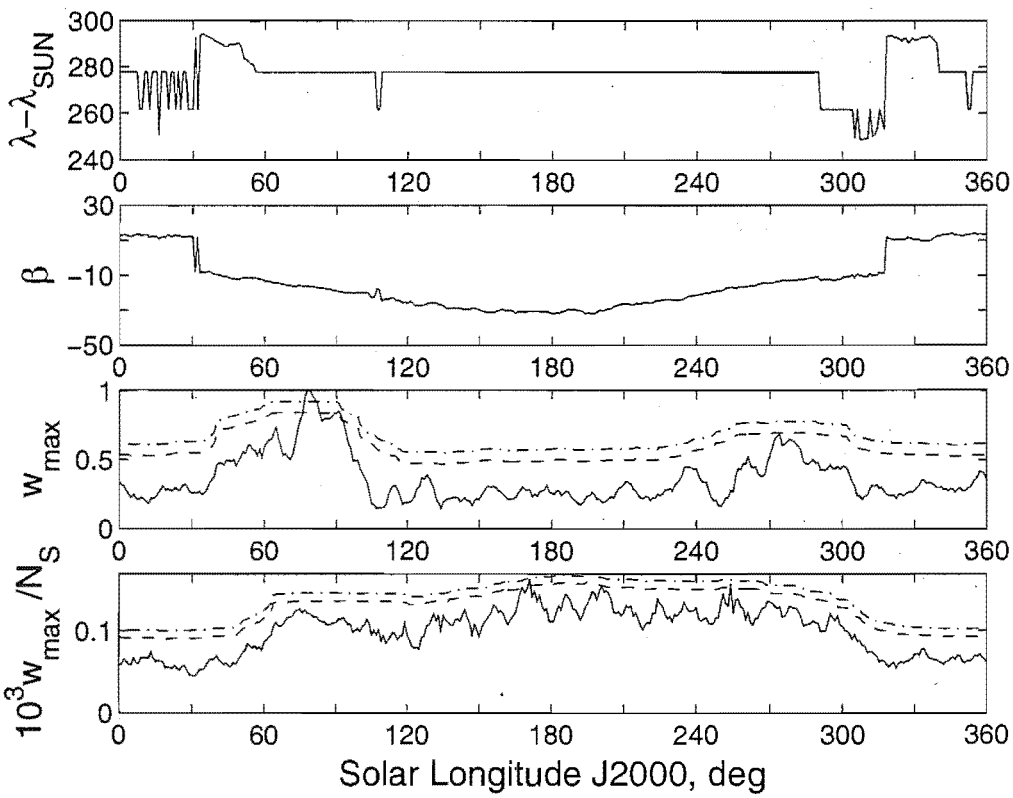

(d) Retrograde Apex Region (Blanked). $(V_G, \Delta\lambda_\odot, a) = (50 \pm 10\ \mathrm{km\,s^{-1}}, \pm 3°, 6°)$.

Figure G.5: *continued.*

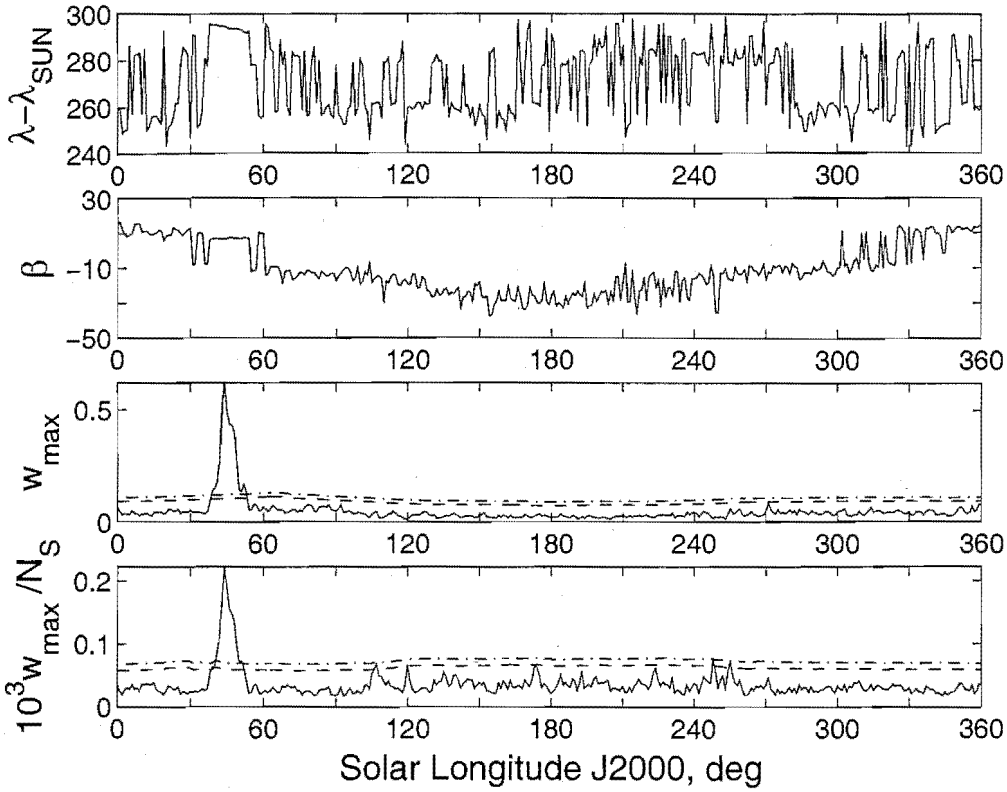

(e) Retrograde Apex Region (Blanked). $(V_G, \Delta\lambda_\odot, a) = (60 \pm 10\ \mathrm{km\,s^{-1}}, \pm 1°, 3°)$.

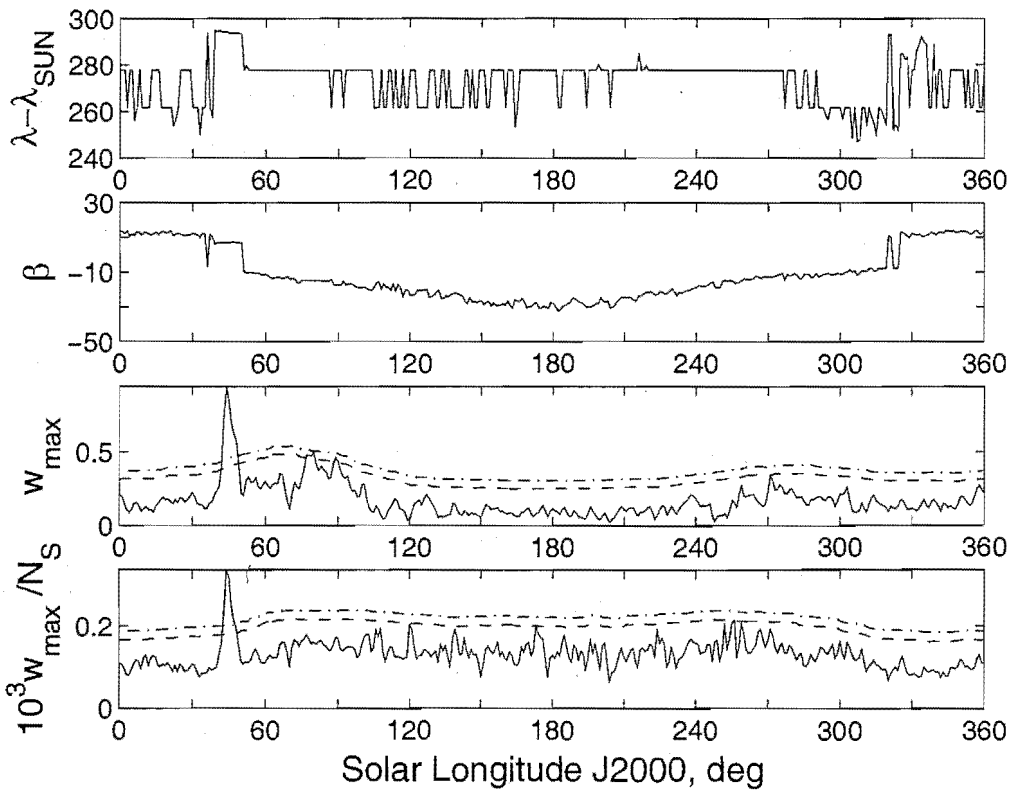

(f) Retrograde Apex Region (Blanked). $(V_G, \Delta\lambda_\odot, a) = (60 \pm 10\ \mathrm{km\,s^{-1}}, \pm 1°, 6°)$.

Figure G.5: *continued.*

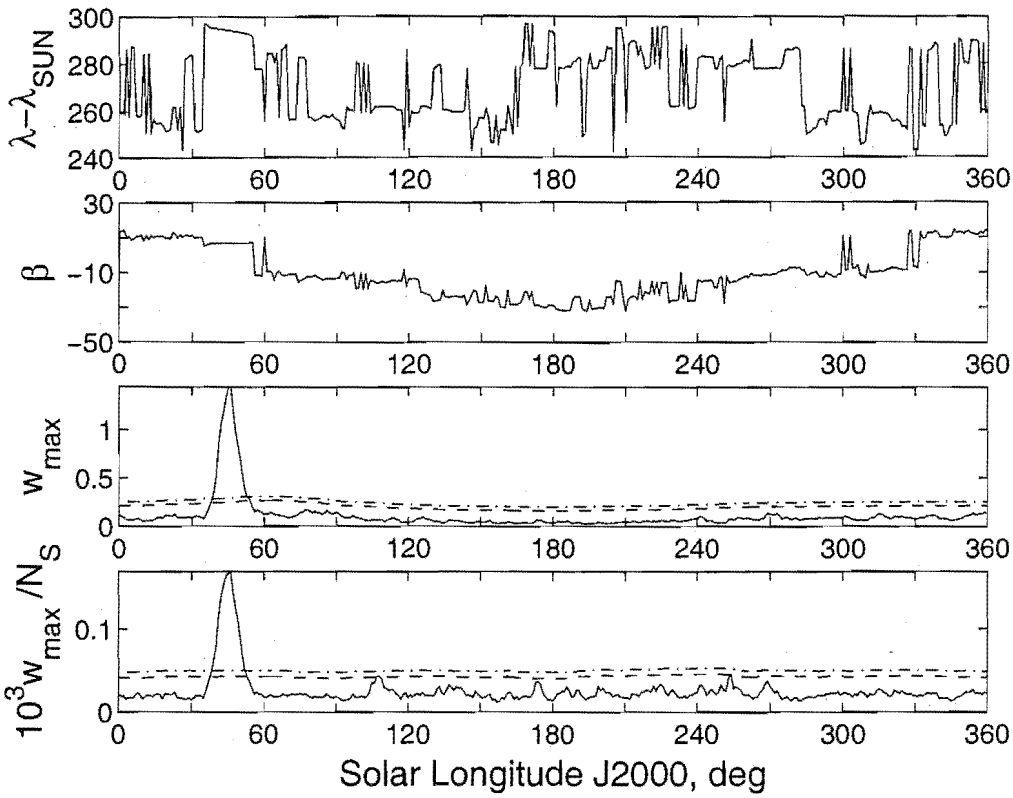

(g) Retrograde Apex Region (Blanked). $(V_G, \Delta\lambda_\odot, a) = (60 \pm 10\ \mathrm{km\,s^{-1}}, \pm 3°, 3°)$.

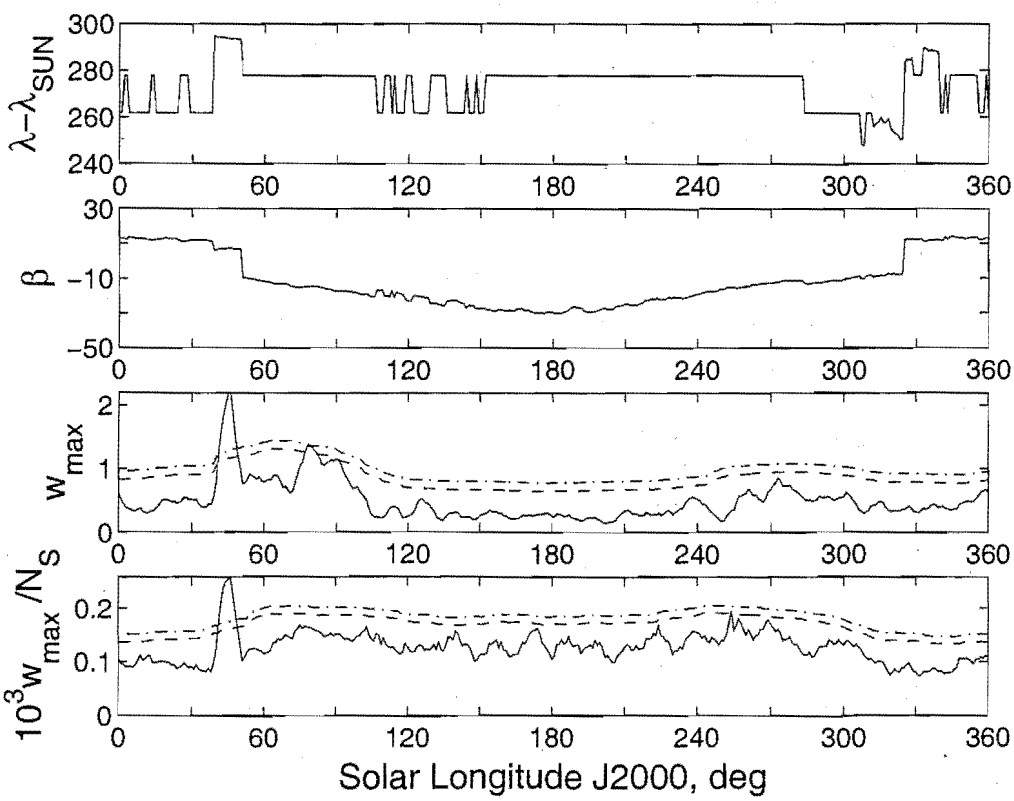

(h) Retrograde Apex Region (Blanked). $(V_G, \Delta\lambda_\odot, a) = (60 \pm 10\ \mathrm{km\,s^{-1}}, \pm 3°, 6°)$.

Figure G.5: *continued.*

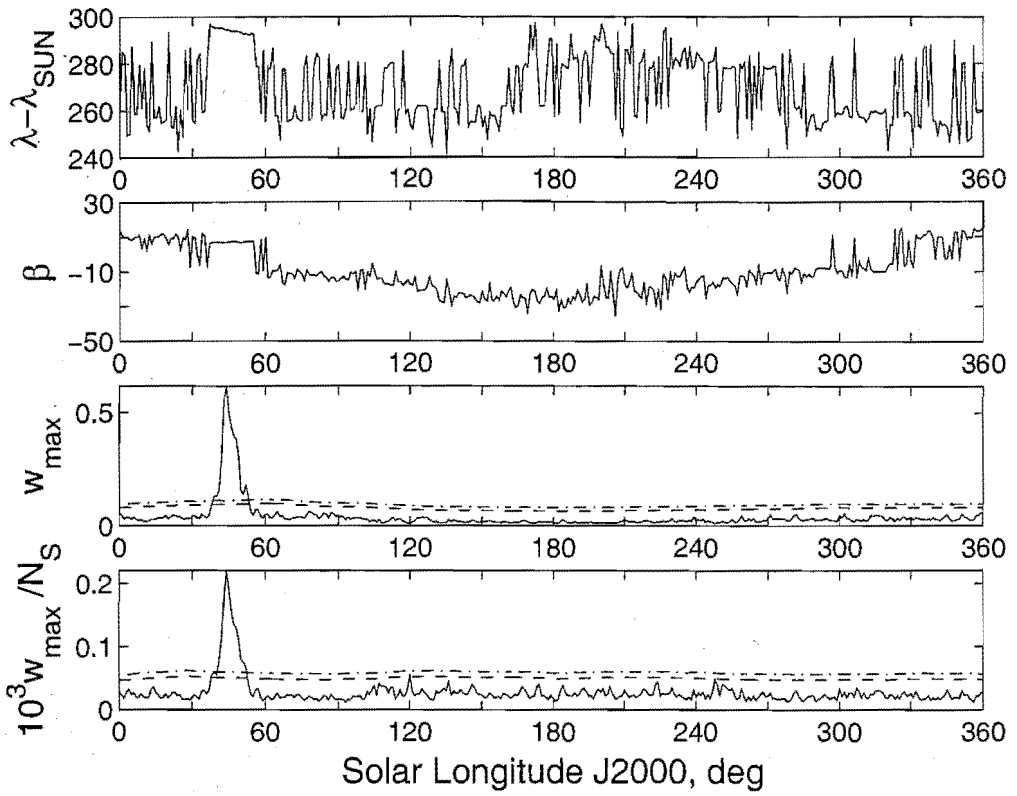

(i) Retrograde Apex Region (Blanked). $(V_G, \Delta\lambda_\odot, a) = (70 \pm 10\ \mathrm{km\,s^{-1}}, \pm 1°, 3°)$.

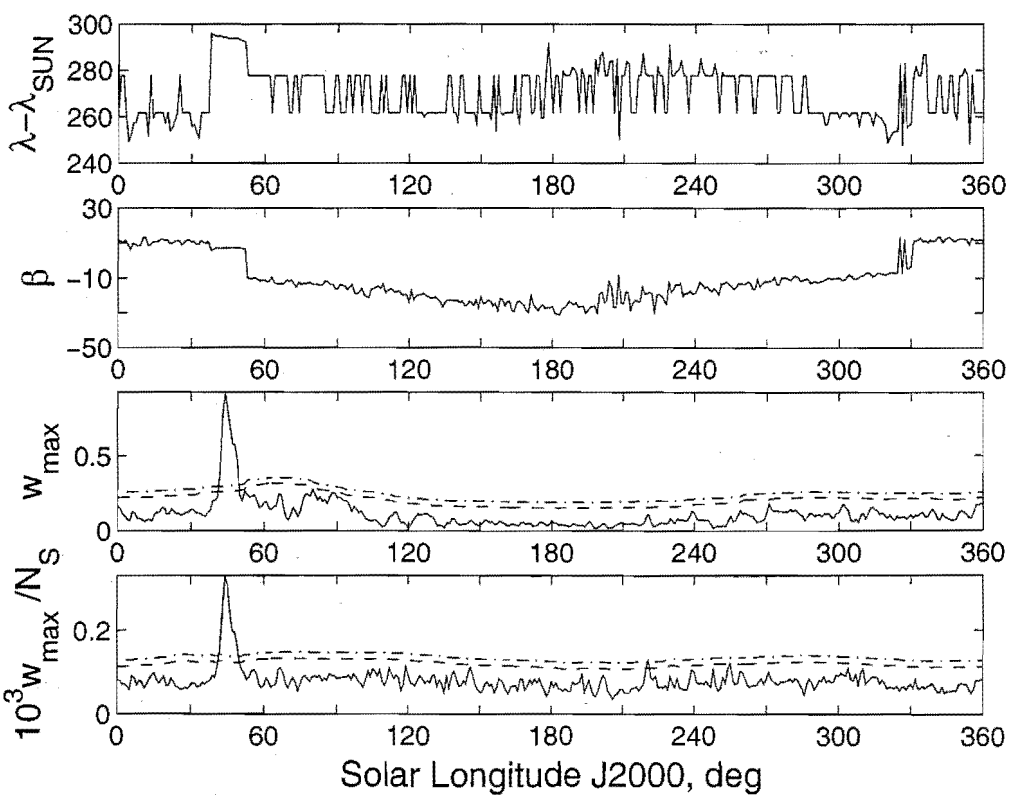

(j) Retrograde Apex Region (Blanked). $(V_G, \Delta\lambda_\odot, a) = (70 \pm 10\ \mathrm{km\,s^{-1}}, \pm 1°, 6°)$.

Figure G.5: *continued.*

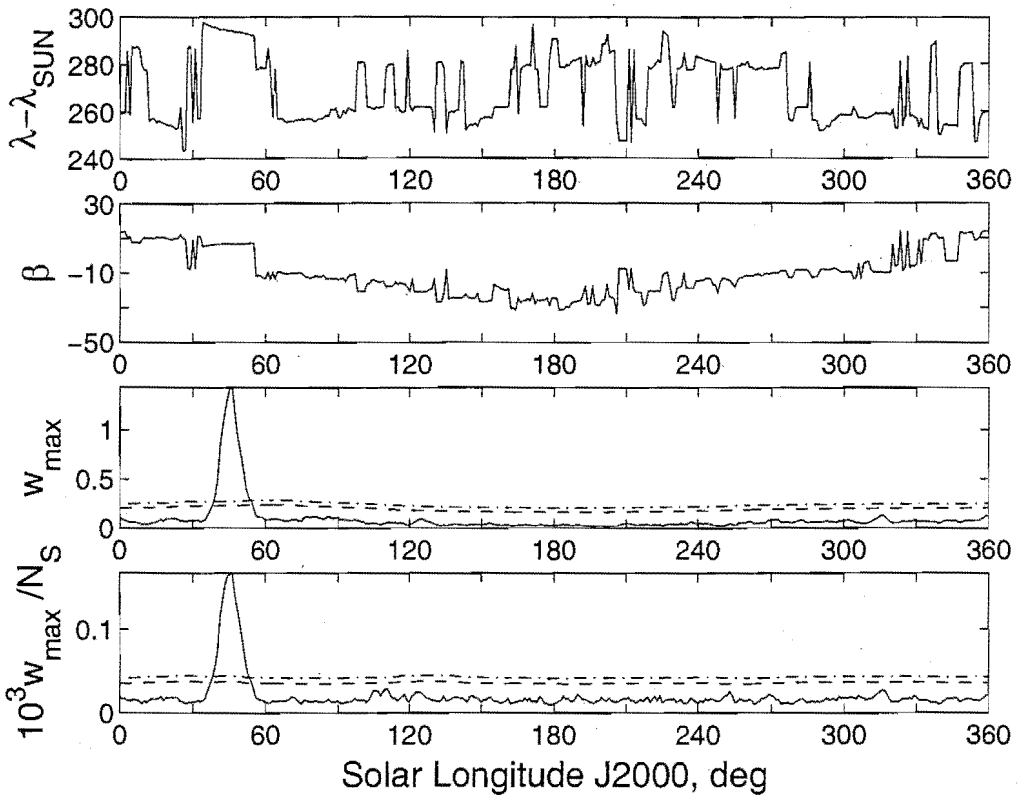

(k) Retrograde Apex Region (Blanked). $(V_G, \Delta\lambda_\odot, a) = (70 \pm 10\ \mathrm{km\,s^{-1}}, \pm 3°, 3°)$.

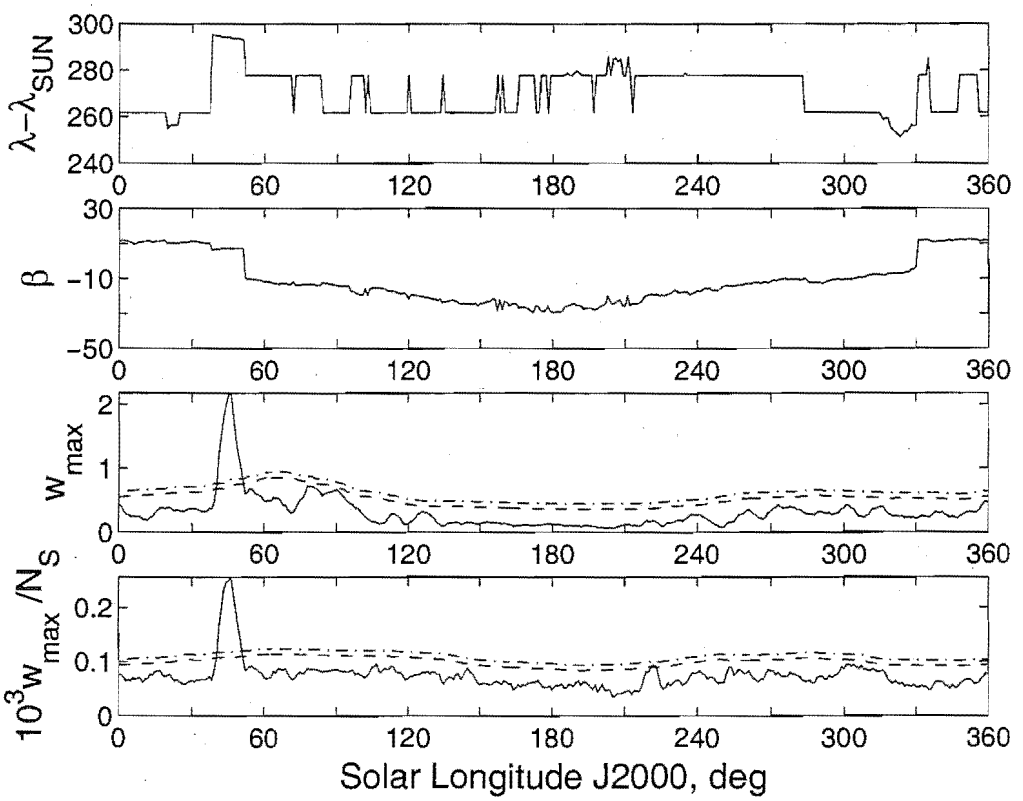

(l) Retrograde Apex Region (Blanked). $(V_G, \Delta\lambda_\odot, a) = (70 \pm 10\ \mathrm{km\,s^{-1}}, \pm 3°, 6°)$.

Figure G.5: *continued.*

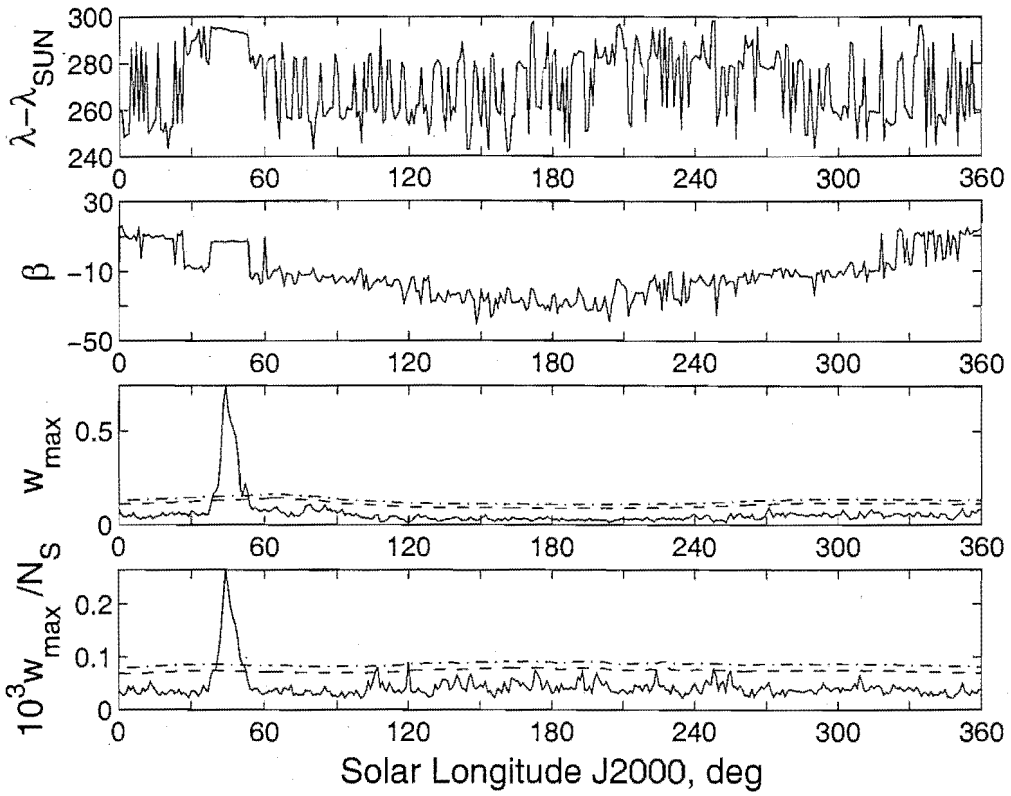

(m) Retrograde Apex Region (Blanked). $(V_G, \Delta\lambda_\odot, a) = ([0, \infty)\ \mathrm{km\,s^{-1}}, \pm 1°, 3°)$.

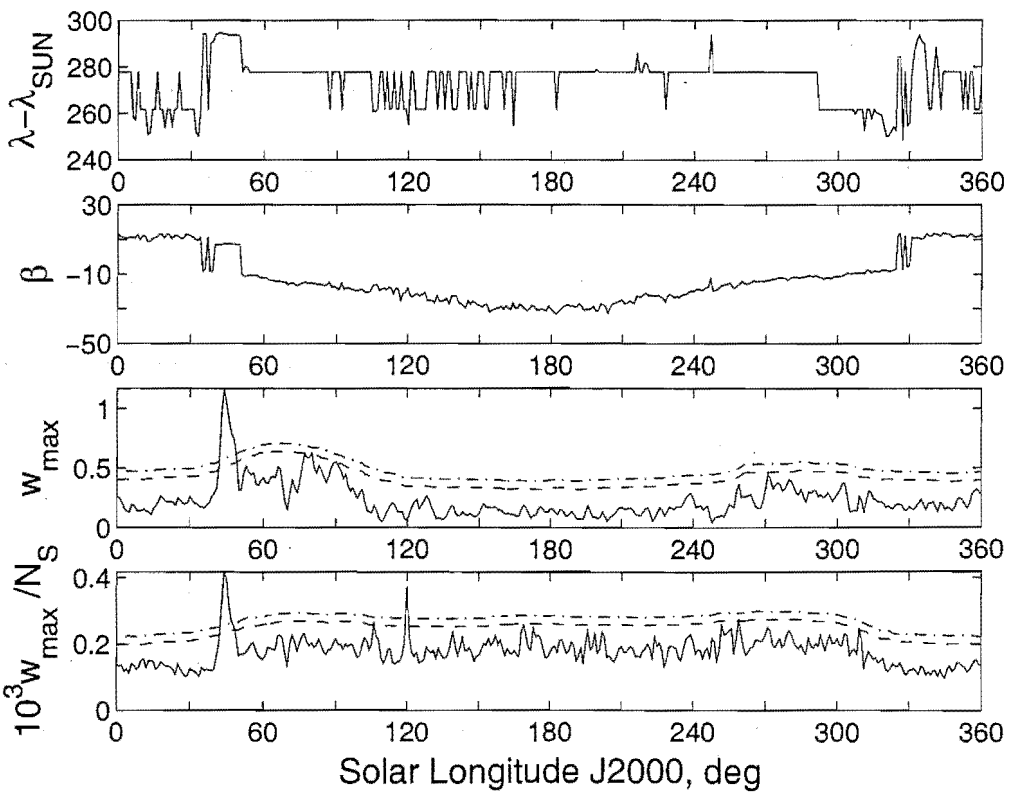

(n) Retrograde Apex Region (Blanked). $(V_G, \Delta\lambda_\odot, a) = ([0, \infty)\ \mathrm{km\,s^{-1}}, \pm 1°, 6°)$.

Figure G.5: *continued.*

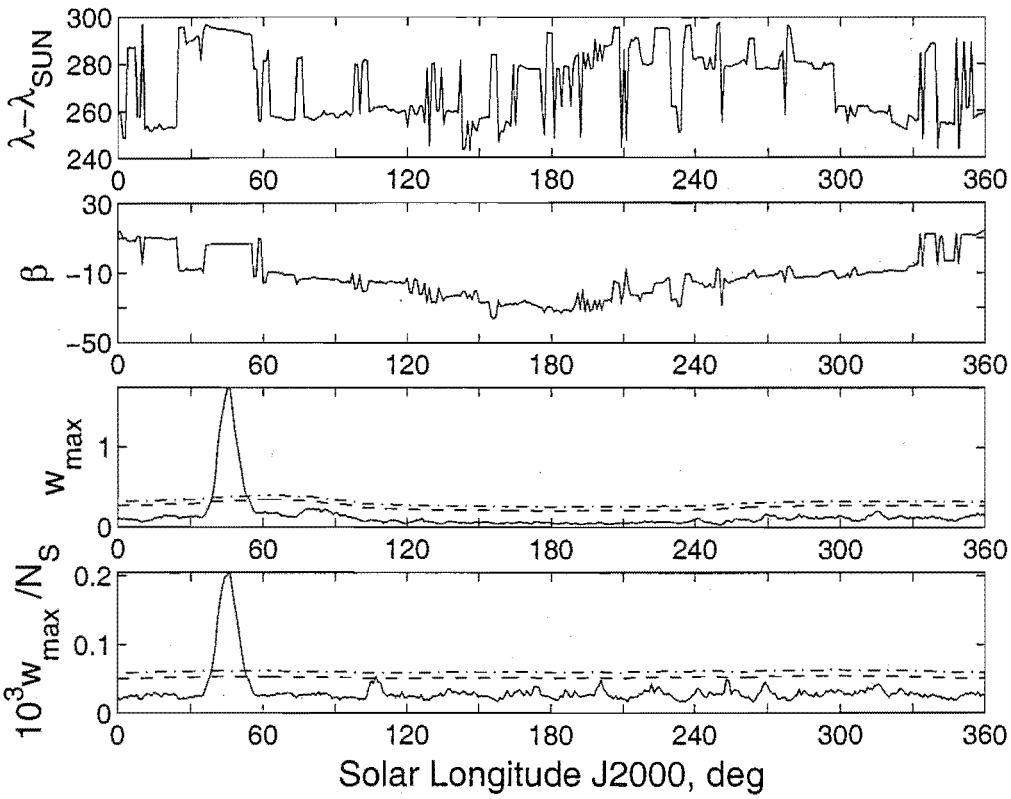

(o) Retrograde Apex Region (Blanked). $(V_G, \Delta\lambda_\odot, a) = ([0, \infty)\ \mathrm{km\,s^{-1}}, \pm 3°, 3°)$.

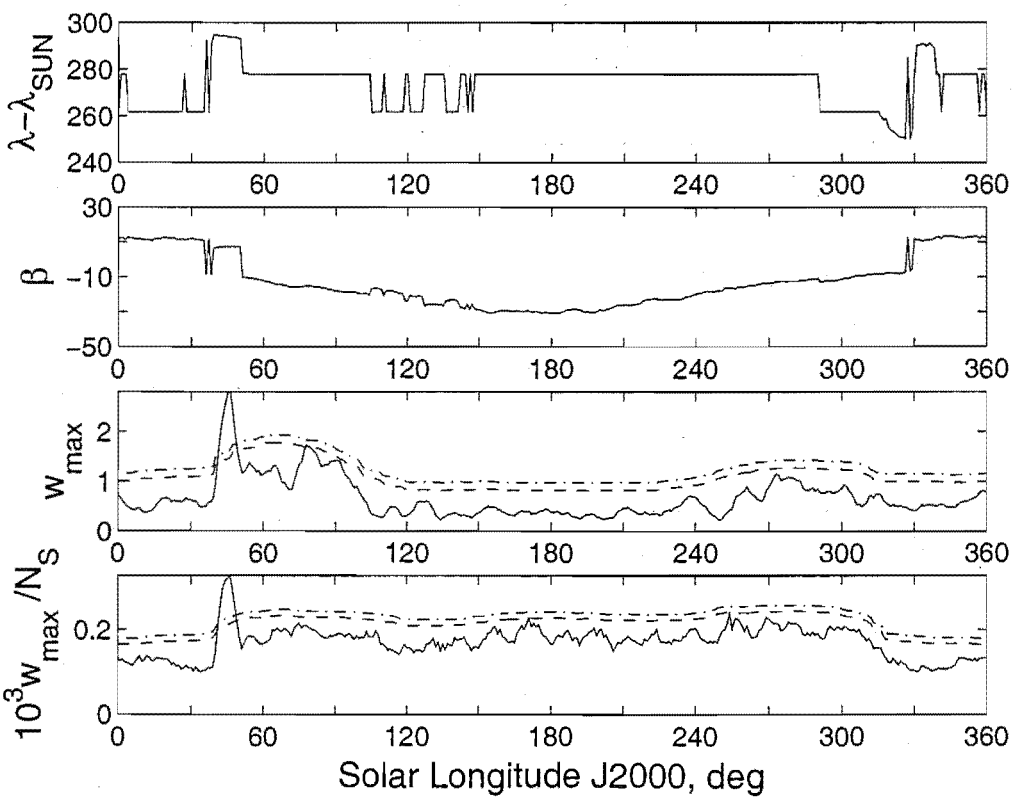

(p) Retrograde Apex Region (Blanked). $(V_G, \Delta\lambda_\odot, a) = ([0, \infty)\ \mathrm{km\,s^{-1}}, \pm 3°, 6°)$.

Figure G.5: *continued.*

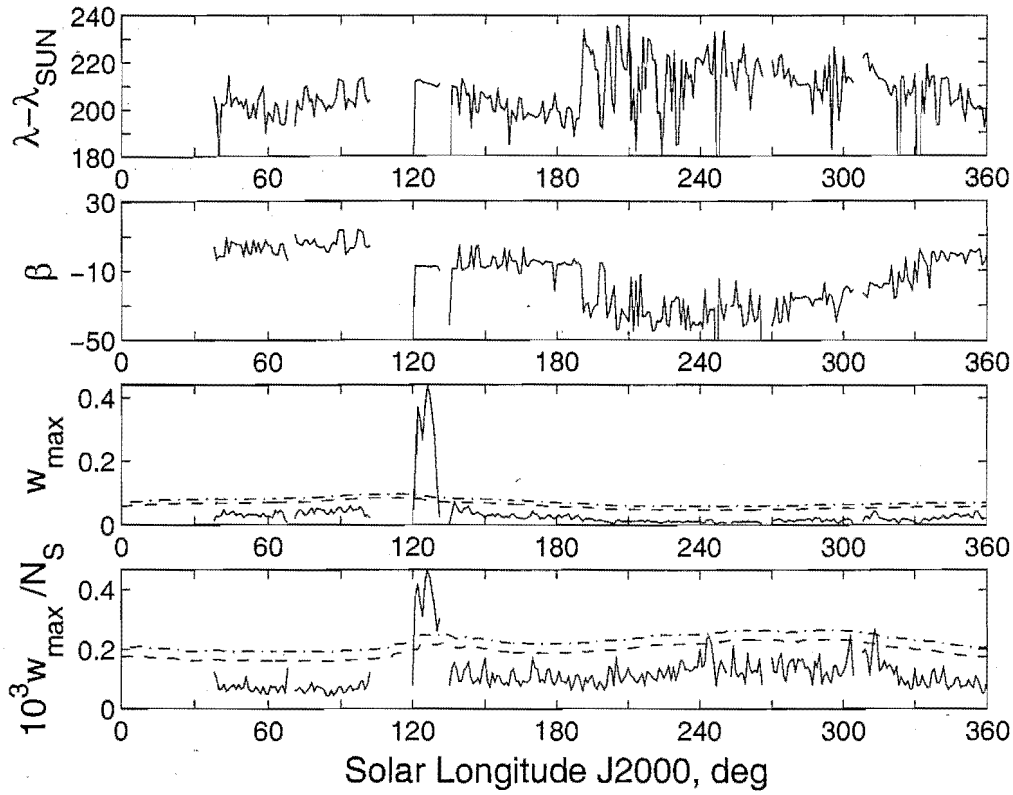

(a) T1995 Antihelion Region. $(V_G, \Delta\lambda_\odot, a) = ([0, \infty)\ \mathrm{km\,s^{-1}}, \pm 1°, 3°)$.

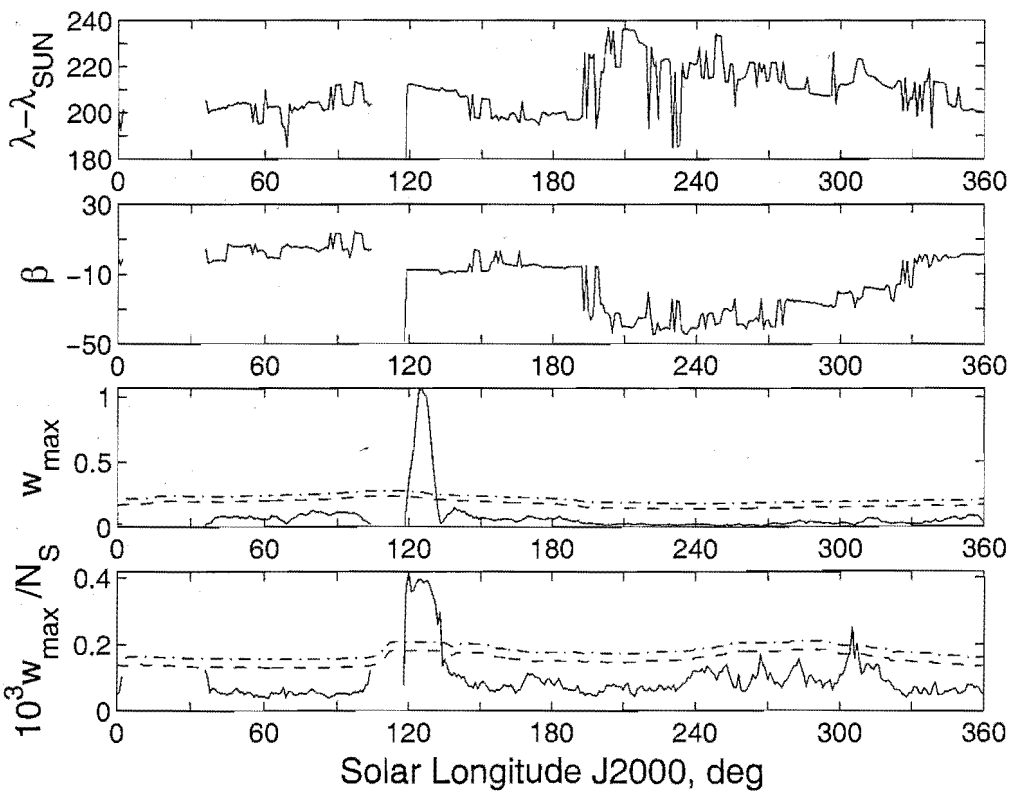

(b) T1995 Antihelion Region. $(V_G, \Delta\lambda_\odot, a) = ([0, \infty)\ \mathrm{km\,s^{-1}}, \pm 3°, 3°)$.

Figure G.6: A wavelet transform enhanced search of the antihelion region, in specific years, using two time windows ($\Delta\lambda_\odot$), one geocentric speed partition (V_G) and one wavelet probe-size (a).

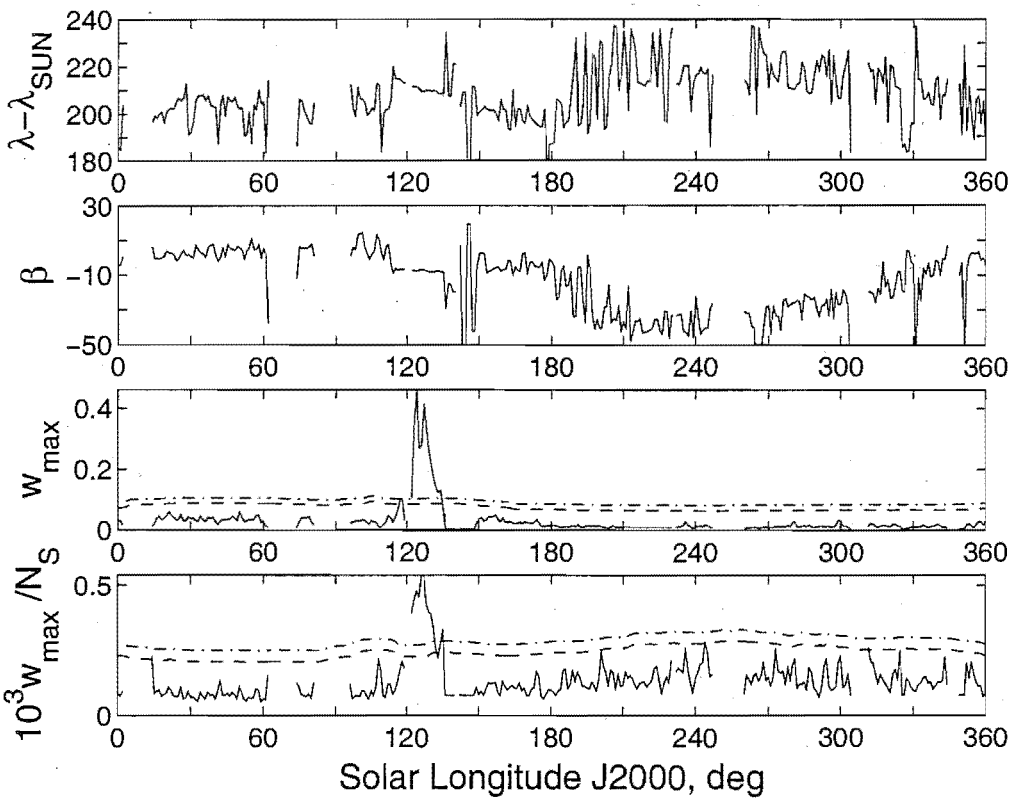

(c) T1996 Antihelion Region. $(V_G, \Delta\lambda_\odot, a) = ([0,\infty)\ \mathrm{km\,s^{-1}}, \pm 1°, 3°)$.

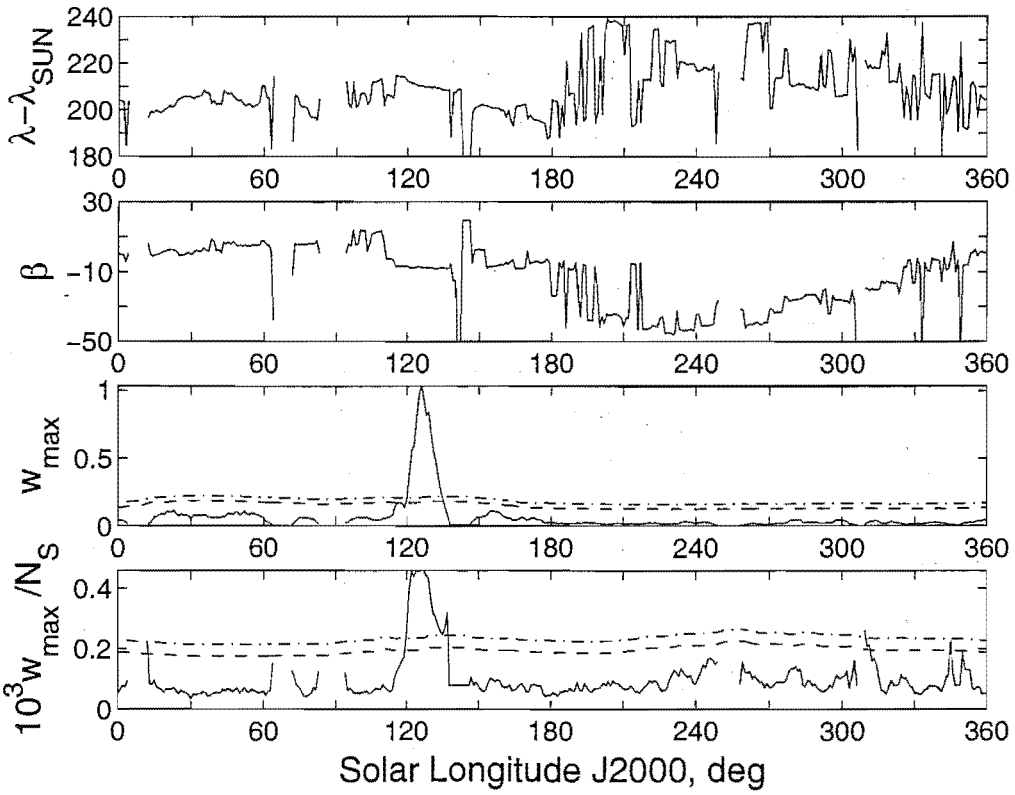

(d) T1996 Antihelion Region. $(V_G, \Delta\lambda_\odot, a) = ([0,\infty)\ \mathrm{km\,s^{-1}}, \pm 3°, 3°)$.

Figure G.6: *continued.*

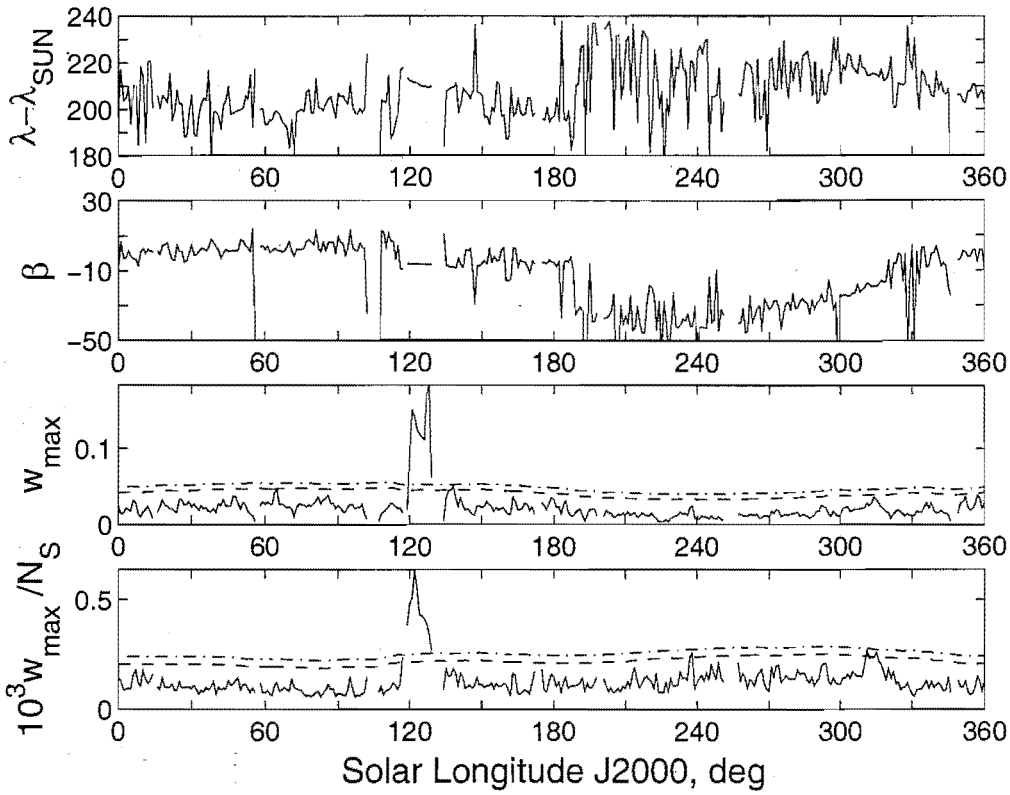

(e) T1997 Antihelion Region. $(V_G, \Delta\lambda_\odot, a) = ([0, \infty)\ \mathrm{km\,s^{-1}}, \pm 1°, 3°)$.

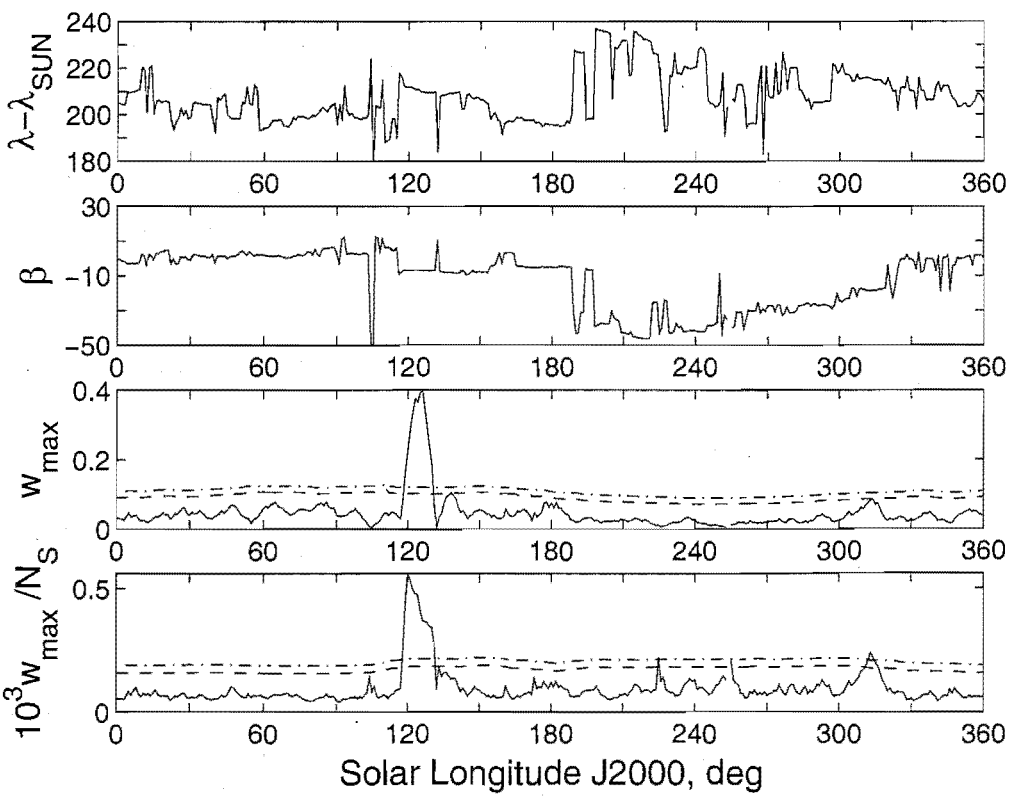

(f) T1997 Antihelion Region. $(V_G, \Delta\lambda_\odot, a) = ([0, \infty)\ \mathrm{km\,s^{-1}}, \pm 3°, 3°)$.

Figure G.6: *continued.*

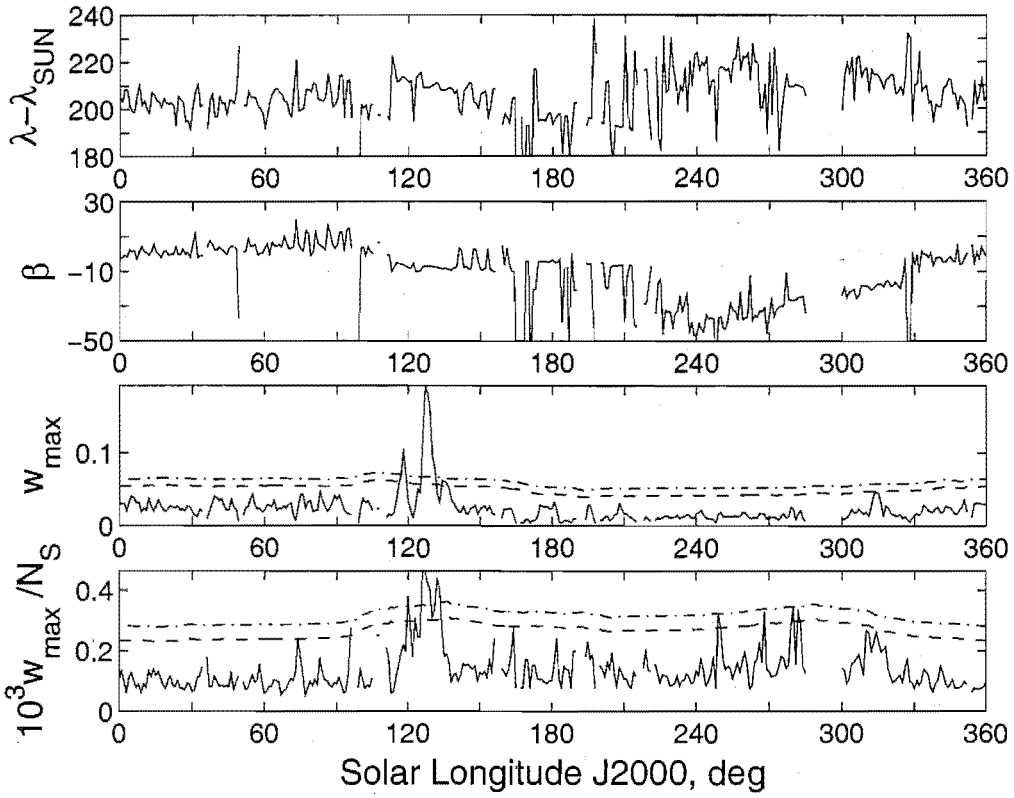

(g) T1998 Antihelion Region. $(V_G, \Delta\lambda_\odot, a) = ([0, \infty)\ \mathrm{km\,s^{-1}}, \pm 1°, 3°)$.

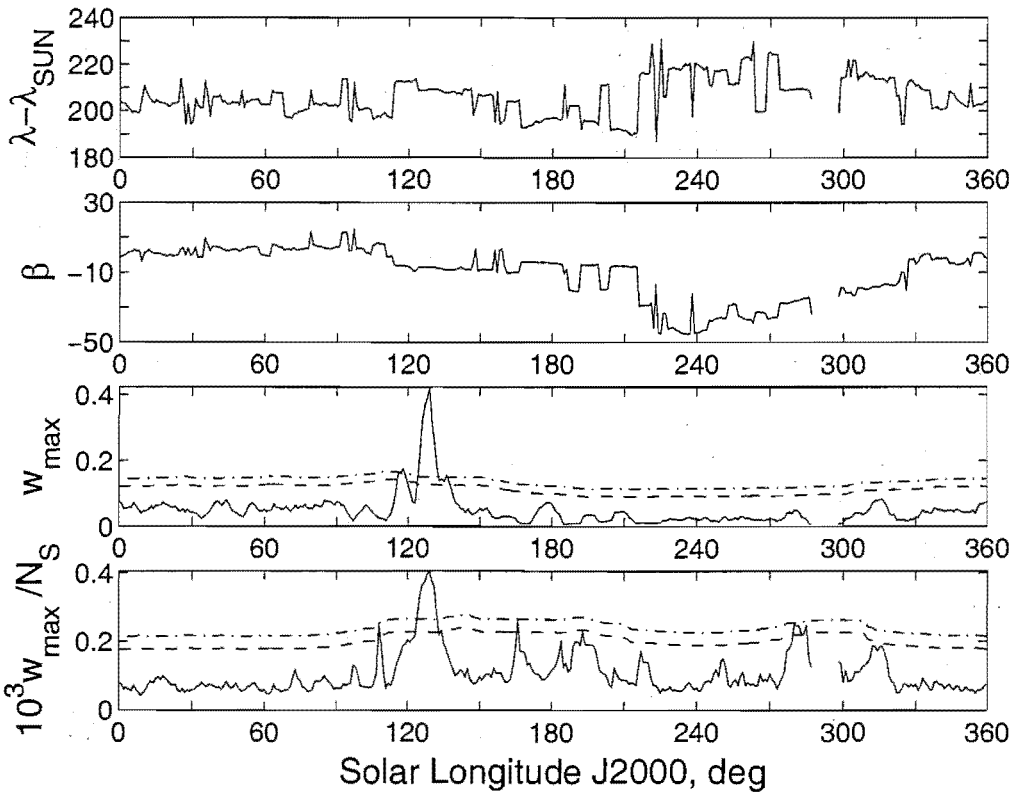

(h) T1998 Antihelion Region. $(V_G, \Delta\lambda_\odot, a) = ([0, \infty)\ \mathrm{km\,s^{-1}}, \pm 3°, 3°)$.

Figure G.6: *continued.*

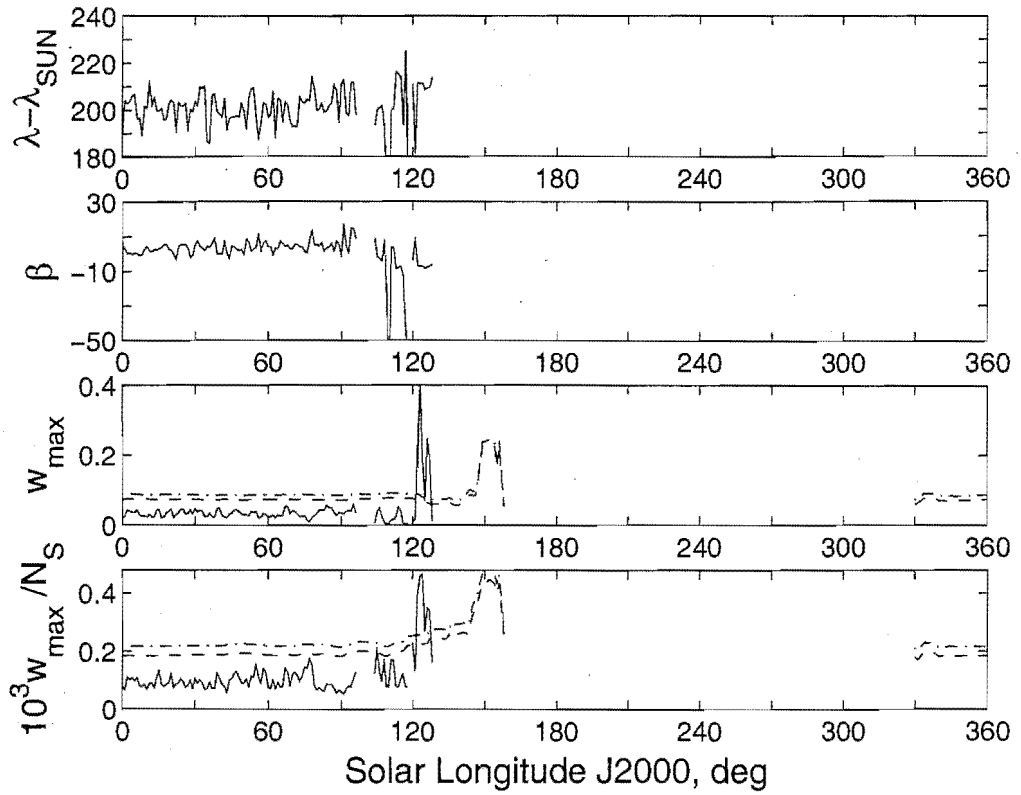

(i) T1999 Antihelion Region. $(V_G, \Delta\lambda_\odot, a) = ([0, \infty)\ \mathrm{km\,s^{-1}}, \pm 1°, 3°)$.

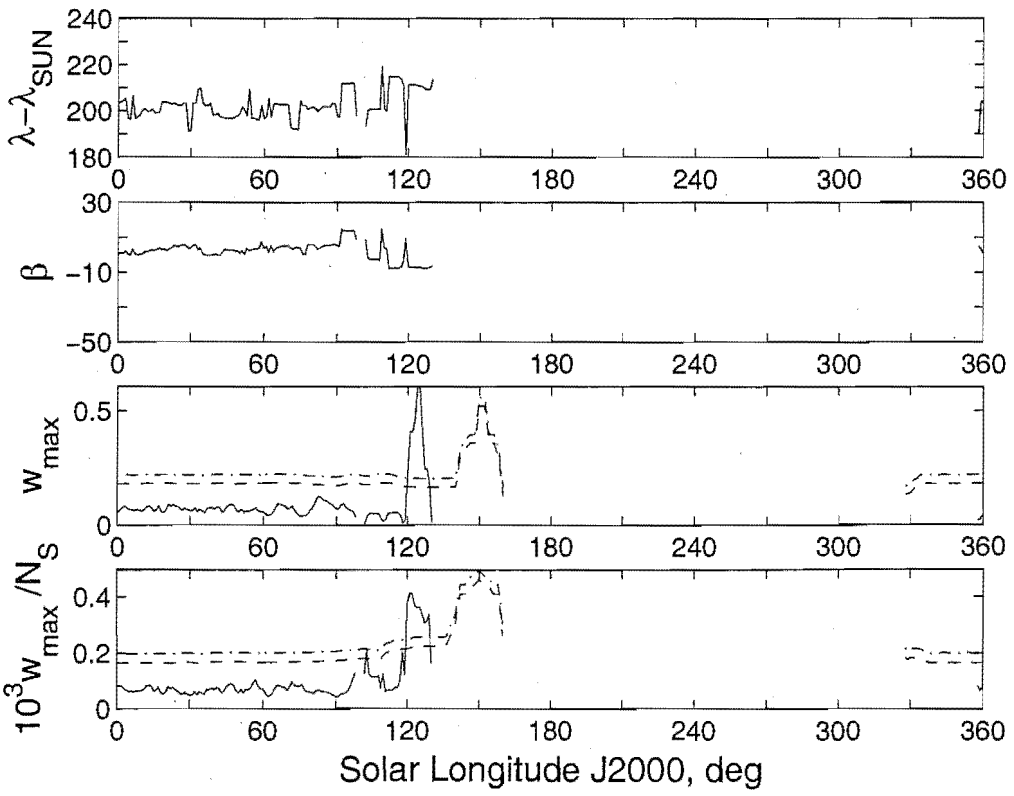

(j) T1999 Antihelion Region. $(V_G, \Delta\lambda_\odot, a) = ([0, \infty)\ \mathrm{km\,s^{-1}}, \pm 3°, 3°)$.

Figure G.6: *continued.*

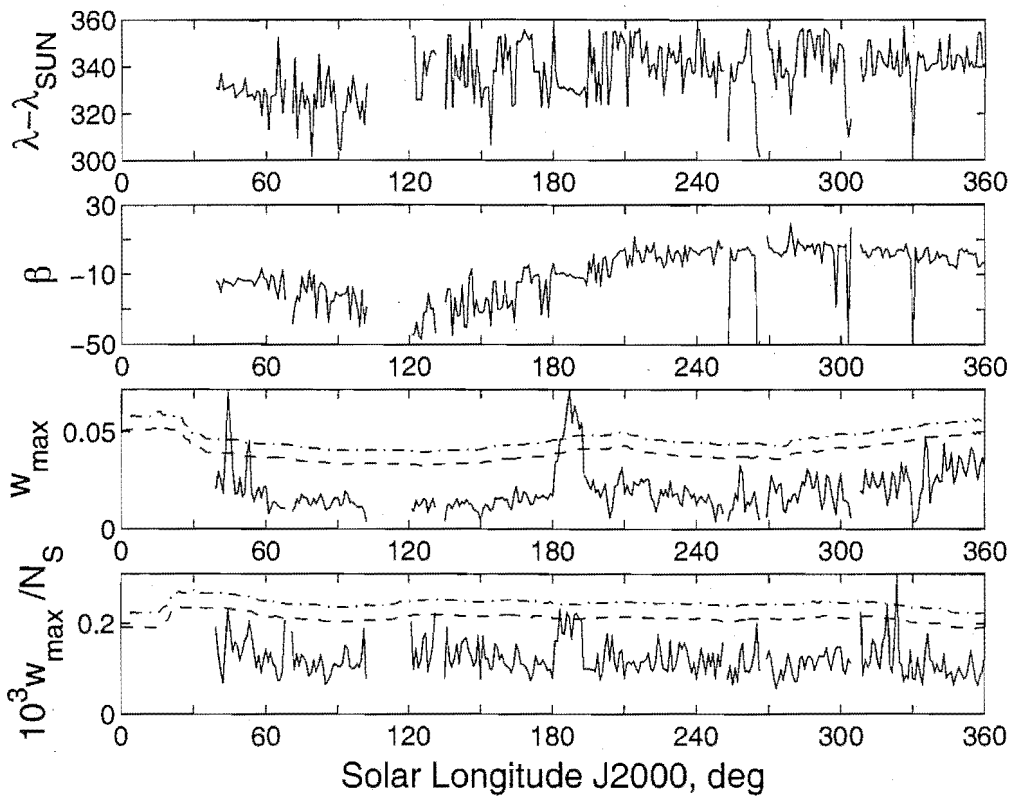

(a) T1995 Helion Region. $(V_G, \Delta\lambda_\odot, a) = ([0, \infty)\ \mathrm{km\,s^{-1}}, \pm 1°, 3°)$.

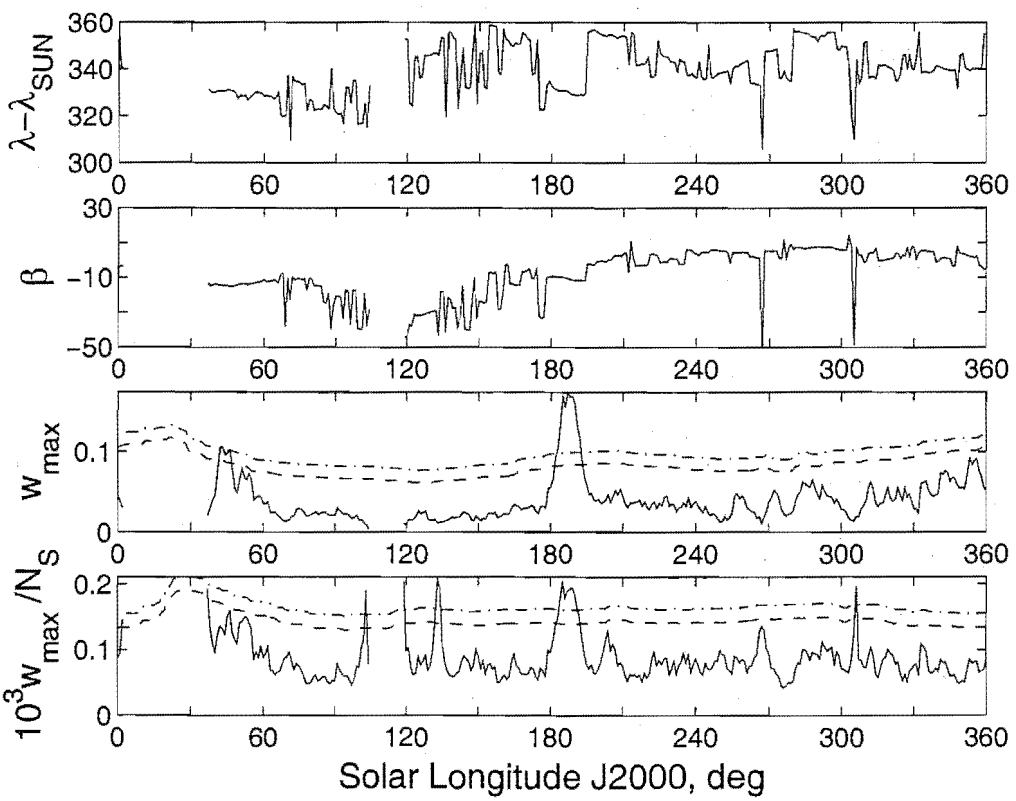

(b) T1995 Helion Region. $(V_G, \Delta\lambda_\odot, a) = ([0, \infty)\ \mathrm{km\,s^{-1}}, \pm 3°, 3°)$.

Figure G.7: A wavelet transform enhanced search of the helion region, in specific years, using two time windows ($\Delta\lambda_\odot$), one geocentric speed partition (V_G) and one wavelet probe-size (a).

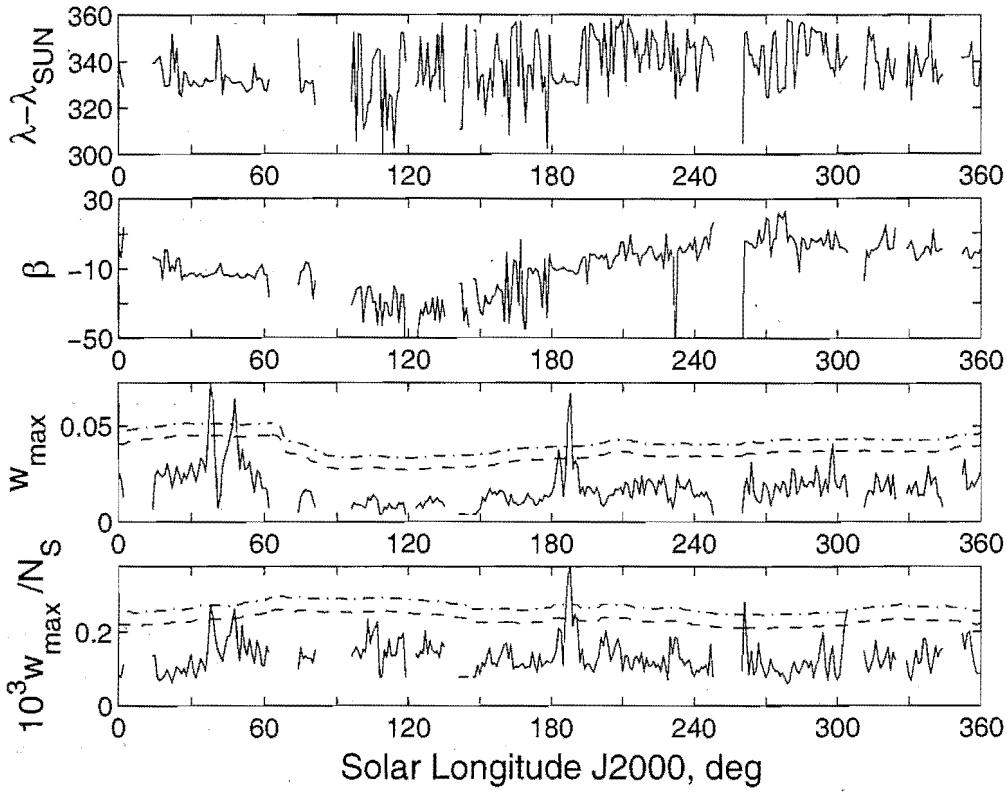

(c) T1996 Helion Region. $(V_G, \Delta\lambda_\odot, a) = ([0, \infty)\ \mathrm{km\,s^{-1}}, \pm 1°, 3°)$.

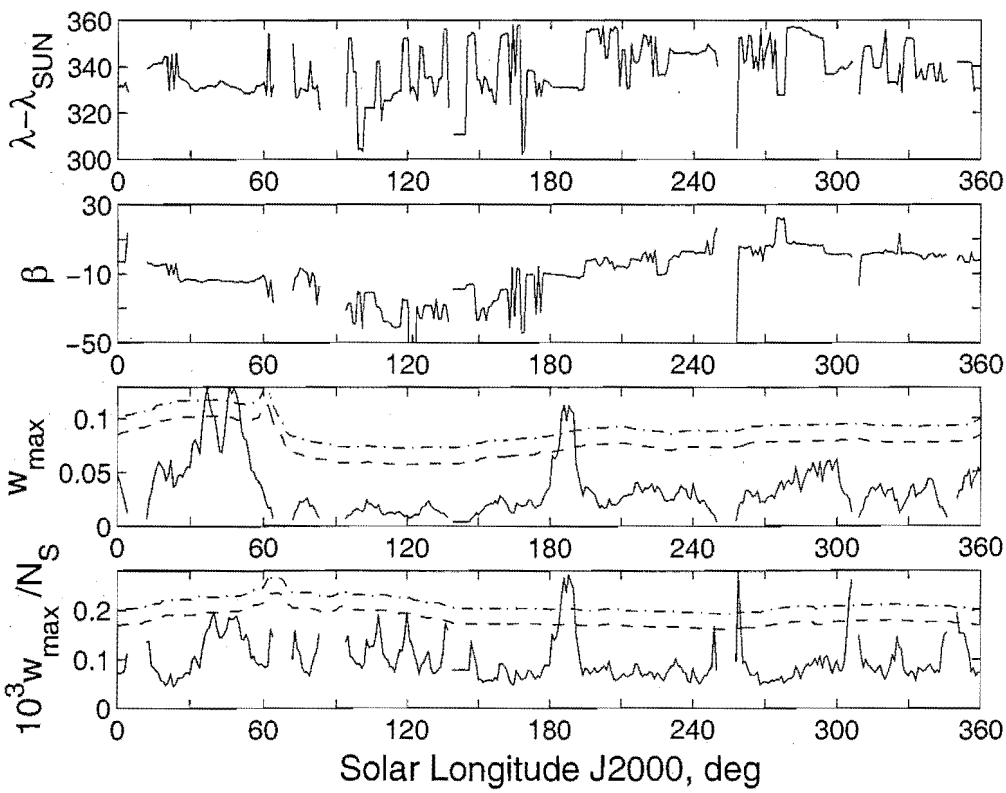

(d) T1996 Helion Region. $(V_G, \Delta\lambda_\odot, a) = ([0, \infty)\ \mathrm{km\,s^{-1}}, \pm 3°, 3°)$.

Figure G.7: *continued.*

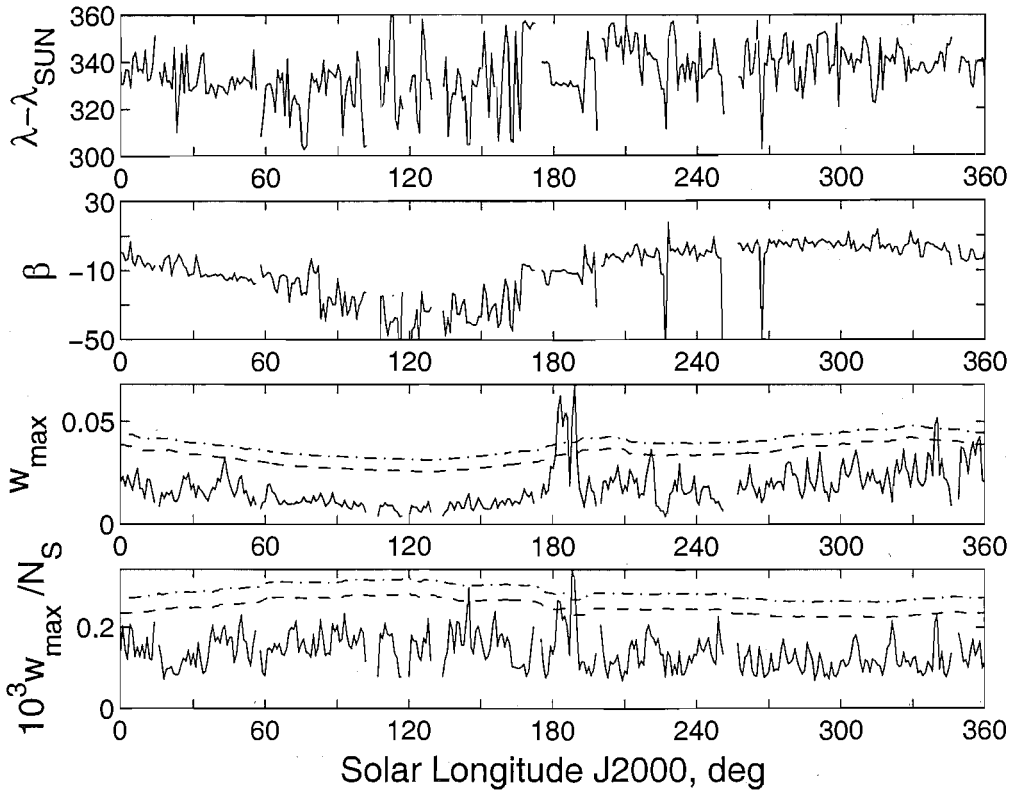

(e) T1997 Helion Region. $(V_G, \Delta\lambda_\odot, a) = ([0, \infty)\ \mathrm{km\,s^{-1}}, \pm 1°, 3°)$.

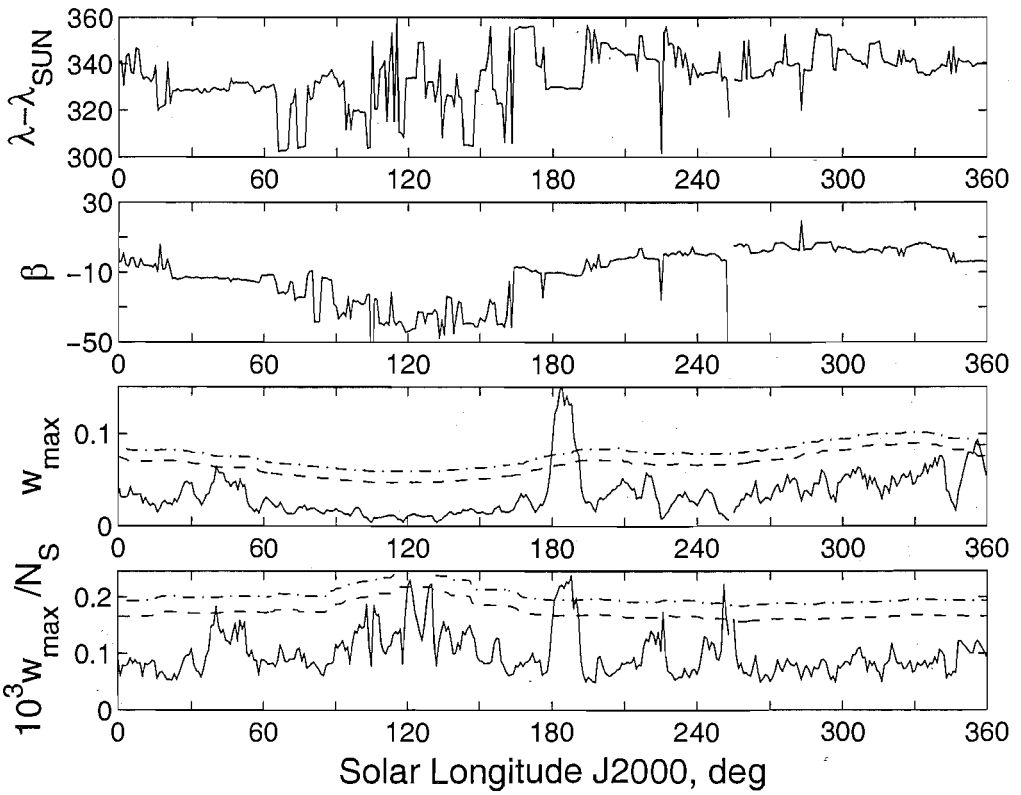

(f) T1997 Helion Region. $(V_G, \Delta\lambda_\odot, a) = ([0, \infty)\ \mathrm{km\,s^{-1}}, \pm 3°, 3°)$.

Figure G.7: *continued.*

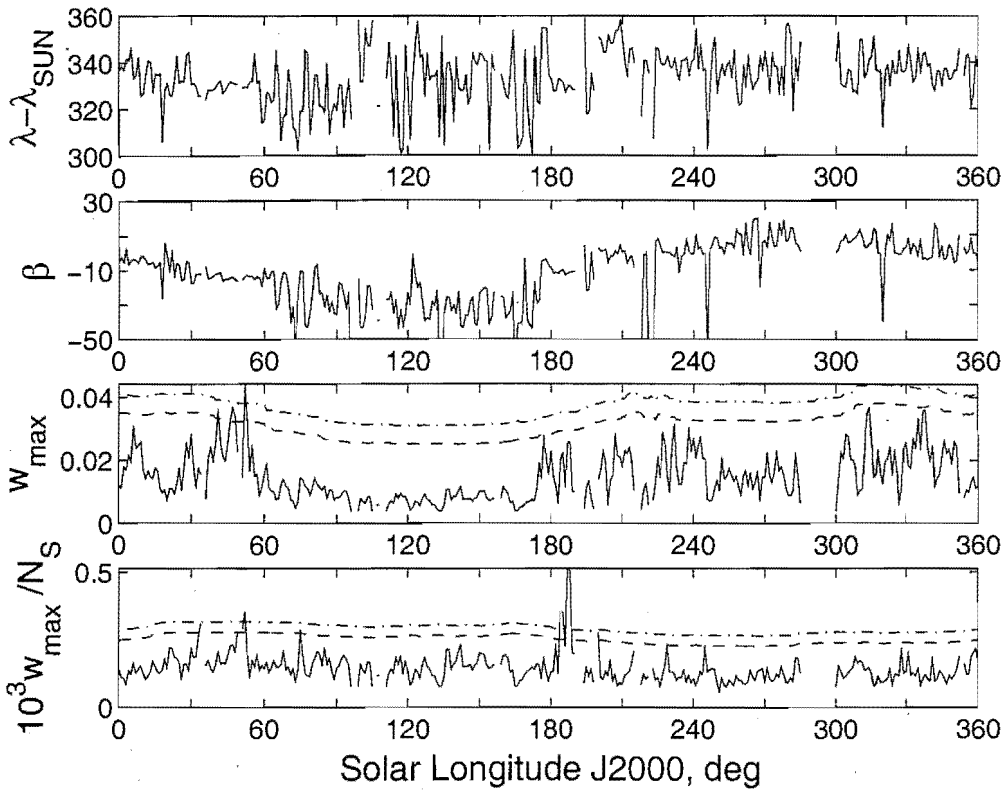

(g) T1998 Helion Region. $(V_G, \Delta\lambda_\odot, a) = ([0, \infty)\ \mathrm{km\,s^{-1}}, \pm 1°, 3°)$.

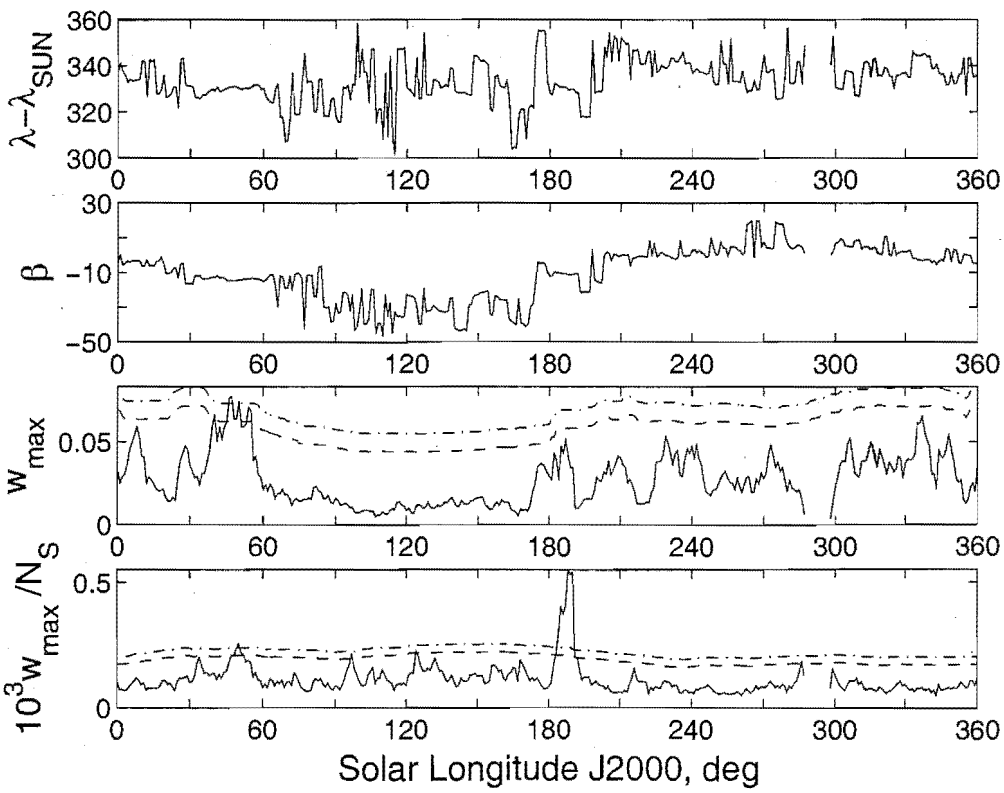

(h) T1998 Helion Region. $(V_G, \Delta\lambda_\odot, a) = ([0, \infty)\ \mathrm{km\,s^{-1}}, \pm 3°, 3°)$.

Figure G.7: *continued.*

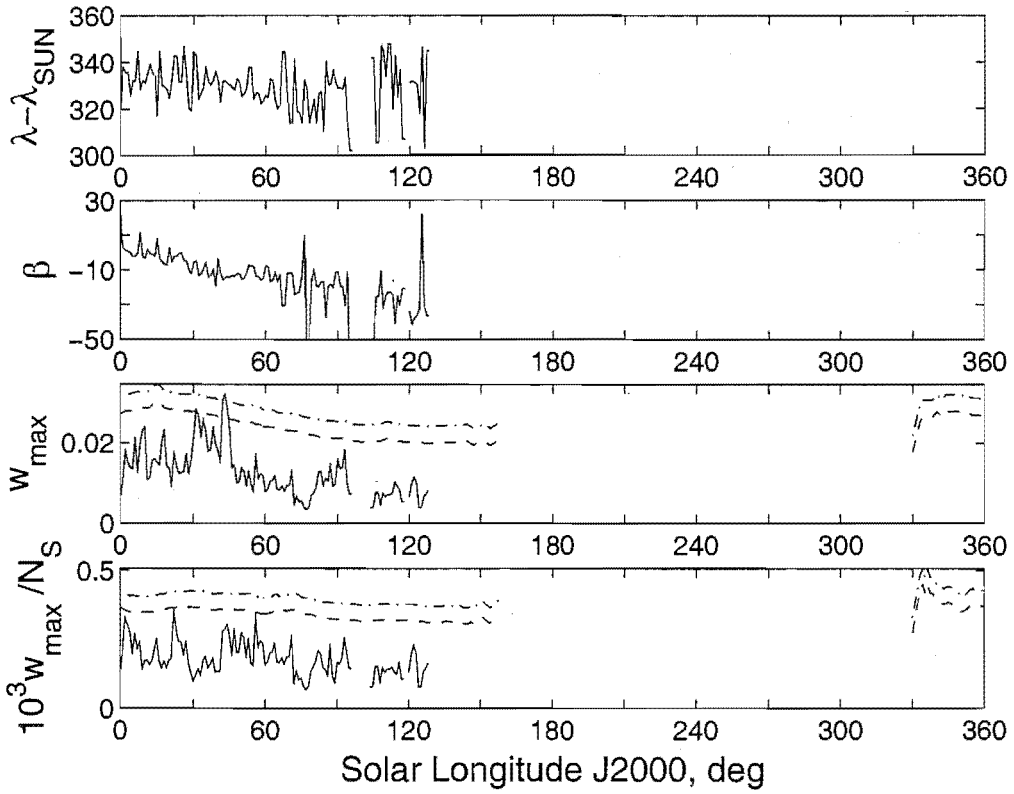

(i) T1999 Helion Region. $(V_G, \Delta\lambda_\odot, a) = ([0, \infty)\ \mathrm{km\,s^{-1}}, \pm 1°, 3°)$.

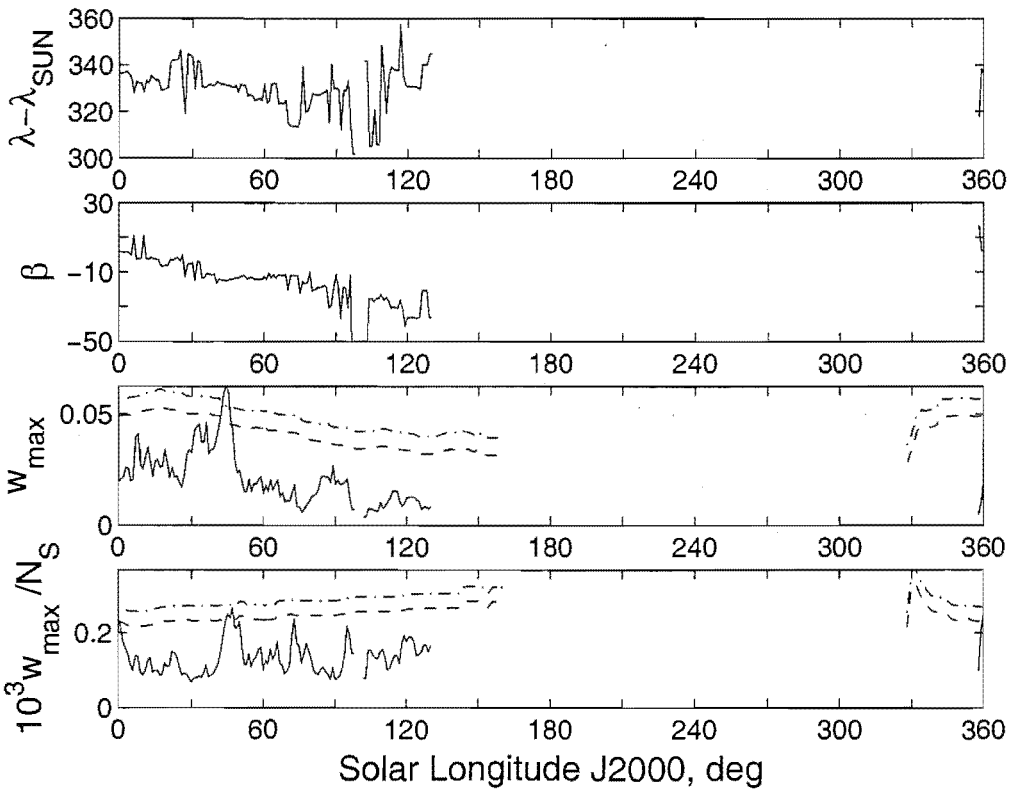

(j) T1999 Helion Region. $(V_G, \Delta\lambda_\odot, a) = ([0, \infty)\ \mathrm{km\,s^{-1}}, \pm 3°, 3°)$.

Figure G.7: *continued.*

Appendix H

Reproduction of ACM '99 Conference Paper

A poster paper presented at the Asteroids, Comets & Meteors 1999 conference at Cornell University, USA.

Orbits of the Southern Hemisphere Meteor Streams Provided By the AMOR Radar Facility

David Galligan and Jack Baggaley,
University of Canterbury,
Christchurch,
New Zealand.

A programme of orbit determinations for particles down to a limiting size of 40 μm operates the multi-station radar system AMOR at latitude 43° S. The high data rate is such that shower mean radiant daily coordinate shifts are clearly distinguished. We present orbital parameters of some catalogued southern hemisphere streams for faint (approximate magnitude +14) meteors in conjunction with an outline of the methodology used to search for them.

The AMOR System

The AMOR Meteor Orbit Radar (Baggaley and Bennett 1996) launched in 1990 is located near Banks Peninsula near Christchurch, New Zealand. It is designed to allow systematic study of the population of meteoroids with diameters ~ 40 μm and masses ~ 0.3 μg in Earth-intersecting orbits.

The radar system comprises three sites of ~ 8 km separation. At the control site a 26.2 MHz transmitter, three receivers and the data acquisition system are located. Two identical remote sites each house a receiver and VHF link in order to feed data back to control.

The velocity of the meteor in the local frame is determined from three parameters: the time-differences between the specular point detection instances on the echo profile at each site; the range to the echo point from timing the return signal and the elevation angle of the echo point as determined by the two other receivers at the control site which act as a dual-wavelength interferometer to give this angle unambiguously.

Once this velocity has been determined a series of reduction steps translate from the local frame of reference to give the original space velocity of the meteoroid from both a heliocentric and a geocentric perspective. A heliocentric orbit is then calculated from the heliocentric velocity and the time of detection.

Since its beginnings in 1990 AMOR has built up a large data set of reduced meteoroid orbits. A set of scheduled upgrades have reduced down-time to $\sim 10\%$. In recent years several hundred orbits a day have been reduced leading to $\sim 10^5$ orbits per year being catalogued. This coverage allows the opportunity to learn more about known streams and to search for new unknown ones.

A systematic study of the AMOR data set is underway in order to determine any underlying stream structure. The main aim of this work is to determine any unknown streams which may be present. As part of this work a survey of previously catalogued streams is underway. This presentation describes some methodology and results from this continuing work.

Current Data Set

The data set currently under study consists of $\sim 5 \times 10^5$ orbits from the latest four equinoctial years[1]. These are all orbits which have passed AMOR's quality checks based on three-station detection of well-defined echo time profiles. The data set is partitioned into four year-long subsets each containing greater than 10^5 orbits.

[1]Here an equinoctial year is defined as the period of time between two consecutive vernal equinoxes. Each such *year* is labelled by the calendar year in which it begins. A degree of solar longitude becomes the calendar day equivalent.

Many parameters are recorded for each orbit: however, those used for the stream-search are the perihelion distance, q; eccentricity, e; inclination, i; argument of perihelion, ω and the longitude of ascending node, Ω.

Introduction to the Analysis Method

Previous surveys of meteoroid shower activity have mostly centred around the study of photographically detected data sets, e.g. (Lindblad 1971a, Lindblad 1971b). Here one normally has a low number of orbits each of which is determined to a high precision. The proportion of stream to non-stream orbits in these data sets is high. Hence the exact choice and application of the stream search method is not crucial to the determined composition of the streams.

Radar meteoroid orbits are inherently more uncertain than their photographic counterparts. The meteoroid's orbit is based on the measurement of its velocity at the time of detection. Those with high geocentric velocities will have higher orbital uncertainties. This deficiency of radar detection is more than compensated for: radar data sets do not rely on darkness and therefore have 24 hour coverage; a high level of possible automation may be achieved in order to perform long-term observation runs; the rate of dust particles detected by a radar system is much greater than that for a photographic system due to radar's higher sensitivity.

Most photographic meteoroid stream searches use the single-linkage search technique. This is one of a class of agglomerative hierarchical clustering algorithms. Here one starts with all orbits in a data set in separate clusters and end with all of them grouped into a single all-encompassing cluster. The method is to attempt to stop the process at suitable intermediate levels in the hierarchy in order achieve clusters which have some meaning.

Early stream searches such as those of Lindblad tend to empirically select two to four spread out cutoff levels and test for clusters at each of these. Recent advances (Jopek and Froeschlé 1997) provide a more automated and hence a more objective approach for determining suitable cutoff points. Here one tests a number of pseudo-random data sets based on the real orbit data set under study. These are put through the cluster analysis method exactly the same as the real set is. From these randomised runs one can get a picture of level of interference of the non-stream background as one progresses through the hierarchy.

Radar meteoroid orbits suffer differential uncertainties which increase as the geocentric speed of the meteor increases. Orbits in the prograde Southern δ Aquarids shower ($\overline{V}_G$=39 km s^{-1}) have much lower uncertainties than those in the retrograde η Aquarids shower ($\overline{V}_G$=64 km s^{-1}). This is because in general (Figure H.1(k)) retrograde meteoroids have higher geocentric speeds than their prograde counterparts.

The result of attempting a single-linkage algorithm on the large radar orbit sets provided by AMOR is that it is necessary to search on many levels of the hierarchy due to the rapidly evolving group structure which occurs (Galligan and Baggaley 1998) as opposed to searching based on a few significant levels (as tested with partial success in Baggaley and Galligan (1997)). For example the Southern δ Aquarids will agglomerate to form a sensible and complete group early in the hierarchy while at the same point the η Aquarids will only have a small minority of their orbits clustered together. One must proceed to a much higher level to attain a similar level of sensibility for the η Aquarids. While this behaviour is partly attributable to the orbital spread caused by uncertainties there is also an effect due to the larger number of prograde orbits near the ecliptic in the uncorrected (for Earth collision and radar detection factors) distribution (Figure H.1(l)).

Modified Single-Linkage Method

Due to the different rates at which distinct clusters emerge from and subside into the non-shower background, the current method attempts to embrace a large number of levels at once. It is not considered necessarily true that a low level in the hierarchy means a high quality grouping and conversely that a grouping at a high level is likely to mainly consist of non-shower background orbits.

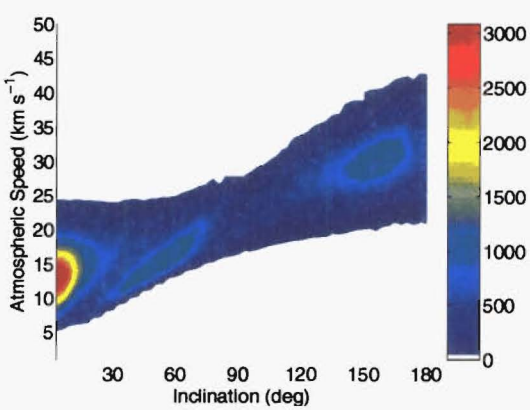

(k) Increase in general atmospheric speed distribution with inclination.

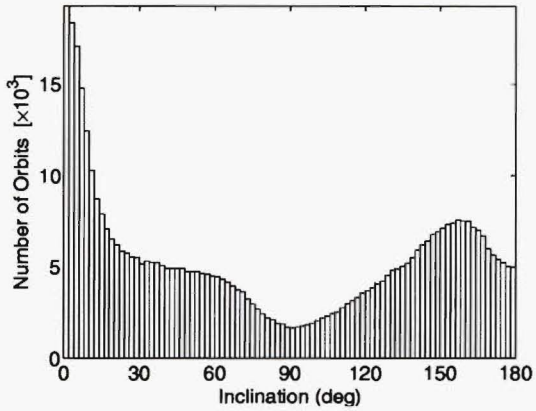

(l) Uncorrected inclination distribution. Note large near-ecliptic population.

Figure H.1: Distributions of the $\sim 5 \times 10^5$ orbits from equinoctial years beginning 1995 to 1998.

Single-linkage cluster analysis is performed at 10^3 or more levels simultaneously. The computer software can presently perform at this level for up to 2×10^5 orbits with a usual realistic limit of 1.5×10^5 at a time. The process is $O(N^2)$ in nature hence increasing much above the current limit is difficult. The dissimilarity function used to judge how close two orbits are is the D-criterion adaptation of Jopek (1993a):

$$[D_H]^2 = (e_2 - e_1)^2 + \left(\frac{q_2 - q_1}{q_2 + q_1}\right)^2 + \left(2 \sin \frac{I_{21}}{2}\right)^2 + \left(\frac{e_2 + e_1}{2}\right)^2 \left(2 \sin \frac{\pi_{21}}{2}\right)^2 . \qquad \text{(H.1)}$$

The standard orbital elements q, e, i, ω and Ω are used to compare orbits in equation H.1 where $I_{21}(i, \omega)$ is the inter-orbital plane inclination and $\pi_{21}(i, \omega, \Omega, I_{21})$ the angle between perihelion positions.

Once the single-linkage cluster hierarchy for the 10^3 levels has been established one would normally then try and decide on an objective criterion for stopping the hierarchy at a particular level. Instead, the current method works by starting at the highest agglomeration level explored in the hierarchy and working down through all levels from there. At present groups are accepted which fulfil the following requirements:

1. Group Size: $5 \leq N_g < 1500$
2. Solar Longitude Range: $\Delta\lambda_\odot < 35°$

These two simplistic conditions work quite well. They have the obvious advantage of speed of application which is very important when large data sets are under study. Condition 1 prevents against runaway group growth: generally it is found that groupings do not grow to this maximum size before merging into the large-scale background (e.g. Figure H.2). Condition 2 prevents low inclination groupings from forming year-round streams through similarity of their longitude of perihelia, $\overline{\omega} = \omega + \Omega$. While the argument of perihelion, ω and longitude of ascending node, Ω for these near-ecliptic streams mean little and hence it is perfectly valid to associate $\overline{\omega}$, it is improbable to find many of these streams existing as they would be quickly cleansed by planetary and Solar perturbation. Absence of condition 2 tends to lead to large-scale clusters being built extending from low to medium inclinations year round. These conditions are admittedly not optimum yet and work is currently underway in this area. They will be changed in future with the possible addition of other limitations on viable groups.

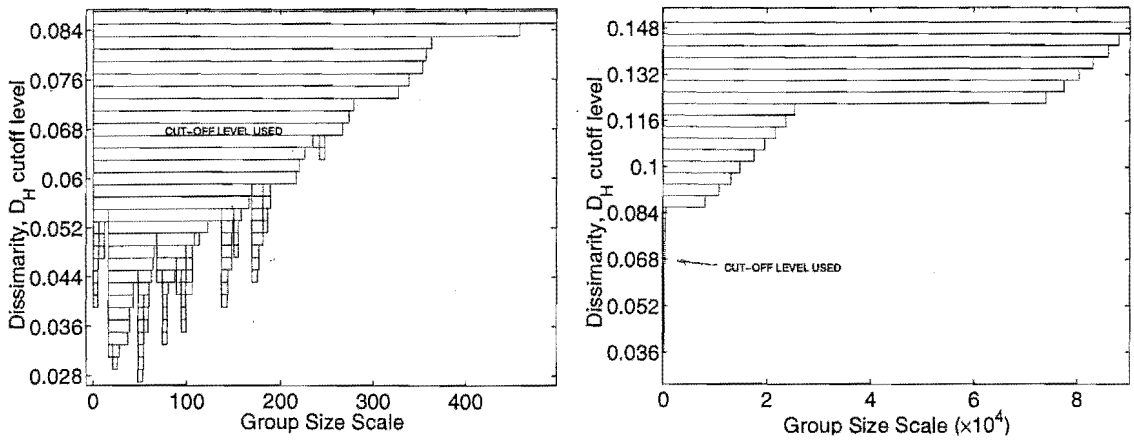

(a) Fine Scale

(b) Coarse Scale

Figure H.2: Examples of dendrograms showing increasing levels of agglomeration as one proceeds up the single-linkage hierarchy. These graphs are of the η Aquarids shower from 1996. Figure H.2(a) shows the grouping structure about $D = 0.0680$ at which the group was cutoff. The top level shown on this graph ($D = 0.0880$) is made up of a single totally unrealistic group containing in excess of 6,000 (not shown above 500) orbits. In the stream search the actual increment between each level was $D = 0.0002$; One may readily see that a small number of levels lie between sensible and insensible groupings. Figure H.2(b) illustrates this point further using a coarser scale. Note the very different x-axis scales on the two graphs.

Once a run has been completed down to the lowest level of agglomeration one has a set of groupings which are the largest they can be according to the set conditions. Some of these groupings will consist of random background orbits especially at the higher agglomerative levels but many contain good distinct and astronomically significant groupings.

Use of data

The data set contains almost half a million orbits over four equinoctial years. Each year is analysed separately in order to produce its own streams for further analysis. At this point each year has produced several thousand minor/major potential streams for each of which a mean orbit is determined.

All four years mean orbits are combined into a single data set. This orbital element set is then fed into the same cluster analysis process again but this time with different group acceptance conditions ($\lambda_\odot < 15°$ and $N_g > 2$). The several thousand groupings which emerge at this stage contain many fully developed streams such as the Daytime Sextantids in which most of the obvious orbits associated with this stream are contained in a single cluster (in this case the cluster contains 766 orbits over three years).

In fact most of the major streams are described by one or two clusters only. However a few, such as the Southern δ Aquarids, are very large streams or in the case of the η Aquarids have large apparent orbit spreads due to measurement uncertainties. These kinds of factors can act to split the stream up, into (usually) a single very large stream containing the dense central core, in addition to many smaller streams, which obviously should be linked to the central stream.

In these cases the processing invokes the clustering algorithm a third time with the same acceptance criterion as for the second time. Streams such as the Daytime Sextantids are not affected by this as they are already stable with their region of orbital element space. However some streams such as the Southern δ Aquarids add several smaller streams together into the central core in order to obtain a more realistic stream.

The process of multi-pass-cluster analysis described above works well in a number of cases:

however, for such streams as the η Aquarids the uncertainty in their orbits is large enough that while the mean eccentricity is almost 1, several obviously related highly homogeneous clumps are formed whose eccentricities are up to 3. Unless one accepts an extremely high D-criterion value for joining these groupings together the large difference in eccentricity is quite sufficient to prevent merging.

We are at present exploring other techniques towards this goal. A final grouping check based on the similarity of the mean corrected radiant points, geocentric velocities and stream occurrence date-range is one option. Alternatively weighting the D-criterion based more on inclination (which enjoys one of the lowest uncertainties in general as compared to orbital size and shape as defined by q and e which generally carry higher uncertainties) would be another option. Difficulties arise here in that the majority of orbits are found with orbital planes near the ecliptic—where one must use q and e more to distinguish streams.

Results

All of the major catalogued southern showers (about 20) are found in the data set under study. Most of these repeat clearly each year with many of them exhibiting a clear radiant shift parallel to the ecliptic. This shift is expected of a stream which is coming from a discrete source direction and for which the only condition that changes is the observation point as the Earth moves in its orbit. Sufficient numbers of meteoroid orbits are needed to provide statistical validity to measured daily mean radiant points in order to see a clear radiant shift.

A summary of some of the catalogued showers found are presented below with mean, standard deviation and standard error being given for each stream parameter mean. In all cases the angular elements are measured in degrees and where appropriate have been reduced to the J2000.0 epoch. Velocities are measured in km s^{-1}. For the mean radiant point shift diagrams the ecliptic is shown as a blue line.

η Aquarids.

The η Aquarids (ETA) are very much the signature stream of AMOR. They are detected year after year in late April to mid-May at consistent rates and effort has been expended to keep equipment operational at the time of the shower each year so that there is now a valuable 10 year archive of ETA showers.

Figure H.3(a) shows the rate change as the Earth progressed through the stream's structure for each of the years from 1995 to 1998. Dropout points along the curves are caused by instrumental effects in general—especially evident in the steep dropout near what would have been the maximum rate in 1997 (the radar is occasionally off for a few calendar days when maintenance periods are undertaken).

In Figure H.3(b), the shift of the mean corrected radiant point as it changes during the shower's presence is given. The numbers on each point are the solar longitude at which the mean was taken. Note that for solar longitudes at either end of the rate curve the corresponding radiant points will have larger uncertainties: however all of the points remain near parallel with the ecliptic in this example.

The mean orbital elements are given in Table H.1 for the 779 orbits contained in the core of the shower. One should note the large standard deviation in q and e for this stream as compared to that in i as discussed earlier. These standard deviations relate to similar uncertainties in the member orbits in this case. If it were not for the sheer number of ETA and their distinct position in orbital element space it is unlikely they would be so well detected. As noted earlier there are many sub-streams mostly with larger eccentricities which appear to belong to the main ETA shower but which are not included by the stream search. Work is underway to examine these further.

YEAR		$\lambda_\odot$ deg	q AU	e	i deg	ω deg	Ω deg	V_A	V_H $\mathrm{km\,s^{-1}}$	V_G	α deg	δ deg	SIZE
ALL	$\overline{x}$	45.9	0.524	0.908	164.9	88.1	45.9	63.3	39.5	63.9	338.8	-1.5	
	s.d.	4.4	0.088	0.140	2.4	14.6	4.4	3.3	3.4	3.5	3.9	1.7	779
	s.e.	0.2	0.003	0.005	0.1	0.5	0.2	0.1	0.1	0.1	0.1	0.1	

Table H.1: Orbital element statistics of the η Aquarids shower from 1995–1998.

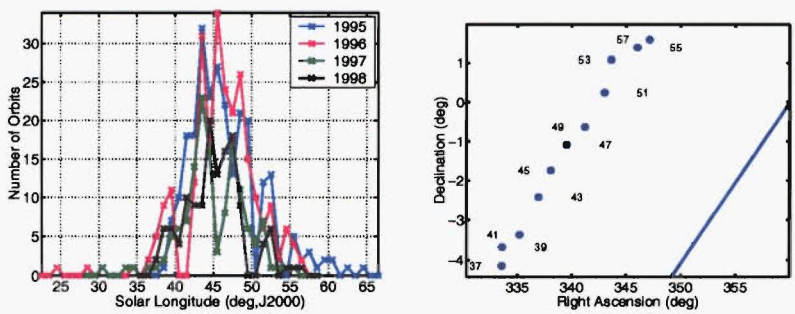

(a) Individual rate curves (b) Radiant shift

Figure H.3: The η Aquarids shower 1995–1998.

Daytime Sextantids.

This October shower is found year after year by AMOR. As a day-time shower it is a good example of the particular importance of a radar system such as AMOR. Fairly constant rates are found for 1995–1997 years (Figures H.4(a) and H.4(b)) while the equipment was down for maintenance in 1998. There were minor equipment down-times near the maximum in 1997 and later in 1996. Despite these features the time of maximum is clear.

The radiant shift over time is shown in Figure H.4(c). Note that for $\lambda_\odot > 193°$ the mean radiant point stops following the ecliptic so well. Here the rate is in decline (see Figures H.4(a) and H.4(b)) so that fewer orbits are contributing to the mean.

The stability of the mean stream orbit over several years is demonstrated in Table H.2. The standard deviations in the mean stream orbits are less than the uncertainties in the individual orbit (Table H.3). Therefore it is possible to consider looking more closely at the micro-structure of the stream—an area which will be examined in the near future. This situation contrasts with the η Aquarids for which the individual orbital uncertainties are comparable to the standard deviations in the stream's mean orbit.

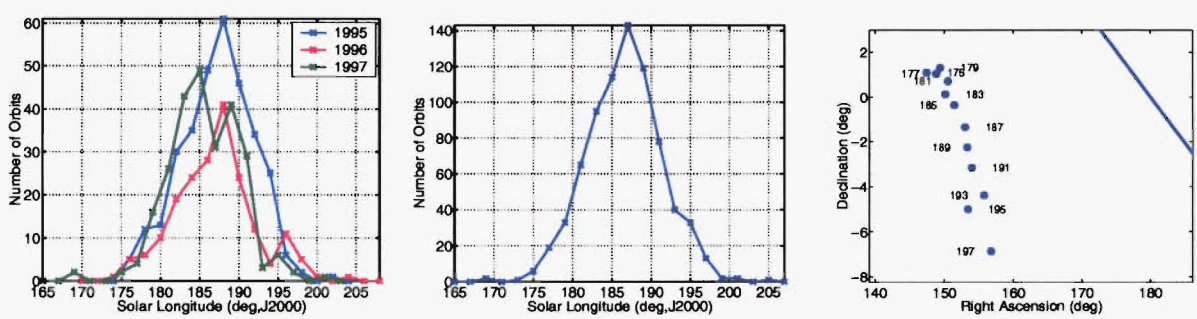

(a) Individual rate curves. (b) Combined rate curves. (c) Radiant shift.

Figure H.4: The Daytime Sextantids 1995–1997.

YEAR		$\lambda_\odot$ deg	q AU	e	i deg	ω deg	Ω deg	V_A	V_H km s^{-1}	V_G	α deg	δ deg	SIZE
1995	$\overline{x}$	187.0	0.157	0.841	22.4	211.5	7.0	31.1	29.5	30.0	153.2	-1.3	
	s.d.	4.5	0.032	0.055	5.6	5.0	4.5	3.8	3.5	4.2	4.7	2.4	319
	s.e.	0.3	0.002	0.003	0.3	0.3	0.3	0.2	0.2	0.2	0.3	0.1	
1996	$\overline{x}$	187.0	0.173	0.825	21.9	213.1	7.0	30.4	29.4	29.3	153.4	-2.0	
	s.d.	5.3	0.033	0.059	6.6	5.9	5.3	3.9	3.8	4.3	5.8	2.9	192
	s.e.	0.4	0.002	0.004	0.5	0.4	0.4	0.3	0.3	0.3	0.4	0.2	
1997	$\overline{x}$	185.8	0.155	0.832	23.4	210.0	5.8	30.4	28.5	29.3	150.2	-1.1	
	s.d.	4.5	0.033	0.058	6.0	5.0	4.5	3.8	3.5	4.2	5.1	3.0	255
	s.e.	0.3	0.002	0.004	0.4	0.3	0.3	0.2	0.2	0.3	0.3	0.2	
ALL	$\overline{x}$	186.6	0.160	0.834	22.6	211.4	6.6	30.7	29.1	29.6	152.2	-1.4	
	s.d.	4.7	0.033	0.057	6.0	5.4	4.7	3.8	3.6	4.2	5.3	2.7	766
	s.e.	0.2	0.001	0.002	0.2	0.2	0.2	0.1	0.1	0.2	0.2	0.1	

Table H.2: The mean orbital elements of the Daytime Sextantids 1995–1997.

	$\lambda_\odot$	q (AU)	e	i	ω	Ω	V_A	V_H	V_G	α	δ
$\overline{x}$	0.0	0.016	0.020	3.0	2.5	0.0	1.2	1.1	1.3	2.1	0.5
s.d.	0.0	0.008	0.005	1.4	1.2	0.0	0.4	0.5	0.4	0.9	0.3

Table H.3: Statistics for the absolute uncertainties of the 766 Daytime Sextantids orbits.

Southern δ Aquarids.

The Southern δ Aquarids (SDA) is a well established shower which is recorded with a high rate each year. Equipment was down during part of the maximum in both 1997 and 1998. Table H.4 shows the mean orbital elements from each year. The 1998 stream mean is very similar to those of 1995 and 1996. However the 1997 stream mean inclination for instance is 45° instead of 32° or 33°. A large part of the maximum was missed for this year. It is easy to skew the statistics if the whole period of the stream is not included. Here only a small number of orbits have been included compared to normal. The mean is consequentially of a much lower validity. Note that the standard error in 1997 is much higher than 1995 or 1996. In 1998 although we had a lower rate a similar picture of the stream was built up to that in 1995 and 1996.

YEAR		$\lambda_\odot$ deg	q AU	e	i deg	ω deg	Ω deg	V_A	V_H km s^{-1}	V_G	α deg	δ deg	SIZE
1995	$\overline{x}$	126.1	0.091	0.945	33.4	151.7	306.1	39.4	35.3	39.0	342.3	-16.9	
	s.d.	4.0	0.046	0.051	18.3	6.8	4.0	5.6	4.4	5.9	6.3	3.2	1378
	s.e.	0.1	0.001	0.001	0.5	0.2	0.1	0.1	0.1	0.2	0.2	0.1	
1996	$\overline{x}$	127.0	0.091	0.945	32.2	151.5	307.0	38.8	34.8	38.4	343.5	-16.9	
	s.d.	4.6	0.032	0.043	16.6	6.0	4.6	5.0	4.7	5.4	6.0	3.1	1265
	s.e.	0.1	0.001	0.001	0.5	0.2	0.1	0.1	0.1	0.2	0.2	0.1	
1997	$\overline{x}$	129.7	0.094	0.938	45.3	152.3	309.7	39.3	33.6	39.0	351.8	-17.5	
	s.d.	9.6	0.038	0.045	18.0	8.1	9.6	5.5	6.6	5.9	9.1	5.1	130
	s.e.	0.8	0.003	0.004	1.6	0.7	0.8	0.5	0.6	0.5	0.8	0.4	
1998	$\overline{x}$	128.1	0.084	0.947	32.9	153.1	308.1	38.8	34.2	38.4	346.0	-16.0	
	s.d.	7.0	0.028	0.035	17.1	6.2	7.0	4.5	4.8	4.8	7.8	4.1	392
	s.e.	0.4	0.001	0.002	0.9	0.3	0.4	0.2	0.2	0.2	0.4	0.2	

Table H.4: Mean orbital elements of the Southern δ Aquarids from 1995–1998.

November Sextantids

This retrograde November stream does not appear in any catalogues. It is very well defined with AMOR recording its appearance for the past four years. The rate curves for each year match well as is hoped for in the case of well established coherent streams.

The radiant at the maximum is near Sextantis Σ1441 about 20° south of Regulus. Following the suggested naming procedure (Baggaley 1999) the designation is 237.6,157.3,-7.6,50.3,ZHR.[2]

[2]ZHR is the equivalent zenithal hourly rate as often used by visual observers.

This stream represents one of a list of possible new streams which are currently being further analysed to determine previously unknown stream presence in the Solar System dust population.

The next step in the exploration of such a stream is a check to see if it was detected in the years previous to 1995. After this step the probability of detection of the grouping is measured. A distinct group with a low probability of detection which is still detected distinctly is judged more significant than an equivalent with a high probability of detection.

Especially in the case of smaller clusters one hopes to find groupings which are repeated year by year. Due to their sizes these smaller groupings are often difficult to perform rigorous statistics on. This is why four separate years of data are being used in the current survey and only placed together after initial reasonably sized clusters have been found in each.

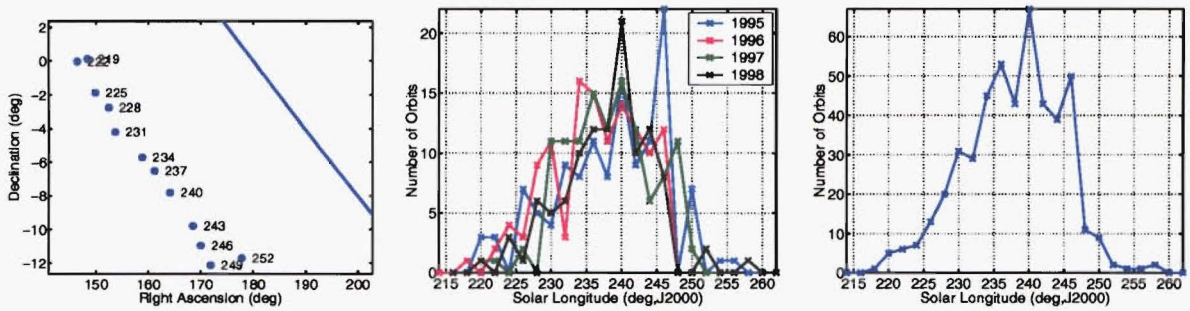

(a) Radiant shift (b) Individual rate curves (c) Combined rate curve

Figure H.5: The November Sextantids activity profiles.

YEAR		$\lambda_\odot$ deg	q AU	e	i deg	ω deg	Ω deg	V_A	V_H $\mathrm{km\,s^{-1}}$	V_G	α deg	δ deg	SIZE
1995	$\overline{x}$	237.8	0.326	0.624	143.6	217.5	57.8	52.0	27.5	52.2	161.7	-7.7	
	s.d.	8.3	0.050	0.102	10.3	15.4	8.3	3.4	4.0	3.6	9.7	3.9	94
	s.e.	0.9	0.005	0.010	1.1	1.6	0.9	0.4	0.4	0.4	1.0	0.4	
1996	$\overline{x}$	236.2	0.290	0.622	139.5	205.7	56.2	49.5	24.8	49.6	156.6	-7.2	
	s.d.	6.5	0.076	0.104	7.3	17.8	6.5	2.6	3.9	2.8	11.8	5.4	88
	s.e.	0.7	0.008	0.011	0.8	1.9	0.7	0.3	0.4	0.3	1.3	0.6	
1997	$\overline{x}$	237.7	0.330	0.550	136.7	201.1	57.7	49.0	24.2	49.1	154.7	-8.2	
	s.d.	5.9	0.094	0.137	8.7	12.3	5.9	1.9	2.5	1.9	10.3	3.7	92
	s.e.	0.6	0.010	0.014	0.9	1.3	0.6	0.2	0.3	0.2	1.1	0.4	
1998	$\overline{x}$	238.5	0.297	0.618	142.7	208.4	58.5	50.1	25.3	50.3	160.2	-7.3	
	s.d.	5.9	0.075	0.115	12.1	13.7	5.9	3.2	3.6	3.3	10.5	3.7	85
	s.e.	0.6	0.008	0.012	1.3	1.5	0.6	0.3	0.4	0.4	1.1	0.4	
ALL	$\overline{x}$	237.6	0.312	0.603	140.6	208.2	57.6	50.2	25.4	50.3	158.3	-7.6	
	s.d.	6.8	0.077	0.119	10.1	16.1	6.8	3.1	3.8	3.2	11.0	4.2	359
	s.e.	0.4	0.004	0.006	0.5	0.9	0.4	0.2	0.2	0.2	0.6	0.2	

Table H.5: The mean orbital elements of the November Sextantids from 1995–1998.

References

Almond, M.: 1951, The summer daytime meteor streams of 1949 and 1950 III. Computation of the orbits", *MNRAS* **111**, 37+.

Andrianov, N. S., Kurganov, R. A., Nasirov, A. M. and Sidorov, V. V.: 1968, Oblique-scattering method for measuring individual radiants and meteor velocities, *IAU Symp. 33: Physics and Dynamics of Meteors*, Vol. 33, pp. 14+.

Andrianov, N. S., Pupysev, U. A. and Sidorov, V. V.: 1970, The distribution of orbit parameters and the changes in incident meteor particle flux density, *MNRAS* **148**, 227+.

Arlt, R., Rendtel, J., Brown, P., Velkov, V., Hocking, W. K. and Jones, J.: 1999, The 1998 outburst and history of the June Bootid meteor shower, *MNRAS* **308**, 887–896.

Babadzhanov, P. B. and Obrubov, Y. V.: 1992a, Evolution of short-period meteoroid streams, *Celestial Mechanics and Dynamical Astronomy* **54**, 111–127.

Babadzhanov, P. B. and Obrubov, Y. V.: 1992b, P/Machholz 1986 VIII and Quadrantid meteoroid stream. Orbital evolution and relationship, *Asteroids, Comets, Meteors*, pp. 27–32.

Baggaley, W. J.: 1995, Radar surveys of meteoroid orbits, *Earth, Moon and Planets* **68**, 127–139.

Baggaley, W. J.: 1999, An improved meteor stream nomenclature. Presented as Poster ACM20-16P at Asteroids, Comets and Meteors '99, Cornell University, Ithaca, USA.

Baggaley, W. J. and Bennett, R. G. T.: 1996, The meteor orbit radar facility AMOR: Recent developments, *Physics, Chemistry and Dynamics of Interplanetary Dust*, Vol. 104, pp. 65–70.

Baggaley, W. J., Bennett, R. G. T., Steel, D. I. and Taylor, A. D.: 1994, The Advanced Meteor Orbit Radar Facility: AMOR, *Q. J. R. Astr. Soc.* **35**, 293–320.

Baggaley, W. J. and Galligan, D. P.: 1997, Cluster analysis of the meteoroid orbit population, *Planet. Space Sci.* **45**(7), 865–868.

Bendjoya, P.: 1993, A classification of 6,479 asteroids into families by means of the wavelet clustering method, *Astron. Astrophys. Supp.* **102**, 25+.

Bronshten, V. A.: 1983, *Physics of Meteoroid Phenomena*, D. Reidel Publishing Company, Dordrecht, Holland.

Ceplecha, Z. K., Borovička, J. I., Elford, W. G., Revelle, D. O., Hawkes, R. L., Porubčan, V. and Šimek, M.: 1998, Meteor phenomena and bodies, *Space Science Reviews* **84**, 327–471.

Cook, A. F.: 1973, A working list of meteor streams, *IAU Colloq. 13: Evolutionary and Physical Properties of Meteoroids*, pp. 183+.

Cook, A. F., Flannery, M. R., Levy II, H., McCrosky, R. E., Sekanina, Z., Shao, C., Southworth, R. B. and Williams, J. T.: 1972, *Meteor Research Program*, NASA CR-2109, Smithsonian Astrophysical Observatory, Washington DC.

Damiani, F., Maggio, A., Micela, G. and Sciortino, S.: 1996, A source detection method for ROSAT/PSPC X-ray images based on wavelet transforms, *ASP Conf. Ser. 101: Astronomical Data Analysis Software and Systems V*, Vol. 5, pp. 143+.

Davies, J. G. and Gill, J. C.: 1960, Radio echo measurements of the orbits of faint sporadic meteors, *MNRAS* **121**, 437–462.

Drummond, J. D.: 1979, On the meteor/comet orbital discriminant D, *Proc. Southwest Reg. Conf. Astron. Astrophys.*, Vol. 5, pp. 83–86.

Drummond, J. D.: 1981, A test of comet and meteor shower associations, *Icarus* **45**, 545–553.

Eastwood, E. and Mercer, K. A.: 1948, A study of transient radar echoes from the ionosphere, *Proc. Phys. Soc.* **61**, 122–134.

Edsall, C. J.: 1996, *Meteor decay constant and echo elevation data for atmospheric parameters*, Master's thesis, University of Canterbury.

Fedynski, V. V.: 1975, *Meteor orbits and rates from Equatorial survey*, Vol. 1 of *Materials of the World Data Center B*, Soviet Geophysical Committee of the Academy of Sciences of the U.S.S.R., Moscow.

Fedynski, V. V.: 1977, *Meteor orbits and rates from Equatorial survey*, Vol. 2 of *Materials of the World Data Center B*, Soviet Geophysical Committee of the Academy of Sciences of the U.S.S.R., Moscow.

Fisher, N. I.: 1993, *Statistical analysis of circular data*, Cambridge University Press.

Freeman, P. E., Kashyap, V., Rosner, R., Nichol, R., Holden, B. and Lamb, D. Q.: 1996, X-ray source detection using the wavelet transform, *ASP Conf. Ser. 101: Astronomical Data Analysis Software and Systems V*, Vol. 5, pp. 163+.

Galligan, D. P. and Baggaley, W. J.: 1998, Methods of cluster analysis of radar meteoroid orbits, *in* V. Porubčan and L. Neslusan (eds), *Meteoroids 98*, Comenius University Press, Slovakia.

Gartrell, G. and Elford, W. G.: 1975, Southern hemisphere meteor stream determinations, *Aust. J. Phys.* **28**, 591–620.

Gustafson, B. S. and Adolfsson, L. G.: 1996, Radiation pressure correction to meteor orbits, *Earth Moon and Planets* **72**, 327–332.

Hawkes, R. L.: 1993, Television meteors, *in* J. Štohl and I. P. Williams (eds), *Meteoroids and their parent bodies*, Astronomical Inst. Slovak Academy of Sciences, Bratislava, pp. 227–234.

Hawkes, R. L., Jones, J. and Ceplecha, Z.: 1984, The populations and orbits of double-station TV meteors, *Bull. Astron. Inst. Czechosl.* **35**, 46–64.

Hawkins, G. S.: 1956, A radio echo survey of sporadic meteor radiants, *MNRAS* **116**(1), 92–113.

Hey, J. S. and Stewart, G. S.: 1947, Radar observations of meteors, *Proc. Phys. Soc.* **59**, 858–883.

Hughes, D. W.: 1978, Meteors, *in* J. A. M. McDonnell (ed.), *Cosmic Dust*, John Wiley & Sons, p. 156.

Hughes, D. W.: 1993, Meteoroids - an overview, *in* J. Štohl and I. P. Williams (eds), *Meteoroids and their parent bodies*, Astronomical Inst. Slovak Academy of Sciences, Bratislava, pp. 15–28.

Jenniskens, P.: 1994, Meteor stream activity I. The annual streams, *Astron. Astrophys.* **287**, 990–1013.

Jones, J. and Brown, P.: 1993, Sporadic meteor radiant distributions - orbital survey results, *MNRAS* **265**, 524.

Jones, J. and Sarma, T.: 1979, Television observations of Perseid meteors, *MNRAS* **189**, 225–232.

Jopek, T. J.: 1993a, Remarks on the meteor orbital similarity D-criterion, *Icarus* **106**, 603–607.

Jopek, T. J.: 1993b, TV meteor streams searching, *in* J. Stohl and I. P. Williams (eds), *Meteoroids and their parent bodies*, Astronomical Inst. Slovak Academy of Sciences, Bratislava, pp. 269–272.

Jopek, T. J. and Froeschlé, C.: 1997, A stream search among 502 TV meteor orbits. An objective approach., *Astron. Astrophys.* **320**, 631–641.

Jopek, T. J., Valsecchi, G. B. and Froeschlé, C.: 1998, Meteor stream identification: a new approach. Application to 3,675 radio meteors, *in* W. J. Baggaley and V. Porubčan (eds), *Meteoroids 1998*, Astronomical Institute of the Slovak Academy of Sciences, Bratislava, pp. 307–310.

Jopek, T. J., Valsecchi, G. B. and Froeschle, C.: 1999, Meteoroid stream identification: a new approach - II. Application to 865 photographic meteor orbits, *MNRAS* **304**, 751–758.

Kashcheev, B. L. and Lebedinets, V. N.: 1967, Radar studies of meteors, *in* G. S. Hawkins (ed.), *Smithson. Contrib. Astrophys.*, Vol. 11, pp. 183–199.

Kashcheev, B. L. and Tkachuk, A. A.: 1980, *Rezul'taty radiolokatsionnykh nabliudenii slabykh meteorov : Katalog orbit meteorov do +12m*, Moskva : [s.n.], 1980.

Kashcheev, B. L. and Voloshchuk, Y.: 1992. Private communication to W. J. Baggaley.

Kresak, L.: 1967, Relation of meteor orbits to the orbits of comets and asteroids, *in* G. S. Hawkins (ed.), *Smithson. Contrib. Astrophys.*, Vol. 11, pp. 9–34.

Kronk, G.: 1988, *Meteor Showers: A Descriptive Catalog*, Enslow Astronomy Series, Enslow. Updated version now available at internet address http://comets.amsmeteors.org.

Lebedinets, V. N.: 1968, *in* L. Kresak and P. M. Millman (eds), *IAU Symposium 33: Physics and Dynamics of Meteors*, Reidel, Dordrecht, The Netherlands, pp. 241–264.

Lebedinets, V. N., Korpusov, V. N. and Manokhina, A. V.: 1981, *Radiolokatsionnye issledovaniia meteorov V Obninske : katalog orbit, sentiabr'-dekabr' 1967*, Moskva : Mezhduvedomstvennyi geofizicheskii kom-t pri Prezidiume AN SSSR, 1981.

Lebedinets, V. N., Korpusov, V. N. and Manokhina, A. V.: 1982, *Radiolokatsionnye issledovaniia meteorov V Obninske : katalog orbit, ianvar'-avgust 1968*, Moskva : Mezhduvedomstvennyi geofizicheskii kom-t pri Prezidiume AN SSSR, 1982.

Lindblad, B. A.: 1971a, A stream search among 865 precise photographic meteor orbits, *Smithson. Contrib. Astrophys.* **12**, 1–13.

Lindblad, B. A.: 1971b, A computerized stream search among 2,401 photographic meteor orbits, *Smithson. Contrib. Astrophys.* **12**, 14–24.

Lindblad, B. A.: 1989, The orbit of the Eta Aquarid meteor stream, *in* C.-I. Larerkvist, P. Magnusson and H. Rickmann (eds), *Third International Symposium on Asteroids, Comets, Meteors.*, Uppsala,Sweden.

Lindblad, B. A., Ohtsuka, K. and Shirakawa, K.: 1994, The orbit of the Eta Aquarid meteor stream, *Planet. Space Sci.* **42**, 113–116.

Lovell, A. C. B.: 1954, *Meteor Astronomy*, The international series of monographs on physics, Oxford University Press.

Marsh, S. H.: 1996, *A Winds Doppler Facility for* AMOR, Master's thesis, Dept. of Physics and Astronomy, University of Canterbury, Christchurch, New Zealand.

Marsh, S. H., Bennett, R. G. T., Baggaley, W. J., Fraser, G. J. and Plank, G. E.: 2000, Measuring meridional mesospheric winds with the AMOR meteor radar, *JASTP* . In Press.

McCrosky, R. E. and Posen, A.: 1961, Orbital elements of photographic meteors, *Smithson. Contrib. Astrophys.* **4**.

McKinley, D. W. R.: 1954, Radio determination of the velocity and radiant of the Delta Aquarid meteors, *Ap. J.* **119**, 519+.

McKinley, D. W. R.: 1961, *Meteor Science and Engineering*, McGraw-Hill.

McKinley, D. W. R. and Millman, P. M.: 1949, Determination of the elements of meteor paths from radar observations, *Canadian J. Res.* **A27**, 53–67.

Nilsson, C. S.: 1963, *Observatory* **83**, 934.

Nilsson, C. S.: 1964, Southern hemisphere survey of meteors, *Aust. J. Phys.* **17**, 205–256.

Ohtsuka, K., Shimoda, C., Yoshikawa, M. and Watanabe, J.-I.: 1997, Activity profile of the Sextantid meteor shower, *Earth Moon and Planets* **77**, 83–91.

Öpik, E. J.: 1951, Collision probabilities with the planets and the distribution of interplanetary matter, *Proc. Roy. Irish Acad.*, Vol. 54 of *A*, pp. 165–199.

Poole, L. M. G.: 1997, The structure and variability of the helion and antihelion sporadic meteor sources, *MNRAS* **290**, 245–259.

Porubčan, V., Hajduk, A., Cevolani, G. and Trivellone, G.: 1996, Lyrid meteor shower observed by a forward scatter meteor radar, *Contributions of the Astronomical Observatory Skalnate Pleso* **26**, 5–9.

Rendtel, J., Arlt, R. and McBeath, A. (eds): 1995, *Handbook for Visual Meteor Observers*, International Meteor Organisation. The information used in this thesis is actually from the 2000 meteor calendar published on the Internet by the International Meteor Organisation at: http://www.imo.net/calendar/cal00.html. Most of the information in this calendar is based on the 1995 handbook.

Sarma, T. and Jones, J.: 1980, Television observations of the Delta-Aquarid shower, *IAU Symp. 90: Solid Particles in the Solar System*, Vol. 90, pp. 167–169.

Sarma, T. and Jones, J.: 1985, Double-station observations of 454 TV meteors, *Bull. Astron. Inst. Czechosl.* **36**, 9–24.

Sekanina, Z.: 1970a, Statistical model of meteor steams I. Analysis of the model, *Icarus* **13**, 459–474.

Sekanina, Z.: 1970b, Statistical model of meteor steams II. Major showers, *Icarus* **13**, 475–493.

Sekanina, Z.: 1973, Statistical model of meteor steams III. Stream search among 19,303 radio meteors, *Icarus* **18**, 253–284.

Sekanina, Z.: 1976, Statistical model of meteor steams IV. A study of radio streams from the Synoptic year, *Icarus* **27**, 265–321.

Skuljan, J.: 2000, *A study of moving groups of stars in our galaxy*, PhD thesis, University of Canterbury.

Slezak, E., Durret, F. and Gerbal, D.: 1994, A wavelet analysis search for substructures in eleven X-ray clusters of galaxies, *Astron. J.* **108**(6).

Southworth, R. B. and Hawkins, G. S.: 1963, Statistics of meteor streams, *Smithson. Contrib. Astrophys.* **7**, 261–285.

Steel, D.: 1996, Meteoroid orbits, *Space Sci. Rev.* **78**, 507–553.

Taylor, A. D.: 1991, *A Meteor Orbit Radar*, PhD thesis, Dept. of Physics and Astronomy, University of Canterbury, Christchurch, New Zealand.

Taylor, A. D., Baggaley, W. J., Bennett, R. G. T. and Steel, D. I.: 1994, Radar measurements of very high velocity meteors with AMOR, *Planet. Space. Sci.* **42**, 135–140.

Thomas, G. E.: 1998, *Meteoric diffusion studies of middle atmospheric dynamical structure*, Master's thesis, University of Canterbury.

Valsecchi, G. B., Jopek, T. J. and Froeschle, C.: 1999, Meteoroid stream identification: a new approach - I. Theory, *MNRAS* **304**, 743–750.

Štohl, J. and Porubčan, V.: 1993, Meteor streams of asteroidal origin, *in* J. Štohl and I. P. Williams (eds), *Meteoroids and their parent bodies*, Astronomical Inst. Slovak Academy of Sciences, Bratislava, pp. 41–48.

Weiss, A. A.: 1960, Radio-echo observations of Southern hemisphere meteor shower activity from 1956 December to 1958 August, *MNRAS* **120**(5).

Whipple, F. L.: 1950, A comet model, I: The acceleration of Comet Encke, *Ap. J.* **111**, 375–394.

Whipple, F. L.: 1954, Photographic meteor orbits and their distribution in space, *Astron. J.* **59**, 201–217.

Whipple, F. L.: 1983, 1983 TB and the Geminid meteors, *IAU Circ.* **3881**, 1+.

Zappalà, V., Bendjoya, P., Cellino, A., Farinella, P. and Froeschlé, C.: 1995, Asteroid families: Search of a 12,487-asteroid sample using two different clustering techniques, *Icarus* **116**(2), 291–314.

Zappalà, V., Cellino, A., Farinella, P. and Knĕzević, Z.: 1990, Asteroid families I. Identification by hierarchical clustering and reliability assessment, *Astron. J.* **100**(6), 2030–2046.

Zappalà, V., Cellino, A., Farinella, P. and Milani, A.: 1994, Asteroid families II. Extension to unnumbered multi-opposition asteroids, *Astron. J.* **107**(2), 772–801.